Transactions of the ASME

Technical Editor
ARTHUR J. WENNERSTROM
Senior Associate Editor
G. K. SEROVY
Associate Editors
Air Pollution Control
H. E. HESKETH
Diesel and Gas Engine Power
G. VanDeMARK
Gas Turbine
G. OPDYKE
Power
R. W. PORTER
Advanced Energy Systems
T. M. BARLOW
Fuels
H. C. ORENDER
Nuclear Engineering
J. SUSNIR

BOARD ON COMMUNICATIONS
Chairman and Vice-President
K. N. REID, JR.

Members-at-Large
W. BEGELL
W. G. GOTTENBERG
D. KOENIG
M. KUTZ
F. LANDIS
J. T. COKONIS
J. E. ORTLOFF
C. PHILLIPS
H.C. REEDER
R. E. NICKELL

President, G. KOTNICK
Executive Director,
PAUL ALLMENDINGER
Treasurer, ROBERT A. BENNETT

PUBLISHING STAFF
Mng. Dir., Publ., J. J. FREY
Dep. Mng. Dir., Pub.,
JOS. SANSONE
Managing Editor,
CORNELIA MONAHAN
Production Editor,
JACK RUMMEL
Editorial Prod. Asst.
MARISOL ANDINO

The Journal of Engineering for Gas Turbines and Power (ISSN 0022-0825) is published quarterly for $100 per year by The American Society of Mechanical Engineers, 345 East 47th Street, New York, NY 10017. Second class postage paid at New York, NY and additional mailing offices. POSTMASTER: Send address change to The Journal of Engineering for Gas Turbines and Power, c/o The AMERICAN SOCIETY OF MECHANICAL ENGINEERS, 22 Law Drive, Box 2300, Fairfield, NJ 07007-2300.

CHANGES OF ADDRESS must be received at Society headquarters seven weeks before they are to be effective. Please send old label and new address.

PRICES: To members, $24.00, annually; to nonmembers, $100.00. Add $6.00 for postage to countries outside the United States and Canada.

STATEMENT from By-Laws. The Society shall not be responsible for statements or opinions advanced in papers or ... printed in its publications (B 7.1, para. 3).

INDEXED by the Engineering Index, Inc.

Journal of Engineering for Gas Turbines and Power

Published Quarterly by The American Society of Mechanical Engineers

Volume 107 • Number 1 • JANUARY 1985

TECHNICAL PAPERS

(Contents Continued)

Some Practical Aspects of Staged Premixed, Low Emissions Combustion

A. Sotheran
Chief Combustion Engineer.

D. E. Pearce
Senior Combustion Engineer.

D. L. Overton
Senior Combustion Engineer.

Rolls-Royce Limited,
Bristol, England

An experimental program to research, develop, and demonstrate an axially staged, premixed low emissions combustor is described, with particular emphasis on the many mechanical and thermal problems which were encountered and which seem characteristic of the type. Of these, the risks of autoignition and flashback in the premixing duct were perhaps, the most severe. Their elimination imposed severe constraints on premixing duct geometry and indeed, dictated the layout of the whole combustor. Nevertheless, it proved possible to retain conventional technology to a large extent including the basic combustor structure and mounting arrangements and normal fuel injector accessibility. Large emissions reduction capability was demonstrated to be possible though not within conventional combustor dimensions.

1 Introduction

As public awareness and concern on environmental matters increased during the early 1970s, it was the policy of Rolls-Royce, in common with other manufacturers, to respond constructively and to undertake to reduce engine pollutant emissions to whatever levels were deemed tolerable by the national and international agencies involved (references [1 and 2]). Adverse speculation on the possible effects of high altitude NO_X emissions from Concorde (references [3 and 4]) provided further pressure and helped to dictate the technical policy which was adopted.

In discussions with the French partner SNECMA, it was decided to evaluate and develop an axially staged combustor with a fully premixed, lean burning, main stage piloted by a conventional idling stage alongside the premixing duct. Various configurations were suggested and an exploratory program was begun to investigate suitable premixing-duct geometries. Tests at full scale geometries and under realistic conditions quickly demonstrated the high risks and dangers of flashback and auto-ignition involved in premixing at high pressures and sub-stoichiometric mixture strengths. Accordingly, in 1975 Rolls-Royce launched a program to design and develop a combustor the geometry of which was wholly configured to ensure thorough but safe premixing of the main stage fuel and air. Another equally important objective was to achieve close control over the mixing of the primary and main stage gases, since this process, in quenching the primary stage but establishing the very precise conditions needed to ensure clean and complete main stage burning, would obviously have crucial influence on all the pollutant emission rates. Finally, as far as possible, it was required to retain certain conventional features. These included the very simple single-piece structure of the conventional annular vaporizer combustor together with its rear mounting arrangement. In addition, it was hoped to be able to mount all the fuel injectors, as normal, in the combustor inlet diffuser.

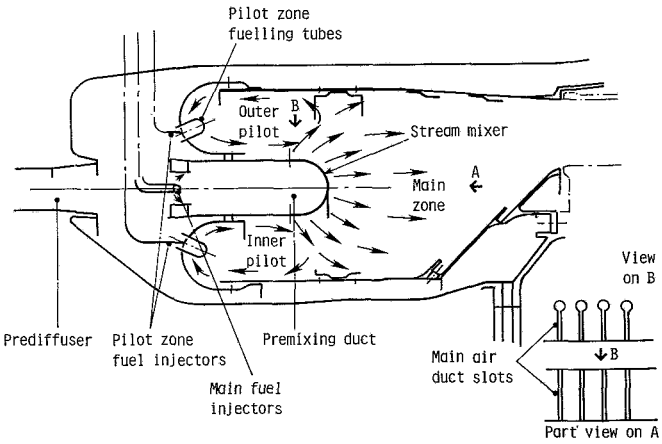

Fig. 1 Axially staged, premixed combustor

These objectives together suggested an arrangement in which a central premixing duct was flanked by the two halves of a split primary stage, as shown on Fig. 1. Once the geometry was decided, an intensive program of design and experimental work on research, scale, and full size combustors was initiated.

2 General Combustor Geometry

Early testing suggested that any flow separation or wakes in the premixing duct, or a thick boundary layer on any part of the walls or even, perhaps, severe velocity profiles could be the cause of auto-ignition in the duct or constitute a route for flashback from the downstream combustion zone. Since the

Contributed by the Gas Turbine Division of THE AMERICAN SOCIETY OF MECHANICAL ENGINEERS and presented at the 29th International Gas Turbine Conference and Exhibit, Amsterdam, The Netherlands, June 4-7, 1984. Manuscript received at ASME Headquarters, January 6, 1984. Paper No. 84-GT-88.

risk of either of these catastrophes could obviously not be tolerated in any practicable combustor, it was clear that the premixing duct geometry and, if necessary, the whole combustor layout, would have to be configured to eliminate all their known causes. To this end it was eventually decided that several severe constraints would have to be imposed on the premixing duct geometry. In order of importance, these were that it must be straight, aligned with the compressor efflux, terminated by a high-blockage device which would act as a flame trap and tapered or stepped down from a well-flared intake towards the flame trap. These arrangements (Fig. 1) were intended not only to eliminate all flow separation or low velocity regions, where fuel might linger and become subject to auto-ignition, but, more positively, to insure uniform velocities and constant fuel residence times so that substantially all the fuel would be equally well prepared in the available time. The final high-blockage was intended to suppress any boundary layers or wakes which, despite all the precautions, had grown or persisted to the end of the duct, since these could otherwise be a route along which the flames could flashback into the premixing duct.

The central location of the premixing duct obviously necessitated a split primary burning stage with its two halves disposed either side of the duct. This called for an extra fuel injection system and introduced a possible problem, which in fact never materialized, of igniting the inner stage.

However, to offset these problems, the layout offered several advantages apart from safe premixing. The flame trap device at the end of the premixing duct could obviously also act as the primary/main stream mixer, and was very well located to perform this task in which it was assisted by the symmetrical geometry. In addition, the premixing duct was very easily fuelled from injectors which could be conventionally mounted from the inlet diffuser casing, and conventional combustor structure and mounting were retained.

3 Combustor Details

The combustor was a single-piece structure mounted from its rear end in common with the annular vaporizer combustor which it was intended to replace [5].

The primary stage aerodynamics were adopted from the "reverse flow" combustors of small helicopter engines and comprised (Fig. 1) a single recirculation driven by the wall cooling films and by a main air supply provided from the inner wall of the stage. The primary admission ports were, in fact, enlargements at either end of the radial slots through which the bulk of the air was supplied to the main burning stage.

In the initial design, the stream mixer at the end of the premixing duct was a simple half-toroid perforated with the radial slots mentioned in the last paragraph. The purpose of the mixer was to quench the high temperature, NO_X producing, combustion in the primary gases and also to generate the right conditions for clean, low-temperature burning in the incoming very lean, premixed main gases. To achieve the first objective the mixing obviously needed to be very thorough. In addition, to insure that all elements of the main stage gases resided long enough in the combustor to burn to completion and to do this without wasting combustor volume, it was also necessary for the stream mixer to fill the whole cross-section of the main combustor stage as quickly as possible, with a uniform gas stream progressing at uniform velocity toward the turbine. As will be seen, the simple slot mixer achieved these objectives very well but proved to be unsatisfactory for various other reasons.

Initially, conventional vaporizer fuel injection was selected for the twin primary burning stages because, for instance, this

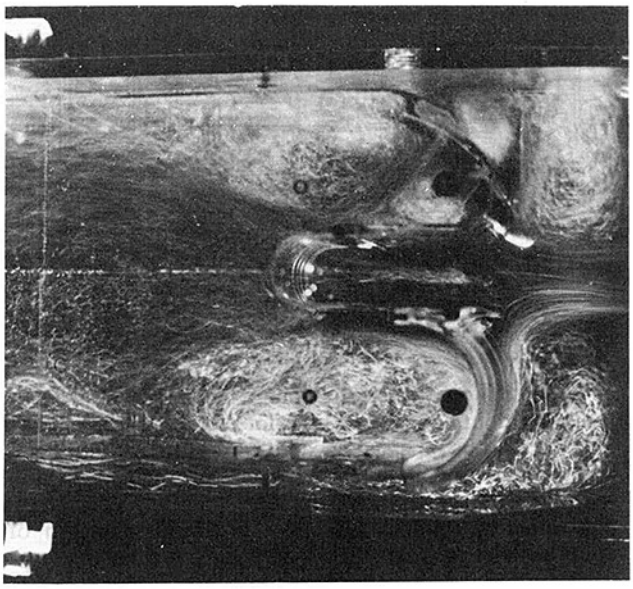

Fig. 2 Flows in staged combustor

type of fuel injection requires only a very simple fuel feed nozzle and is insensitive to the combustor head movements which result from the single-piece, rear mount design. The optimum means to admit the main stage fuel into the premixing duct was the subject of a special experimental exercise described below. Eventually a simple drilled manifold (actually in sections) and splash plate system was adopted.

It was recognized when the combustor was first proposed that it involved various risks and potential malfunctions which could necessitate appropriate design compromises. For instance, depending on how prone to premature ignition the premixing/prevaporizing system should prove to be, the fuel residence time in the duct could be reduced or increased to suit the situation. This could be done simply by adjusting the location of the fuel injection point and, if necessary, extending the premixing duct forward. The possibility was also considered of providing two fuel injection locations, one giving a short premixing length to minimize preignition risks at takeoff, the other for maximum premixing at altitude cruise when NO_X reductions are most important and the risks of auto-ignition are lower.

The degrees of quenching and mixing between the primary and main burning stages were obviously related and could not necesarily be optimized simultaneously. While rapid quenching of the primary stage would reduce NO_X emission rates at full engine power, it would tend to increase emission rates of CO and unburned hydrocarbon at engine idle by prematurely terminating the primary burning. It was intended to adjust the number and shape of mixer radial slots until a satisfactory compromise was obtained.

The success of the lean, premixed, prevaporized burner in reducing NO_X emissions depends to a large extent on the uniformity of the gases, both before and after burning, so that a uniform exit temperature pattern should be an automatic end product of a successful design. Accordingly, it was decided not to include a final "dilution" section in the initial design of the staged combustor but to pass all the air not used for wall cooling through the burning zones. This maximized the combustion space available for burning, but it also imposed severe constraints on the stoichiometries of the two burning stages. Since no variable geometry was contemplated, the only control which could be exerted on the zone mixture strengths was via the chosen air and fuel flow splits between the two stages. While it was known that the idle efficiency of the vaporizer primary stage was fairly insensitive

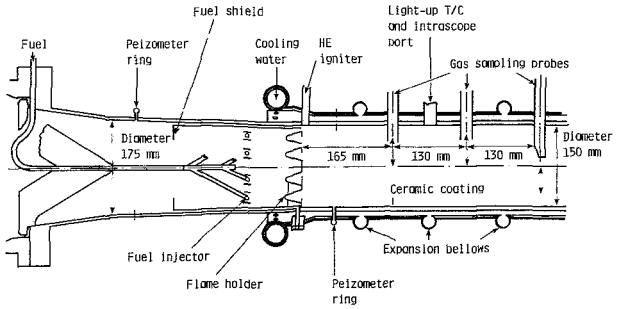

Fig. 3 Premixing research combustor

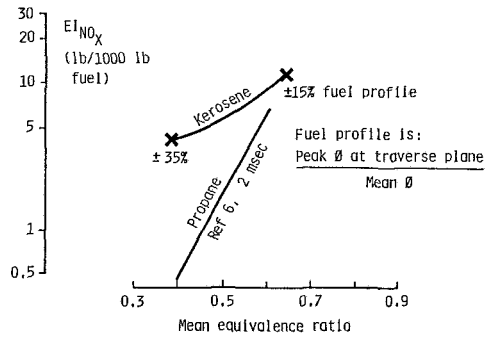

Fig. 4 Premixing rig results

to the stoichiometry of the zone when followed by a conventional dilution zone, it was not certain that this characteristic could be repeated ahead of a rapid quench system. If both primary and main burning stages proved (incompatibly) sensitive to stage mixture strengths, then it was anticipated that either a variable fuel split or the introduction of a dilution zone could provide the needed extra control.

4 Supporting Research

4.1 Aerodynamic Rigs. Various flow visualization rigs were used to help develop the geometries which were needed to generate the aerodynamics appropriate in the different zones of the combustor. The basic shapes and proportions of the combustor and, for instance, the depth of premixing duct giving the intended flow characteristics were first assessed on a water surface table model at the Royal Aircraft Establishment Pyestock. These tests also suggested appropriate locations for the primary stage cooling rings to enable the cooling films to help drive the primary stage recirculation.

Figure 2 shows the flow in a later two-dimensional model of the combustor. In this, the flow is indicated by polystyrene beads, of which there were enough to allow the velocity of the gases to be deduced from the local brightness of the picture. The light patches are low-velocity regions, while in the dark, high-velocity regions, individual beads can be detected and indicate the flow direction.

The flow is first seen exiting at the right of the picture from the combustor inlet prediffuser into the dump. The majority of the flow, about 70 percent, enters the premixing duct filling it from wall to wall. The intake flow is clean with very little spillage. The light streak at the center of the premixing duct is the wake of the fuel injector which, of course, is a potential location for auto-ignition since it could possibly entrap fuel for long periods. To help avoid this occurrence, the injector was designed to fire the fuel radially into the high-velocity gas stream on either side of the injector and on to splash rings (not shown in the picture) which are aligned with the gas stream. As the picture shows, the injector wake is re-energized well ahead of the stream mixer and so provides no opportunity for the burning to flash back from the combustion section.

The low-velocity gases of the two primary stages are easily identified as the light areas either side of the premixing duct. The upper primary stage is penetrated by a row of jets which were introduced to establish a pair of counter-rotating vortices since, without them, the flow in the rather elongated recirculation zone, illustrated by the lower primary stage, tended to be rather ill defined. As explained later, the double vortex primary stage was found to improve idle efficiency very significantly in the burning experiments.

The transition between the primary and main stage regions is, again, well defined in the photograph, and it can be seen that the main stage gases substantially and fairly quickly fill the cross-section of the combustor with rearward moving, uniform-velocity gases.

The acceptability of the flow proportions, velocity profiles, and so on was further confirmed on appropriate airflow rigs. An undesirable consequence of the central premixing duct, especially in combination with a dilutionless combustor configuration, is that the only air ducted to either side of the combustor is the liner cooling air and this is naturally taken from the low-energy gases at either side of the compressor exit radial velocity profile. As a result, the chosen pressure loss of the combustor may need to be higher than would otherwise be necessary to provide an adequate air supply to the wall cooling devices. This feature is shared by all lean burning combustors to some extent but was worsened, in the present case, by the tendency of the main stage gases, when concentrated at the stream mixer exit, to lower the local pressure level. This effect significantly enhanced the gas flow rate through the mixer at the expense of the remaining combustor features and, until it had been identified and allowed for, caused substantial deviations from the intended flow distribution.

4.2 Premixing Research. Development of the combustor was continuously dogged by auto-ignition and flashback failures and a separate rig was manufactured and tested to define the design rules for the premixing duct of the real combustor (Fig. 3). These rules required a clean intake to the premixing section and smooth wall tapering to a high-blockage duct end, in this case comprising an array of small, afterburner-style flameholders to stabilize the downstream burning process. A fuel shield was also provided to insure that the boundary layer of the burning section was not fuelled, at least initially, and to eliminate one cause of flashback into the premixing section. The progress of the burning and the local emission concentrations could be measured at various stations in the burner section, and the fuel injection system could be moved axially to vary the fuel residence time in the premixing duct. The fuel injection was a system of manifolds and splash plates which had been developed to establish a reasonably uniform fuel distribution within a very short length.

Since, unlike in the engine combustor, the premixing and burner section flow areas were approximately the same, it was not possible to simulate engine velocities in both sections simultaneously. The rig was therefore tested at engine premixing duct velocities – the Mach number was about 0.1 – and it was intended to compensate for the excessive burner section velocities by appropriate choice of burning length and residence time.

While the arrangements eliminated auto-ignition problems in the premixing duct very successfully, the flameholders proved subject to overheat and burn-out problems which, as might be expected, were later experienced by the stream mixer of the demonstrator combustor. A further serious problem of obvious relevance to the real combustor was that, at engine-practical premixing lengths and times, significant proportions

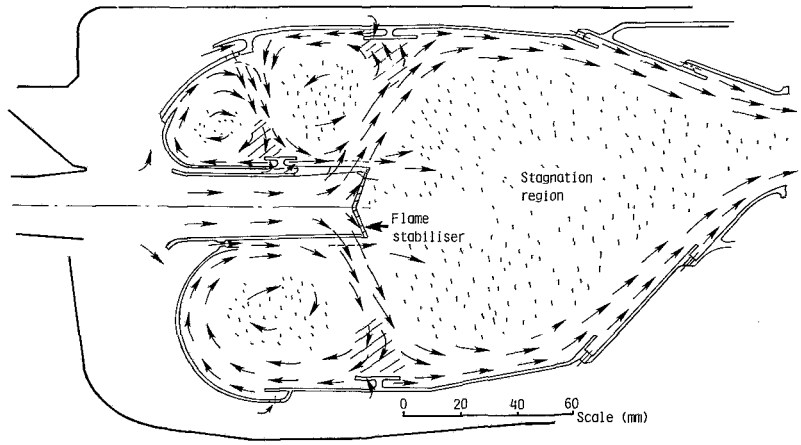

Fig. 5 Flow with bluff body stabilizer

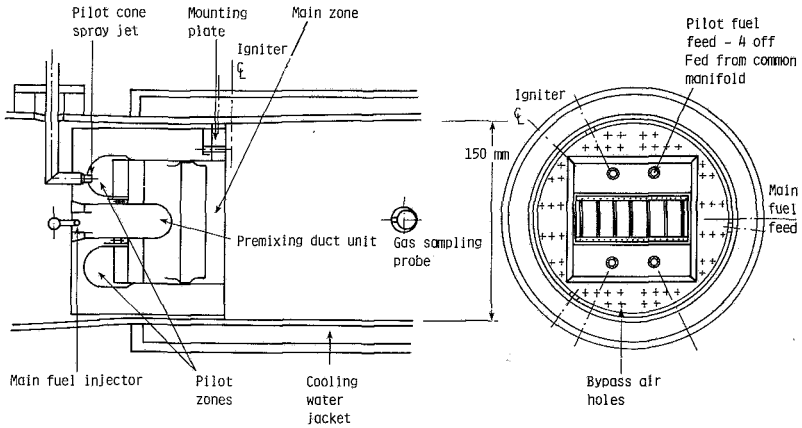

Fig. 6 Premixing duct integrity rig

of the fuel remained unevaporated, became "collected" by the flameholders, and were shed off from the corners between the annular and radial gutters in significant concentrations. This applied particularly at low equivalence ratios with deleterious effects on both burning efficiency and NO_X emissions. Figure 4 shows typical NO_X emission concentrations measured 0.4 m from the flameholders equivalent to a burning time of approximately 3 ms. The results are corrected from the actual test conditions (1 MPa, 725K) to those used by Anderson [6] in his premixed propane burner. While the kerosene NO_X rates were similar to the propane results at 0.65 equivalence ratio, at weaker conditions, where it was intended to operate the demonstrator combustor, the propane emission rates were very much exceeded. This is probably explained by the poor fuel distribution patterns which were still evident at the sampling station as indicated on the figure.

Burning efficiencies, on the other hand, were so low, at about 90 percent, as to question the whole credibility of a premixed kerosene burner as a low emissions device suitable for application as a preturbine combustor. Fortunately another experiment, with two stage burning, had already given encouraging results from which it was presumed that the unpiloted, premixed burner experiment had little relevance to the staged engine combustor.

4.3 Stream Mixer Geometry. The stream mixer was required to accomplish a number of objectives which were each crucial to the satisfactory operation of the combustor. As listed earlier, these were to provide a flame trap between the premixing duct and the burning stages, to mix the primary and main gases, to terminate the high NO_X production rate primary stage burning and to initiate and pilot the main burning. It was also used to feed and to help drive the primary stage gas recirculations. However, the proper role of the mixer was not fully appreciated at the outset of the program and it was originally intended to end the premixing duct with the kind of bluff body flame stabilizer which had been used in various earlier fundamental investigations of unpiloted premixed combustion. Various deficiencies of this device were quickly identified in the premixing experiments as described earlier. In addition, it failed totally to establish the uniformly mixed and uniform velocity main stage flow which was intended (Fig. 5). As a result the stabilizer was replaced by a stream mixer comprising a half-toroid end to the annular premixing duct with radial slots enlarged at their extremities to form the primary stage air ports (Fig. 1). This system provided "escape routes" into the main stage for the primary gases which had been lacking in the previous arrangement, and also established a continuous sandwich of alternately primary and main stage gases and hence quickly mixed them together. It also filled the main burner section from wall to wall and generally satisfied the stated objectives described in the previous section.

Unfortunately, although cooling films were provided on the hot side of the stream mixer walls (Fig. 1), these failed to maintain contact and hence did not provide adequate protection for the semicircular lands between the radial slots. From the severity of the failures it was clear that reliable geometries would not be easily derived and, to avoid the delays and expense of repeated trials on the full-scale combustor, the premixing research rig described in an earlier section was adapted to evaluate a number of candidate stream mixer arrangements (Fig. 6). In this rig, a rectangular sector

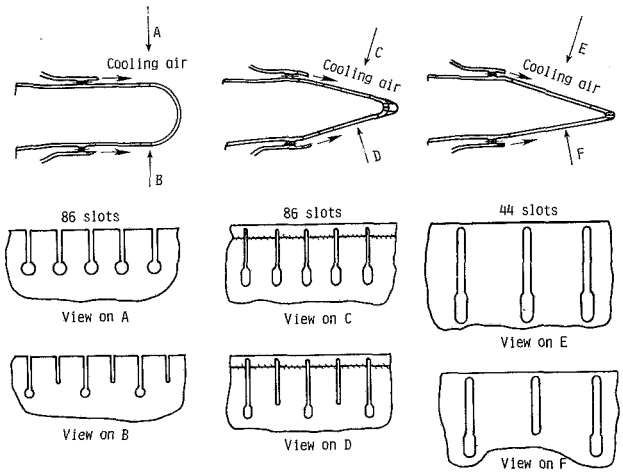

Fig. 7 Stream mixer geometries

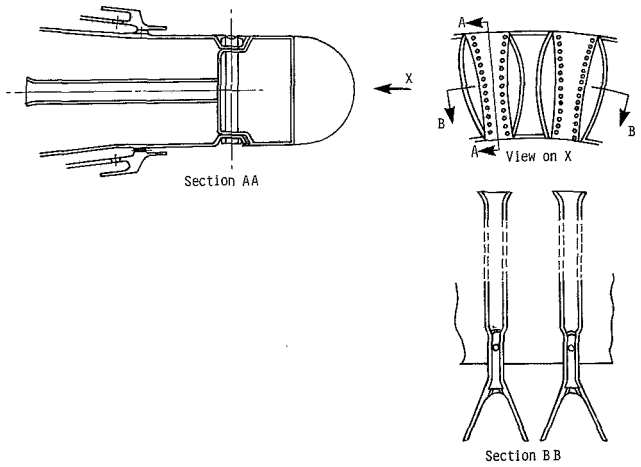

Fig. 8 Petal mixer

of the combustor primary stage was mounted in a 150 mm diameter pressure drum which allowed the stream mixer to be evaluated under severe conditions. The premixing duct of the sector combustor was arranged to be easily detached and replaced so that numbers of stream mixer geometries could be quickly compared.

Among the many geometries tested was the V-sectioned end-piece shown in Fig. 7. Since this proved to be only partly successful, a system to provide very positive cooling on the hot-side faces of the mixer hardware was devised (Fig. 8) and this proved successful up to the most severe conditions of interest at the time (1.2 MPa, 750K). Figure 8 shows how adjacent "petals" are shaped and located to define radial slots which enlarge toward their extremities. Pairs of petals are attached to an air manifold which supplies the cooling films on the hot face of each petal and which is fed in turn by a forward facing tube which extends forward to a plane upstream of the fuel injectors. In this way a clean supply of cooling air is obtained to insure that no burning will occur in the cooling films.

Obviously these very elaborate measures, though successful enough, were adopted only reluctantly and it would be hoped to replace them with a simpler arrangement. Fortunately, the petal mixer can be constructed from mechanically weak, refractory materials which eliminates the need for the cooling system.

4.4 Fuel Injection. Main fuel injection was from individually fed sections forming an annular ring located centrally in the premixing duct and firing radially inwards and outwards on to splash plates. The ring was constructed in sections to retain conventional fuel injector accessibility. The splash plates were distanced from the ring to give an even spread of fuel into the main burning zone, that is after it had passed through the stream mixer which, it was known from the earlier premixing research experiment, substantially modified the fuel distribution. The optimum location of the splash rings was determined by visual inspection of the fuel spread in cold air flow visualization tests using water injection, since the premixing experiments had shown that in the engine combustor, even at high inlet temperature conditions, significant quantities of fuel could remain in liquid form as it passed through the stream mixer.

The primary stage fuel injection was by adapted forms of the Rolls-Royce vaporizer. In the standard vaporizer the fuel and air mixture is fired upstream against the combustor head. Cooling of the head is by external impingement, by the compressor efflux gases. No internal cooling is provided in order to maintain over-rich conditions on the inside surface of

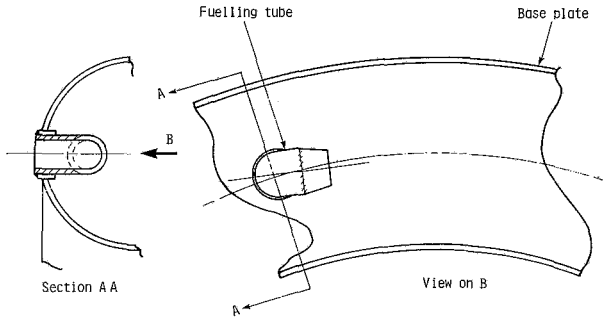

Fig. 9 Primary fuel injectors

the head and hence to avoid any substantial heat input. In the present application it was intended to use the wall cooling films to drive the primary stage flow recirculations so that upstream fuel injection would have inevitably fuelled the cooling films and introduced the risk of overheating the combustor.

To avoid these problems single bend L-shaped vaporizers firing circumferentially round the primary zone were initially adopted (Fig. 9) but these gave an unacceptably strong swirl motion to the whole primary stage flow. To prevent this a cross jet of fresh air was fired at the vaporizer efflux from the slotted end of a tube let into the combustor head. These arrangements were later integrated into a single unit as shown in Fig. 10.

4.5 Primary Stage Development. Primary stage geometry and technology was evaluated and developed in a special model combustor which was designed to be easily dismantled and rebuilt. In addition, it was small enough to be tested at severe conditions of inlet temperature and pressure reasonably economically.

The primary stage model comprised a full scale outer-half of the real combustor but rotated on a smaller mean diameter (Figs. 11 and 12). This geometry was chosen rather than a conventional sector to give a circular outer casing which could accommodate high working pressures and because it was intended to use the circumferentially firing primary stage vaporizes described in the previous section. All the features of the demonstrator combustor were incorporated as Fig. 11 shows. The figure also shows how the cooling films were directed anticlockwise to drive the primary recirculation.

The suggested improvements were first evaluated on this rig and only the most promising were transferred to the demonstrator combustor. Most of these have been described earlier but a particularly important modification, only briefly

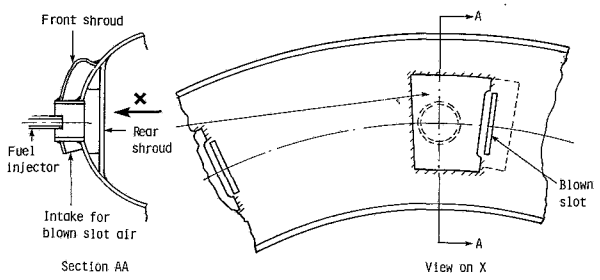

Fig. 10 Surface air blast primary fuel injection

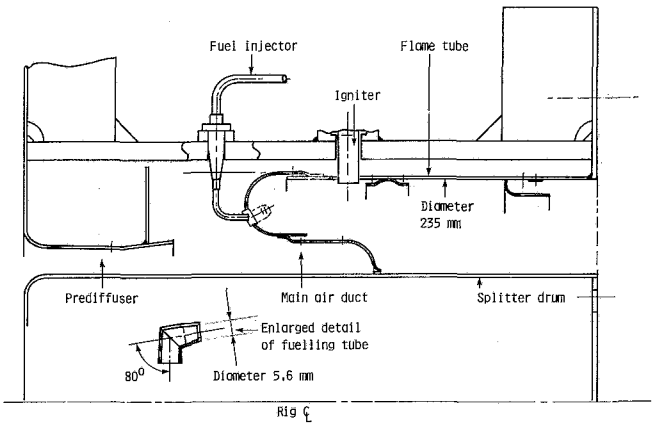

Fig. 11 Primary stage development rig

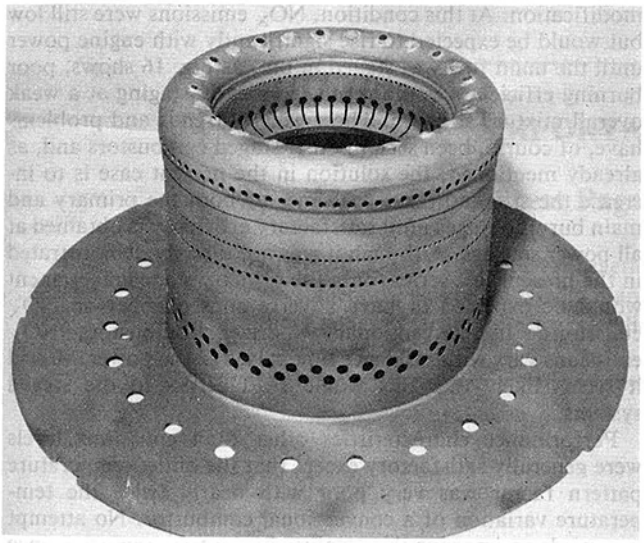

Fig. 12 Primary stage development rig

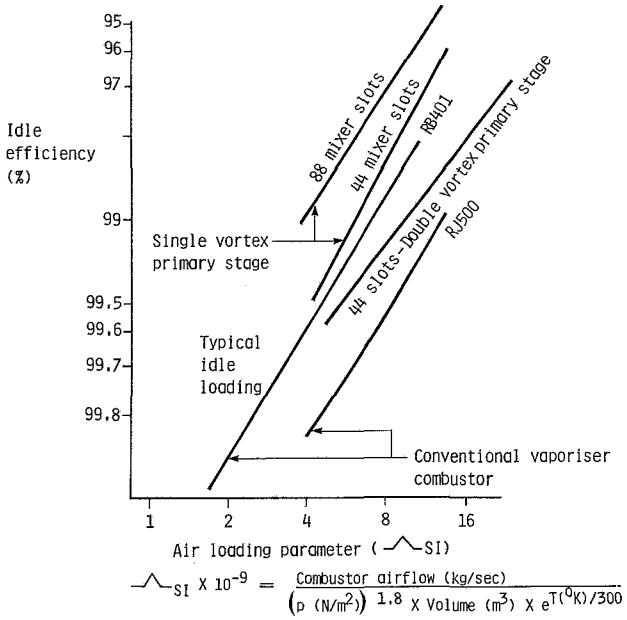

Fig. 13 Idle efficiency of staged and conventional combustors

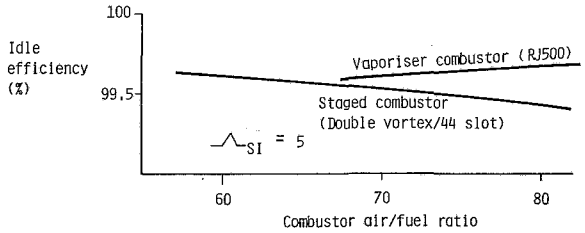

Fig. 14 Primary idle efficiency versus air/fuel ratio

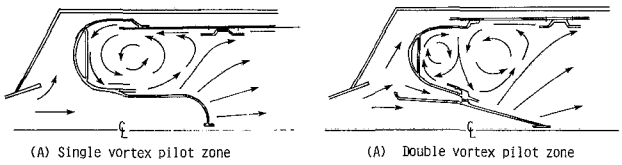

Fig. 15 Primary stage flow patterns

mentioned in an earlier section, was the change to a twin-vortex primary stage. After some development it became possible to match the idle performance of the conventional vaporizer combustor, as proved later on the demonstrator combustor, (Figs. 13 and 14), and to obtain high efficiency and little sensitivity to zone stoichiometry over a wide range of conditions. However, the split geometry of the low emissions combustor primary stage meant that each half was much longer than it was deep. Attempts to fill these rectangular sections with a single recirculation failed and to remedy this situation the double vortex primary stage was adopted. In this, a row of air jets was introduced to divide two counter-rotating recirculations and to feed both of them with a portion of their air supply (Fig. 15).

Figure 13 shows idle efficiency conventionally plotted against an "air loading parameter" which depends on the compressor exit gas conditions at idle and the combustor volume. The figure shows efficiency for a number of staged combustor geometries compared with those of good conventional combustors. An important feature of the conventional combustor is a device which removes fuel from the combustor walls before it can become entrapped in the cooling films and carried from one to the next and so on to combustor exit without ever burning. The directions of the staged combustor primary recirculations, exhausting into the combustor mid-region rather than into the wall cooling films, was chosen to provide a similar effect. Figures 13 and 14 show that, with the various measures adopted, the best of the staged combustors closely matched conventional combustor performance and that, like the conventional combustor, it displayed the relative insensitivity to primary stage or overall stoichiometry which seems to be a feature of very high efficiency combustors.

The primary stage rig proved to be a reliable indicator of the performance and mechanical characteristics of the demonstrator combustor except in one important aspect. When the demonstrator combustor was idled on one primary stage only, a portion of fuel which was still incompletely burnt on reaching the stream mixer section migrated into the

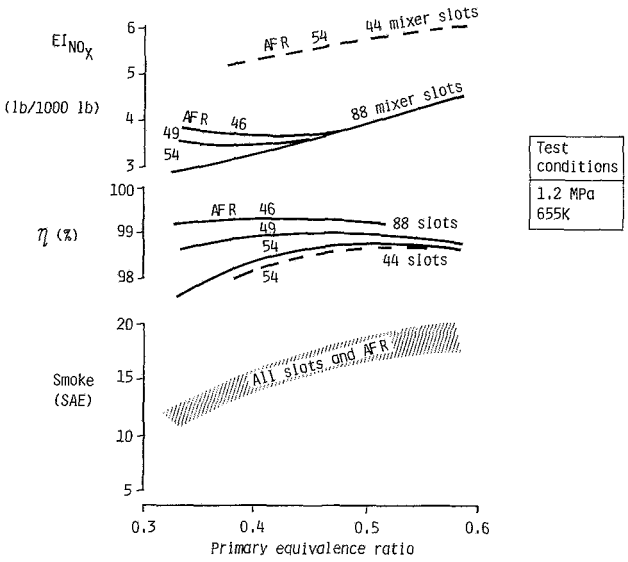

Fig. 16 Full power emissions

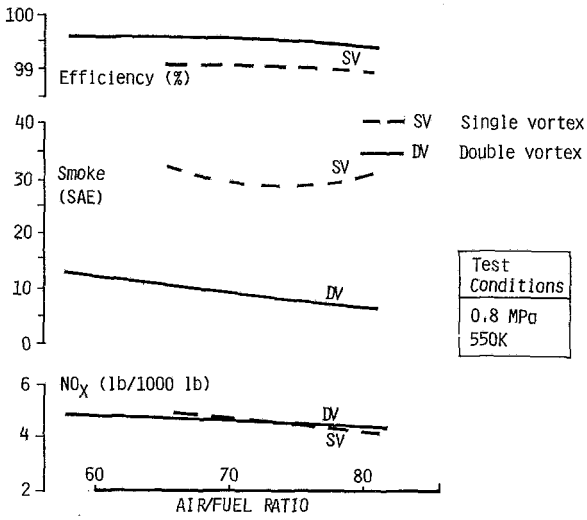

Fig. 17 Intermediate power emissions

unfuelled, nonoperating half of the combustor, and was consequently chilled and never finished burning. As a result, efficiency was lower than indicated by the primary stage rig and an early intention to operate at low engine speeds on one primary stage only was consequently abandoned.

5 Demonstrator Combustor

Most of the mechanical problems and performance characteristics of the combustor were first encountered in the earlier supporting experiments and have already been mentioned. By the time the demonstrator combustor was tested, various deficiencies had already been identified. To begin with and, most importantly, because the combustor was designed to fit the casing of an existing combustor and retained its main dimensions, it transpired to be too small in both its primary and main burning stages. For instance the presence of the central premixing duct represented a substantial loss of primary stage burning volume which was not compensated by any improvement in the "air loading" performance beyond that of a good conventional combustor. While this loss could be made good to some extent by reducing the airflow into the primary stage (without incurring the adverse effects on full power smoke which the conventional, unstaged combustor would inevitably suffer), there was no opportunity to make good the inadequate main stage residence time and consequent poor efficiency at high power, since this would have involved lengthening the combustor. In subsequent designs of conventional and staged combustors for a 25:1 pressure ratio, civil engine, the first designed to achieve all but the NO_X (EPA) emissions regulations and the second using staged system characteristics measured in the present and related programes, the staged system required 20 percent additional length relative to the conventional combustor.

Figures 13, 14, and 16 give a selection of results from the demonstrator combustor obtained by gas sampling traverses at combustor outlet. Figure 16 shows satisfactory full power NO_X and smoke emissions and their dependence on the primary equivalence ratio. NO_X emission levels were less than half those from the conventional combustor and were influenced by the overall equivalence ratio but only at low values of primary equivalence ratio. Full power efficiency was strongly dependent on main stage equivalence ratio and, even at its best, was still unsatisfactorily low.

The figures show that by reducing the number of mixer slots, and hence the rapidity at which the primary stage was quenched, the idle efficiency was improved (Fig. 13) at the expense of full power NO_X emissions and efficiency (Fig. 16).

Figure 17 gives intermediate power emissions with primary fuel only and shows how the double vortex primary stage improved smoke emissions very considerably at this condition. There was also some improvement in efficiency while NO_X emissions were not affected, presumably because the mean primary residence times were not changed by this modification. At this condition, NO_X emissions were still low but would be expected to rise significantly with engine power until the main fuel was staged in but, as Fig. 16 shows, poor burning efficiency would result from early staging at a weak overall mixture strength. These general trends and problems have, of course, been seen in other staged combustors and, as already mentioned, the solution in the present case is to increase the size and residence times of both the primary and main burning stages until satisfactory efficiency is obtained at all power settings. Although it was not directly demonstrated in the present test series, only the primary stage enlargement would be expected to have adverse consequences on NO_X emissions. In conventional vaporizer combustors NO_X emissions vary with residence time raised to the power 0.6 and it seems likely that this would read across to the staged systems.

Performance characteristics other than emissions levels were generally satisfactory except that the outlet temperature pattern factor was very poor with nearly twice the temperature variation of a conventional combustor. No attempt was made to improve these values in the tests reported since these were concentrated mainly on emission rates. The addition of a dilution section to the combustor to control pattern factors would lengthen the combustor and could spoil emissions performance, so that it seems that improved control over fuel and air movements throughout the combustor would be needed to improve these values.

6 Conclusions

In view of the geometrical restrictions on the demonstrator combustor design, the performance achieved was fairly promising and the supporting rigs suggested that, with suitable enlargements to both primary and main stages, good emissions performance could be achieved, by an axially staged, premixed combustor. The combustor also demonstrated that although staging and premixing introduced very severe mechanical and thermal problems, these can be accommodated without major changes to conventional

structural or mounting arrangements. Part load emissions and control over the outlet temperature pattern factors remain the most important problems.

References

1 Environmental Protection Agency, "Control of Air Pollution from Aircraft and Aircraft Engines, Proposed Standards," *Federal Register*, Vol. 37, 1972, pp. 26487–26300.

2 International Civil Aviation Organisation, "Control of Aircraft Engine Emissions," Circular 134-AN/94, 1977.

3 Broderick, A. J., and Hard, T. M. (eds.), *Proceedings of the Third Conference on the Climatic Impact Assessment Program*, Feb. 26–Mar. 1, 1974, DOT-TSC-OST-74-15, Nov. 1974.

4 Meteorological Office, "The Report of the Committee on Meteorological Effects of Stratospheric Aircraft (COMESA)," 1972–1975, Parts 1 and 2, 1975.

5 Sotheran, A., "The Rolls-Royce Annular Vaporiser Combustor," ASME Paper 83-GT-49, Mar. 1983.

6 Anderson, D., "Effects of Equivalence Ratio and Dwell Time on Exhaust Emission from an Experimental Premixing, Prevaporising Burner," ASME Paper 75-GT-69, Mar. 1975.

J. Odgers

D. Kretschmer

J. Halpin

Universite Laval,
Quebec, Quebec, Canada G1K 7P4

Weak Limits of Premixed Gases

Experimental values of weak and rich limits, for a wide range of fuel-oxygen-inerts mixtures (H_2, CO, CH_4, C_3H_8, O_2, Ar, He, N_2, CO_2), are presented for a number of tube diameters. The significance of the results is discussed, and with the use of other published data, a weak limit correlation is proposed that demands knowledge only of the fuel composition, its calorific value, and the specific heat of the stoichiometric products at 298 K. The correlation is applicable to simple or complex mixtures, with or without inert addition, and applies over an initial temperature range from 298–1000 K. It is also capable of application to a much wider range of fuels than those investigated experimentally. The accuracy of the parameter is as good as, or better, than those currently in use.

Introduction

Current industrial gas turbines are faced with the problem of having to burn a very wide range of fuels, both liquids and gases. The latter exhibit a large variation of calorific value, and it is usual to classify them as follows:

High BTU gases	>500 BTU/scf	(>18,6 MJ/m^3)
Medium BTU gases	300–500 BTU/scf	(11,2–18,6 MJ/m^3)
Low BTU gases	100–300 BTU/scf	(3,7–11,2 MJ/m^3)

The lowest value is generally considered to represent a reasonable limit for satisfactory combustion within a typical gas turbine. High and medium calorific fuels may be used without difficulty, but the low calorific fuels present the gas turbine user with several problems.

In a typical liquid fueled engine the mass of the fuel is about 2 percent of the air flow, and after the bleed, the mass flow in the turbine is usually marginally less than in the compressor. With low BTU fuels, however, the fuel mass flow forms a substantial part of the total mass flow, and there is a possibility of a compressor-turbine mismatch. There are also problems associated with introducing the fuel into the air within the primary zone, and many low BTU fuels have narrow limits of combustion. It is with this latter problem that the present work is concerned.

A Brief Discussion of Weak Limit Phenomena. Any flame will cease to propagate when the heat release rate becomes less than a certain critical quantity. This is the heat required to overcome the effects of heat losses, chain-breaking reactions, and/or third body or other quenching reactions at the wall. Whether or not one accepts one or the other as more important, in practice all limits relate to the thermal characteristics of the mixture (including diffusion) and the nature of the fuel molecule.

A major problem is to isolate such thermal characteristics from apparatus effects. Even a simple apparatus demonstrates the sensitivity problem. Thus, e.g., for limits determined within a simple cylindrical tube, the direction of propagation becomes very important. Limits determined by upward propagation differ from those obtained in horizontal tubes or by firing vertically downward (see Fig. 1 [1]).

It can be seen that the limits change in the order of 15 percent, depending upon the position of the tube. Thus immediately one is faced with defining the "correct" limit.

In firing, the heat of the ignition source initiates a small flame kernel which may, or may not, sustain flame spread within the mixture. The hot products of this initial kernel rise within the tube so as to preheat the reactants and also to set up convection currents. Hence, near the limits there is a range of mixtures that will ensure propagation in an upward direction but not in the downward sense. Such mixtures are very important from the fire safety viewpoint, but it is generally conceded that the downward propagation limit represents the more fundamental value, since convection effects are minimized. This is why, for the experiments discussed below, downward propagation was used.

The effects of walls (tube diameter) upon limits may be readily demonstrated (Fig. 2). It will be noted that tubes of small diameter rapidly narrow both weak and rich limits. In contrast, wide tubes have little or no effect upon the limits.

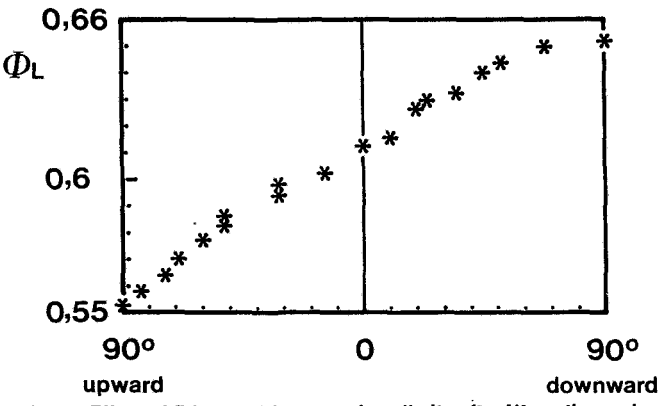

Fig. 1 Effect of firing position upon lean limits after [1]: methane-air, atmospheric conditions

Contributed by the Gas Turbine Division of THE AMERICAN SOCIETY OF MECHANICAL ENGINEERS and presented at the 29th International Gas Turbine Conference and Exhibit, Amsterdam, The Netherlands, June 4–7, 1984. Manuscript received at ASME Headquarters December 9, 1984. Paper No. 84-GT-144.

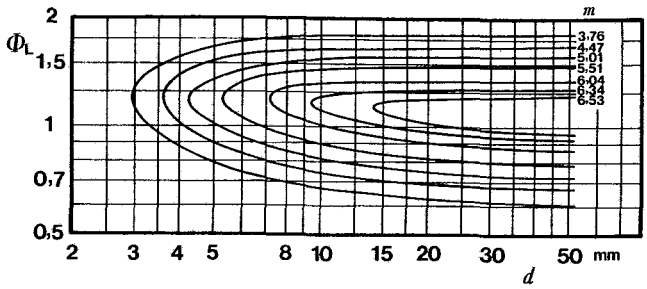

Fig. 2 The effect of tube diameter d and inerts content m on burning limits: propane-oxygen-nitrogen, atmospheric conditions

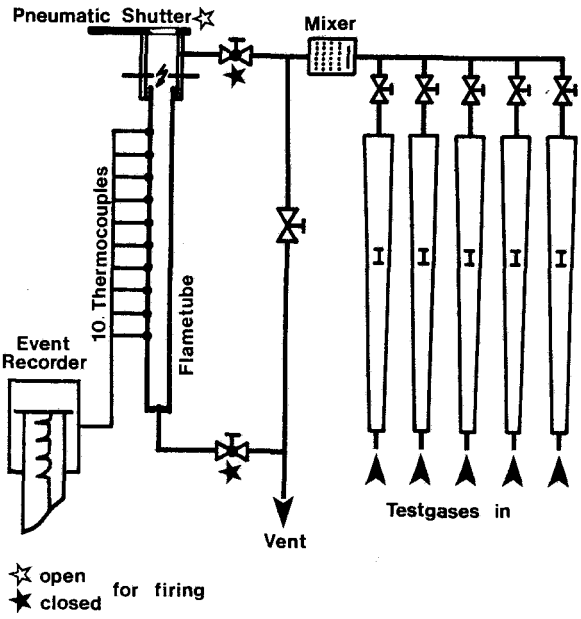

Fig. 3 Schematic of apparatus

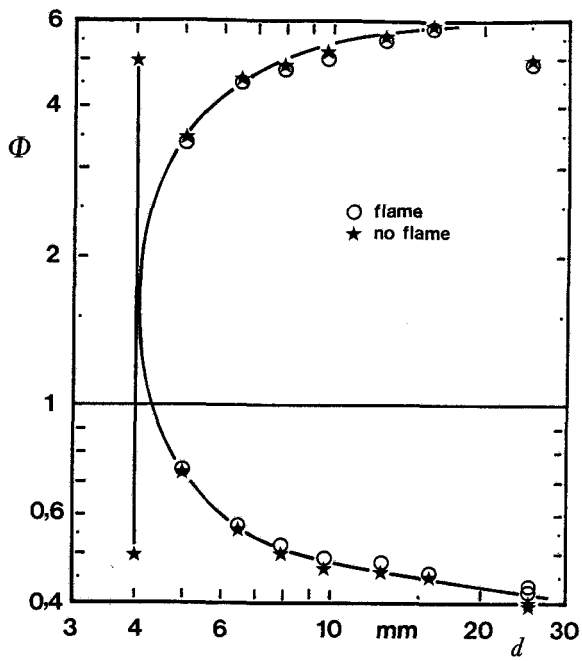

Fig. 4 Burning limits: CO—moist air, atmospheric conditions

For the analysis of the work described below, the minimum tube diameter that had no significant effect upon flame limits was set to 20 mm. Hydrogen mixtures, because of the greater reactivity, could be fully burned without any apparent effects in tubes of somewhat smaller diameter (say 10 mm). The materials used to fabricate the tubes appear to have little or no effect, providing they are not catalytic. Clear plastic tubing was selected for the present tests for visibility, ease of fabrication, low conductivity, and cheapness.

Apparatus

A schematic of the apparatus is given in Fig. 3. Any or all of five test gases are separately metered by rotameters. These are manufactured to a very high precision and equipped with a logarithmic scale such that they have an accuracy of ±0.5 percent of the reading. The gases then pass via a mixing chamber into the combustion section, from which they are led to an incineration burner. Sufficient gas is passed through the equipment (twenty volumes) to purge it from all previously used gases, and then the gases are bypassed, leaving a sealed tube filled with the test gas. By means of remote switching, the pneumatic shutter is opened smoothly and at a constant speed, and by means of a low energy spark, the gas is ignited within the ignition chamber. The mixture then burns with downward propagation through the firing tube. In order to attenuate pressure waves, a gauze plug is positioned at the base of the tube. As the combustion front travels down the tube, it passes a series of thermocouples set flush within the inner wall. The thermocouples act as heat sensors and transmit a signal to the event recorder. Knowing the distances between the thermocouples, it is then possible to determine the rate of flame travel.

Due to the use of a pneumatic shutter and an ignition chamber, ignition and transition to flame are very smooth, and only rarely are tests subjected to significant variation of flame velocity within the firing tube sections. However, such tests are rejected, and almost always the second tests show very good consistency.

Flame extinction needs to be carefully defined, since occasionally, the flame will progress part way down the tube before extinguishing. For the purpose of this work, total extinction (i.e., no flame at all within the firing tube) was defined by a "go or no-go" system. In this, the limit was defined as midway between the two most proximate values of "flame" and "no flame." Repeat tests indicate that, in terms of equivalence ratio, the weak limits are within ±0.02 and rich limits within ±0.4. A typical experimental loop is given in Fig. 4.

Nomenclature

C_p = molar specific heat, J/(mol.K)
C_p^* = specific heat of the stoichiometric products per mole of fuel, J/(mol.K)
d = tube diameter, m
d_c = critical combustor diameter, m
d_q = quenching diameter, m
E = activation energy, J/mol
l_q = quenching distance, m
m = inerts to oxygen mole ratio
p_0 = pressure, Pa
Q = net calorific value, J/mol
q_v = net calorific value per unit volume, J/normal m^3 (BTU/scf)
R = gas constant, J/(mol.K)
T = temperature, K
T_a = temperature at mean reaction rate, K
T_b = temperature of the burned gas, K
T_0 = initial temperature, K
X = correlation group (equation (4)), K
y = fuel composition parameter
Φ = equivalence ratio
Φ_L = equivalence ratio at the burning limit
Θ = temperature correction factor

Table 1 Extinction limits—range of variables (Downward propagation, atmospheric pressure)

		This work	Other work [1-13]
H_2-O_2-N_2	m	3.76 to 14	3.76
	T_0 K	300	298 to 673
	d mm	3.8 to 25	10 to 210
	Φ	0.224-5.34	0.12-6.95
H_2-O_2-Ar	m	6-20	
	T_0 K	300	
	d mm	3.8-9.7	
	Φ	0.21-4.61	
H_2-O_2-He	m	6-8	
	T_0 K	300	
	d mm	3.8	
	Φ	0.22-3.35	
CO-O_2-N_2	m	3.76-9	3.76
	T_0 K	300	300-673
	d mm	2.5-5	2.5-80
	Φ	0.4-4.82	0.31-8.19
CH_4-O_2-N_2	m	3.76	0-6.635
	T_0 K	300	298-1073
	d mm	25	20-80
	Φ	0.59-1.56	0.136-3.88
CH_4-O_2-N_2-CO_2	m		3.76-5.335
	T_0 K		300
	d mm		>20
	Φ		0.532-0.981
CH_4-O_2-N_2-H_2O	m		3.76-5.35
	T_0 K		300
	d mm		>20
	Φ		0.532-0.979
CH_4-O_2-N_2-Ar	m		3.76-8.645
	T_0 K		300
	d mm		>20
	Φ		0.532-0.973
CH_4-O_2-N_2-He	m		3.76-6.83
	T_0 K		300
	d mm		17->20
			0.532-0.975
CH_4-H_2-O_2-N_2	m	3.76-6.8	
	T_0 K	300	
	d mm	25	
	Φ	0.224-0.894	
C_3H_8-O_2-N_2	m	3.76-6.34	3.76
	T_0 K	300	300
	d mm	3.2-25	>20
	Φ	0.57-1.99	0.536-2.68
Commercial gases in air [17]	m		3.76
	T_0 K		300
	d mm		>20
	Φ		0.27-4.6
Hydrocarbons - O_2-N_2 [15]	m		0-3.76
	T_0 K		290-673
	d mm		20-75
	Φ		0.105-14.5
CHO-O_2-N_2 [6]	m		3.76
	T_0 K		300
	d mm		25-275
	Φ		0.351-2.57
Total number of points		341	391

Test Results

The full range of variables is listed in Table 1. Fuels ranged from hydrogen through carbon monoxide to simple and complex hydrocarbons and include oxygenated carbon compounds; in all some 40 different compounds. The test results are limited to atmospheric pressure, but inlet temperatures are considered from 298-1073 K. Inert gases include nitrogen, carbon dioxide, argon, helium, and water, and the inerts/oxygen mole ratios vary from 0 to 20. The values of equivalence ratio lie between 0.105 and 14.5, although the analysis of the data is restricted to weak mixtures. Experimental measurements were made with a range of tube diameters from 3.8 to 210 mm, and this has enabled the limiting diameter for minimizing wall effects to be reasonably well defined. Again the limit analysis does not consider tubes exhibiting wall effects.

Table 2 Reproducibility of results (Weak extinctions, large tube diameters, ambient conditions, downward firing, this work, and [1-13])

Equivalence Ratio At Burning Limit:				
No.	H_2-Air	CO-Air	CH_4-Air	C_3H_8-Air
1	0.24	0.42	0.6	0.605
2	0.23	0.41	0.6	0.63
3	0.23	0.41	0.64	0.575
4	0.22	0.42	0.62	0.57
5	0.25	0.4	0.61	0.63
6	0.24	0.45	0.59	0.69
7	0.24	0.48	0.62	0.68
8	0.25	0.45	0.59	0.645
9	0.23	0.464	0.62	0.62
10	0.25	0.44	0.59	0.61
11	0.26	0.39	0.62	0.58
12	0.17		0.64	0.536
13	0.24		0.62	0.577
14	0.25		0.58	0.588
15	0.25		0.53	
16	0.2		0.532	
17	0.26		0.533	
18	0.25		0.644	
19	0.12		0.532	
20			0.529	
$\bar{x}$	0.231	0.430	0.592	0.61
S_x	0.034	0.028	0.040	0.042
$S_{\bar{x}}$	0.008	0.009	0.009	0.01
Max. Deviat.	+0.126 −0.481	+0.116 −0.093	+0.088 −0.106	+0.131 −0.121

Typical experimental results are illustrated in Figs. 2 and 4-8. They indicate a good concurrence between the experiments carried out in the course of the present work and the results obtained by other workers (where available).

The effect of the initial temperature upon the lean limit is shown in Fig. 8. It would seem that the experimental results are consistently richer than the predicted values. This is due to the prediction being based upon *all* the data used in this report (see also Fig. 13) at ambient temperature. At 298 K, the experimental data do not agree with the mean values considering all data. This could well be an apparatus characteristic.

Repeatability and Reproducibility. As indicated before, the repeatability of the present apparatus is quite good. Comparison with other workers readily demonstrates that the reproducibility between various workers using different apparatus increases the error severalfold. Table 2 illustrates typical results from various sources and, based upon the data, a standard deviation of some 4 percent seems reasonable with a maximum error of 13 percent. It is realized that one hydrogen point exhibits a deviation of 48 percent, but it is felt that this one test may well be erroneous in some way.

Flame Quenching—Weak Limit Relationships. Heat losses and/or third body reactions at the wall are very important in determining flame propagation, and several theories have been proposed to explain these phenomena. Two definitions of flame quenching are used:

- Quenching Distance, l_q: This is the distance between two parallel plates at which a flame just fails to propagate.
- Quenching Diameter, d_q: This is the limiting diameter of a small burner which will just prevent flash-back.

Various attempts have been made to relate the two from a theoretical viewpoint, but the most useful relationship to-date is an empirical one

$$d_q \approx 1{,}4 l_q$$

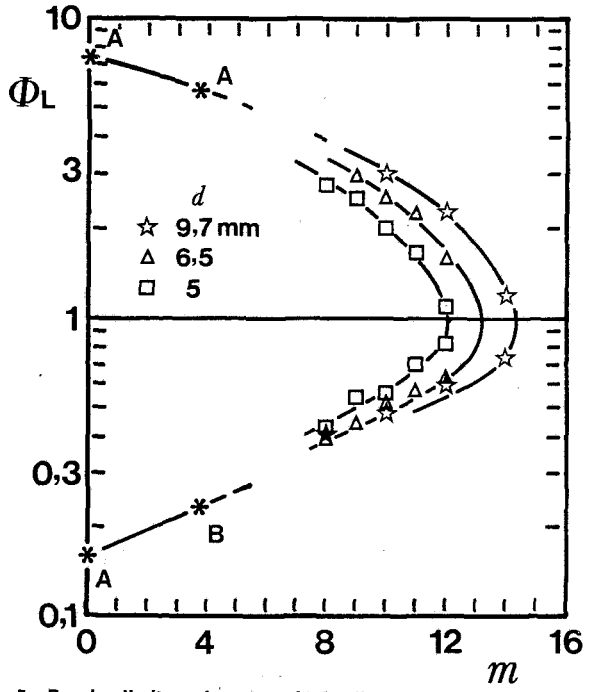

Fig. 5 Burning limits as function of tube diameter d and inerts content m: H_2-O_2-N_2 ambient conditions (A: [1], 16-21 mm; B: mean values from Table 2, 16-210 mm)

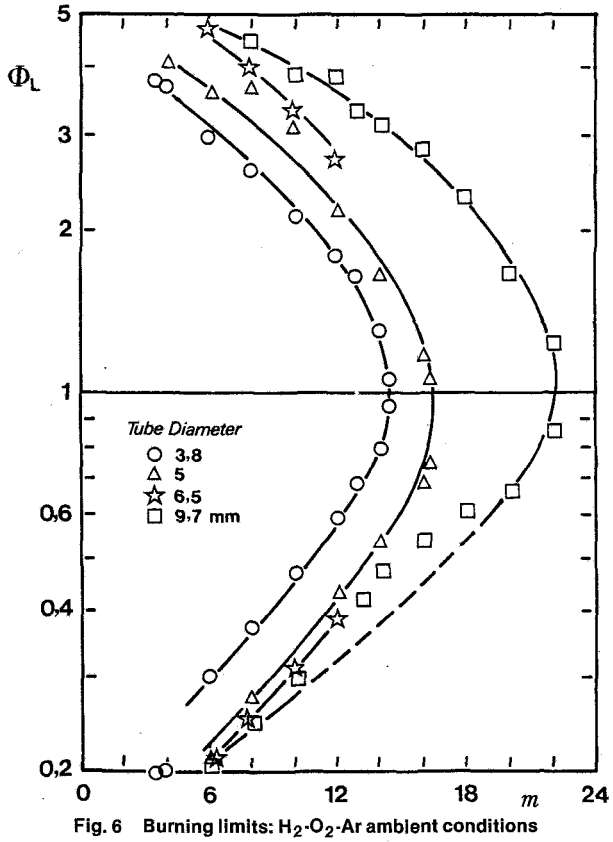

Fig. 6 Burning limits: H_2-O_2-Ar ambient conditions

When one examines published data for quenching diameters, the values cited are usually small (say 2–6 mm). On the other hand, flame limits within tubes are cited for much larger diameters. The diameter which corresponds to these limits may be referred to as "extinction diameter." It seems reasonable to suggest that quenching and extinction diameters are strongly related and probably identical. Figure 7 suggests

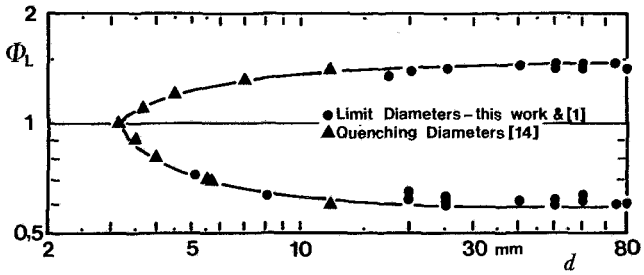

Fig. 7 Extinction and quenching diameters: methane-air ambient conditions

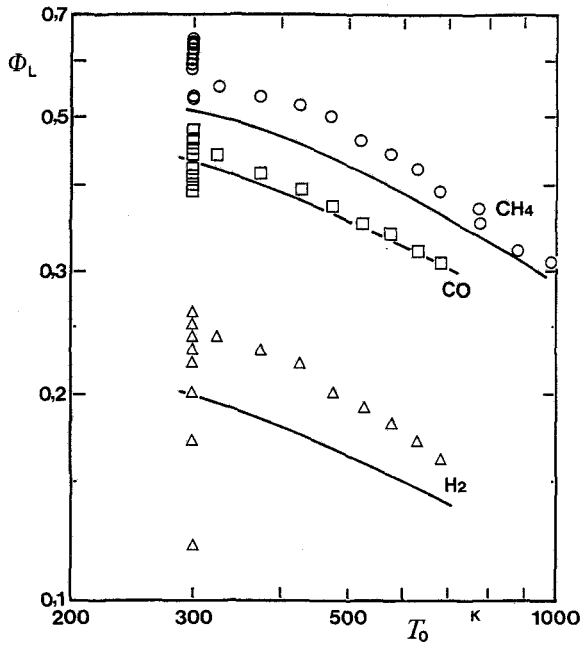

Fig. 8 Effects of initial temperature on lean limts: in air at atmospheric pressure; ambient temperature data see Table 2; data at other temperatures from [1]; lines from equation (3)

Table 3 Experimental values of critical diameters

System	m	d_c weak mm	d_c rich mm
H_2-Air	3.76	8–10	10
CO-Air	3.76	20–25	20–25
CH_4-Air	3.76	20–25	20–25
C_3H_8-Air	3.76	20–25	20–25
C_3H_8-O_2-N_2	5	25–30	20–25
	6	25–30	20–25

that this assumption has some substance, and confirmation is provided by Figs. 9 and 10.

Wall Effects. For ambient conditions (i.e., $p_0 \approx 100$ kPa, $T_0 \approx 300$ K) Figs. 2, 4–7, and 10 enable the tube diameters to be found, above which there is little or no effect on the limits. Table 3 lists values obtained. These diameters will be termed "critical" diameters, d_c. The practical implications are that any combustor having a diameter less than d_c might well suffer a loss of flame stability and (based upon flame velocity measurements) that near the limit there might well be a fall-off in efficiency. The information available to date is not considered to be sufficient to enable a satisfactory analysis of the phenomena, other than that given in Table 3.

Rich Extinctions. A considerable amount of new rich extinction data have accrued as a result of the present work and has been thought worthy of report (Figs. 2, 4–6, 10, 12).

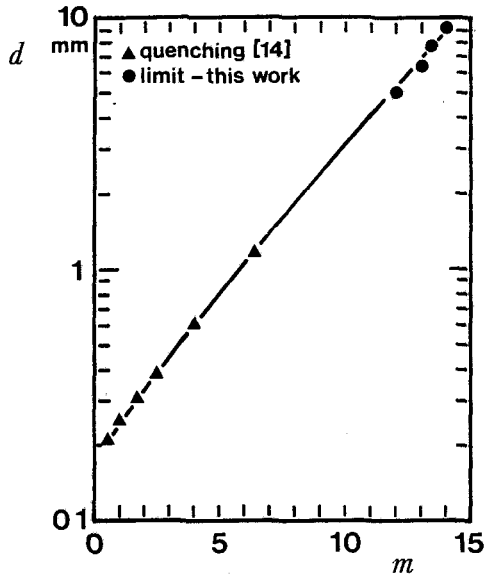

Fig. 9 Quenching and extinction diameters: H_2-O_2-N_2, $\Phi = 1$, ambient conditions

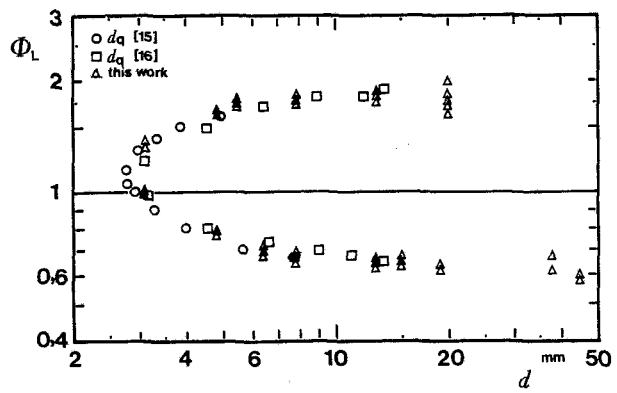

Fig. 10 Quenching diameters and burning limits: propane-air atmospheric conditions

However, the present indications are that the complex combustion of rich mixtures precludes the simple treatment according to the weak mixtures (below).

Low-BTU Fuels. For some years it has been the practice to classify gases into high-, medium-, and low-BTU categories. The classification, while useful, is by no means comprehensive, especially the low-BTU category, which is very sensitive to variations in composition. During the course of the present work, three fuels (propane, carbon monoxide, and hydrogen) were individually diluted to yield low-BTU fuels. The limits of these fuels are given in Fig. 11, and they indicate that high proportions of hydrocarbons in low-BTU fuels will give rise to severe extinction problems. The data for Fig. 11 are taken from [1] for methane. In another series of experiments, mixtures of hydrogen and methane were diluted with nitrogen to produce "100-BTU" and "200-BTU" fuels. Both weak and rich limits were determined and the results are given in Fig. 12. The data show how quickly the limits narrow as the proportion of methane is increased.

Weak Limit Prediction

Theoretical approaches to the prediction of limits have been attempted from time to time [1, 17, 18]. Typical is the formula cited by Lewis and Von Elbe [19]

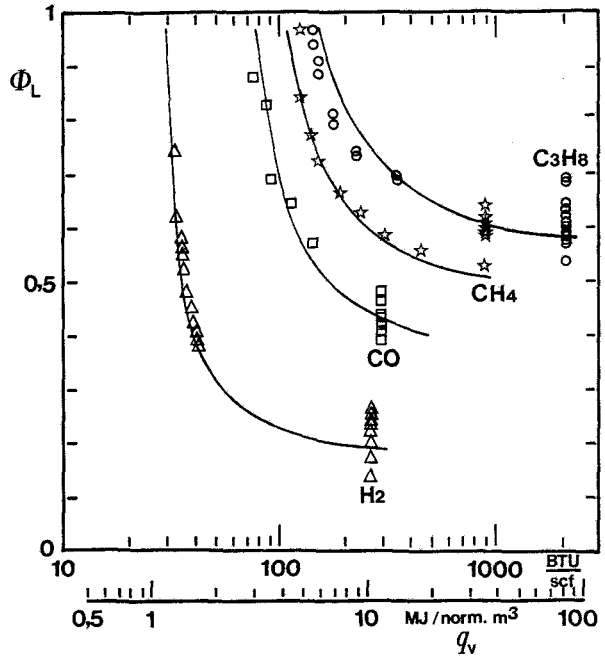

Fig. 11 Lean limits of inert containing fuels in air: mixtures comprise fuel + nitrogen to yield appropriate volumetric calorific value; ambient conditions; propane, hydrogen, carbon monoxide—this work; methane from [1], pure fuel data see Table 2, lines from equation (3)

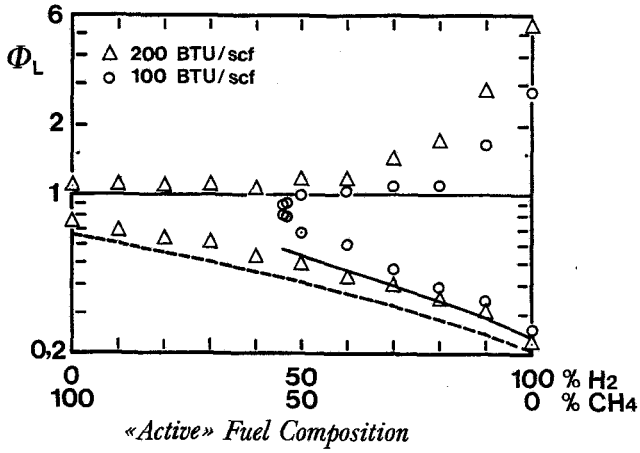

Fig. 12 Burning limits, "Low-BTU gases": H_2-CH_4-N_2-air, ambient conditions, 25-mm-tube, lines from equation (3)

$$\frac{E}{RT_b}\left(1-\frac{T_a}{T_b}\right)=1 \tag{1}$$

Because of the manner of its derivation, the temperature corresponding to the average reaction rate, T_a, has to have a value close to that of the burned gas, T_b. Other workers replace T_a by the temperature corresponding to flame extinction, but it is obvious that this raises its own problems, since if this temperature is known, the limits are automatically defined.

The empirical approach that has been most used is attributed to Le Chatelier [20]. For mixtures of gases, this supposes

$$L=\frac{a+b+c+\ \ldots}{a/A+b/B+c/C+\ \ldots} \tag{2}$$

a, b, and c are the number of moles of individual gases in the mixture, and A, B, and C are the individual limits. The procedure is fairly satisfactory, but it demands that the in-

Table 4 Fuel factors

Fuel	$\frac{H+O}{H+C+O}$	y
Single components		
H_2	$2/2=1$	1
CH_4	$4/(4+1)=0.8$	1.893
CO	$1/(1+1)=0.5$	2.05
C_3H_8	$8/(3+8)=0.727$	2.172
CH_3OH	$4/5=0.8$	1.893
HCOOH	$3/4=0.75$	2.088

Mixed fuels:

For any fuel mixture, the fuel factor is the molar average of the individual component fuel factors, e.g.,

20 percent H_2 + 80 percent CH_4 For H_2 $y=1$
For CH_4 $y=1.893$

therefore $y_{mix}=0.2\times1+0.8\times1.893=1.714$

dividual limits are known at the conditions of operation. Often this information is not available, expecially at temperatures and pressures other than atmospheric. Pressure effects present a great challenge to prediction techniques, since the limited experimental evidence suggests that, while some fuels show widening of limits, other fuels exhibit the opposite effects. Fortunately over the range of gas turbine operation (say 0.1–4 MPa), there is generally little effect upon lean limits. Thus any prediction technique which can take into account mixed gases and the effects of initial temperature could be of considerable use to the gas turbine engineer, either directly (some engineers claim that for gaseous fuels weak extinction within the primary zone approximates to the premixed lean limits) or indirectly (by ratioing a known limit by the premixed limits of the "known" and "unknown" fuels). The following technique offers considerable promise for the satisfactory determination of the lean limits of premixed gases.

Equation (1) clearly shows that the limit is a function of reaction rate, the rate temperature, and the burned gas temperature at the appropriate equivalence ratio. Limit temperatures for hydrocarbon/air mixtures are reasonably constant, but the presumption of a unique limit temperature fails immediately when one considers hydrogen and/or carbon monoxide mixtures. However, the work on the measurements of flame speeds (not reported here) strongly suggests that for the range of mixtures investigated (Table 1) the flame speeds approaching the limit mixtures are very similar. This might imply a constant reaction rate. In this case it was felt that the maximum flame temperature might provide a useful correlation parameter. An early attempt at such a correlation [21] met only with limited success.

Although the correlation derived below is empirical, there are theoretical justifications for the various parameters. It was still felt that some sort of reaction temperature should be representative at extinction, and the stoichiometric temperature offered a natural choice. However, its calculation for an enormously wide range of fuel-inert-oxygen mixtures might prove onerous. A representative group, Q/C_p^*, was therefore substituted. Here, Q is the molar calorific value (net) of the combustible fuel fraction, and C_p^* is the specific heat per mole of fuel of the products of reaction for any C-O-H-inerts system referred to a stoichiometric mixture and 298 K. The selection of these terms meant that all data were readily accessible.

Experimental data (e.g., Figs. 11 and 12) indicated that the fuel composition and structure played an important role in deciding the value of the weak limit, and hence it became necessary to include a representative term.

Many gases comprise one or more fuel components diluted with inerts and/or oxygen. Using the Le Chatelier technique,

Table 5 Specific heats

Species	C_p J/(mol K)	Species	C_p J/(mol K)
CO_2	37.048	Ar	20.89
H_2O	33.729	He	20.89
N_2	29.178		

this is compensated for by the technique known as "air subtraction." For the present purposes, it was thought better to include such inerts with the oxidant, but as will be seen, this resulted in the need to use an iterative procedure to determine the limit equivalence ratio. Correction for initial temperature effects was applied by deducing an empirical factor from published results. Pressure effects were neglected, since all evidence shows them to be small over the range of interest. The final correlation took the form

$$\Phi_L=0.725/X^{1.3} \tag{3}$$

where

$$X=10^{-3}\times Q\times\Theta/(C_p^*\times y) \tag{4}$$

where y is a parameter taking into account fuel composition, Q is the net molar calorific value, Θ is the temperature correction factor. Evaluation of experimental data yielded for y

$$y=2.457-4.9\times\left|\frac{H+O}{H+C+O}-0.63\right|^{1.22} \tag{5}$$

C and H represent the number of carbon and hydrogen atoms, while O is the number of oxygen atoms in the fuel that are double bonded to carbon atoms. Table 4 gives typical values for several fuels. As previously stated, the specific heat term C_p^* is calculated as the specific heat at 298 K of the stoichiometric products per mole of fuel. For example, consider a methane-oxygen-nitrogen mixture. Then

$$CH_4+2O_2+xN_2\rightarrow CO_2+2H_2O+xN_2 \tag{6}$$

$$C_p^*=1\times C_{p,CO_2}+2\times C_{p,H_2O}+x\times C_{p,N_2} \tag{7}$$

Specific heat values are listed in Table 5.

The initial temperature correction was obtained by consideration of published results in [1]

$$\Theta=\frac{Q/C_py \text{ at } T_0}{Q/C_py@298}=0.24\frac{T_0}{298}+0.76 \tag{8}$$

Using equations (3–5), and (8), and Tables 4 and 5, it is possible to predict the weak limits of either single or multicomponent fuels in oxygen-inert mixtures.

For a fuel without inerts, the stoichiometric composition to be used is straightforward. Assume a fuel F of the type $C_aH_bO_c$, burning with oxygen and inerts I in the oxidant mixed in a molar ratio of $I/O_2=m^*$. Then we have

$$F+\left(a+\frac{b}{4}-\frac{c}{2}\right)O_2+\left(a+\frac{b}{4}-\frac{c}{2}\right)m^*I \tag{9}$$

or

$$F+AO_2+Am^*+I \tag{10}$$

If the fuel contains inerts, the real stoichiometric composition cannot be used, the "effective" composition has to be found by iteration. Let us assume the same oxidant as the foregoing, and the same fuel as above mixed with an inert "J" in the proportions of x moles of fuel to $(1-x)$ moles of inert; then at the limit we have

$$\Phi_L[xF+(1-x)J]+xAO_2+xAm^*I \tag{11}$$

All inerts have to be grouped in the oxidant

$$\Phi_L xF+xAO_2+[xAm^*I+\Phi_L(1-x)J] \tag{12}$$

or, for Φ mol of combustible

$$\Phi_L F+AO_2+\left[Am^*I+\Phi_L\frac{1-x}{x}J\right] \tag{13}$$

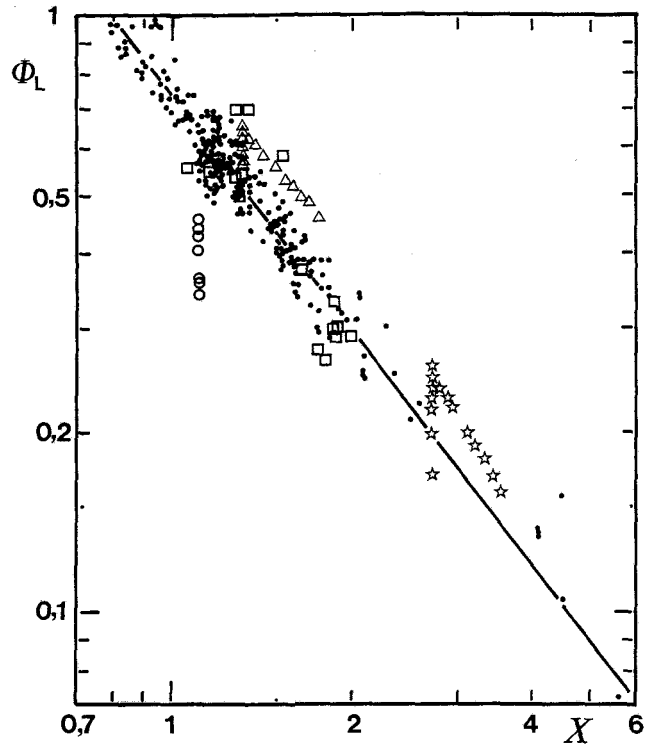

Fig. 13 Lean burning limits—all data: Squares, industrial gases; Triangles, methane; Stars, hydrogen; Circles, acetone; Line, equation (3)

and the corresponding "effective" stoichiometric composition

$$F + AO_2 + \left[Am^*I + \Phi_L \frac{1-x}{x} J\right] \tag{14}$$

Since the equivalence ratio at the limit is the unknown, this composition has to be found by iteration:

- Assume a value for the limit, Φ_1
- Determine the correlation group X_1 for Φ_1
- Using X_1 determine a new value for the limit Φ_2
- Repeat as necessary

Discussion

The present work has yielded a wide range of experimental data pertinent to weak and rich extinction for a variety of fuels, inerts, and tube diameters. To this work has been added the consideration of previous results by other workers. The results indicate that downward flame propagation yields limits which are 15 to 20 percent narrower than those for upward propagation. While downward firing should be more suitable for fundamental interpretation, if safety is of paramount concern, then the wider limits of upward propagation should be taken into account.

To date, attempts to correlate either the effects of tube diameter (wall effects) or rich limits have not met with sufficient success to merit them being included here. For rich mixtures, the method of Le Chatelier appears to be the most appropriate, although it can give rise to considerable inaccuracy when applied to complex mixtures, especially at conditions other than atmospheric. For all cases, unless the inert content of the gas is very high, say $m>6$, provided that the combustor diameter is in excess of 25 mm, its effects upon flame limits may be considered to be negligible.

The major objective of the present work has been to provide a prediction technique for weak limits. The proposed correlation group offers several advantages over previous techniques:

(*i*) It requires no previous knowledge of individual gas limits with the appropriate inert content.

(*ii*) A simple temperature correction factor enables the limits to be predicted over the temperature range 298 to 1000 K.

(*iii*) It requires only a prior knowledge of the fuel composition plus the specific heat data of relatively few products at 298 K (Table 5)

(*iv*) The accuracy of prediction is as good as, or better than, other published techniques.

(*v*) As far as can be judged from the published test data, the correlation applies to a very wide range, not only of hydrogen, carbon monoxide, and hydrocarbon fuels but also to several carbon-hydrogen-oxygen compounds.

Figure 13 gives a plot of all the points considered, either from the present experiments or from the literature. Several interesting comments may be made:

(*i*) The correlation line tends to lie towards the base of the points. This is by deliberate choice, since it is felt that the weakest experimental values may have more fundamental significance than the richer ones.

(*ii*) Certain fuels (acetone, methane, hydrogen) have been sufficiently tested at the same condition to illustrate the reproducibility for a single fuel (see Table 2). It is not known why all the acetone points fall below the line, since other ketones examined fall close to the line, but White [9] admits to difficulties in experimentation.

(*iii*) An important factor is that the industrial fuels correlate reasonably well, and this indicates the usefulness of the correlation. These fuels [1, 10–13] have been burned in gas turbines. Several are quite complex mixtures.

Experimental investigations are continuing, and it is hoped to extend the correlations to cover rich mixtures, tube size, and geometry in the near future.

Acknowledgments

The authors are indebted to the Canadian National Science and Engineering Research Council for the financial support of this work. They also thank the several students, especially Miss A. Ouellet, for their able assistance with the experimental part of the program.

References

1 Coward, H. F., and Jones, G. W., Bulletin No. 503, Bureau of Mines, US Gov't Printing Office, 1952.

2 Odgers, J., White, I., and Kretschmer, D., "The Experimental Behaviour Of Premixed Gases In Tubes: The Effect Of Diluent Gases," ASME JOURNAL OF ENGINEERING FOR POWER, Vol. 102, No. 2, Apr. 1980.

3 White, A. G., "Limits For The Propagation Of Flame In Inflammable Gas-Air Mixtures, III, The Effect Of Temperature On The Limits," *J. Chem. Soc.*, Vol. 127, 1925.

4 White, A. G., "Limits For The Propagation Of Flame In Inflammable Gas-Air Mixtures, I, Mixtures Of Air And One Gas At The Ordinary Temperature And Pressure," *J. Chem Soc.*, Vol. 125, 1924.

5 Le Chatelier, H., and Boudouard, O., "Limits Of Flammability Of Gaseous Mixtures," *Bull. Soc. Chim.*, Vol. 19, Paris, 1908.

6 Leprince-Ringuet, F., "Limits Of Flammability Of Fire-damp," *Compt. Rend.*, Vol. 158, Paris, 1914.

7 Mason, W., and Wheeler, R. V., "Effect Of Temperature And Of Pressure On The Limits Of Flammability Of Mixtures Of Methane And Air," *J. Chem. Soc.*, Vol. 113, 1918.

8 Payman, W., and Wheeler, R. V., "The Effect Of Pressure On The Limits Of Inflammability Of Mixtures Of Paraffin Hydrocarbons With Air," *J. Chem. Soc.*, Vol. 123, 1923.

9 White, A. G., "Limits For The Propagation Of Flame In Vapour-Air Mixtures, I, Mixtures Of Air And One Vapour At Ordinary Temperature And Pressure," *J. Chem. Soc.*, Vol. 121, 1922.

10 Crouch, W. B., Schlenger, W. B., Klapatch, R. D., and Vitti, G. E., "Recent Experimental Results On Gasification Combustion Of Low BTU Gas For Gas Turbines, Part II, Gas Turbine Combustor Test Results And Combined Cycle System," *Combustion*, Vol. 45, No. 10, Apr. 1974.

11 Perry, J. H., ed., *Chemical Engineers Handbook*, 3d ed., McGraw-Hill, New York, 1950.

12 Spiers, H. M., *Technical Data On Fuels*, The British Committee, World Power Conference, London, 1961.

13 Hefner, W. J., and Gassner, R. L., "Gas Turbine Fuel Consideration," *Proc. Symp. on Gas Turbine Operations and Maintenance*, National Research Council of Canada, Calgary, June 6-7, 1977.

14 Barrett, H. C., and Hibbard, R. R., "Basic Considerations In The Combustion of Hydrocarbon Fuels With Air," NACA Report No. 1300, Propulsion Chemistry Div., Cleveland, Ohio, 1957.

15 Harris, M. E., Grumer, J., von Elbe, G., and Lewis, B., "Burning Velocities, Quenching And Stability Data On Nonturbulent Flames Of Methane And Propane With Oxygen And Nitrogen," *Proceedings of the 3rd Symp. (Int.) on Combustion*, Williams and Wilkins, 1949.

16 Gibbons, L. C., Barrett, H. C., and Gerstein, M., "Effect Of Molecular Structure On Combustion Behaviour," *Ind. Eng. Chem.*, Vol. 46, No. 10, Oct. 1954.

17 Fenn, J. B., "Lean Flammability Limit And Minimum Spark Ignition Energy," *Ind. Eng. Chem.*, Vol. 43, No. 12, Dec. 1951.

18 Lovachev, L. A., Babkin, V. S., Bunev, V. A., V'Yun, A., Krivulin, V. N., and Baratov, A. N., "Flammability Limits: An Invited Review," *Combustion & Flame*, Vol. 20, 1973.

19 Lewis, B., and von Elbe, G., *Combustion, Flames And Explosions Of Gases*, Academic Press, New York, 1961.

20 Le Chatelier, H., "Limits Of Flammability Of Gaseous Mixtures," *Bull. Soc. Chim.*, Vol. 19, Paris, 1898.

21 Odgers, J., Kretschmer, D., and Halpin, J., "Weak Limits Of Premixed Gases," 1983 Spring Technical Meeting, The Combustion Institute-Canadian Section, Kingston, Ontario, May 1983.

The Effect of Oxygen Concentration on Ignition of Fuel Spray in Low-Pressure Air Flow

Y. H. Zhao

N. K. Chen

J. S. Chin

Mem. ASME
Jet Propulsion Laboratory,
Beijing Institute of Aerospace
and Astronautics,
People's Republic of China

Further experimental research has been carried out on the ignition improvement by oxygen addition in a small pilot combustion chamber taken from an existing aero-engine. Both uniform mixture method and local oxygen injection method have been investigated. The results show that oxygen addition improves low-pressure ignition performance significantly. Local oxygen injection makes much better use of oxygen added. Experimental results show low evaporation percentage of fuel spray responsible for the poor ignition performance. Based on thermal ignition theory, a semianalytical equation has been obtained to predict the relative enlargement of maximum ignition velocity by oxygen addition, the equation can correlate experimental data very well. To form a stagnant region with suitable oxygen concentration is the most important factor in the design of ignitor with oxygen addition.

Introduction

In previous papers [1, 2], both experimental research and analytical work showed that oxygen addition is very useful for improving the high-altitude ignition performance of aero-gas turbine engines. In [1], the effect of oxygen addition on low-pressure ignition performance of an aero-gas turbine engine was investigated on a full-scale engine. It is gratifying to see the final results on an existing aero engine. But it is impossible to get an insight into the mechanism that controls the ignition of fuel spray, since on engine tests some parameters cannot be changed independently. In [2], the analysis showed that the thermal ignition theory can be used to predict the minimum ignition energy reduction by oxygen addition both for quiescent and flowing mixture.

But it is difficult to analyze the minimum ignition energy of a fuel spray in a flowing air stream with oxygen addition. The present paper has reported some further research results on the effect of oxygen addition on ignition, mainly on the effect of oxygen concentration on the ignition of fuel spray in low-pressure air flow and with a comparison of the effectiveness of oxygen usage by uniform oxygen addition and local oxygen injection. The experimental data and analysis show clearly that the oxygen concentration at the sprak region together with the formation of a stagnant zone is the key factor controlling the effectiveness of oxygen addition.

Apparatus and Procedures

The layout of the ignition test rig is shown in Fig. 1. The ignitor (5) taken from an existing engine is essentially a small combustion chamber with a tiny swirl fuel injector and two electrodes. Air is drawn in from the atmosphere by a vacuum pump (2), and by adjusting the exhaust regulator valve (1) and inlet throttle valve (8), the pressure and air flow rate can be controlled to the desired values. The mninimum air pressure achieved is $1.96 \cdot 10^4$ N/M^2. Oxygen is provided through a solenoid valve (7), and by providing a long length for mixing the oxygen added and the air flow, the oxygen enriched air flow to the ignitor can be considered as a uniform mixture of oxygen and nitrogen. This is one method of oxygen addition – uniform mixture method. Alternatively, oxygen may be supplied locally into the ignitor through an oxygen nozzle of 2 mm diameter; injected countercurrently to the air stream, this is named as local oxygen injection. The air and oxygen flow rates are measured by float gas meters. The fuel flow rate is determined by the pressure drop of the fuel injector with experimentally calibrated fuel injector characteristic curve (mass flow rate versus pressure drop). The determination of oxygen flow rate includes the correction for the change of oxygen pressure and temperature. Since the air flow Mach number is rather low (<0.15), the air velocity is determined by the measured air static pressure, temperature, air mass flow rate, and the flow area. The exhaust system includes a low-pressure plenum chamber (ϕ 420 $\times$ 12 mm, 415 mm high) with two quartz glass windows on side walls for observation and photography. At the outlet of the plenum chamber is the flame arrestor for safety consideration. A drainage valve (12) is installed at the lowest position of the system to avoid any fuel accumulation in the exhaust pipe. The electrodes are connected to the induction ignition coil. The spark energy is close to 50 mj.

The test procedure is as follows:

Start the vacuum pump, adjust the inlet throttle valve and exhaust regulator valve to obtain the required pressure and air flow rate. If oxygen is added the oxygen flow rate is controlled by adjusting the supply pressure. After the stable

Contributed by the Gas Turbine Division of THE AMERICAN SOCIETY OF MECHANICAL ENGINEERS and presented at the 29th International Gas Turbine Conference and Exhibit, Amsterdam, The Netherlands, June 4-7, 1984. Manuscript received at ASME Headquarters January 9, 1984. Paper No. 84-GT-147.

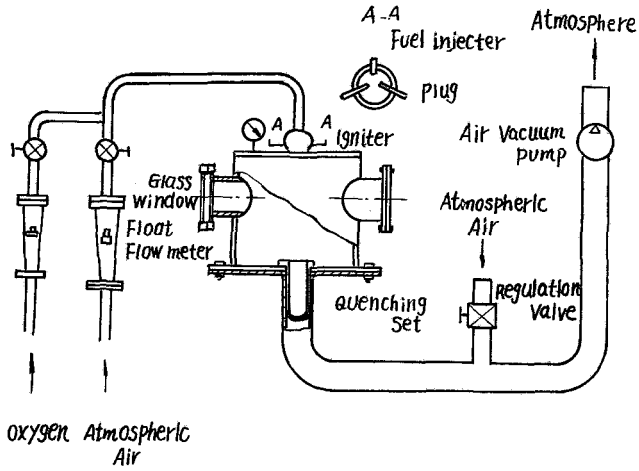

Fig. 1 Ignition test rig

1. regulator valve
2. vacuum pump
3. observation window
4. low-pressure plenum chamber
5. ignitor
6. pressure gage
7. solenoid valve
8. hand valve
9. flow meter
10. hand valve
11. flame arrestor
12. drainage valve

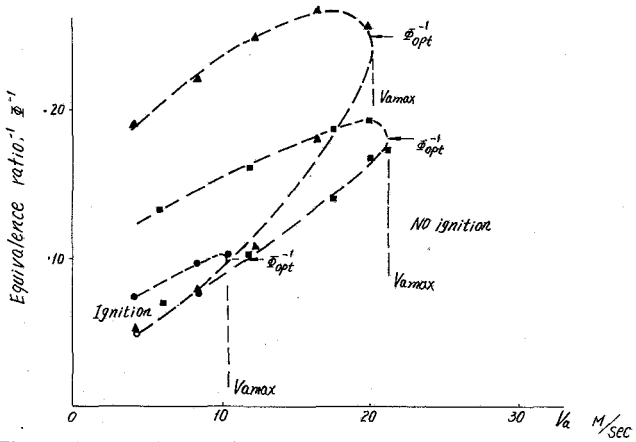

Fig. 2 Ignition loop without oxygen addition at various pressure levels.

T_a = 282.7 K
▲ $P_a = 88.2 \cdot 10^4$ N/M²
■ $P_a = 61.7 \cdot 10^4$ N/M²
● $P_a = 33 \cdot 10^4$ N/M²

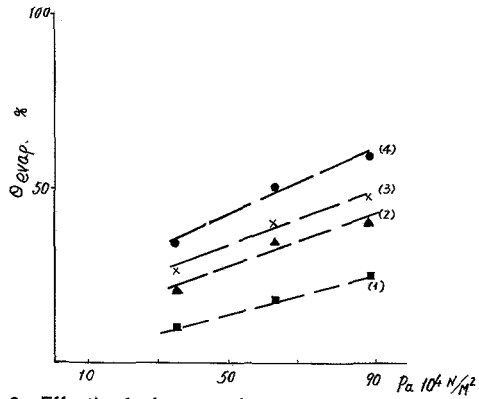

Fig. 3 Effective fuel evaporation percentage versus air pressure

■ (1) No oxygen addition
▲ (2) G_{O_2} = 0.024 g/sec
× (3) G_{O_2} = 0.0506 g/sec
● (4) G_{O_2} = 0.20 g/sec

condition has been obtained, change the fuel supply pressure to reach the fuel rich or fuel lean ignition limit. Then change air pressure or air flow rate or oxygen flow rate, follow the same steps until a complete ignition loop is obtained. The criterion for successful ignition is that after the electrical spark has been turned off, a stable flame is self- sustained continuously. But the maximum ignition operation time is 10 s.

The fuel used in the present research is Chinese aviation kerosine, RP-2.

The test parameters are within the following ranges

air pressure	$1.96 \cdot 10^4 - 88.2 \cdot 10^4$ N/M²
air temperature	283 K
fuel air ratio	0.116-1.49
oxygen fraction	(volume) $O_2/O_2 + N_2$,0.21-0.30

Uniform Oxygen Addition

As a base line, the ignition loops without oxygen addition for three pressure levels are shown in Fig. 2, where the reciprocal of equilivance ratio, Φ^{-1}, is plotted against the air flow velocity. The fuel lean limit (upper limit) is actually obtained at overall equivalence ratios much greater than 1, so the overall situation is fuel rich. But at the center of the spark region, the effective or gaseous (vaporized) fuel–air ratio is lean at this limit, since at room temperature, only a very small portion of liquid fuel has been vaporized. It is obvious that at lower pressure the ignition loop will shrink and the ignitible overall equivalence ratio (fuel–air ratio) and air velocity range become much narrower. At $V_a = V_{amax}$, there is only one equivalence ratio Φ which can provide ignitible mixture at the spark region. It is reasonable to assume that at V_{amax}, the effective, or vaporized fuel–air ratio at the spark region is stoichiometric, or the equivalence ratio based on vaporized

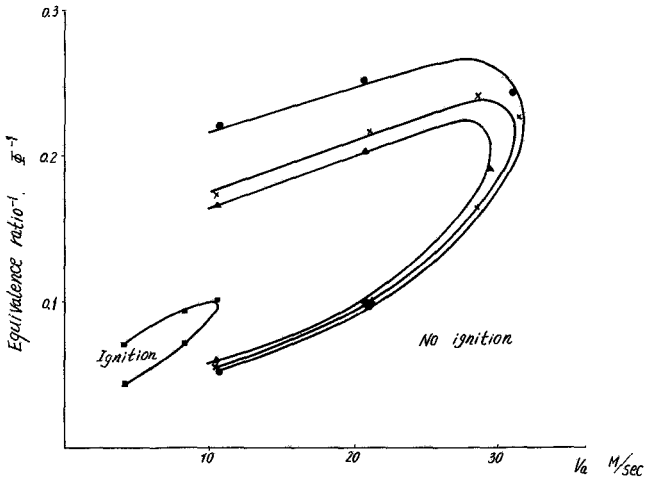

Fig. 4(a)

T_a = 282.8 K
P_a = 34.3 · 10^4 N/M²
■ G_{O_2} = 0
▲ 0.024 g/sec
× 0.0506 g/sec
● 0.20 g/sec
at V_a = 10.4 M/sec
G_a = 1.69 g/sec

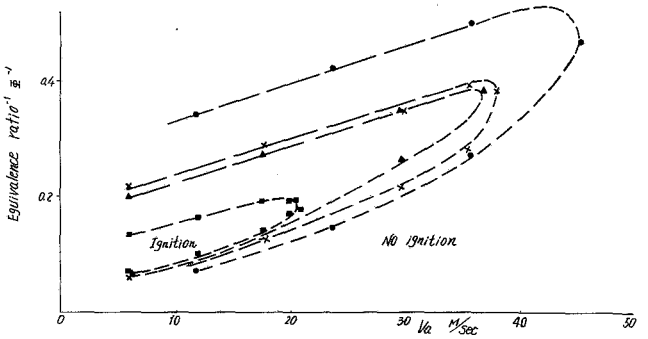

Fig. 4(b)

T_a = 283.2 K
P_a = 61.7 · 10^4 N/M²
■ G_{O_2} = 0
▲ 0.024 g/sec
× 0.0506 g/sec
● 0.20 g/sec
at V_a = 21 M/sec
G_a = 6.15 g/sec

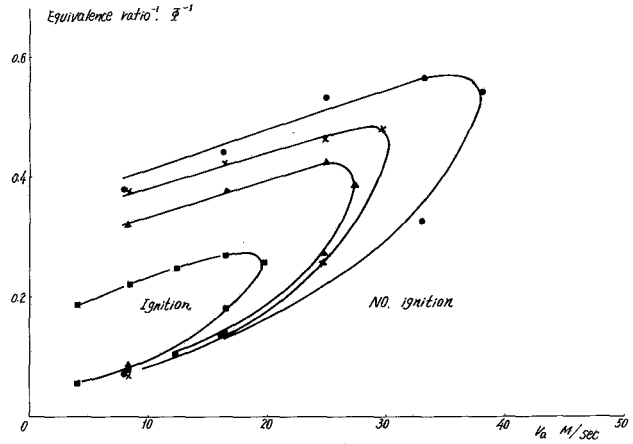

Fig. 4(c)

T_a = 282.4 K
P_a = 882 · 10^4 N/M²
■ G_{O_2} = 0
▲ 0.024 g/sec
× 0.0506 g/sec
● 0.20 g/sec
at V_a = 19.8 M/sec
G_a = 8.2 g/sec

Fig. 4 Ignition loop with uniform oxygen addition

fuel is 1. The effective or vaporized fuel equivalence ratio can be expressed as:

$$\Phi_{\text{eff}} = \Phi_{\text{overall}} \cdot \theta_{\text{evap}}$$

where

Φ_{eff} effective, or vaporized fuel equivalence ratio,
Φ_{overall} overall equivalence ratio
θ_{evap} effective fuel evaporation percentage

At $V_{a\max}$, $\Phi_{\text{eff}} = 1$, $\Phi_{\text{overall}} = \Phi_{\text{opt}}$, thus we have.

$$\theta_{\text{evap}} = \Phi_{\text{opt}}{}^{-1}$$

From Fig. 2, we obtain the effective fuel evaporation percentage for different pressure levels as follows:

Pa	$10^4 \cdot N/M^2$	88.2	61.7	33
θ_{evap}	%	25	18	10

The reason why the effective fuel evaporation percentage increases with pressure is that, the final evaporation percentage is a product of the atomized percentage and the evaporation percentage of the atomized fuel, although the second one does decrease with pressure, but the first one increases sharply with pressure, as can be observed clearly.

As shown in Fig. 3, the effective fuel evaporation percentage is nearly a linear function of air pressure. Figure 3 shows that under low pressure the effective evaporation percentage is very low , most part of liquid fuel injected plays an adverse function for the ignition, the droplets absorb the heat provided by the spark kernel. For the ignitor configuration used the main reason for the low evaporation percentage is low air temperature with a close distance between the fuel injector and the electrodes. Much fuel has not atomized when the droplets reach the spark region.

Figure 4 shows the ignition loops with uniform oxygen addition for three pressure levels. The ignition loops have expanded significantly with oxygen addition, particularly at low pressure level. Also the ignition loop expands more with higher oxygen flow rate, as expected. The ignition limit on fuel "lean" side expands much more than on fuel rich side. This can be explained because with oxygen addition the temperature of initially formed spark flame kernel will be higher, and that will cause more liquid fuel droplets to be vaporized within the kernel, help to broaden to fuel "lean" limit, but contribute very little to fuel rich limit. In Fig. 4 the equivalence ratio was defined as stoichiometric fuel-air ratio with out consideration of oxygen addition. At $V_a = V_{a\max}$, it is also reasonable to assume that the stoichiometric fuel-oxygen (including the added oxygen) exists within the spark region. Following the same manner, the authors are able to calculate the effective fuel vaporization percentage for oxygen addition condition at different pressure levels, as shown in Fig. 3. They are all linear functions of air pressure. The slope is nearly the same. The effective fuel evaporation fraction is also plotted against oxygen fraction O_2/O_2+N_2 in Fig. 5. From Fig. 3 and Fig. 5, it is concluded that the effective fuel evaporation percentage increases with pressure and oxygen concentration. It is interesting to see the importance of fuel evaporation within spark flame kernel for successful ignition. The ignition limits of equivalence ratio are plotted against air pressure at constant air flow velocity $V_a = 20$ M/s in Fig. 6. In fact, at

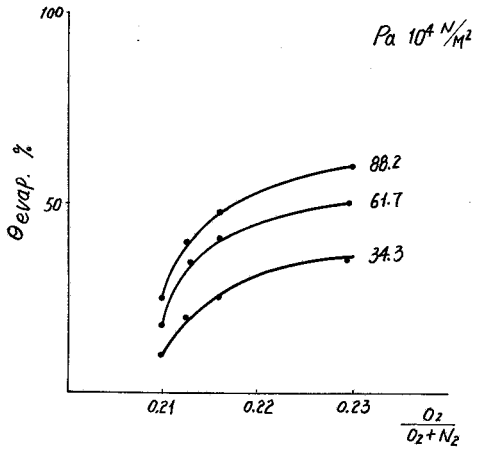

Fig. 5 Effective fuel evaporation percentage versus oxygen fraction

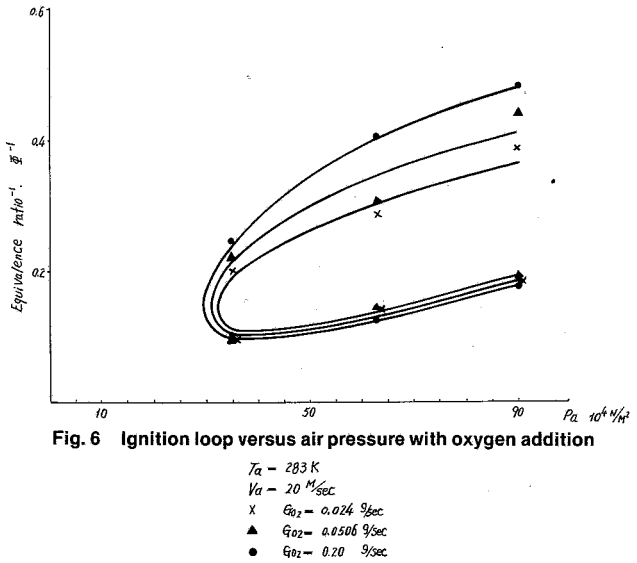

Fig. 6 Ignition loop versus air pressure with oxygen addition

$V_a = 20$ M/s, if there is no oxygen addition, there will be nearly no ignition even at Pa = 88.2 • 10^4 N/M^2. Figure 6 shows clearly again that more oxygen addition will broaden fuel "lean" limit but change fuel rich limit only a little. It shows again the imporance of fuel evaporation on ignition.

Figure 7 shows the maximum ignition velocity versus air pressure for different oxygen addition.It is obvious that at low pressure, the effect of oxygen addition on ignition improvement is more effective.

If we calculate the relative enlargement of maximum ignition velocity defined as

$$\frac{(V_{amax})_{O_2}}{(V_{amax})_{air}}$$

and plot it against oxygen fraction O_2/O_2+N_2, the results are shown in Fig. 8.

Analysis

In [3], the authors presented an ignition model for minimum ignition energy of a flowing combustible mixture with oxygen addition. An equation was proposed for the minimum ignition energy of a combustible flow as follows:

$$H_{\min} = \frac{\beta \cdot C_p(T_f - T_o) \exp(E/RT_f) \cdot (2V_a \cdot t + S)}{N_o \cdot \rho} \quad (1)$$

where:

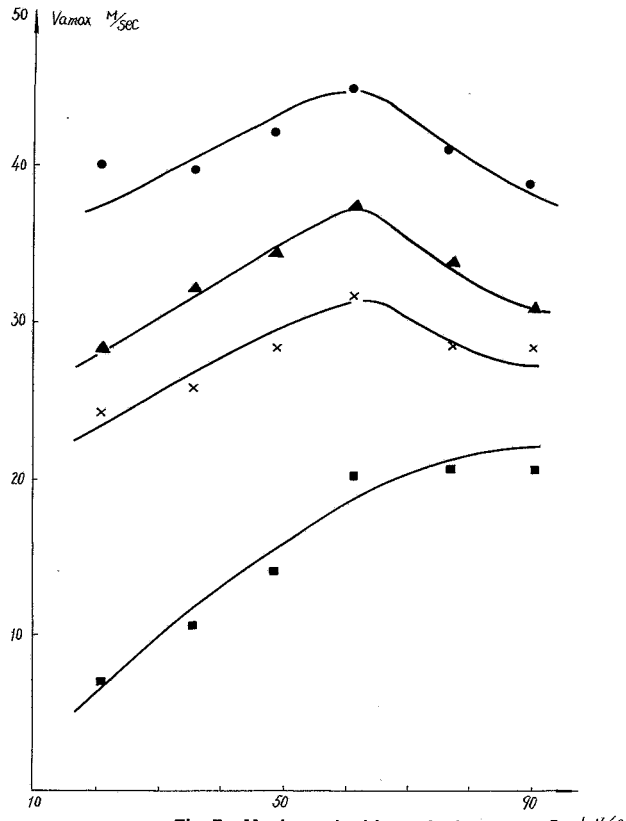

Fig. 7 Maximum ignition velocity

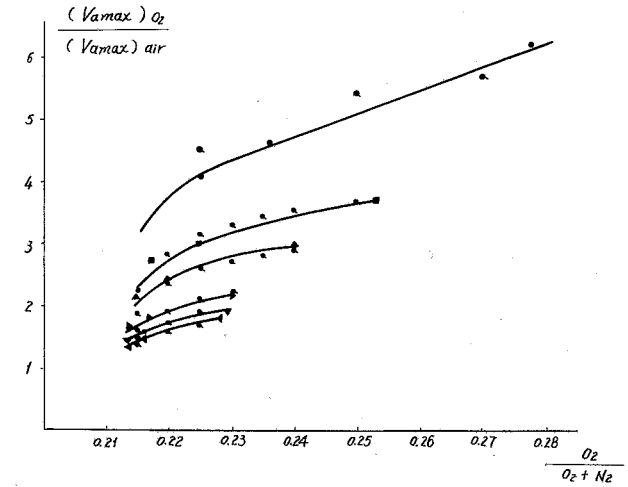

Fig. 8 Relative enlargement of maximum ignition velocity by uniform oxygen addition, experimental data, and prediction

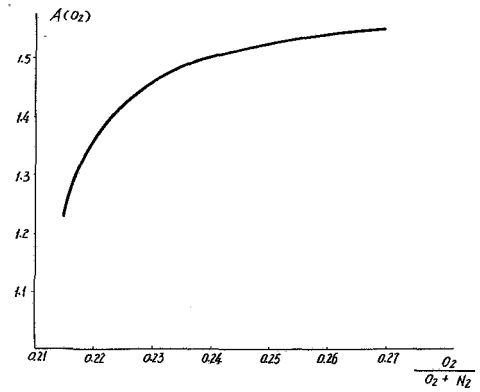

Fig. 9 Ignition improvement factor by oxygen addition

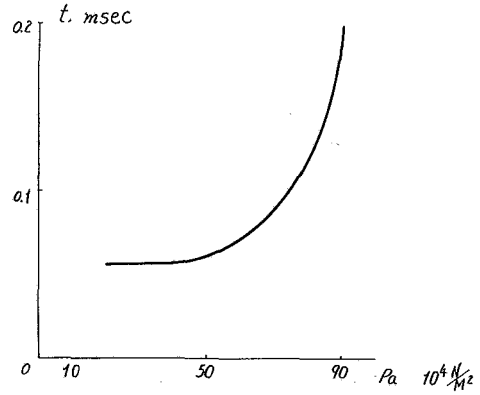

Fig. 10 Correlated spark duration time

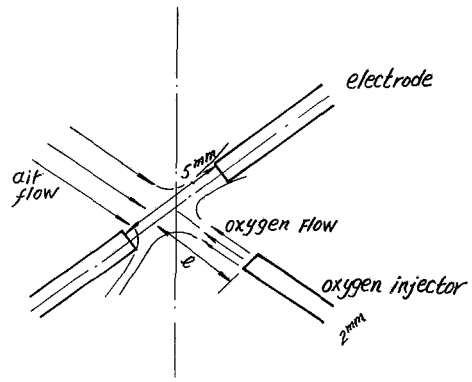

Fig. 11 Local oxygen injection

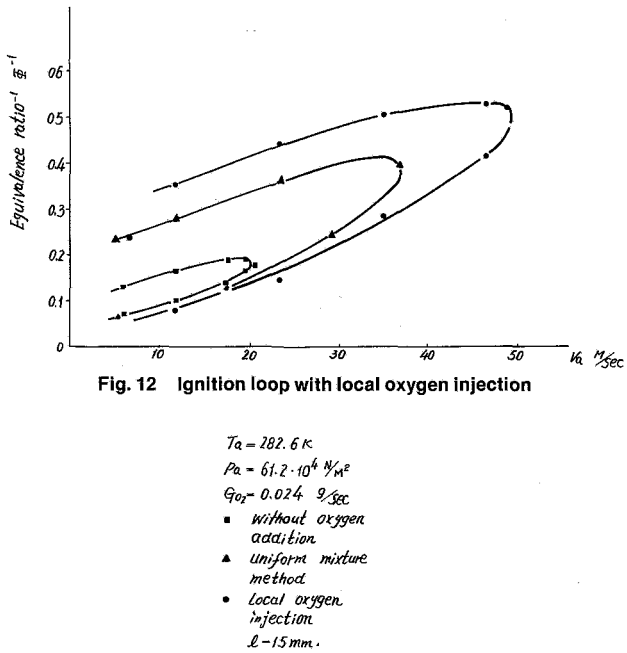

Fig. 12 Ignition loop with local oxygen injection

H_{min} = minimum ignition energy
C_p = specific heat
T_f = flame temperature
T_o = initial temperature
E = activation energy
R = gas constant
t = spark duration time
S = electrode gap distance, in present research $S = 5$ mm
N_o = oxygen concentration
ρ = density
β = constant

Thus the relative enlargement of maximum ignition velocity can be expressed as

$$\frac{2(V_{amax})_{O_2} \cdot t + S}{2(V_{amax})_{air} \cdot t + S} = \frac{C_{pair} \cdot (T_{fair} - T_o)}{C_{pO_2} \cdot (T_{fO_2} - T_o)} \times \left(\frac{No_{O_2}}{No_{air}}\right) \cdot e^{\frac{E}{R} \cdot \left(\frac{1}{T_{fair}} - \frac{1}{T_{fO_2}}\right)} \quad (2)$$

where the subscription O_2 means the conditions with oxygen addition. The right-hand side of the foregoing equation is mainly a function of oxygen concentration, expressed as $A(O_2)$, then the equation can be rewritten as:

$$\frac{(V_{amax})_{O_2}}{(V_{amax})_{air}} = A(O_2) + \frac{S \cdot [A(O_2) - 1]}{2 \cdot t (V_{amax})_{air}} \quad (3)$$

It is not very difficult to calculate $A(O_2)$ as a function of oxygen fraction $O_2/O_2 + N_2$ by equation (2). The calculated result is shown in Fig. 9. But it is not very easy to estimate the spark duration t as function of air velocity and air pressure. Since the maximum air velocity for ignition $(V_{amax})_{air}$ is also a function of air pressure, thus it is reasonable to correlate t as a function of air pressure by the experimental data as shown in Fig. 10. Using equation (3) with t from Fig. 10, $A(O_2)$ from Fig. 9 and $(V_{amax})_{air}$ from Fig. 7, the authors are able to calculate $(V_{amax})_{O_2}/(V_{amax})_{air}$ for different air pressure and oxygen fraction. The calculated values are also shown in Fig. 8 along with the experimental data, and the agreement is excellent. From Fig. 8, it is clear that equation (3) is capable of predicting the relative enlargement of maximum air velocity for ignition by oxygen addition. But the key is how to determine the spark duration for different air velocity and air pressure.

Local Oxygen Injection

In order to compare the effectiveness of oxygen addition by uniform mixture method or by local oxygen injection method, an oxygen injector is installed as shown in Fig. 11. The result is shown in Fig. 12, where the ignition loop without oxygen addition is also presented for comparison purpose. It is always the case that local oxygen injection makes better use of the oxygen added. This may be expressed in the following way. From Fig. 12 for local oxygen injection $(V_{amax})_{O_2 local} = 49.3$ M/s and $(V_{amax})_{O_2 local}/(V_{amax})_{air} = 2.29$; from Fig. 8 we can estimate that in order to obtain the same ignition improvement if it were obtained by uniform mixture method the oxygen percentage would have been 24 percent. That means the oxygen flow rate would have been 0.56 g/s. Now as for local oxygen injection, the oxygen flow rate is only 0.024 g/s.

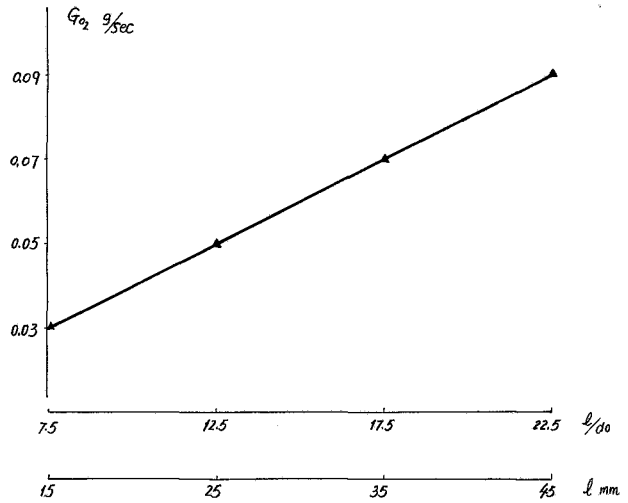

Fig. 13 Oxygen flow rate versus oxygen injection distance for constant ignition performance

$T_a = 283.2K$
$p_a = 61.2 \cdot 10^4\ N/m^2$
$\bar{\varepsilon}^{-1} = 0.283$
$G_a = 14.3$ g/sec
$d_o = 2mm$

The explanation is very simple, the most important factor for successful ignition is the oxygen concentration within spark region, a low oxygen flow rate with local oxygen injection can create a rather high oxygen concentration within spark region just as it is created by a high oxygen flow rate with uniform mixture method.

Another interesting result is obtained by changing the oxygen injection distance l (mm) and increasing the oxygen flow rate to keep the ignition performance constant. Thus a curve of oxygen flow rate versus oxygen injection distance or l/d can be plotted as shown in Fig. 13. In Fig. 13, it is a straight line. This result tells us that there are two factors influencing the ignition improvement by local oxygen injection: the first one is oxygen content within the spark region, the second one is to maintain a low velocity stagnation zone within the spark region. When the oxygen injection distance l is increased, oxygen flow rate, thus oxygen injection velocity must be increased to maintain the oxygen content and the flow velocity within spark region constant. Estimated by jet theory, the straight line in Fig. 13 can be fully interpreted as required by the constant oxygen content and nearly stagnant condition in spark region. Of course, oxygen injection distance l can be only shortened within certain limit; too short a distance will cause quenching effect.

Conclusion

1 Oxygen addition is particular benefitial for low-pressure ignition improvement.

2 Local oxygen injection makes better use of oxygen addition.

3 Equation

$$\frac{(V_{a\max})_{O_2}}{(V_{a\max})_{air}} = A(O_2) + \frac{S \cdot [A(O_2) - 1]}{2 \cdot t (V_{a\max})_{air}}$$

can be used to estimate the enlargement of maximum ignition velocity by oxygen addition.

References

1 Chen, N. K., Zhao, Y. H., Wu, S. S., Zhao, Q. S., and Chin, J. S., "Effect of Oxygen Addition on Low-Pressure Ignition Performance of Aero Gas Turbine Engine at Simulated Altitude Facility," *Journal of Energy*, Nov. 1982, AIAA Paper No. 81-1471, 1981.

2 Chin, J. S., "The Analysis of the Effect of Oxygen Addition on Minimum Ignition Energy," AIAA Paper No. 82-1160, 1982; to be published in *Journal of Energy*.

3 Chin, J. S., "The Effect of Oxygen Addition on the Minimum Ignition Energy of a Homogeneous Combustile Mixture," Research Report BH-B 429, Beijing Institute of Aeronautics Astronautics, 1979.3.

Fuel Effects on Gas Turbine Combustion—Ignition, Stability, and Combustion Efficiency

A. H. Lefebvre[1]
Purdue University,
School of Mechanical Engineering,
West Lafayette, Ind. 47907

An analytical study is made of the substantial body of experimental data acquired during recent Wright-Patterson Aero Propulsion Laboratory sponsored programs on the effects of fuel properties on the performance and reliability of several gas turbine combustors, including J79-17A, J79-17C (Smokeless), F101, TF41, TF39, J85, TF33, and F100. Quantitative relationships are derived between certain key aspects of combustion, notably combustion efficiency, lean blowout limits and lean light-off limits, and the relevant fuel properties, combustor design features, and combustor operating conditions. It is concluded that combustion efficiency, lean blowout limits, and lean lightoff limits are only slightly dependent on fuel chemistry, but are strongly influenced by the physical fuel properties that govern atomization quality and spray evaporation rates.

Introduction

The most dominant fuel issues of today are those of cost and availability. The steps now being taken to ensure future supplies of fuels for gas turbines, in addition to various measures of fuel conservation, include the exploitation of alternative fuel sources and the acceptance of a broader specification for aviation fuels. It is clearly of paramount importance that prediction techniques be established for estimating accurately, for any given combustor, the impact of any change in fuel specification on hardware durability and the key aspects of combustion performance.

One impediment to the attainment of this goal is that the effect of a change in fuel properties is not constant for all combustors but varies between one combustor and another, due to differences in operating conditions and differences in design. An additional complicating factor is that the various properties and characteristics of petroleum fuels are so closely interrelated that it is virtually impossible to change any one property without affecting many others. Thus the classical approach to experimental research, which is based on examination of the effects of varying one independent parameter, while maintaining the others constant, is precluded from the outset.

As far as the actual combustion process is concerned, it is found that chemical reaction rates vary only slightly between the various hydrocarbon fuels of interest to the aircraft gas turbine. This is partly because these fuels exhibit only slight differences in adiabatic flame temperature, but also because before entering the true reaction zone, all the fuels are largely pyrolyzed to methane, other 1-2 carbon atom hydrocarbons, and hydrogen. Hence, the gas composition in the reaction zone is substantially independent of the parent fuel. Thus provided the discussion is restricted to the anticipated range of aircraft fuels, as reflected in Table 1, any differences that occur in ignition performance, lean-blowout limits and combustion efficiency, will be caused mainly by differences in the physical properties of the fuel insofar as they control the quality of atomization and the ensuing rate of evaporation.

Basic Data

In recent years the USAF, Army, Navy, and NASA, along with engine manufacturers, have initiated programs to determine the effects of anticipated future fuels on existing engines. As a result of these studies, data have become available that yield new and useful insights into fuel property effects on combustion performance. These data, that are contained in [1–6], provide the basic material for this investigation.

In addition to a considerable body of evidence on the effects of fuel property variations on the combustion performance and durability characteristics of the combustors investigated, [1–6] also contain detailed information of all the relevant chemical and physical properties of the fuels employed. These fuels were supplied by the U.S. Air Force for combustion system evaluation. They included a current JP4, a current JP8, five blends of the JP4, five blends of the JP8 and, in some cases, a No. 2 diesel fuel. The blends were intended to achieve three different levels of hydrogen content; i.e. 12, 13 and 14 percent by mass.

The rationale for the diesel fuel was to approximate the Experimental Referee Broad Specification (ERBS) aviation fuel that emanated from the NASA-Lewis Workshop on Jet Aircraft Hydrocarbon Fuel Technology [7]. The JP4, JP8 fuels, and their blends were chosen to span systematically the

[1] Reilly Professor of Combustion Engineering.

Contributed by the Gas Turbine Division of THE AMERICAN SOCIETY OF MECHANICAL ENGINEERS and presented at the 29th International Gas Turbine Conference and Exhibit, Amsterdam, The Netherlands, June 4–7, 1984. Manuscript received at ASME Headquarters January 6, 1984. Paper No. 84-GT-87.

Table 1 Test fuel chemical and physical properties

Fuel components		Hydrogen content H	Heating value	Density	Viscosity	Surface tension	Vapor pressure
Base fuel	Blending agents	weight %	(net) MJ/kg	$\rho_{300\,K}$ kg/m^3	$\nu_{300\,K}$ mm^2/s	$\sigma_{300\,K}$ mN/m	$P_{300\,K}$ kPa
JP-4	–	14.5	43.603	752.7	0.924	23.27	12.04
JP-8	–	14.0	43.210	799.5	1.849	25.85	2.15
JP-8	Gulf mineral seal oil	13.9	43.189	801.2	2.071	25.92	1.97
JP-8	2040 solvent	12.0	41.947	852.3	1.809	27.62	1.16
JP-8	Xylene bottoms	13.0	42.724	813.4	1.428	26.38	1.48
JP-8	Xylene bottoms	12.0	42.129	827.6	1.160	26.66	1.33
JP-8	2040	13.0	42.556	825.2	1.804	26.42	1.38
JP-4	2040	12.0	42.203	829.7	1.141	25.22	7.38
JP-4	2040	13.0	42.629	796.3	1.028	23.75	8.61
JP-4	Xylene	12.0	42.196	808.0	0.830	25.21	6.17
JP-4	Xylene	13.0	42.682	786.5	0.835	24.20	9.06
JP-4	Xylene & GMSO	14.0	43.366	769.6	1.057	23.45	10.25
2-D	–	13.1	42.691	837.2	3.245	27.35	1.59

possible fuel variations in key properties that might be dictated in the future on grounds of availability and cost, and the use of non-petroleum sources for jet fuel production.

The key chemical and physical properties of the fuels selected are listed in Table 1. Additional information on the distillation characteristics of the test fuels is contained in Fig. 1.

Fuel Atomization

The quality of the experimental data contained in [1–6] is generally high. Although detailed information on the main liner dimensions and airflow distribution is somewhat sparse, it was usually possible to deduce these parameters to an acceptable level of accuracy. Only in one area, namely that of fuel atomization, did lack of accurate information prove a real impediment to the investigation. It is strongly advised that in future experimental studies on fuel effects every effort should be made to determine mean drop size and drop-size distribution for all fuels over wide ranges of combustor operating conditions.

In the absence of actual measured values, the mean drop size (SMD) was calculated using one of the following two expressions

For airblast atomizers [8]

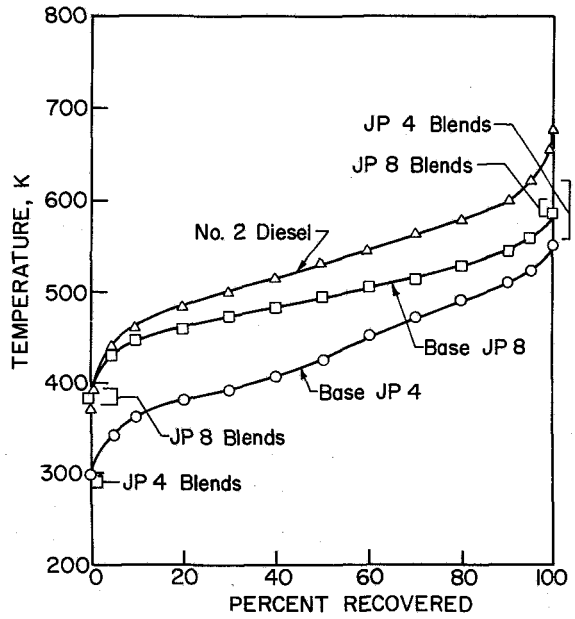

Fig. 1 Distillation characteristics of test fuels [2]

Nomenclature

A = area, m^2
B = mass transfer number
b = constant in equation (18)
A', B' = constants in equations (27 and 32)
C_1, C_2, C_3 = constants in equation (13)
C_4, C_5 = constants in equation (33)
c_p = specific heat at constant pressure, J/kg K
D_h = hydraulic mean diameter of atomizer air duct at exit plane, m
D_L = liner diameter or height, m
D_0 = initial mean drop size of fuel spray, m
D_p = atomizer prefilmer diameter, m
D_r = mean drop size relative to that for JP4
E_{min} = minimum ignition energy, J
f_c = fraction of total combustor air employed in combustion
f_{pz} = fraction of total combustor air employed in primary-zone combustion
f_f = fraction of fuel vaporized within combustion zone
k = thermal conductivity, J/ms K
L = length
L_c = length of combustion zone, m
L_L = total liner length, m
LCV = lower calorific value of fuel, J/kg
LCV_r = lower calorific value relative to JP4
$\dot{m}$ = mass flow rate, kg/s
n = reaction order
P = pressure, kPa
ΔP = pressure differential, kPa
q = fuel/air ratio
q_c = fuel/air ratio in combustion zone
q_{ov} = combustor overall fuel/air ratio
q_{LBO} = fuel/air ratio at lean blowout, g fuel/kg air
q_{LLO} = fuel/air ratio at lean lightup, g fuel/kg air

$$\frac{\text{SMD}}{D_h}\left[1+\frac{\dot{m}_F}{\dot{m}_A}\right]\left[0.33\left(\frac{\sigma_F}{\rho_A U_A{}^2 D_p}\right)^{0.6}\left(\frac{\rho_F}{\rho_A}\right)^{0.1} + 0.068\left(\frac{\mu_F{}^2}{\rho_F \sigma_F D_p}\right)^{0.5}\right] \quad (1)$$

For pressure swirl atomizers [9]

$$\text{SMD} = 0.071\,\sigma_F{}^{0.25}\,\nu_F{}^{0.25}\,\dot{m}_F{}^{0.25}\,\Delta P_F{}^{-0.5}\,\rho_g{}^{-0.25} \quad (2)$$

Equation (1) takes full account of variations in fuel properties (σ_F, ρ_F, and μ_F), air properties (ρ_A and U_A) and atomizer geometry (D_p and D_h). The values of the constants and exponents in this equation were established in a number of experimental studies that covered much wider ranges of fuel and air properties than are needed for the present investigation. Thus the main source of error in the use of equation (1) stems from uncertainties surrounding the values to be assigned to the atomizer dimensions. With equation (2), problems arise in the calculation of ρ_g, since the primary-zone temperature cannot be estimated accurately. Another potentially serious source of error that applies to both equations is that all the experimental work involved in their formulation was carried out under cold, i.e., nonburning, and fairly quiescent conditions. Clearly drop sizes could be appreciably different in the true combustor environment due to the combined effects of high temperature, high turbulence, and strong airflow currents.

Combustion Efficiency

The main factors affecting the level of combustion efficiency are evaporation rates, mixing rates, chemical reaction rates, and the air loading on the combustor. Thus combustion efficiency may be expressed as [10]

$$\eta_c = (\text{air flow rate})^{-1}\left(\frac{1}{\text{evaporation rate}}+\frac{1}{\text{mixing rate}}+\frac{1}{\text{reaction rate}}\right)^{-1} \quad (3)$$

In practical combustion systems, the maximum rate of heat release at any given operating condition may be governed either by evaporation, mixing or chemical reaction, but rarely by all three at the same time. However, over the range of operating conditions where the combustion process is in transition from one regime to another, it is inevitable that two of the three key steps will participate in determining the overall combustion efficiency. Before exploring this situation, it is of interest to examine the separate effects on combustion efficiency of chemical reaction, mixing, and evaporation.

Reaction Rate-Controlled Systems. If evaporation and mixing rates are both infinitely fast, then equation (3) leads directly to the well-known θ parameter [9]

$$\eta_{c_\theta} = \oint\left[\frac{P_3{}^{1.75} A_L D_L{}^{0.75} \exp T_3/300}{\dot{m}_A}\right] \quad (4)$$

This equation is ideally suited and has been widely used in the correlation of experimental data on combustion efficiency obtained with well atomized, light distillate fuels, such as JP4 and Jet A.

As the length of the combustion zone is usually proportional to its diameter or height, H, the foregoing equation may be expressed in terms of combustor volume, V_c, with little loss of accuracy, i.e.,

$$\eta_{c_\theta} = \oint\left[\frac{P_3{}^{1.75} V_c \exp(T_3/300)}{\dot{m}_A}\right] \quad (5)$$

Mixing Rate-Controlled Systems. If evaporation and chemical reaction rates are both infinitely fast, equation (3) becomes

$$\eta_c = \oint(\text{mixing rate/air flow rate})$$

Starting from the assumption that the rate of mixing between the turbulent air jet and the surrounding gas is given by the product of eddy diffusivity, mixing area, and density gradient, it can be shown that [9]

$$\eta_{c_m} = \oint\left[\frac{P_3 A_L}{\dot{m}_A T_3{}^{0.5}}\right]\left[\frac{\Delta P_L}{P_3}\right]^{0.5} \quad (6)$$

Evaporation Rate-Controlled Systems. The third case to consider is when mixing and reaction rates are fast enough for fuel evaporation to be the rate-controlling step. Now for a volume of air, V, containing fuel drops whose initial drop size is D_0, the average rate of fuel evaporation is given by [9]

$$\dot{m}_F = 8(\rho_g/\rho_F)\,(k/c_p)_g\,(V_c/D_0^2)\,q_c \ln(1+B) \times (1+0.22\text{Re}_{D_0}{}^{0.5}) \quad (7)$$

It is assumed that as the fuel evaporates, it instantly mixes and burns with the surrounding air. Thus combustion efficiency is obtained as the ratio of the mass of fuel evaporated within the combustion zone to the mass of fuel supplied, i.e.,

Nomenclature (cont.)

R = gas constant (286.9 m^2/s^2K)
Re_{D_0} = Reynolds number based on initial mean drop size, $(U\rho_A D_0/\mu_A)$
SMD = Sauter mean diameter of fuel spray, m
T = temperature, K
T_{bn} = boiling temperature at normal atmospheric pressure, K
ΔT = temperature rise, K
U = velocity, m/s
V = combustion volume (general), m^3
V_c = total combustion zone volume (= predilution zone volume), m^3
V_{pz} = primary zone volume, m^3
x = constant in equation (18)
μ = dynamic viscosity, kg/ms
ν = kinematic viscosity, m^2/s
ϕ = equivalence ratio
λ_{eff} = effective value of evaporation constant, m^2/s
λ_r = value of λ_{eff} relative to that for JP4
η_c = combustion efficiency
η_{c_θ} = combustion efficiency based on chemical kinetics
η_{c_e} = combustion efficiency based on fuel evaporation
η_{c_m} = combustion efficiency based on mixing rates
ρ = density, kg/m^3
$\oint$ = function of

Subscripts

A = air
F = fuel
g = gas
ad = adiabatic value
st = stoichiometric value
c = combustion zone, or air casing, value
pz = primary zone value
3 = combustor inlet value
4 = combustor outlet value
L = liner

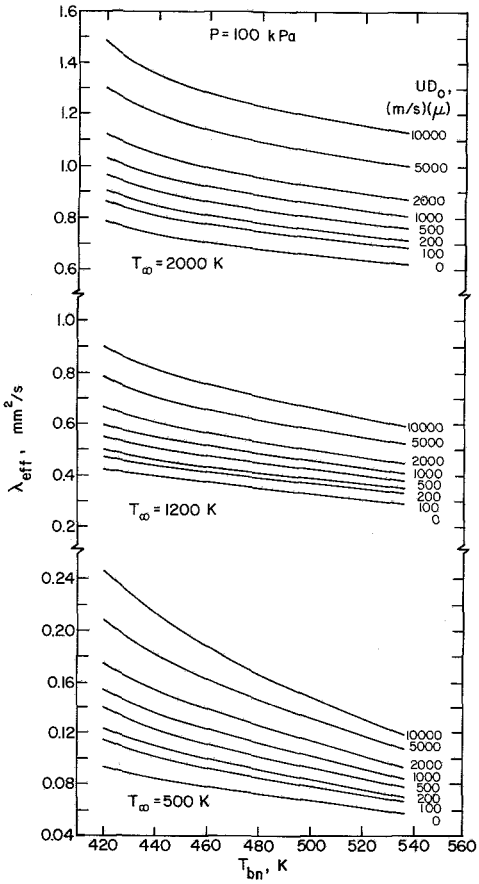

Fig. 2 Variation of effective evaporation constant with normal boiling point at a pressure of 100 kPa

$$\eta_{c_e} = \frac{\dot{m}_F}{q_{ov}\dot{m}_A} \tag{8}$$

$$= \frac{\dot{m}_F}{f_c q_c \dot{m}_A} \tag{9}$$

where f_c is the fraction of the total air flow, $\dot{m}_A$, that participates in combustion.

Substitution of $\dot{m}_F$ from equation (7) into equation (9) gives

$$\eta_{c_e} = 8(\rho_g/\rho_F)\,(k/c_p)_g\,(V_c/f_c\dot{m}_A D^2)x \ln(1+B)(1+0.22\mathrm{Re}_D{}^{0.5}) \tag{10}$$

By making the substitution

$$\lambda_{\mathrm{eff}} = \frac{8(k/c_p)_g \ln(1+B)(1+0.22\mathrm{Re}_{D_0}{}^{0.5})}{\rho_F} \tag{11}$$

where λ_{eff} is an average or "effective" value of the evaporation constant during the drop lifetime [11], equation (10) becomes

$$\eta_{c_e} = \lambda_{\mathrm{eff}}\rho_g V_c[f_c\dot{m}_A D_0{}^2]^{-1} \tag{12}$$

It should be noted that the form of equations (10) and (12) allows η_{c_e} to exceed unity. When this occurs it simply means that the time required for fuel evaporation is less than the time available, so the fuel is fully vaporized within the primary recirculation zone. In these circumstances η_{c_e} should be assigned a value of unity.

Equations (10) and (12) relate combustion efficiency to combustor dimensions (via V_c), combustor operating conditions (via k_g, c_{p_g} and ρ_g), fuel nozzle characteristics (via D_0), and fuel type (via ρ_F and B, or λ_{eff}).

Values of λ_{eff} are shown plotted in Fig. 2. This figure contains plots of λ_{eff} versus T_{bn} at three levels of ambient temperature, namely 500, 1200, and 2000 K. For each value of temperature several lines are drawn to represent different values of UD_0, where U is the relative velocity betweeen the fuel drop and the surrounding gas, and D_0 is the initial drop diameter. Similar plots, for ambient pressures of 1000 kPa and 2000 kPa, may be found in [11].

The parameter T_{bn}, fuel boiling temperature (K) at normal atmosphere pressure, was chosen to represent the fuels' propensity for evaporation. It is recognized that no single chemical or physical property is completely satisfactory for this purpose. However, the average boiling point (50 percent recovered) has much to commend it, since it is directly related to fuel volatility and fuel vapor pressure. It also has the virtue of being easy to measure, and is usually quoted in fuel specifications.

From a practical standpoint the concept of λ_{eff} has considerable advantages, since it takes into account the reduced rate of evaporation that occurs during the initial droplet heat-up period, as well as the enhancement of fuel evaporation rates due to the effects of forced convection. Thus plots of λ_{eff} of the type shown in Fig. 2 greatly simplify calculations on rates of spray evaporation and drop lifetimes.

General Case. For the general case in which evaporation, mixing, and chemical reaction processes could all influence the total rate of combustion, either singly or in combination, an appropriate expression for combustion efficiency may be obtained by substituting equations (5), (6), and (12) into equation (3) to obtain

$$\eta_c = \left[\frac{P_3 V_c}{\dot{m}_A}\right]\left[\frac{C_1 f_c D_0^2 T_g}{\lambda_{\mathrm{eff}}} + \frac{C_2 L_c T_3{}^{0.5}}{(\Delta P_L/P_3)^{0.5}} + \frac{C_3}{P_3{}^{0.75}\exp(T_3/300)}\right]^{-1} \tag{13}$$

The constant C_1 in the foregoing equation is included in order to take into account possible effects of droplet interaction on the rate of fuel evaporation. C_2 represents a turbulent diffusion coefficient, while C_3 is the collision factor for the chemical reaction.

Reaction Rate- and Evaporation Rate-Controlled Systems. In practice, it is difficult to assess the importance of mixing rates to combustion efficiency. This is due partly to lack of accurate information on the liner pressure drop parameter, $\Delta P_L/P_3$, but mainly to the fact that mixing rates tend to be limiting only at conditions where the level of combustion efficiency is close to 100 percent, so that deficiencies in performance due to mixing are difficult to discern. For these reasons, it is often preferable to express combustion efficiency as the product of the θ efficiency, η_{c_θ}, and the evaporation efficiency, η_{c_e}, i.e.,

$$\eta_c = \eta_{c_\theta} x \eta_{c_e} \tag{14}$$

The second term on the right-hand side of equation (14) i.e., η_{c_e} from equation (12), represents the fraction of the fuel that is vaporized within the combustion zone. For $\eta_{c_e} \geq 1$, $\eta_c = \eta_{c_\theta}$, and equation (14) reverts to the θ parameter, which denotes the fraction of fuel vapor that is converted into combustion products by chemical reaction.

From analysis of the available experimental data on combustion efficiency the following expressions for η_{c_θ} and η_{c_e} were derived.

$$\eta_{c_\theta} = 1 - \exp\left[\frac{-0.022 P_3{}^{1.3} V_c \exp(T_c/400)}{f_c \dot{m}_A}\right] \tag{15}$$

and

$$\eta_{c_e} = 1 - \exp\left[\frac{-36\times10^{-6} P_3 V_c \lambda_{\mathrm{eff}}}{T_c D_0{}^2 f_c \dot{m}_A}\right] \tag{16}$$

It should be noted in equation (15) that the pressure

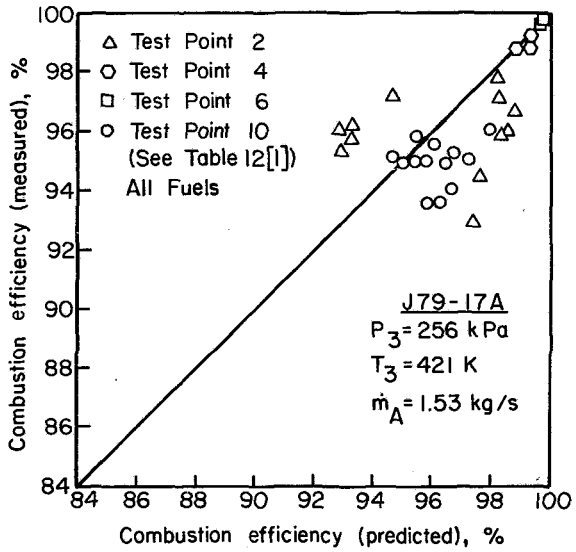

Fig. 3 Comparison of measured and predicted values of combustion efficiency for J79-17A combustor

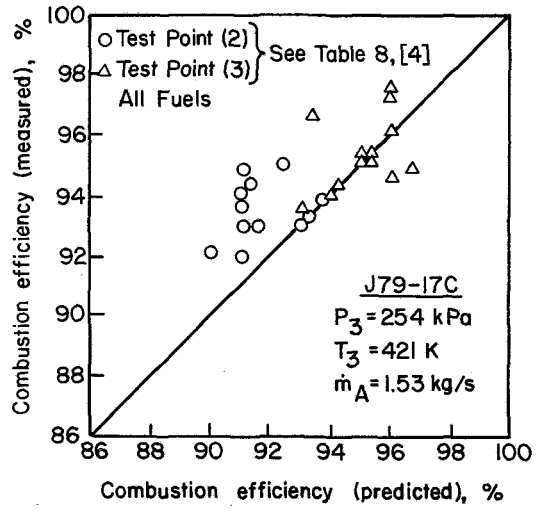

Fig. 4 Comparison of measured and predicted values of combustion efficiency for J79-17C combustor

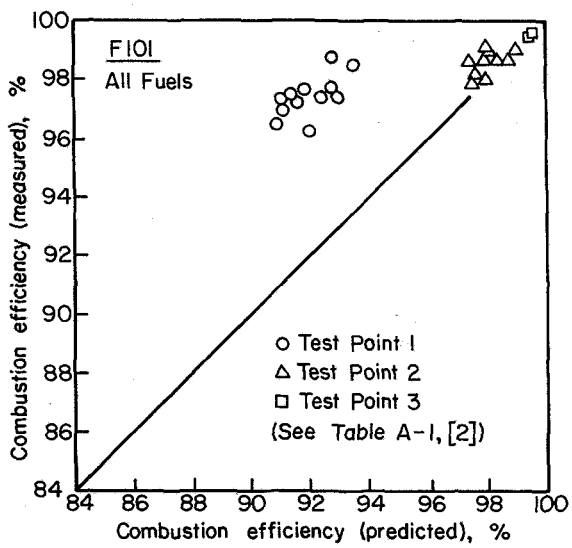

Fig. 5 Comparison of measured and predicted values of combustion efficiency for F101 combustor

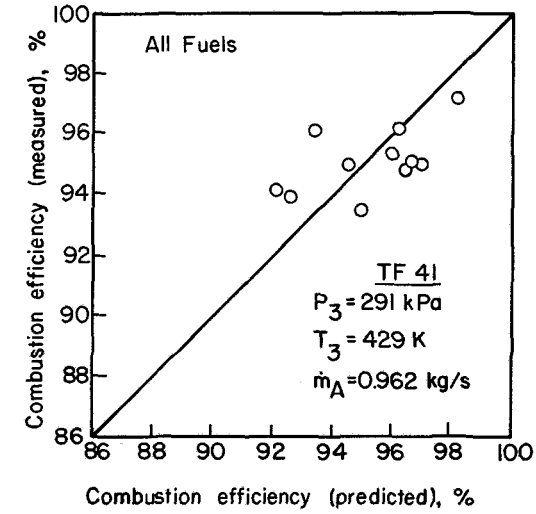

Fig. 6 Comparison of measured and predicted values of combustion efficiency for TF 41 combustor

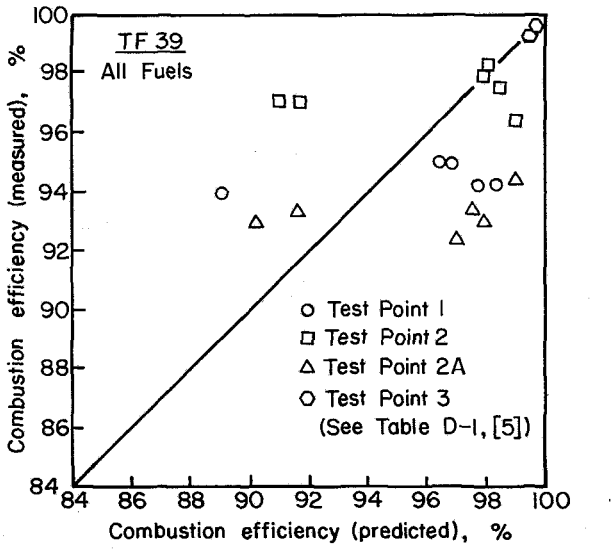

Fig. 7 Comparison of measured and predicted values of combustion efficiency for TF39 combustor

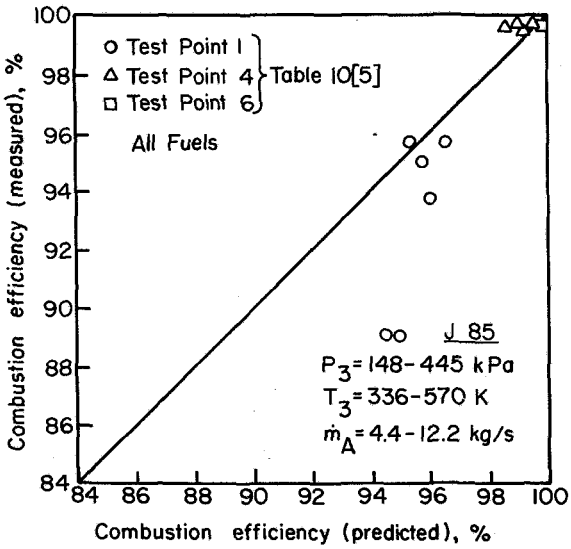

Fig. 8 Comparison of measured and predicted values of combustion efficiency for J85 combustor

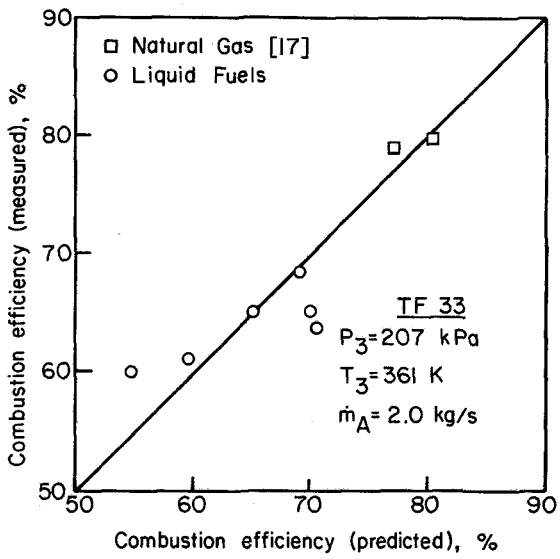

Fig. 9 Comparison of measured and predicted values of combustion efficiency for TF 33 combustor

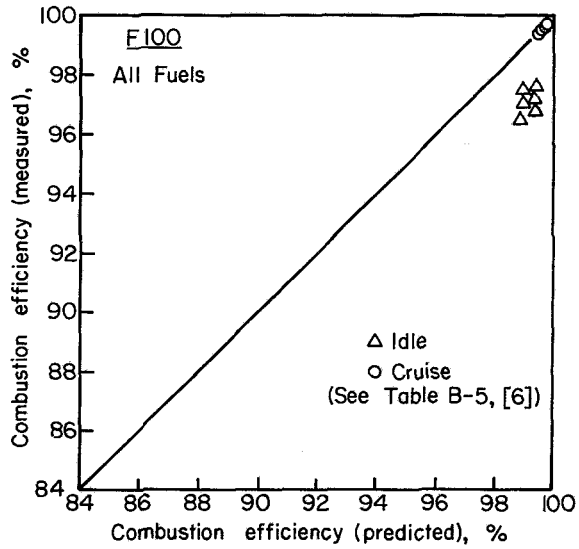

Fig. 10 Comparison of measured and predicted values of combustion efficiency for F100 combustor

dependence is reduced from 1.75 to 1.3. This is because the exponent of 1.75 was determined from tests conducted in the pressure range from 40 to 200 kPa. In the present study, the data on combustion efficiency were obtained at higher pressure levels, where the intervention of mixing rates tends to lower the pressure exponent, in this case to a value of 1.3. Another noteworthy point is that temperature dependence is now expressed in terms of T_c rather than T_3. Either may be used (with suitable adjustment to the constant), but T_c was found to give the best correlation. T_c is the adiabatic flame temperature in the primary zone, assuming complete combustion of the fuel. It is calculated from the expression

$$T_c = T_3 + \Delta T_c \tag{17}$$

where ΔT_c is obtained from standard temperature rise charts for the fuel in question, using appropriate values of P_3, T_3, and q_c $(=q_{ov}/f_c)$.

Values of mean drop size, D_0, may be calculated from equation (1) or equation (2) using the information on fuel nozzle characteristics supplied in [1–6]. The very satisfactory correlation of combustion efficiency data provided by equation (14) is demonstrated in Figs. 3–10. These figures include all the relevant data on combustion efficiency contained in [1–6]. However, it should be noted that for some combustors the combustion efficiency data provided did not include all fuels. Moreover, where both predicted and measured values of combustion lie close to 100 percent, the results obtained for all fuels are virtually the same and are indicated on the graphs by a single point.

Lean Blowout

Until the early 1970s, the problem of lean blowout was always regarded as relatively minor. To a large extent this was due to the almost universal use of pressure-swirl spray atomizers of the duplex or dual-orifice type. The poor mixing characteristics of these pressure-swirl atomizers create many performance problems, not the least being a high rate of soot formation in the primary zone. However, this same poor mixing of fuel and primary air has the useful advantage of allowing combustion to occur, albeit with low combustion efficiency, at mixture strengths well below the normal weak extinction limit. In fact, lean blowout limits in excess of 1000 AFR, based on overall combustor values of air and fuel flow rates, used to be quite commonplace. In recent years, the continuing trend toward improved fuel-air mixing prior to combustion in order to reduce pollutant emissions, especially NO_x and smoke, has led to a narrowing of stability limits and to increasing concern over the attainment of satisfactory lean blowout performance.

For homogeneous fuel-air mixtures, flame blowout occurs when the rate of heat liberation in the primary zone becomes insufficient to heat the incoming fresh mixture up to the required reaction temperature. With heterogeneous mixtures, however, an additional factor is the time required for fuel evaporation. For fuel sprays of low volatility and large mean drop size this time is relatively long and is often the main factor limiting the overall rate of heat release. In the analysis of lean blowout limits, it is convenient to consider homogeneous mixtures first and then to examine how the results obtained should be modified to take account of fuel evaporation.

For homogeneous mixtures, it has been shown that the lean blowout fuel/air ratio depends on the inlet air velocity, pressure, and temperature, and on the size of the combustion zone [12]. The relationship is of the form

$$q_{\mathrm{LBO}} \alpha \left[\frac{\dot{m}_A}{V P_3{}^n \exp(T_3/b)} \right]^x \tag{18}$$

where n is the reaction order, and x is a constant to be determined experimentally. Equation (18) was used by Ballal and Lefebvre [12] to correlate measured values of weak extinction equivalence ratio for propane-air flames stabilized on bluff-body flameholders, using experimental data to determine optimum values of n, b, and x.

Equation (18) may also be used to predict the lean blowout limits of combustion chambers supplied with heterogeneous fuel-air mixtures, provided that the rate of fuel evaporation is sufficiently high to ensure that all the fuel is fully vaporized within the primary combustion zone. If the fuel does not fully vaporize, then clearly the "effective" fuel/air ratio will be lower than the nominal value. However, if the fraction of fuel that is vaporized is known, or can be calculated, it can be combined with equation (18) to yield the fuel/air ratio at lean blowout, i.e.,

$$q_{\mathrm{LBO}_{(\mathrm{heterogeneous})}} = q_{\mathrm{LBO}_{(\mathrm{homogeneous})}} x f_f{}^{-1} \tag{19}$$

where f_f is the fraction of fuel that is vaporized within the primary combustion zone.

From analysis of the factors governing the rate of evaporation of a fuel spray, it was found [13] that

$$f_f = 8(\rho_g/\rho_F)\,(k/c_p)_g \ln(1+B)x \\ (V_{pz}/\dot{m}_{pz}D_0{}^2)(1+0.22\,\mathrm{Re}_{D_0}{}^{0.5}) \quad (20)$$

or, substituting for

$$\lambda_{\mathrm{eff}} \simeq \frac{8(k/c_p)_g \ln(1+B)(1+0.22\,\mathrm{Re}_{D0}{}^{0.5})}{\rho_F} \quad (21)$$

$$f_f = \frac{8\rho_g V_{pz}\lambda_{\mathrm{eff}}}{\dot{m}_{pz}D_0{}^2} = \frac{8\rho_g V_{pz}\lambda_{\mathrm{eff}}}{f_{pz}\dot{m}_A D_0{}^2} \quad (22)$$

If the value of f_f determined from equations (20) and (22) exceeds unity, this means that the time required for fuel evaporation is less than the time available so that the fuel is fully vaporized within the recirculation zone. f_f should then be assigned a value of 1.0, so that

$$q_{\mathrm{LBO(heterogeneous)}} = q_{\mathrm{LBO(homogeneous)}} \quad (23)$$

Substitution of $q_{\mathrm{LBO(hom)}}$ from equation (18) and f_f from equation (22) into equation (19) gives

$$q_{\mathrm{LBO}} \propto \frac{f_{pz}\dot{m}_A{}^{(1+x)}D_0{}^2}{V_{pz}{}^{(1+x)}P_3{}^{(1+nx)}\exp(xT_3/b)\lambda_{\mathrm{eff}}} \quad (24)$$

An additional term to be incorporated into equation (24) is the heating value of the fuel. This stems from the assumption that for any given operating condition the lean blowout temperature is the same for all hydrocarbon fuel-air mixtures. This means that fuels with a high gravimetric heat content should be capable of burning down to weaker mixture strengths than fuels having a lower heat content. With this modification, equation (24) becomes

$$q_{\mathrm{LBO}} \propto \left[\frac{f_{pz}}{V_{pz}{}^{(1+x)}}\right]\left[\frac{\dot{m}_A{}^{(1+x)}}{P_3{}^{(1+nx)}\exp(xT_3/b)}\right]\left[\frac{D_0{}^2}{\lambda_{\mathrm{eff}}\mathrm{LCV}}\right] \quad (25)$$

The first term on the right-hand side of the foregoing expression is a function of combustor design. The second term represents the combustor operating conditions. The third term embodies the relevant fuel-dependent properties.

Unfortunately, the available experimental data do not allow the values of n and x to be determined with any degree of accuracy. This is mainly because that for gas turbine combustors the air mass flow rate is always roughly proportional to air pressure, which makes it very difficult to isolate their separate effects on q_{LBO}. All that can reasonably be deduced from equation (25) is that the exponents of $\dot{m}_A$ and V_{pz} should be the same and that the pressure exponent should be somewhat higher by an amount depending on the effective reaction order. Analysis of the experimental data on q_{LBO} suggests, in fact, that the pressure exponent is about 30 percent larger than that of the air mass flow rate. Also, the temperature dependence corresponds to the relationship

$$q_{\mathrm{LBO}} \propto \exp -(T_3/300)$$

Thus the simplest form in which equation (25) can be expressed that is consistent with the experimental data is

$$q_{\mathrm{LBO}} = \left(\frac{A''f_{pz}}{V_{pz}}\right)\left(\frac{\dot{m}_A}{P_3{}^{1.3}\exp(T_3/300)}\right)\left(\frac{D_0{}^2}{\lambda_{\mathrm{eff}}\mathrm{LCV}}\right) \quad (26)$$

where A'' is a constant whose value depends on the geometry and mixing characteristics of the combustion zone and must be arrived at experimentally. Having determined the value of A'' at any convenient test condition, equation (26) may then be used to predict the lean blowout fuel/air ratio at any other operating condition.

One problem with equation (26) is that of assigning appropriate values of V_{pz} to all the combustors under consideration. Although values of f_{pz}, the fraction of the total combustor airflow entering the primary zone, were either quoted directly in [1–6], or could easily be estimated, only in one or two cases could the corresponding primary-zone volume be assessed to the desired level of accuracy. To surmount this problem it was decided to substitute the predilution volume, V_c, into equation (26), instead of V_{pz}. This could be justified on the grounds that more accurate values of V_c were available and, in fact, had already been used in the correlation of combustion efficiency data. Moreover, as the ratio of primary-zone volume to predilution volume tends to be fairly constant for most conventional combustion chambers, using V_c instead of V_{pz} has the virtue of consistency without undue sacrifice in accuracy.

A more serious drawback to equation (26) is that its solution demands an accurate knowledge of mean drop size over the entire range of operating conditions. As drop sizes were neither measured nor can they be estimated with sufficient accuracy, this obstacle would appear to rule out the application of this equation to the present task. However, since the main objective is to study fuel effects, the problem can be circumvented by rewriting equation (26) in a different form, such that the fuel-dependent properties are expressed relative to those of the baseline fuel, JP4. With these modifications, equation (26) becomes

$$q_{\mathrm{LBO}} = \frac{A'f_{pz}\dot{m}_A}{V_c P_3{}^{1.3}\exp(T_3/300)} \times \frac{D_r{}^2}{\lambda_r \mathrm{LCV}_r} \times \left(\frac{D \text{ at } T_F}{D \text{ at } 277.5\ \mathrm{K}}\right)^2 \quad (27)$$

where:

D_r = mean drop size relative to that for JP4
LCV_r = lower calorific value relative to that for JP4
λ_r = effective evaporation constant relative to that for JP4 at T_{pz} and P_3

The term $(D \text{ at } T_F)^2/(D \text{ at } 277.5)^2$ is introduced to take into account the variation in drop size arising from a change in fuel temperature from the initial baseline value, which is taken as 277.5 K.

The correlations of lean blowout limits provided by equation (27), using appropriate values of A', are illustrated in Figs. 11–21. The close agreement exhibited betweeen the predicted and the measured values of lean blowout fuel/air ratio is clearly very satisfactory. However, because the measured values of q_{LBO} for the F101 seemed much too high, only the correlation obtained with one fuel is shown in Fig. 15 to demonstrate the ability of equation (27) to predict the effect of changes in T_3 and T_F on the lean blowout limits of this combustor.

For each combustor, a value of A' was chosen for insertion into equation (27) that would provide the best fit to the experimental data. These values of A'' are given in Table 2. It was anticipated that similar types of primary zones would yield similar values of A', which would clearly be ad-

Table 2 Values of A' and B' employed in equations (27) and (32)

Engine	A'	$A'f_{pz}$	B'	$B'f_{pz}$
J79-17A	185	42	870	199
J79-17C	100	31	–	–
F101	79	32	222	99
TF 41	46	13	228	634
TF 39	123	37	704	211
J85	213	64	597	179
TF 33	85	25.4	726	274
F100	65	23	483	170

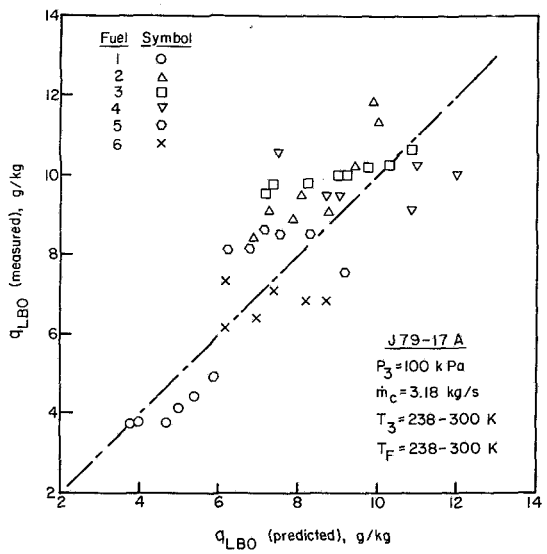

Fig. 11 Comparison of measured and predicted values of q_{LBO} for J79-17A combustor (Fuels 1-6)

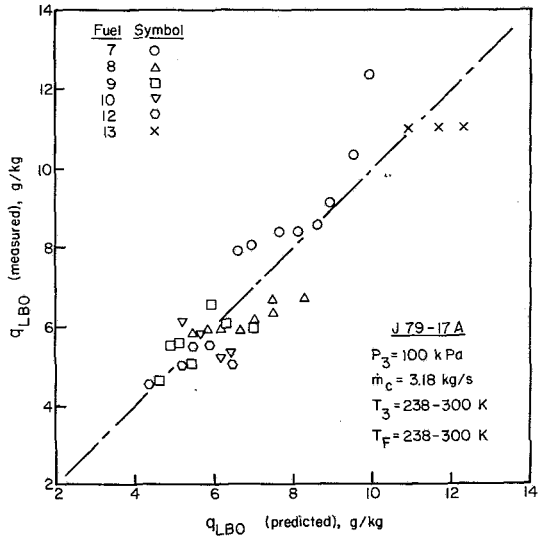

Fig. 12 Comparison of measured and predicted values of q_{LBO} for J79-17A combustor (Fuels 7-13)

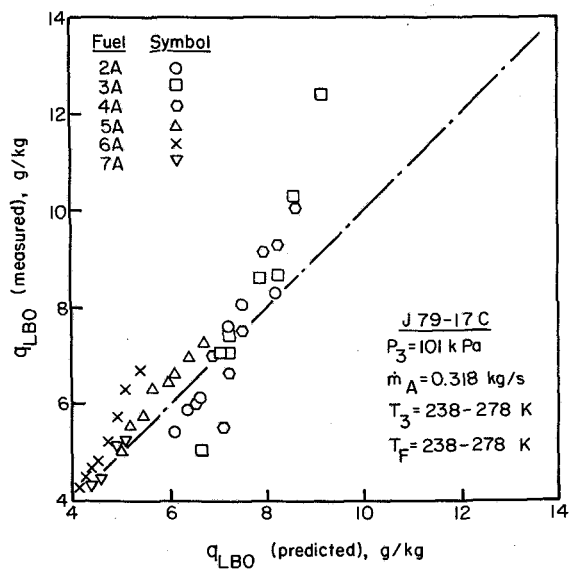

Fig. 13 Comparison of measured and predicted values of q_{LBO} for J79-17C combustor (Fuels 2A-7A)

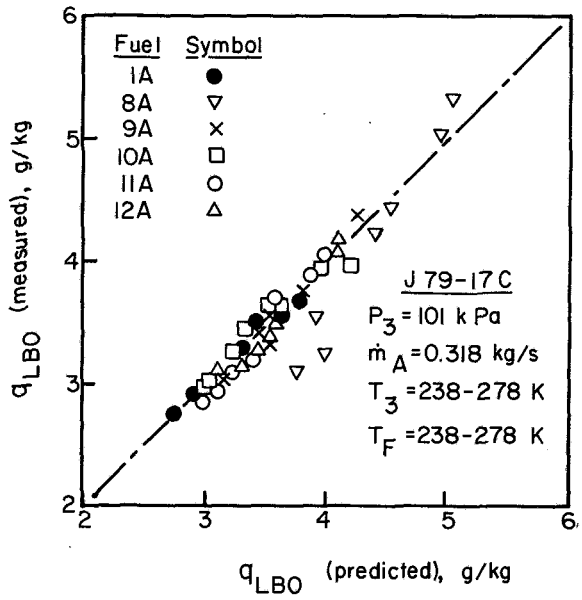

Fig. 14 Comparison of measured and predicted values of q_{LBO} for J79-17C combustor (Fuels 1A and 8A-12A)

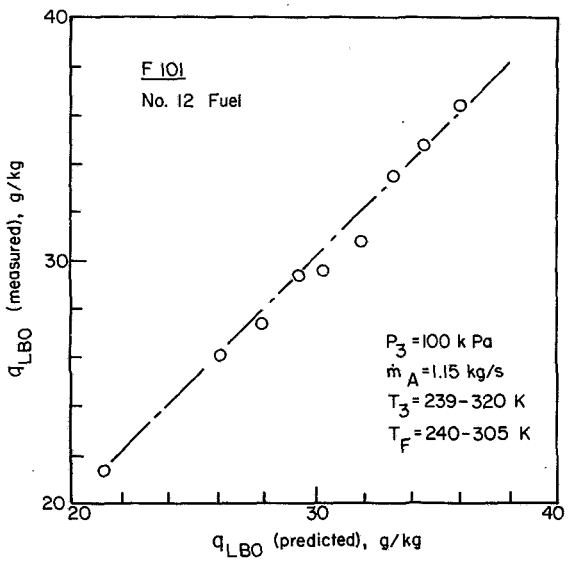

Fig. 15 Comparison of measured and predicted values of q_{LBO} for F101 combustor

vantageous from the standpoint of predicting the lean blowout limits of future combustor designs. Although the variation in the values of A' exhibited in Table 2 virtually prohibits such extrapolation, it should be borne in mind that these values embody all the errors incurred in the estimates of combustion volume, the fraction of air involved in primary combustion, and the mean drop size. If these parameters could be established accurately, then it should be possible to determine an appropriate value of A' for each characteristic primary zone/nozzle configuration. By combining A' with f_{pz}, the deviation is reduced somewhat, as illustrated in Table 2. The exceptionally low value of $A'f_{pz}$ for the TF41 combustor can be attributed to its excellent atomization characteristics at low fuel flows, stemming from the use of an exceptionally low primary nozzle flow number. Initially, an unusually high value of $A'f_{pz}$ was calculated for the F101 combustor. This could be the result of an error in the recording of either fuel flow rate of air flow rate, due possibly to the fact that the tests were conducted on a 54 deg segment

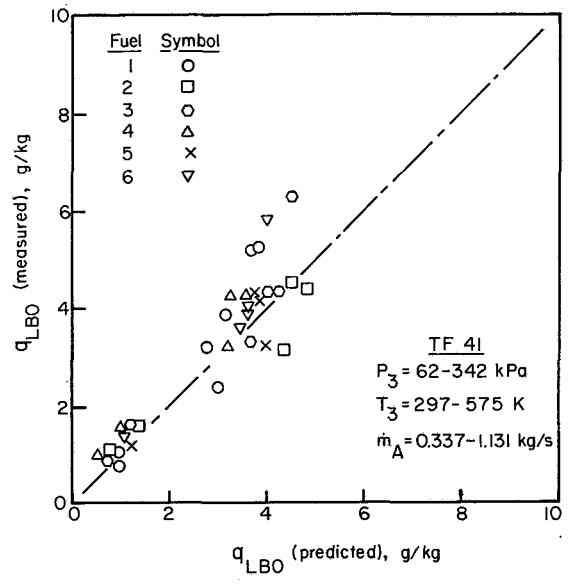

Fig. 16 Comparison of measured and predicted values of q_{LBO} for TF 41 combustor (Fuels 1-6)

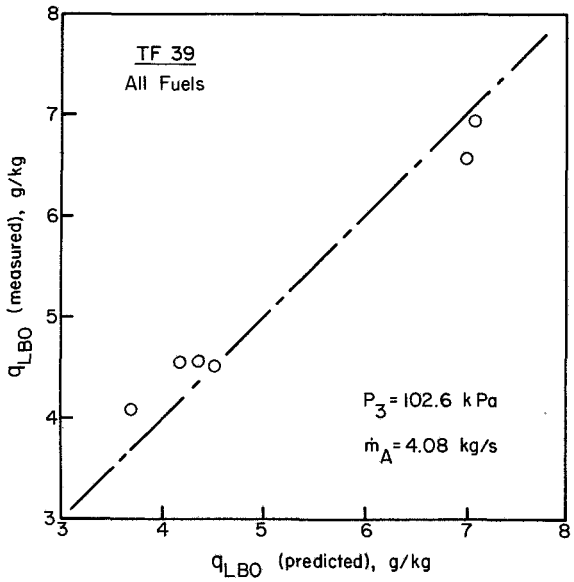

Fig. 18 Comparison of measured and predicted values of q_{LBO} for TF 39 combustor. Plotted points represent average of five values of fuel and air temperatures between 255 and 277 K.

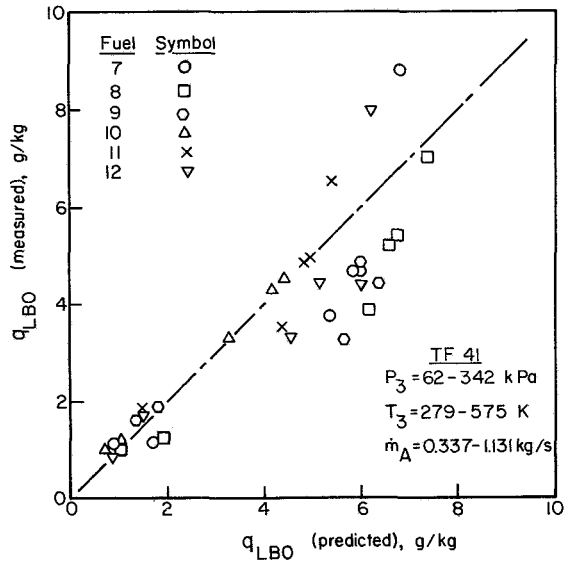

Fig. 17 Comparison of measured and predicted values of q_{LBO} for TF 41 combustor (Fuels 7-12)

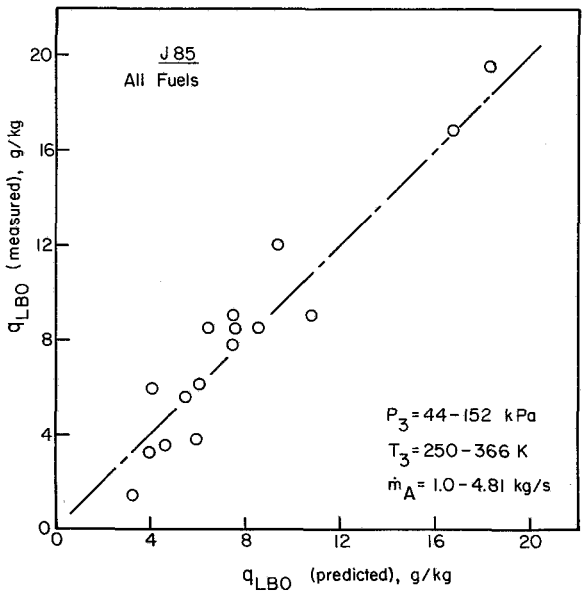

Fig. 19 Comparison of measured and predicted values of q_{LBO} for J85 combustor

of the full annular combustor. If the tabulated results in [2] were accepted at face value, they would imply that the engine was in danger of flame-out at take off, which is highly unlikely. Dividing the published values of q_{LBO} by (360/54) reduces $A'f_{pz}$ to 32, which is fully consistent with the results obtained for the other combustors.

Ignition

In recent years, a series of detailed experimental studies has been carried out on the influence of electrical and flow parameters on minimum spark energy in flowing mixtures of fuel drops and air [14–16]. These studies have led to a better conceptual understanding of the basic ignition process and have provided a useful theoretical foundation for relating ignition characteristics to all the operating variables involved. They confirm practical experience in showing that ignition is made easier by increases in pressure, temperature and spark energy, and is impeded by increases in velocity and turbulence intensity. They also emphasize that ignition performance is markedly affected by fuel properties through the way in which they influence the concentration of fuel vapor in the immediate vicinity of the igniter plug. These influences arise mainly through the effect of volatility on evaporation rates and also through the effects of surface tension and viscosity on mean fuel drop size. The amount of energy required for ignition is very much larger than the values normally associated with gaseous fuels at stoichiometric fuel/air ratio. Much of this extra energy is absorbed in the evaporation of fuel droplets, the actual amount depending on the distribution of fuel throughout the primary zone and on the quality of atomization.

The process of ignition is envisaged to occur in the following manner. Passage of the spark creates a small, roughly spherical, volume of air (the spark kernel) whose temperature is sufficiently high to initiate rapid evaporation

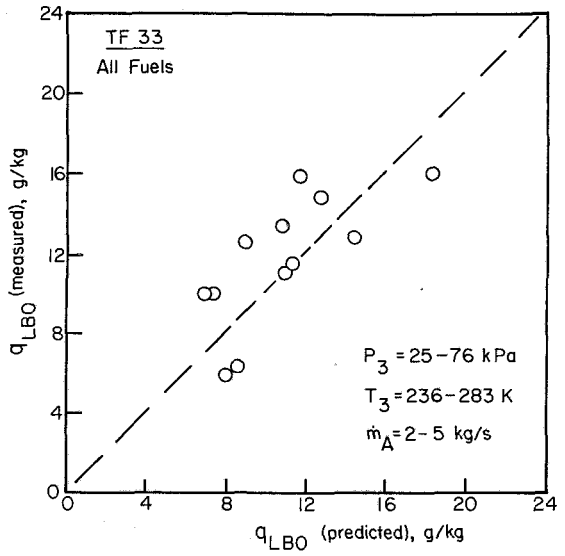

Fig. 20 Comparison of measured and predicted values of q_{LBO} for TF 33 combustor

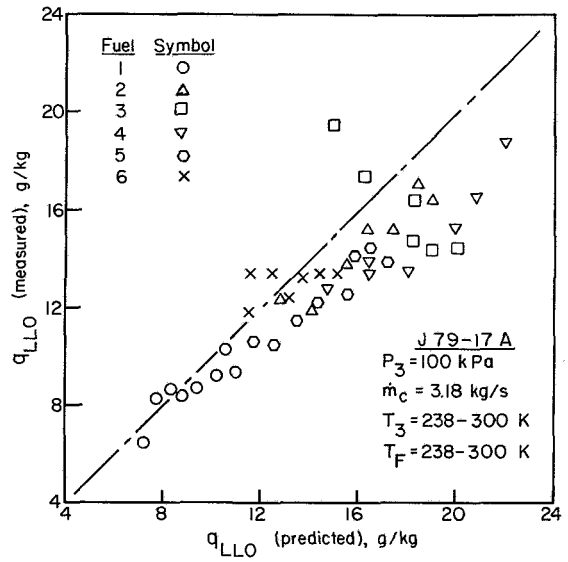

Fig. 22 Comparison of measured and predicted values of q_{LLO} for J79-17A combustor (Fuels 1–6)

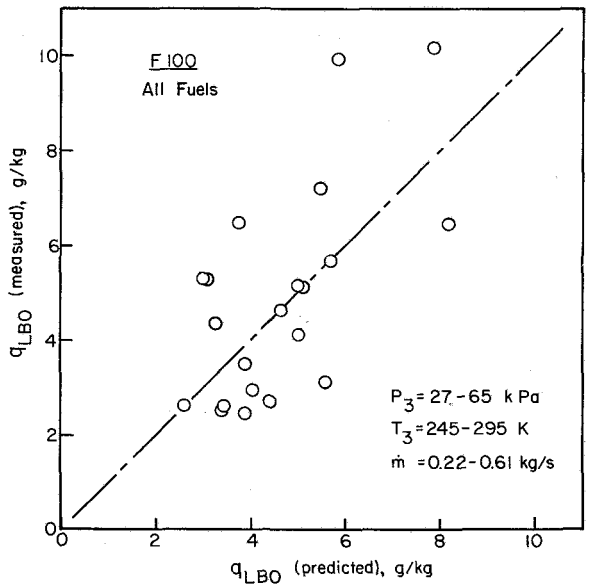

Fig. 21 Comparison of measured and predicted values of q_{LBO} for F100 combustor

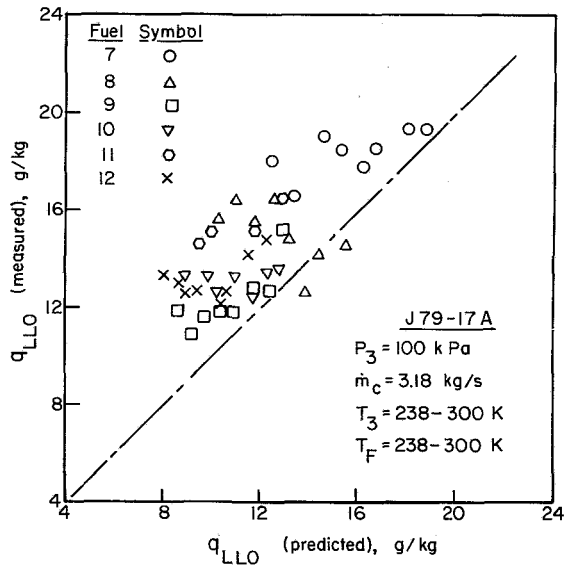

Fig. 23 Comparison of measured and predicted values of q_{LLO} for J79-17A combustor (Fuels 7–12)

of the fuel drops contained within the volume. It is assumed that reaction rates and mixing times are infinitely fast so that any fuel vapor created within the spark kernel is instantly transformed into combustion products at the stoichiometric flame temperature. If the rate of heat release by combustion exceeds the rate of heat loss at the surface of the inflamed volume, then the spark kernel will grow in size to fill the entire combustion volume. If, however, the rate of heat release is less than the rate of heat loss, the temperature within the spark kernel will fall steadily until fuel evaporation ceases altogether. This concept leads to the definition of "quenching distance" as the critical size that the inflamed volume must attain in order to propagate unaided, while the amount of energy required from an external source to achieve this critical size is termed the "minimum ignition energy."

Analysis of the relevant heat transfer and evaporation processes [16] yields the following expression for the quenching distance of quiescent or slow-moving monodisperse mists

$$d_q = \left[\frac{\rho_F D_0^2}{\rho_A \phi \ln(1+B_{st})}\right]^{0.5} \quad (28)$$

It should be noted that the foregoing equation was derived directly from basic considerations of the mechanisms of heat generation within the kernel and heat loss from its surface and contains no experimental or arbitrary constants.

Equation (28) and similar expressions for polydisperse sprays of the type provided by most practical atomizing devices, provide simple relationships between quenching distance and the key spray properties. Essentially, they state that quenching distance is directly proportional to drop size and is inversely proportional to the square root of gas pressure. An increase in ϕ and reduction in ρ_F both reduce d_q, because they promote evaporation by increasing the surface area of the fuel. Similarly, an increase in B will also accelerate evaporation and thereby decrease d_q. Values of E_{min} may be obtained by inserting the calculated values of d_q from equation (28) into the following expression

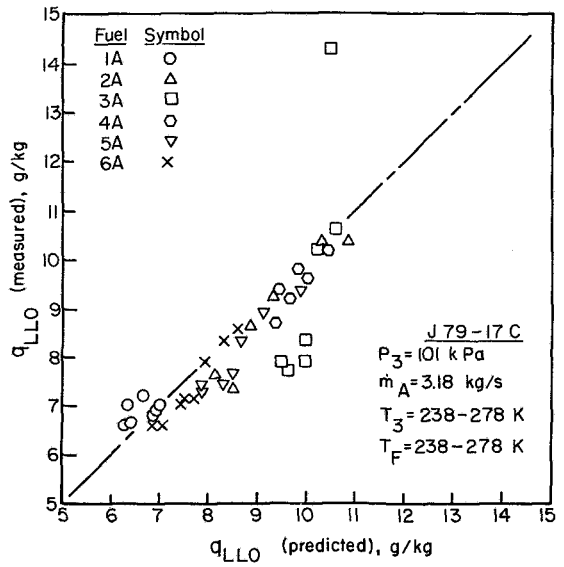

Fig. 24 Comparison of measured and predicted values of q_{LLO} for J79-17C combustor (Fuels 1A-6A)

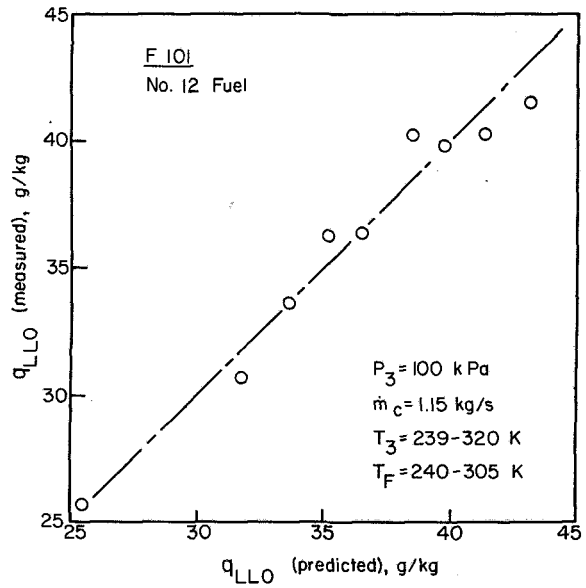

Fig. 26 Comparison of measured and predicted values of q_{LLO} for F101 combustor

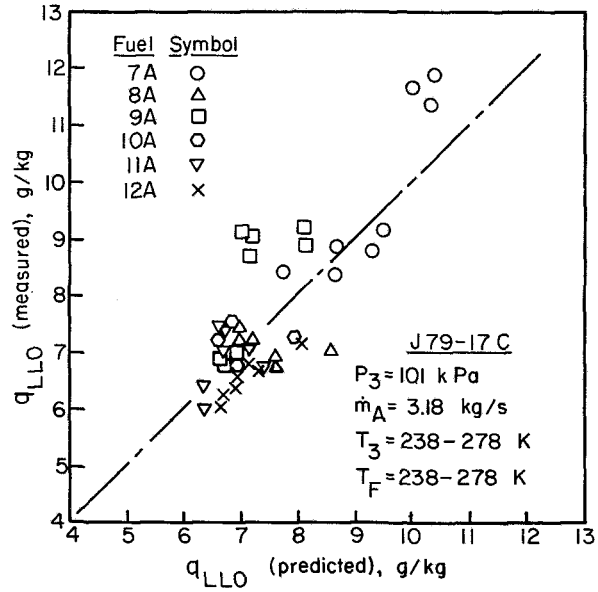

Fig. 25 Comparison of measured and predicted values of q_{LLO} for J79-17C combustor (Fuels 7A-12A)

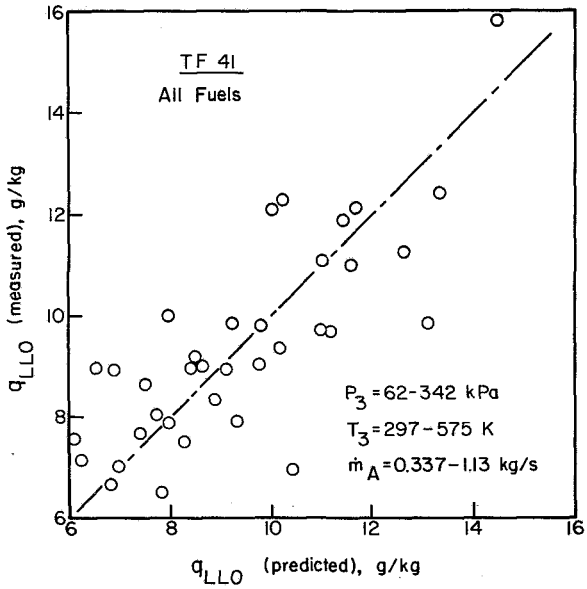

Fig. 27 Comparison of measured and predicted values of q_{LLO} for TF 41 combustor

$$E_{\min} = c_{p_A} \rho_A \Delta T_{st} (\pi/6) d_q^3 \quad (29)$$

Subsequently, Ballal and Lefebvre [16] extended the model described above to include (*i*) the effects of finite chemical reaction rates, which are known to be significant for very well-atomized fuels at low pressures and low equivalence ratios, and (*ii*) the effect of heat loss from the spark kernel by turbulent diffusion. Thus the model has general application to both quiescent and flowing mixtures of air with either gaseous, liquid, or evaporated fuel, or any combination of these fuels.

From a gas turbine viewpoint, the value of the type of model described above lies not so much in its ability to predict minimum ignition-energy requirements, since the available spark energy is determined by the specifications of the igniter plug and the high-energy unit; rather, its importance is in highlighting the key parameters that control ignition and in providing quantitative relationships or "rates of exchange" between these parameters.

Consider, for example, a combustor that normally operates on kerosine fuel. It is required to know what improvement in atomization quality would be needed to achieve the same ignition performance when diesel oil is burned. Now the relevant fuel properties are density and volatility, the latter being represented in the quenching-distance equations by the mass-transfer number B. From equation (28), we have

$$d_q \propto \left[\frac{\rho_F D_0^2}{\ln(1 + B_{st})} \right]^{0.5} \quad (30)$$

Thus for unchanged ignition performance, i.e., unchanged d_q, we can write

$$\frac{(D_0)_{\text{diesel}}}{(D_0)_{\text{ker}}} = \left[\frac{[\ln(1 + B_{st})/\rho_F]_{\text{diesel}}}{[\ln(1 + B_{st})/\rho_F]_{\text{ker}}} \right]^{0.5} \quad (31)$$

Now for diesel oil, $\rho_f = 900$ and $B_{st} = 2.80$; for kerosine, $\rho_F = 775$ and $B_{st} = 3.75$. Substituting these values into equation (31) gives

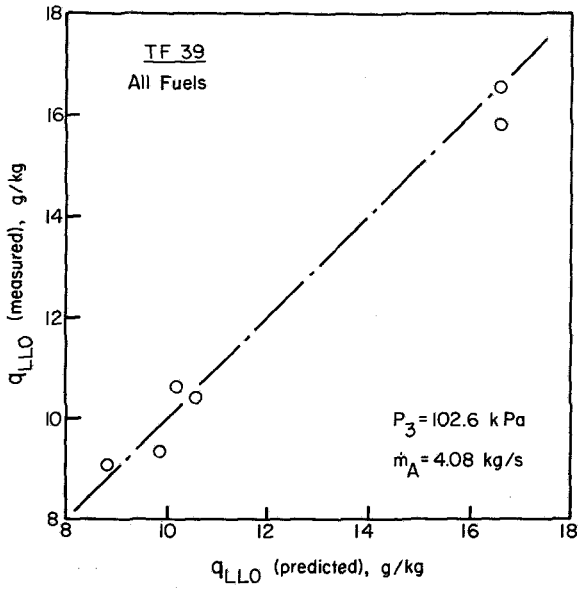

Fig. 28 Comparison of measured and predicted values of q_{LLO} for TF 39 combustor

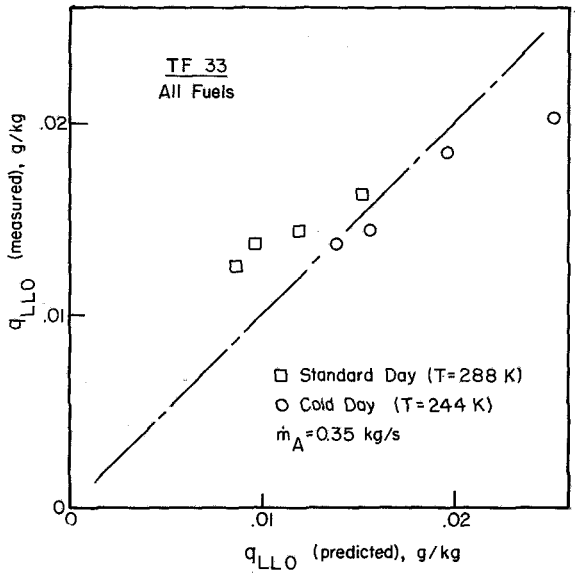

Fig. 30 Comparison of measured and predicted values of q_{LLO} for TF 33 combustor

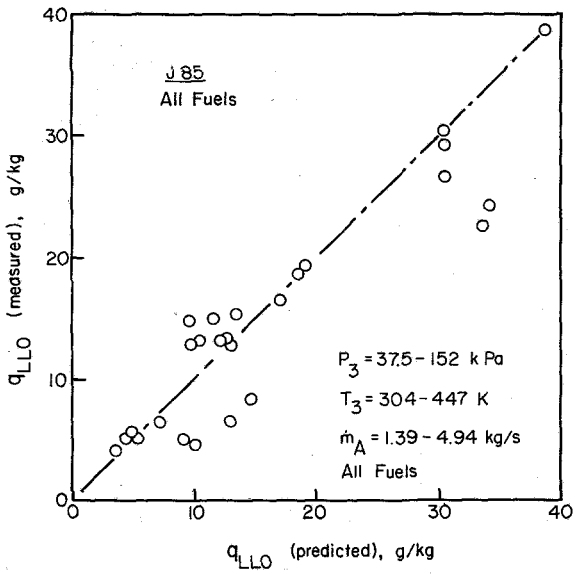

Fig. 29 Comparison of measured and predicted values of q_{LLO} for J85 combustor

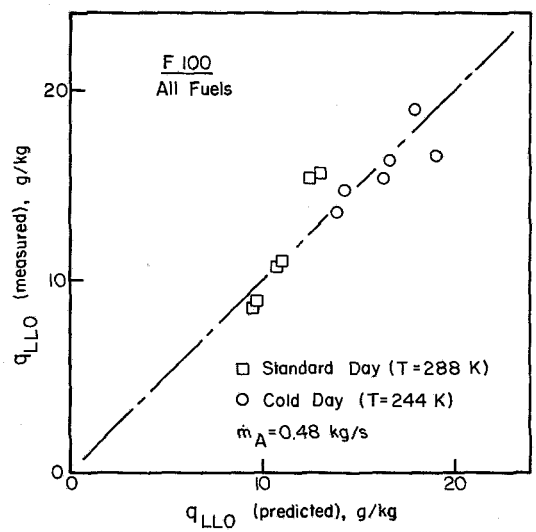

Fig. 31 Comparison of measured and predicted values of q_{LLO} for F100 combustor

$$\frac{(D_0)_{\text{diesel}}}{(D_0)_{\text{ker}}} = 0.86$$

which suggests that for diesel oil the SMD should be reduced by about 14 percent to retain the ignition performance obtained with kerosine.

Data Analysis. Application of the foregoing theoretical concepts to the analysis of the experimental data on ignition contained in [1-6] was inhibited, as for the lean blowout data, by lack of accurate information on mean drop size. So again recourse was made to relationships in which the key fuel properties are not expressed in absolute terms but in values relative to those of the baseline fuel, JP4. This approach leads to the following equation for lean lightup fuel/air ratio.

$$q_{\text{LLO}} = \frac{B' f_{pz} \dot{m}_A}{V_c P_3^{1.5} \exp(T_3/300)} \times \frac{D_r^2}{\lambda_r \text{LCV}_r} \times \left[\frac{D \text{ at } T_F}{D \text{ at } 277.5 \text{ K}}\right]^2 \quad (32)$$

This equation is virtually identical to equation (27), except for a higher pressure dependence: $P_3^{1.5}$ versus $P_3^{1.3}$.

The correlation of lightup data obtained with equation (32) is illustrated in Figs. 21-31. The level of agreement between predicted and experimental values is considered satisfactory, especially in view of the well-known lack of consistency that usually characterizes experimental data on spark ignition. The values of B' and $B' f_{pz}$ for the various combustors are listed in Table 2.

A curious anomaly exists in regard to the ignition data obtained from the J79 17C combustor. For this combustor, the results indicate a correlating parameter of the form

$$q_{\text{LLO}} = C_4 + \frac{C_5 f_{pz} \dot{m}_A}{V_c P_3^{1.5} \exp(T_3/300)} \times \frac{D_r^2}{\lambda_r \text{LCV}_r} \times \left(\frac{D \text{ at } T_F}{D \text{ at } 277.5 \text{ K}}\right)^2 \quad (33)$$

Assigning values of 3.92 and 200 to C_4 and C_5, respectively, provides the excellent correlation illustrated in Figs. 24 and 25.

For the F101 combustor, it was found that, in common with the lean blowout data discussed earlier, the reported lightoff fuel/air ratios were unusually high. Thus only the results obtained with the fuel having the highest number of test points (Fuel No. 12, [2]) are shown in Fig. 26 to illustrate the level of prediction attained. As for the lean blowout case, it was again assumed that a computational error had arisen in the calculation of fuel/air ratios due to tests being performed on a 54 deg sector rig, and a correction factor of (54/360) was again used to calculate the values of B' and $B'f_{pz}$ shown in Table 2 for the F101 combustor.

Discussion of Results

Combustion Efficiency. Equations (15) and (16) generally confirm the results of previous investigations on the effects on combustion efficiency of changes in combustion volume and combustor operating conditions. Equation (16) also demonstrates the adverse effect of low fuel volatility on combustion efficiency, especially at operating conditions where atomization quality is relatively poor. This, of course, is well known from practical experience, but the main attribute of equation (16) lies in the direct quantitative relationships it provides between atomization quality (via SMD), fuel volatility (via λ_{eff}), and combustion efficiency, which allow the effect on combustion efficiency of any change in fuel type or fuel nozzle characteristics to be readily estimated.

The study has also shown that in the correlation of combustion efficiency some care must be exercised in the choice of pressure exponent for the inlet air pressure, P_3. For values of combustion efficiency between 50 to 85 percent, which is the range of most importance in determining the combustor size needed to meet any stipulated high altitude relight performance, the optimum value of pressure exponent is around 1.75 [9, 10]. However, for the correlation of combustion efficiencies between around 85 to 100 percent, which is the range of primary concern for ground idle, and for the emissions of carbon monoxide and unburned hydrocarbons, a lower value is indicated. The results of the present study show that satisfactory correlation of data in this range can be achieved using a pressure exponent in equation (15) of 1.3.

Lean Blowout. The close grouping of the values of $A'f_{pz}$ for all the combustors listed in Table 2 gives cause for optimum in regard to the prediction of lean blowout limits for new combustor designs. For example, from inspection of Table 2 it is apparent that if $A'f_{pz}$ were assigned a fixed value of 29, its insertion into equation (27) would enable this equation to predict the lean blowout limits of five of the eight combustors to an accuracy of within ± 21 percent. Of the remaining three combustors, the TF 41 could be expected to have an exceptionally low value of $A'f_{pz}$ due to the unusually low primary flow number of its dual-orifice atomizer.

It is not being suggested that the prediction of lean blowout limits for new combustors to an accuracy of within 21 percent should be considered satisfactory or acceptable. However, the fairly close affinity between the values of $A'f_{pz}$ exhibited in Table 2 for several different types of combustor suggests that prospects are good for predicting to within close and acceptable limits the lean blowout limits of future combustor designs and should serve to encourage further experimental and analytical efforts in this area.

Ignition. The correlations obtained for lean lightoff limits highlight the important role played by the atomization process in creating an adequate concentration of fuel vapor in the spark region. Moreover, by providing quantitative relationships between fuel volatility (B or λ_{eff}), atomization quality (D_0), operating conditions (P_3, T_3, and $\dot{m}_A$), and combustion volume (V_c), equation (32) may be used to estimate the increase in combustor volume and/or improvement in atomization quality needed to recover the loss in altitude relight capability caused by changing the fuel to one of lower volatility.

Despite the well-known inconsistencies that tend to plague ignition data, the values of $B'f_{pz}$ listed in Table 2 do not exhibit appreciable scatter. The unusually low primary flow number of the TF 41 fuel nozzle, which gave rise to an exceptionally low value of $A'f_{pz}$, also produces a correspondingly low value of $B'f_{pz}$. Of the remaining six combustors, the lean lightoff data from five could be correlated to an accuracy of within ± 24 percent by assigning a value of 222 to $B'f_{pz}$. This result must be regarded as representing useful progress towards establishing accurate prediction formulae for lean lightoff limits.

Conclusions

1 The most important factors governing combustion performance are liner size, liner pressure drop, and combustion operating conditions, with fuel effects playing a secondary role. However, since in modern high-pressure ratio engines the combustor is called upon to perform satisfactorily for long periods at extreme conditions on current fuels, it follows that any factor, however secondary, that creates a more adverse combustor environment, could have a large and disproportionate effect on combustion performance.

2 The physical properties that govern atomization quality and evaporation rates affect lightup characteristics, weak extinction limits, and combustion efficiency. However, the influence of fuel chemistry on these performance parameters is quite small and stems from the effects of slight variations in lower calorific value on combustion temperature.

3 Based on considerations of the fundamental physical and chemical processes involved in fuel atomization, evaporation, mixing and combustion, expressions have been derived that allow the effects of changes in combustor size, combustor operating conditions, fuel type, and fuel temperature on lean blowout performance, lean lightoff characteristics, and combustion efficiency to be correlated satisfactorily.

Recommendations for Future Work

1 It is strongly recommended that any future experimental studies of fuel effects on gas turbine combustion should include measurements of mean drop size and drop-size distribution in the fuel spray at various representative engine operating conditions. Such measurements would be of great value in assessing the relative importance of chemical composition and physical properties in regard to the effects of a change in fuel type on combustion performance and could also lead to the establishment of more accurate formulae for the prediction of lean lightoff and lean blowout limits and combustion efficiency.

2 The rather similar ignition and stability characteristics exhibited by the different types of combustor examined in this study is an encouragement to further analytical and experimental efforts in this area. The envisioned study would focus mainly on the effects of fuel type, fuel spray characteristics, and primary-zone aerodynamics on lean lightoff, lean blowout, and combustion efficiency. The most important spray characteristics are mean drop size, drop-size distribution, and radial and circumferential fuel distribution. The test program should include both pressure-swirl and airblast fuel nozzles. These atomizers would be used in conjunction with various primary-zone configurations carefully selected to represent current practice as well as anticipated future designs. The aerodynamic features of interest include liner pressure drop, swirler characteristics,

and turbulence properties, as well as the distribution of primary air between air swirler and primary holes. The experimental work need not be expensive, since an air supply at normal atmospheric pressure and temperature would suffice for most of the test program, although a limited number of tests at other levels of air temperature would clearly be advantageous. As pattern factor is not a consideration, an annular combustor could be simulated adequately by a segment embracing three or more fuel nozzles, or even by a duct of rectangular cross section. Research along these lines involving a few basic primary zone geometries, operating at conditions where the relevant aerodynamic and fuel spray characteristics are accurately known, would appreciably enhance current capabilities in regard to the prediction of lean blowout limits, lean lightoff limits and combustion efficiency.

Acknowledgments

Support of the work reported here by the Fuels Branch of the Air Force Aero Propulsion Laboratory, Wright-Patterson Air Force Base, Ohio, is gratefully acknowledged. The Air Force Technical Monitors employed on this program were Dr. Thomas A. Jackson in the initial phase, and Mr. Curtis M. Reeves for the remainder of the program.

References

1 Gleason, C. C., Oller, T. L., Shayeson, M. W., and Bahr, D. W., "Evaluation of Fuel Character Effects on J79 Engine Combustion System," AFAPL-TR-79-2015, June 1979.

2 Gleason, C. C., Oller, T. L., Shayeson, M. W., and Bahr, D. W., "Evaluation of Fuel Character Effects on F101 Engine Combustion System," AFAPL-TR-79-2018, June 1979.

3 Vogel, R. E., Troth, D. L., and Verdouw, A. J., "Fuel Character Effects on Current, High-Pressure Ratio, Can-Type Turbine Combustion Systems," AFAPL-TR-79-2072, Apr. 1980.

4 Gleason, C. C., Oller, T. L., Shayeson, M. W., and Kenworthy, M. J., "Evaluation of Fuel Character Effects on J79 Smokeless Combustor," AFWAL-TR-80-2092, Nov. 1980.

5 Oller, T. L., Gleason, C. C., Kenworthy, M. J., Cohen, J. D., and Bahr, D. W., "Fuel Mainburner/Turbine Effects," AFWAL-TR-81-2100, May 1982.

6 Russell, P. L., "Fuel Mainburner/Turbine Effects," AFWAL-TR-2081, Sept. 1982.

7 Longwell, J. P., "Jet Aircraft Hydrocarbon Fuels Technology," NASA Conference Publication 2033, June 7–9, 1977.

8 Lefebvre, A. H., "Airblast Atomization," *Prog. Energy Combust. Sci.*, Vol. 6, 1980, pp. 231–261.

9 Lefebvre, A. H., *Gas Turbine Combustion*, McGraw-Hill, 1983.

10 Lefebvre, A. H., "Theoretical Aspects of Gas Turbine Combustion Performance," College of Aeronautics Note, Aero. No. 163, Cranfield, Bedford, England, 1960.

11 Chin, J. S., and Lefebvre, A. H., "Effective Values of Evaporation Constant for Hydrocarbon Fuel Drops," *Proceedings of the Twentieth Automotive Technology Development Contractors Coordination Meeting*, 1983, pp. 325–331.

12 Ballal, D. R., and Lefebvre, A. H., "Weak Extinction Limits of Turbulent Flowing Mixtures," ASME JOURNAL OF ENGINEERING FOR POWER, Vol. 101, No. 3, 1979, pp. 343–348.

13 Ballal, D. R., and Lefebvre, A. H., "Weak Extinction Limits of Turbulent Heterogeneous Fuel/Air Mixtures," ASME JOURNAL OF ENGINEERING FOR POWER, Vol. 102, No. 2, 1980, pp. 416–421.

14 Lefebvre, A. H., "An Evaporation Model for Quenching Distance and Minimum Ignition Energy in Liquid Fuel Sprays," paper presented at Fall Meeting of Combustion Institute (Eastern Section), 1977.

15 Rao, K. V. L., and Lefebvre, A. H., "Minimum Ignition Energies in Flowing Kerosene/Air Mixtures," *Combustion and Flame*, Vol. 27, No. 1, 1976, pp. 1–20.

16 Ballal, D. R., and Lefebvre, A. H., "General Model of Spark Ignition for Gaseous and Liquid Fuel/Air Mixtures," *Proceedings of the Eighteenth Symposium (International) on Combustion*, 1981, pp. 1737–1746.

Optical Measurements of Soot Size and Number Density in a Spray-Atomized, Swirl-Stabilized Combustor

C. P. Wood
Staff Research Associate.

G. S. Samuelsen
Professor of Mechanical Engineering.

UCI Combustion Laboratory,
Mechanical Engineering,
University of California,
Irvine, Calif. 92717

In-flame optical measurements of soot particulates in a turbulent, recirculating (i.e., complex flow) model laboratory combustor are described. A nonintrusive optical probe based on large-angle (60 and 20 deg) intensity ratio scattering was used to yield a point measurement of soot particulate in the size range of 0.08 to 0.38 μm. A shale-derived JP-8 stock, isooctane, and mixtures of isooctane with various ring and aromatic compounds blended to yield the smoke point of the JP-8 stock were separately injected as a liquid spray through a twin-fluid atomizer. One blend was also introduced prevaporized through a hollow-cone nozzle. The addition of ring compounds to the base isooctane as well as operation on JP-8 increased the amount of soot produced, although the total amount of soot produced depended on fuel type for those fuels of equivalent smoke point. The spatial distribution of soot as well as the amount produced was found to be sensitive to nozzle atomization quality and injection momentum. The amount of soot produced was reduced by a reduction in fuel loading. However, injection of fuel in a prevaporized state both increased the amount of soot produced and changed spatially the region over which soot was distributed. Scanning electron micrographs of extracted samples established that the optical technique resolved the large particle wing of the soot size distribution.

Introduction

Fuel flexibility is a viable and realistic approach to assure adequate availability of aviation fuel through this century. To achieve this position, the relationship of fuel properties and composition to combustion hardware performance and durability must be identified more precisely. Such information is necessary if fuel specifications are to be successfully relaxed to a level that both maintains the required performance of the combustion system (and other subsystems) and permits the desired latitude in the portion of hydrocarbon resources (petroleum, oil shale, coal, tar sands, etc.) that can be utilized to produce aviation fuel. These potential changes in fuel processing and fuel source make future fuel composition effects on gas turbines a primary consideration and concern.

Currently, the specification limit on aromatics for aviation fuel is a maximum of 20 percent (Jet A) or 25 percent (JP-4, JP-5, JP-8) by volume. The limit is set to preclude a series of combustion-related problems associated with the production of soot, examples of which include increased flame radiation, deposit of carbonaceous material, and emission of particles. Radiation and deposition influence hardware durability and performance, while the emission of particles results in aesthetic and tactical problems. The aromatic content is of special interest because a relaxed specification for aromatics could ease the demand for hydrogen addition in the refining of low hydrogen resources. An upper limit of 35 percent aromatics has been discussed [1].

To accommodate an increased fuel aromaticity, the production of soot from combustors operating on relaxed-specification fuels must be reduced. Toward this end, experimental evidence is needed with respect to the effects that fuel properties, fuel-additive properties, and combustor operating conditions have on soot formation and burnout. Of particular interest are the mass emission, size distribution, and composition of the soot particulate. Extractive probe measurements have been used in the past to derive this set of information (e.g., [2, 3, and 4]) but, in complex flows where backmixing can exacerbate and widely distribute perturbations introduced by the presence of a physical probe, caution must be exercised in the use of such methods [5]. This may include limiting the measurements to the combustor exit-plane, far downstream of the recirculation zone. Such a limit substantially restricts the information available. Excluded is the spatial distribution of local soot size and soot number

Contributed by the Gas Turbine Division of THE AMERICAN SOCIETY OF MECHANICAL ENGINEERS and presented at the 29th International Gas Turbine Conference and Exhibit, Amsterdam, The Netherlands, June 4–7, 1984. Manuscript received at ASME Headquarters January 9, 1984. Paper No. 84-GT-153.

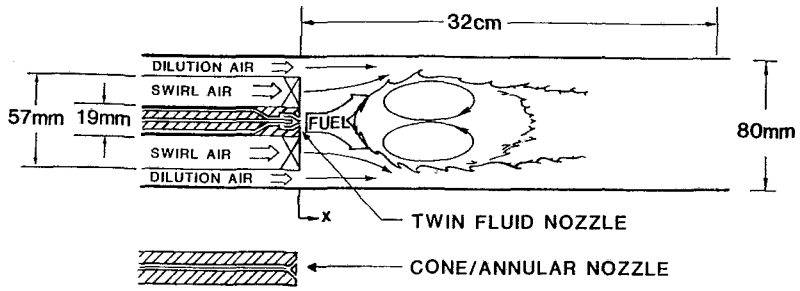

Fig. 1 Dilute swirl combustor

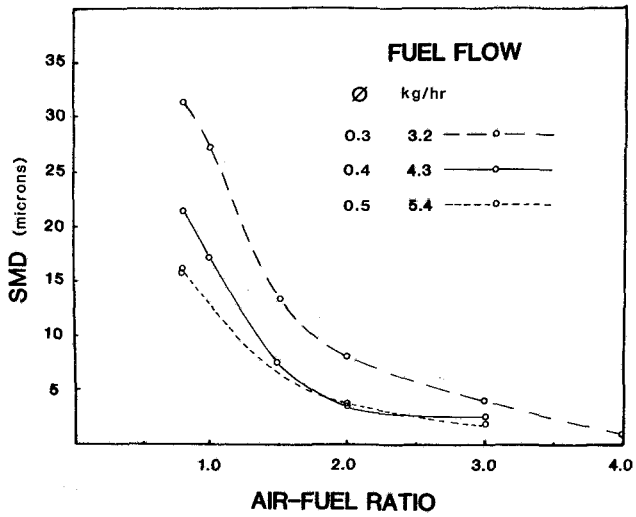

Fig. 2 Nozzle characterization

density in the near wake of the recirculation zone and within the recirculation zone itself. Such measurements must be nonintrusive and therefore rely on optical techniques. Although optical techniques have been successfully employed to measure soot in relatively simple flows (flat flames and diffusion flames), limited applications to complex flows have only recently been demonstrated [5, 6].

In a recent study [6], we addressed the application of a nonintrusive, optical probe to a complex flow where the principal objective was to evaluate the performance of large angle intensity ratioing for optically measuring the local soot size and soot number density in the reaction zones of a complex flow. Isooctane and blends of isooctane with pure hydrocarbons of varying aromaticity were introduced prevaporized. In the present study, the objectives were to (*i*) introduce the fuels as liquid sprays and add to the fuels tested a shale-derived JP-8, and (*ii*) conduct an exploratory assessment of the impact of key parameters (fuel molecular structure, atomization quality, injection state) on the spatial distribution of soot in a model laboratory complex flow combustor.

Experiment

(a) Approach. The approach was to optically measure the spatial distribution of local soot size and number density in a model laboratory complex flow combustor. Radial profiles were measured at three axial locations for a shale-derived JP-8, isooctane, and three fuel blends introduced through a twin-fluid atomizer. The three fuel blends were mixed to yield the same ASTM smoke point as the JP-8 in order to assess the effect of fuel molecular structure on soot yield in a complex flow. The effect of atomization quality was addressed for the shale-derived JP-8, and a parametric variation was conducted on one fuel blend to assess the effect of injection state (prevaporized versus liquid fuel injection) on soot yield. The optical technique employed was scattering intensity ratioing at two angles, 60 and 20 deg.

(b) Combustor. The combustor employed was a model laboratory complex flow combustor developed in a series of tests [7, 8]. The configuration is presented in Fig. 1. The Dilute Swirl Combustor (DSC) features an aerodynamically controlled, swirl-stabilized recirculation zone to simulate important features of practical combustors (e.g., swirl and highly turbulent recirculation).

For the present work, the housing consisted of an 80-mm-i.d. cylindrical stainless steel tube that extended 32 cm from the plane of the nozzle. Rectangular, flat windows (25 × 306 mm) were mounted perpendicular to the horizontal plane on both sides of the combustor tube to provide a clear, optical access for the laser measurements.

A set of swirl vanes (57-mm-o.d.) were concentrically located within the tube around a 19-mm-o.d. centrally positioned fuel delivery tube. Dilution and swirl air were metered separately. The dilution air was introduced through flow straighteners in the outer annulus. The swirl air passed through swirl vanes with 100 percent blockage, which imparted an angle of turn to the flow of 60 deg. For the swirl-to-dilution air flow ratio of 1.66 used in the present study, the swirl number obtained by integrating across the swirl vanes was 1.3; that obtained by integrating the total inlet mass flux was 0.5. Prototype 60 deg swirl vanes with a 70 percent blockage, used in the initial study for prevaporized fuel injection [6], were not adequate for the liquid injection. Higher blockage provides a wider range of stable operation for the liquid injected fuels.

Fuel was introduced through a twin-fluid injector designed for the present study by Parker-Hannifin. Sauter Mean Diameter (SMD) was measured using a Malvern ST2200 laser diffraction instrument as a function of nozzle air-to-fuel mass ratio and compared to data generated by Parker-Hannifin [9]. The data are presented in Fig. 2. Although the values of SMD approach the limit of resolution for the Malvern as nozzle air-to-fuel ratio is increased, the trend toward enhanced atomization quality is clearly evident. The intensity ratioing results of the present work were obtained for an air-to-fuel mass ratio of 3.0. For the shale-derived JP-8, data were also obtained at air-to-fuel ratios of 2.5 and 3.5 to assess the effect of this parameter on soot size and spatial distribution. A cone-annular nozzle was used for the one fuel blend introduced in a prevaporized state.

The combustor was operated at atmospheric pressure to provide for the necessary optical access and ease of operation with the relatively complex and unhardened optical system employed. The effect of pressure, an important parameter in the production of soot, is appropriate for evaluation once the utility and applicability of the optical system is established and adaptability of elevated pressure systems to optical access is demonstrated.

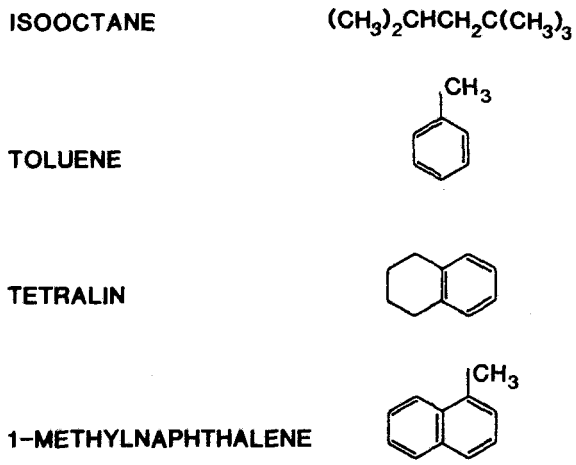

Fig. 3 Fuel molecular structure

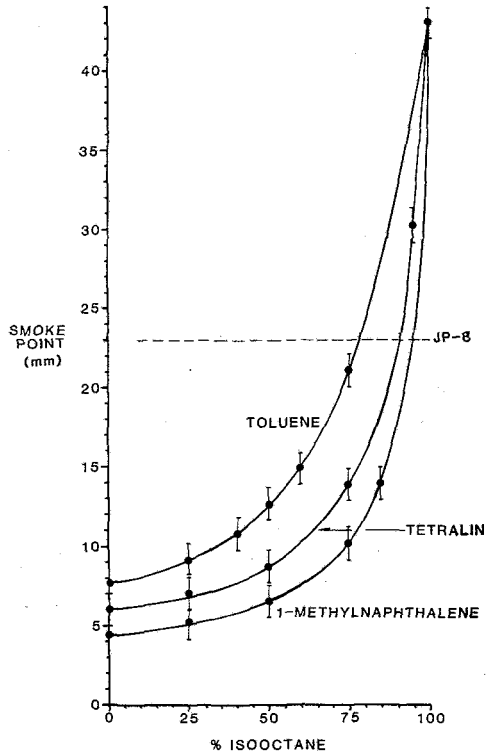

Fig. 4 ASTM smoke point

(c) **Fuels.** A shale-derived JP-8 and four liquid fuels of varying molecular structure representative of compounds found in petroleum, shale, and coal-derived fuels were used in this study. Isooctane (2, 2, 4-trimethylpentane) served as the base fuel as it represents a major component of JP-8 and serves as the reference fuel in the ASTM smoke point test. The three remaining fuels consisted of mixtures of isooctane with one of three compounds with varying degrees of saturation and ring number (Fig. 3)—toluene, tetralin (1, 2, 3, 4-tetrahydronaphthalene), or 1-methylnaphthalene.

The amount of hydrocarbon blended with the isooctane was selected to yield the same ASTM smoke point as that obtained for the JP-8 stock. The amount of each compound blended with isooctane was determined by first preparing a curve of smoke point versus volume percent isooctane (Fig. 4). Table 1 summarizes the composition and the actual smoke point found for each blend. The smoke points, while not identical,

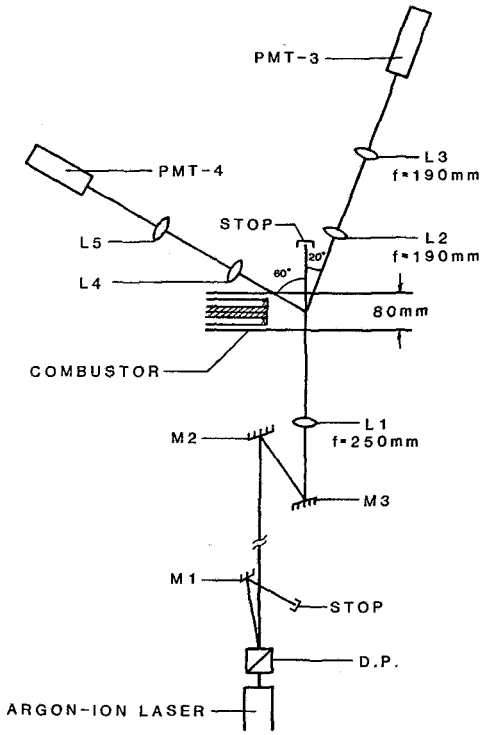

Fig. 5 Optical configuration

Table 1 Fuel summary

Fuel[a]	Smoke point[b]	H wt. %
Isooctane	43.0	15.79
JP-8	23.0	13.89[c]
Blend 1 21% toluene/ 79% isooctane	24.0	14.02
Blend 2 8% tetralin/ 92% isooctane	25.3	15.06
Blend 3 5% 1-methylnaphthalene/ 95% isooctane	22.2	15.16

[a] Blend composition stated in volume percent
[b] Distance above base of burner in mm at which sooting first occurs
[c] Wright Patterson AFB
Source: [4]

are equivalent within the achievable accuracy of the smoke point test (± 1 mm) shown by the error bands in Fig. 4.

(d) **Optical System.** The method adopted for the point-measurement of particle size and number density of soot particulate was scattering intensity ratioing. Figure 5 illustrates the optical configuration, a modification of that used previously [5]. This earlier work utilized collection optics at 10 and 5 deg off the optical axis. The current work employed collection optics at 60 and 20 deg to reduce the smallest size of particles that could be resolved from 0.3 to 0.08 μm.

A 5-watt Model 165 Spectra-Physics argon-ion laser operating in the multiline mode was used as the source of light. The laser lines were separated by a dispersion prism to resolve the blue line (488.0 nm). The beam was focused to a 110 μm waist dia using a 50-mm-dia F/5 focusing lens. The scattered intensity was detected at 60 and 20 deg which provided a particle size detection band of $0.08\ \mu m < d < 0.38\ \mu m$. Other angles were available but 60 deg/20 deg provided the smallest resolvable size (0.08 μm) of those pairs available.

The scattered light was focused to two photomultiplier tubes (RCA Model 8575) having quantum efficiencies of

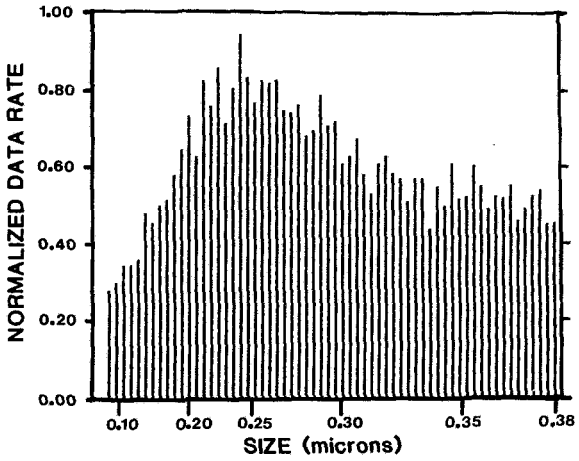


```
DATE: 21SEP83
SERIES: ISOTET      RUN: 1006 21SEP83
COMMENT: D=DATA HV=1200/1220  LASER=1W
R/R=0.83 X/R=3.0 EQ/R=0.5  V=7.5M/S

MAX RAW COUNT = 764
TOTAL RAW COUNT = 30131
SAMPLE TIME: 11.4 SECONDS

          LISTING OF RAW COUNTS

          BIN                    BIN
RATIO     COUNT  RATIO           COUNT

.946      225    .31             584
.913      239    .299            492
.881      278    .289            508
.85       279    .278            545
.82       285    .268            467
.791      387    .259            429
.763      367    .25             492
.736      405    .241            506
.71       418    .232            472
.685      472    .224            459
.661      522    .216            410
.637      594    .209            461
.615      506    .201            458
.593      670    .194            352
.572      615    .187            442
.552      696    .181            398
.532      575    .174            491
.513      652    .168            414
.495      764    .162            421
.478      672    .156            487
.461      620    .151            445
.444      669    .145            393
.429      665    .14             423
.414      669    .135            418
.399      605    .13             443
.385      597    .126            369
.371      616    .121            393
.358      549    .117            419
.345      563    .113            433
.333      634    .109            362
.321      573    .105            364
```

Fig. 6 Representative optical data (isooctane/tetralin, $\phi = 0.5$, $r/R = 0.83$, $x/R = 3.0$)

approximately 15 percent at the 488.0 nm wavelength with pinhole aperature diameters of 200 μm. The supply voltage to the tubes was approximately 1200 V.

The output signal from the photomultiplier tubes was passed into a Spectron Development Laboratories (SDL) Model LA-1000 logarithmic amplifier, which converted the negative current to a positive voltage and was scaled for +10 V peak output when the input current was −1 mA. The amplified signals were then fed to a SDL Model RP-1001 Intensity Ratio Processor (RP). The RP registered and processed the peaks of the two signals provided certain criteria were met. The d-c voltages input from the two channels of the logarithmic amplifier were processed by an analog subtractor circuit in the RP, which amplified the signal

Table 2 Test matrix

Fuel[a]	Overall equivalence ratio ϕ	Nozzle air-to fuel ratio	Injection state	Fig.
Isooctane	0.3,0.5	3.0	liquid	9
JP-8	0.3	2.5,3.0,3.5	liquid	10
Blend 1- 21% toluene/ 79% isooctane	0.3,0.5	3.0	liquid	9
Blend 2- 8% tetralin/ 92% isooctane	0.3,0.5 0.3,0.5	3.0 NA[b]	liquid prevap.	9 9,11
Blend 3- 5% 1-methyl-naphthalene/ 95% isooctane	0.3,0.5	3.0	liquid	7,9

[a] Blend composition stated as volume percent
[b] NA = not applicable

with a gain of 5 and converted the signal to an 8-bit binary number. The RP had a variable lower threshold voltage, allowing a measure of control over the rejection of background noise.

The binary output was fed to an Apple II microcomputer, which resolved this output into 62 bins. The size distribution was determined by the number of counts in each bin, where each bin encompassed a discrete size range. The counts in each bin were then divided by the time required to collect them, resulting in a count rate (counts/s). A histogram was then generated of normalized data rate versus size (in microns). The normalization of this histogram was under the operator's control through the system software. The histogram could be normalized to itself (giving the bin with the highest sooting rate an intensity of 1.0); it could be normalized to the highest sooting rate among all the histograms generated for a particular fuel; or it could be normalized to the highest sooting rate among any number of fuels or operating conditions. The results of this normalization procedure are evident in Figs. 7, 9, 10, and 11.

The interpretation of the measured intensity ratio is based on the analysis of the Mie scattering properties of a homogeneous, isotropic spherical particle. Soot, a nonspherical scatterer with an index of refraction of some uncertainty, therefore requires special consideration. An evaluation of such effects, considered in an earlier study, concluded that the combined error was 20–30 percent with some broadening of the distribution [5].

Calibration of the optical system was performed routinely at the beginning of each run session using polystyrene particles of a known size (mean diameter = 0.255 μm, standard deviation = 0.9 percent). Calibrations were regularly checked as well at the end of each run session to verify that the optical quality of the combustor windows had not degraded. In addition, consistency in the performance of the combustor and optical system was monitored over a period of weeks by periodically repeating the isooctane/tetralin data set. After attaining thermal equilibrium, nine points in the flow field were monitored for soot data rate and size distribution. At any given station, the variation in the peak of the size distribution of the soot never exceeded 10 percent of the nominal value at that station. The data rate was more variable. Along the outer perimeter of the combustor (e.g., $r/R = 0.83$), where nominal sooting rates exceeded 1500 Hz, the variation in data rate was approximately 30 percent. At the interior stations, where sooting rates were nominally below 300 Hz, the data rate varied from 47 to 71 percent, depending on the station, with the greater variability correlated with lower data rate. The variability of the data rates is not unreasonable at this point in the system

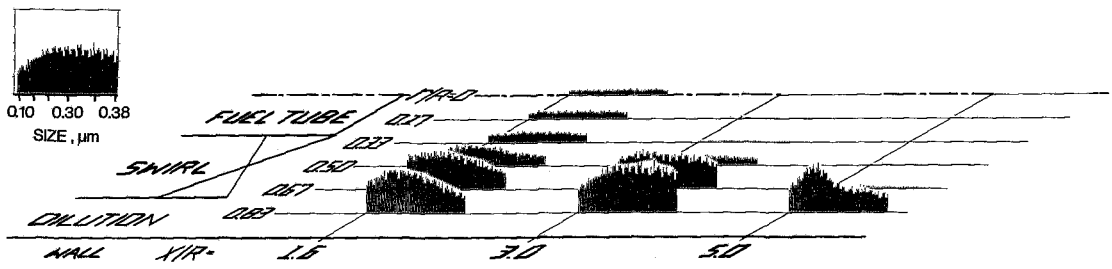

Fig. 7 Spatial map (isooctane/1-methylnaphthalene, $\phi = 0.5$)

Table 3 Data rate (Hz)

Fuel	Equivalence ratio ϕ	Location							Injection state	Fig.
		Axial x/R	Radial r/R							
			0	0.17	0.33	0.50	0.67	0.83		
Isooctane	0.5	1.6	57	70	66	61	109	247	liquid	9(*a*)
		3.0	0	0	0	0	7	26		
		5.0	0	0	0	0	0	1		
Blend 1	0.5	1.6	30	72	122	204	406	581	liquid	9(*b*)
21% toluene/		3.0	0	0	1	6	65	296		
79% isooctane		5.0	0	0	0	4	59	419		
Blend 2	0.5	1.6	236	305	389	700	1521	1982	liquid	6,9(*c*),11(*c*)
8% tetralin/		3.0	1	6	61	444	1775	2643		
92% isooctane		5.0	0	1	3	9	98	1746		
Blade 3	0.5	1.6	260	346	450	770	1482	1612	liquid	7,9(*d*)
5% 1-methylnaphthalene/		3.0	0	5	61	429	1532	1991		
95% isooctane		5.0	0	1	2	6	90	1399		
JP-8	0.3	1.6	26	25	24	22	24	21	liquid	10(*a*)
(A/F = 3.0)		3.0	22	22	20	14	12	19		
		5.0	105	134	122	25	10	15		
JP-8	0.3	1.6	45	46	53	61	42	20	liquid	10(*b*)
(A/F= 2.5)		3.0	425	330	311	166	29	28		
		5.0	1812	1686	1211	470	88	20		
JP-8	0.3	1.6	13	10	11	35	236	372	liquid	10(*c*)
(A/F= 3.5)		3.0	11	11	10	12	56	269		
		5.0	6	8	10	24	92	191		
Blend 2	0.5	1.6	1505	1221	874	468	142	103	prevaporized	11(*a*)
8% tetralin/		3.0	1054	775	928	373	143	244		
92% isooctane		5.0	183	394	1761	934	861	3373		
Blend 2	0.3	1.6	1120	980	857	603	239	239	prevaporized	11(*b*)
8% tetralin/		3.0	313	345	887	416	282	488		
92% isooctane		5.0	284	677	2364	1023	1914	3816		
Blend 2	0.5	2.3	1200	1590	1347	1175	1631	2236	prevaporized	11(*d*)
8% tetralin/		3.7	1269	1293	1717	2104	2361	2708	(weak swirl)	
92% isooctane		5.0	1164	1081	1291	1686	2032	2405		

development. Several parameters of the measurement system can influence the rate, including the alignment and focusing of two optical detectors at a coincident point and the signal processor thresholds. In addition, the condition of the twin-fluid injector was found to have a marked effect on data rate. The specific orientation of the injector with respect to the combustor flow field was found to change the sooting rate at specific points in the flow field, presumably because of resulting changes in fuel distribution caused by small asymmetries in the atomized spray. The effect of nozzle configuration and performance on fuel distribution and soot production is an area of active interest and will be explored in more detail in future work.

(e) Test Matrix. The test matrix for the present study is presented in Table 2. Tests were conducted at overall equivalence ratios of 0.3 and 0.5, except for the JP-8, which was tested only at 0.3. (At equivalence ratios greater than 0.3, a portion of the atomized JP-8 was found to penetrate the recirculation zone and impinge on the walls of the combustor). The nominal air-to-fuel rate for the nozzle was 3.0 for the JP-8, isooctane, and three blends. The nozzle air was in addition to the main air (swirl plus dilution) and corresponded to 10 and 6 percent of the main air at $\phi = 0.5$ and $\phi = 0.3$, respectively. Although not optimum for each individual case, an air-to-fuel ratio of 3.0 was selected as the operating condition that provided the most satisfactory

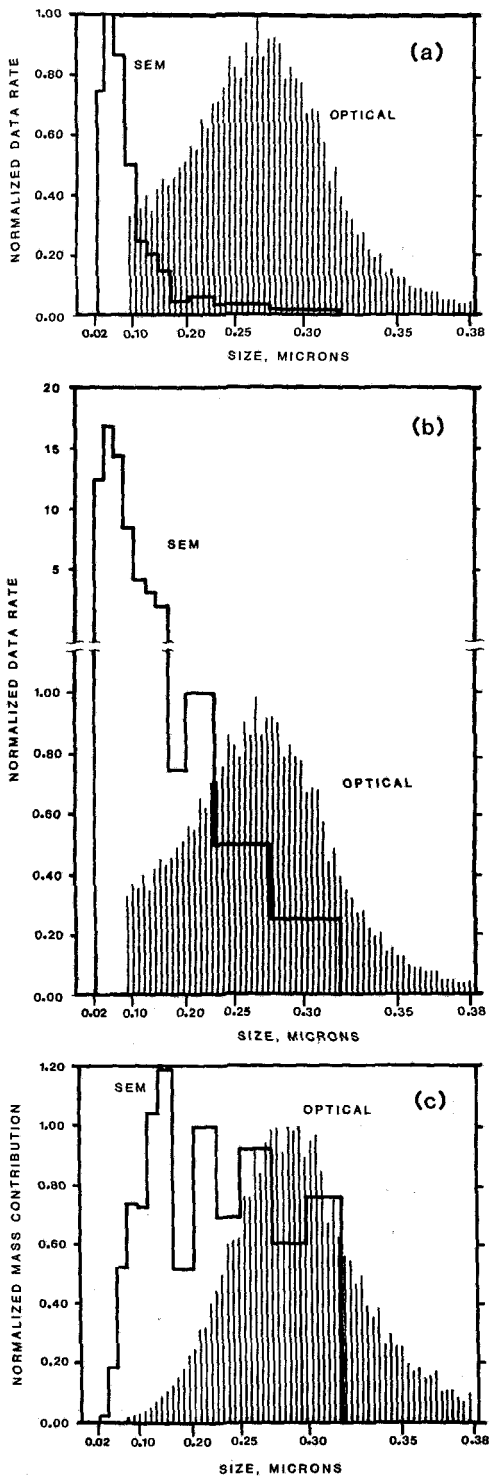

Fig. 8 Validation [6] (isooctane/toluene, ϕ = 0.5, prevaporized): (a) number density; (b) number density renormalized; (c) mass density

performance (highest stability) for the group of fuels tested. The effect of atomization quality was demonstrated for the shale-derived JP-8. The combustor was operated at a reference velocity of 7.5 m/s.

Results

The results are presented in two groups. The performance and utility of the optical system for in-situ, nonintrusive measurements of soot size and number density are first evaluated. Second, the effects of fuel molecular structure, fuel loading, nozzle performance, and injection state on the spatial variation of soot size and number density within the combustor are assessed.

(a) Data Presentation. An example of the data provided by the optical system is shown in Fig. 6 for the tetralin blend at ϕ = 0.5. The histogram represents the distribution of intensity ratio for 30131 validated samples. The total data rate for this case (2643 Hz) is the number of validated samples (30131) divided by the total sample time (11.4 s) and represents the sum of the bin data rates for each of the 62 bins comprising the histogram. The total data rate for each sampling location for this case and for all fuels and conditions tested is listed in Table 3.

The utility of a point measurement is the ability to map the combustor for soot size and number density. An example of such a mapping is presented in Fig. 7 for the 1-methylnaphthalene blend at ϕ = 0.5. Radial profiles of optically measured soot size and number density are presented at three axial locations within the combustor. The locations of peak soot concentration for the 1-methylnaphthalene blend can be identified (x/R = 1.6; r/R = 0.83), and the reduction of soot downstream is clearly evident.

The effects of fuel molecular structure, nozzle performance, and injection state on the soot field are presented in Figs. 9, 10, and 11, respectively. In Fig. 7, as well as in Figs. 9, 10, and 11, radial and axial locations are nondimensionalized to the combustor radius (R = 40 mm). All the histograms in Figs. 7, 9, and 10 represent results obtained with the fuels injected as liquids and are, as a result, normalized as a group to the peak bin data rate in the set (JP-8, Fig. 10(*b*)). In Fig. 11, the state of fuel injection is varied. Hence these histograms are normalized to the peak bin data rate in this set (prevaporized isooctane/tetralin, Fig. 11(*b*)). To assist in comparing the histograms in each three-dimensional plot and within each set of results, the histogram with the peak bin data rate in the field is reproduced and dimensioned in the upper left corner of each plot. Because the peak bin data rate in Fig. 7, for example, is normalized to the peak bin data rate of JP-8 in Fig. 10(*b*), the height of the histogram in the upper left corner of Fig. 7 is less than unity.

(b) Evaluation. To validate the optical system, the optical probe was positioned at the entrance of an extractive probe used previously [5]. The extractive probe was located at an axial location (x/R = 5.0) and radial location (r/R = 0.83) well displaced from the centerline where flow perturbation was expected to be minimized. A scanning electron microscopy analysis of the extracted sample was compared to the optical data. The results, reported previously [6], are summarized here for completeness.

The morphology of the soot is agglomerates of smaller (~0.05 μm) spherical particles, which is consistent with the morphology and size observed in other combustor studies (e.g., [4, 5, 6, 10, 11]). An example of the size distribution derived from a scanning electron micrograph (SEM) of the extracted sample is compared to the optical measurement for an isooctane/toluene blend in Fig. 8(*a*). Particle sizes observed optically are also revealed by the SEM data. However, the range of particle sizes resolved by the 60 deg/20 deg intensity ratioing (*i*) is at the large particle end of the SEM distribution, (*ii*) encompasses only a small portion of the total number of particles, (*iii*) includes the agglomerates, and (*iv*) excludes the primary particles.

Although the optical data do not include the peak size of the actual distribution (~0.05 μm, the size of the primary particles), the optical data appear to accurately reflect a secondary peak located in the large particle wing of the SEM data. To more effectively compare the two sets of data, the

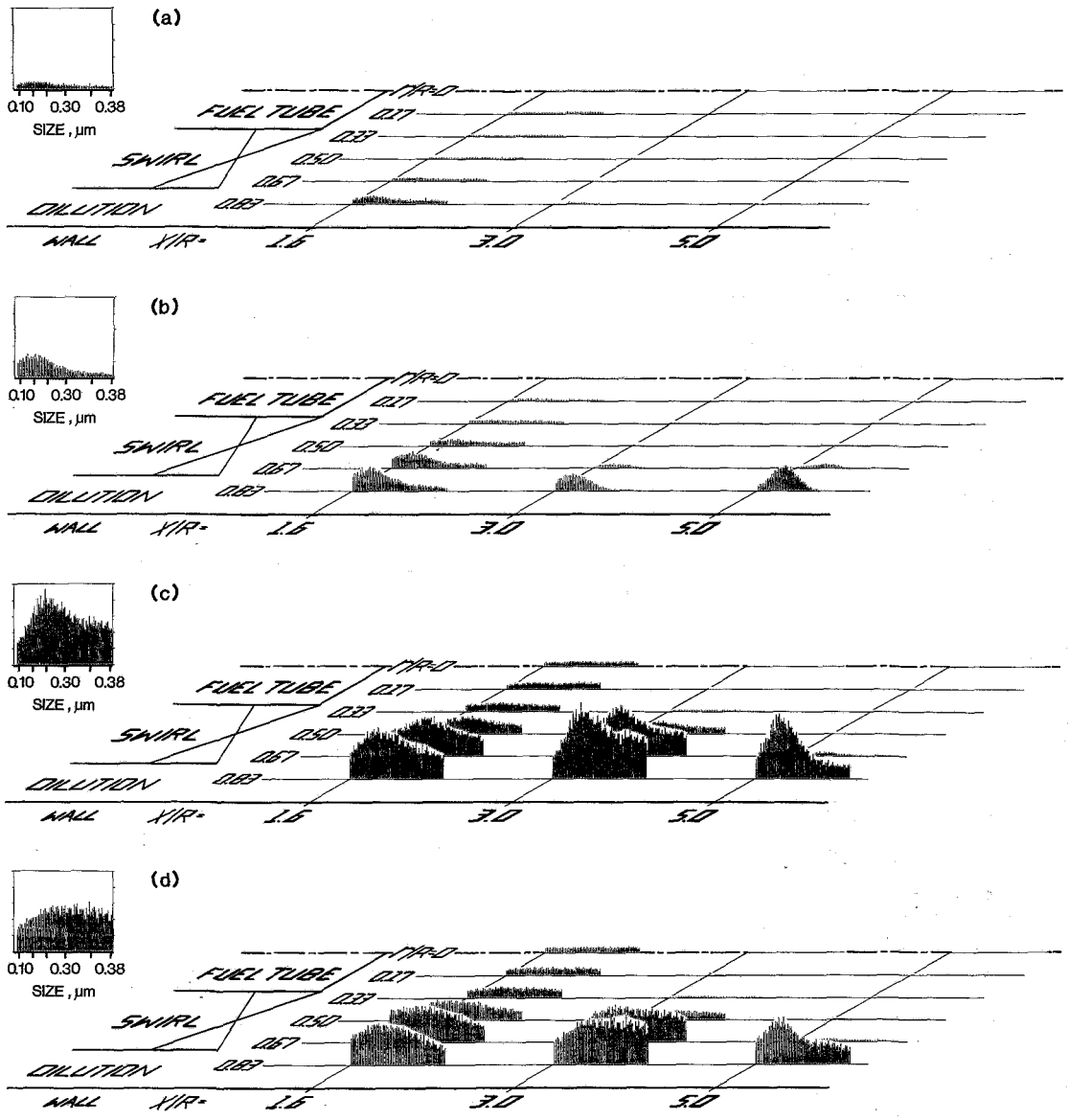

Fig. 9 Fuel molecular structure (ϕ = 0.5): (*a*) isooctane; (*b*) isooctane/toluene; (c) isooctane/tetralin; (*d*) isooctane/1-methylnaphthalene

SEM data are renormalized in Fig. 8(*b*) to the secondary peak in data rate that occurs in the large particle wing of the SEM distribution ($d_p \sim 0.22$ μm). The optically measured peak in data rate appears to be real and reflects a discontinuity in particle size associated with agglomerate growth. However, the extent to which the optically measured data rate is reduced on the small particle side of the peak may be exaggerated due to an inaccuracy in the optical technique associated with the Gaussian intensity profile of the incident laser beam. A relatively small particle passing through the laser beam at the wing of the Gaussian intensity profile may not scatter enough light to the detectors to meet established threshold levels on the RP, whereas a larger particle, passing through the same region of the beam, will scatter enough light to be recorded. This acts to artificially suppress the low end of the distribution. This inaccurcy is amenable to an analytically derived "probe volume" correction which could be implemented through the reduction software, in essence giving the system a flat response throughout the range of sizes it is theoretically capable of measuring. Other sources of inaccuracy are discussed in [6].

In Fig. 8(*c*), both the optical and SEM distributions are presented in terms of mass density. Although the difference in relative peak levels is not as pronounced, it is nonetheless still striking.

(c) Parametric Assessment.

Fuel Molecular Structure. The results for the effect of fuel molecular structure on soot size and number density are presented in Fig. 9 for isooctane and the three blends (79 percent isooctane/21 percent toluene; 92 percent isooctane/8 percent tetralin; 95 percent isooctane/5 percent 1-methylnaphthalene) prepared to yield the same smoke point as a JP-8 stock. The data are normalized to the peak bin data rate observed for JP-8 at an air-to-fuel ratio = 2.5, ϕ = 0.3 (Fig. 10(*b*)). The total data rates for each location are tabulated in Table 3.

It is first noteworthy to compare the results for the isooctane blends (Figs. 9(*b*,*c*,*d*)) with the results for the pure isooctane (Fig. 9(*a*)). The data rates for the blends are higher than the data rates observed for the pure isooctane. Hence the addition of ring compounds (as small as 5 percent by volume in the case of 1-methylnaphthalene) has a substantial impact on the soot produced.

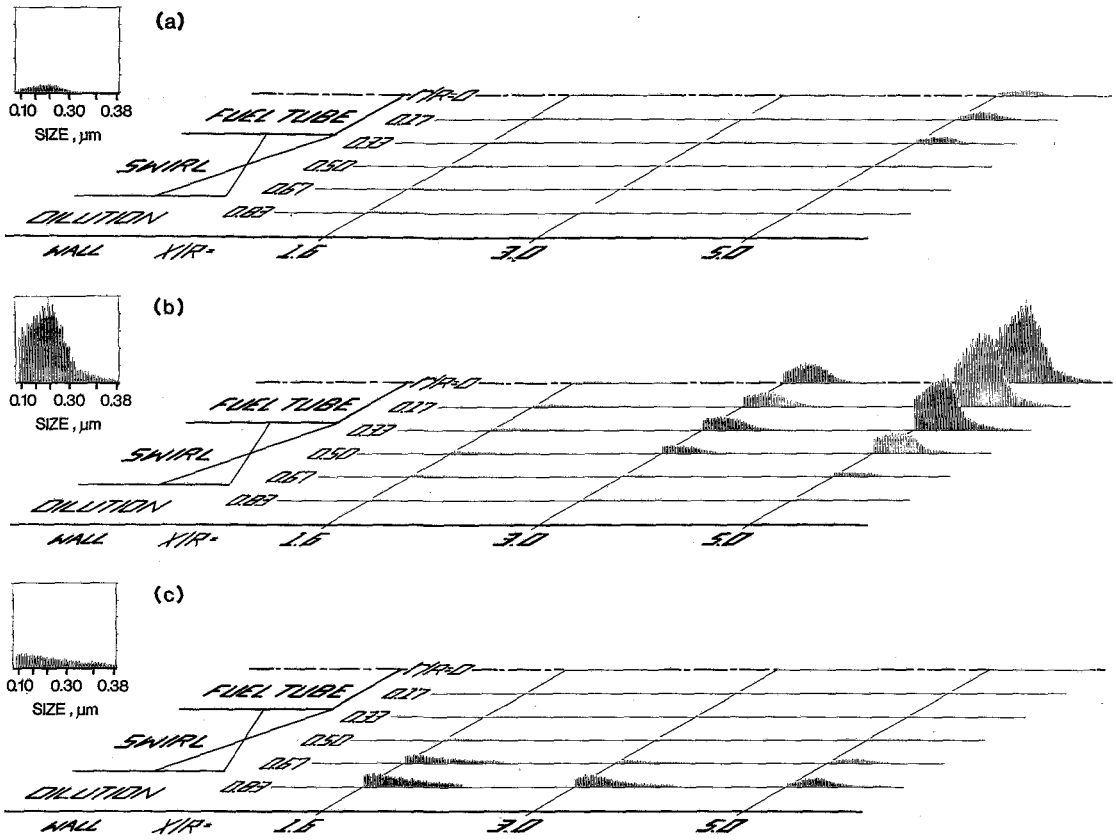

Fig. 10 Nozzle performance (JP-8, $\phi = 0.3$): (a) A/F = 3.0; (b) A/F = 2.5; (c) A/F = 3.5

For the isooctane and all three blends, soot is observed at all radial stations at the $x/R = 1.6$ axial station, but only at the outer radial stations at $x/R = 3.0$ and 5.0. This is attributed to (*i*) the intersection of the $x/R = 1.6$ axial station with the recirculation zone, the outer boundary of which extends to approximately 80 mm ($x/R = 2.0$), and (*ii*) the injection of the fuel into the outer boundary ("shear layer") of the recirculation zone. Note that the data rate is of the same magnitude for radial stations within the recirculation zone ($0 < r/R < 0.50$), which is consistent with the presence of a zone of strong backmixing.

The peak data rate for the isooctane and fuel blends occurs at the outer radial positions, coincident with the injection of fuel into the shear layer. Downstream of the recirculation zone ($x/R = 3.0$, 5.0), the soot particles are transported radially outward as a consequence of the strong swirl.

The data rate for isooctane drops dramatically at the two downstream locations and, at $x/R = 5.0$, the soot particulate is completely burned out. The addition of ring compounds, by contrast, not only results in more soot produced, but shows evidence of only marginal burn out.

The distribution of soot particulate has both similarities and significant differences in this data set. The distributions are similar in the relatively uniform distribution in the recirculation zone. The flatness of the distribution reflects an early stage of particulate formation prior to the onset of agglomerate growth. Evidence for the agglomerate growth is reflected in distributions measured at locations displaced from the recirculation zone, namely at $x/R = 1.6$ ($0.67 \leq r/R \leq 0.83$), $x/R = 3.0$, and $x/R = 5.0$. The distribution differs as to where within the combustor the agglomerate begins to build. The buildup of the agglomerate peak occurs further away from the recirculation zone as the molecular complexity of the ring compound increases. This reflects the longer time for fuel pyrolysis and/or longer time for polymerization as the fuel complexity increases.

Data were also obtained at a reduced fuel loading ($\phi = 0.3$) for the isooctane and three fuel blends. Virtually no soot particulate was detected by the optical probe at any of the eighteen sampling points within the combustor (e.g., total data rates were less than 1 Hz). In direct contrast, the total data rates for the shale-derived JP-8 at $\phi = 0.3$ were not insignificant (Table 3, Fig. 10(*a*)). It is also noteworthy that the highest sooting rate occurs at the centerline for the JP-8. This is attributed to the probable collapse of a portion of the fuel jet onto the centerline at this lower nozzle fuel flow rate. Such a collapse has been detected with two-color anemometry by Brum and Samuelsen [8] and the subsequent centerline formation of soot has been verified with high-speed video recordings.

Finally, the fuel blends, mixed to the same smoke point as the shale-derived JP-8, produced different soot yields (area-weighted soot flux) at the last axial plane sampled ($x/R = 5.0$, Figs. 9(*b–d*)). The double-ring tetralin and 1-methylnaphthalene blends both yielded a higher soot level than the single-ring toluene blend. The tetralin blend yielded the highest production of the three. At $\phi = 0.3$ the JP-8 yielded significant soot, whereas the blends yielded no soot at this lower equivalence ratio.

Nozzle Performance. To assess the effect of nozzle performance, the nozzle air-to-fuel (A/F) ratio for one fuel, the JP-8, was varied from the nominal value of 3.0 by changing the air flowrate at a constant fuel flowrate corresponding to $\phi = 0.3$ (Fig. 10). At a degraded level of performance ($A/F = 2.5$), the soot production went up markedly (Fig. 10(*b*)). This demonstrates the importance of nozzle performance in dictating sooting levels. As further

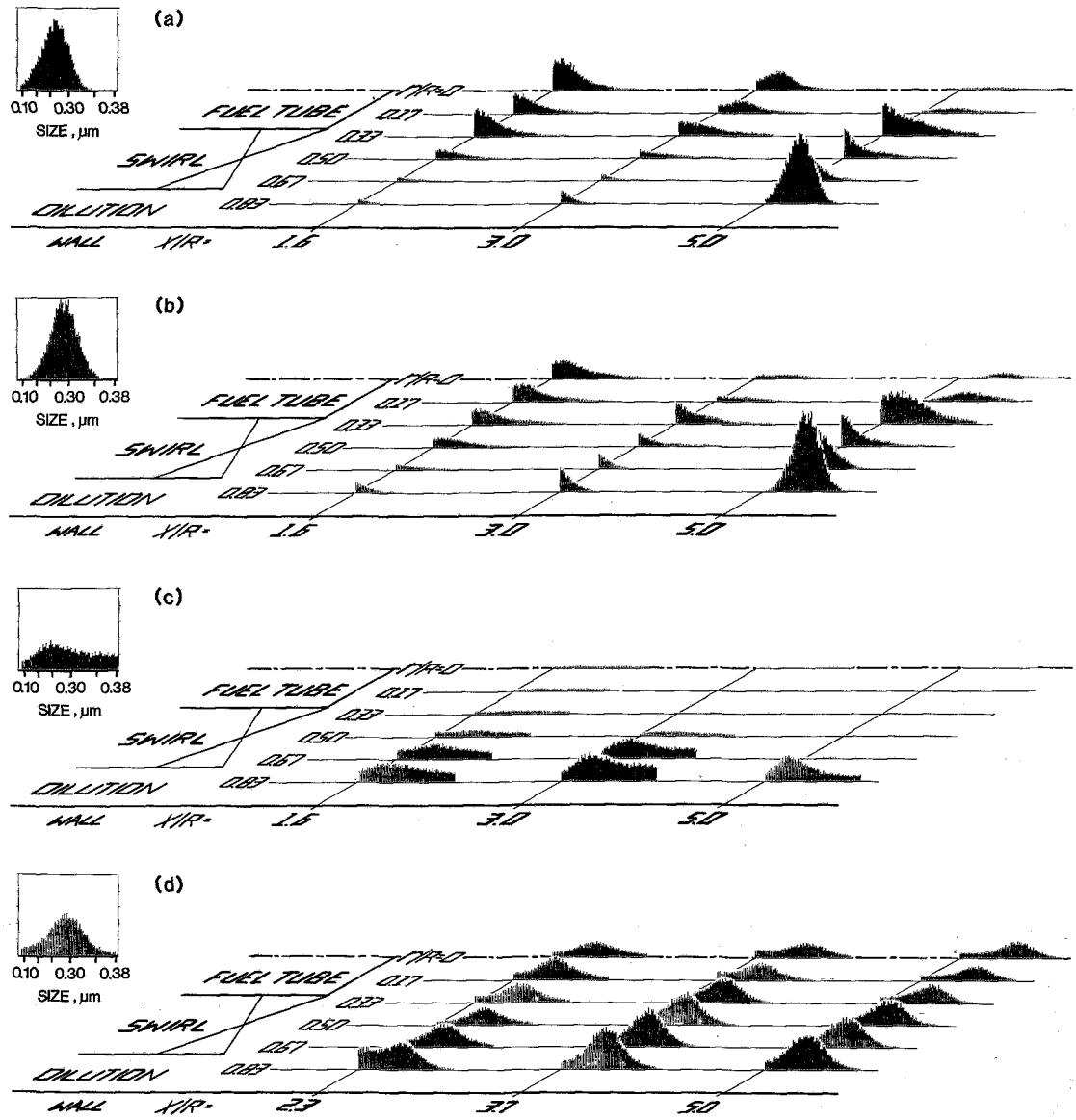

Fig. 11 Injection state (isooctane/tetralin): (*a*) prevaporized injection, $\phi = 0.5$; (*b*) prevaporized injection, $\phi = 0.3$; (*c*) liquid injection, $\phi = 0.5$; (*d*) prevaporized injection, diminished swirl intensity, $\phi = 0.5$

evidence for this, note that the spatial distribution of soot for $A/F = 3.5$ (Fig. 10(*c*)) is different from that measured for $A/F = 3.0$ and 2.5 Figs. 10(*a*,*b*)), and similar to the spatial distributions measured for the blends at $\phi = 0.5$, $A/F = 3.0$ (Figs. 9(*b*,*c*,*d*)). This is attributed to a higher fuel momentum associated with the higher A/F (in the case of the JP-8 at $\phi = 0.3$) and higher fuel flow rate (in the case of the blends at $A/F = 3.0$), thereby preventing collapse of fuel onto the centerline.

Prevaporization. One blend (92 percent isooctane/8 percent tetralin) was injected prevaporized through a cone-annular nozzle (see Fig. 1) to assess the sooting propensity when evaporation of injected droplets is not a factor in the injection and subsequent fuel/air contacting. The results are shown in Fig. 11 for $\phi = 0.5$ (Fig. 11(*a*)) and $\phi = 0.3$ (Fig. 11(*b*)). (The tetralin blend injected in the liquid state at $\phi = 0.5$ is shown in Fig. 11(*c*) and is normalized to Fig. 11(*b*) for comparison.) The soot yield was greater for the fuel injected prevaporized and soot was present at all points measured in the combustor. This is consistent with previous results [6], shown in Fig. 11(*d*), where the swirl was not as intense. This difference in sooting behavior is attributed to the different fuel distribution in the recirculation zone resulting from (*i*) the state of the fuel when injected, and (*ii*) the nozzle. Fuel injected as a vapor enhances the early mixing with the air, and rapidly breaks down the jet penetration. The resulting flames reflects a fuel rich, diffusion type core that extends out of the combustor, giving enhanced sooting levels at the interior radial positions along the entire length of the duct. In contrast, fuel injected as liquid droplets can direct the fuel into the outer boundary of the swirl-induced recirculation zone (the shear layer) resulting in enhanced processing of the fuel within the recirculation zone. This decreases the diffusion type character of the flame, reduces the soot produced, and limits the presence of soot to the outer portion of the combustor.

Summary and Conclusions

An optical system based on large angle intensity ratioing has been used to measure soot particulate in an aerodynamically complex flow field representative of a practical turbine combustor. The utility of such a diagnostic

tool is the provision of detailed mapping to identify the regions of soot formation and burnout. To demonstrate the utility and applicability of the technique, parametric variation on fuel molecular structure, fuel loading, nozzle performance, and injection state were performed. The results are summarized in the following list of observations and conclusions:

Summary of Observations.

- Blends of ring compounds in isooctane (as little as 5 percent 1-methylnaphthalene) produced substantially more soot than the isooctane alone.
- Blends mixed to the same smoke point as a shale-derived JP-8 and injected as liquid sprays yielded less soot than the JP-8 and varied among the blends in the yield of soot with the multi-ring tetralin and 1-methylnaphthalene blends producing substantially more soot than the single-ring toluene blend.
- The soot yield for the blend injected prevaporized was higher than for the fuel injected as a liquid. Whereas soot was virtually absent in the core of the combustor for the blends injected as liquids, the soot was spatially distributed more evenly throughout the combustor for the blend injected prevaporized. This is attributed to the reduced momentum of the prevaporized fuel jet and subsequent collapse of a portion of the fuel onto the centerline.
- Although the shale-derived JP-8 yielded more soot than the blends mixed to the same smoke point, an increased nozzle air-to-fuel ratio substantially reduced the soot produced and indicates that nozzle performance and combustor aerodynamics can be tailored to reduce the soot yield to approximately that of the blends. Nozzle air-to-fuel ratio not only changed the soot yield but also changed the spatial distribution of soot. At low air-to-fuel ratios, both the fuel jet momentum and atomization quality is degraded, a portion of the fuel collapses onto the centerline, and soot is produced in the core of the combustor. At high air-to-fuel ratios, the fuel is injected and processed in the shear layer of the recirculation zone.

Conclusions.

- The spatial distribution of soot, as well as the soot yield in a complex flow combustor, is a function of not only fuel molecular structure and fuel loading, but of flow aerodynamics and pattern of fuel injection. This result points to (*i*) the importance of *aerodynamics* and *nozzle performance*, alone and in combination, in controlling the amount of soot produced, and (*ii*) the requirement for spatially resolved, nonintrusive optical measurements in order to guide combustor design, nozzle design, and fuel property specifications for future fuels.
- To unravel and delineate the coupling between the aerodynamics and nozzle performance, and for the results derived from nonintrusive optical measurements in aerodynamically complex flows to be of quantitative as well as qualitative value:
  - -Optical techniques must be pursued to extend the resolvable size to encompass sizes below 0.05 μm.
  - -Spatially resolved measurements of the velocity and temperature must be acquired to facilitate interpretation of the soot field data.

Acknowledgments

The results presented were obtained in a soot formation/alternative fuels study in progress at the UCI Combustion Laboratory and supported by the Air Force Engineering and Service Center, Research and Development Directorate, Environics Division (Air Force Contract FO-8635-83-C-0052) with Captain Paul Kerch as the project manager. The authors gratefully acknowledge (*i*) the assistance of Roger Rudoff and Randy Smith in the collection, reduction, and presentation of the data, (*ii*) the assistance of Tom Jackson and Robyn Charles for their work in the spray analysis of the Parker-Hannifin twin-fluid injector, (*iii*) the cooperation of Parker-Hannifin in the provision of the nozzle and the valuable technical discussions with Mr. Harold Simmons and Mr. Curt Harding, and (*iv*) the kindness of KVB Engineering and Dr. Larry Muzio for providing use of the Malvern droplet analyzer. The optical particulate measurement system was developed under subcontract to Spectron Development Laboratories, with Dr. Chie Poon serving as the principal in the design.

References

1 Churchill, A. V., DeLaney, C. L., and Lander, H. R., "Future Aviation Turbine Fuels," *J. Aircraft*, Vol. 15, No. 11, 1978, pp. 731–734.

2 Prado, G. P., Lee, M. L., Hites, R. A., Hoult, D. P., and Howard, J. B., "Soot and Hydrocarbon Formation in a Turbulent Diffusion Flame," *Sixteenth Symposium (International) on Combustion*, The Combustion Institute, 1976, pp. 649–661.

3 Wyatt, W. R., Clark, J. A., Peters, J. E., and Mellor, A. M., "Size Distribution and Surface Area Measurements of Gas Turbine Combustor Smoke," *Journal of Energy*, Vol. 3, No. 5, 1979, pp. 285–290.

4 Himes, R. M., Hack, R. L., and Samuelsen, G. S., "Chemical and Physical Properties of Soot as a Function of Fuel Molecular Structure in a Swirl-Stabilized Combustor," ASME JOURNAL OF ENGINEERING FOR GAS TURBINES AND POWER, Vol. 106, No. 1, Jan. 1984, pp. 103–108.

5 Hack, R. L., Samuelsen, G. S., Poon, C. C., and Bachalo, W. D., "An Exploratory Study of Soot Sample Integrity and Probe Perturbation in a Swirl-Stabilized Combustor," ASME JOURNAL OF ENGINEERING FOR POWER, Vol. 103, No. 10, 1981, pp. 759–771.

6 Samuelsen, G. S., Wood, C. P., and Jackson, T. A., "Optical Measurements of Soot Size and Number Density in a Complex Flow, Swirl-Stabilized Combustor," Combustion Problems in Turbine Engines, AGARD Conference Proceedings, No. 353, North Atlantic Treaty Organization, Oct. 1983.

7 Brum, R. D., and Samuelsen, G. S., "Assessment of a Dilute Swirl Combustor as a Bench Scale, Complex Flow Test Bed for Modeling, Diagnostics, and Fuels Effects Studies," AIAA Paper No. 82-1263, 1982.

8 Brum, R. D., and Samuelsen, G. S., "Two-Component Laser Anemometry Measurements in a Nonreacting and Reacting Complex Flow Model Combustor," WSS/CI Paper 82-53, 1982.

9 Parker-Hannifin. private communication by Mr. Curt Harding, 1983.

10 Sawyer, R. F., "Experimental Studies of Chemical Processes in a Model Gas Turbine Combustor," *Emissions From Continuous Combustion Systems*, edited by W. Cornelius and W. G. Agnew, Plenum, New York, 1972, pp. 243–254.

11 Fenton, D. L., Luebcke, E. H., and Norstrom, E., "Physical Characterization of Particulate Material From a Turbine Engine," ASME Paper 79-GT-179, 1979.

T. Ahmad
Staff Research Engineer.

S. L. Plee
Staff Research Engineer.

J. P. Myers
Senior Research Engineer.
Engine Research Department,
General Motors Research
Laboratories,
Warren, Mich. 48090

Computation of Nitric Oxide and Soot Emissions From Turbulent Diffusion Flames

An existing steady-state, locally homogeneous flow model of turbulent spray combustion was modified to predict NO emission from a spray flame and soot emission from a gas-jet flame. The effect of turbulent fluctuations on the reaction rates was accounted for. The predicted NO emission from an n-pentane spray with a changing injection velocity could be correlated with the convective time scale of the flow. Calculation of soot emission from a burning turbulent gas jet indicated that the centerline soot concentration reaches a peak upstream of the maximum temperature location and then decreases due to soot oxidation and dilution by air entrainment.

Introduction

Detailed models of spray combustion in practical devices are desirable because they have potential for reducing the need for cut-and-try methods during the combustion chamber development. Modeling of combustion in practical systems requires development of turbulence models of flow and the combustion process. Additionally, if the prediction of pollutant emission is desirable, the interaction between turbulence and kinetics must also be considered. Due to the lack of information about the kinetics of pollutant formation and destruction in spray flames and about the effect of turbulent fluctuations on reaction rates, detailed models of emissions from spray-combustion systems are virtually nonexistent. However, significant progress has been made toward the development of combustion models for these flames. These models have been classified as either locally-homogeneous-flow (LHF) models, where the phases are assumed to be in kinematic and thermodynamic equilibrium, or as two-phase flow (TPF) models, where the transport between the phases is considered [1]. Although the LHF models are generally valid only when the spray drops are small, these models require minimal injector specifications and have significant advantages over the TPF models in terms of computation time.

In the present study, a LHF model of steady spray combustion has been modified to calculate NO and soot emissions from turbulent diffusion flames. An n-pentane spray was selected for the NO calculations. However, due to uncertainty in the formation and oxidation rates of soot, a simpler flow system, namely a gas-jet, was considered for soot computations.

Calculation Procedure

The Flow Model. The flow model used in this investigation has been utilized by Mao et al. [2]. Reference [2] provides the details of the formulation of the equations of motion and their numerical solution. The model considers a steady, axisymmetric, turbulent spray issuing from a simple hole-type fuel injector into a quiescent infinite medium.

Employing the assumptions and approximations utilized by the model, the following conservation equations for No and soot can be derived.

$$\bar{\rho}\bar{u}\frac{\partial Y_i}{\partial x} + \bar{\rho}\bar{v}^{\circ}\frac{\partial Y_i}{\partial r} - \frac{1}{r}\frac{\partial}{\partial r}\left(r\frac{\mu_t}{\sigma_i}\frac{\partial Y_i}{\partial r}\right) = \bar{S}_i \qquad (1)$$

where

$$\bar{\rho}\bar{v}^{\circ} = \bar{\rho}\bar{v} + \overline{\rho' v'} \qquad (2)$$

The source terms $\bar{S}_i$ represents the net time-averaged reaction rate for the production of species i (NO or soot). The source term for soot $\bar{S}_s$, can be written in terms of the formation and oxidation components as follows.

$$\overline{S_s} = \overline{S_{s,\text{form}} + S_{s,\text{ox}}} \qquad (3)$$

Modeling of the source terms involves selection of appropriate kinetic expressions from the literature as well as consideration of the interaction between turbulence and chemical kinetics.

Treatment of Source Terms

NO Kinetics. The NO source term is written as

$$S_{\text{NO}} = 10^3 M_{\text{NO}}\frac{d[\text{NO}]}{dt} \qquad (4)$$

where the rate of NO formation and destruction, $d[\text{NO}]/dt$, is described by the extended Zeldovich mechanism using the customary N-atom, steady-state approximation (see, e.g., [3, 4]). The simplest scheme for evaluating $d[\text{NO}]/dt$ is to also assume that the concentrations of O_2, N_2, OH, and O-atom are in equilibrium and that the NO formation process is slow compared to the time required for the other species to equilibrate. Because of its simplicity, this technique is used extensively in modeling NO formation from practical combustion systems and is generally more valid at high pressures

Contributed by the Diesel and Gas Engine Division for publication in the JOURNAL OF ENGINEERING FOR GAS TURBINES AND POWER. Manuscript received by the Diesel and Gas Engine Division March 19, 1984.

and in lean mixtures [4]. The equilibrium concentrations required by $d[NO]/dt$ were computed from the LHF model (see [2]), while the rate coefficients were taken from [5, 6].

Soot Kinetics. The amount of soot emitted by a flame depends on the competition between the formation and oxidation reactions. Thus the net instantaneous formation rate is given by the sum of formation and oxidation rates, as shown in equation (3). In most situations, formation and oxidation are inherently coupled. Therefore, the accuracy of a formation rate expression, which is almost invariably based on the measurement of net soot produced, depends on the choice of the oxidation mechanism.

Soot Formation. Numerous theories on the mechanisms of carbon formation have been proposed whose details are available in several excellent papers in the literature, see for example [7]. The present study is restricted to the relatively small body of literature related to quantitative estimation of the rate of soot formation [8, 9].

In the present study, the term $S_{s,\text{form}}$ in equation (3) was modeled using two schemes: an arbitrary one-equation empirical scheme that assumes soot formation to be a first-order reaction with respect to the fuel

$$S_{s,\text{form}} = \left(\frac{dm_s}{dt}\right)_{\text{form}} = Zm_f \exp(-E/RT) \tag{5}$$

and the multistep mechanism proposed by Tesner et al. [8]

$$\frac{dn}{dt} = a_o m_f \exp(-E/RT) + (f-g)n - g_o nN \tag{6}$$

$$\left(\frac{dm_s}{dt}\right)_{\text{form}} = (a - bN)np_w \tag{7}$$

Soot Oxidation. Similar to soot formation, considerable controversy exists over the exact mechanism of soot oxidation. Appleton [10] has reviewed the literature and concluded that in practical combustion systems, the semiempirical expression proposed by Nagle and Strickland-Constable provides the best method for estimating soot oxidation rates. However, in a recent study, Neoh et al. [11] found that the Nagle and Strickland-Constable expression drastically underestimated soot burnout rates under fuel-rich and near-stoichiometric conditions, because it considers only the oxidation by O_2 and ignores oxidation by OH radicals. In the present study, the oxidation of soot by OH radicals has also been accounted for using the expression proposed by Fenimore and Jones [12]. Thus the total soot oxidation rate would be

$$S_{s,\text{ox}} = \left(\frac{dm_s}{dt}\right)_{\text{ox}} = -\frac{60m_s}{\rho_s D_p}(\omega_{o_2} + \omega_{\text{OH}}) \tag{8}$$

Magnussen [9] has developed an eddy-dissipation scheme for soot oxidation that assumes oxidation of soot and fuel are mutually related and are controlled not by kinetics but by local mixing in eddies of the Kolmogorov scale. Thus

$$\left(\frac{dm_s}{dt}\right)_{\text{ox}} = \frac{dm_f}{dt}\frac{\bar{m}_s}{\bar{m}_f} \tag{9}$$

He developed an expression for the fuel consumption rate, dm_f/dt, in terms of local turbulence parameters. Using this oxidation scheme with Tesner's [8] soot formation model, Magnussen [9] obtained reasonable agreement with soot concentration in an acetylene-jet flame.

The combinations of formation and oxidation schemes used in this study to model S_s are summarized in Table 1.

Interaction Between Turbulence and Kinetics. In a one-step, first-order reaction represented by an Arrhenius expression, the turbulent fluctuations in the species con-

Nomenclature

a = constant (1/s)
a_0 = constant (particle/kg-s)
b = constant (m^3/particle-s)
C_s = soot concentration (g/m^3)
D_p = particle diameter (m)
d_{inj} = fuel injector diameter (m)
E = activation energy (kJ/mole)
EINO = NO emissions index (g/kg)
EIS = soot emissions index (g/kg)
f = constant (1/s)
g = constant (1/s)
g_o = constant (m^3/s-particle)
m = mass concentration (kg/m^3)
M = molecular weight (g/mole)
N,n = number concentration of soot particles and nuclei, respectively (particle/m^3)
p_w = average particle mass (kg/particle)
Re = Reynolds number
R = gas constant (kJ/mole-K)
r = jet radius (m)
S = source term (kg/m^3-s)
T = temperature (K)
t = time (s)
u = velocity in axial direction (m/s)
U_{inj} = fuel injection velocity (m/s)
v = velocity in radial direction (m/s)
x = distance along the jet or spray axis
Y = mass fraction
Z = preexponential constant (1/s)
σ = turbulent Schmidt number
γ^* = mass fraction of the total fluid contrained in the fine structures
χ = reactiveness of the fuel in fine structures
μ_t = turbulent viscosity (kg/m-s)
ω = surface oxidation rate of soot (g/cm^2-s)
ρ = density (kg/m^3)
[ ] = molar concentration (mole/cc)

Subscripts

form = formation
f = fuel
i = species i
inj = injection conditions
j = species j
max = maximum conditions
NO = mechanism involving NO
O_2,OH = mechanism involving O_2 and OH, respectively
ox = oxidation
s = soot or carbon

Superscripts

$-$ = mean or time-averaged condition
$*$ = conditions in the fine structure
o = conditions in the fluid surrounding the fine structures
$'$ = turbulence quantity

Table 1

Scheme	Term	Source
1	$S_{s,\text{form}}$	equation (5)
	$S_{s,\text{ox}}$	equation (8)
2	$S_{s,\text{form}}$	Tesner's model[a] [8] equations (6, 7)
	$S_{s,\text{ox}}$	Magnussen's model [9] equation (9)

[a]In this case, in addition to the conservation equations for NO and soot (equation (1)), a conservation equation for the radical nuclei n was also solved using Tesner's and Magnussen's expressions for production and destruction of n, respectively.

Table 2

	NO calculations	Soot calculations
Fuel	n-penetane	Propane
d_{inj}	2.0×10^{-4} m	2.54×10^{-3} m
Ambient pressure	6 MPa	0.1 MPa
Injection velocity	40, 69, 90 m/s	80.7 m/s

Table 3

U_{inj} (m/s)	$\bar{T}_{\max}$ (K)	$[\text{NO}]_{\max}$ (ppm)	$(x/d_{\text{inj}})^*_{\max}$
40	2143	589	450
69	2158	460	500
90	2165	348	500

*Location of the maximum centerline mean temperature and NO concentration

centrations and temperature can significantly influence the time-averaged reaction rate due to the nonlinear dependence of the reaction rate on the thermodynamic state variables. Therefore, for the calculation of NO and soot emissions, the influence of turbulence on their rate expressions must be accounted for. Borghi [13] has developed a series-expansion solution for the time-averaged reaction rate for CO combustion in a turbojet plume. This expression involves terms such as $\overline{T' Y_i'}$ and $\overline{T' Y_j'}$. Evaluation of these terms is a formidable task because it requires solutions of their conservation equations [13].

Magnussen [9] has developed a simpler eddy-dissipation concept to account approximately for the effect of turbulence-kinetics interaction. This concept assumes that the mixing at a molecular level, which is a prerequisite for chemical reaction, occurs in the fine eddy structures whose characteristic dimension is similar to the Kolmogorov microscale.

Following Magnussen [9], the time-averaged form of the source terms are weighted averages of the reaction rates in the fine structures and the surrounding fluid. The source terms for NO and soot are

$$\bar{S}_{\text{NO}} = S^*_{\text{NO}} \chi\gamma^* + (1 - \chi\gamma^*) S^o_{\text{NO}} \tag{10}$$

and

$$\bar{S}_s = (S^*_{s,\text{form}} + S^*_{s,\text{ox}}) \chi\gamma^* + (1 - \chi\gamma^*)(S^o_{s,\text{form}} + S^o_{s,\text{ox}}) \tag{11}$$

The parameters γ^* and χ represent the mass fraction of the total fluid contained in the fine structures and the ratio between the local concentration of reacted fuel and the total fuel concentration, respectively. Magnussen [9] provides expressions for γ^* and χ in terms of the local properties of the flow and the fluid. The fine-structure and the surrounding-fluid properties T^*, Y_i^*, T^o, and Y_i^o were computed from γ^*, χ, and the mean fluid properties (see [9] for details). All kinetic expressions used for the source terms were approximated in this manner to account for the effect of turbulent unmixedness.

Results and Discussion

NO Emissions. NO computations were performed for a high-pressure, n-pentane spray. The conditions considered are summarized in Table 2.

A pressure of 6 MPA was considered because at a supercritical pressure the two-phase effects were expected to be relatively less important and the locally homogeneous flow approximation more valid. Since the conservation equations for NO and soot involved kinetic expressions, the gradients of the source terms were expected to be large in the flame zone. The numerical stability of the solution was ensured by using 59 computation nodes in the radial direction instead of the 29 which the code originally employed. Throughout this study, the original turbulence-model constants were used [2].

The kinetic equations were modified to account for the turbulent fluctuations in the manner discussed previously. This step was necessary because using the mean temperature, and concentrations in the rate expressions yielded unreasonably low predictions of NO concentration (about 1 ppm maximum).

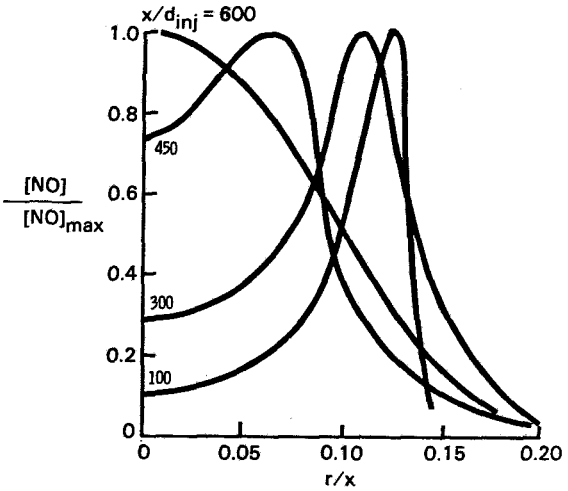

Fig. 1 Radial profiles of normalized NO concentration at different axial locations

General Characteristics. The general characteristics of the profiles for NO and mean temperature are in agreement with the measurements in a C_2H_2 jet flame [9], a H_2-air flame [14], a C_3H_8 jet flame [15, 16], and a kerosene spray flame [16], all at atmospheric pressure. Figure 1 shows typical radial profiles of normalized NO concentration at various axial locations. A comparison of the NO profiles in Fig. 1 with the calculated profiles for mean temperature (not shown) shows that the NO concentration peaks nearly coincide with the temperature peak in the radial direction. Experimentally, Bilger and Beck [14], as well as Onuma et al. [16], noticed that the NO concentration peaked slightly on the rich side of the stoichiometric location near the location of maximum temperature.

Effect of Injection Velocity. Figure 1 illustrates the centerline axial profiles of NO concentration for different fuel-injection velocities. As observed in the case of radial profiles, the peak centerline NO concentration coincides with the peak temperature along the axis, the location of the peak being only slightly dependent on the fuel-injection velocity (see Table 3).

The insensitivity of the location of the temperature [17] and NO peaks to the injection velocity is a characteristic of diffusion flames with pure forced-convection structures and negligible buoyancy. Thus the decrease in NO concentration with increasing U_{inj} can be interpreted as a residence-time effect.

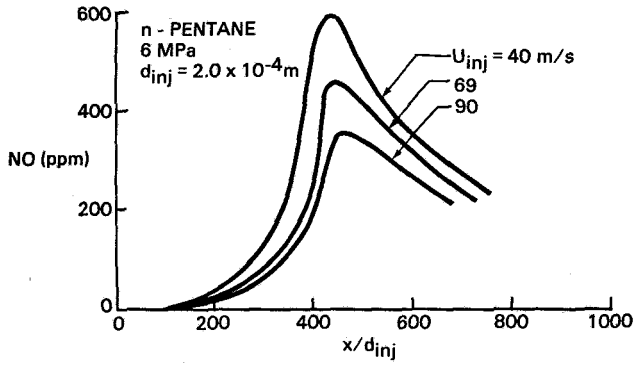

Fig. 2 Axial profiles of NO concentration for different injection velocities

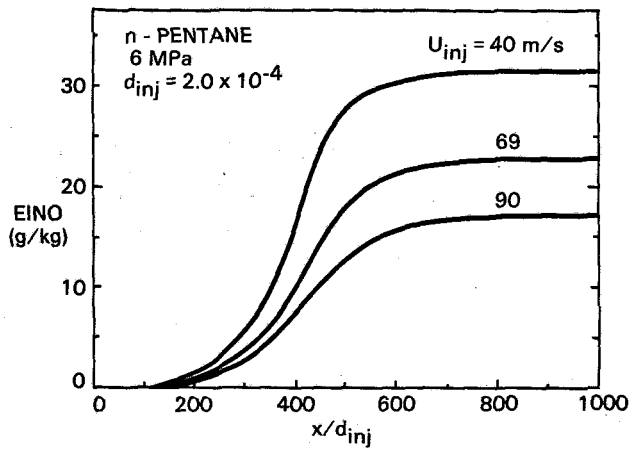

Fig. 3 Axial profiles of NO emission index for different injection velocities

In Figure 3, the total NO flow rate through each axial cross section, expressed as emission index (g NO/kg fuel), is plotted against the axial distance from the nozzle tip normalized by the injector diameter. The NO flow rate is obtained by numerically integrating the radial profiles of NO concentration, mean density, and mean velocity over the cross section. A similar decrease in NO with increasing injection velocity has been reported for H_2 and C_3H_8 diffusion flames [14, 15].

In [18], the dependence of the characteristic NO formation rate given by the ratio of EINO (or $Y_{NO,max}$) to the integral time scale of the flow, d_{inj}/U_{inj}, was plotted against the Reynolds number of the injected fluid. At low injection velocities, the characteristic formation rates showed some Re_{inj} dependence. However, in the high-Re_{inj} regime, where the flame structure is fully developed, the formation rate became independent of Re_{inj}. Consistent with the findings of Mellor [19] for gas turbine combustors, this result implies that the NO emission correlates only with the integral time scale of the flow. The emission index rises rapidly near the flame tip and then becomes constant as the NO reactions freeze in the downstream region due to a rapid temperature drop and air entrainment. The fact that EINO becomes constant past the flame tip also suggests that NO decomposition is insignificant.

Soot Emissions. As discussed earlier, modeling soot formation is much more difficult than modeling NO formation because soot kinetics are far from understood, even in the simplest combustion systems. Therefore, for simplicity, a turbulent gas jet was considered for soot calculations.

Becker and Yamazaki [17, 20] have reported measurements of soot concentration and mean temperature profiles in

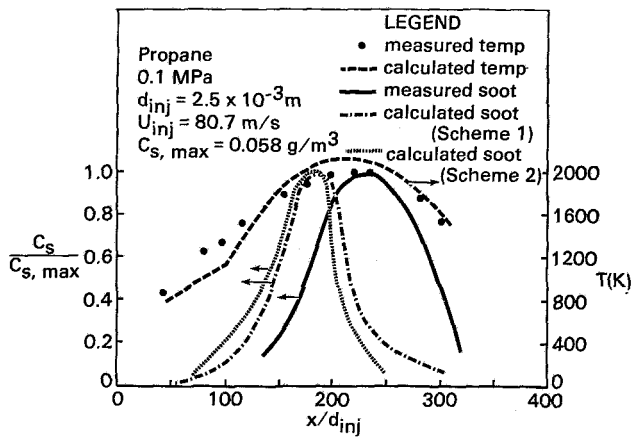

Fig. 4 Comparison of calculated and measured mean temperatures and soot concentrations along the jet axis

propane jet flames over a wide range of injection velocities. The conditions considered here for soot calculations (Table 2) represent a high-Reynolds-number case considered by Becker and Yamazaki [17, 20].

The two combinations of formation and oxidation schemes given in Table 1 were used in the calculations. The formation constant Z in equation (5) and constant a in Tesner's model found in equation (7) were adjusted to 8×10^9 and 3.5×10^8, respectively, to match the measured maximum centerline soot concentration of 0.058 g/m^3 for this flame [20]. Following Glassman and Yaccarino [21], a value of 352 kJ/mole was used for E in equation (5). No adjustments were made to the turbulence-model constants and the oxidation rate coefficients.

Major sources of uncertainty in soot calculations include approximations involved in treating the effect of turbulent unmixedness on reaction rates, the crude global nature of formation expressions, and errors in temperature calculations. Tesner's model was developed originally for C_2H_2 flames whose sooting characteristics are known to be different from those of saturated hydrocarbon flames [7]. Therefore, the values of the activation energy and of chain branching and termination coefficients determined by Tesner et al. [8] are not expected to be valid for other fuels. Furthermore, the activation energy used in the one-equation formation scheme (equation (5)) was determined from potentially less accurate sooting-height measurements for a laminar diffusion flame burning butane [21]. Although the preexponential constants were adjusted to match the maximum centerline soot concentration in both schemes, the shapes of the axial and radial concentration profiles are expected to be dependent on the activation energy.

General Characteristics. Figure 4 compares the calculated profiles of centerline mean temperature and normalized soot concentration with the measurements reported by Becker and Yamazaki [17, 20]. A good agreement was found between the calculated and measured flame lengths based on the location of the maximum centerline temperature ($x/d_{inj} \approx 220$). In the region $x/d_{inj} \leq 100$, the theory underestimated the temperature, the maximum disagreement being about 20 percent. A comparison reported by Mao et al. [2] for a propane jet flame also shows somewhat similar characteristics in the near-injector zone. The calculation errors in the high-mixture-fraction region result primarily from the approximations involved in formulating the equilibrium properties used by the code as an input [2]. Fortunately, the reaction rates for the kinetically controlled species are insignificant in this region because of the low temperature. Thus, the errors in the calculation of temperature in the near-injector region should not significantly affect the computed soot concentration.

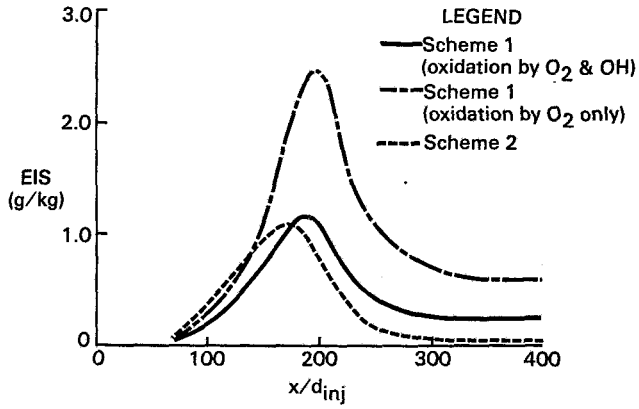

Fig. 5 Comparison of the predictions of different soot oxidation schemes

In the high-temperature region ($150 \leq d_{inj} \leq 300$), the maximum discrepancy between the theory and the data was found near the flame tip and was of the order of 120 K. In this region, the errors in formulating the equilibrium properties are expected to be small, therefore, this discrepancy can be attributed to the assumptions of the model, in particular, the assumption of negligible radiation. Although the temperature overestimate in this region would affect the soot calculations, a better agreement between calculated and measured temperatures should not be expected due to the limitations of both theory and experiment in treating sooty turbulent flames.

The axial profiles of soot concentration, normalized by the maximum centerline concentration ($C_{s,max}$) computed from the two schemes, are also shown in Fig. 4. The shapes of the predicted and measured profiles are similar, the soot concentration reaching a maximum in the vicinity of the flame tip and then decreasing to a small value. The most interesting feature of the calculated soot profiles is the similarity between the two despite the widely different natures of the formation and oxidation expressions. Both schemes predict maxima in soot concentration on the fuel-rich side of the flame tip, i.e., at $x/d_{inj} \approx 180$. However, the soot data show a peak at $x/d_{inj} \approx 240$, which is slightly on the fuel-lean side but for all practical purposes can be assumed to coincide with the temperature peak. A detailed discussion of the discrepancy between the experimental and theoretical location of the peak soot concentration is given in [18].

The net soot concentration in a flame is determined by a balance between soot formation and oxidation rates. In the region between the injector nozzle and the flame tip, the soot concentration increases because the formation process dominates due to high fuel and low O_2 concentrations in this region. Thus formation dominates oxidation and the soot concentration increases initially with axial distance from the nozzle. At the point where the oxidation rate almost equals the formation rate, the maximum soot concentration is observed. Following this point, the soot concentration decreases due to high rates of oxidation (which now dominate formation) as well as because of radial turbulent diffusion and dilution by entrainment of air.

A comparison of the profiles predicted by the two schemes indicates that scheme 2 predicts a faster development of the soot field than scheme 1 partly due to the reason that a higher activation energy was used in scheme 2. Scheme 2 also predicts a sharper drop-off in soot concentration on the fuel-lean side of the flame tip than does scheme 1.

Oxidation by OH Radicals. The significance of soot oxidation by OH was examined by setting equal to zero the term ω_{OH} in the oxidation equation in scheme 1. In Fig. 5, the calculated soot emissions index (EIS) for this case is compared with the one obtained by considering oxidation by both O_2 and OH. EIS for both cases peaks at about $x/d_{inj} \approx 180$ and then decreases due to oxidation. Note that the decrease in EIS following the peak is entirely due to soot oxidation, since the dilution because of air entrainment does not influence the soot mass flow across a radial plane. The case in which only the oxidation by O_2 was considered yields considerably larger quantities of soot through the flame, the final emissions indices being 0.26 and 0.69 with and without the OH mechanism, respectively. Thus ignoring soot oxidation by OH radicals could result in significant overprediction of the net soot emitted.

EIS computations using scheme 2 are also illustrated in Fig. 5. The net EIS predicted by scheme 2 was almost an order of magnitude less than that predicted by scheme 1 (EIS = 0.025). This result suggests that Magnussen's eddy-dissipation mechanism [9] predicts oxidation rates much higher than the kinetic mechanism.

Summary

A locally homogeneous-flow, steady-state spray combustion model has been modified to calculate NO and soot emissions from turbulent spray and jet flames. The NO calculations were performed for a n-pentane spray burning at 6 MPa for different fuel-injection velocities. The major results of this study are as follows:

1 Turbulent fluctuations significantly affect the reaction rates for NO and soot in turbulent flames, so ignoring this effect results in serious underprediction of the concentrations of kinetically controlled species.

2 For a high-Reynolds-number spray, the temperature field was insensitive to the fuel-injection velocity. Furthermore, variations in NO emission with a changing injection velocity could be correlated with the convective time scale of the flow.

3 With adjustment in the preexponential constants, both soot models examined in this study predicted correctly the overall profile of the soot concentration field.

4 The oxidation of soot by OH radicals could be significant in the region between the injector and the flame tip.

Acknowledgments

The authors gratefully acknowledge the helpful suggestions throughout this investigation of Professor G. M. Faeth of the Pennsylvania State University.

References

1 Faeth, G. M., "Spray Combustion Models—A Review," AIAA Paper No. 79-0293, 1979.

2 Mao, C-P., Szekely, Jr., G. A., and Faeth, G. M., "Evaluation of a Locally Homogeneous Flow Model of Spray Combustion," AIAA *Journal of Energy*, Vol. 4, 1980, pp. 78-87.

3 Westenberg, A. A., "Kinetics of NO and CO in Lean, Premixed Hydrocarbon-Air Flames," *Combust. Sci. Tech.*, Vol. 4, 1971, pp. 59-64.

4 Caretto, L. S., "Mathematical Modeling of Pollutant Formuation," *Prog. Energy Combust. Sci.*, Vol. 1, 1976, pp. 47-71.

5 Baulch, D. L., Drysdale, D. D., and Horne, D. G., "Homogeneous Gas Phase Reactions of the H_2-N_2-O_2 System." *Evaluated Kinematic Data for High Temperature Reactions*, Butterworths, London, 1973.

6 Flower, W. L., Hanson, R. K., and Kruger, C. H., "Kinetics of the Reaction of Nitric Oxide With Hydrogen," *Fifteenth Symposium (International) on Combustion*, The Combustion Institute, Pittsburgh, 1975, pp. 823-832.

7 Wagner, H., Gg., "Soot Formation in Combustion, *Seventeenth Symposium (International) on Combustion*, The Combustion Institute, Pittsburgh, 1979, pp. 3-19.

8 Tesner, P. A., Snegiriova, T. D., and Knorre, V. G., "Kinetics of Dispersed Carbon Formation," *Combust. Flame*, Vol. 17, 1971, pp. 253-260.

9 Magnussen, B. F., "Modeling of Reactions Processes in Turbulent Flames with Special Emphasis on Soot Formation and Combustion," *Particulate Carbon—Formation During Combustion*, edited by D. C. Siegla and G. W. Smith, Plenum Press, New York, 1981, pp. 321-341.

10 Appleton, J. P., "Soot Oxidation Kinetics at Combustion Temperatures, *Atmospheric Pollution by Aircraft Engines*, AGARD CP-125, Paper No. 20, 1973.

11 Neoh, K. G., Howard, J. B., and Sarofim, A. F., "Soot Oxidation in Flames," *Particulate Carbon—Formation During Combustion*, edited by D. C. Siegla and G. W. Smith, Plenum Press, New York, 1981, pp. 261–282.

12 Fenimore, C. P., and Jones, G. W., "Oxidation of Soot by Hydroxyl Radicals," *J. Phys. Chem.*, Vol. 71, 1967, pp. 593–597.

13 Borghi, R., "Chemical Reaction Calculations in Turbulent Flows: Application to a Co-Containing Turbojet Plume," *Advances in Geophysics*, edited by H. E. Landsberg and J. Mieghem, Vol. 18B, 1974, pp. 349–365.

14 Bilger, R. W., and Beck, R. F., "Further Experiments on Turbulent Jet Diffusion Flames," *Fifteenth Symposium (International) on Combustion*, The Combustion Institute, Pittsvurgh, 1975, pp. 541–552.

15 Takagi, T., Ogasawara, M., Fujii, K., and Daizo, M., "A Study of Nitric Oxide Formation in Turbulent Diffusion Flames," *Fifteenth Symposium (International) on Combustion*, The Combustion Institute, Pittsburgh, 1975, pp. 1051–1059.

16 Onuma, Y., Ogasawara, M., and Inoue, T., "Further Experiments on the Structure of a Spray Combustion Flame," *Sixteenth Symposium (International) on Comnbustion*, The Combustion Institute, Pittsburgh, 1977, pp. 561–567.

17 Becker, H. A., and Yamazaki, S., "Soot Concentration Field of Turbulent Propane/Air Diffusion Flames," *Sixteenth Symposium (International) on Combustion*, The Combustion Institute, Pittsburgh, 1977, pp. 681–691.

18 Ahmad, T., Plee, S. L., and Myers, J. P., "Computation of Nitric Oxide and Soot Emissions from Spray and Gas-Jet Flames," ASME Paper No. 82-WA/HT-1, 1982.

19 Mellor, A. M., "Semi-Empirical Correlations for Gas Turbine Emissions, Ignition and Flame Stabilization," *Prog. Energy Combust. Sci.*, Vol. 6, 1980, pp. 347–358.

20 Becker, H. A., and Yamazaki, S., "Entrainment, Momentum Flux and Temperature in Vertical Free Turbulent Diffusion Flames," *Combust. Flame*, Vol. 33, 1978, pp. 123–149.

21 Glassman, I., and Yaccarino, P., "The Temperature Effect in Sooting Diffusion Flames," *Eighteenth Symposium (International) on Combustion*, The Combustion Institute, Pittsburgh, 1981, pp. 1175–1183.

Free-Stream Turbulence and Pressure Gradient Effects on Heat Transfer and Boundary Layer Development on Highly Cooled Surfaces

K. Rued
Research Assistant.

S. Wittig
Professor.
Mem. ASME

Lehrstuhl und Institut für
Thermische Strömungsmaschinen,
Universität Karlsruhe (T.H.),
D-7500 Karlsruhe 1,
West Germany

Heat transfer and boundary layer measurements were derived from flows over a cooled flat plate with various free-stream turbulence intensities (Tu = 1.6–11 percent), favorable pressure gradients ($k = \nu_e/u_e^2 \cdot du_e/dx = 0 \div 6 \cdot 10^{-6}$) and cooling intensities (T_w/T_e = 1.0–0.53). Special interest is directed towards the effects of the dominant parameters, including the influence on laminar to turbulent boundary layer transition. It is shown, that free-stream turbulence and pressure gradients are of primary importance. The increase of heat transfer due to wall cooling can be explained primarily by property variations as transition, and the influence of free-stream parameters are not affected.

Introduction

Extremely high thermal and mechanical loading are typical characteristics of modern gas turbine blading. A reliable design of cooled gas turbine blades concerning both cooling efficiency and hardware durability is, therefore, highly dependent on an accurate prediction of heat transfer rates along the blade surfaces. A numerical calculation procedure, capable of predicting airfoil boundary layers and heat transfer, has to consider various influence parameters such as free-stream turbulence, wall to free-stream temperature ratio, surface curvature, pressure gradients, and surface roughness. The development and application of new numerical codes, commonly based on finite difference techniques for the solution of the basic boundary layer equations, including turbulence models, requires extensive and reliable experimental data [1].

In an effort to separate the influence parameters of gas turbine flow, previous analytical and experimental studies were directed towards idealized, nearly isothermal flat-plate conditions to describe the effects of free-stream turbulence on the boundary layer development and heat transfer characteristics (e.g., [2–4]). These studies indicate that the primary effect of an increase in free-stream turbulence is the upstream displacement of the onset of transition.

The effects of free-stream turbulence on turbulent boundary layer profiles lead to slightly fuller profiles and higher turbulence levels, resulting in higher momentum thicknesses, smaller form parameters, and increased heat transfer as well as skin friction coefficients (e.g., [3, 5, 6]). The effects are more evident when turbulent boundary layers of the same momentum thickness Reynolds number are compared. With respect to the influence of the turbulence intensity at the same streamwise location, the effects are partly vanished by the upstream displacement of transition.

In analyzing the combined influence of free-stream turbulence and pressure gradient, it was shown for nearly isothermal flows that the sign of the pressure gradient is of dominant influence. In addition, the relative strength of the two effects is to be considered. Adverse pressure gradients promote the onset of transition, whereas favorable pressure gradients stabilize the boundary layer and thus counteract the effect of free-stream turbulence, which may – dependent upon the strength of flow acceleration – result in a delay of transition onset and in an increase of transition length (e.g., [4, 7, 8]). In addition to the influence on the boundary layer transition, relatively strong effects on the heat transfer rates due to the presence of pressure gradients are observed.

The present program was initiated to provide new experimental boundary layer and heat transfer data for highly cooled surfaces, combining sequentially the effects of free-stream turbulence, wall cooling, and relatively strong favorable pressure gradients with emphasis on the laminar to turbulent boundary layer transition. For the initial stage of the experiments described in this paper, free-stream velocities up to 150 m/s, temperature ratios from $0.53 < T_w/T_e < 1.0$ and free-stream turbulence levels of Tu = 1.6–11 percent were chosen. The maximum pressure gradient parameter defined as $k = \nu_e/u_e^2 \cdot du_e/dx$ for the accelerating flow is $k = 6 \cdot 10^{-6}$.

Contributed by the Gas Turbine Division of THE AMERICAN SOCIETY OF MECHANICAL ENGINEERS and presented at the 29th International Gas Turbine Conference and Exhibit, Amsterdam, The Netherlands, June 4–7, 1984. Manuscript received at ASME Headquarters January 12, 1984. Paper No. 84-GT-180.

Experimental Setup and Diagnostics

The test section used for the experimental analysis of the boundary layer and heat transfer characteristics is shown in Fig. 1. The test section itself consists of a 440 × 125 mm^2 copper plate that is divided into 28 insulated segments. Each of the segments is cooled separately to ensure a constant plate surface temperature. The heat flux within the cooled segments is derived from one-dimensional heat conduction analysis, i.e., from the temperature difference determined by thermocouple measurements in the segments. The results are supported by finite element heat conduction calculations and enthalpie balances within the boundary layer. The local Stanton number is readily obtained from the local heat flux. To ensure a laminar starting boundary layer, the leading edge, which is uncooled for the first 15 mm, has an elliptical profile, and suction of the entering boundary layer is applied. The two-dimensionality and the laminar form of the starting boundary layer was confirmed by detailed profile measurements. Variation of the free-stream turbulence is accomplished by calibrated turbulence grids located 170 mm upstream of the plate's leading edge.

The free-stream turbulence is determined by Laser-Doppler anemometry as already described in detail in an earlier paper [9]. Pressure gradients along the plate are achieved by contoured upper channel walls. Two different acceleration parameter distributions of

$$k(x) = \frac{\nu_e}{u_e^2} \cdot \frac{du_e}{dx} \tag{1}$$

where chosen as illustrated in Fig. 2. The strong variations of $k(x)$ due to contour 2, which is closer to actual gas turbine flow, are evident with k_{max} approximately 3.2 • 10^{-6}. Contour 1 shows smaller but more uniform acceleration parameters.

Detailed boundary layer measurements were obtained in planes with 120, 220, 320, and 420 mm distance from the plate's leading edge. Pitot tube and total temperature measurements – the probe diameters were 0.4 and 0.25 mm, respectively – were applied. The Pitot tube total pressure profile was corrected following McMillan [10]. The turbulent

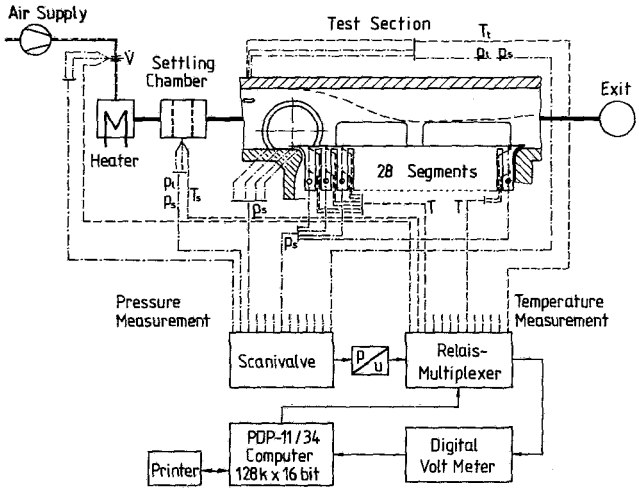

Fig. 1 Test section and instrumentation

skin friction was derived using the Preston technique [11] and additionally utilizing the law of the wall as shown in equation (2).

$$\frac{u}{u_\tau} = \frac{1}{0.41} \cdot \ln\left(\frac{y \cdot u_\tau}{\nu}\right) + 5.1 \tag{2}$$

with

$$u_\tau = \sqrt{\tau_w/\rho}$$

Only small discrepancies of less than 3 percent were observed. For the cooled plate in a hot gas flow, the properties were calculated using the reference temperature scheme following Holmes and Luxton [12]. The assumptions are confirmed by Laser-Dual-Focus (LDF) measurements [13, 14] of the boundary-layer profile.

The data acquisition is accomplished using a Scanivalve and a Relay-multiplexer, both controlled by a minicomputer (PDP 11/34), as indicated in Fig. 1.

Nomenclature

c_f = skin friction coefficient = $\dfrac{2\tau_w}{\rho_e \cdot u_e^2}$

c_{fo}, c'_{fo} = skin friction coefficients without free-stream turbulence

L = length of the plate

$L_e{}^u$ = dissipation length $\dfrac{-(\overline{u'^2})^{3/2}}{U \cdot \dfrac{d}{dx}(\overline{u'^2})}$

k = acceleration parameter

k_{max} = characteristic value of k for contour 2

Pr = molecular Prandtl number

$\dot{q}$ = heat flux

Re_x = Reynolds number = $u_e \cdot x/\nu_e$

Re_θ = Reynolds number based on momentum thickness

Re_{L0} = Reynolds number based on plate length and free-stream conditions at leading edge

St = Stanton number $\dot{q}_w/\rho_e \cdot u_e \cdot c_p (T_t - T_w)$ based on local free-stream conditions, c_p = specific heat

T = temperature

Tu = local free stream turbulence $\sqrt{\dfrac{1}{3}(\overline{u'^2}+\overline{v'^2}+\overline{w'^2})}/u_e$

Tu_o = free-stream turbulence at leading edge

u = velocity

u', v', w' = velocity fluctuations (u', v' = measured, $v' = w'$)

u_τ = skin friction velocity = $\sqrt{\tau_w/\rho}$

x = distance from the leading edge

y = distance from the wall

ρ = density

δ = boundary layer thickness

θ = $\int_0^\delta \dfrac{\rho \cdot u}{\rho_e u_e}\left(1 - \dfrac{u}{u_e}\right) dy$

ν = viscosity

ζ = uncooled starting length of the plate

Subscripts

e = free stream

w = wall

t = total

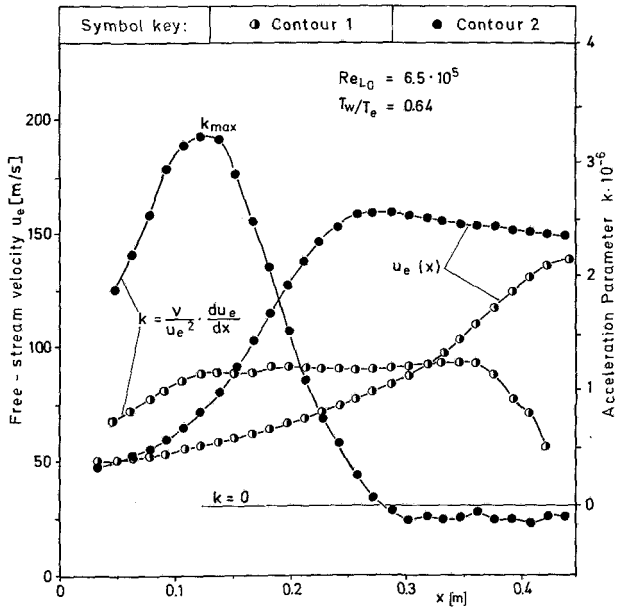

Fig. 2 Free-stream velocity and acceleration parameter k along the plate (flow conditions 6 and 7 in Table 1)

Experimental Conditions

The experimental conditions for the analysis of the influence of turbulence level, pressure gradients, and wall cooling are summarized in Table 1. The wall temperature was kept nearly constant ($T_w \approx 305$ K) under all conditions, whereas the free-stream temperature was adjusted. Figure 3(*a*) illustrates the decay of the turbulence intensity along the plate with zero pressure gradient (compare Rüd et al. [6]). The observed decays agree fairly well with those of Baines and Peterson [15]. Figure 3(*b*) compares the characteristic change of the turbulence intensities with and without pressure gradients. In determining the turbulence levels, it should be noted that the free-stream velocity increases strongly under the negative pressure gradients chosen.

In checking whether the turbulence is isotropic, the following ratios of the measured fluctuations were determined along the plate

$$\frac{\sqrt{\overline{v'^2}}}{\sqrt{\overline{u'^2}}} = \begin{cases} 0.7 \div 0.9 \text{ for } dp/dx = 0 \\ 0.9 \div 1.2 \text{ for } dp/dx < 0 \end{cases}$$

Results and Discussion

Influence of Free-Stream Turbulence on Heat Transfer and Skin Friction. The heat transfer measurements without pressure gradients reveal the influence of free-stream turbulence on the boundary layer transition and the heat transfer. The results are summarized in Figs. 4 and 5.

Figure 4 illustrates the variation of the transition onset, which is defined as indicated (see turbulence intensity 1.6 percent). Despite a moderately cooled wall ($T_w/T_e = 0.8$), the transition Reynolds numbers of 3.7×10^5 and 1.7×10^5 for turbulence levels of 1.6 and 2.3 percent, respectively, agree well with those found in the literature for uncooled plates [2]. Increasing the free-stream turbulence up to 8.7 percent leads to an upstream displacement of the transition towards the leading edge. In comparing the Stanton numbers with the relations given by Kays [16] for laminar and turbulent heat transfer in nearly isothermal flow, it is shown that for laminar boundary layers the Stanton numbers found with wall cooling are higher by approximately 7.5 percent, a relatively small

Table 1 Flow conditions

Nr.	dp/dx	T_e K	$T_W/T_{e,o}$ –	$u_{e,o}$ m/s	$Re_{L_o} \cdot 10^{-6}$ –
1 *K*	= 0.0	340	1.0	40	0.8
2	= 0.0	375	0.8	47	0.9
3	= 0.0	478	0.64	53	0.657
4	= 0.0	570	0.53	38	0.36
Contour = 1					
5 *K*	= $1.2\,10^{-6}$	381	0.8	35	0.64
6	= $1.2\,10^{-6}$	470	0.64	49	0.64
Contour = 2					
7 K_{max}	= $3.2\,10^{-6}$	463	0.64	48	0.654
8	= $5.65\,10^{-6}$	385	0.8	20	0.352
9	= $5.7\,10^{-6}$	467	0.64	27	0.345
10	= $6.3\,10^{-6}$	570	0.53	34	0.33

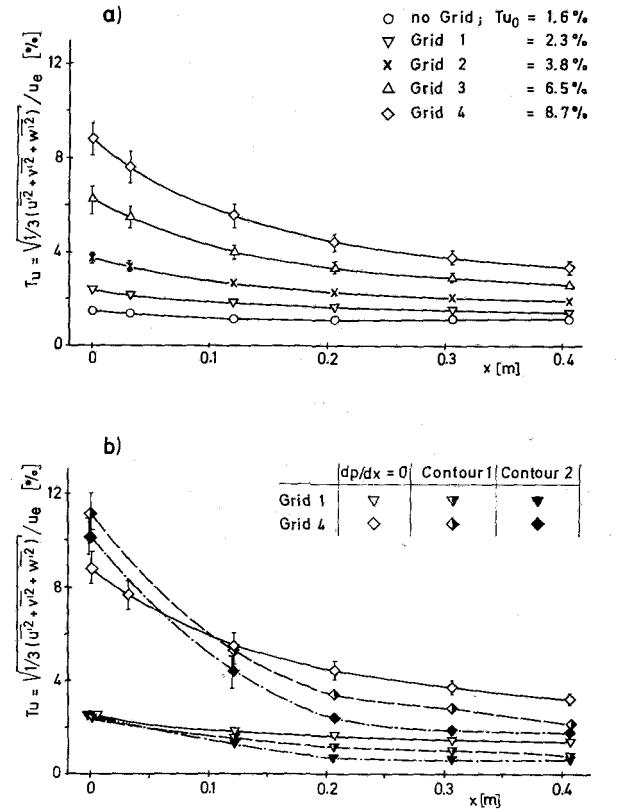

Fig. 3 Free-stream turbulence development along the test section with and without pressure gradients

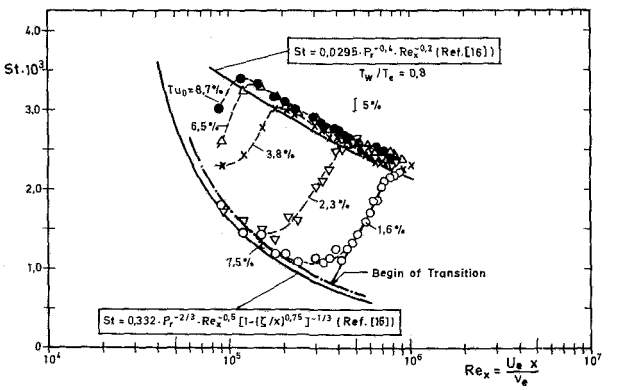

Fig. 4 Influence of free-stream turbulence on heat transfer and boundary layer transition

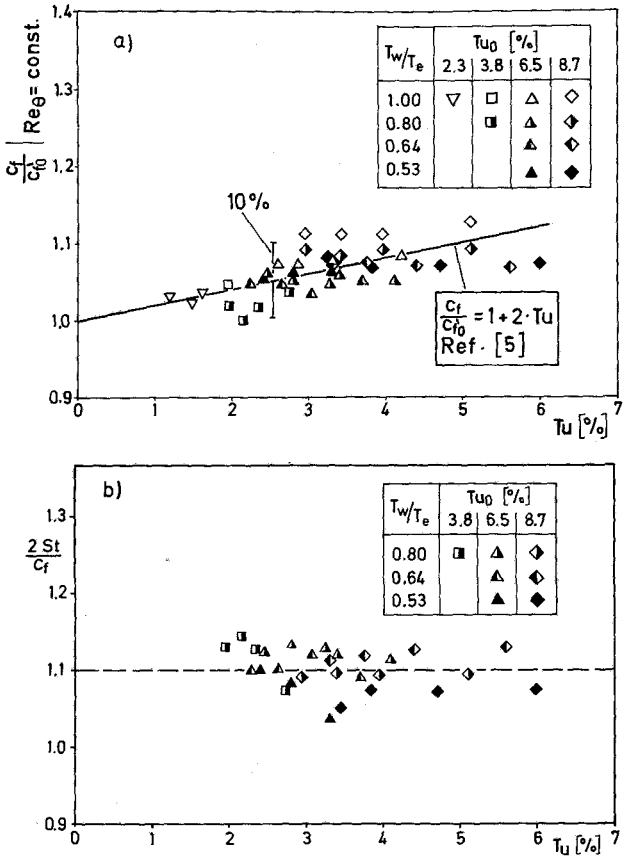

Fig. 5 Influence of free-stream turbulence on turbulent skin friction and heat transfer

effect which, however, is also confirmed at lower temperature ratios (T_w/T_e = 0.64 and 0.53) where the difference between the analytical relation and our measurements exceeds 20 percent. This observation is supported by the measurements with pressure gradients as will be shown later (Fig. 9). In modifying Kay's relation, the Stanton numbers for a broad range of temperature ratios can be correlated as follows

$$St = A \cdot Re_x^{-0.5} \cdot Pr^{-2/3} \cdot \left[1 - \left(\frac{\zeta}{x}\right)^{0.75}\right]^{-1/3} \quad (3)$$

with

$$A = 0.342 \cdot (T_w/T_e)^{-0.25}$$

For turbulent flow, a tendency to slightly increasing Stanton numbers with turbulence intensity is observed; its effect, however, is found to be partly within the measurement reproducibility (3 percent). Here, too, a cooling-dependent increase with temperature ratio up to approximately 10 percent is obtained.

Detailed information on the turbulent boundary layer characteristics was derived from accurate boundary layer measurements as shown in Figs. 5(*a*) and 5(*b*). In comparing the skin friction for the boundary layer profiles with Reynolds numbers based on the momentum thicknkess with Re_θ = 500 ÷ 2000, which is considered to be characteristic for gas turbine flow, the influence of free-stream turbulence intensity as given by Simonich [5] is largely confirmed. c_{fo}' is the temperature-corrected skin friction using Back and Cuffel's [17] suggestion

$$c_{fo}'/c_{fo} = \left[\frac{2}{1 + T_w/T_e}\right]^{0.66} \quad (4)$$

with

$$c_{fo} = 0.024 \cdot Re_\theta^{-0.25}$$

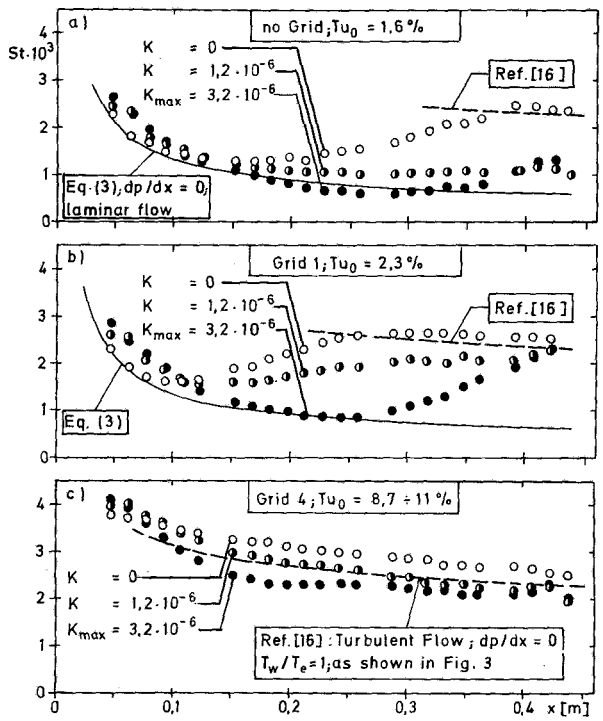

Fig. 6 Influence of pressure gradient on heat transfer and boundary layer transition
($Re_{L_o} = 6.5 \cdot 10^5$; $T_w/T_e = 0.64$)

c_{fo} for turbulence-free main flow was derived from averaging the nearly identical data of Murlis [18], Wieghard (see [18]) and Coles [19] (compare [6]). It should be noted that the observed characteristic scale of turbulence L_e^u is of the order of the boundary layer thickness. This should provide a maximum influence of turbulence [5]. Furthermore, as our newest detailed LDF-measurements [14] confirm the validity of the applied temperature correction for the reference skin friction, no additional influence of the wall cooling is evident. The independence of temperature is also illustrated in Fig. 5(*b*), where the Reynolds analogy 2·St/*cf* is shown to be largely independent of the turbulence level. The analogy factor is observed to be constant with a mean value of 1.1, which leads to the conclusion that heat transfer rates increase in the same amount as the skin friction coefficients of Fig. 5(*a*).

Pressure Gradient Effects. In analyzing the effects of strong negative pressure gradients, systematic comparisons of the flow with and without acceleration were performed. Identical starting conditions at the leading edge (Re_{Lo} = const.) were used and acceleration was achieved employing the two contoured upper walls as described in chapter 2 and shown in Fig. 2. For an entrance Reynolds number of $Re_{Lo} = 6.5 \cdot 10^5$ and strong wall cooling (T_w/T_e = 0.64) the results are shown in Fig. 6 with various turbulence intensities. Here, the Stanton numbers are defined using the local free-stream conditions. In comparing the results with those of zero pressure gradient flow (k = 0) it can be seen, that the delayed transition, which is more pronounced for the strong acceleration ($k_{max} = 3.2 \cdot 10^{-6}$) leads to a reduction of the Stanton numbers in the downstream part of the plate. In the leading edge region, however, an increase of the laminar heat transfer coefficients of approximately 20 percent due to free-stream acceleration is observed. At high turbulence intensities, transition occurs immediately behind the leading edge, as shown in Fig. 6(*c*). The effects of the strong acceleration result in a lower local Stanton number. It is obvious that the high free-stream turbulence level prevents a

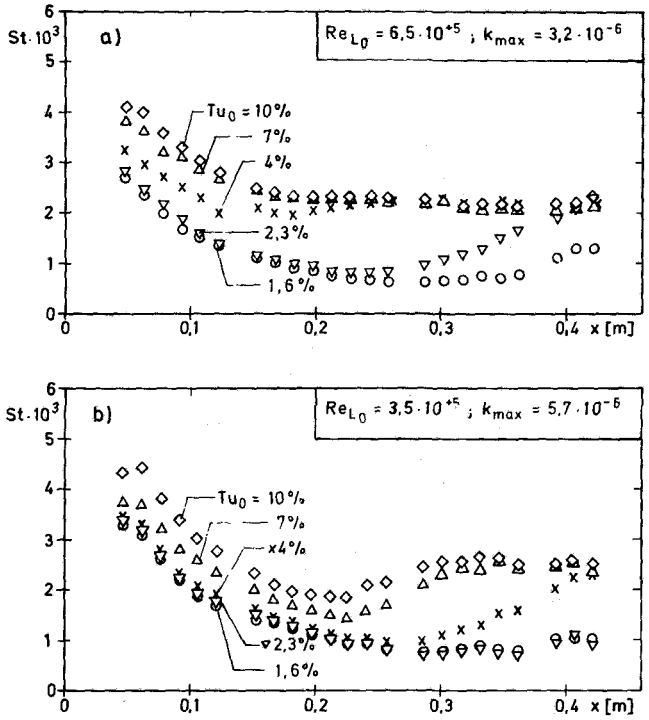

Fig. 7 Influence of Reynolds number on heat transfer and boundary layer development in accelerating flows ($T_w/T_e = 0.64$)

pronounced relaminarization even for high acceleration parameters.

If the acceleration parameter k is increased by reducing the entrance Reynolds number from $Re_{Lo} = 6.5 \cdot 10^5$ to $3.5 \cdot 10^5$, i.e., k_{max} is increased by a factor 1.86, the result as shown in Fig. 7 is obtained. Even at high turbulence intensities (Fig. 7(*b*)), the transition is delayed and for low turbulence levels up to 4 percent no transition occurs during the acceleration ($x < 0.27$ m). Laminar heat transfer is observed for $Tu_o = 1.6$, 2.3, and 4 percent. Despite an increase in Stanton numbers with raising turbulence levels, the heat transfer shows even for $Tu_o = 7$ and 10 percent similarities to laminar flow. As the boundary layer, however, is of transitional character, it cannot be classified, in our opinion, as laminar, despite its apparent overall behavior. Similar effects were observed in cascade flow [21]. However, they were interpreted as a rise in laminar heat transfer. These effects lead to pronounced difficulties in applying numerical codes, especially existing turbulence models.

Wall Cooling. Some aspects of wall cooling have already been discussed in chapter 4.1. The correlation of equation (3) indicates an increase of the laminar heat transfer with decreasing temperature ratio. In contrast it was shown for turbulent flows, that the increase of heat transfer and skin friction due to free-stream turbulence is not strongly dependent on temperature ratio. Still, effects of the wall cooling on the heat transfer itself in turbulent boundary layers were observed, as already mentioned, and shown in Fig. 8 and in Fig. 5 for zero-pressure gradient flow using the temperature-corrected c_{fo}' and the Reynolds analogy. The data in Fig. 8 are derived as function of the Reynolds number based on momentum thickness and compared with results of Chi and Spalding [20]. The agreement is quite acceptable. In altering the temperature ratio from $T_w/T_e = 1.0$ to 0.53 an increase of the Stanton numbers of 10 to 15 percent is observed.

Figure 9 illustrates the influence of the wall cooling in accelerating flow. Two flows with similar distributions of the pressure gradient parameter k along the plate but different

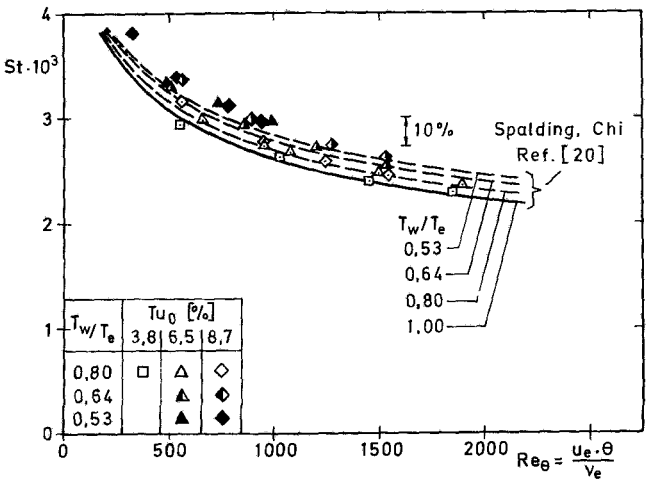

Fig. 8 Influence of wall-cooling on heat transfer in turbulent boundary layers

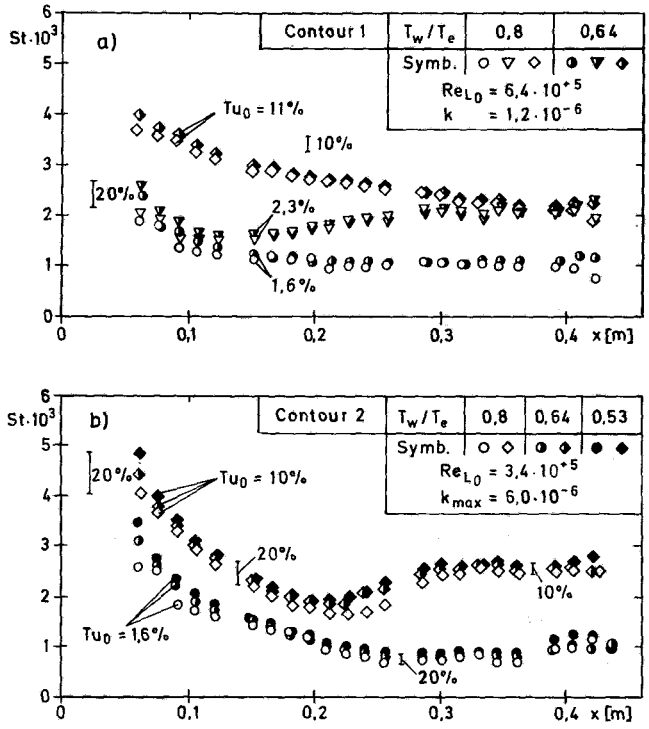

Fig. 9 Heat transfer and boundary layer development for two different pressure gradient flows with varying cooling intensities

temperature ratios T_w/T_e and turbulence levels Tu are presented. As can be seen, the transitional characteristics are not changed and the increase of Stanton number with wall cooling is of the same order as found in flows without pressure gradient. This leads to the conclusion, supported by recent measurements [14], that the variation of the fluid properties across the boundary layer and not the change of the turbulence structure are primarily responsible for the increase of heat transfer coefficients.

The detailed measurements of the influence of free-stream turbulence, pressure gradient distribution, i.e., acceleration and wall to free-stream temperature ratio are presently used in analyzing the accuracy of newly developed field methods as well as integral procedures.

Acknowledgment

Thanks are due to Dr.-Ing. K.-H. Sill, Dipl.-Ing. S. Eriksen and Dr.-Ing. G. Scheuerer for continuous discussions and to

cand. mach. E. Schnell for his support in data reduction. Financial support was provided by the "Forschungsvereinigung für Verbrennungskraftma-schinen (FVV)". Dr.-Ing. D. Mukherjee was actively involved in initiating the program.

References

1 Nealy, D. A., Mihelc, M. S., Hylton, L. D., Gladden, H. J., "Measurements of Heat Transfer Distribution over the Surfaces of Highly Loaded Turbine Nozzle Guide Vanes," ASME Paper No. 83-GT-53, presented at ASME Gas-Turbine Conference, Phoenix, Ariz., Mar. 1983.

2 Abu-Ghanam, B. J., and Shaw, R., "Natural Transition of Boundary Layers—The Effects of Turbulence, Pressure Gradients and Flow History," T.N. Turbomachinery Section, Department of Mechanical Engineering, University of Liverpool, Apr. 1979.

3 Blair, M. F., and Werle, J. R., "The Influence of Free Stream Turbulence on the Zero Pressure Gradient Fully Turbulent Boundary Layer," UTRC, East Hartford, Conn., Rep.-No. R-80-914388-12.

4 Junkham, G. H., and Serovy, G. K., "Effects of Free-Stream Turbulence and Pressure Gradient on Flat-Plate Boundary Layer Profiles and Heat Transfer," ASME *Journal of Heat Transfer*, Vol. 169, 1967.

5 Simonich, J. C., and Bradshaw, P., "Effect of Free-Stream Turbulence on Heat Transfer through a Turbulent Boundary Layer," ASME *Journal of Heat Transfer* 1978, Vol. 100.

6 Rüd, K., Sill, H., and Wittig, S., "Einfluß der Freistromturbulenz auf den Wärmeübergang an stark gekühlten Oberflächen," *VDI-Bericht*, No. 487 "Thermische Strömungsmaschinen '83" VDI-Verlag, 1983, pp. 171–180.

7 Blair, M. F., "Influence of Free-Stream Turbulence on Boundary Layer Transition in Favourable Pressure Gradients," ASME Paper No. 82-GT-4, presented at ASME Gas Turbine Conference, London, Apr. 1982.

8 Turner, A. B., "Local Heat Transfer Measurements on a Gas Turbine Blade," *Journal of Mech. Eng. Sci.*, Vol. 13, No. 1, 1971.

9 Eriksen, S., Wittig, S., Sakbani, K., and Rüd, K., "Comparison of Laser-Doppler-, Laser-Dual-Focus- and Probe Measurements in Laminar and Fully Turbulent Boundary Layers," *Proceedings of Int. Symposium on Application of Laser-Doppler Anemometry to Fluid Mechanics*, Lisbon, July 1982.

10 McMillan, F. A., "Experiments on Pitot Tubes in Shear Flow," Gt. Brit. ARC Rep. and Mem. 3028, London, 1959.

11 Patel, V. C., "Calibration of Preston Tube and Limitations on its Use in Pressure Gradients," *Journ. of Fluid Mech.*, Vol. 23, pt. 1, 1965, pp. 185–208.

12 Holmes, W. E., and Luxton, R. E., "Measurement of Turbulent Skin Friction by a Preston Tube in the Presence of Heat Transfer," *Journal of Mech. Eng. Sci.*, Vol. 9, No. 3, 1967.

13 Wittig, S., Eriksen, S., Schulz, A., and Hassa, C., "Laser-Doppler- und Laser-Zwei-Focus-Messungen in laminaren und turbulenten Wandgrenzschichten," *VDI-Bericht*, No. 487 "Thermische Strömungsmaschinen '83," VDI-Verlag 1983, pp. 181–189.

14 Eriksen, S., Wittig, S., Rüd, K., "Optical Measurements of the Transport Properties in a Highly Cooled Turbulent Boundary Layer at Low Reynolds Number," *Proc. of the 4th Symposium on Turbulent Shear Flow*, Sept. 12–14, 1983, Karlsruhe, W. Germany.

15 Baines, W. D., and Peterson, E. G., "An Investigation of Flow Through Screens," ASME *Transactions* Vol. 73, 1970, pp. 467–480.

16 Kays, W. M., *Convective Heat and Mass Transfer*, McGraw-Hill Book, 1966.

17 Back, L. H., Cuffel, R. F., and Massier, P. F., "Effect of Wall Cooling on the Mean Structure of a Turbulent Boundary Layer in Low-Speed Gas Flow," *Int. Journal of Heat and Mass Transfer*, Vol. 13, 1970, pp. 1029–1047.

18 Murlis, J., "The Structure of a Turbulent Boundary Layer at Low Reynolds Number," PhD thesis, University of London, June 1975.

19 Coles, D. E., "The Turbulent Boundary Layer in a Compressible Fluid," Rand Report, R-403-PR, 1962.

20 Chi, S.W., and Spalding, D. B., "Influence of Temperature Ratio on Heat Transfer to a Flat Plate Through a turbulent Boundary Layer in Air," *Proc. 3rd. Int. Heat Transfer Conf.*, Vol. 2, AICHE, 1966.

21 Krishnamoorthy, V., "Effect of Turbulence on Heat Transfer in a Laminar and Turbulent Boundary Layer Over a Gas Turbine Blade," ASME Paper No. 82-GT-146, presented at the ASME Gas Turbine Conference, London, Apr. 1982.

Airfoil Heat Transfer Calculation Using a Low Reynolds Number Version of a Two-Equation Turbulence Model

J. H. Wang[1]
Wang Associates,
Milford, Conn.

H. F. Jen

E. O. Hartel

AVCO-Lycoming Division,
Stratford, Conn. 06497

A two-dimensional, boundary-layer program, STAN5, was modified to incorporate a low-Reynolds number version of the K-ϵ, two-equation turbulence model for the predictions of flow and heat transfer around turbine airfoils. The K-ϵ, two-equation model with optimized empirical correlations was used to account for the effects of free-stream turbulence and transitional flow. The model was compared with experimental flat plate data and then applied to turbine airfoil heat transfer prediction. A two-zone model was proposed for handling the turbulent kinetic energy and dissipation rate empirically at the airfoil leading edge region. The result showed that the predicted heat transfer coefficient on the airfoil agreed favorably with experimental data, especially for the pressure side. The discrepancy between predictions and experimental data of the suction surface normally occurred at transitional and fully turbulent flow regions.

Introduction

The improvement of the efficiency of gas turbines necessitates the elevation of inlet gas temperature while maintaining acceptable metal temperature level. For that purpose, air bled from compressor is usually used to cool the first-stage turbine airfoils. Since the additional cooling air will offset, somewhat, the benefit gained from higher turbine inlet temperature, its efficient use is one of the most critical tasks in turbine design. The optimized cooling scheme must result from the accurate predictions of the gas-side heat transfer rate on the turbine blades.

Several fundamental mechanisms influence the prediction of heat transfer to gas turbine airfoils. These include:

1 Laminar, transitional, and turbulent flows
2 Gas stream turbulence
3 Strong accelerating and decelerating flow conditions
4 Stagnation flow at the airfoil leading edge
5 Airfoil surface curvature
6 Film cooling injection location and geometry and its interaction with main gas stream
7 Secondary flow
8 Body force
9 Shock and boundary layer interaction
10 Flow unsteadiness and periodicity

The ideal flow and heat transfer model for incorporating all above factors is the Navier-Stokes solution of the entire cascade/blade channel. The Navier-Stokes solution approach, however, is still under development. The current design practice in the industry usually assumes two-dimensional boundary-layer flow around turbine airfoils to account for the first five factors. Despite the simplifying assumptions for the problem, the solution has yet achieved a desirable accuracy level as compared to the published data. Under the assumption of two-dimensional, boundary-layer flow, the heat transfer coefficient of a turbine airfoil can be obtained by solving the momentum and energy equations along with suitable boundary conditions for both laminar and turbulent flows. For turbulent flows, however, there are some additional turbulent transport terms in the governing equations. These terms must be modeled by some kind of turbulence models.

Survey of literature indicates that, to date, the zero- and one-equation turbulence models are the most popular methods for predicting heat transfer over turbine airfoil [1–3]. These lower-order turbulence models require the prescription of the mixing-length scale distribution through extensive data correlation for complex flow environment, such as turbine airfoils. These models become complicated in order to incorporate the crucial flow mechanisms on turbine airfoils. The mixing length approach yields reasonably good results for the flow problems similar to the correlated data but it sometimes does not predict well for the turbine airfoils, which have different flow conditions from the data used in the empirical correlation. The use of higher-order turbulence models will minimize the need of those empirical functions and can apply to a broader-range flow conditions. Since gas

Contributed by the Gas Turbine Division of THE AMERICAN SOCIETY OF MECHANICAL ENGINEERS and presented at the 29th International Gas Turbine Conference and Exhibit, Amsterdam, The Netherlands, June 4–7, 1984. Manuscript received at ASME Headquarters January 24, 1984. Paper No. 84-GT-261.

[1] Currently at Physical Research, Inc., Palo Verdes, Calif.

Table 1 Constants for the two-equation model

C_μ	C_1	C_2	σ_K	σ_ϵ	f_1
0.09	1.55	2.0	1.0	1.3	1.0

$f_2 = 1.0 - 0.3 \exp(-\mathrm{Re}_t^2)$
$f_\mu = \exp[-2.5/(1+\mathrm{Re}_t/50)]$
where $\mathrm{Re}_t = K^2/\nu\epsilon$

transitional and relaminarization flow, and curved surfaces, and its documented experience in the open literature [4–7]. The applications of the same model but with different turbine designers are constantly striving for efficiency improvement with higher inlet temperature, sophisticated cooling schemes have been frequently introduced. New physical models should possess the potential of applying to the new cooling schemes.

It is known that the high gas stream turbulence in turbine environments results in significant heat transfer coefficient enhancement. Hylton et al. [1] introduced a turbulence viscosity term in the turbulent eddy viscosity formulation to account for gas stream turbulence effects. The approach did not include the turbulence decay in the cascade due to channel curvature and velocity field around the airfoils. So et al. [3] employed a simplified turbulent energy equation at the boundary-layer edge to include the decay effect. One of the alternate methods is to use the K-ϵ, two-equation model and to impose a boundary condition at the edge of the boundary layer.

In view of the drawbacks of zero- and one-equation turbulence model for turbine heat transfer predictions, it is our goal to implement a higher-order turbulence model for predicting flow field and heat transfer coefficient over turbine airfoils. A literature survey on the available turbulence models concluded that the low-Reynolds-number version of K-ϵ, two-equation model proposed by Jones and Launder [4] is one of the most suitable methods for turbine airfoil flow environment because of its applicability for viscous sublayer, correlations are also reported by Dutoya and Michard [8] in which the computations did not start from the immediate vicinity of the stagnation point on the leading edge.

Hylton et al. [1] indicated that, in their initial assessment study, Jones and Launder's model did not give satisfactory results for predicting heat transfer over C3X turbine airfoils. Similar difficulty was encountered by the authors and was attributed to the improper prescription of the initial and boundary conditions for turbulent kinetic energy and its dissipation rate at airfoil leading edge region. The free-stream boundary conditions suitable for flat-plate turbulent flow are not valid in the vicinity of the airfoil stagnation region dominated by laminar flow. The modified initial and boundary conditions are introduced in conjunction with a two-zone model to deal with the effect of stagnation flow and the variation of turbulent kinetic energy and its dissipation rate around the airfoil. Empirical correlations are obtained as a criterion at the boundary of these two zones.

This paper summarizes the results for the applications of the low-Reynolds number version of K-ϵ, two-equation model to various problems. First, the turbulence model along with suitable boundary conditions is discussed. The model is then applied to different flat-plate flow conditions to study the effects of pressure gradient and flow transition. It is followed then by the prediction of heat transfer coefficients for two different airfoils. Finally, the conclusions drawn from this study are discussed. In this study, the effect of streamline surface curvature is not included.

Formulation of the Problem

Governing Equations. The formulation for boundary-layer flows are well documented in the open literature [9–11]. For a two-dimensional, steady-state turbulent, boundary-layer flow, the equations read
Continuity:

$$\frac{\partial(\rho U)}{\partial X} + \frac{\partial(\rho V)}{\partial Y} = 0 \tag{1}$$

Nomenclature

a = exponential constant for the mean flow velocity: $U_G \sim X^a$
c = specific heat
CF = skin friction factor $\tau_w/0.5\rho U_G^2$
C_1, C_2, C_μ = empirical constants in equations (8) and (9) and listed in Table 1
D = diameter for the turbine airfoil leading edge
f_1, f_2, f_μ = empirical functions in equations (8) and (9) and listed in Table 1
g_c = the constant in Newton's Second Law
I = static enthalpy of fluid
I^* = stagnation enthalpy of fluid
i' = fluctuating static enthalpy
J = the proportionality factor in the First Law of Thermodynamics
K = turbulent kinetic energy
l_m = classical mixing length
l = integral length scale of turbulence eddy
L_x = turbulence characteristic length scale
Pr = Prandtl number
Re = Reynolds number
S = source term for the energy equation
Tu = free-stream turbulence intensity, $\sqrt{\bar{u}'^2}/U_G$
U = local mean velocity parallel to wall
V = local mean velocity normal to wall
u' = fluctuating velocity parallel to wall
v' = fluctuating velocity normal to wall
U = dimensionless velocity
X = Cartesian coordinate in the main flow direction
Y = Cartesian coordinate normal to the wall
Y^+ = dimensionless value of Y: $U_\tau Y/\nu$
δ = boundary layer thickness
$\tilde{\epsilon}$ = dissipation rate of turbulent kinetic energy
ϵ = isotropic dissipation rate of turbulent kinetic energy
κ = von Karman mixing-length constant
μ = dynamic viscosity
ν = kinematic viscosity
ρ = density
σ = Schmidt number
τ = shear stress

Subscripts

D = airfoil leading edge diameter
G = free-stream condition
w = wall
t = turbulent eddy, turbulence
x = axial distance

Momentum:

$$\rho U\frac{\partial U}{\partial X}+\rho V\frac{\partial U}{\partial Y}=-g_c\frac{dP}{dX}+\frac{\partial}{\partial Y}\left\{\left(\mu\frac{\partial U}{\partial Y}-\overline{u'v'}\right)\right\} \quad (2)$$

Energy:

$$\rho U\frac{\partial I^*}{\partial X}+\rho V\frac{\partial I^*}{\partial Y}=\frac{\partial}{\partial Y}\left\{\left(\frac{k}{C}\frac{\partial I^*}{\partial Y}\right)-\overline{\rho i'v'}+\frac{\mu}{Jg_c}\frac{\partial}{\partial Y}\left(\frac{U^2}{2}\right)\right\}+S \quad (3)$$

Where I^* is the stagnation enthalpy of the fluid, defined as $I^* = I+U^2/2g_cJ$, and I is the static enthalpy.

To solve the foregoing equations, the second-order correlations $\overline{u'v'}$ and $\overline{i'v'}$ must be replaced by a turbulent model. Where u' and i' are the fluctuations in velocity and static enthalpy, respectively. The second-order closure model states that these correlations can be expressed by

$$\overline{-u'v'}=\frac{\mu_t}{\rho}\frac{\partial U}{\partial Y} \quad (4)$$

$$\overline{-i'v'}=\frac{\mu_t}{\mathrm{Pr}_t\rho}\frac{\partial I^*}{\partial Y} \quad (5)$$

Where μ_t is the turbulent viscosity and Pr_t is the turbulent Prandtl number. According to Jones and Launder's K-ϵ, two-equation model, these two turbulent properties are given by

$$\mu_t=c_\mu f_\mu\rho K^2/\epsilon \quad (6)$$

$$\mathrm{Pr}_t=0.9 \quad (7)$$

Where K and ϵ are the turbulent kinetic energy and the isotropic dissipation rate (i.e., $\epsilon=\bar{\epsilon}-2\nu(\partial K^{1/2}/\partial Y)^2$, where ϵ is the dissipation rate.) The values for K and ϵ are obtained by solving the following two transport equations

$$\rho\frac{DK}{Dt}=\frac{\partial}{\partial Y}\left\{\left(\mu+\frac{\mu_t}{\sigma_K}\right)\frac{\partial K}{\partial Y}\right\}+\mu_t\left(\frac{\partial U}{\partial Y}\right)^2-\rho\epsilon-2\mu\left(\frac{\partial K^{1/2}}{\partial Y}\right)^2 \quad (8)$$

$$\rho\frac{D\epsilon}{Dt}=\frac{\partial}{\partial Y}\left\{\left(\mu+\frac{\mu_t}{\sigma_\epsilon}\right)\frac{\partial\epsilon}{\partial Y}\right\}+C_1f_1\frac{\epsilon}{K}\mu_t\left(\frac{\partial U}{\partial Y}\right)^2-C_2f_2\frac{\rho\epsilon^2}{K}+\frac{2\mu\mu_t}{\rho}\left(\frac{\partial^2U}{\partial Y^2}\right)^2 \quad (9)$$

Different correlations for the constants C_1, C_2, C_μ, f_1, f_2, f_μ, σ_k, and σ_ϵ have been proposed in the literature [4-8]. A comparison study of all these correlations for a fully developed turbulent flow on a flat plate showed no significant difference in the results. However, the original correlations given by Jones and Launder in [4] gave slightly better results for the turbine airfoils. The correlations are selected for all the flow problems presented in this study. These constants are presented in Table 1.

Initial Conditions. For flat-plate problems, the initial profiles of velocity and stagnation enthalpy are obtained using a spline curve fitting routine through the experimental data. When the experimental data are not available, the fully developed turbulent or laminar flow profiles are used depending on the inlet flow Reynolds number.

Turbulent Flow.

(*a*) Velocity:

$$U(y)=\frac{U_\tau}{\kappa}(\ln Y^+ +5.0) \quad (10)$$

where

$$Y^+=U_\tau Y/\nu, \text{ and } U_\tau=(\tau_w/\rho)^{1/2} \quad (11)$$

(*b*) Turbulent kinetic energy and dissipation rate

$$\mu_t = \rho C_\mu{}^{1/4}K^{1/2}l_m=\rho K^{1/2}l \quad (12a)$$

$$= \rho l_m{}^2\left(\frac{\partial U}{\partial Y}\right) \quad (12b)$$

Combining equations (12*a*) and (12*b*) yields

$$K=(dU/dY)^2l_m{}^2/C_\mu{}^{1/2} \quad (13)$$

Combining equations (6) and (12*a*) yields

$$\epsilon=f_\mu C_\mu{}^{3/4}K^{3/2}/l_m \quad (14)$$

$$\text{but } f_\mu = 1.0 \text{ for large } \mathrm{Re}_t$$

where l_m is the classical mixing length scale that is determined from the following expressions

$$l_m=\kappa Y \text{ for } Y\leqq 0.09\delta/\kappa \quad (15a)$$

$$l_m=0.09\delta \text{ for } Y>0.09\delta/\kappa \quad (15b)$$

For flow with free-stream turbulence intensity, additional terms are added to equations (13) and (14) to yield

$$K=(dU/dY)^2l_m{}^2/C_\mu{}^{1/2}+K_GY/\delta \quad (16)$$

$$\epsilon=f_\mu C_\mu{}^{3/4}K^{3/2}/l_m+\epsilon_GY/\delta \quad (17)$$

where

$$K_G=1.5(U_G\cdot Tu)^2 \quad (18)$$

$$\epsilon_G=f_\mu C_\mu{}^{3/4}K_G{}^{3/2}/l_m \quad (19)$$

Laminar Flow With Free Stream Turbulence.

$$U(Y)=U_Gf(Y) \quad (20)$$

where $f(Y)$ is the Blasius function.

The mixing-length scale for laminar flow subject to free-stream turbulence intensity level is unknown. For transitional flow, Wilcox [12] used a length scale that depends on the free-stream turbulence intensity level. In the present model, equation (15*a*) is assumed to be applicable up to the edge of the laminar boundary layer. Then equations (16) and (17) are still applicable to the flow problem starting with laminar flow conditions, but f_μ depends on the turbulence Reynolds number, Re_t, as shown in Table 1. A special treatment is required for turbine airfoil stagnation point to be discussed in the Comparison section.

Boundary Conditions. The boundary conditions for flat-plate and turbine airfoil must be treated separately because the latter has a complex flow behavior around the leading edge region.

Flat Plate.

At $y=0$:

$$I=I_w \text{ and } U_w=K_w=\epsilon_w=0 \quad (21)$$

At $y=\delta$:

$$U_G\frac{dK_G}{dX}=-\epsilon_G \quad (22)$$

$$U_G\frac{d\epsilon_G}{dX}=-C_2f_2\epsilon_G{}^2/K_G \quad (23)$$

Equations (22) and (23) are the asymptotic forms of equations (8) and (9) as the transverse gradients vanish.

Turbine Airfoil. The turbulence structure around the leading edge of turbine airfoils is very complex and only limited experimental study has been presented in the literature for the flow around a circular cylinder. Because of the thin boundary layer thickness, the capability of measuring the turbulence properties across the layer may not be available. From an analytical point of view the ideal method for ob-

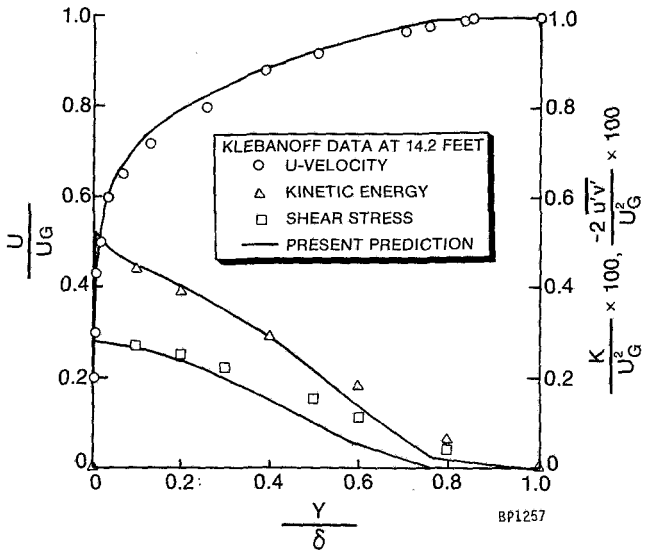

Fig. 1 Comparisons for flat plate with zero pressure gradient

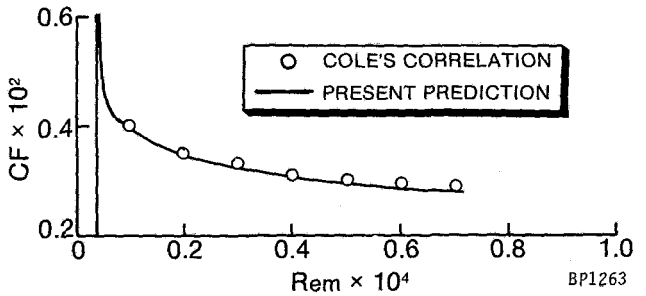

Fig. 2 Comparison on wall frictional factor

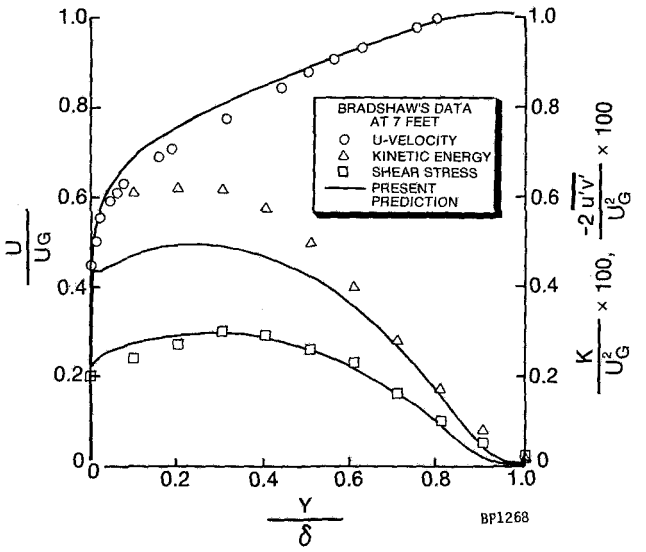

Fig. 3 Comparisons for flat plate with adverse pressure gradient, $a = -.15$

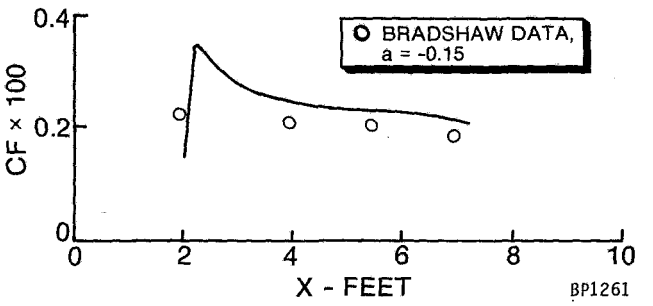

Fig. 4 Comparison on wall frictional factor

taining the boundary conditions is to solve the turbulent kinetic energy and dissipation rate equations with Euler equations for the entire cascade flow field. In order to circumvent the problem, a two-zone model for K and ϵ is proposed.

Bearman [13] conducted an experimental study of the distortion of grid-generated turbulence approaching the stagnation region of a two-dimensional bluff body. The study concluded that the mean stagnation streamline turbulence attenuates like the mean flow if the free-stream turbulence scale (or eddy size) L_x is much larger than the typical body dimension, such as the airfoil leading edge diameter D. The data of the study also showed the rapid attenuation of the turbulent kinetic energy at locations extremely close to the wall. On the basis of Bearman's study the assumption of constant turbulence intensity around the airfoil leading edge is made for the first zone before the main flow accelerates and reaches a critical velocity which is obtained using numerical optimization technique. Equations (18) and (19) are then applied.

As the boundary layer thickness grows to the end of the first zone and the computation approaches the "critical velocity," V_c, the linear relationship due to wall effect between turbulent velocity and local free-stream velocity gradually becomes invalid. The computation grid gradually extends into the turbulence structure region dominant by the main velocity field. In this region the turbulent kinetic energy and its dissipation rate will vary without viscous layer effect. The typical boundary conditions equations (22) and (23) are then applied at the boundary-layer edge. In other words, when the free-stream velocity reaches the "critical velocity," the decay of free-stream turbulence intensity will take place. From numerical experiments, different critical velocities are required for suction and pressure surfaces because of different flow fields around the leading edge.

The Solution Scheme. The numerical method for solving the governing equations along with suitable boundary conditions is the one presented by Crawford [10]. The computer program STAN5 given in [10] is modified to include the two-equation model.

Comparison With Measured Data

Flat Plate Equilibrium Flow Without Pressure Gradient. Klebanoff [14] measured the velocity profile and turbulent properties for a fully developed turbulent flow on a flat plate. The free-stream velocity is 50 ft/s, and the measured station is 14.2 ft from the virtual leading edge. The momentum thickness Reynolds number was about 7.7×10^3. For this problem, a fully developed flow profile is assumed at a distance 1 ft from the leading edge. A total of 83 points across the boundary layer is used. The ratio between two consecutive grid points is 1.2 and the first grid point is 8.28×10^{-10} ft from the wall. The CPU for this problem is 0.43 min on the IBM system 370/3081.

The predicted profiles for velocity, turbulent kinetic energy, and turbulent shear stress are compared with Klebanoff's data in Fig. 1. The comparison indicates that the results from the low-Reynolds-number K-ϵ model agree well with the experimental data. The predicted friction factor versus momentum thickness Reynolds number is also compared with Coles's [15] correlation in Fig. 2. It shows that the predicted friction factors change rapidly in the initial stages of the calculations. This is due to the effect of initial conditions.

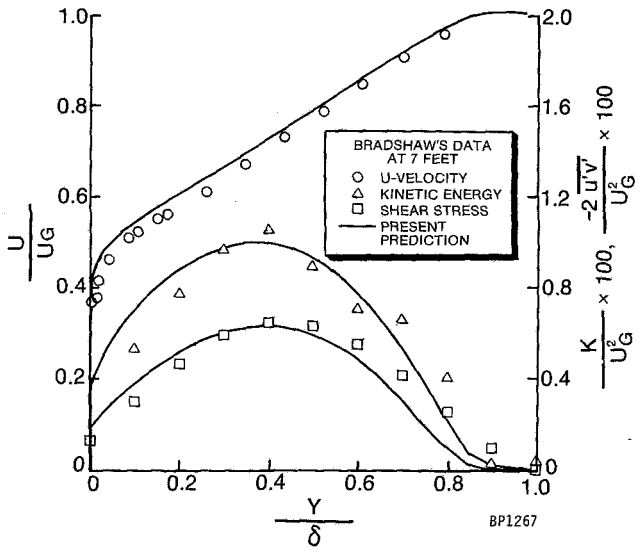

Fig. 5 Comparison for flat plate with adverse pressure gradient, $a = -.255$

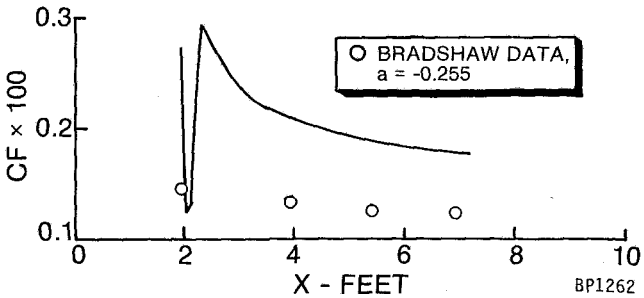

Fig. 6 Comparison on wall frictional factor

This effect diminishes within a short distance from the starting point.

For the same flow condition, a high-Reynolds-number version of K-ϵ, two-equation model, along with suitable wall functions is also tested. A total of 30 points across the boundary layer is used. The results, which are not presented here, are in excellent agreement with the low-Reynolds-number model.

Fully Developed Turbulent Flow on a Flat Plate With Adverse Pressure Gradient. This is turbulent flows under mild and severe adverse pressure gradients reported by Bradshaw [16]. The free-stream velocity is represented by $U \sim X^a$. Two different flow conditions are evaluated: $a = -0.15$ and $a = -0.255$.

For $a = -0.15$, Figs. 3 and 4 display the comparisons between the prediction and experimental data for velocity, turbulent kinetic energy, turbulent shear stress, and friction factor. The same comparison for $a = -0.255$ is presented in Figs. 5 and 6. These comparisons indicate that for flow with adverse pressure gradient, the profiles for velocity, and turbulent shear stress are generally well predicted although some discrepancies are observed for turbulent kinetic energy at $a = -0.15$. The friction factor shown in Fig. 6 for $a = -0.255$ is overpredicted. The same discrepancy was reported in [17], and this could be the deficiency of the K-ϵ model for strongly adverse pressure gradient.

Transitional Flow on Flat Plate. The model is applied to verify its capability of simulating transitional flow process on an adiabatic flat plate. The calculations start at a fully developed laminar flow condition of Reynolds number, $Re_x = 1 \times 10^3$.

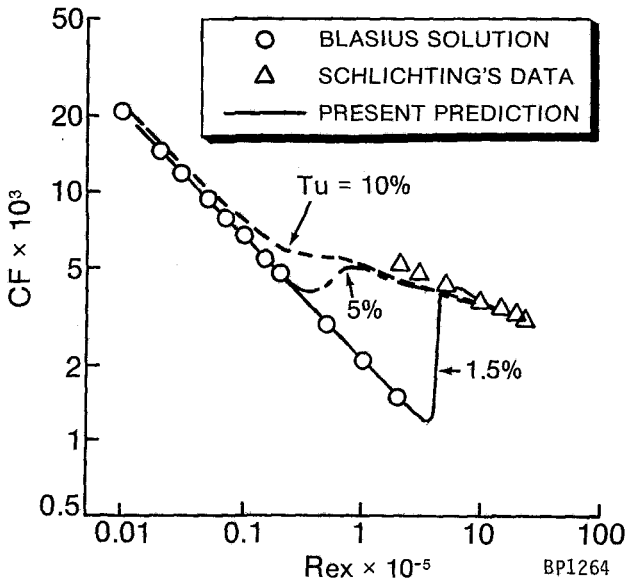

Fig. 7 Transitional flow on a flat plate

Table 2 Operating conditions for turbine airfoils

Run	Pa	T (°R)	M2	Re_1 (X10^5)	Re_D (X10^4)	Re_2 (X10^6)	Tu %
C3X airfoil (M_1 = .17)							
149	4743	1431	0.92	3.9	6.0	1.51	6.5
159	4681	1461	0.90	3.8	5.8	1.45	8.3
109	6208	1433	0.90	5.2	8.0	1.96	6.5
112	6220	1410	0.90	5.3	7.8	2.01	8.3
145	7807	1426	0.90	6.4	9.8	2.43	6.5
157	7990	1473	0.89	6.4	9.8	2.44	8.3
Turner's airfoil							
1	3268.8	654.2	0.75	4.36	3.2	1.03	5.9
2	3268.8	654.2	0.75	4.36	3.2	1.03	2.2

Three different free-stream turbulence intensity levels were tested: Tu = 1.5, 5, and 10 percent. Figure 7 depicts the predicted friction factors along the flat plate. The experimental data for fully developed laminar and turbulent flows are also included in the figure for comparison. Similar results are reported in [8] by using the same model but different correlations and constants. Although no comparisons are made for the friction factors in the transitional flow regime, the present model does demonstrate its ability to simulate the behavior of flow transition subject to different free-stream intensities. It should be noted that a slightly higher than laminar value is predicted for $Tu = 10$ percent in the laminar region. A total of 78 points is used for the solution and the CPU time for each run is 0.61 min.

Heat Transfer on Turbine Airfoils. The heat transfer prediction over turbine airfoils presents the greatest challenge to the applicability of K-ϵ model for complex flow problems. Two different turning-angle cascade airfoils are evaluated: large turning-angle airfoil, C3X airfoil of [1] (shown in Fig. 8) and smaller turning-angle airfoil, Turner airfoil of [19]. The cascade operation conditions selected for the comparison with the present low-Reynolds-number K-ϵ model are given in Table 2. Hylton et al. [1] compared the C3X and Turner airfoil data with the predictions of the original STAN5 and the DDA's modified version of STAN5 with a sophisticated mixing-length model. It shows that the results of DDA's

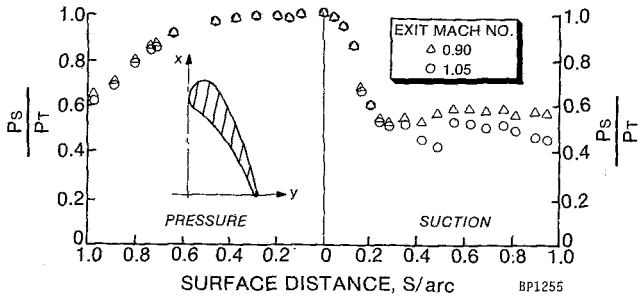

Fig. 8 C3X vane pressure distribution

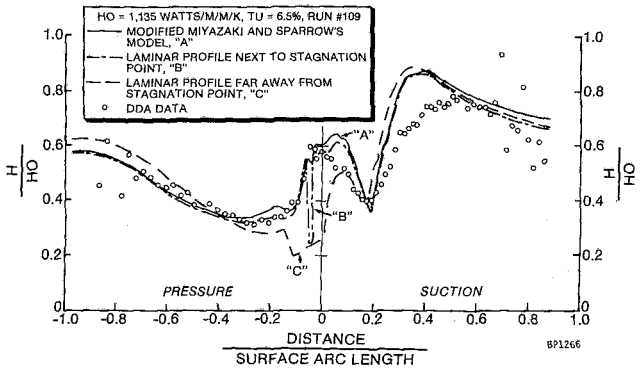

Fig. 9 Effect of initial condition

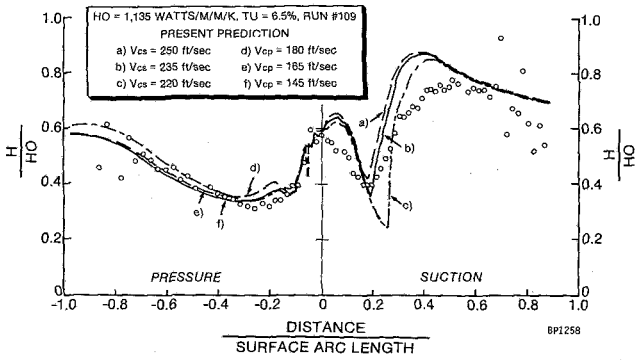

Fig. 10 Effect of critical velocity

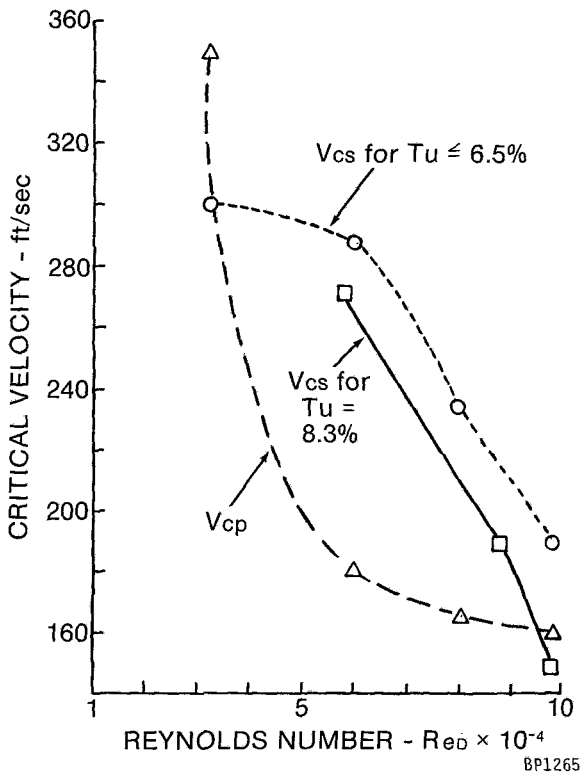

Fig. 11 Empirical correlations on critical velocity

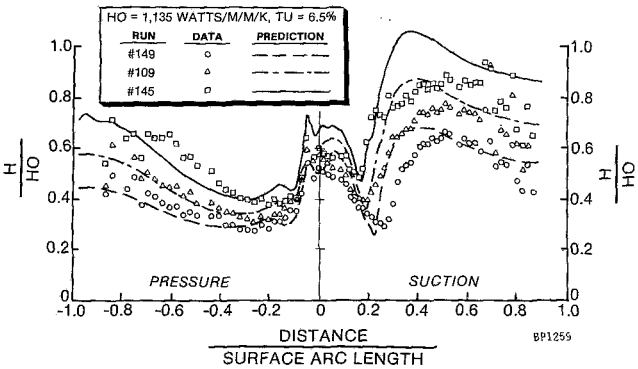

Fig. 12 Heat transfer comparison on C3X

modified model gives closer correlation with the data. However, the discrepancies between predictions and data increase progressively with exit Reynolds number, and the model is complicated in implementation.

A study was performed to evaluate the effect of initial conditions on the heat transfer prediction. Three different methods were used for generating the initial profiles for velocity and stagnation enthalpy:

(*a*) Using a fully developed laminar flow profile at a point very close to the stagnation point. The prediction is the "A" curve of Fig. 9.

(*b*) Using the modified Miyazaki and Sparrow's model developed in [1] for flow at the stagnation point of a cylinder subject to free-stream turbulence intensity. Keller's Box method [18] is used to solve the governing equations. The resulting velocity and temperature profiles are then used as the initial conditions for the low-Reynolds-number $K\epsilon$ model. The prediction is the "B" curve in Fig. 9.

(*c*) Using a fully developed laminar flow profile some distance (2–6 percent arc-length) away from the stagnation point. This is the "C" curve. Two-zone model is not needed in this approach.

All methods gave similar results, except for the region at the airfoil leading edge. "A" method is much easier to use, but "B" method yields more accurate result at the stagnation point, which is critical to the turbine cooling design. It is interesting to know that the predictions of "C" method for the fully turbulent flow regime are not affected by the initial conditions. "B" method was chosen in the study for generating the initial conditions for C3X and "A" method for Turner airfoil and "two-zone" model as described in the preceding section was used for the boundary conditions. For an airfoil whose surface velocity field is significantly different from that of C3X and Turner's airfoils, the "C" method is recommended.

The effect of the "critical velocity" on the heat transfer prediction is shown in Fig. 10. Although the predicted results for fully turbulent flows remain the same, the predicted heat transfer in the laminar and transitional flow region is very sensitive to the specification of these velocities. The numerical optimization is required to obtain the optimal "critical velocity," which can yield better correlation with the data.

Figure 11 displays the values for V_c used in the present study for C3X and Turner airfoils. It shows that V_{cs} decreases with Re_D and decreases slightly for free-stream turbulence intensity level greater than a threshold value 6.5 percent. On

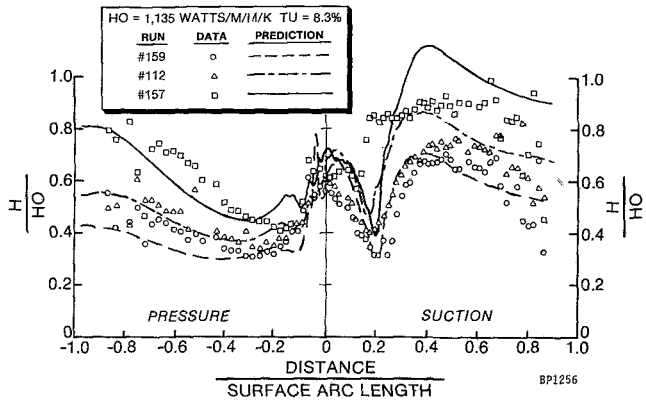

Fig. 13 Heat transfer comparison on C3X airfoil, Tu = 8.3 percent

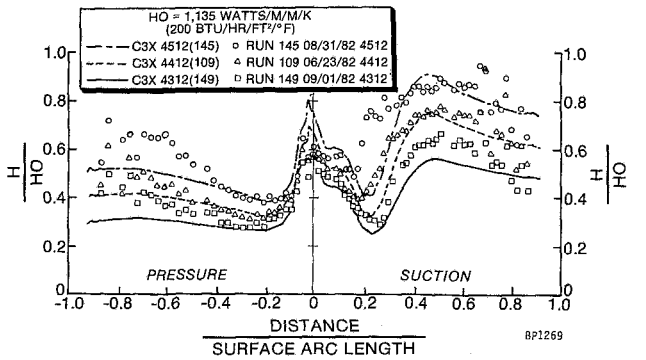

Fig. 14 Predicted heat transfer coefficients using mixing length model of [1]

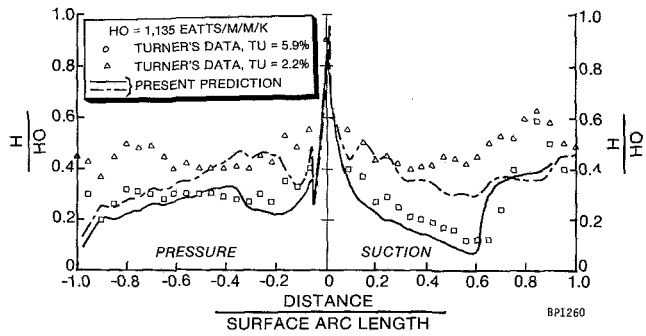

Fig. 15 Heat transfer prediction for Turner's airfoil

the other hand, for Re_D less than 6×10^4, V_{cp} decreases rapidly with Re_D; and for Re_D greater than 6×10^4, V_{cp} decreases slightly with Re_D. For the cases studied, V_{cp} is independent of free-stream turbulence intensity level. Further comparison for different airfoils is required to test the accuracy of the present correlation.

Figures 12 and 13 show the effects of varying Reynolds number with free-stream turbulence intensity equal to 6.5 and 8.3 percent, respectively. It shows that the overall heat transfer increases progressively with the increasing Reynolds number. This effect is well predicted with the present model especially on the pressure surface. The results of DDA's mixing length model are reproduced in Fig. 14 for comparison with the present K-ϵ model.

Figures 12 and 13 show that the predicted heat transfer over the pressure side of the airfoil agree fairly well with experimental data. However, the heat transfer over the first 20 percent of the suction surface is overpredicted. This is believed due to the effect of streamline surface curvature. The surface curvature effect on the suction surface [20] will reduce the prediction by about 10 to 20 percent to correlate better with the data. Although DDA's mixing length results agreed well with the data better than the present study, the former method did not include curvature effect and the latter is able to accommodate the curvature effect as demonstrated in [20].

The second airfoil is that reported by Turner [19] for an exit Mach number of 0.75. Since the distribution of static pressure on the airfoil surface is not reported, the free-stream velocity profile is estimated from the reported data for Mach number of 0.77. In doing so, it is very likely that the boundary conditions used could cause some inaccuracy for the heat transfer predictions. The grid system is the same as that for the C3X airfoil. The initial profiles are generated by assuming fully laminar flow at a point close to the stagnation point.

Two different mainstream turbulence intensity levels were tested: Tu = 5.9 percent and 2.2 percent. The predictions are compared with Turner's data in Fig. 15. The comparison shows that the trends of the heat transfer due to mainstream intensity level are well predicted, except for the trailing edge of the airfoil. It is also observed that the present model does not overpredict the heat transfer for the leading edge. This is because the inlet Reynolds number for this case is much lower than that for the C3X airfoil and the effect of surface curvature at the leading edge is not as significant. The overall heat transfer coefficient prediction could be improved if a better aerodynamic velocity field were used at the boundary layer edge.

Conclusions and Recommendations

The low-Reynolds-number version of the K-ϵ, two-equation model is implemented for predicting several boundary layer flows. For flows on a flat plate with and without pressure gradient, the results of the K-ϵ model agree reasonably well with experimental data. The model has the capability of simulating transitional flow process on a flat plate subject to various free-stream turbulence intensity levels. When the K-ϵ model is applied to predict heat transfer over a cascade airfoil, a two-zone model is proposed to deal with boundary conditions for turbulent kinetic energy and its dissipation rate. Empirical correlations are obtained to define the "critical velocity" separating the two zones for boundary condition specification.

The K-ϵ model is used to predict heat transfer for two different airfoils. Results demonstrate that the model is capable of predicting the general trend of heat transfer on both sides of the airfoil. On the suction side of the airfoils, the model without surface curvature correlations gives higher predictions for transitional and turbulent regions. On the pressure side, however, the present results generally agree very well with the data. Further comparisons with data for different airfoils at various operating conditions are required to verify the accuracy of the present model and to develop the empirical "critical velocity" of the proposed "two-zone" model for turbine airfoil problems.

Finally, it is recommended that detailed experiments around the leading edge of the airfoil are performed for replacing the present two-zone model for free-stream turbulent properties.

References

1 Hylton, L. D., Mihelc, M. S., Turner, E. R., Nealy, D. A., and York, R. E., "Analytical and Experimental Evaluation of the Heat Transfer Distribution Over the Surfaces of Turbine Vanes," NASA CR 168015, May 1983.

2 Forest, A. E., "Engineering Predictions of Transitional Boundary Layers," AGARD-CP-224, 1977.

3 So, R. M. C., Edelfelt, I. H., Elovic, E., and Kercher, D. M., "A Two-

Dimensional Boundary-Layer Program for Turbine Airfoil Heat Transfer Calculation," ASME Paper No. 82-GT-93, 1982.

4 Jones, W. P., and Launder, B. E., "The Prediction of Laminarization With a Two-Equation Model of Turbulence," *International Journal of Heat and Mass Transfer*, 1972, p. 301.

5 Jones, W. P., and Launder, B. E., "The Calculation of Low-Reynolds-Number Phenomena With a Two-Equation Model of Turbulence," *International Journal of Heat and Mass Transfer*, Vol. 16, 1973, p. 1189.

6 Koosinlin, M. L., Launder, B. E., and Sharma, B. I., "Prediction of Momentum, Heat and Mass Transfer in Swirling Turbulent Boundary Layers," ASME *Transactions*, 1974, p. 204.

7 Priddin, C. H., "The Behavior of the Turbulent Boundary Layer on Curved Porous Walls," Ph.D. thesis, Faculty of Engineering, University of London, 1975.

8 Dutoya, D., and Michard, P., "A Program for Calculating Boundary Layers and Heat Transfer Along Compressor and Turbine Blades," *Numerical Methods in Heat Transfer*, John Wiley & Sons, Ltd, 1981.

9 Patankar, S. V., and Spalding, D. B., *Heat and Mass Transfer in Boundary Layers*, 2d ed., *Intertext*, London, 1970.

10 Crawford, M. E., and Kays, W. M., "STAN5—A Program for Numerical Computation of Two-Dimensional Internal/External Boundary Layer Flows," NASA CR-2742, 1976.

11 Schlichting, H., *Boundary Layer Theory*, 5th ed., McGraw-Hill, New York, 1968.

12 Wilcox, D. C., "A Model for Transitional Flows," AIAA paper 77-126, Jan. 1977.

13 Bearman, P. W., "Some Measurement of the Distortion of Turbulence Approaching a Two-Dimensional Bluff Body," *Journal of Fluid Mechanics*, Vol. 53, 1972, p. 3.

14 Klebanoff, P. S., "Characteristics of Turbulence in a Boundary Layer With Zero Pressure Gradient," NACA Report 1247, 1953.

15 Coles, D. E., and Hirst, E. A., *Computation of Turbulent Boundary Layers*, AFOSR-IFP-Stanford Conference, Stanford University, 1968.

16 Bradshaw, P., "The Turbulent Structure of Equilibrium Boundary Layers," NPL AERO Report 1184, 1966.

17 Chambers, T. L., and Wilcox, D. C., "Critical Examination of Two-Equation Turbulence Closure Models," AIAA paper 76-352, July 1976.

18 Cebeci, T., and Smith, A. M. O., *Analysis of Turbulent Boundary Layers*, Academic Press, 1974.

19 Turner, A. B., "Local Heat Transfer Measurements on a Gas Turbine Blade," *Journal of Mechanical Engineering Sciences*, Vol. 13, 1971, p. 1–12.

20 Wang, J. H., and Jen, H. F., "Heat Transfer Prediction Using Two-Equation Turbulence Model With Surface Curvature Effect," Lycoming IRAD report 183.14, Dec. 1983.

Effect of Nonuniform Geometries on Flow Distributions and Heat Transfer Characteristics for Arrays of Impinging Jets

L. W. Florschuetz

H. H. Tseng

Department of Mechanical and Aerospace Engineering, Arizona State University, Tempe, Ariz. 85287

Two-dimensional arrays of circular jets impinging on a surface parallel to the jet orifice plate are considered. The jet flow, after impingement, is constrained to exit in a single direction along the channel formed by the jet orifice plate and the impingement surface. Experimental results for the effects of streamwise nonuniform array geometries on streamwise flow distributions and heat transfer characteristics are presented. A flow distribution model for nonuniform arrays is developed and validated by comparison with the measured flow distributions. The model is then employed to compare nonuniform array streamwise resolved heat transfer coefficient data with previously reported uniform array data and with a previously developed correlation based on the uniform array data. It was found that uniform array results can, in general, serve as a satisfactory basis from which to predict heat transfer coefficients at individual spanwise rows of nonuniform arrays. However, significant differences were observed in some cases over the first one or two rows downstream of the geometric transition line of the nonuniform array.

Introduction

Two-dimensional arrays of circular jets impinging on a surface parallel to the jet orifice plate are considered. The configurations are intended to model those of interest in current and contemplated gas turbine airfoil midchord cooling applications. The geometry of the airfoil applications considered dictates that the jet flow, after impingement, exits in the chordwise (i.e., streamwise) direction toward the trailing edge. The accumulated flow from upstream jet rows in the array acts as a crossflow to downstream rows. In this study, experimental results for the effects of nonuniform array geometries on flow distributions and heat transfer characteristics were obtained. The objective was to determine the degree of confidence the designer can place in streamwise resolved heat transfer coefficients for nonuniform arrays that are based on experimental results from uniform arrays. The nonuniform arrays for which measurements were made are comprised of two different regions, each of which has a uniform geometry. Either hole spacing or hole diameter has a different value in the two regions. A previously developed flow distribution model for uniform arrays [1] was extended to nonuniform arrays and was validated by comparison with the measured flow distributions. The validated flow distribution model was then employed to compare nonuniform array streamwise resolved heat transfer coefficient data with uniform array data previously obtained with the same test rig [1, 2], and with a previously reported correlation based on the uniform array data [1]. To the authors knowledge, no other results for arrays of nonuniform geometry have been reported in the open literature. Several studies of uniform geometry, two-dimensional arrays of circular impinging jets for which the exhaust flow is constrained to exit in a single direction, and which were motivated by turbine cooling applications, have been reported in addition to the work already cited [3, 4,5].

Experimental Facility

The basic test model geometry for the nonuniform arrays is identical to that previously utilized for a comprehensive series of uniform array tests [1, 2], except that the arrays are now composed of two adjacent uniform array geometries, each of which has different values for one of the three geometric parameters, x_n, y_n, or d. This is illustrated in Fig. 1 for the case where y_n is the parameter whose value changes. The upstream region is denoted as Region 1, the downstream region as Region 2, with corresponding subscripts used to distinguish quantities having different values in the two regions. For quantities having identical values, no subscript is used. These geometric configurations were incorporated into the test facility previously utilized for the uniform array tests.

The nonuniform array geometries for which tests were conducted are summarized in Table 1. Heat transfer tests were conducted for all cases listed, with flow distribution tests

Contributed by the Gas Turbine Division of THE AMERICAN SOCIETY OF MECHANICAL ENGINEERS and presented at the 29th International Gas Turbine Conference and Exhibit, Amsterdam, The Netherlands, June 4–7, 1984. Manuscript received at ASME Headquarters January 11, 1984. Paper No. 84-GT-156.

conducted for those cases so indicated. Most of the tests were for arrays with nonuniform spanwise hole spacings and nonuniform hole diameters. These arrays had a total of ten spanwise rows of holes, just as did the uniform arrays for which results were previously reported [1, 2]. One test is included for an array with a nonuniform streamwise hole spacing. This array had a total of 6 spanwise rows.

Arrays with a nonuniform hole spacing, x_n or y_n, were prepared from previously machined uniform array jet plates by either plugging or taping over selected holes on the upstream side of the jet plate. For arrays with nonuniform hole diameters, new jet plates were machined. Each had five spanwise rows of holes of a smaller diameter in one region, and five rows of a larger diameter in the other region. They were designed so they could be reversed end-to-end in the streamwise direction in the test facility. Thus each could be used to give a small-to-large hole diameter transition in the streamwise direction, as well as a large-to-small diameter transition.

Experimental Procedures and Data Reduction

The details of the experimental procedures and data reduction techniques for the nonuniform geometry flow distribution tests were identical to those previously described for uniform arrays [1] and will not be repeated here. It should be noted, however, that jet hole discharge coefficients for each subarray (region) within a nonuniform array were assumed constant. This was justified, since the resulting crossflow-to-jet velocity ratios were never large enough to significantly affect the discharge coefficients [6], just as was the case for the prior uniform array geometries. For nonuniform arrays in which one of the two regions was formed by blocking selected holes in a uniform array jet plate, the discharge coefficients for both regions were set equal to the previously measured $\bar{C}_D$ for the original jet plate. For arrays with nonuniform hole diameters, which were newly machined jet plates, C_D for each region was set equal to the originally measured $\bar{C}_D$ for the uniform jet plate of corresponding geometry. For these cases, the $\bar{C}_D$ values used for the two regions may differ to some extent. The experimental procedures and data reduction techniques for the nonuniform array heat transfer tests were also essentially as utilized for the prior uniform array tests. The estimate of the composite experimental uncertainty on the resulting Nusselt numbers also remains at ± 5 percent.

Flow Distributions

A theoretical model for the row-by-row flow distributions for the nonuniform geometries was developed on the same basis as that originally presented by Florschuetz et al. [1] for uniform geometries. That is, a uniform discrete hole array is assumed to be replaced (temporarily) by a surface over which the jet flow is continuously distributed. The flow is treated as incompressible and as one-dimensional along the channel, with negligible effect of channel wall shear (i.e., the channel pressure drop is assumed to be caused solely by the acceleration of the crossflow resulting from injection of jet flow). The jet discharge coefficient is assumed uniform over the array. The model leads to a linear second-order ordinary differential equation for the crossflow (channel flow) mass velocity as a function of streamwise location. Boundary conditions are a specified crossflow velocity of zero at the upstream end of the array ($x=0$) and a specified velocity at the downstream end ($x=L$) determined from the total jet flow rate.

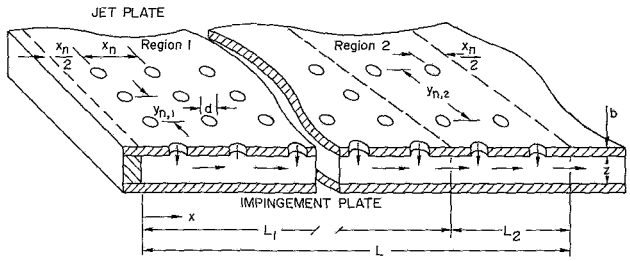

Fig. 1 Example of basic test model geometry and nomenclature for nonuniform array

Consider now a nonuniform array in which any one or more of the geometric parameters x_n, y_n, or d undergo one or more changes in value in the streamwise direction along the array (e.g., Fig. 1). In order to extend the model, the nonuniform array may be regarded as composed of a series of coupled *uniform* geometry subarrays (regions). Consider a nonuniform array composed of n regions. The boundary conditions at the entrance ($x=0$) and exit ($x=L$) of the nonuniform array remain the same as for a uniform array. But now two matching conditions must be satisfied at each of the $(n-1)$ interfaces between the n regions. Both the crossflow rate (therefore, the crossflow mass velocity) and the channel pressure must be continuous across each interface. Thus there are n second-order differential equations with two boundary conditions and $2(n-1)$ matching conditions, for a total of $2n$ supplementary conditions for the general case. Detailed formulation and solution for the general case may be found in [7].

The nonuniform jet plates tested in the present study each had two regions. The governing equations and closed-form solutions for this case are given in both [7] and [8]. For the jet mass velocity

Nomenclature

A_0^* = open area ratio, $\pi/[4(x_n/d)\,(y_n/d)]$
b = local thickness of jet plate at jet hole location
C_D = jet plate discharge coefficient
c_p = constant pressure specific heat
d = jet hole diameter
G_c = crossflow mass velocity based on channel cross-sectional area
G_j = jet mass velocity based on jet hole area
G_j^* = superficial jet mass velocity based on jet plate area
h = heat transfer coefficient at impingement surface
L = streamwise length of jet plate and impingement surface (Fig. 1)
Nu = Nusselt number, hd/k
q = heat flux at impingement surface
Re_j = jet Reynolds number, $G_j d/\mu$
Re_j^* = superficial jet Reynolds number, $G_j^* d/\mu$
St = Stanton number, $h/c_p \bar{G}_j$
x = streamwise location along jet plate or impingement surface (Fig. 1)
$\tilde{x}$ = normalized streamwise location, x/L
x_n = streamwise jet hole spacing
y_n = spanwise jet hole spacing
z = channel height (jet exit plane-to-impingement surface spacing)

Greek

μ = dynamic viscosity

Subscripts and Superscripts

1,2 = uniform geometry regions of nonuniform array, 1 for upstream region, 2 for downstream region
$(\bar{\ })$ = overbar refers to mean value over jet plate or over specified region of jet plate

Table 1 Nonuniform array geometries tested

Non-uniform parameter	Array geometry[a] Region 1	Region 2	No. of rows Region 1	Region 2	d (cm)	Test series #
x_n	B(10,8,3)I	B(5,8,3)I	4	2	0.254	1X[b]
y_n	B(5,8,3)I	B(5,4,3)I	8	2	0.254	2Y[b]
	B(5,4,3)I	B(5,8,3)I	4	6	0.254	3Y[b]
	B(5,8,3)I	B(5,4,3)I	2	8	0.254	4Y[b]
	B(5,4,3)I	B(5,8,3)I	1	9	0.254	5Y[b]
	B(10,8,3)I	B(10,4,3)I	8	2	0.127	6Y
	B(5,8,2)I	B(5,4,2)I	8	2	0.254	7Y
	B(10,8,2)I	B(10,4,2)I	8	2	0.127	8Y
	B(10,8,2)I	B(10,4,2)I	5	5	0.127	9Y
					d_1 (cm)	
d	B(10,8,2)I	B(5,4,1)I	5	5	0.127	1D[b]
	B(5,4,1)I	B(10,8,2)I	5	5	0.254	2D[b]
	D(15,6,3)I	D(10,4,2)I	5	5	0.254	3D
	D(10,4,2)I	D(15,6,3)I	5	5	0.381	4D

[a] $(x_n/d, y_n/d, z/d)$
Prefix designates overall array length:
$B(L = 12.7$ cm), $D(L = 38.1$ cm)
Suffix designates hole pattern: I = Inline
[b] Flow distribution (row-by-row) measured in addition to heat transfer coefficients

Note: $b = d$, for test series 1X and for 2Y–9Y
b = larger of d_1 or d_2, for test series 1D–4D

$$\frac{G_{j,k}}{\bar{G}_j} = \frac{A_0^*}{A_{0,k}^*} \frac{B_k}{\sinh B_k \tilde{L}_k} (E_k \cosh B_k \tilde{x} + F_k \sinh B_k \tilde{x}) \quad k = 1,2$$

and for the crossflow-to-jet velocity ratio

$$\left(\frac{G_c}{G_j}\right)_k = \frac{1}{\sqrt{2}\, C_{D,k}} \frac{E_k \sinh B_k \tilde{x}' + F_k \cosh B_k \tilde{x}'}{E_k \cosh B_k \tilde{x} + F_k \sinh B_k \tilde{x}} \quad k = 1,2$$

where $\tilde{x}' = \tilde{x} - (1/2) \cdot (x_{n,k}/L)$, $B_k = \sqrt{2}(A_0^* C_D)_k L/z$ and $\tilde{L}_k = L_k/L$. For Region 1 ($k = 1$)

$$E_1 = \frac{1}{(\coth B_1 \tilde{L}_1 + \coth B_2 \tilde{L}_2) \sinh B_2 \tilde{L}_2}, F_1 = 0$$

and for Region 2 ($k = 2$),

$$E_2 = \cosh B_2 \tilde{L}_1 - E_1 \cosh B_2, \quad F_2 = E_1 \sinh B_2 - \sinh B_2 \tilde{L}_1$$

The solution corresponding to one of the test cases for which y_n was the nonuniform parameter is plotted in Fig. 2. The upper plot shows the jet mass velocity (G_j) at each spanwise row normalized by the mean value over all ten rows of the array. The lower plot shows the ratio of the crossflow velocity (G_c) immediately upstream of a given row to the jet velocity at the row. Data points based on the flow distribution measurements are also indicated and seen to be in excellent agreement with the theory. The closure value (0.97) indicated in the legend of the figure is the ratio of the sum of the measured individual spanwise row flow rates to the total jet flow rate as measured at a metering section upstream of the jet plenum. For the case shown in Fig. 2, with $z/d = 3$, the flow distribution is rather uniform and the effect of the step change in y_n is not readily apparent in the $G_j/\bar{G}_j$ plot. The effect, however, shows up clearly in the G_c/G_j plot.

The results presented in Figs. 3 and 4 are for arrays in which the jet hole diameter over the downstream half of the array is either double (Fig. 3) or one-half (Fig. 4) that over the upstream half. Since each of these cases involves a substantial region over which both the spanwise hole spacing and channel height ($y_n/d = 4$ and $z/d = 1$) are relatively small, the flow distributions are quite nonuniform, and the effect of the step change in hole diameter is quite apparent. These cases provide a more severe test of the model than the case shown in Fig. 2, but the agreement is still excellent.

It may be of interest to note that the first (i.e., upstream) region of a nonuniform array may be thought of as a uniform array *without* initial crossflow[1], while a downstream region may be thought of as a uniform array *with* initial crossflow (the initial crossflow arising from the upstream regions). In a prior study of uniform arrays with initial crossflow [6], it was shown that the flow distribution becomes less uniform as $(y_n/d)\,(z/d)$ decreases and as the initial crossflow increases. With these ideas in mind the trends for $G_j/\bar{G}_j$ in Figs. 3 and 4 may be interpreted. In Fig. 3 the upstream region has both a large value of (y_n/d) (z/d) *and* zero initial crossflow conditions, leading to the essentially uniform observed and predicted flow distribution in that region. The downstream region has both a small value of $(y_n/d)\,(z/d)$ *and* a finite initial crossflow leading to the highly nonuniform observed and predicted flow distribution in that region. In Fig. 4, we have a case where the $(y_n/d)\,(z/d)$ and initial crossflow conditions for each region tend to oppose each other in their effects on the flow distribution. This results in the flow distributions of intermediate nonuniformity observed and predicted for each of the two regions of this array.

Nonuniform Array Heat Transfer Characteristics

In this section examples of the experimentally determined streamwise profiles of heat transfer coefficients for the nonuniform arrays are presented. Results for arrays with nonuniform hole spacings are plotted as Nusselt number profiles (Nu = hd/k). Results for arrays with nonuniform hole diameters are plotted as Stanton numbers, defined using the mean jet mass velocity over the entire array (St = $h/c_p \bar{G}_j$), so that the plots correctly represent the streamwise variation of the heat transfer coefficient itself.

In the following two subsections, a series of plots is presented, all having the same basic format and all displaying the same types of comparisons (Figs. 5–10). Each plot is for a specific nonuniform array geometry, as indicated on the plot. The location of the interface between the two uniform regions comprising the nonuniform array is marked by the vertical dashed line. The primary result shown on each plot is the set

[1] When a channel flow approaches an array along an upstream extension of the channel formed by the jet orifice plate and the impingement surface, it is referred to as an initial (or independent) crossflow [6, 8].

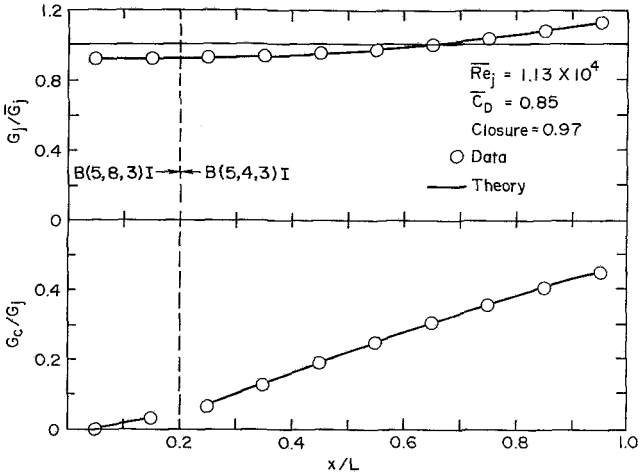

Fig. 2 Flow distribution data for nonuniform y_n array compared with theory: Test #4Y

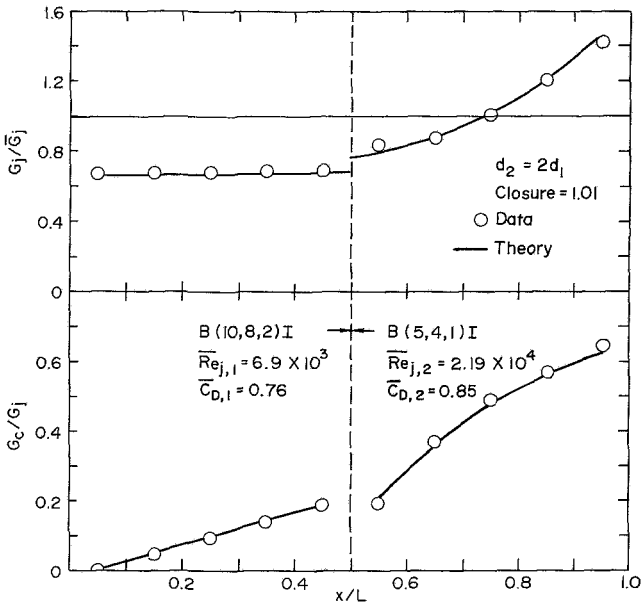

Fig. 3 Flow distribution data for nonuniform diameter array compared with theory: Test #1D

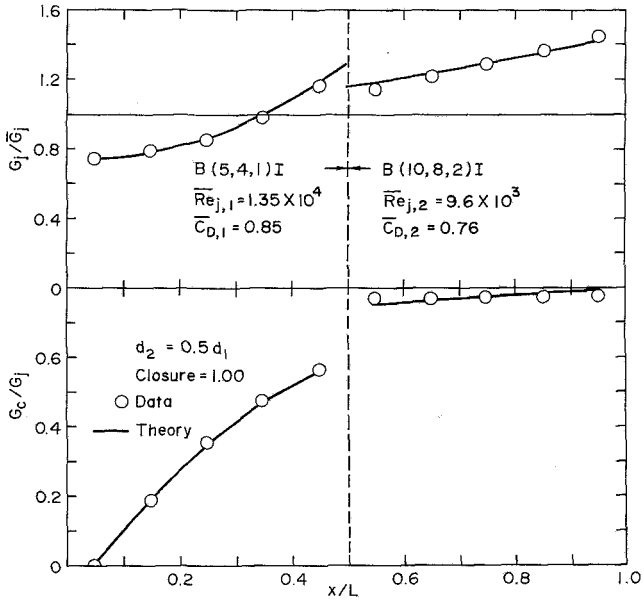

Fig. 4 Flow distribution data for nonuniform diameter array compared with theory: Test #2D

of 10 spanwise averaged, streamwise resolved, Nu (Or St) values for the nonuniform array geometry indicated on the plot. These points are always represented by the upright solid triangles. Each point represents the average Nu (or St) value over the heat transfer surface increment x_n centered immediately opposite the corresponding spanwise row of jet holes in the array.

A second set of points on each plot, always represented by inverted open triangles, is based on the previously reported data for uniform arrays [1, 2]. Each point shown is for the same values of the parameter set (Re_j, G_c/G_j, x_n/d, y_n/d, z/d) that existed for the nonuniform array data point to which it is compared. The validated flow distribution models for both uniform arrays [1], and nonuniform arrays (prior section) were utilized in performing this comparison. For Region 1 (the upstream region), G_c/G_j values match the corresponding uniform geometry values row by row. However, for Region 2 (the downstream region) this does not hold. Therefore, the uniform array row numbers utilized to match the G_c/G_j values are noted for Region 2 over the abscissa of the plot. In some cases, it was necessary to interpolate Nu as a function of G_c/G_j between adjacent rows of the uniform array. Normally, the adjacent values were quite close so that linear interpolation was satisfactory. In these cases, the pairs of adjacent row numbers utilized are indicated for Region 2 over the abscissa of the plot. In several cases the ranges of values of G_c/G_j for corresponding uniform and nonuniform geometry tests did not completely overlap. Where possible, uniform array points for comparison were then determined from available uniform array initial crossflow data [8]. The row numbers are again indicated and also marked by an asterisk.

Finally, included on each plot are the Nu (or St) values calculated from the correlation originally developed in [1]. This correlation was based entirely on the data from the prior comprehensive series of uniform array geometry tests. The correlation gives $Nu = f(Re_j, G_c/G_j, x_n/d, y_n/d, z/d)$. The specific form used was equation (10) from [1]. The uncertainty interval for the correlation was ± 11 percent for a 95 percent confidence level. It was applied at each spanwise row of the nonuniform arrays tested. In Figs. 5–10, the position of the points so calculated is indicated by a solid line to facilitate comparison with the data points.

The nonuniform array data and the comparisons presented in these figures is discussed below in two major categories: first, the effects of a nonuniform hole spacing with emphasis on the spanwise spacing (Figs. 5–8), and second, the effects of a nonuniform hole diameter (Figs. 9 and 10).

Nonuniform Hole Spacings. Examination of the nonuniform array data (solid triangles) in Fig. 5 indicates that a doubling of y_n from Region 1 to Region 2 can cause a significant decrease in Nu across the transition line, the change being larger when it occurs upstream (Fig. 5(*a*)) as compared to further downstream (Fig. 5(*b*)). Figure 6 indicates the reverse transition (reducing y_n by one-half) causes less significant changes across the transition line, especially when the transition occurs far downstream (Fig. 6(*b*)). However, it is clear that reducing y_n from Region 1 to Region 2 always increases Nu across the transition line to some degree, as illustrated by Figs. 6–8. In most of these cases the downward trend of Nu in Region 1 is halted across the transition line and sometimes reversed in Region 2.

For Region 1, the data points from the nonuniform array tests are consistent with those from the uniform array in every case (Figs. 5–8). Indeed, the largest difference is just 6.3

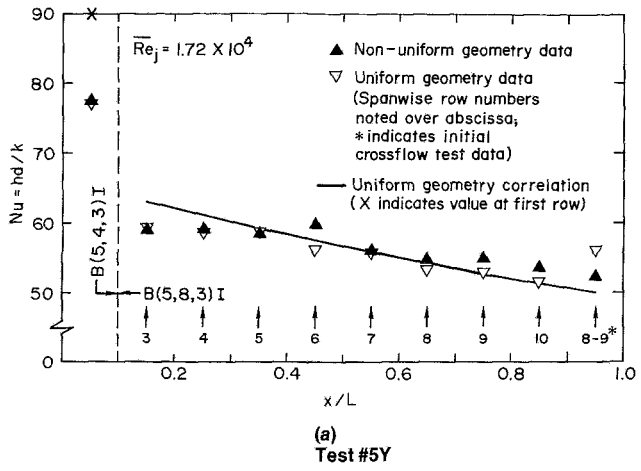

(a) Test #5Y

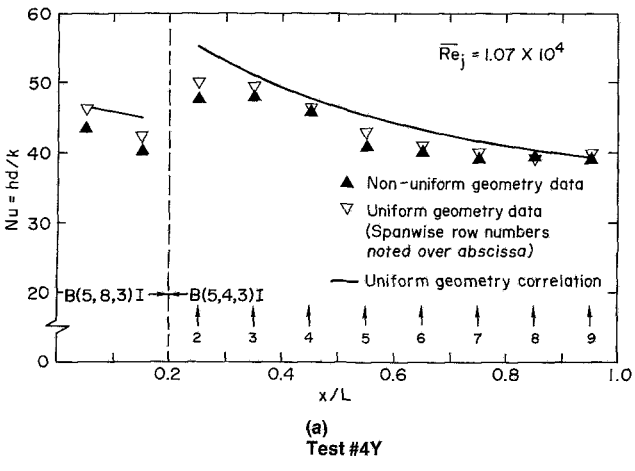

(a) Test #4Y

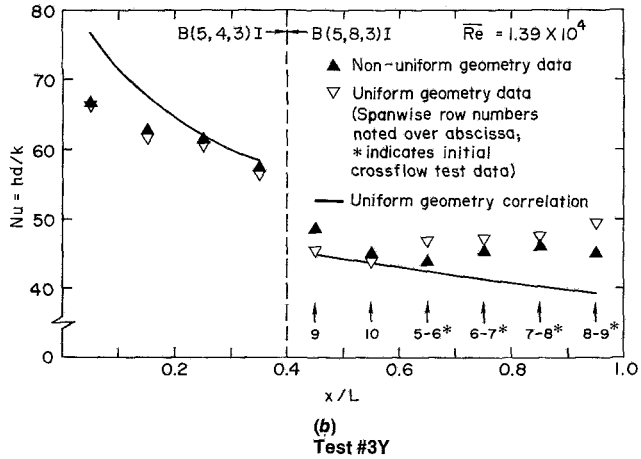

(b) Test #3Y

Fig. 5 Nusselt number data for nonuniform arrays ($y_{n2} = 2y_{n1}$) compared with uniform array data and correlation

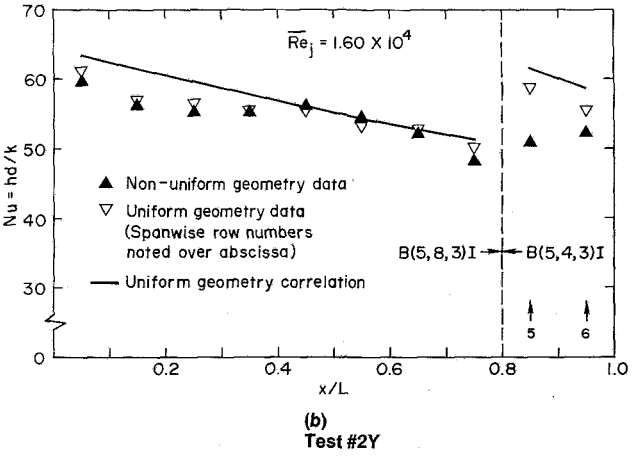

(b) Test #2Y

Fig. 6 Nusselt number data for nonuniform arrays ($y_{n2} = 0.5y_{n1}$) compared with uniform array data and correlation

percent with an average difference of only 2.5 percent. With respect to any given row in Region 1 of the nonuniform array, details of the flow field history upstream of the row should be identical with the history for the corresponding row in the uniform array. The good consistency of the data for Region 1 provides confidence that the differences sometimes observed in Region 2 immediately downstream of the transition line represent real effects. These effects will now be discussed.

There is little difference observed between the data points even at the first row following the transition line when y_n is doubled from Region 1 to Region 2 (Fig. 5). However, it does appear from Fig. 5(*b*)) that at this row the nonuniform array data point indicates a somewhat larger Nu than existed for the uniform array (7 percent). Conversely, when y_n was cut in half, the nonuniform array point at the first row in Region 2 fell below the uniform array point by anywhere from 13 to 19 percent (see, e.g., Figs. 6(*b*), 7, and 8), except for the case of Fig. 6(*a*), where it fell below by only 5 percent. Since the data points are being compared for the same G_j (which is averaged over jet hole area of a given spanwise row) and same G_c (which is averaged over channel cross-sectional area), significant differences in Nu are undoubtedly related to local differences in the two flow fields. These differences arise due to differing histories of the crossflow approaching respective rows being compared, even though the crossflow rate magnitudes are the same. Qualitative explanations of these Nusselt number differences may be attempted, but must remain tentative because of the great complexity of the interacting cross and jet flows within a two-dimensional array of jets. The explanations given below are related largely to the consideration that the spanwise distribution of the crossflow is not uniform but rather periodic with a period equal to the spanwise hole spacing.

It is well known that as the crossflow velocity approaching an impinging jet is increased from zero the heat transfer coefficient at the impingement surface opposite the jet decreases. Data reported in [8] show that heat transfer coefficients opposite a downstream row within an array can be significantly larger than those opposite the first spanwise row of an array subject to an initial crossflow, even though compared at the same Re_j and G_c/G_j values. This is because the crossflow within an inline array tends to become channelized between the streamwise rows of the array [9]. That is, the crossflow velocity between adjacent jets in a downstream row is larger than the mean value over the channel cross section, while the crossflow velocity approaching directly in line with the jets is smaller than the mean value. The initial crossflow, which approaches the first spanwise row, is uniform across the span of the channel. Therefore, jets at a downstream spanwise row in an array see smaller local crossflow velocities approaching them than do jets in the first upstream row even though they are subject to the same total crossflow rate. In other words, a jet within an in-line array tends to be partially shielded from accumulated crossflow by upstream jets in the same line, and therefore produces a larger heat transfer coefficient than a jet which is not so shielded.

Now consider a nonuniform in-line array for which the spanwise hole spacing downstream of the geometric transition

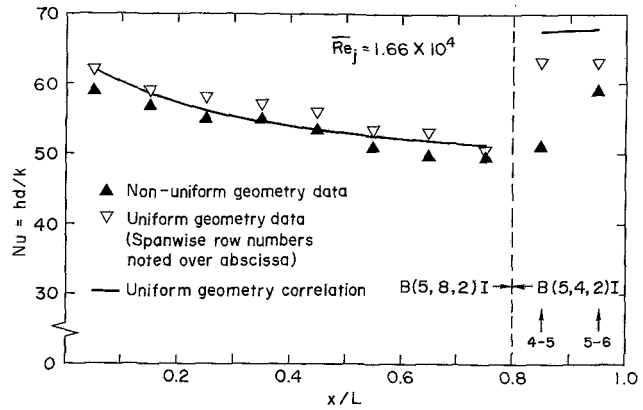

Fig. 7 Nusselt number data for nonuniform array ($y_{n2} = 0.5y_{n1}$) compared with uniform array data and correlation: Test #7Y

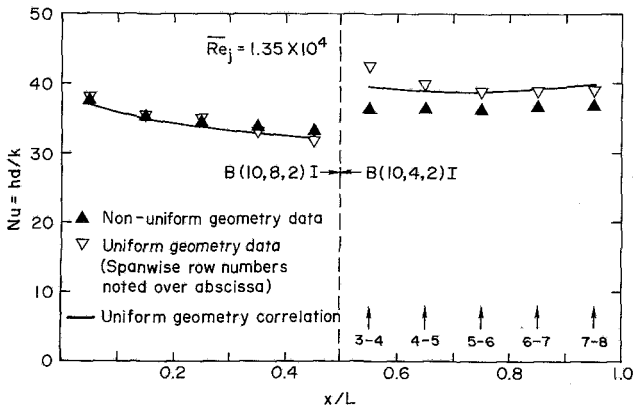

Fig. 8 Nusselt number data for nonuniform array ($y_{n2} = 0.5y_{n1}$) compared with uniform array data and correlation: Test #9Y

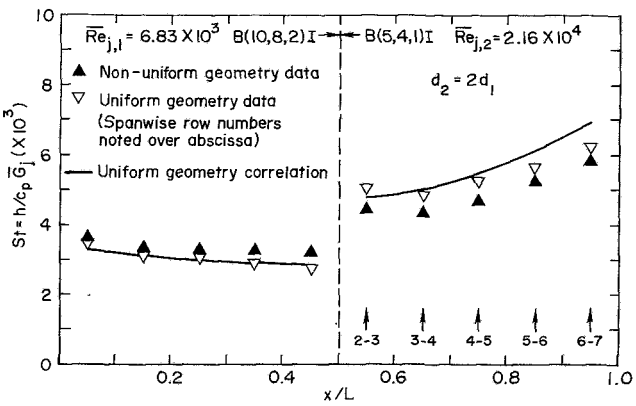

(a)
Test #1D

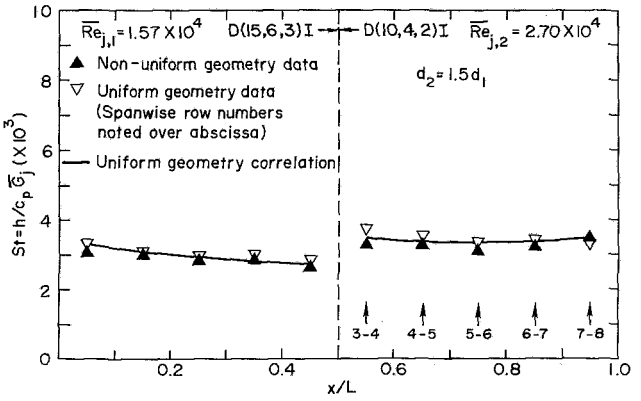

(b)
Test #3D

Fig. 9 Stanton number data for nonuniform diameter arrays ($d_2 > d_1$) compared with uniform array data and correlation

line is one-half the upstream value. Then alternate jets in the first spanwise row downstream of the geometric transition line are not shielded from accumulated crossflow by upstream jets. This results in smaller heat transfer coefficients opposite this spanwise row than if it were part of a uniform in-line array where every jet in the row would be partially shielded. Each Nusselt number in Figs. 6–8 for the first row of Region 2 was already observed to be smaller than the corresponding value based on uniform array data.

When y_n is doubled (as in Fig. 5) each jet in the first row of Region 2 is still partially shielded by upstream jets as it would be if part of a uniform array. In addition, part of the total crossflow, that from alternate jets in the last row of Region 1, flows directly between adjacent pairs of jets in the first row of Region 2. Its influence in decreasing the Nusselt numbers of the jets in the first row of Region 2 would thus tend to be reduced, relative to what it would be as part of a uniform array. This tendency is reflected in Fig. 5(*b*), though the difference is small. No difference whatever shows up in the case of Fig. 5(*a*), where the geometric transition occurs far enough upstream so that G_c/G_j is still quite small. The explanations outlined above are closely related to the previously reported interpretation of Nusselt number differences between corresponding uniform inline and staggered arrays [9].

Comparing Fig. 5(*a*) to 5(*b*) and Fig. 6(*a*) to 6(*b*) (and to Figs. 7 and 8), it appears that data point differences immediatedly downstream of the transition line are larger when the transition line is farther downstream. For all of the cases where a significant difference between the corresponding data points occurs in the first row after the transition line, the difference becomes noticeably smaller at the second row after the transition line and continues to decrease at succeeding rows. The use of the correlation appears to be essentially as well-justified for nonuniform y_n arrays as it is for uniform arrays, except, in some cases, at the first one or two rows after the transition line.

Heat transfer data were obtained for one nonuniform x_n array (Test #1X, Table 1). For this array, x_n was reduced by one-half from Region 1 to Region 2. Nusselt numbers for the two rows in Region 2 were compared as above with uniform array results indicating no significant difference even at the first row downstream of the transition line.

Nonuniform Hole Diameters. Stanton number (St = $h/c_p\bar{G}_j$) profiles for four different arrays with nonuniform hole diameters are presented in Figs. 9 and 10. Since the Reynolds numbers are defined in terms of the jet hole diameter, mean values are specified for each of the two uniform subarrays (regions).

The nonuniform array data points (upright solid triangles) in Fig. 9 show that increasing the hole diameter for Region 2 relative to Region 1 results in higher heat transfer coefficients in Region 2 than in Region 1. Figure 10 shows the reverse trend for a decrease in hole diameter. The differences are more pronounced when the diameters change by a factor of 2 than when they change by a factor of 1.5.

When Region 2 has the larger diameter (e.g., Fig. 9(*a*)), the ratio of hole area to heat transfer surface area is also larger, so that even for the same jet velocities, one might expect higher heat transfer coefficients. Examination of the corresponding flow distribution (Fig. 3) indicates Region 2

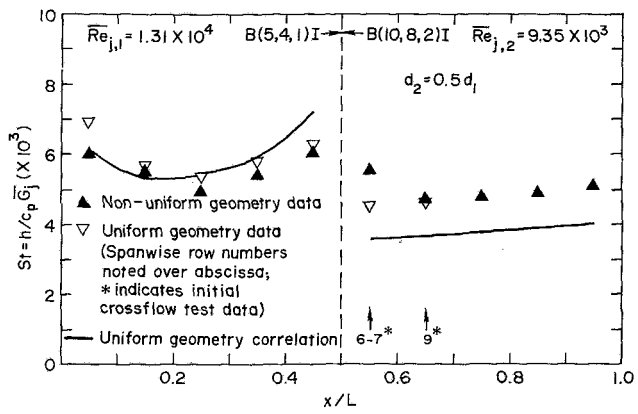

(a)
Test #2D

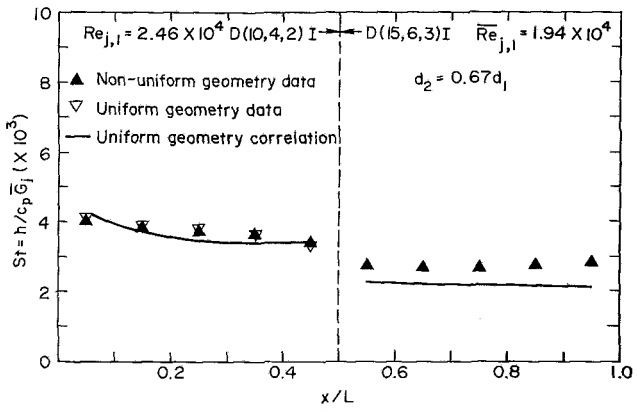

(b)
Test #4D

Fig. 10 Stanton number data for nonuniform diameter arrays ($d_2 < d_1$) compared with uniform array data and correlation

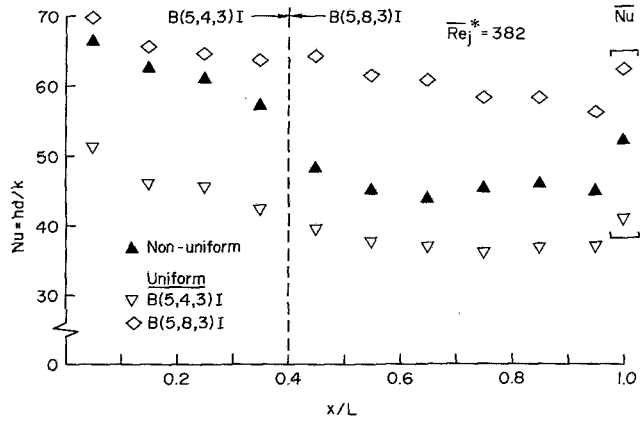

(a) Same total jet flow rates

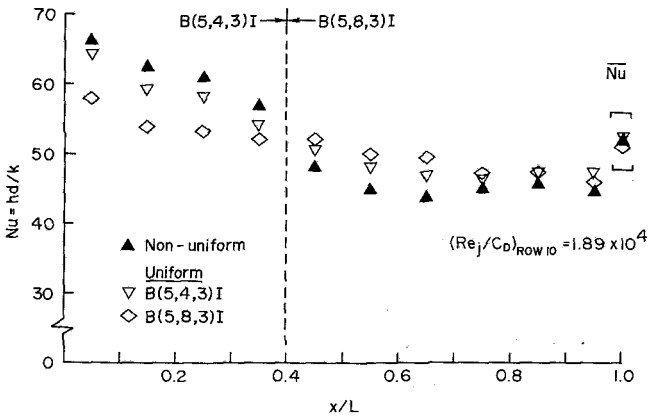

(b) Same pressure drops

Fig. 11 Nusselt number profile for nonuniform y_n array compared with profiles for corresponding uniform array geometries

also has larger jet velocities. Thus two effects combine resulting in higher heat transfer coefficients in Region 2 relative to Region 1.

When Region 2 has the smaller diameter (e.g., Fig. 10(*a*)), the open area ratio effect, assuming the same jet velocities, would tend to reduce the heat transfer coefficients. The corresponding flow distribution (Fig. 4) shows the jet velocities in Region 2 to be equal to or higher than those of Region 1 just as they were for the contrasting conditions of the preceding paragraph. However, here the counteracting open area ratio effect apparently dominates enough to cause lower heat transfer coefficients in Region 2 relative to Region 1.

When the corresponding uniform and nonuniform array heat transfer coefficient data points are compared, an effect of the upstream history of the flow field again shows up immediately downstream of the transition line just as it did for the nonuniform y_n cases. The difference is significant only in Fig. 10(*a*), but disappears at the second row of Region 2, so here the significant "entrance length" is no more than one row. It should be pointed out that none of the available uniform array data, with or without an initial crossflow, had G_c/G_j values in the necessary range for comparisons at the last three rows of the array of Fig. 10(*a*) or for the entire Region 2 of the array of Fig. 10(*b*). These points were also, of course, outside the applicable range of the correlation, as were those for the first two rows of Region 2, Fig. 10(*a*), where uniform array initial crossflow data points [8] were used for comparison. Otherwise the curves based on the correlation are consistent with the data for both regions in all of these figures.

Additional Comparisons. The previous two subsections have been concerned primarily with the nature of the nonuniform array heat transfer coefficient profiles and consideration of how well these streamwise resolved heat transfer coefficients may be predicted from uniform array data or from the correlation based on uniform array data. Here, an example of a direct comparison between a two-region nonuniform array and the two uniform arrays having the same geometric parameter sets (x_n/d, y_n/d, z/d) is provided. The array of Test #3Y (Fig. 5(*b*)) with a nonuniform y_n is used as the example. The basis of comparison must, however, be precisely defined. The heat transfer characteristics of the arrays are first compared for the same total jet flow rate per unit of heat transfer surface area (or equivalent jet plate surface area), $\bar{G}_j^*$. For jet plates of uniform hole diameter the comparison may be made for the same value of mean jet Reynolds number based on this superficial mass velocity, $\bar{Re}_j^*$. The comparison is presented in Fig. 11(*a*). The Nu profile for the nonuniform array is more highly nonuniform than either profile for the corresponding uniform arrays, and falls between these profiles. The nonuniform $\overline{Nu}$ falls about midway between the uniform array values in this example. It is interesting to observe that, in both Regions 1 and 2, the nonuniform array Nusselt numbers lie closer to the values for the uniform array with the differing y_n/d than they do to the values for the uniform array with the same y_n/d.

The same cases are compared again in Fig. 11(*b*) on a different basis. Here the comparison is for the same pressure drop from jet plenum to jet array channel exit. This pressure drop is essentially that existing across the final downstream

row of holes in the array (Row 10 for the present arrays). For incompressible flow, the pressure drop will be the same if G_j (or Re_j) is the same, assuming the same discharge coefficient for each array. For the arrays compared here C_D differed slightly. Taking this into account, the same pressure drop will exist for the same value of Re_j/C_D at Row 10. The value at which the comparison was made is specified on the figure. Compared on this basis the Nu profiles differ less than when compared for the same total jet flow rate. The mean values for this example are almost identical, but as before the mean for the nonuniform array lies between the uniform array values. Now, however, the nonuniform array has larger Nusselt numbers than either uniform array in Region 1, but smaller values than either in Region 2.

These comparisons serve to illustrate that, depending on the designer's flow and pressure drop constraints, the use of nonuniform arrays can serve to adjust the level and distribution of cooling furnished by the array, providing the flexibility to better match the external heat load magnitude and distribution.

Concluding Remarks

A midchord internal cooling scheme utilizing two-dimensional arrays of jets, in addition to the high heat transfer coefficients possible, provides the flexibility and potential for optimizing cooling performance by tailoring the array geometry to appropriately match the external thermal loading. This may often require the use of arrays having nonuniform geometric parameter values. Since it is not feasible to generate measurements or test results for every possible arrangement the designer may need to consider in his performance and trade-off analyses, it is important that he has available some means of calculating expected performance for various array geometries.

Comparisons made in preceding sections of the paper verified that reliable uniform array heat transfer data can be used to determine heat transfer coefficients for the upstream region of a nonuniform array. In addition, it was found that for downstream regions accurate determinations can be made beyond the second row following the geometric transition line, and for many conditions at the first and/or second rows as well (put more concisely, the maximum significant "entrance length" following the geometric transition appears to be two rows). Heat transfer coefficients for "entrance length" rows based on uniform array data may be larger or smaller than the actual values for the nonuniform array, depending on the type of geometric transition. If the spanwise spacing is increased downstream, the uniform array based value may be somewhat low. If it is decreased, the value will tend to be high. If the diameter is increased the uniform array based value will tend to be high, while for a decrease in diameter it will tend to be low. The largest difference observed for any nonuniform array tested was about 20 percent. It has been observed [10] that if, in Figs. 5–10(*a*), a straight line is drawn from the uniform array based data point at the *last* row of Region 1 to the uniform array based point at the *second* row of Region 2, it very nearly passes through the nonuniform array point at the *first* row of Region 2. In every case, except Fig. 5(*a*), where the transition line occurs after the first row, using such a "rule of thumb" results in a prediction for the first row downstream of the geometric transition line that is as good or better than that obtained by relying on the uniform array based value at that row.

Finally, it was found that heat transfer coefficient predictions for nonuniform arrays based on the correlation originally presented in [1] may, in general, be made with essentially the same confidence as for uniform arrays, as long as the crossflow-to-jet velocity ratios are within the range of results on which the correlation was based. Exceptions occur, in some cases, for the first one or possibly two rows immediately downstream of the geometric transition in the nonuniform array. At these rows the correlation may still be applied but with more caution, because the confidence will not be as high.

Acknowledgment

The support of the National Aeronautics and Space Administration, Lewis Research Center, is hereby gratefully acknowledged.

References

1 Florschuetz, L. W., Truman, C. R., and Metzger, D. E., "Streamwise Flow and Heat Transfer Distributions for Jet Array Impingement with Crossflow," ASME *Journal of Heat Transfer*, Vol. 103, 1981, pp. 337–342.

2 Metzger, D. E., Florschuetz, L. W., Takeuchi, D. I., Behee, R. D., and Berry, R. A., "Heat Transfer Characteristics for Inline and Staggered Arrays of Circular Jets with Crossflow of Spent Air," ASME *Journal of Heat Transfer*, Vol. 101, 1979, pp. 526–531.

3 Kercher, D. M., and Tabakoff, W., "Heat Transfer by a Square Array of Round Air Jets Impinging Perpendicular to a Flat Surface Including the Effect of Spent Air," ASME JOURNAL OF ENGINEERING FOR POWER, Vol. 92, 1970, pp. 73–82.

4 Saad, N. R., Mujumdar, A. S., Abdel Messeh, W., and Douglas, W. J. M., "Local Heat Transfer Characteristics for Staggered Arrays of Circular Impinging Jets with Crossflow of Spent Air," ASME Paper 80-HT-23, 1980.

5 Behbahani, A. I., and Goldstein, R. J., "Local Heat Transfer to Staggered Arrays of Impinging Circular Air Jets," ASME JOURNAL OF ENGINEERING FOR POWER, Vol. 105, 1983, pp. 354–360.

6 Florschuetz, L. W., and Isoda, Y., "Flow Distributions and Discharge Coefficient Effects for Jet Array Impingement with Initial Crossflow," ASME JOURNAL OF ENGINEERING FOR POWER, Vol. 105, 1983, pp. 296–304.

7 Tseng, H. H., "Effect of Nonuniform Geometry on Jet Array Impingement Flow Distributions and Heat Transfer Characteristics," M.S. thesis, Arizona State University, Tempe, Ariz., 1983.

8 Florschuetz, L. W., Metzger, D. E., Su, C. C., Isoda, Y., and Tseng, H. H., "Jet Array Impingement Flow Distributions and Heat Transfer Characteristics—Effects of Initial Crossflow and Nonuniform Array Geometry," NASA Contractor Report 3630, Department of Mechanical and Aerospace Engineering, Arizona State University, Tempe, Ariz., Nov. 1982.

9 Florschuetz, L. W., Berry, R. A., and Metzger, D. E., "Periodic Streamwise Variations of Heat Transfer Coefficients for Inline and Staggered Arrays of Circular Jets with Crossflow of Spent Air," ASME *Journal of Heat Transfer*, Vol. 102, 1980, pp. 132–137.

10 Hippensteele, S. A., NASA Lewis Research Center, personal communication.

Turbine Heat Flux Measurements: Influence of Slot Injection on Vane Trailing Edge Heat Transfer and Influence of Rotor on Vane Heat Transfer

M. G. Dunn
Aerodynamic Research Department,
Calspan Advanced Technology Center,
Buffalo, N.Y. 14225

This paper describes the measurement of heat flux distributions obtained for a Garrett TFE 731-2 hp turbine. Measurements were obtained for a full turbine both with and without injection and for the nozzle guide vanes with and without a rotor. A shock tube is used as a short-duration source of heated air and miniature thin-film gages are used to obtain the heat flux measurements. Results are presented for values of the blowing parameter $(\rho_c V_c / \rho_\infty V_\infty)_{at\ SLOT}$, *in the range of 0.8–1.3. The injection gas (air) as a percentage of turbine weight flow,* W_c / W_o, *was in the range of 2.1–3.5 percent. A comparison is presented between results obtained with the rotor operating at 100 percent of corrected speed and those obtained with the rotor replaced by a row of flow straighteners. The results suggest that: (i) the reduction of heat flux due to injection is a function of the blowing parameter, the temperature ratio, and the physical location relative to the tip or hub endwall and (ii) the presence of the rotor has a significant affect on the vane trailing edge Stanton number, increasing it by 15 to 25 percent. The vane leading edge and midchord regions were generally unaffected.*

Introduction

The efficiency of aircraft gas turbine engines is strongly affected by the maximum allowable turbine inlet temperature, and the performance improvements that can be achieved by increases in this parameter are substantial. Such increases are limited by heat transfer considerations; for this reason, many contemporary research efforts are directed at obtaining a better understanding of cooling schemes that can be incorporated into component designs in order to permit higher gas temperature operation.

A measurement and analysis program that utilizes a Garrett TFE 731-2 HP turbine has been on-going at Calspan. Until the present time, the major emphasis of this program has been placed on making accurate measurements of heat flux distributions in a full-scale rotating turbine stage in the absence of cooling. However, the 731-2 hp turbine under normal operating conditions utilizes pressure surface trailing edge slot cooling. It was thus decided to operate the stage with active slot cooling and to compare the resulting measurements with the existing no-injection data base.

Contributed by the Gas Turbine Division of THE AMERICAN SOCIETY OF MECHANICAL ENGINEERS and presented at the 29th International Gas Turbine Conference and Exhibit, Amsterdam, The Netherlands, June 4–7, 1984. Manuscript received at ASME Headquarters January 12, 1984. Paper No. 84-GT-175.

The interaction of rotor blades with stator vanes and endwalls is also an important consideration to the designers of gas turbine engines. In general, it is difficult to obtain measurements under essentially identical gas-dynamic conditions with and without a rotor but within the same experimental facility. The experimental facility at Calspan offers a unique opportunity in that the rotor wheel of the full-stage configuration can be replaced with a row of flow straighteners and then measurements of vane heat flux distributions can be obtained for comparison with full-stage results. A vane-only measurement program was previously conducted at Calspan [1] but under significantly different physical and gas-dynamic conditions than used for the measurements reported herein.

The experimental technique being used is the short-duration, shock-tunnel approach, in which fast-response, thin-film thermometers are used to measure the surface-temperature histories at prescribed positions on the various component parts. Heat transfer rates are then inferred from the temperature histories, using standard data reduction procedures. For the measurements described herein, 180 deg of the stator utilized cooling.

Previous results of this measurement program were reported as they became available. The first of these [2] described the flow-establishment process within the model

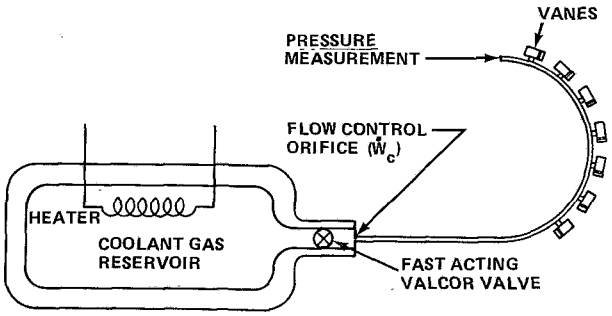

Fig. 1 Sketch of coolant system

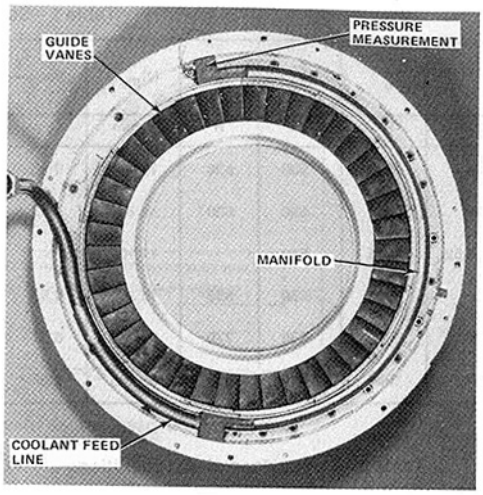

Fig. 2 Photograph of guide vanes and coolant manifold

containing the turbine hardware and the results of total temperature and pressure measurements, which confirmed that the gas-dynamic behavior of the flow was as designed. The second [1] reported heat flux results obtained at many locations within the nozzle guide vane. The geometry used in [1] and [2] was a 180-deg stator sector but without a downstream rotor. Turning vanes were placed downstream of the nozzles to remove a substantial portion of the flow turning introduced by the vanes. The third paper in this series [3] included heat flux measurements for a full 360 deg stator and the associated downstream rotor in order to obtain full-stage data. The full-stage heat flux results for the stator were used to calculate a Stanton number and the results were compared with the previous [2] measurements obtained with the vanes in the absence of the rotor. The comparisons presented in [3] suggested that the rotor can have an upstream influence on the boundary-layer development on the vane.

In [4], the initial 180 deg-sector data were compared with the predictions obtained using a flat-plate correlation, a two-dimensional parabolic boundary layer code (STAN5), and a three-dimensional viscous code (NANCY I). The measurements obtained for the blades were later compared [5] with the predictions of [4]. In addition, the comparisons earlier presented in [4] were updated to correct the heat flux data for temperature variations in the thermal properties of the substrate.

The most recent publication [6] in this series reported the results of a measurement program to obtain Stanton number distributions for the vanes and endwall, the rotor blade, the rotor tip, the rotor platform, and the shroud for which: (*a*) the rotor speed and flow function were representative of typical engine values and (*b*) the ratio of wall temperature to gas total temperature, T_w/T_o, was set at values of 0.21, 0.33, and 0.53.

The measurements described in this paper were obtained for vane pressure surface slot injection. Many film cooling papers have appeared in the literature, but the majority of these have dealt with discrete hole injection. All of the reported slot injection results were obtained for flat-plate type flows in the absence of endwall and/or acceleration effects. Louis [7] has correlated his and previous [8–10] slot injection data with a generalized correlation parameter, which is a function of the coolant to free-stream temperature ratio, the blowing parameters, the coolant Reynolds number, and the downstream location relative to the slot. Later, Louis [11] revised this correlation to include both discrete hole and slot injection and in the process he eliminated the Reynolds number dependence and used the slot gap (or height) to normalize the downstream location. Metzger et al. [12] have obtained slot injection data in a flat-plate geometry, and they have demonstrated an acceptable prediction of their experimental results based on the work of Patankar and Spalding [13]. Earlier, Stollery and El-Ehwany [14] obtained a relationship that was useful for correlating slot-injection data at locations significantly downstream of the injection site.

During the past 30 years, many authors [15–19] have investigated the vane-blade interaction phenomena either theoretically or by use of a variety of experimental techniques. In general, these previous studies have principally addressed the aerodynamic interaction as it relates to flow through compressors with somewhat less attention being given to turbine flows. Dring et al. [19] have presented the results of a measurement program for which both aerodynamic and heat flux data were obtained using a large-scale rotating rig. These authors found that the presence of the rotor did have an influence on the stator vane airfoil heat flux distribution, a result that is qualitatively consistent with the results reported in this paper.

The heat flux measurements described here were obtained for turbine hardware that utilizes slot injection on the vane pressure surface. For the injection portion of this paper, one-half the stator row (180 deg) was supplied with cooling air, while the cooling slots on the remaining 180-deg sector were sealed. The vane trailing edge for both pressure and suction surfaces downstream of the injection location were instrumented with thin-film gages. For the measurements

Nomenclature

A = stator inlet area
H_o = total enthalpy
$H_W(T)$ = wall enthalpy
N_{phy} = physical rotor speed
$\dot{q}(T)$ = measured heat flux corrected for variable thermal properties of the pyrex substrate

$$(\text{Stanton No.})_{\text{INLET}} = \frac{\dot{q}(T)}{(\dot{w}_o/A)\,(H_o - H_w(T))}$$

$T = T_w + \Delta T$
T_w = initial wall temperature
ΔT = measured temperature rise of pyrex substrate
T_o = total temperature
$\dot{w}_o$ = physical weight-flow rate
V = velocity obtained from $(\dot{w}/A)$
ρ = pyrex density or gas density

Subscripts

c = coolant
∞ = local free-station condition

Table 1 Summary of experimental conditions

RUN	T_o	T_w	T_c	$N)_{PNY}$	$\theta = \frac{T_c}{T_o}$	$m = \frac{\rho_c V_c}{(\rho_\infty V_\infty)_{AT\ SLOT}}$	$\frac{T_o - T_w}{T_o - T_c}$	$\frac{\rho_c V_c}{\mu_c}$	$\dot{W}_c$	$\dot{w}_o]$ VANE INLET	$\dot{w}_c/\dot{w}_o$
#	°R	°R	°R	rpm	-	-	-	1/ft	#/sec	#/sec	%
44,45,46	1000	530	530	19,800	0.53	1.1	1.0	1.5^7	0.6	22.0	2.9
47,48,49	1000	530	530	20,500	0.53	1.3	1.0	1.8^7	0.8	22.0	3.5
50,51,58,59	1000	530	-	19,100	-	-	-	-	0.0	22.0	0
53,54	1000	530	530	19,200	0.53	0.9	1.0	1.3^7	0.6	22.0	2.5
56,57,60	1000	530	770	18,200	0.77	0.8	2.0	1.6^7	0.5	22.0	2.1
61,62,63	1000	530	650	19,500	0.65	1.0	1.3	1.4^7	0.6	22.0	2.5

Table 2 Comparison of test conditions

	FULL STAGE	VANE ONLY
MEASURED REFLECTED-SHOCK PRESSURE, psia	1078	1080
CALCULATED REFLECTED-SHOCK TEMPERATURE, °R	998	1009
STATOR INLET TOTAL TEMPERATURE, °R	998	1009
MEASURED STATOR INLET TOTAL TEMPERATURE, °R	–	1013
MEASURED STATOR TOTAL PRESSURE, psia	99.3	97.8
CYLINDER IN CROSS FLOW STAGNATION PT.HT.TR. AHEAD OF STATOR, BTU/ft² sec	46.7	44.9
MEASURED AVG. ΔT OF STAGNATION PT. THIN-FILM GAGES, °R	93.0	92.8
CALCULATED AVG. WEIGHT FLOW, lb/sec	22.0	21.8

described in the second part of this paper, the rotor was replaced with a row of flow straighteners, and heat flux measurements were obtained with and without the rotor.

Experimental Apparatus

The experimental apparatus used in this work is well documented [3, 5, 6], and thus only that portion of the apparatus that is new to this work will be briefly described. A shock tube is used as a short-duration source of heated air and miniature thin-film gages are used to obtain heat flux measurements. The coolant system used to supply the stator is sketched in Fig. 1. The coolant gas total temperature, T_c, is set at a predetermined value in the reservoir. The Valcor valve is opened just prior (on the order of 50–100 ms) to the arrival of the model test-gas flow so that the coolant gas weight flow, $\dot{w}_c$, can be established. The magnitude of $\dot{w}_c$ is maintained by the flow control orifice (all flow control orifices used here are standard ASME design) located between the reservoir and the vane coolant inlet holes. Care is taken to maintain the reservoir pressure at a sufficiently high value so that when the test flow is established in the model, and thus the pressure level existing at the slot is transmitted to the feed system plenum, the pressure ratio across the orifice is sufficient to maintain a choked orifice. The weight flow of coolant gas can then be calculated from the geometry and the coolant reservoir conditions. The pressure history downstream of the orifice is measured in the manifold feeding the vane inlet holes. Figure 2 is a photograph of the coolant manifold mated to the nozzle guide vane ring. A rubber gasket is used to provide a gas-metal interface seal between the manifold and the vanes.

In order to obtain the stator-only results, the rotor was replaced with 41 flow straighteners located downstream of the stator, one straightener for each vane. The leading edge of the straightener was placed at an axial distance equal to 65 percent of an axial vane chord from the exit plane of the vane. The flow straighteners were kept thin, and they were placed sufficiently far downstream that the likelihood of radial displacement should have been small. A detailed calculation of the flow field was not performed, but it would be appropriate to perform such a calculation.

The measurement program described here utilized the instrumented vane (with coolant slot plugged), rotor, and shroud described in [6], two additional vanes instrumented in the trailing edge region, and the flow straighteners described above. The slot of the instrumented vane used in [6] was altered as follows. In [6], the pressure surface slot looked like a rearward facing step (0.012-in.). An epoxy was used to blend the step to the pressure surface contour so that a comparison could be made between downstream results with and without the step for the identical blade instrumentation. Because we did not want to destroy the trailing edge instrumentation, it was not possible to completely smooth the airfoil contour.

Experimental Conditions

Table 1 gives the experimental conditions for which heat flux measurements were performed. This table includes the following quantities: (*a*) the stator inlet total temperature, T_o, calculated from the shock-tube conditions; (*b*) the measured model wall temperature, T_w; (*c*) the turbine weight flow, $\dot{w}_o$, calculated knowing the area of the exit channel, the orifice area, the turbine work extraction, the pressure in the exit channel, and the inlet total temperature; (*d*) the measured rotor speed; (*e*) the blowing parameter, $\rho_c V_c/\rho_\infty V_\infty$) at slot, where $\rho_\infty V_\infty$ is calculated at the slot location; (*f*) the coolant weight flow, $\dot{w}_c$, calculated from the known coolant reservoir conditions and the geometry; (*g*) the coolant Reynolds number per foot; (*h*) the temperature ratio $T_o - T_w/T_o - T_c$; and (*i*) the coolant injected as a percentage of stator inlet weight flow.

Table 2 gives a comparison between the experimental conditions and measured parameters for the full-stage and vane-only results presented in this paper. This table includes the following quantities: (*a*) the stator inlet total temperature, T_o, measured using a rake of thermocouple probes and also independently calculated from the shock-tube conditions; (*b*) the measured model wall temperature, T_w; (*c*) the weight flow rate, $\dot{w}_o$; (*d*) the measured shock-tube, reflected-shock pressure; (*e*) the measured wall static pressure just ahead of the stator; and (*f*) the average stagnation-point heat flux to a cylinder in cross flow obtained just ahead of the stator.

For the vane-only experiments, the stagnation temperature, T_o, was measured across the channel just ahead of the stator. The thermocouples are constructed using 0.0005-in.-dia. or 0.001-in.-dia. butt-welded chromel-alumel wire housed in 0.050-in.-dia. stainless steel tubes. The thermocouples were found to reach a steady-state temperature within a time period consistent with the model flow-establishment period. It is shown in Table 1 that the measured total temperature is close to the calculated total temperature (1012 R versus 1009 R).

The intent of Table 2 is to illustrate that, in general, the experimental conditions achieved at the stator inlet for the vane-only measurements essentially reproduced those achieved for the full-stage measurements. The respective

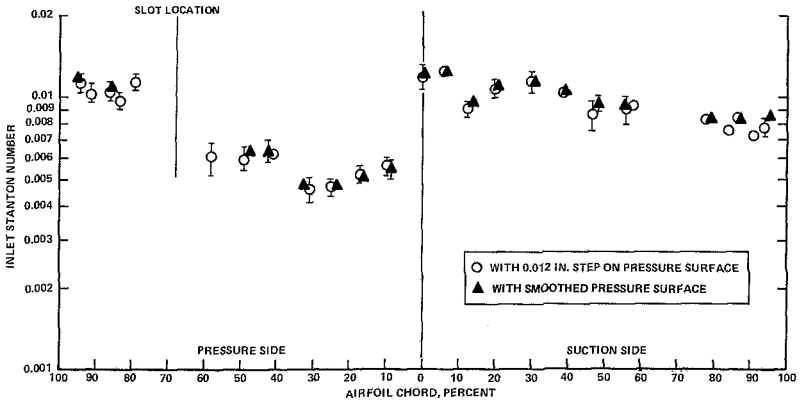

Fig. 3 Influence of pressure surface rearward facing step on vane midspan Stanton number distribution

values of the stagnation point heat transfer rates for the cylinder in crossflow are in reasonably good agreement. The final entry in this table illustrates that the average weight flow values, $\dot{w}_o$, determined for the full-stage and vane-only measurements are also in good agreement.

Experimental Results

The Stanton number used here is based on conditions at the stator inlet and was evaluated using the relationship

$$(\text{Stanton No.})_{\text{INLET}} = \frac{\dot{q}(T)}{(\dot{w}_o/A)\,(H_o - H_w(T))}$$

Most of the data that have been obtained to date at Calspan for this turbine are presented here. The standard deviation was computed [20] for the total data set at the given test condition. The experimental reproducibility was generally within ±5 percent for most locations. When these results are presented on the data plots, the symbol will indicate the mean value and the bar indicates the standard deviation. The absence of a bar means that the standard deviation was within the symbol.

Influence of Rearward Facing Step on Trailing Edge Stanton Number

The instrumented vane (shown later on the inset of Fig. 5) was modified in an attempt to change the abrupt nature of the slot into a more gradual contour without disturbing the trailing edge heat flux gages. The height of the slot is on the order of 0.00043 m (0.012 in.). The calculated turbulent boundary layer displacement thickness for these experimental conditions is 0.00004 (0.001 in.). The corresponding turbulent boundary layer thickness would be of the same order as the slot height, suggesting that even by smoothing the slot contour it might not be possible to alleviate the influence of the step. Figure 3 presents the results obtained for the vane midspan region with the unaltered slot and no coolant flow compared to those obtained with the filled and smoothed slot. The resulting distributions appear to be essentially the same suggesting that the smoothing had no influence on the results.

Influence of Coolant Weight Flow on Trailing Edge Convective Heat Flux

As illustrated in Table 1, at a fixed value of the ratio T_c/T_o = 0.53, data were obtained at three coolant weight flow values, $\dot{w}_c/\dot{w}_o$ = 2.5, 2.9, and 3.5 percent. For the purposes of a coolant discussion, a more relevant parameter with which to normalize the coolant flow would be $\rho_\infty V_\infty$) at slot. Using the two-dimensional flow field predictions presented in [4], the value of $\rho_\infty V_\infty$ at the slot location was calculated and

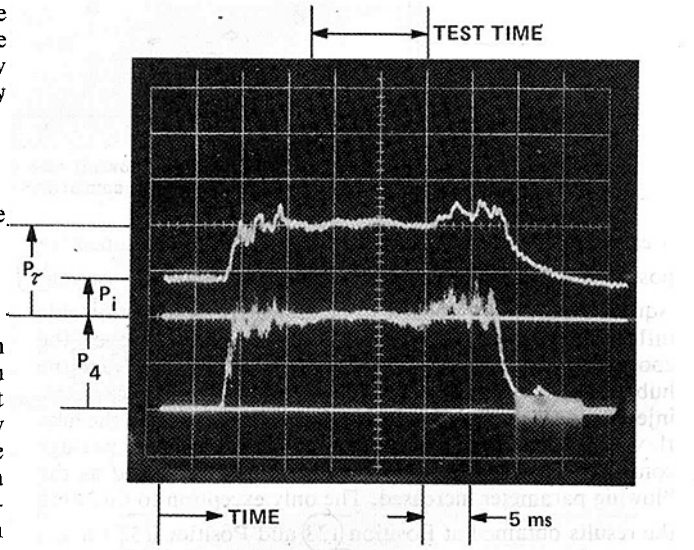

UPPER TRACE: VANE INTERNAL (COOLANT) PRESSURE JUST PRIOR TO FLOW ARRIVAL (P_i) AND VANE INTERNAL (COOLANT) PRESSURE DURING TEST TIME (P_T)

LOWER TRACE: STATIC PRESSURE AT (4) JUST UPSTREAM OF VANE (P_4)

Fig. 4 Typical internal and external pressure histories for vane during slot injection measurements

thus the blowing parameter, given by $\rho_c V_c/\rho_\infty V_\infty)_{\text{at slot}}$, corresponding to the three injection conditions becomes 0.9, 1.1, 1.3.

The operation of the coolant gas supply system was described earlier, and it was noted that the coolant flow was initiated at a time approximately 50 to 100 ms prior to arrival of the test-gas flow at the vane location. Figure 4 is an oscilloscope record illustrating the pressure histories recorded in the coolant gas feed line downstream of the orifice (see Fig. 1) and the pressure measured at location four just upstream of the stator. The pressure level indicated by P_i is the value existing prior to arrival of the test gas, and P_t is the coolant system pressure history after arrival of the test gas. The time histories of P_t and P_4 are shown to be very similar.

Figure 5 is a comparison of the spanwise distribution of the ratio of convective heat flux with injection divided by the convective heat flux without injection, $q_{\text{inj}}/q_{\text{no inj}}$, for the vane region downstream of the injection site at three values of $\dot{w}_c/\dot{w}_o$: 2.6, 2.9, and 3.4 percent. The hub endwall is in the center of the plot and the tip endwall is at the outer edges. The vane suction surface is essentially uninfluenced by the

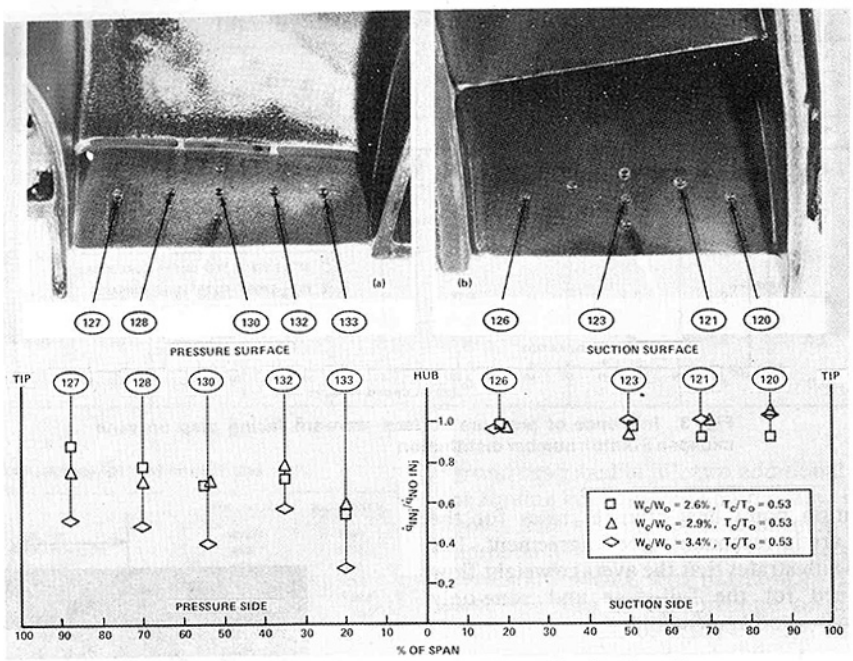

Fig. 5 Influence of blowing rate on spanwise distribution of convective heat flux downstream of slot with blowing

presence of the injected coolant. The data points obtained for positions (120) and (121) at an injection value of 2.6 percent (square symbol) are not felt to be indicative of a suction side influence. On the pressure surface, the magnitude of the coolant effect appears to depend on the location relative to the hub endwall. For a given value of the blowing parameter, injection near the hub results in a larger depression in the heat flux. This is felt to be the result of the internal cooling passage construction. The heat flux ratio generally decreased as the blowing parameter increased. The only exception to this were the results obtained at Position (133) and Position (132) for 2.6 and 2.9. However, at Position (133), the results are sufficiently close together that the difference is immaterial. It is of interest to note that the results obtained at Position (132) are out of line with the others. This is felt to be due to the gage location, immediately downstream of a slot support as can be seen on the photograph of Fig. 5(*a*), which results in the gage being partially shielded from the coolant flow.

Figure 6 is a plot of the airfoil midspan Stanton number results compared for four values of $\dot{w}_c/\dot{w}_o$; 0, 2.6, 2.9 and 3.4 percent, with the data all obtained at $T_c/T_o = 0.53$. The suction surface results downstream of the slot location are not influenced by the coolant injection. The pressure surface Stanton number is reduced with increasing blowing. The data point at 90 percent chord and $\dot{w}_c/\dot{w}_o = 3.4$ percent is somewhat below the other data. However, the location of this particular gage is near the trailing edge, and when compared with the spanwise distribution shown on Fig. 5, it is not inconsistent with other data.

Influence of Coolant Temperature on Convective Heat Flux

Figure 7 is a plot of the vane midspan Stanton number distribution at $\dot{w}_c/\dot{w}_o = 2.6$ and $T_c/T_o = 0.53$ and $T_c/T_o = 0.65$. Because the flow channel through which the heated coolant gas flows was at room temperature, it should be anticipated that when the heated coolant gas arrives at the slot, it will be cooler than when it left the reservoir. For the case of $T_c/T_o = 0.65$ ($T_c = 650$ R), it was estimated that the coolant gas would be cooler by approximately 20°F or less.

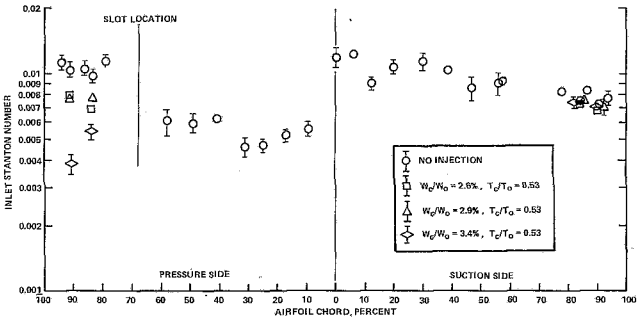

Fig. 6 Influence of slot cooling on vane midspan Stanton number distribution

The suction surface trailing edge results were uninfluenced by coolant injection. Comparing these two sets of pressure surface trailing edge data indicates that for $T_c/T_o = 0.53$ the Stanton number was reduced by approximately 32 percent, whereas for $T_c/T_o = 0.65$ the Stanton number was reduced by approximately 26 percent. For greater values of T_c, the reduction in Stanton number was correspondingly less.

Influence of Rotor on Vane Heat Transfer

Figure 8 illustrates the influence of the rotor on the distribution of Stanton number for the vane midspan. The open circles are the full-stage data for $T_w/T_o = 0.53$, the filled circles are the vane-only data obtained at essentially identical experimental conditions ahead of the stator (see Table 2) as the open circle data, and the filled square is the previous [1] vane-only data that were obtained at $T_w/T_o = 0.21$. An appropriate correction for the variable substrate thermal properties has been applied to these high-T_o data [6]. The chordwise coverage of these older measurements is not as extensive as the more recent ones.

Comparison of the open and filled circles shown on Fig. 8 for the pressure side of the vane suggests that for the $T_w/T_o = 0.53$ data, the Stanton number distribution is relatively unaffected by the rotor. A similar comparison on the suction side suggests that over the last 40 percent of the axial chord,

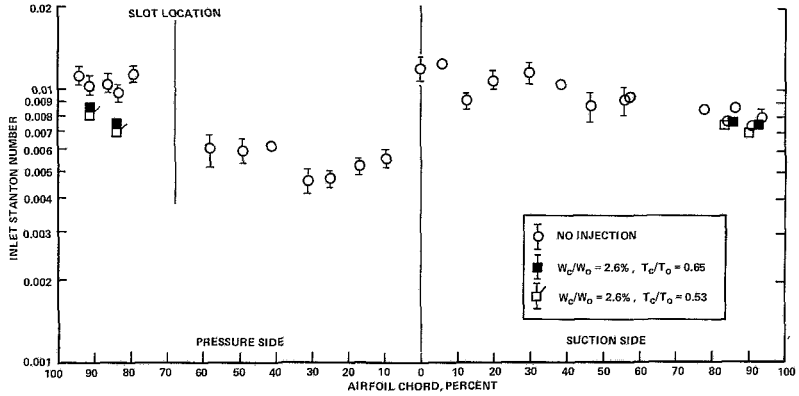

Fig. 7 Influence of coolant temperature on Stanton number for vane midspan

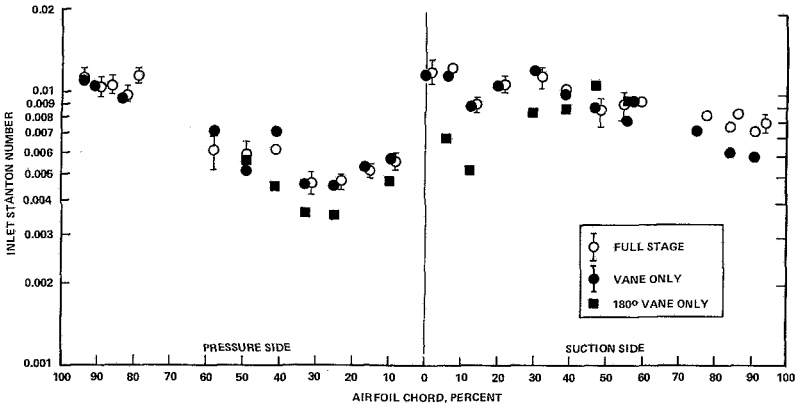

Fig. 8 Influence of rotor on distribution of Stanton number for vane midspan

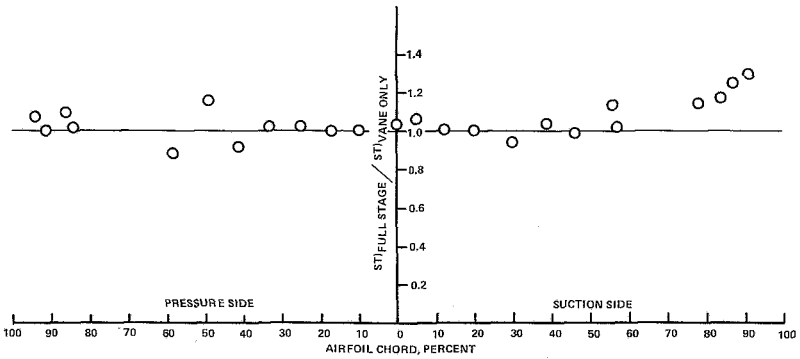

Fig. 9 Ratio of Stanton number with and without rotor for vane midspan

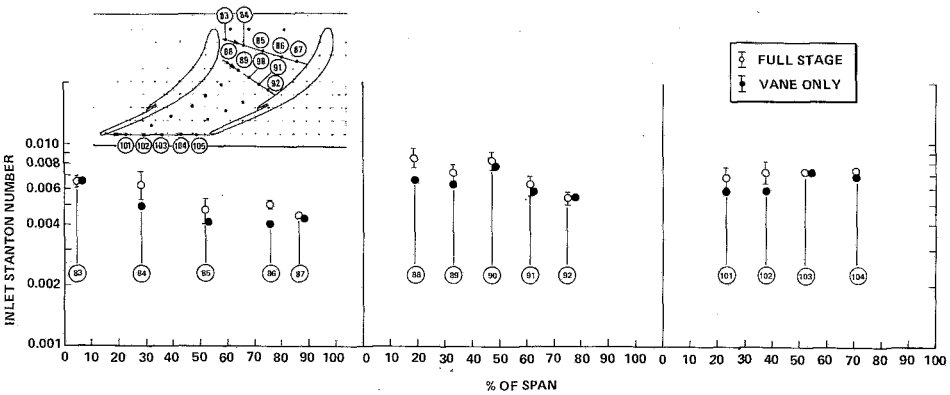

Fig. 10 Distribution of Stanton number at selected locations on vane endwall

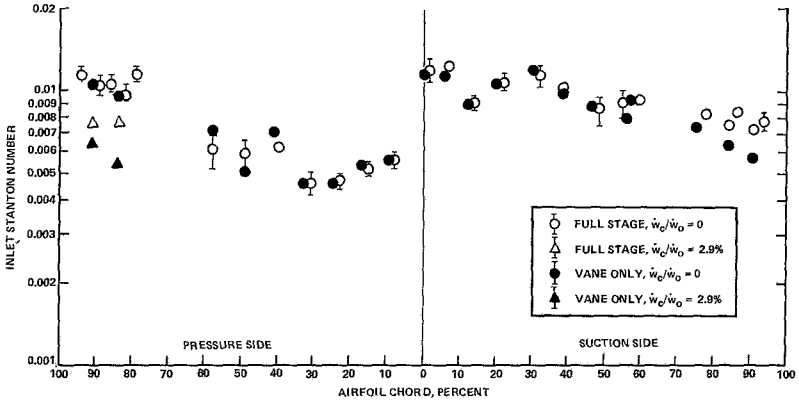

Fig. 11 Influence of rotor on vane midspan Stanton number distribution with pressure surface trailing edge cooling

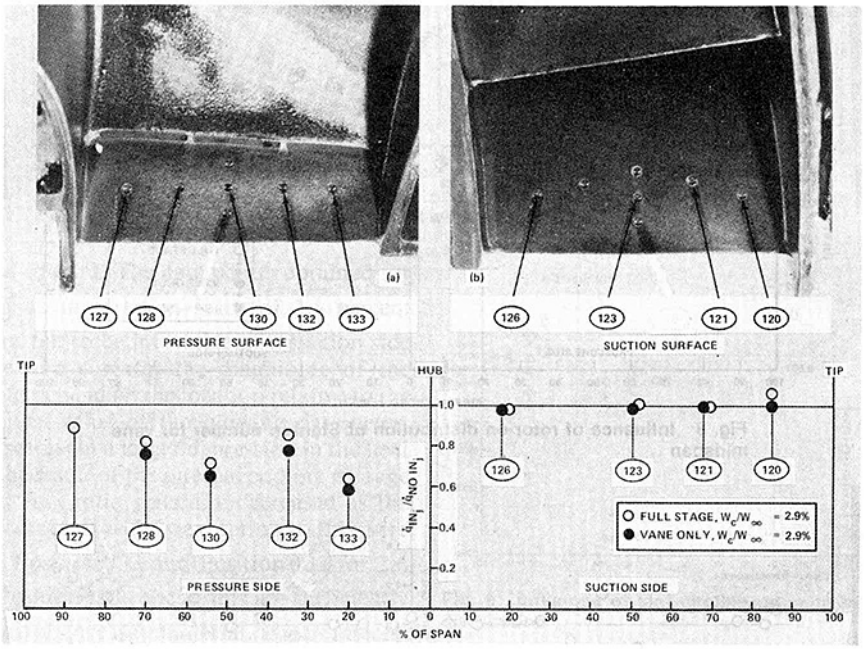

Fig. 12 Influence of rotor on spanwise distribution of convective heat flux downstream of slot with blowing

the presence of the rotor results in a 15 to 25 percent increase in the Stanton number. Between 0 and 60 percent of axial chord, the with and without rotor results are in reasonably good agreement.

The data presented in Fig. 8 have been replotted in Fig. 9 as the ratio of Stanton number)$_{\text{full stage}}$/Stanton number)$_{\text{vane-only}}$ versus chord position for the vane midspan. With the exception of three points in the vicinity of 50 percent chord on the pressure surface, this ratio is within 5 percent of 1.0 over the pressure surface midspan and also for a significant portion of the suction surface. However, beyond 60 percent chord on the suction surface, the presence of the rotor has a significant influence on the vane Stanton number distribution, causing the ratio to approach 1.25 at 91 percent chord.

The filled square data presented on Fig. 8 are the very early [1] vane-only data obtained at Calspan but at a value of $T_w/T_o = 0.21$. With the exception of suction-surface data points at 6 and 11 percent, the filled square data are reasonably consistent with the filled circle data. In order to perform this comparison, it was necessary to approximate the substrate surface temperatures using the $T_w/T_o = 0.21$ data reported in [7]. In addition, a Reynolds number correction (ratio to 0.2 power) was required, because the data reported in [1] were obtained at a lower Reynolds number than those reported here and in [7].

Figure 10 presents distributions of the Stanton number along three selected lines on the vane tip endwall with and without the rotor. The circled numbers are heat flux gage position numbers. The Stanton numbers are plotted as a function of percent of span, with 0 percent being at the suction surface and 100 percent of span being at the pressure surface as shown on the inset of Fig. 10. At several locations, the filled circles are about 10–15 percent below the open circles and the associated standard deviation, but at other locations they are in excellent agreement with the open circles. These results suggest that the rotor may have an influence on the endwall heat transfer distribution, but it isn't as well defined as the influence observed on the vane suction surface trailing edge. Additional endwall data have been obtained and the results of further analysis will be described at a later date.

Earlier in this paper, measurements were described that were obtained with cooling air being expelled from the vane pressure surface trailing edge slots. As part of the full-stage/vane-only measurements, the injection measurements were repeated. Figure 11 presents the Stanton number distributions obtained using pressure-surface, trailing-edge cooling, both with and without a rotating component. On the

vane suction surface, the results are consistent with the previously discussed Fig. 6. Figure 12 is a plot of the ratio $\dot{q}_{INJ}/\dot{q}_{NO\ INJ}$ as a function of percent span for a location downstream of the slot. The inset photographs and the circled position numbers provide a reference for the measurement locations relative to the slot. The values of $\dot{q}$ used to form the plotted ratios are those associated with either the vane-only or with the full-stage measurements. The values shown for the suction surface again indicate that blowing does not influence that surface. The pressure surface values suggest that without the rotor, blowing at the same rate provides a slightly greater depression in the convection heat flux than was observed with the rotor present. In the absence of injection, the rotor had no affect on the pressure surface results. With injection, the flow field changes and thus the conditions for the rotor-stator interaction change.

Conclusions

Full-stage turbine hardware (Garrett TFE 731-2 hp turbine) has been utilized to obtain heat flux measurements with vane trailing edge cooling and with the rotor present versus being replaced with stationary flow straighteners for representative operating conditions. The reduction in heat flux was found to be dependent upon the blowing parameter and the temperature ratio, T_c/T_o. The vane suction surface heat flux was not influenced by the pressure surface injection.

The presence of the rotor is shown to have a significant influence on the vane suction surface Stanton number, increasing it by 15 to 25 percent for axial chord positions beyond 60 percent. The corresponding pressure surface distribution in the absence of cooling was found to be essentially unafffected by the rotor presence.

Acknowledgments

This work was supported by the U.S. Air Force, Wright Aeronautical Laboratories, Aero-Propulsion Laboratory, Air Force Systems Command, Wright-Patterson AFB, Ohio, and the Naval Air Propulsion Center, Trenton, New Jersey, under Contract No. F33615-81-C-2017.

The author would also like to thank T.C. Booth and D. Winstanley of the Garrett Turbine Engine Company, K. Mach of WPAFB, and W. J. Rae of The State University of New York at Buffalo, for many helpful discussions during the course of this work. Success of this work would not have been possible without the dedicated efforts of J. R. Moselle, G. Lukis, M. Urso, and S. J. Sweet of Calspan.

References

1 Dunn, M. G., and Stoddard, F. J., "Application of Shock-Tube Technology to the Measurement of Heat Transfer Rate to Gas Turbine Components," 11th International Symposium on Shock Tubes and Waves, July 1977.

2 Dunn, M. G., and Stoddard, F. J., "Measurement of Heat Transfer Rate to a Gas Turbine Stator," ASME Paper No. 78-GT-119, ASME JOURNAL OF ENGINEERING FOR POWER, Vol. 101, No. 2, Apr. 1979.

3 Dunn, M. G., and Hause, A., "Measurement of Heat Flux and Pressure in a Turbine Stage," ASME Paper No. 81-GT-88, ASME JOURNAL OF ENGINEERING FOR POWER, Vol. 104, No. 1, Jan. 1982.

4 Winstanley, D. K., Booth, T. C., and Dunn, M. G., "The Predictability of Turbine Vane Convection Heat Transfer," Paper No. AIAA-81-1435, presented at the AIAA/SAE/ASME 17th Joint Propulsion Conference, July 27-30, 1981, Colorado Springs, Colo.

5 Dunn, M. G., and Holt, J. L., "Turbine Stage Heat Flux Measurements," Paper No. 82-1289, AIAA/ASME 18th Joint Propulsion Conference, 21-23 June 1982, Cleveland, Ohio.

6 Dunn, M. G., Rae, W. J., and Holt, J. L., "Measurement and Analysis of Heat-Flux Data in a Turbine Stage: Part I: Description of Experimental Apparatus and Data Analysis; Part II: Discussion of Results and Comparison with Predictions," 28th International Gas Turbine Conf., Phoenix, Arizona, 27-31 March 1983.

7 Louis, J. F., "Shock Tunnel Studies of Heat Transfer and Film Cooling Effectiveness," *Proc. of the 10th International Shock Tube Symposium*, Kyoto, Japan, 1975.

8 Hatch, J. E., and Papell, S. S., "Use of a Theoretical Flow Model to Correlate Data for Film Cooling or Heating an Adiabatic Wall by Tangential Injection of Gases of Different Fluid Properties," NASA TN-D-130, Nov. 1959.

9 Papell, S. S., and Trout, A. M., "Experimental Investigation of Air Film Cooling Applied to an Adiabatic Wall by Means of an Axially Discharging Slot," NASA TN-D-9, Aug. 1959.

10 Zysin, V. A., and Zolotogorov, M. S., "Study of Film-Cooling Effectiveness of Some Gas-Turbine Stator Surfaces," *Heat Transfer—Soviet Research*, Vol. 4, No. 3, May-June 1972, pp. 6-10.

11 Louis, J. F., "Heat Transfer in Turbines," AFWAL-TR-81-2099, Oct. 1981.

12 Metzger, D. E., Carper, J. H., and Warren, J. M., "Predicted Film Cooling Near Flush Slots—Comparison with Experiment," *J. of Aircraft*, Vol. 9, No. 12, Dec. 1972, pp. 857-863.

13 Patankar, S. V., and Spalding, D. B., "A Finite-Different Procedure for Solving the Equations of the Two-Dimensional Boundary Layer," *International Journal of Heat and Mass Transfer*, Vol. 10, 1967, pp. 1389-1411.

14 Stollery, J. L., and El-Ehwany, A. A., "A Note on the Use of a Boundary Layer Model for Correlating Film-Cooling Data," *International Journal of Heat and Mass Transfer*, Vol. 8, No. 1, 1965, pp. 55-65.

15 Kemp, N. H., and Sears, W. R., "Aerodynamic Interference Between Moving Blade Rows," *J. Aero. Sci.*, Vol. 20, No. 9, Sept. 1953, pp. 585-597.

16 Kemp, N. H., and Sears, W. R., "The Unsteady Forces Due to Viscous Wakes in Turbomachine," *J. Aero. Sci.*, Vol. 22, No. 7, July 1955, pp. 478-483.

17 Giesing, J. P., "Nonlinear Interaction of Two Lifting Bodies in Arbitrary Unsteady Motion," ASME *Journal of Basic Engineering*, Sept. 1968, pp. 387-394.

18 Parker, R., "Relation Between Blade Row Spacing and Potential Flow Interaction Effects in Turbomechanics," *Proceedings of the Institute of Mechanical Engineering*, Vol. 184, Pt. 3G, No. 11, 1969-70, pp. 1-8.

19 Dring, R. P., Joslyn, H. D., Hardin, L. W., and Wagner, J. H., "Turbine Rotor-Stator Interaction," ASME JOURNAL OF ENGINEERING FOR POWER, Vol. 104, Oct. 1982, pp. 729-742.

20 Bevington, P. R., *Data Reduction and Error Analysis for the Physical Sciences*, McGraw-Hill, New York, 1969.

B. Jubran
Department of Mechanical Engineering
and Engineering Production,
University of Wales,
Institute of Science and Technology,
Cardiff, CF1 3NU England

A. Brown
Mechanical Engineering Department,
Royal Military College of Science,
Shrivenham, Swindon,
Wilts, SN6 8LA England

Film Cooling From Two Rows of Holes Inclined in the Streamwise and Spanwise Directions

This paper describes the results of an experimental investigation into the film cooling effectiveness of two rows of holes inclined in the stream and spanwise directions. The effects of hole and row spacings and combinations of inclinations are investigated in the presence of free-stream pressure gradients and turbulence for a typical range of blowing rates.

Introduction

Film cooling as a means of protecting the surface of gas turbine components exposed to high-temperature gases has been recognized for the last three decades. During this period, a vast amount of information about the process has been generated, much of which has direct application to gas turbine blades. Frequently, the injection of coolant through multiple rows of holes is used to protect blade surfaces.

In the recent past, the attention of some researchers has been directed to discrete hole film cooling leading to single row and multiple row cooling. Goldstein et al. [1] investigated the effect of angled injection through a discrete hole angled at 90 and 35 deg to the free-stream flow direction. Film cooling from a circular hole with lateral inclination of 15 and 35 deg to the free-stream flow direction was studied by Goldstein et al. [2], and Hartsel [3] revealed the aerodynamic penalties of lateral angled injection on both suction and pressure surfaces of aerofoils.

Film cooling through a row of inclined holes spaced at various pitch to diameter ratios was investigated by Liess and Carnell [4], Liess [5], Bergeles et al. [6, 7], and Brown and Saluja [8]. The general conclusions were that the maximum film cooling effectiveness in the vicinity of the holes is achieved with a blowing rate of about 0.5, above which jets lift off allowing the free stream to flow under the injectant and reduce the cooling. Further from the holes, the film cooling tends to increase with increasing blowing rate, where the jets reattach to the surface. The laterally averaged film cooling effectiveness increases with reduced pitch to diameter ratio, but the same is not always true for local effectiveness values, especially on the centerline downstream from a hole. Kruse [9] showed that a double row of holes provided better cooling than a single row, and in a study of multiple rows of film cooling holes, Le Brocq et al. [10] concluded that a staggered pattern of holes gave superior cooling than holes in line. Bergeles et al. [6, 7], Jabbari et al. [11], and Afejuku et al. [12] experimented on two staggered rows of holes with injection angles of 35, 30, and 90 deg, respectively.

Very limited work has been carried out on the influence of free-stream turbulence and velocity gradients on film cooling. Launder and York [13] reported a drop in film cooling effectiveness due to increased free-stream turbulence intensity in the presence of a favorable pressure gradient. Brown and Saluja [8] showed for a row of holes that higher free-stream turbulence intensity lowers the centerline effectiveness for locations within 15 hole dia from the hole for blowing rates less than 1.25. The laterally averaged effectiveness was lowered for all blowing rates at locations within 5 hole dia of the hole, whereas at 15-dia distance, it was lowered for blowing rates less than 0.7 and increased for rates above. In general, the Brown and Saluja [8] findings were in agreement with those of Brown and Minty [14] for injection from a single slot of aspect ratio 2.0 in adverse, zero, and favorable pressure gradients and Launder and York [13] mentioned above. Kadotani and Goldstein [15] studied the effect of free-stream turbulence, both intensity and scale on a turbulent jet. They concluded that the free-stream intensity and scale affected a number of parameters: boundary-layer thickness; mixing between the free-stream and the injected flow that increases with increasing intensity and scale; shape of the injected flow due to vortex formation (also see Bergeles et al. [6, 7]; and the height of penetration of the injected flow. The effect of free-stream velocity gradients on discrete hole film cooling has been investigated by Launder et al. [16], Launder and York [13], Nicolas and LeMeur [17], Liess [5], Brown and Minty [14], and Brown and Saluja [8], but at first glance no consistency of view emerges; however, more will be spoken of this later.

In this paper, the effect of coolant injection through two staggered rows of holes covering a range of combination of injection angles, row spacing, and pitch to diameter ratios on adiabatic film cooling is described. A brief look at the effect of free-stream turbulence and velocity gradient is discussed.

Experimental Rig and Experimentation

The experimental investigation was carried out in a low-

Contributed by the Gas Turbine Division of THE AMERICAN SOCIETY OF MECHANICAL ENGINEERS and presented at the 29th International Gas Turbine Conference and Exhibit, Amsterdam, The Netherlands, June 4-7, 1984. Manuscript received at ASME Headquarters February 6, 1984. Paper No. 84-GT-286.

speed recirculatory wind tunnel that provided a uniform free stream at controlled velocity up to 15 m/s and temperature up to 60°C. Cold air was injected through the base of the working section. Temperature measurements were made on the base of the working section downstream of the cold air injection tubes in the streamwise and lateral directions, and velocity and turbulence measurements were made in the exit regions of the tubes and in the boundary layers, jets, and free stream. Cholesteric liquid crystals were applied to the working surface for temperature-flow visualization as a backup to the thermocouple temperature measurements. The injection configurations investigated were two symmetrically staggered rows of holes of constant hole diameter equal to 19.4 mm spaced either 5 or 10 hole dia apart in the streamwise direction; the pitch to diameter ratio in either row of holes was 3 or 5.4; and the angles of injection were either 30 deg or 90 deg to the streamwise direction and 90 deg or 45 deg to the lateral direction. A summary of the injection configurations is given in Table 1, and a sketch of the test plate is given in Fig. 1. The effects of free-stream turbulence intensity and velocity gradient on film cooling were also considered, the values of turbulence intensity were 0.03 and 0.14 and velocity gradient factors were 0 and 1.11×10^{-6}.

In the absence of cold injection, the free-stream velocity at the first row of holes was 10 m/s throughout the measurements described in this article, giving a value of 2.55×10^5 for the free-stream Reynolds number at the first row of holes. The ratio of free-stream displacement thickness to hole diameter for the first row of holes was 0.077 and the length to diameter ratio of the air injection tubes was 14.74 for the case of 30 deg inclination. During film cooling measurements, the temperature of the free stream was maintained about 30°C above the temperature of the injected coolant, and the ratio of coolant to free-stream density, ρ_c/ρ_∞, was about 1.1. The velocity ratio, U_c/U_∞, was variable up to a value of 1.2 and so the blowing rate, $M = \rho_c U_c/\rho_\infty U_\infty$, was variable up to 1.35. The corresponding upper limit for the momentum flux ratio, $I = \rho_c U_c^2/\rho_\infty U_\infty^2$, was about 1.6. The major portion of work described in this article was for zero free-stream velocity gradient and a turbulence intensity of about 0.03.

Experimental Results

Throughout the measurements made to establish the data presented in this article, care was taken to note possible sources of error and an error analysis based on the method of Kline and McClintock [18] was carried out. The error analysis indicated a ± 7 percent uncertainty in film cooling measurements. For a single hot-wire constant temperature anemometer, Riberio and Whitelaw [19] found that velocity and turbulence intensity measurements are accurate within 1 and 8 percent, respectively, provided the flow is essentially one dimensional. Larger uncertainties are to be expected in the presence of reverse flow and vortices.

Local film cooling effectiveness was determined for seven blowing rates from 0.2 to 1.3 at six lateral and for many streamwise stations for all models listed in Table 1 for free-stream turbulence intensity of 0.03 and zero velocity gradient. The coolant flow was equally divided between both rows of holes. In addition, some meausurements were made at a free-stream turbulence intensity of 0.14 and a velocity gradient factor 1.11×10^{-6}. A substantial number of data were generated which are summarized without loss of the essential features of the measurements in the remainder of this article.

Some local effectiveness measurements for models A, B, C, and F are shown in Figs. 2, 3, 4, and 5, respectively. Corresponding velocity and turbulence intensity measurements are shown in Figs. 6, 7, 8, and 9. The effect of row spacing, hole pitch, angle of injection, turbulence intensity, and velocity gradient on film cooling effectiveness were determined and are illustrated in Figs. 10–14, respectively. Comparison with the measurements of other workers, namely, Bergeles [6, 7], Saluja [20], Jabari et al. [11] and Sasaki et al. [21], are made in Figs. 15, 16, and 17.

Table 1

Model	Streamwise Angle Row 1	Streamwise Angle Row 2	Lateral Angle Row 1	Lateral Angle Row 2	Row Spacing	Hole spacing Row 1	Hole spacing Row 2
A	30°	30°	90°	90°	10D	5.4D	5.4D
B	30°	30°	90°	90°	5D	5.4D	5.4D
C	30°	30°	90°	90°	10D	3D	3D
D	90°	30°	90°	90°	10D	3D	3D
E	30°	90°	90°	90°	10D	3D	3D
F	30°	90°	90°	45°	10D	3D	3D

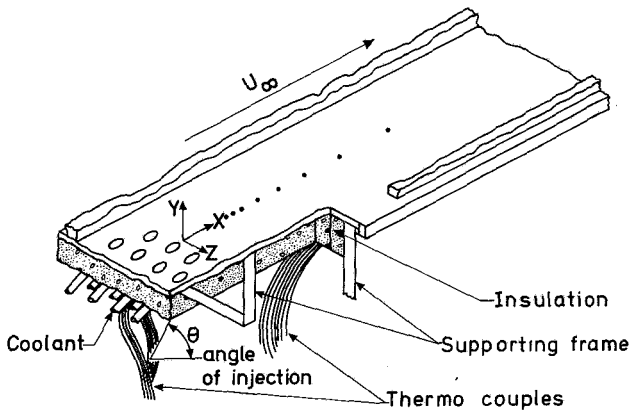

Fig. 1 Schematic of experimental apparatus

Discussion and Conclusions of the Measurements

The effect of increasing the distance between the two rows of holes is detrimental to both local and averaged film cooling

Nomenclature

D = hole diameter
I = momentum flux ($=\rho_c U_c^2/\rho_\infty \mu U_\infty^2$)
K = velocity gradient factor ($=\nu/U_\infty^2(dU_\infty/dX)$)
M = blowing rate ($=\rho_c U_c/\rho_\infty U_\infty$)
P = hole pitch
Tu = turbulent intensity ($=U'/U_\infty$)
u = local X-component of velocity
U' = turbulent velocity
U_c = injectant velocity on centerline of hole
U_∞ = free stream velocity
X = distance measured downstream from the first row of holes
X_2 = distance measured downstream from the second row of holes
Y = distance measured normal to the surface
Z = distance measured laterally across the surface
η = local effectiveness, that is, the ratio of the difference between the hot mainstream and local film temperature and the hot mainstream and cold air injection temperature
η_c = centerline effectiveness
$\bar{\eta}$ = laterally averaged effectiveness
ν = kinematic viscosity
ρ_c = coolant density
ρ_∞ = free-stream density

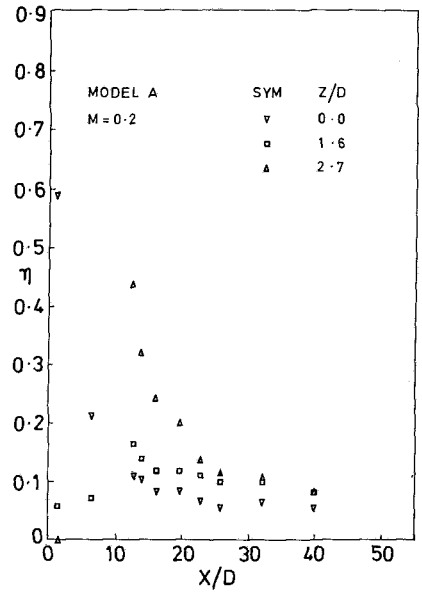

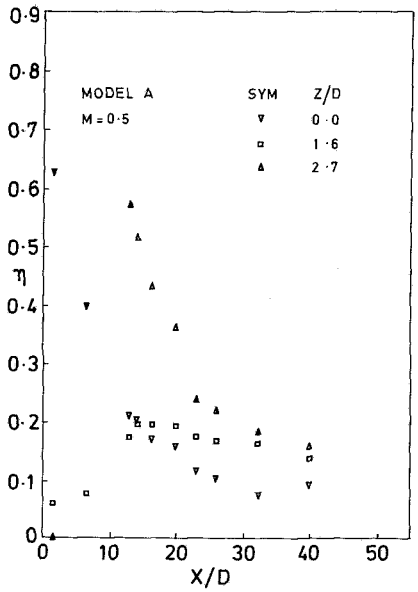

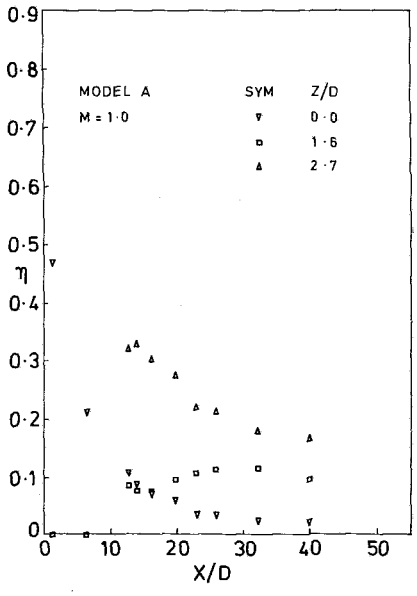

Figs. 2 Local effectiveness distribution of model A

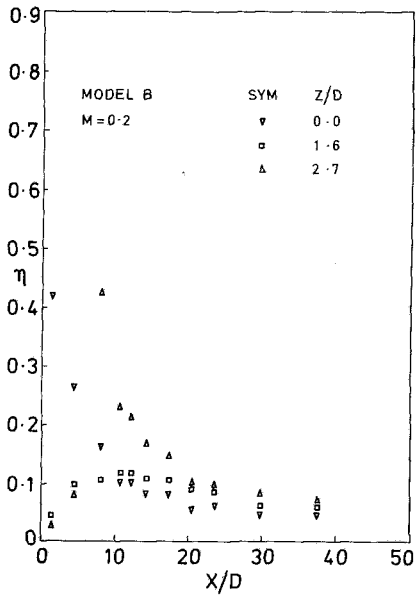

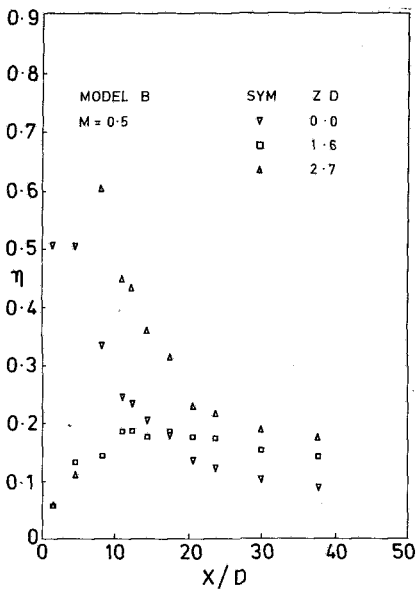

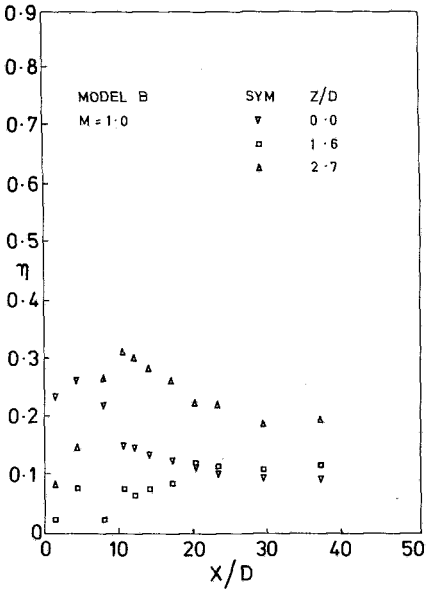

Figs. 3 Local effectiveness distribution of model B

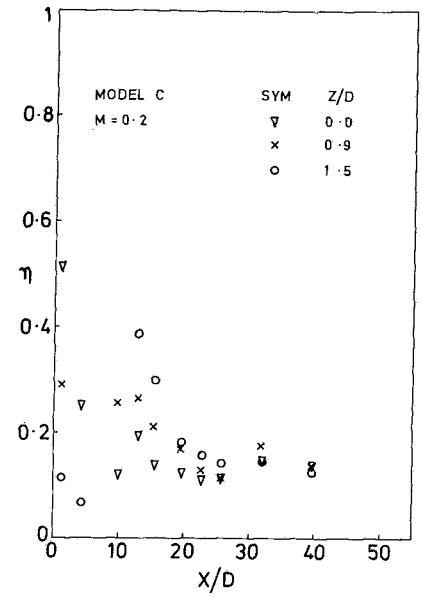

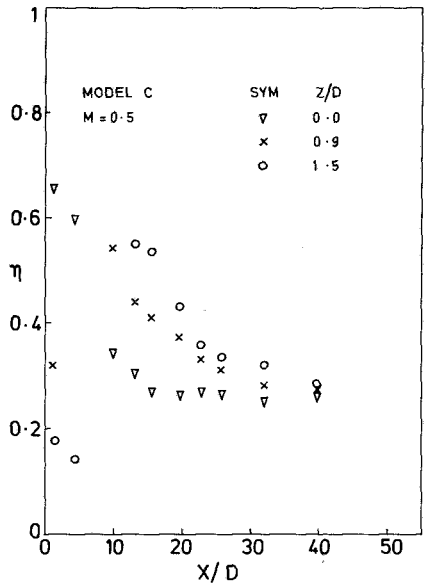

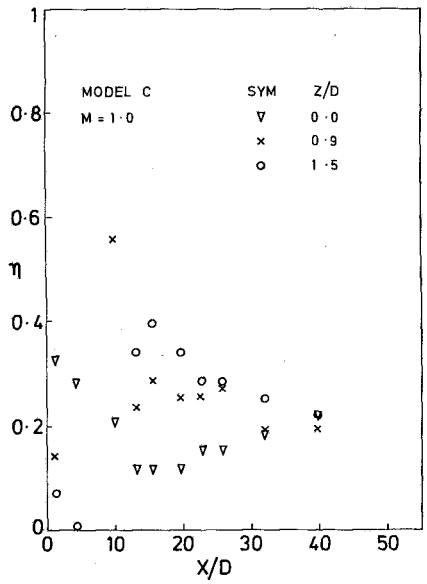

Figs. 4 Local effectiveness distribution of model C

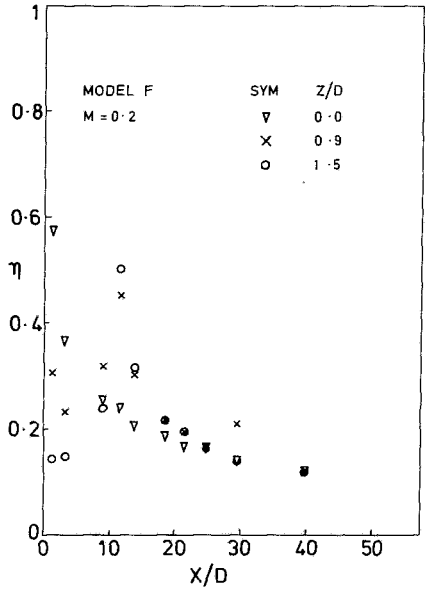

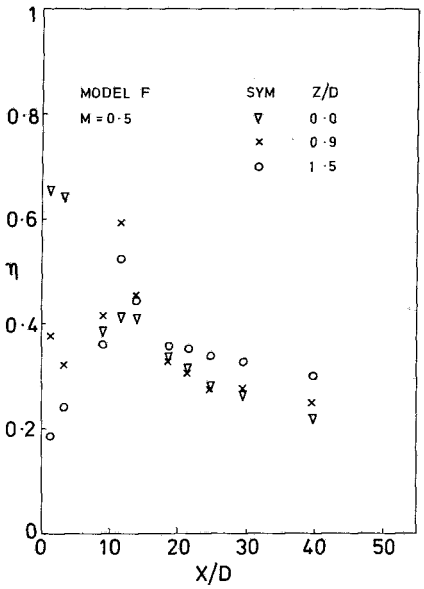

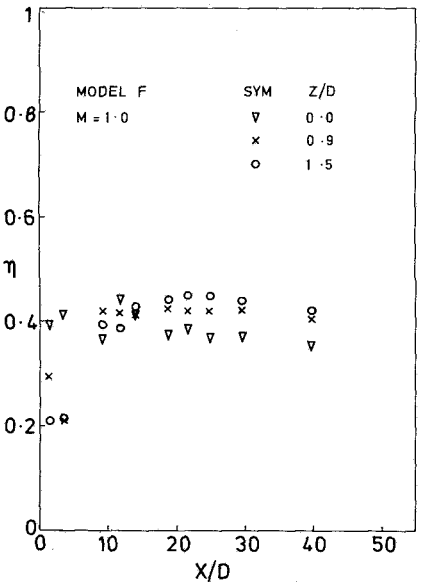

Figs. 5 Local effectiveness distribution of model F

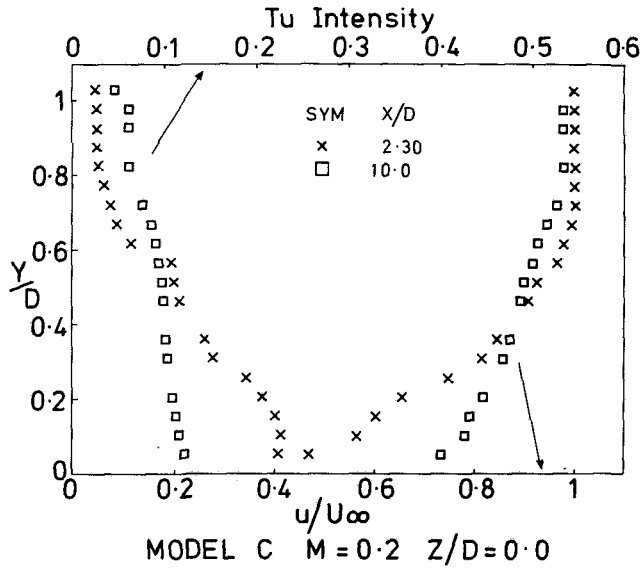

Fig. 6 Typical velocity and turbulence distributions for low blowing rate on a hole centerline

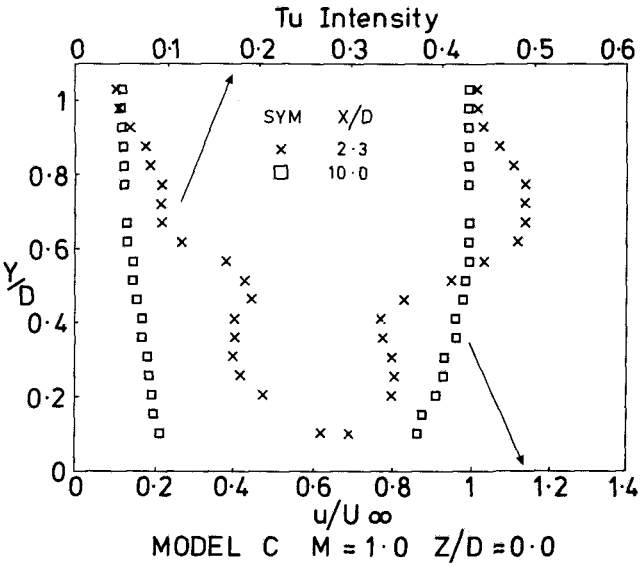

Fig. 8 Typical velocity and turbulence distributions for high blowing rate on a hole centerline

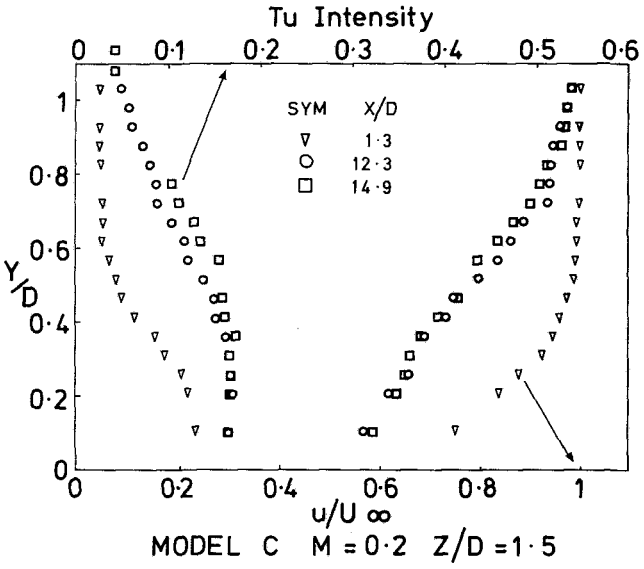

Fig. 7 Typical velocity and turbulence distributions for low blowing rate at midpitch

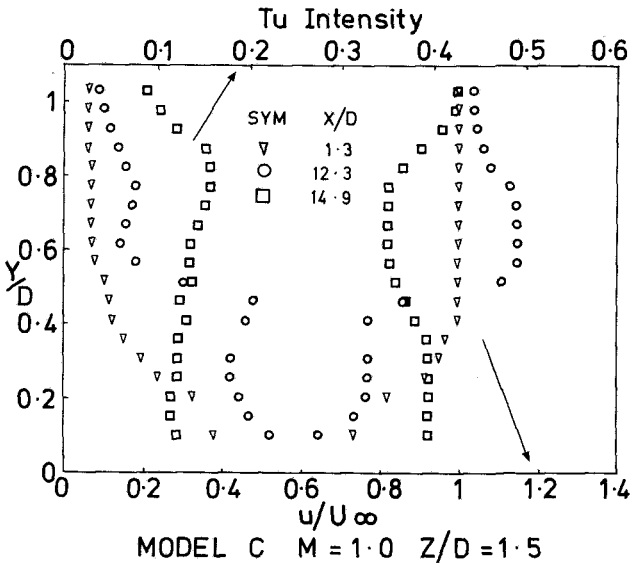

Fig. 9 Typical velocity and turbulence distributions for high blowing rate at midpitch

effectiveness downstream of the second row of holes for all blowing rates, as can be seen from Fig. 10 and by comparing the measurements in Figs. 2 and 3. The differences are most pronounced close to the second row of holes for all blowing rates and further downstream at high blowing rates in particular. Afejuku et al. [12] reported similar trends in their investigations on average film cooling effectiveness using a mass transfer measuring technique. An implication is that film cooling effectiveness downstream of the second row of holes is dependent on the state of development of the film (the merging of individual jets) from the first row. Increasing row spacing increases the development length for a film from the upstream row, which consequently is more nearly two dimensional when the second row is encountered. Increasing the blowing rate results in the requirement for a larger development length to achieve two-dimensional conditions within the upstream film, and hence the effect of row spacing on film cooling is more pronounced at high blowing rates.

The averaged effectiveness for rows of holes with pitch to diameter ratios of 5.4 and 3.0, models A and C, are illustrated in Fig. 11, from which it can be seen that for all blowing rates and all streamwise positions, $P/D = 3.0$ is superior to 5.4. The same conclusion, though to a lesser extent, can be drawn for local film cooling effectiveness as can be seen by comparing the measurements given in Figs. 2 and 4. Saluja [20] suggested that a modified blowing parameter ($= MD/P$) may be more meaningful than M as an indicator of film cooling performance. The modified blowing parameter normalizes the injectant mass flow flux. The foregoing trends are reinforced when $\bar{\eta}$ is plotted against MD/P, except at low values of MD/P, where the performance of the two P/D models are much the same (see Fig. 11). Brown and Saluja [8] found the same for a single row of holes over a range of P/D from 8.0 to 2.67.

The main purpose of the tests described in this article was to simulate some of the conditions found on a film-cooled turbine blade. The very shape of a blade necessitates that the rows of coolant holes will have different angles of injection,

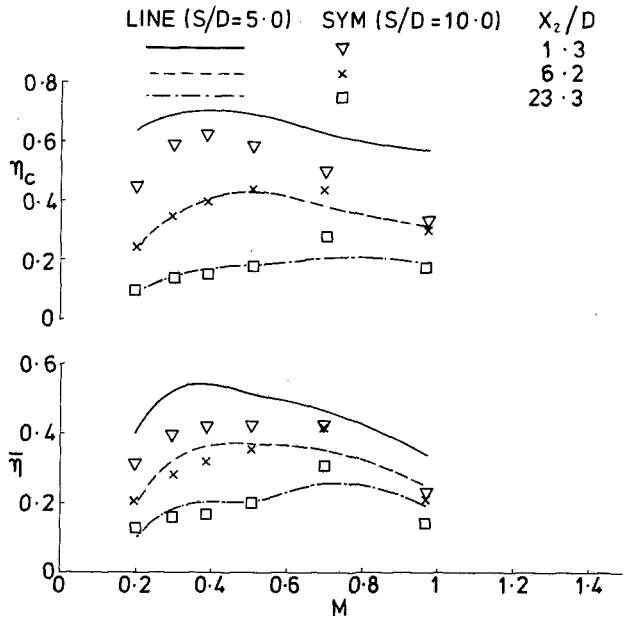

Fig. 10 The effect of row spacing on centerline and averaged effectiveness

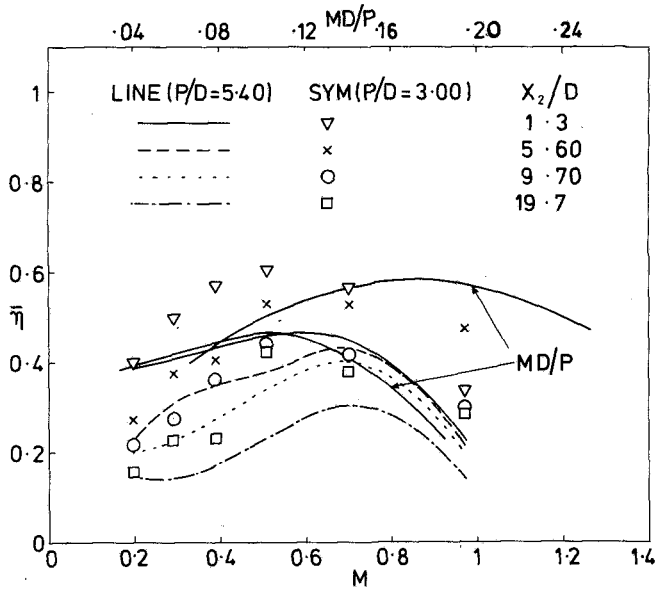

Fig. 11 The effect of pitch to diameter ratio on averaged effectiveness

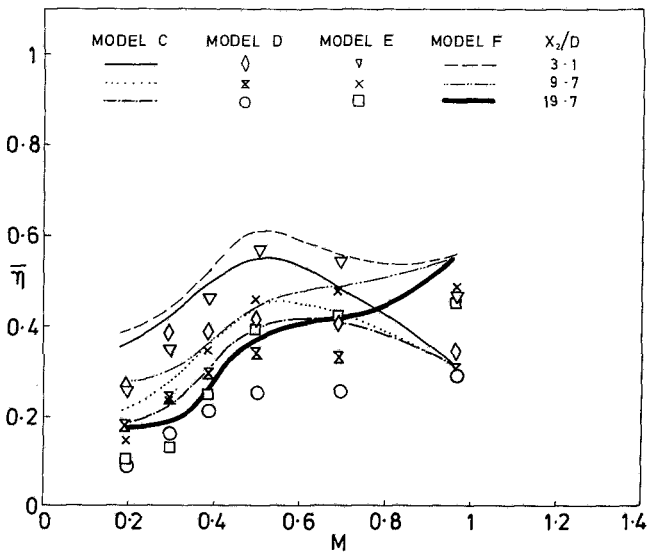

Fig. 12 Comparison of models, C, D, E, and F

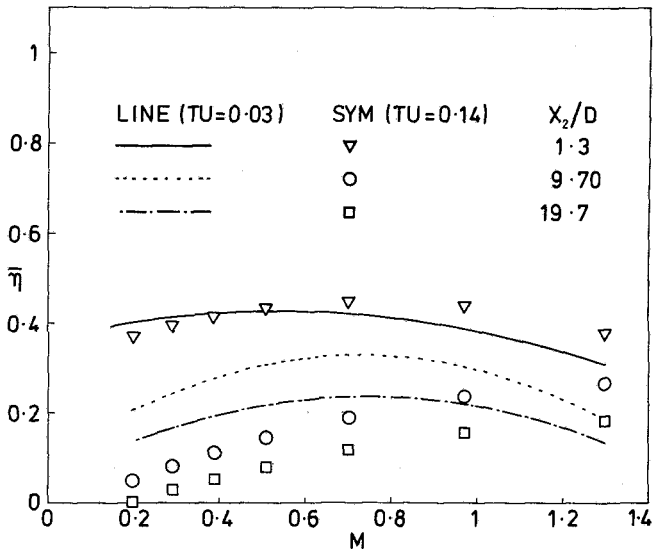

Fig. 13 Effect of turbulence intensity on averaged effectiveness

hence the ranges of angles of models C to F inclusive. Plots of averaged film cooling effectiveness for these four models are given in Fig. 12 and local values of models C and F are given in Figs. 4 and 5, respectively. For all blowing rates, model C is superior to D for averaged effectiveness downstream of the second rows of holes. A similar improvement of C over E is so for blowing rates less than about 0.7, above which E is superior to C. Model F is as good as model C for low blowing rates and superior for high blowing rates when judged in terms of averaged effectiveness downstream of the second row of holes. The comparisons between the models based on averaged effectiveness downstream of the second row of holes was confirmed from local effectiveness in the same region, see Figs. 4 and 5. The liquid crystal visualization, not reproduced in this article as they are in color, confirmed these findings. The effect of angling the injection in the lateral direction for the second row of holes is quite pronounced at higher blowing rates between the two rows of holes as well as downstream of the second row. The very narrow spread of local effectiveness at any streamwise position downstream of the second row of holes for model F and the very uniform value of $\eta \simeq 0.4$ for large blowing rates up to $X/D = 50$ are extremely attractive features of this model. However, there could well be adverse aerodynamic effects.

It is known that free-stream turbulence intensity and velocity gradient influence film cooling performance, and in view of this, some measurements have been made for $U'/U_\infty = 0.14$ with zero velocity gradient and for velocity gradient factor $K(=(\nu/U_\infty^2)dU_\infty/dx) = 1.11 \times 10^{-6}$ at the first row of holes with a turbulence intensity of 0.03 (see Figs. 13 and 14, respectively). From Fig. 13, it can be seen that the averaged effectiveness downstream of the second row of holes for model A is reduced by increased turbulence intensity for all streamwise positions and low blowing rates, an enhancement occurs close to holes for $M > 0.7$ and far downstream for $M > 1.0$. Similar results were found by Brown and Saluja [8] for a single row of holes, Brown and Saluja [22] for multiple rows of holes on an aerofoil, and by Launder and York [13] and Brown and Minty [14] for single holes. The

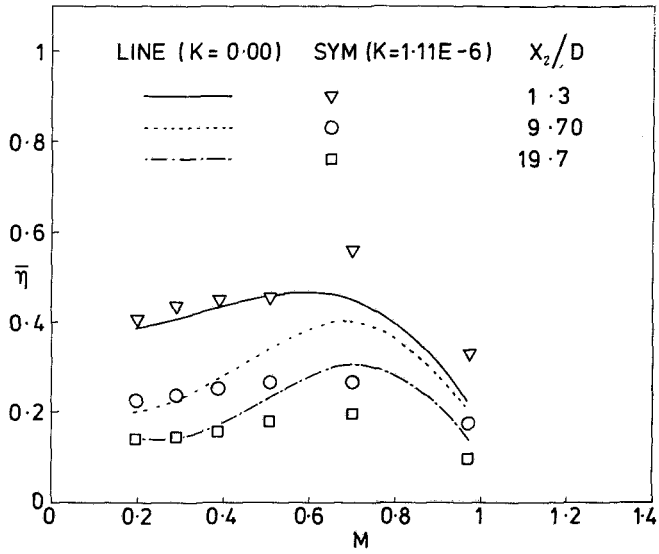

Fig. 14 Effect of velocity gradient factor on averaged effectiveness

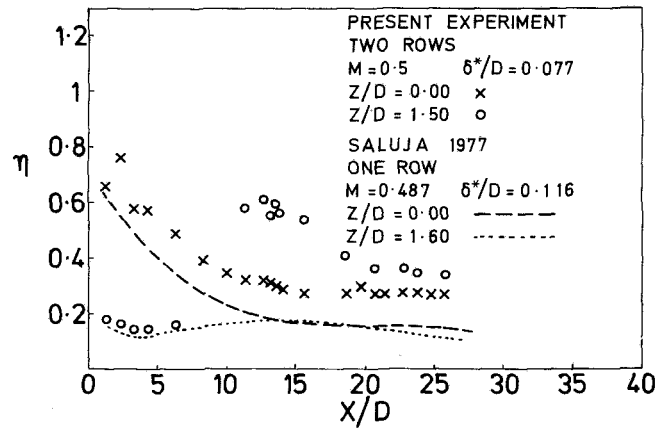

Fig. 15 Comparison of present local effectiveness measurements with those of Saluja 1977

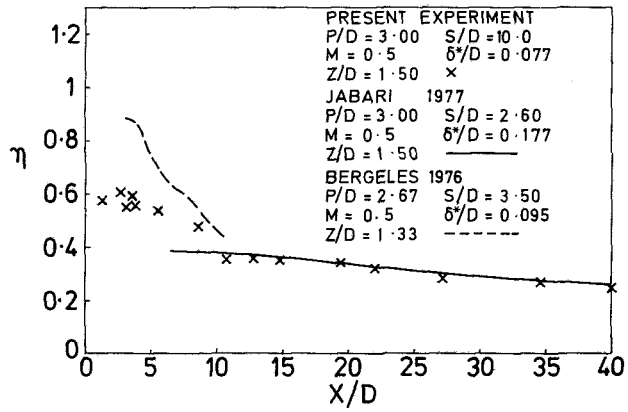

Fig. 16 Comparison of present local effectiveness measurements with those of Jabari 1977 and Bergeles 1976

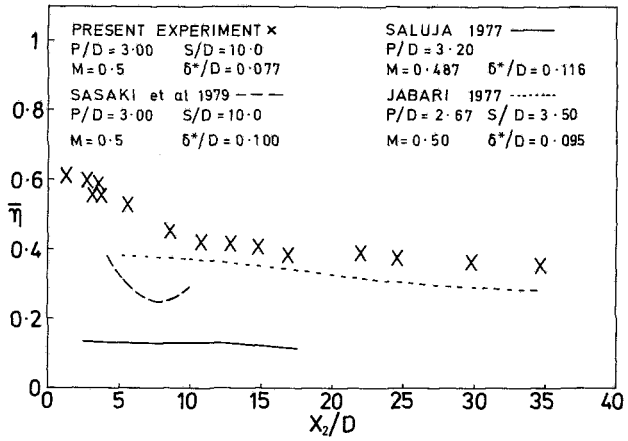

Fig. 17 Comparison of presented averaged effectiveness measurements with those of Saluja 1977, Jabari 1977, and Sasaki 1979

effect of free-stream turbulence intensity on models B, C, D, E, and F was in general agreement with that of model A. The published work on the effect of free-stream velocity gradient on film cooling indicates some disagreement on the subject. Liess [5] measured the effect of favorable velocity gradients on film cooling effectiveness downstream from a row of holes and found the effectiveness was reduced for low values of the blowing rate. Jabarri [11] had similar results to Liess. Brown and Saluja [8] found the same as Liess for a row of holes for $M < 0.7$, but for $M > 0.7$ the centerline effectiveness was superior and averaged the same for a favorable gradient compared with zero gradient. From Fig. 14, the presence of a favorable pressure gradient enhances the averaged effectiveness close to the second row of holes for all blowing rates, whereas, further downstream, there is virtually no effect for low blowing rates, but for $M > 0.4$ the averaged effectiveness is reduced. Launder and York [13] and Brown and Minty [14] found that steep streamwise accelerations substantially improve the effectiveness for discrete hole cooling systems. The disagreements on the effect of favorable velocity gradients becomes clearer if distinctions are made between centerline and averaged effectiveness and between very close proximity to the holes and further downstream. Bergeles et al. [6, 7] indicated the presence of horseshoe vortices with discrete hole injection, the strength of which to a large extent control the mixing between free stream and injectant close to the holes. The observations on effectiveness imply that an accelerating flow suppresses the vortices and hence enhances both centerline and averaged effectiveness close to the holes. Accelerating flow has more momentum than zero velocity gradient flow further downstream, so enhancing the mixing between free stream and injectant and reducing the effectiveness. The effective of turbulence are as expected.

Although the present measurements have been compared with others in the foregoing discussion, for completeness comparisons are made graphically in Figs. 15, 16, and 17 for one row and two rows of cooling holes configurations for simple pitch to diameter and displacement thickness to diameter ratios. The present measurements compare favorably with the two rows of cooling holes results of other workers and clearly show the improved cooling of two rows of holes over one row.

Acknowledgments

The authors wish to thank Mrs. Y. J. Abrams, Mrs. J. G. D. Price, and Mrs. P. Jenkins for their help in preparing this article.

References

1 Goldstein, R. J., Eckert, E. R. G., and Ramsey, J. W., "Film Cooling With Injection Through a Circular Hole," ASME JOURNAL OF ENGINEERING FOR POWER, Vol. 90, 1968, pp. 384-395.

2 Goldstein, R. J., Eckert, E. R. G., Erikson, V. L., and Ramsey, J. W.,

"Film Cooling Following Injection Through Inclined Circular Tubes," NASA CR72612, 1969.

3 Hartsel, J. E., "Prediction of Effects of Mass Transfer Cooling on the Blade Row Efficiency of Turbine Aerofoils," AIAA No. 71-11, 1972.

4 Liess, C., and Carnel, J., "Applications of Film Cooling to Gas Turbine Blades," AGARD *Conf. Proc. 73*, Paper No. 23, 1971.

5 Liess, C., "Experimental Investigation of Film Cooling With Ejection From a Row of Holes for Application to Gas Turbine Blades," ASME Paper No. 74-GT-5, 1974.

6 Bergeles, G., Gosman, A. D., and Launder, B. E., "The Near-Field Character of a Jet Discharged Normal to a Mainstream," ASME *Journal of Heat Transfer*, Vol. 98, 1976, pp. 373-378.

7 Bergeles, G., Gosman, A. D., and Launder, B. E., "The Prediction of Three-Dimensional Discrete-Hole Cooling Processes, Part 1: Lamianr Flow," ASME *Journal of Heat Transfer*, Vol. 98, 1976, pp. 379-386.

8 Brown, A., and Saluja, C. L., "Film Cooling From a Single Hole and a Row of Holes of Variable Pitch to Diameter Ratio," *Int. J. Heat Mass Transfer*, Vol. 22, 1979, pp. 525-533.

9 Kruse, H., "Film Cooling Measurements," DEVLR Report No. 352-74/9, 1974.

10 Le Brocq, P. V., Launder, B. E., and Priddin, C. H., "Discrete Hole Injection as a Means of Transpiration Cooling, An Experimental Study," *Proc. Inst. Mech. E.*, Vol. 187, 1973, pp. 149-157.

11 Jabbari, M. Y., "Film Cooling and Heat Transfer With Air Injection Through Staggered Rows of Holes Into an Accelerating Flow," Ph.D. thesis, University of Minnesota, Minneapolis, Minn. 1973.

12 Afejuku, W. O., "Superposition of Cooling Films," Ph.D. thesis, University of Nottingham, 1977.

13 Launder, B. E., and York, J., "Discrete Hole Cooling in the Presence of Freestream Turbulence and Strong Favourable Pressure Gradient," *Int. J. Heat Mass Transfer*, Vol. 17, 1974, pp. 1403-1409.

14 Brown, A., and Minty, A. G., "The Effects of Mainstream Turbulence Intensity and Pressure Gradient on Film Cooling Effectiveness for Cold Air Injection Slits of Various Aspect Ratios," ASME Paper No. 75-WA/HT-17, 1975.

15 Kadotani, K., and Goldstein, R. J., "Effects of Mainstream Variables on Jet Issuing From a Row of Inclined Round Holes," ASME JOURNAL OF ENGINEERING FOR POWER, Vol. 101, Apr. 1979.

16 Launder, R. D., Fish, R. W., and Suo, M., "The External Heat Transfer Distribution on Film-Cooled Turbine Vanes," AIAA Paper No. 72-9, 1972.

17 Nicoles, J. J., and Lemeur, A., "Curvature Effects on a Turbine Blade Cooling Film," ASME Paper No. 74-GT-156, 1974.

18 Kline, S. J., and McClintock, F. A., "Describing Uncertainties in Single-Sample Experiments," *Mechanical Engineering*, 1953, pp. 3-8.

19 Riberio, M. M., and Whitelaw, J. H., "Verification of Turbulence Models With Hot-Wire Anemometry," HTS/72/20, 1972, Imperial College, Mechanical Engineering Report.

20 Saluja, C. L., "Film Cooling From Rows of Discrete Holes," Ph.D. thesis, University of Wales Institute of Science and Technology, Cardiff, 1977.

21 Sasaki, K., Takahara, K., Kumagai, T., and Hamano, J., "Film Cooling Effectiveness for Injection From Multirows of Holes," ASME JOURNAL OF ENGINEERING FOR POWER, Jan. 1979, Vol. 101.

22 Brown, A., and Saluja, C. L., "Film Cooling From Three Rows of Holes on Adiabatic, Constant Heat Flux and Isothermal Surfaces in the Presence of Variable Free-Stream Velocity Gradients and Turbulence Intensity," ASME Paper No. 79-GT-24.

The Prediction of Flow Through Leading Edge Holes in a Film Cooled Airfoil With and Without Inserts

E. S. Tillman
Mechanical Engineering Department,
University of Bridgeport,
Bridgeport, Conn. 06601

E. O. Hartel

H. F. Jen

Heat Transfer Department,
Avco-Lycoming Division,
Stratford, Conn. 06497

A method for predicting cooling air flow rates using tests on cylindrical models of typical turbine blade leading edges has been extended to include blades with inserts and blades with reversed-angled holes. When an insert is used, the pressure loss across the insert can be determined from flow tests and added to other losses in the flow path to determine cooling flow rates. Calculated and experimentally determined flow rates are compared with good agreement. The second experiment was performed to determine internal loss coefficients for reverse-angled holes oriented so the flow makes a reverse turn to enter the holes. The reversed flow case produced significantly greater internal loss coefficients than when the same holes were oriented in the direction of flow. These results were used to predict flow from arrays of reverse- angled holes and from a cylinder containing both reverse-angled holes and nonreversed holes. In all cases, good agreement was found between predicted and measured flow rates.

Introduction

The use of film cooling for the thermal protection of high-temperature components in gas turbines has resulted in significant improvements in operating life. However, the design of film cooling systems represents one of the most difficult engineering problems in modern gas turbine technology. Before the design engineer can predict local metal temperatures, the flow rate of air from the film cooling holes must be calculated. Particularly critical regions are the leading edges of the high temperature turbine airfoils. The discharge of air from individual leading edge holes is essentially the same as flow through a thick plate orifice with both upstream and downstream cross flow. In a previous paper by Tillman and Jen [1], it was shown that the effects of crossflow at the inlet and outlet of individual holes could be expressed as loss coefficients which could be determined from simple experiments on scale models of individual cooling holes. An analytical technique for predicting flow from arrays of leading edge cooling holes was presented. Comparisons between predicted and measured cooling flow rate, with generally good agreement, were presented for cylindrical models of typical turbine blades.

The present paper extends the study of (1) to two important cases which were not presented in the earlier paper. The first case involved the prediction of cooling air flow from blades with angled holes that are oriented so the internal flow must turn more than 90 deg to enter the holes. This is referred to as reverse orientation in this paper. The second case involves the study of blades in which the cooling air is distributed along the spanwise length of the blade by an insert. The final portion of the paper presents flow visualization studies of cooling jets ejecting from arrays of holes. These pictures reflect the problem of producing a uniform distribution of cooling flow in a film cooled turbine component.

Loss Coefficients for Orifice Flow

A sketch of flow through an orifice machined in the wall of a thick wall cylinder is shown in Fig. 1. If the orifice flow is small relative to the total flow along the tube, then $V_{T1} \simeq V_{T3}$ and the static pressure is essentially constant along the tube. For ideal flow, Bernoulli's equation can be written between points 1 and 2 as

$$P_{T_1} = P_{S_1} + \frac{\rho}{2} V_{T_1}{}^2 = P_{S_2} + \frac{\rho}{2} V_j{}^2 \qquad (1)$$

Equation (1) can be solved for V_j, which is then multiplied by the orifice area at 2, A_j, to give the ideal flow rate through the orifice. However, the flow does not fill the orifice exit plane, and viscous effects cause the velocity, V_j, to deviate from the value predicted by equation (1). As shown by White [2], the traditional method of calculating orifice flow is to include these effects into a single empirically determined coefficient of discharge, C_D, defined by

$$Q = C_D A_j \sqrt{\frac{2}{\rho_j}(P_{T_1} - P_{S_2})}$$

Contributed by the Gas Turbine Division of THE AMERICAN SOCIETY OF MECHANICAL ENGINEERS and presented at the 29th International Gas Turbine Conference and Exhibit, Amsterdam, The Netherlands, June 4–7, 1984. Manuscript received at ASME Headquarters December 5, 1983. Paper No. 84-GT-4.

$$= C_D A_j \sqrt{\frac{2(P_{S_1} - P_{S_2})}{\rho_j (1 - (V_T/V_j)^2)}} \quad (2)$$

In typical pipe flow problems, the ratio $(V_T/V_j)^2$ can be replaced by the ratio of orifice area to pipe cross-sectional area. However, for this study, it was more convenient to calculate the flow rate from the pressure differential, $(P_{T1} - P_{S2})$. Experimental values for C_D were presented in [1] as functions of the orifice Reynolds number for three different orifice geometries. In all these tests, the value of V_T was essentially zero. If these values of C_D are used in equation (2) for a case where V_T is significant relative to V_j, the calculated flow will be in error, because the tube velocity, V_T, induces distortions in the flow field at the entrance of the orifice. This added effect can be expressed as an internal loss coefficient defined as

$$\delta_i = \frac{(P_{T_1} - P_{S_2})_{\text{Tube Flow}} - (P_{T_1} - P_{S_2})_{\text{Tube Flow} = 0}}{\rho_j V_j^2/2} \quad (3)$$

where the pressure differences, $(P_{T1} - P_{S2})_{\text{tube flow}}$ and $(P_{T1} - P_{S2})_{\text{tube flow} = 0}$ are measured at the same value of orifice flow. This flow can then be expressed as

$$Q = C_D' A_j \sqrt{\frac{2}{\rho_j}(P_{T_1} - P_{S_2})_{\text{Tube Flow}}}$$

$$= C_D A_j \sqrt{\frac{2}{\rho_j}(P_{T_1} - P_{S_2})_{\text{Tube Flow} = 0}} \quad (4)$$

a comparison of equation (3) and (4) shows that

$$\delta_i = \frac{1}{C_D'^2} - \frac{1}{C_D^2} \quad (5)$$

Thus the internal loss coefficient is actually a correction to the normal coefficient of discharge, C_D, which accounts for the influence of the transverse velocity, V_T, past the entrance of the orifice. It was shown in [1] that δ_i can be expressed as a function of $(V_j/V_T)^2$. Experiments on single hole models were used to develop empirical curves for each hole geometry.

It is more convenient for calculation purposes to consider δ_i as a correction to the pressure differential across the orifice, through equation (3), than as a correction to C_D. Thus if V_T and the differential pressure are known and a value of V_j can be assumed, δ_i can be determined from the corresponding empirical curve and a correction to the differential pressure can be calculated. This technique forms the basis for the iterative flow prediction program described in [1].

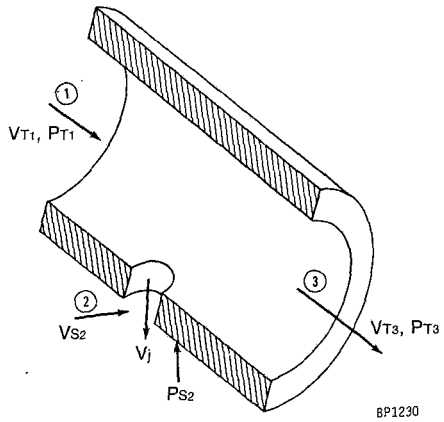

Fig. 1 Sketch of flow from test cylinder

The effect of external flow past the orifice can be handled in a similar manner to the internal flow by the use of an external loss coefficient, where δ_o is defined by

$$\delta_o = \frac{(P_{T_1} - P_{S_2})_{V_\infty} - (P_{T_1} - P_{S_2})_{V_\infty = 0}}{\rho_j V_j^2/2} \quad (6)$$

It was shown by Sasaki et al. [3] and confirmed in [1] that δ_o can be expressed as a function of the momentum ratio, K_o, where

$$K_o = \frac{\rho_j V_j^2}{\rho_\infty V_s^2} \quad (7)$$

and V_s is the local transverse velocity at the orifice exit. The correlations presented in [1] for δ_o are used in the present study, because the use of the reversed hole orientation or inserts only affects the flow conditions at the entrance of the holes.

Reverse Single-Hole Experiments

The experimental development of internal loss coefficients for the reverse orientation was performed using the same single-hole test cylinders that were described in [1]. Two cylinders were machined from aluminum, each with three test holes. Both cylinders were 10.16 cm (4.00 in.) dia by 10.16 cm (4.00 in.) long with 20.3 mm (0.80 in.) wall thickness. On each cylinder, the three test holes were located at the middle and spaced 120 deg apart around the circumference: one was drilled at 90 deg to the cylinder axis; one was drilled at 45 deg to the cylinder axis; and one was drilled at 30 deg to the cylinder axis. In one cylinder, the test holes were 10.16 mm

Nomenclature

A_{IH} = flow area of insert holes
A_j = flow area of single cooling hole
A_T = cross-sectional flow area inside cylinder
C_D = coefficient of discharge without external and internal flow effects
C_D' = coefficient of discharge based on effective pressure difference
C_p = pressure coefficient, $(P_T - P_\infty)/1/2\,\rho_\infty v_\infty^2$
d = test hole diameter
D = tube outside diameter
L = test hole length
M = blowing velocity ratio, V_j/V_∞
N = number of cooling hole rows
P_A = total pressure inside annulus
P_I = total pressure inside insert
P_p = plenum static pressure
P_s = surface static pressure at hole location
P_T = total pressure inside cylinder
P_∞ = wind tunnel static pressure
Q = volume flow rate through test hole, $Q = V_j A_j$
Q_I = volume flow rate through all insert holes
Q_{CH} = volume flow rate through all cooling holes
Re_d = Reynolds number based on hole diameter and hole flow
Re_D = Reynolds number based on outside tube diameter and external flow
Re_T = Reynolds number based on inside tube diameter and internal flow
V_j = hole velocity
V_s = surface velocity
V_T = tube axial velocity
V_∞ = wind tunnel velocity
δ_o = external additive loss coefficient
δ_i = internal loss coefficient
ρ_J = air density in coolant jet
ρ_∞ = air density in wind tunnel

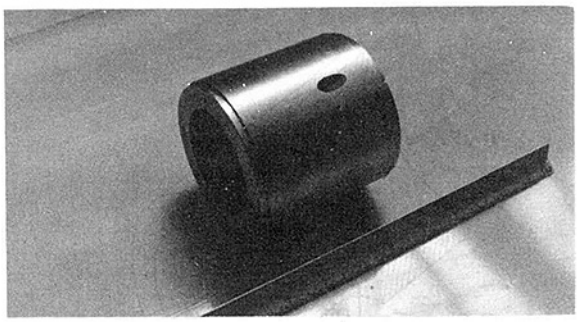

Fig. 2 Single-hole test cylinder

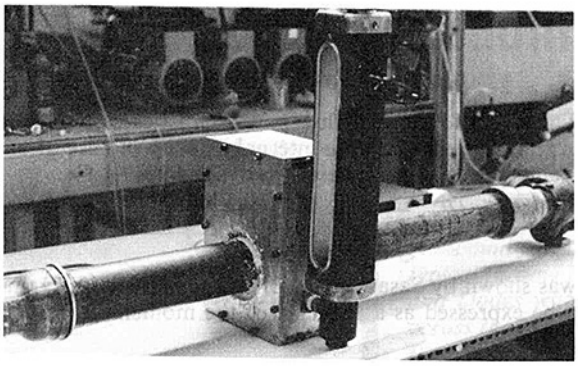

Fig. 3 Test plenum for discharge coefficient measurement

(0.40 in.) dia and in the other the test holes were 5.08 mm (0.20 in.) dia., giving hole L/d ratios of 2.0 and 4.0, respectively. Only one hole was tested at a time. The other two were blocked off with tape and wax. A photograph of one test cylinder is shown in Fig. 2.

Each cylinder was mounted in the test plenum shown in Fig. 3. A schematic diagram of the test apparatus is shown in Fig. 4. The plenum was made from 1.27cm (0.50-in.) aluminum plate with outside dimensions 11.65 cm (4.56 in.) long, 17.78 cm (7.00 in.) wide, and 25.4 cm (10.00 in.) high. The plenum served to collect the flow discharging from the test hole so the flow rate could be measured. The size was chosen so that a minimum of 10 jet diameters existed between the test hole and the top cover to minimize wall interference effects. All seams were sealed with a commercial silicone caulking compound and were secured with machine screws. The entire plenum was leak tested with soap solution prior to each test run.

Air was supplied to the test cylinder from a Model 2007H Spencer Turbine through a flexible hose to the supply pipe. This pipe was made from standard 2-1/2-in. pipe and was 30.48 cm (12 in.) long. The i.d. of the supply pipe was approximately 3 mm smaller than the i.d. of the test cylinder, so there was little disturbance to flow entering the cylinder. A perforated plate was mounted at the entrance of the supply tube to insure uniform flow. The discharge tube was similar in design to the supply tube, except that it was 45.7 cm (18 in.) long. A gate valve was used to control the amount of bypass flow. A second perforated plate was mounted just upstream of the valve for flow uniformity.

The flow rate through the hole was controlled by a hand operated valve mounted at the discharge end of a commercial rotometer, which was connected to the exit port of the plenum. The velocity in the test cylinder was measured with a standard 1/8 in. pitot tube connected to a Setra System Inc. Model No. 239 pressure transducer with a Model 300C digital read out device. The pressure differential, $P_T - P_S$, was measured by connecting the total pressure side of the pitot tube to one side of the transducer and the static pressure tap in the plenum to the other side. The actual pressure in the plenum was measured with a mercury manometer, since it was

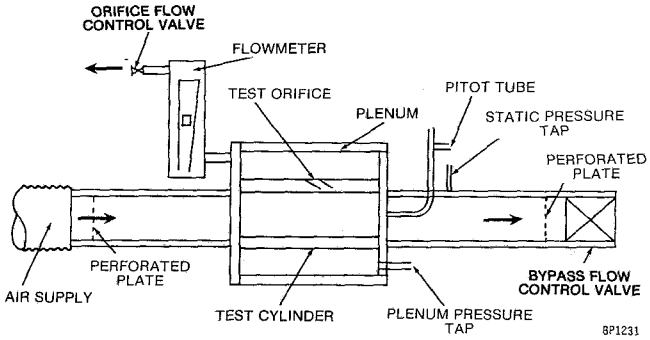

Fig. 4 Schematic diagram of test plenum

usually higher than the maximum range of the pressure transducer. The air temperature was measured with a thermocouple and a Leeds and Northrup type 932 Numatron, which was accurate to ± 1°F. The accuracy of the factory calibrated pressure transducer was checked against a precision micromonometer and found to be 0.3 percent over the range used. The flowmeters were supplied by Fischer and Porter Co. and were accurate to ± 2 percent of full scale. It was estimated that the tube velocity measurements were accurate to within 5 percent.

The results of the reverse flow tests were shown in Figs. 5 and 6 for holes with $L/d = 2$. Similar curves were obtained for holes with $L/d = 4$, showing that the effect of the aspect ratio of the hole is slight. The curves representing $\mathrm{Re}_T = 0$ are particularly interesting since they represent undisturbed discharge from the holes into the plenum. These curves are very similar to the curves shown in Fig. 6 of [1], which were obtained for discharge into the open air, thus demonstrating that the test plenum is large enough to eliminate wall interference effects. The coefficients of discharge shown in Figs. 5 and 6 were used to calculate internal loss coefficients for the 45-deg and 30-deg reverse flow cases. These results are presented for comparison. If these results are compared to the normal orientation results presented in Figs. 8 and 9 of [1], two important differences can be noted. First, in the low ranges of $(V_j/V_T)^2$, the loss coefficients for the reverse orientation are higher than the corresponding values for the normal orientation. This is due to the fact that the flow must make a reverse turn over the sharp-angled inner edge of the hole, which causes separation. The other difference is that the loss coefficients remain positive over the entire range of $(V_j/V_T)^2$ for the reversed hole orientation. Thus there is no "ram effect," as found with the normal orientation.

The effect that the amount of turning has on the internal loss coefficient can be best seen from Fig. 9. In this figure, results from [1] for the 30-deg and 45-deg holes tested at normal orientation and for the 90-deg holes are included with the results of this study. It can be seen that, particularly at high values of $(V_j/V_T)^2$, the effect of turning angle on the internal loss coefficient is slight.

Multi-Hole Cylinder Tests. A second test series was performed using multi-hole cylindrical models of a typical film cooled turbine blade leading edge. These models were described in detail in [1]. The cylinders were made from standard 5.08-cm (2.00-in.)-dia. aluminum tubing with a 9.5 mm (0.375 in.) wall thickness. The cylinders were 20.32 cm (8.0 in.) long with holes drilled over the middle 15.24-mm (6.00-in.) section. Five cylinders were used: the first two had 2.54-mm (0.10-in.)-dia holes and the other three had 5.08-mm (0.20-in.)-dia holes. All holes were arranged in a staggered array, about 2.5 dia apart. The first and third cylinders had holes oriented at 45 deg to the tube axis, while the second and fourth cylinders had holes oriented at 30 deg to the tube axis. The final cylinder combined 45-deg normal holes, 45-deg

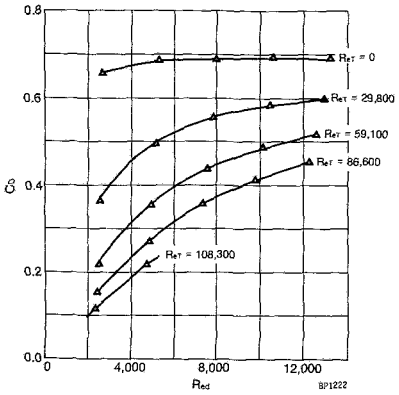

Fig. 5 Discharge coefficient at 45 deg reversed flow

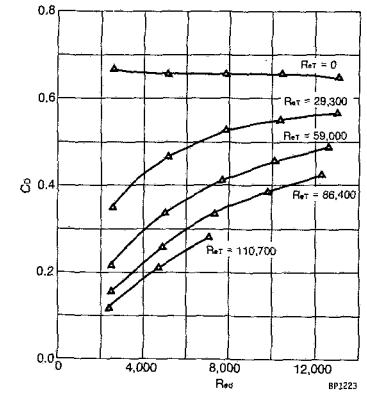

Fig. 6 Discharge coefficient at 30 deg reversed flow

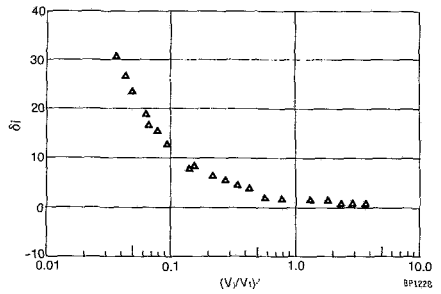

Fig. 7 Internal loss coefficient at 45 deg reversed flow

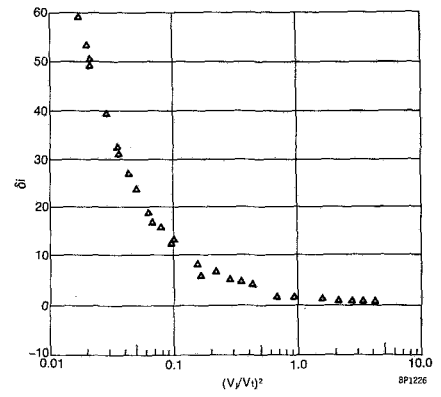

Fig. 8 Internal loss coefficient at 30 deg reversed flow

reversed holes and 90-deg holes to simulate a turbine blade where the end holes are reversed because of machining restrictions. A photograph of this composite cylinder is shown in Fig. 10.

Each cylinder was mounted on support tubes across the test section of the University of Bridgeport low-speed wind tunnel. The test section was 0.43 m (17 in.) wide by 0.30 m (12 in.) high, so blockage effects were small. The cooling air was supplied to the cylinder by the same system described previously. The supply tube was attached to the end of the cylinder so that all holes in the first four cylinders saw reverse flow. Commercial flowmeters were used to measure the total cooling flow rate. The wind tunnel velocity, measured by a built-in manometer system was set at two different values, corresponding to cylinder Reynolds numbers of 20,000 and 50,000. The total supply pressure to the test cylinder was measured relative to the wind tunnel static pressure by the pressure transducer system used for the single hole tests. The cooling flow was set at various values corresponding to average blowing ratios, M, of 0.5 to 3.0 and the pressure differential required to produce this flow was measured. These results are shown in Fig. 11. The experimental values were compared to the analytically predicted flow rates discussed in the next section.

Analytical Predictions For Multiple-Hole Cylinders. A computer program was described in [1] that predicted both the flow through individual holes in any array and the total flow. This program required input constants for the empirical curves which represented the internal and external loss coefficients as well as the coefficient of discharge. The input variables were the wind tunnel velocity and the pressure differential, $P_T - P_\infty$. This program was used to predict flow for the reverse hole orientations. It was only necessary to supply constants representing the reverse hole internal loss coefficients, since the curves of δ_o and C_D are the same regardless of hole orientation. A modification to the program was required for the composite cylinder. Constants were supplied for both normal and reversed 45-deg holes, as well as for 90-deg holes. The program then read in the appropriate constants for each new group of holes as the calculation proceeded along the cylinder.

The calculated results are presented in Fig. 11 along with the corresponding measured flow rates. In general, the agreement is good between the predicted and measured values. As was the case with the earlier studies, the poorest agreement was at the lowest flow rates. This can be explained, in part, by the fact that the flow meters are least accurate at low flows. However, this does not explain why the calculated values are always high at low values of M. One reason may be that the tube pressure is lower than the free-stream stagnation pressure at $M = 0.5$. Thus back flow may occur through the holes near the stagnation region. This idea was checked by covering the middle row of holes with tape to eliminate back flow. Although this improved agreement, it was still not as close as the agreement at higher flow rates.

Impingement Insert Experiment

In some gas turbine blades, the cooling air is distributed along the blade by an insert. If the cross-sectional area of the insert is large enough so that the axial velocity is low, then the internal static pressure is uniform and equal to the total pressure. The insert acts as a plenum so each supply hole has essentially the same entrance condition and supply pressure.

In the leading edge region, the holes in the insert are located so that the ejected coolant impinges on the inside of the blade behind the stagnation region. The air then flows around the insert to supply the cooling holes that are located away from the stagnation region. For typical gas turbine applications, the velocity in the annulus between the insert and wall is not large enough to cause significant internal losses. The approach taken in this study was that the pressure loss across the insert holes and the pressure loss across the cooling holes were independent of each other and could be considered separately.

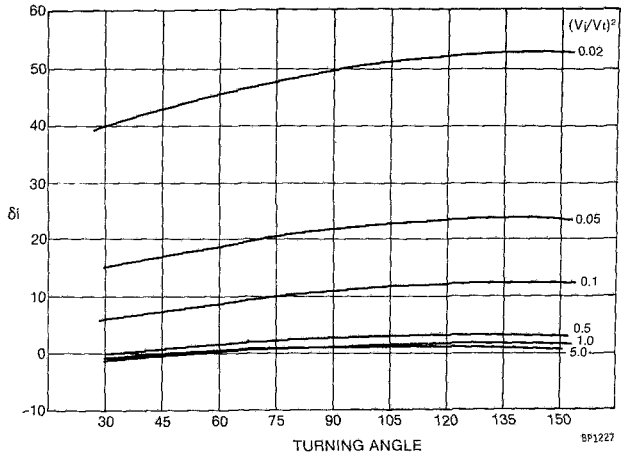

Fig. 9 Effect of turning angle on δ_i

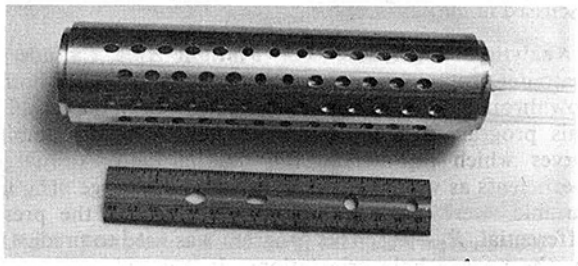

Fig. 10 Test cylinder with composite hole

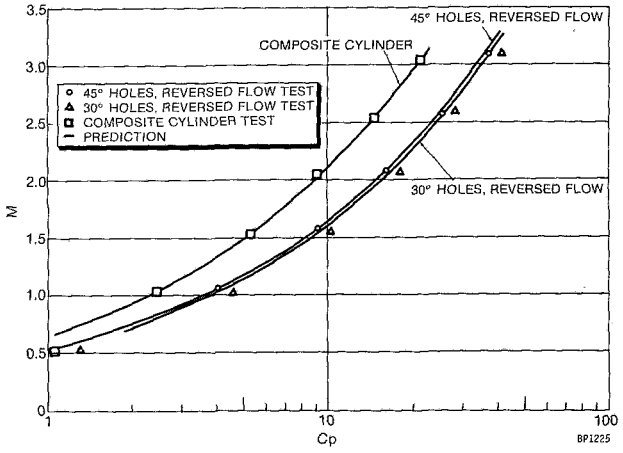

Fig. 11 Comparison of reversed flow cylinders

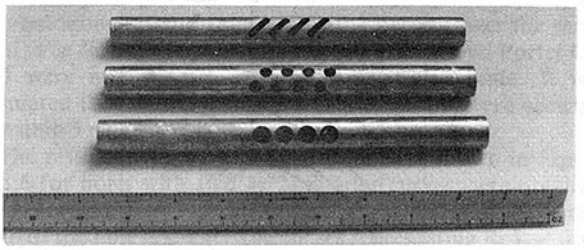

Fig. 12 Impingement inserts

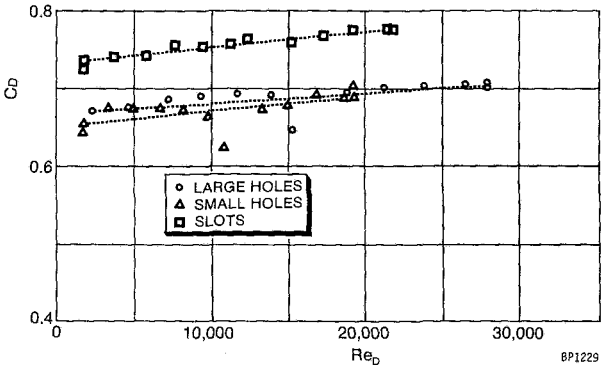

Fig. 13 Discharge coefficient of inserts

The total pressure loss across the system would be the sum of the two losses.

Three model inserts were made from 1.9-cm (0.75-in.)-dia. aluminum tubing. The inserts were designed to fit inside the multi-hole cylindrical leading edge models described above and in [1]. The inside cross-sectional area of the test cylinders was proportionately much smaller than the inside flow area of a typical turbine blade. Thus, the inserts could not supply air to all the holes along the 15.24-cm (6.00-in.) active length of the test cylinders without developing excessive velocities at the entrance of the inserts. The inserts were designed to supply air along the 5.08-cm (2.00-in.) middle section of the test cylinders and the air was supplied through both ends of the insert. Bushings were used to block off the unused length of the test cylinders. Three different inserts were made: each with a different hole pattern typical of current designs. The first had four large holes, the second had eight smaller holes, and the third had diagonal slots. The total hole area was approximately the same for each insert. A photograph of the three inserts is shown in Fig. 12.

The first tests were performed to determine the coefficient of discharge of each insert when discharging into the open air. The air supply system, previously used in the reverse flow tests, was connected through a tee fitting to both ends of an insert tube. A static pressure tap was located at the midpoint of each insert opposite the discharge holes. The pressure was measured relative to the atmosphere with the digital manometer system previously described. The coefficient of discharge is plotted versus the hole Reynolds number for the three inset designs in Fig. 13. These data points were entered into a least-squares curve fitting routine to develop a correlation curve for each insert.

The next series of tests consisted of running each of the three inserts in four multi-hole cylinders in the low-speed wind tunnel. The test cylinders were the same ones used in [1]. Cylinders 1, 2, and 3 had five rows of 5.08-mm (0.20-in.)-dia holes in a staggered array oriented at 90 deg, 45 deg, and 30 deg, respectively. The fourth cylinder had nine rows of 2.54-mm (0.10-in)-dia holes in a staggered array oriented at 90 deg. The wind tunnel velocity was adjusted to give cylinder Reynolds numbers of 20,000 and 50,000. Thus, a total of 24 different test combinations were run. The cooling air supply for each test was adjusted to give blowing ratios of between 0.5 and 3.0. All instrumentation was similar to that described above for the reverse flow tests. The only difference in test procedure was that both the pressure in the insert and the pressure in the annular space (between the insert and the test cylinder) were measured relative to the wind tunnel static pressure. The results of representative tests are presented in Fig. 14. These values were compared to the analytical predictions discussed in the next section.

Analytical Predictions for Cylinders With Impingement Inserts. An analytical method was developed for the prediction of flow through a multi-hole cylinder with an insert. The method was based on the method developed for cylinders without inserts which was described in detail in [1]. It was assumed that the coefficient of discharge for the insert, measured for free discharge, would remain unchanged when

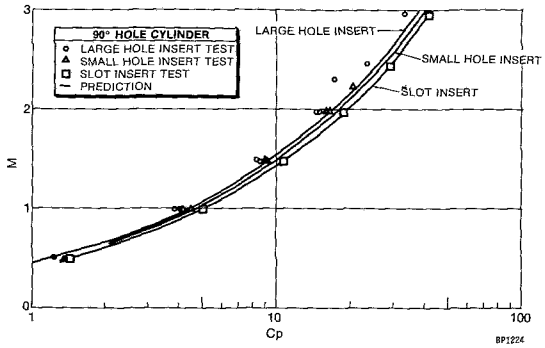

Fig. 14 Comparison of impingement insert cylinders

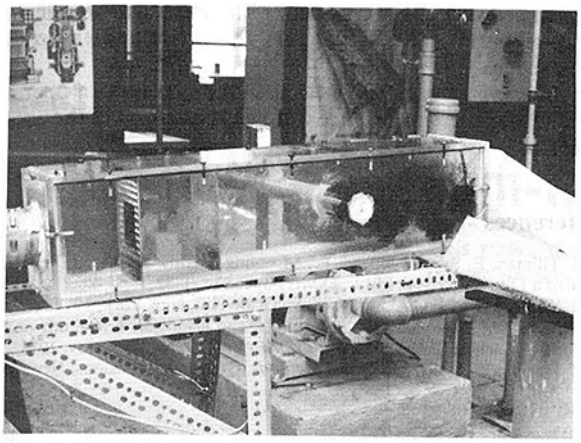

Fig. 15 Flow visualization water tunnel

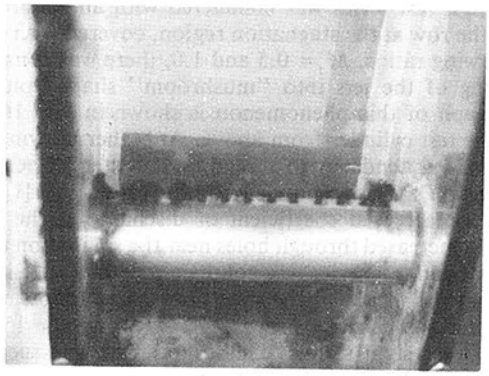

Fig. 16 Flow pattern of a single row of holes at cylinder stagnation point

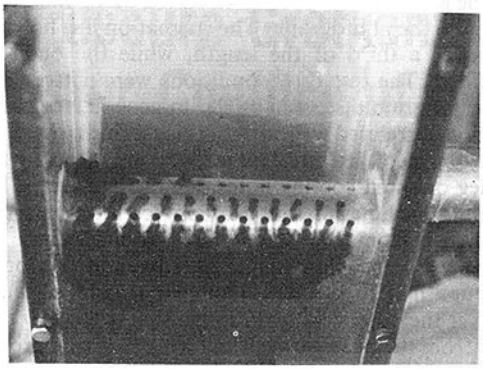

Fig. 17 Flow pattern of 90 deg cylinder. $M = .5$

the insert was run inside the cylinder. It was further assumed that the velocities inside the cylinder, i.e., in the annulus, were so low that the inside loss coefficients would be negligible. The effect that the air ejecting from the insert had on flow through the cooling holes was also assumed to be negligible. This assumption was based on the facts that few of the insert holes lined up directly with the cooling holes in the cylinder, and the major effect would be on the holes located at the stagnation region. Since these holes contribute little to the overall flow, the error induced on total calculated flow would be small. The final assumption was that the coefficients of discharge and the external loss coefficients for the cooling holes would not be influenced by the insert.

A program was written which used an assumed annular pressure, P_A, to calculate the flow through the insert holes and the cooling holes for given input values of the insert pressure, P_I, wind tunnel pressure, P_∞, and wind tunnel velocity. The flow through the insert holes can be calculated by

$$Q_I = A_{IH} C_D(R_e) \sqrt{\frac{2(P_I - P_A)}{\rho}} \tag{8}$$

while the flow through the cooling holes can be expressed as

$$Q_{CH} = fn(P_A - P_\infty, V_\infty) \tag{9}$$

In equation (9), the functional relationship is expressed in the form of the cooling hole program developed in [1] but modified by the removal of the inside loss coefficients.

Both the empirically based calculation routines, represented by equations (8) and (9), were written as subroutines in the program. The method of bisection, as presented by Hornbeck [4], was used to find the annular pressure which made Q_T and Q_{CH} equal within a specified tolerance.

The calculated results are compared to the measured values in Fig. 14. It can be seen that good agreement was found for all combinations of cylinders and inserts tested. The results imply that coupling between the insert and cooling hole flow is weak and that the method of separation is valid. The results also show that the shape of the insert cooling holes is significant only in that it effects the coefficient of discharge.

Flow Visualization Studies

Several flow visualization experiments were conducted to gain a greater understanding of flow from arrays of cooling holes. Three aspects of the problem were studied. The first was directed toward the behavior of jets at the stagnation region, the second involved the distribution of cooling flow along the cylinder, and the third was concerned with interference effects between rows.

The studies were conducted in the water flow duct shown in Fig. 15. The inside dimensions of this duct were 20.3 cm (8.00 in.) high, 17.8 cm (7.00 in.) wide and 91.4 cm (36.00 in.) long. The duct was constructed from 12.7-cm (0.5-in)-thick plexiglass. Two perforated plates were mounted upstream of the test cylinder for flow uniformity. The discharge end was covered with a plate with twelve 1.75-cm (0.69-in.)-dia. holes, uniformly spaced to prevent channeling. The duct flow was supplied directly from a surge tank connected to the laboratory supply main. The flow rate was measured at the beginning of each run by a weigh barrel and was controlled by a hand operated valve. The water flowed through the duct on a once-through basis to a drain. Because of supply pressure limitations, the maximum velocity in the duct was 0.14 m/s (0.46 ft/s). This corresponds to a cylinder Reynolds number of 7200. Although the test Reynolds number is less than the range of 20,000 to 50,000 usually encountered on turbine blade leading edge, it was within the turbulent range and was assumed adequate for these studies. The cooling flow was simulated by dye colored water, which was supplied from a pressurized supply tank through a commercial flow meter. All three test series were conducted with cylinder number 1 mounted horizontally across the flow duct.

The first test series was conducted with all cooling holes, except the row at the stagnation region, covered with tape. At low blowing ratios, $M = 0.5$ and 1.0, there was considerable spreading of the jets into "mushroom" shaped plumes. A photograph of this phenomenon is shown in Fig. 16, which views the test cylinder from above. At higher blowing ratios, there was less tendency to spread and greater jet penetration was seen. This corresponded to the results of [1], which showed a decreased coefficient of discharge as the blowing ratio was increased through holes near the stagnation region.

The second test series was conducted with all cooling holes open and the inside of the cylinder partially blocked to increase the axial velocity to a level where inside loss coefficients were significant. A photograph of one such test is shown in Fig. 17. In this photograph, the internal flow is from right to left, and the duct flow is from the top of the picture toward the bottom. The poor distribution along the length can be seen from the photograph. The stagnation line holes supply coolant over a third of the length, while the outer row is almost filled. The test flow conditions were entered into the computer program discussed in [1]. In general, the calculated distribution correlated well with the visual findings.

The problem of jet interference was also investigated for the 90 deg oriented cooling holes. As can be seen in Fig. 17, the leading edge holes discharge at a much lower rate than the holes further from the stagnation region because of the decreased pressure differential at the stagnation region. Thus, even though half of the flow from the stagnation line holes passes over the outer row, the momentum is too low to affect the flow from the outer rows. The flow prediction program of [1] was based on the assumption that interference effects are slight. The generally good agreement between experimental and calculated total flow confirmed this assumption.

Conclusions

The following conclusions can be drawn from the results presented in this paper:

1 The inside loss coefficient for angled holes in reverse flow are higher than corresponding values for the normal orientation.

2 The inside loss coefficients are relatively weak functions of turning angle.

3 The method of separation is valid for the calculation of reversed hole flow.

4 The flow through cylinders with inserts can be calculated by considering the losses across the insert and the cooling holes separately.

5 Flow visualization confirms that under certain operating conditions severe imbalance can be experienced in the cooling hole flow.

References

1 Tillman, E. S., and Jen, H. F., "Cooling Airflow Studies at the Leading Edge of a Film-Cooled Airfoil," ASME Paper 83-GT-82.

2 White, F. M., *Fluid Mechanics*, McGraw-Hill, New York, 1979.

3 Sasaki, M., Takahara, K., Sakata, K., and Kumagai, T., "Study on Film Cooling of Turbine Blades," *Bulletin JSME*, Vol. 19, No. 137, Nov. 1976.

4 Hornbeck, R. W., *Numerical Methods*, Quantum Publishers, New York.

Effects of the Condition of the Approach Boundary Layer and of Mainstream Pressure Gradients on the Heat Transfer Coefficient on Film-Cooled Surfaces

N. Hay

D. Lampard

C. L. Saluja

Department of Mechanical Engineering,
University of Nottingham,
Nottingham NG7 2RD England

This paper describes an investigation of the sensitivity of the heat transfer coefficient under the film to the state of the approach boundary layer for injection through a row of holes on a flat plate. The investigation is done for a range of blowing parameters using a heat-mass transfer analogy. Injection angles of 35 deg and 90 deg are covered. Additionally, for the same injection geometries, the effect of injection in the presence of mild adverse, mild favorable, and strong favorable mainstream pressure gradients is investigated. The results indicate that the heat transfer coefficient under the film is sensitive neither to the condition of the approach boundary layer nor to the presence of a mild adverse pressure gradient, but it is significantly lowered by a favorable pressure gradient, particularly at low blowing parameters.

1 Introduction

In the companion paper [1], the present authors described the effect of film injection on a flat plate on the heat transfer coefficient in the presence of a fully developed turbulent boundary layer with zero mainstream pressure gradient. In a practical application of film cooling to a component like a gas turbine blade, the film injection may be on a curved surface, in a region where the mainstream boundary layer is laminar or transitional and in the presence of adverse or favorable mainstream pressure gradients. For a realistic design of a film cooled component, it is necessary to know the effect of each of these parameters on the film cooling process. Only limited studies have been made of these effects.

Some data exist on the effects of these parameters on film cooling effectiveness, but data on the heat transfer coefficient are very limited. The present investigation aims to provide for flat-plate data on the effects on the heat transfer coefficient of (*a*) the condition of the approach boundary layer and (*b*) the presence of adverse and favorable pressure gradients.

2 The Effects of the Condition of the Approach Boundary Layer

Background. The authors are aware of only one previous study, namely, that by Goldstein and Yoshida [2], in which the effect of the condition of the approach boundary layer was investigated. Laminar and turbulent mainstream boundary layers were considered, and it was reported that the heat transfer coefficient under the film differed very little with the two states of the approach boundary layer.

In the experimental investigation reported in this section of this paper, the effects of the condition of the approach boundary layer on the heat transfer coefficient were covered in two tests, one with a fully turbulent boundary layer, and one with a transitional boundary layer at the point of injection, with nearly zero mainstream pressure gradient over the film-cooled region. The experimental data were obtained through a heat-mass transfer analogy using the swollen polymer technique described in the companion paper [1]. The same two injection angles (35 and 90 deg) and the same pitch-to-diameter ratio (3.0) were again used, together with the same range of injection blowing parameters (0.5 to 2.0).

Experimental Apparatus and Test Conditions. The experimental apparatus and facilities used in the present work were the same as described in the companion paper [1], with the only difference that the flat roof of the working section of the wind tunnel was replaced by a contoured roof to produce the desired condition of the approach boundary layer at the point of film injection. The profile of the roof is shown in Fig. 1.

The condition of the mainstream with the flat roof of the previous work [1] is referred to as Case (*a*) (see Fig. 1) and that with the contoured roof is referred to as Case (*b*).

Contributed by the Gas Turbine Division of THE AMERICAN SOCIETY OF MECHANICAL ENGINEERS and presented at the 29th International Gas Turbine Conference and Exhibit, Amsterdam, The Netherlands, June 4-7, 1984. Manuscript received at ASME Headquarters December 27, 1983. Paper No. 84-GT-47.

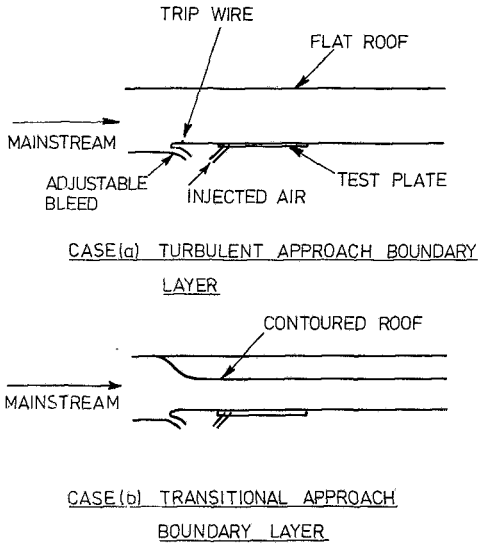

Fig. 1 Profiles of contours – condition of the approach boundary layer study

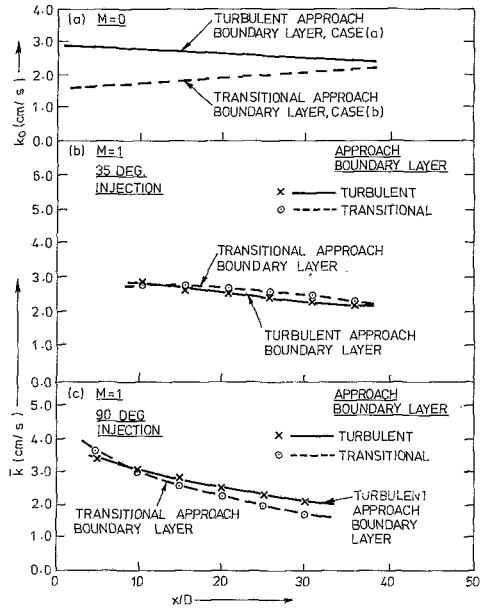

Fig. 2 Effect of the approach boundary layer on the mass transfer coefficient with no injection and on the laterally averaged mass transfer coefficient under a film

In both cases, the mainstream velocity was maintained nominally at 25 m/s at the point of injection. To establish the condition of the approach mainstream boundary layer, velocity profiles were obtained on a dummy test plate which had no film cooling holes. The measurements were made at the centerline of the floor.

The condition of the boundary layer in Cases (*a*) and (*b*) is summarized below.

Case (*a*). The measured velocity profiles were found to resemble closely the 1/7th power law turbulent boundary layer. The ratio of the boundary layer displacement thickness to injection hole diameter, δ^*/D, was 0.63 at the point of injection. The acceleration parameter, V $[=(\nu/U_m^2)(dU_m/dx)]$, was nominally zero, i.e., the flow was with zero pressure gradient.

Case (*b*). Upstream of the point of injection, the contoured roof provided strong acceleration. In this region, and further downstream, the boundary layer was transitional. At the point of injection, the ratio δ^*/D was 0.16 and over the film cooled area, V was again nominally zero so that the flow was as in Case (*a*) with zero pressure gradient.

Results and Discussion. The variation of the mass transfer coefficient with no injection, k_o, is shown in Fig. 2(*a*) for Cases (*a*) and (*b*). The variation for Case (*a*) has been shown, [1], to agree closely with that inferred from a heat transfer correlation for a turbulent boundary layer under zero pressure gradient conditions.

For Case (*b*), k_o increases in the streamwise direction, as might be expected under a transitional boundary layer, and the level is considerably lower than for Case (*a*).

Comparison of laterally averaged mass transfer coefficients, $\bar{k}$, for Cases (*a*) and (*b*) are shown in Figs. 2(*b*) and (*c*) for both injection angles for a blowing parameter of nearly unity. The results for turbulent and transitional approach boundary layers are seen to be in close agreement. This is typical of results over the full range of blowing parameters used, agreement being within 15 percent throughout, and the results showing no trend dependent upon the approach boundary layer condition. The observed level of agreement is within the experimental uncertainty of ±7.5 percent and it seems clear that the mass transfer coefficient under the film is not sensitive to the approach boundary layer.

This conclusion has important implications both for the real gas turbine situation and for the present investigation into the effects of pressure gradients. In the former instance, it implies that the blade cooling engineer has one fewer parameter to match when seeking heat transfer data to apply on a blade. For the present work, it implies that we can extract the effects of mainstream pressure gradient from results obtained with varying approach boundary layer thickness. This will be discussed in more detail in section 3 of this paper.

3 The Effects of Mainstream Pressure Gradients

Background. Some research workers have investigated

Nomenclature

D = injection hole diameter
h = local heat transfer coefficient
$\bar{h}$ = laterally averaged heat transfer coefficient
k = local mass transfer coefficient
$\bar{k}$ = laterally averaged mass transfer coefficient
M = blowing parameter $(\equiv \rho_c U_c/\rho_m U_m)$
U = velocity
V = acceleration parameter $[\equiv (\nu/U_m^2)(dU_m/dx)]$
x = streamwise distance downstream of the injection hole(s) measured from the trailing edge of the hole(s)
z = lateral distance measured from the center of the injection hole
δ^* = boundary layer displacement thickness
ν = kinematic viscosity
ρ = density

Subscripts

A.P.G. = adverse pressure gradient
c = coolant
F.P.G. = favourable pressure gradient
m = mainstream
o = with no injection or at the point of injection
Z.P.G. = zero pressure gradient

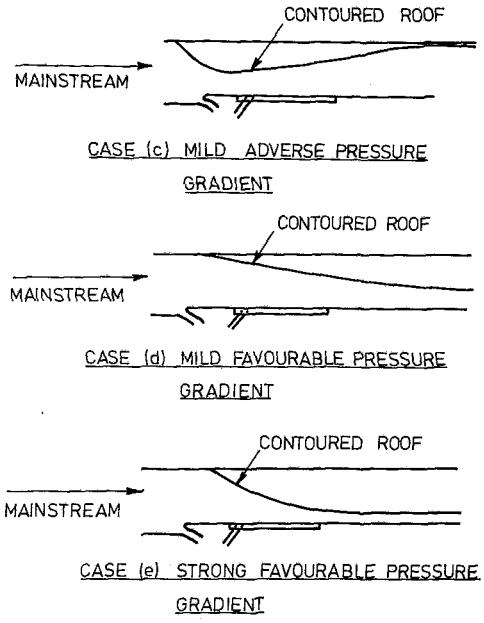

Fig. 3 Profiles of contours – mainstream pressure gradient study

the effect of mainstream pressure gradients on the heat transfer coefficient, but the data available for injection geometries of practical importance to the cooling of gas turbine blades are very limited.

The effects of an accelerating mainstream on the heat transfer coefficient have been investigated by Hartnett et al. [3] and Seban and Back [4] for tangential slots and by Warren and Metzger [5] for an angled slot. Liess [6] and Jabbari and Goldstein [7] have considered, respectively, injection through a row of holes, and injection through a single hole and a double row of staggered holes. All have reported a reduction in heat transfer coefficient over at least some part of the range of blowing parameter used although the effect was generally weak. Only the most strongly accelerated flow studied by Warren and Metzger [5] gave a significant reduction in heat transfer coefficient. For that case, the mainstream acceleration was sufficiently strong to cause boundary layer relaminarisation.

Most of the heat transfer data available in the literature for the effects of mainstream pressure gradient are for an accelerating mainstream and little information is available for the decelerating mainstream. The work reported in this section of the present paper was undertaken to provide data on the effects of injection on the heat transfer coefficient in the presence of both adverse and favorable mainstream pressure gradients. The acceleration parameters used were typical of those existing on gas turbine blades in regions away from the leading edge. The experimental technique, injection geometries, and range of blowing parameters used were the same as in section 2 of this paper.

Experimental Apparatus and Test Conditions. The experimental apparatus and facilities used in the present work were again the same as described in the companion paper [1], with the only difference that the flat roof of the working section of the wind tunnel was replaced by contoured roofs. The contoured roofs are shown in Fig. 3, and these imposed the desired mainstream pressure gradients in the film cooled region downstream of the point of injection. The conditions of the mainstream with the contoured roofs are referred to as Cases (*c*), (*d*), and (*e*) as shown in Fig. 3.

In all the cases described in this section, the mainstream velocity was maintained nominally at 25 m/s at the point of injection. The variation of mainstream velocity normalized

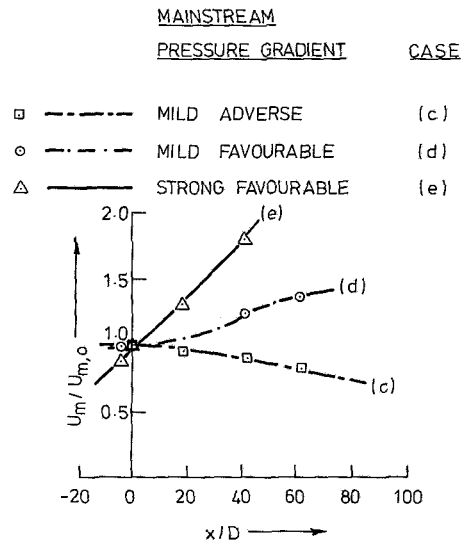

Fig. 4 Variation of the mainstream velocity in the streamwise direction

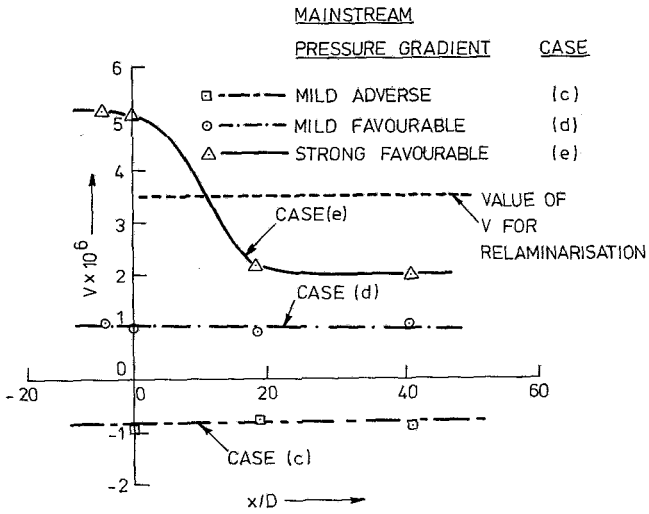

Fig. 5 Variation of the acceleration parameter in the streamwise direction

with mainstream velocity at the point of injection, $U_{m,o}$, is shown in Fig. 4. The variation of the acceleration parameter, V, in the streamwise direction for the three cases is shown in Fig. 5.

The condition of the mainstream boundary layer over the film cooled area in the absence of film injection was established by obtained boundary layer velocity profiles on a dummy test plate which had no film cooling holes. The measurements were made at four streamwise locations on the centerline of the floor.

The condition of the boundary layer in Cases (*c*), (*d*), and (*e*) is summarized below:

Case (*c*). From Fig. 4, the mainstream was mildly decelerated, its velocity reducing by only 10 percent in 40 dia downstream of the injection point. From Fig. 5, V was nearly constant at about -0.85×10^{-6} over the film-cooled region. The measured velocity profile was found to resemble closely the 1/7th power law turbulent boundary layer at the point of injection, with $\delta^*/D=0.19$.

Case (*d*). The contoured roof used provided mild acceleration of the mainstream as is shown in Fig. 4, the velocity increasing by about 25 percent at 40 dia downstream of the point of injection. The ratio δ^*/D was 0.21 at the point of

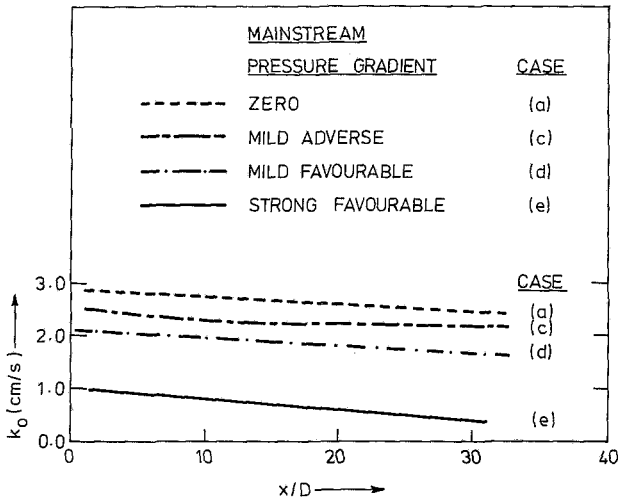

Fig. 6 Variation of the mass transfer coefficient with no injection in the streamwise direction

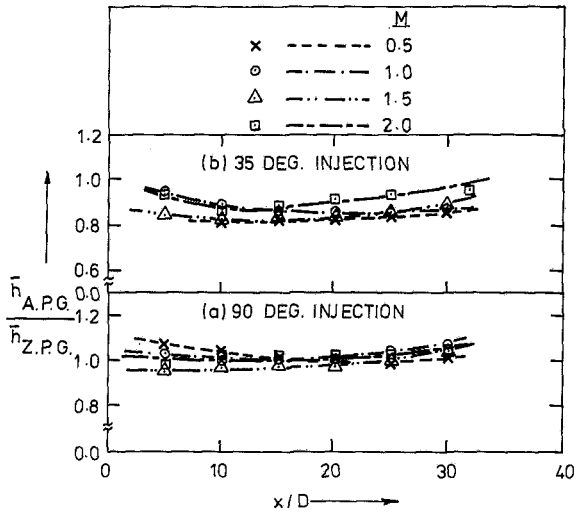

Fig. 7 Effect of adverse mainstream pressure gradient on the laterally-averaged heat transfer coefficient under a film

injection. The acceleration parameter was nearly constant at about 1×10^{-6} over the film-cooled area.

Case (*e*). The mainstream was strongly accelerated in the streamwise direction (see Fig. 4), the increase in mainstream velocity at 40 dia being about 80 percent over the value at the point of injection. The ratio δ^*/D was 0.10 at the point of injection, and V reduced from about 5×10^{-6} at this point to a nearly constant value of about 2×10^{-6} beyond 20 dia downstream. The boundary layer was transitional upstream of the point of injection. It has been reported by Moretti and Kays [8] that for $V \geq 3.5 \times 10^{-6}$, complete relaminarization of boundary-layer flow takes place. Since V values are in excess of this critical value over a part of the test surface, relaminarization of the boundary layer must have been taking place. The measured velocity profiles confirmed that this, in fact, was the case.

The variation of mass transfer coefficient with no injection, k_o, in the streamwise direction in the Cases (*c*), (*d*), and (*e*) is presented in Fig. 6. Also shown in the figure is the variation of k_o for zero pressure gradient (Case (*a*)). It can be seen that with the deceleration imposed (Case (*c*)), k_o is lowered by 10–15 percent from the zero pressure gradient values. For the mild favourable pressure gradient (Case (*d*)), k_o is reduced by 25–30 percent from the zero pressure gradient values. It was suggested by Moretti and Kays [8] that mainstream acceleration suppresses the generation of turbulence in a turbulent boundary layer and this could be the cause of the observed reduction of the heat transfer coefficient. For the strong favourable pressure gradient (Case (*e*)), there is significant reduction of k_o, 70–80 percent of the zero pressure gradient values.

As noted earlier, relaminarization of the mainstream boundary layer flow was taking place in the presence of the strong favorable pressure gradient. The reason for the reduction observed is that while the zero mainstream pressure gradient curve corresponds to a turbulent boundary layer, the strong favorable pressure gradient curve corresponds to a relaminarizing boundary layer, as was shown earlier (Fig. 5).

It must, however, be pointed out that in Cases (*a*), (*c*), (*d*), and (*e*), not only were there differences in the mainstream pressure gradient downstream of the injection location ($x/D = 0$), but there were also differences upstream. These latter differences affect the approach boundary layer, and hence are partly responsible for the observed k_o variation in Fig. 6. In particular, it will be noted that k_o in the presence of the mild adverse pressure gradient is less than that for the zero pressure gradient case. This contrasts with the increase expected from the known behavior of turbulent boundary layers in adverse pressure gradients and arises from the effect of the strong acceleration of the flow in the region upstream of the injection point. However, it has been shown in section 2 for zero pressure gradient that, in the presence of injection, a large change in approach boundary layer condition (from thick, turbulent to thin, transitional) produces no measurable change in the heat transfer coefficient under the injected film. It seems reasonable to suppose that the heat transfer coefficients under films injected into regions with nonzero pressure gradients are similarly insensitive to approach boundary layer conditions.

Results and Discussion. The results are presented in terms of the ratio of mass transfer coefficient under the film in the presence of the pressure gradient to that with zero pressure gradient conditions at the same location and injection rate. That is, we plot $k_{\text{F.P.G.}}/k_{\text{Z.P.G.}}$, $k_{\text{A.P.G.}}/k_{\text{Z.P.G.}}$, etc., to give the factor by which the mass transfer coefficient (or heat transfer coefficient) has been altered due to the imposition of a pressure gradient. The value of $k_{\text{Z.P.G.}}$ used in this normalizing process are those from Case (*a*). As noted earlier, the heat transfer coefficient under the film is insensitive to the condition of the approach boundary layer so that presentation of the results in this form reveals solely the effect of the pressure gradient.

Adverse Mainstream Pressure Gradient. Figure 7(*a*) illustrates the effect of the adverse mainstream pressure gradient on the laterally averaged heat transfer coefficient with 90-deg film injection. The variation of $\bar{h}_{\text{A.P.G.}}/\bar{h}_{\text{Z.P.G.}}$ shows no distinct trend with M. Also for all the blowing parameters, the ratios are in the range of 0.96–1.08. Bearing in mind that the uncertainty associated with these ratios is ± 10.5 percent, we can conclude that for 90-deg injection, a mild adverse pressure gradient does not have any significant effect.

In Fig. 7(*b*), the laterally averaged results for 35-deg injection are shown. The values of the ratio of the heat transfer coefficients reach about 0.83–0.97. Again, there is no distinct effect of blowing parameter but overall the ratio of the heat transfer coefficients with 35-deg injection is reduced slightly as compared to its value with 90-deg injection.

Favorable Mainstream Pressure Gradient. In contrast to the effect of adverse pressure gradient noted earlier, the favorable pressure gradients show significant effects: the ratio of heat transfer coefficients is distinctly lower than unity, and

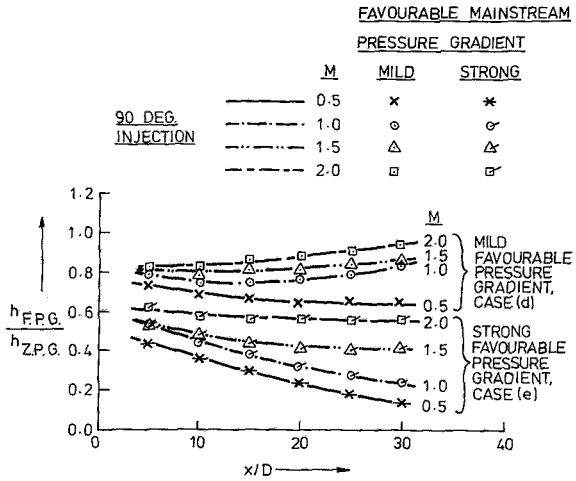

Fig. 8 Effect of favorable pressure gradients on the local heat transfer coefficient under a film for 90-deg injection

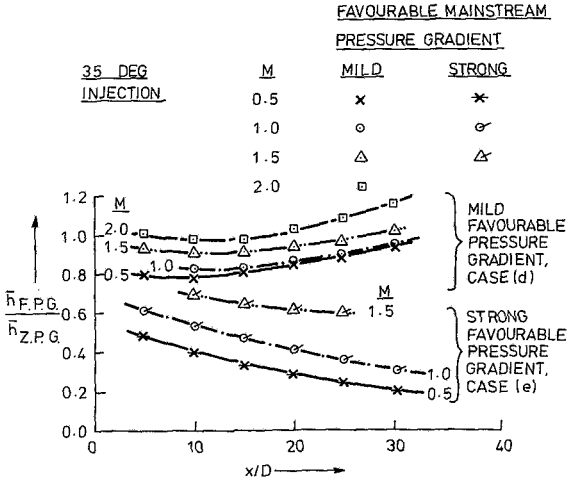

Fig. 9 Effect of favorable pressure gradients on the laterally averaged heat transfer coefficient under a film for 35-deg injection

there is a definite variation with the blowing parameter. Figure 8 shows the effects of both mild favorable and strong favorable pressure gradients on the heat transfer coefficient for 90-deg injection on the centerline ($z/D=0$).

For the mild favorable pressure gradient, at locations close to the injection holes, the heat transfer coefficient with injection ranges between 70 and 80 percent of that for zero mainstream pressure gradient. Beyond about 20 dia downstream, $h_{F.P.G.}/h_{Z.P.G.}$ is in the range of 0.65–0.95, rising with the blowing parameter. As mentioned earlier, the level of turbulence in a boundary layer is reduced in the presence of a favorable mainstream pressure gradient. The present results suggest that an injected film is similarly affected particularly at low injection rate. As the blowing parameter is raised, the injected stream creates a greater disturbance in the mainstream boundary layer and causes the heat transfer coefficient ratio $h_{F.P.G.}/h_{Z.P.G.}$ to rise towards unity.

It can also be seen in Fig. 8 that in the presence of the strong favorable pressure gradient, the heat transfer coefficient ratio at $M=0.5$ is reduced to 40 percent close to the injection point and falls further to 15 percent at $x/D\simeq 30$. The value of the ratio at a given location rises as the blowing parameter is increased. The effect of injection is to overcome relaminarization and reintroduce turbulence in the film. As more and more coolant is injected, an increase in the ratio of the heat transfer coefficients of 200–300 percent of the value at $M=0.5$ is observed. At a blowing parameter of about 2, the heat transfer coefficient with injection reaches 60 percent of the corresponding value with injection with zero pressure gradient.

From Fig. 8, it is also evident that the ratio $h_{F.P.G.}/h_{Z.P.G.}$ at a given location and blowing parameter in the presence of a strong favorable pressure gradient is much lower than its value in the presence of a mild favorable pressure gradient. The difference in the effects of the strong and mild favorable pressure gradients is larger at low blowing rates and decreases as the blowing rate is increased. This indicates that at a large blowing parameter, the effect of the injection dominates the effect of the imposed mainstream pressure gradient.

For both mild and strong favorable pressure gradients, the laterally averaged heat transfer coefficients ratio $\bar{h}_{F.P.G.}/\bar{h}_{Z.P.G.}$ was found to behave in a similar way to the ratio of local values discussed above.

The results for 35-deg injection are shown in Fig. 9. This time, laterally averaged values are shown. With this injection angle, for the mild favorable pressure gradient, the ratio $\bar{h}_{F.P.G.}/\bar{h}_{Z.P.G.}$ is about 0.80–1.00 at low values of x/D and about 0.85–1.1 at large values of x/D. For the strong favorable pressure gradient, the ratios are significantly lower, at about 0.45–0.70 at low values of x/D and about 0.20–0.60 at large values of x/D. As with the 90-deg results, for a given location, as M increases, the ratio $\bar{h}_{F.P.G.}/\bar{h}_{Z.P.G.}$ also increases. With this injection angle, the ratios of heat transfer coefficients were found to be greater than with 90-deg injection, typically by 15 percent.

The effect of acceleration on the adiabatic film cooling effectiveness for injection through a row of holes has been reported by Liess [6] and Brown and Saluja [9] and shown to be negative in that it would lead to an increase in metal surface temperature. However, since as we have just seen this is coupled with a simultaneous decrease in heat transfer coefficient, the overall result as far as the metal surface temperature is concerned, will not be so severe and may on balance be even beneficial.

Conclusions

(*i*) The condition of the approach boundary layer makes hardly any difference to the heat transfer coefficient under the film.

(*ii*) The presence of an adverse pressure gradient does not have any significant effect on the heat transfer coefficient under the film.

(*iii*) For injection at a low blowing parameter of 0.5 in the presence of a mild favorable pressure gradient, the heat transfer coefficient reduces to 70–80 percent of the value with zero mainstream pressure gradient. As the blowing parameter is raised, the heat transfer coefficient approaches the zero pressure gradient values.

(*iv*) The effect of a strong favorable pressure gradient is to decrease the heat transfer coefficient drastically, particularly at low blowing rates due to the relaminarizing effect of the pressure gradient. As the injection rate increases, there is a tendency for the relaminarization effect to be overcome and the heat transfer coefficient also increases, although full recovery to zero pressure gradient levels does not take place within the range of blowing rates considered here.

Acknowledgment

The research reported here was carried out in the Department of Mechanical Engineering at the University of Nottingham with a grant from the Science and Engineering Research Council. The use of facilities and the financial support are gratefully acknowledged.

References

1 Hay, N., Lampard, D., and Saluja, C. L., "Effects of Cooling Films on the Heat Transfer Coefficient on a Flat Plate With Zero Mainstream Pressure Gradient," this issue of ASME JOURNAL OF ENGINEERING FOR GAS TURBINES AND POWER, pp. 105–110.

2 Goldstein, R. J., and Yoshida, T., "The Influence of a Laminar Boundary Layer and Laminar Injection on Film Cooling Performance," ASME Paper No. 81-HT-38, 1981.

3 Hartnett, J. P., Birkbeck, R. C., and Eckert, E. R. G., "Velocity Distribution, Temperature Distribution, Effectiveness and Heat Transfer in Cooling a Surface With a Pressure Gradient," *International Development in Heat Transfer*, Pt. IV, ASME, New York, 1961, pp. 682–689.

4 Seban, R. A., and Back, L. H., "Heat Transfer and Effectiveness for a Turbulent Boundary Layer With Tangential Fluid Injection," ASME *Journal of Heat Transfer*, Vol. 82, No. 4, Nov. 1960, pp. 303–312.

5 Warren, J. M., and Metzger, D. E., "Heat Transfer With Film Cooling in the Presence of Laminarizing Mainstream," ASME Paper No. 72-HT-11, 1972.

6 Liess, C., "Experimental Investigation of Film Cooling With Ejection From a Row of Holes for the Application to Gas Turbine Blades," ASME JOURNAL OF ENGINEERING FOR POWER, Vol. 97, Jan. 1975, pp. 21–27.

7 Jabbari, M. Y., and Goldstein, R. J., "Effect of Mainstream Acceleration on Adiabatic Wall Temperature and Heat Transfer Downstream of Gas Injection," *Proceedings of the Intl. Heat Transfer Conf.*, Toronto, Vol. 5, 1978, pp. 249–251.

8 Moretti, P. M., and Kays, K. M., "Heat Transfer to a Turbulent Boundary Layer With Varying Surface Temperature—An Experimental Study," *International Journal of Heat and Mass Transfer*, Vol. 8, 1965, pp. 1187–1202.

9 Brown, A., and Saluja, C. L., "Film Cooling From a Single Hole and a Row of Holes of Variable Pitch to Diameter Ratio," *International Journal of Heat and Mass Transfer*, Vol. 22, 1979, pp. 523–533.

Effects of Cooling Films on the Heat Transfer Coefficient on a Flat Plate With Zero Mainstream Pressure Gradient

N. Hay

D. Lampard

C. L. Saluja

Department of Mechanical Engineering,
University of Nottingham,
Nottingham, NG7 2RD, U.K.

The influence of injection of cooling films through a row of holes on the heat transfer coefficient on a flat plate is investigated for a range of mass flux ratio using a heat-mass transfer analogy. Injection angles of 35 deg and 90 deg are covered. The experimental technique employed uses a swollen polymer surface and laser holographic interferometry. The results presented show the change in local heat transfer coefficient over the no-injection values at the centerline and off-centerline locations for various streamwise stations. The effect of injection on laterally averaged heat transfer coefficients is also assessed.

Introduction

The desirability of employing high temperature working gases in modern gas turbines of aero-engines has given considerable impetus in recent years to research into the technique of "film cooling." This technique involves localized injection of cold air through discrete holes into the mainstream boundary layer flowing over the surfaces to be cooled. Thus the surfaces of the vulnerable components of the engine such as turbine blades are kept within acceptable temperature limits.

On film cooled surfaces, the thermal flux, q_f, required for thermal analysis has usually been determined using the equation:

$$q_f = h_f(T_{aw} - T_w) \tag{1}$$

where h_f is the heat transfer coefficient with injection, T_w the wall temperature and T_{aw} the temperature of the abiabatic wall usually expressed in the nondimensionalized form as the adiabatic film cooling effectiveness, η_{ad}, defined as:

$$\eta_{ad} = (T_m - T_{aw})/(T_m - T_c) \tag{2}$$

Here T_m is the mainstream recovery temperature and T_c is the recovery temperature of the injected coolant stream.

Some workers, for example, Metzger et al. [1], Choe et al. [2] have expressed the thermal flux, q_f, to a film cooled surface by the equation

$$q_f = h(T_m - T_w) \tag{3}$$

where h is the heat transfer coefficient with injection and T_w is the temperature of the isothermal wall. The parameter h in equation (3) reflects the effect of film injection.

If the heat flux with no injection, q_0, is expressed as:

$$q_0 = h_0(T_m - T_w) \tag{4}$$

combining equations (1) to (4), we have

$$q_f/q_0 = h/h_0 = (h_f/h_0)(1 - \eta_{ad}\theta) \tag{5}$$

where θ is defined as:

$$\theta = (T_m - T_c)/(T_m - T_w) \tag{6}$$

The linearity of h with θ for incompressible flow has been demonstrated experimentally by Metzger et al. [1]. For the case $\theta = 0$, equation (5) gives $h = h_f$ and this has been used by Metzger et al. [3] and by Ville and Richards [4] to determine h_f by extrapolation from measurements of h made over a range of θ.

In the experimental investigation described in this paper, the value of the local heat transfer coefficient with injection, h, was estimated through the analogous mass transfer coefficient. Isothermal conditions on a test surface were simulated by maintaining the concentration of the mass transferring fluid on the film cooled surface constant during a test. Also, the concentration of the mass transferring fluid in the mainstream as well as in the secondary stream was maintained at zero so that θ was equal to zero. For this condition, $h = h_f$ as has been pointed out before. Thus it will be possible to compare the results obtained by this method with other results such as those of Liess [5] and Eriksen and Goldstein [6] where the heat transfer coefficient based on an adiabatic wall temperature (h_f) was measured instead of h.

Previous Work

The majority of researchers into film cooling have concentrated on the behavior of the adiabatic film cooling effectiveness since it varies over a wide range on film cooled surfaces. It has been the practice in the past to assume that the

Contributed by the Gas Turbine Division of THE AMERICAN SOCIETY OF MECHANICAL ENGINEERS and presented at the 29th International Gas Turbine Conference and Exhibit, Amsterdam, The Netherlands, June 4–7, 1984. Manuscript received at ASME Headquarters, December 27, 1983. Paper No. 84-GT-40.

heat transfer coefficient is not significantly modified by the injection of the coolant and its value with injection has been assumed to be equal to the value when no injection was present. This assumption may be valid for locations at some distance downstream of the point of injection and for low film injection rates, but it is certainly not true for some locations on film cooled surfaces where the effect of injection on the hydrodynamic boundary layer is significant. For such locations, a knowledge of the variation of the local heat transfer coefficient with injection as well as that of the film cooling effectiveness is required for the thermal analysis of the blade, and this has motivated some research workers to investigate the heat transfer coefficient. The information available is however limited.

Liess [5] reported heat transfer measurements for injection through a row of 35 deg holes with a lateral spacing of 3.0 diameters. He showed that close to the injection holes, the heat transfer coefficient increased by up to 60 percent above the no-injection value and further downstream, the increase was up to 25 percent. Using an injection geometry similar to that of Liess [5], Eriksen and Goldstein [6] showed that at low blowing parameters, the heat transfer coefficient with film injection was approximately equal to the heat transfer coefficient with no film injection. Above a blowing parameter M of 0.5, h_f became progressively greater than h_0 as M increased. Metzger and Fletcher [7] explored the variation of the laterally averaged heat transfer coefficient downstream of a row of holes on a flat plate. Significant increases (up to 50 percent) in the heat transfer coefficient close to the injection holes for large blowing rates were found. Similar results for injection through two rows of staggered holes on the suction surface of turbine vanes and for injection on a flat surface were reported respectively by Lander et al. [8] and Jabbari and Goldstein [9].

Most of the heat transfer data available in the literature is for 35 deg injection and little information is available for 90 deg injection. The work reported in this paper has been undertaken to provide heat transfer data for 90 deg and 35 deg injection. Also, the experimental techniques employed by most of the previous workers afforded laterally averaged heat transfer coefficients although some have also provided local heat transfer coefficients at a few lateral locations. In the present work, a comparatively novel technique has been employed which offers the great advantage of providing the variation of the local heat transfer coefficient over the entire film cooled surface.

Experimental Method

In the present work a new and powerful technique, developed by Dr. N. Macleod of Edinburgh University is employed and this offers the advantages of speed, simplicity and high precision over the conventional means of determining mass transfer coefficients. It is also comparatively inexpensive to use. The technique is, in fact, a combination of the "swollen polymer technique" [10] and of "laser holographic interferometry" [11]. The mass-transferring test surface consists of a coating of a polymer which is swollen in a reversible manner in an organic fluid of suitable volatility. Exposure of the swollen polymer to airstreams causes the swelling agent to evaporate, resulting in a change in the polymer coating thickness. The time of exposure is controlled so that the concentration of the swelling agent in the polymer and its vapor pressure over the polymer surface are maintained almost constant and lateral diffusion of the swelling agent within the polymer is insignificant. Under these circumstances, as shown by Macleod and Todd [10], the rate of change of the polymer thickness at any location is proportional to the local mass transfer coefficient.

Laser holographic interferometry is employed to measure the thickness changes of the polymer at various points. The values of the local mass transfer coefficient at various locations are determined following the procedure outlined by Kapur and Macleod [12]. For this, a knowledge of the physical properties of the polymer and of the swelling agent, the geometry of the optical setup, and the order of the fringes at the locations are required.

The problem of fringe order identification is partly overcome in the present work by measuring the recession at a reference point on the test surface using an air-gage. The pressure reading on the air gaging system is noted just before the first holographic exposure and then just after the second holographic exposure. From the two measurements, the absolute value of the polymer thickness change and hence the order of a fringe passing through the reference point is determined.

For identification of the order of all the fringes on the interferogram, it is also necessary to determine the way the order of fringes changes (increases, decreases or remains constant) in any direction. To this end, "live" fringes are constructed and their movements are observed in a manner described previously by the present authors [13] following the work of Macleod [14]. This information was also ascertained in some cases by the use of two air gages separated by a distance in the streamwise direction.

Experimental Apparatus and Test Conditions

The tests were conducted in a low speed wind tunnel using a removable flat plate as the film cooled surface. The wind tunnel described by Foster and Lampard [15] was used with minor modifications to suit the present program. The

Nomenclature

D = injection hole diameter
D^* = diffusion coefficient
h = local heat transfer coefficient, defined in equation (3)
h_f = local heat transfer coefficient, defined in equation (1)
$\bar{h}$ = laterally averaged heat transfer coefficient
k = local mass transfer coefficient
K = acceleration parameter $[=(\nu/U_m^2)(dU_m/dx)]$
L = distance between the origins of aerodynamic and concentration boundary layers
M = blowing parameter $(\equiv \rho_c U_c/\rho_m U_m)$
q = thermal flux
Re = Reynolds number
S = lateral spacing of holes
T = temperature
U = velocity
x = streamwise distance downstream of the injection hole (s) measured from the trailing edge of the hole (s)
z = lateral distance measured from the center of the injection hole
α = injection angle
δ = boundary layer thickness
δ^* = boundary layer displacement thickness
η = film cooling effectiveness, defined in equation (2)
θ = nondimensionalized wall temperature, defined in equation (6)
ν = kinematic viscosity
ρ = density

Subscripts

ad = adiabatic
aw = adiabatic wall
c = coolant
f = with film cooling
m = mainstream
0 = with no injection
w = wall

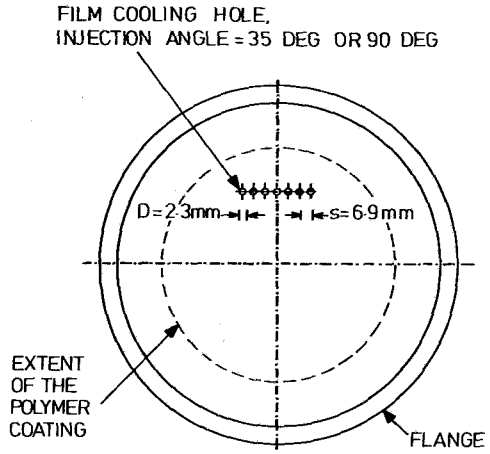

Fig. 1 Test plate

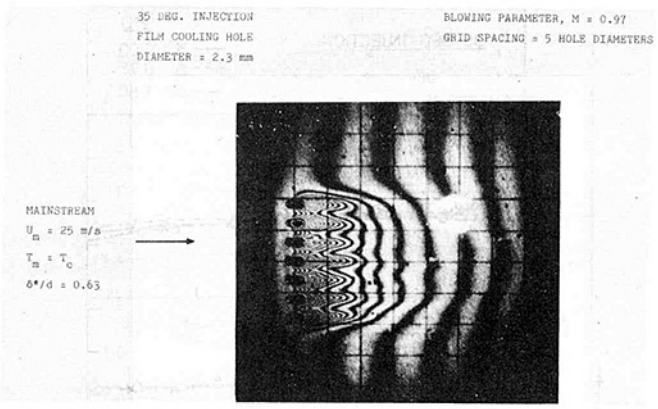

Fig. 2 Interference fringes depicting contours of constant mass transfer coefficient (or of analogous heat transfer coefficient) for injection through a row of holes, pitch/diameter = 3

Table 1 Experimental test conditions

Injection hole diameter, D	: 2.30 mm
Pitch/diameter, S/D	: 3.0
Number of rows	: 1
Injection angle, α	: 35, 90 deg
Mainstream velocity, U_m	: 25 m/s
Blowing parameter, $M(\equiv \rho_c U_c/\rho_m U_m)$	: 0.5–2.0
Boundary layer displacement thickness, δ^*	: 0.63 D
Mainstream acceleration parameter, $K[=(\nu/U^2{}_m)(dU_m/d_x)]$	: zero
Mainstream Reynolds number, Re_D	: 0.38×10^4

mainstream flow was supplied by a laboratory compressor plant at a nominal velocity of 25 m/s. Upstream of the secondary air injection locations, the tunnel floor boundary layer was first bled off and then tripped. Velocity measurements were made in the boundary layer at the centerline of the working section on a dummy test plate which had no film cooling holes. The measured velocity distributions were found to compare closely to a 1/7th power law turbulent boundary layer velocity distribution. The ratio of the boundary layer displacement thickness to injection hole diameter was 0.63 at the point of injection and the origin of the aerodynamic boundary layer was 0.455 m upstream of the injection locations. All the tests were conducted with zero mainstream pressure gradient.

The base of the working section of the wind tunnel had a 290 mm diameter circular cutout through it. A circular test plate (shown in Fig. 1) carrying a coating of about 0.5 mm thickness of the swollen polymer over part of its top surface was inserted in the cutout and clamped in position to expose it to the film cooling and mainstream flows. Two test plates were used. Each test plate had 7 circular tubes of 2.3 mm I.D. for the injection of secondary air streams. The pitch-to-diameter ratio of the injection holes was 3.0. In one test plate, the injection holes were normal to the surface and in the other they were at 35 deg to the surface.

Secondary air was drawn from the same supply as the mainstream and after metering by rotameters, it was fed to the circular injection tubes via a plenum chamber containing gauze screens. The injection tubes were long enough to ensure fully developed flow at their exit.

The experimental test conditions employed during the present work are summarized in Table 1.

The holographic setup described previously by the present authors [13] was also used in this investigation for construction and reconstruction of holograms.

Results and Discussions

Tests were carried out with 90 deg and 35 deg holes at blowing rates of 0.5, 1.0, 1.5, and 2.0. A typical interferogram is shown in Fig. 2. Each fringe in the figure depicts a contour of equi-recession of the swollen polymer or of constant mass transfer coefficient. Using the ancillary measurements made with an air-gage at a reference point and utilizing the observations made with live fringes, the order of all the interference fringes was identified thus yielding the variation of the mass transfer coefficient. During the experimental work, all major sources of error were carefully noted. An error analysis carried out following the method of Kline and McClintock [16] indicated a ±7.5 percent uncertainty in the values of the measured mass transfer coefficients.

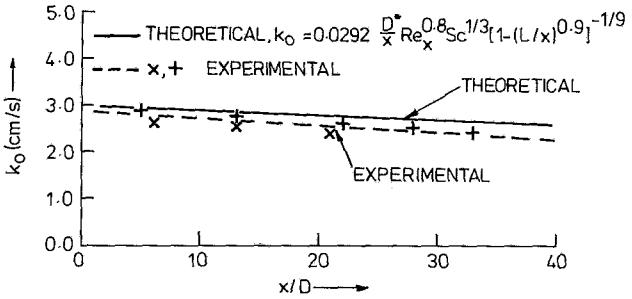

Fig. 3 Variation of the mass transfer coefficient without injection, k_0, in the streamwise direction

In the present work, the Lewis number is about 4.1 and not unity as required for the validity of the heat-mass transfer analogy. Therefore it was considered desirable to express the results in terms of the change in the coefficient due to film injection. To do this, a subsidiary test was run in which the test plate was exposed to the mainstream with the plate turned 180 deg to the direction of the mainflow so that the variation of mass transfer coefficient due to the mainstream only was obtained over the area of interest. This is shown in Fig. 3. Also shown in the figure is the theoretical variation of k_0 calculated from the analogous heat transfer equation given by Knudsen and Katz [17]:

$$k_0 = 0.0292(D^*/x)\,\mathrm{Re}_x^{0.8}\mathrm{Sc}^{1/3}[1-(L/x)^{0.9}]^{-1/9} \qquad (7)$$

The expression $[1-(L/x)^{0.9}]^{-1/9}$ in equation (7) is a correction factor suggested by Rohsenow and Hartnett [18] to account for the fact that the origin of the concentration boundary layer and that of the aerodynamic boundary layer were at a distance L apart. The experimental results shown in Fig. 3 were obtained from two separate runs. They differ by about 8 percent. Also, the mean experimental curve drawn

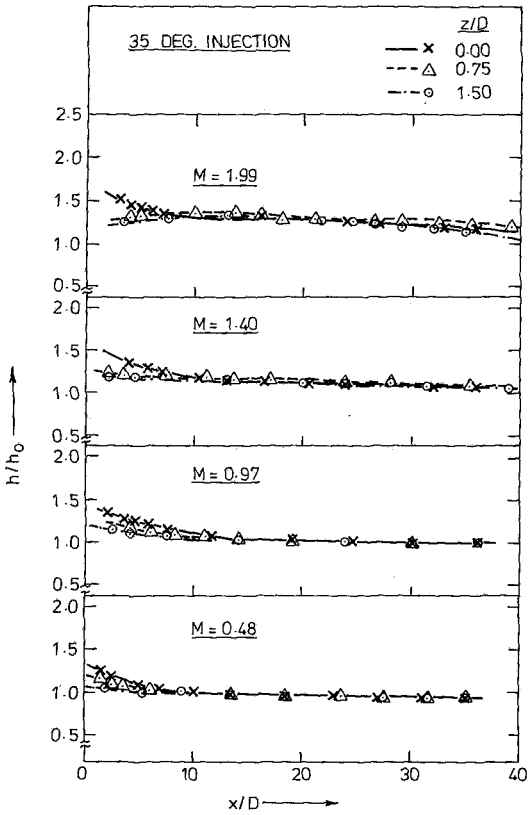

Fig. 4 Variation of the heat transfer coefficient ratio h/h_0 with distance downstream x/D

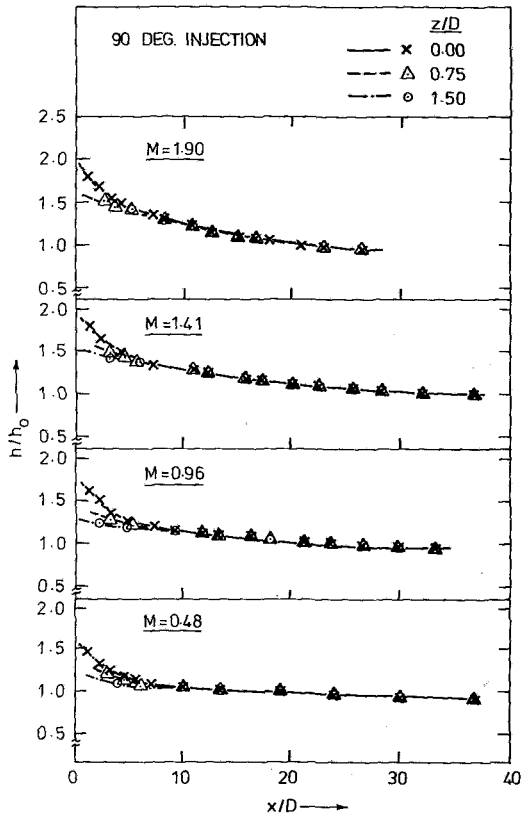

Fig. 5 Variation of the heat transfer coefficient ratio h/h_0 with distance downstream x/D

through both sets of data lies within 8.5 percent of the theoretical curve. It should be recognized that this discrepancy may arise in part from error in determining the location of the origin of the aerodynamic boundary layer.

As shown in Fig. 2, each hologram obtained was found to have nearly parallel fringes on either side of the injection region. Mass transfer coefficients in this region were found to agree well with the experimental values obtained from the exposure of the test surface to the mainstream only. The ratio of the heat transfer coefficient with injection to the heat transfer coefficient without injection, h/h_0, at a location on the film cooled region was found from the ratio of the order of a fringe in the film cooled region to the order of a fringe in the region not affected by injection following an approach described previously by the present authors [13]. The uncertainty associated with the ratio of the two heat transfer coefficients was estimated to be ±10.5 percent.

The ratio of the analogous heat transfer coefficients, h/h_0, obtained is plotted in Fig. 4 for 35 deg injection and in Fig. 5 for 90 deg injection for the centerline, quarter-pitch, and mid-pitch positions. For both injection angles, at locations close to the injection holes ($x/D < 10$), there is significant variation of h/h_0 in the lateral direction. For 35 deg injection, h/h_0 can be as high as 1.40 for $M = 0.97$ and 1.50 for $M = 1.99$. For 90 deg injection, measured values of h/h_0 reach 1.60 for $M = 0.96$ and 1.80 for $M = 1.90$. As the jets come out of the injection holes, they disturb the mainflow and high levels of turbulence result which enhance the local heat transfer coefficient. Levels of turbulence of the order of 40 percent in the region just downstream of injection were reported previously by one of the present authors [19] for injection through a row of 30 deg holes. With normal injection, the level of turbulence is expected to be still higher. The level of disturbance varies significantly across a span in the vicinity of the injection holes. The variation of the heat transfer coefficient is thus significant in the lateral direction until the emerging jets begin to interact and merge when the variation becomes small. Beyond about 10 diameters downstream, the variation in the lateral direction is seen to be small for both injection angles. For such locations, with 35 deg injection, h/h_0 is nearly unity for $M = 0.48$ and 0.96 whereas it is about 1.10 for $M = 1.40$ and about 1.25 for $M = 1.99$. With 90 deg injection, h/h_0 ranges from about 1.05 to about 1.30 at $x/D = 10$ but drops to about 1.0 at x/D of 30 for all the blowing parameters used.

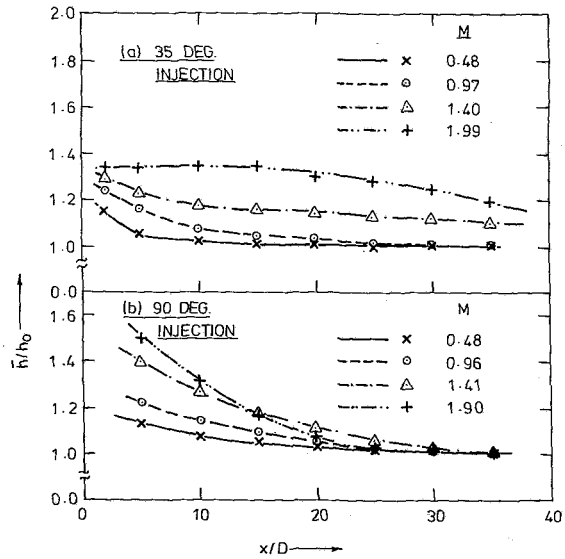

Fig. 6 Variation of the heat transfer coefficient ratio $\bar{h}/h_0$ with distance downstream x/D

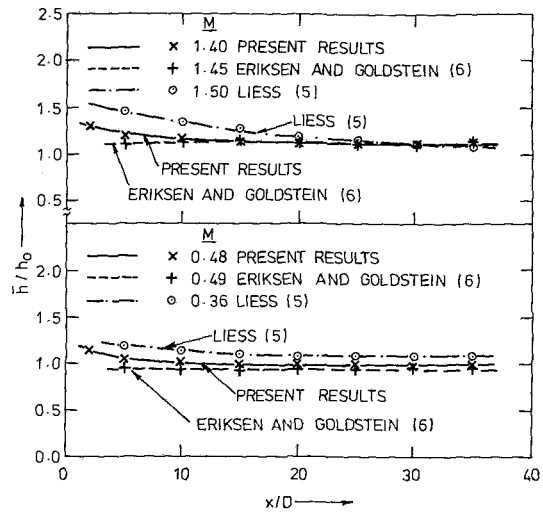

Fig. 7 Comparison of the present 35 deg results with the results of references [5] and [6]

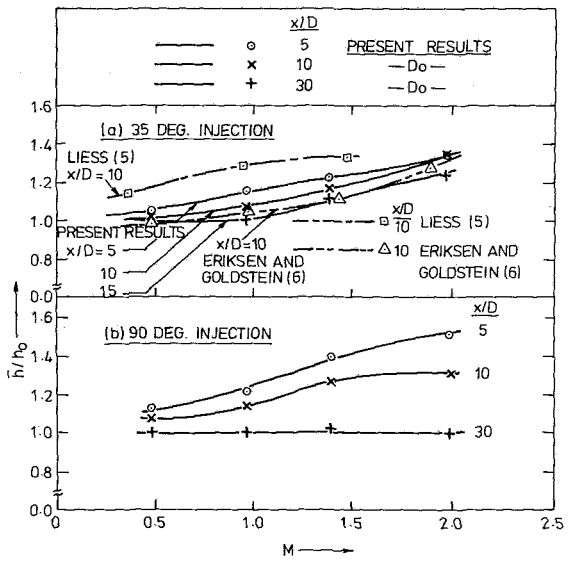

Fig. 8 Variation of the heat transfer coefficient ratio $\bar{h}/h_0$ with the blowing parameter M

The ratio of the laterally averaged heat transfer coefficient with injection to the heat transfer coefficient with no injection, $\bar{h}/h_0$, was found by dividing the average value of the order of fringes over one pitch at a streamwise position in the film cooled region by the order of a fringe at the same streamwise position in the region not affected by injection. These are the data which are of more interest from a design standpoint. This ratio is plotted for the four blowing parameters in Figs. 6(*a*) and 6(*b*) for 35 deg and 90 deg injection, respectively. For 35 deg injection, $\bar{h}/h_0$ varies from 1.15 to 1.35 for low x/D and between 1.00 and 1.25 for large x/D. For 90 deg injection, the ratio varies from about 1.15 to about 1.55 at low x/D. At large x/D, $\bar{h}/h_0$ tends toward unity. The reasons for the differences in the average heat transfer coefficient for the two injection angles are discussed later.

In Fig. 7, some of the present results for $\bar{h}/h_0$ for 35 deg injection are compared with the available results of Liess [5] and of Eriksen and Goldstein [6] which are for the same injection geometry. At a low blowing parameter of about 0.5, the present results fall between the results reported in

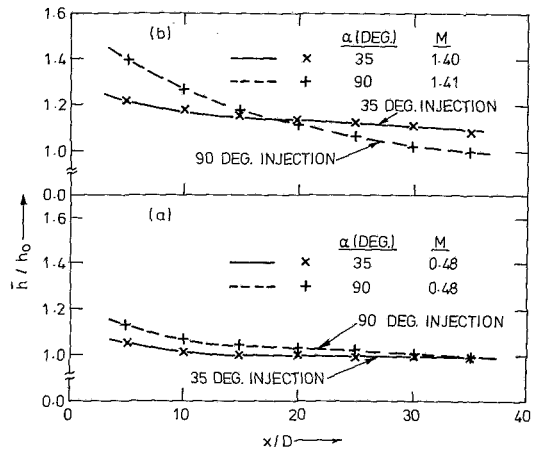

Fig. 9 Comparison of the 35 deg and 90 deg results with each other

references [5] and [6] over the whole of the film cooled area. For the nominal blowing parameter of 1.5, the present results also fall between the results of references [5] and [6] at $x/D < 20$, although they are closer to the data of Eriksen and Goldstein [6]. At larger distances downstream, there is very close agreement between the three sets of data.

To illustrate the implications of the results, an example of film cooling of a gas turbine blade through a row of 90 deg holes with a lateral spacing of 3 hole diameters is considered. For a location of x/D of 10 and M equal to 1.40, η_{ad} is 0.15 (from Foster and Lampard [15]) and h_f/h_0 is 1.27 from the present results. In a modern advanced aeroengine, a typical value of θ is between 1.25 and 1.75 (Ville and Richards [4]). From equation (5) for $\theta = 1.50$, q_f/q_0 is 0.984 but if it is assumed that $h_f/h_0 = 1$, q_f/q_0 is 0.775 i.e., the assumption that the film injection does not affect the heat transfer coefficient results in about 20 percent underestimation of thermal load and hence overestimation of the life of the film cooled component.

The variation of $\bar{h}/h_0$ with the blowing parameter M is plotted in Figs. 8(*a*) and 8(*b*) for 35 deg and 90 deg injection, respectively. For each injection angle, results are given for streamwise distances, x/D of 5, 10, and 30. Over the range of the blowing parameter covered, $\bar{h}/h_0$ increases as M is increased. A similar trend of variation of the ratio with the blowing parameter has been observed by Liess [5] and Eriksen and Goldstein [6] as shown in Fig. 8(*a*). The present results also show that, for 35 deg injection, the ratio is close to unity at low values of the blowing parameter at all the three locations but is significantly higher than unity at higher values of the blowing parameter. For 90 deg injection, the ratio is close to unity at large x/D for all the blowing parameters but is higher than unity at low x/D.

A comparison of the $\bar{h}/h_0$ results for 35 deg and 90 deg injection is shown in Fig. 9(*a*). The results are for a blowing parameter of 0.48 but are representative of the results obtained for blowing parameters of less than unity. The increase over h_0 is greater for the 90 deg injection than for the 35 deg injection at most of the streamwise positions. This is obviously due to the greater interaction and disturbance caused by 90 deg injection. The results obtained with a blowing parameter greater than unity show slightly different trends. A typical plot of $\bar{h}/h_0$ against x/D for the two injection angles of 90 deg and 35 deg is shown in Fig. 9(*b*) for $M = 1.40$. For x/D less than 20, the ratio $\bar{h}/h_0$ is greater for 90 deg injection as noted for lower blowing rates but at larger x/D, the trend reverses. The effect of injection falls off much faster with 90 deg injection than with 35 deg injection. It has been observed by Afejuku et al. [20] that normal injection results in much faster mixing and consequent jet dilution than 35 deg in-

jection. Velocity measurements by Foster and Lampard [15] have revealed that jets injected at 35 deg maintain their jet structure for a longer distance downstream than jets injected normally. This explains why the effect of injection on the heat transfer coefficient persists to larger distances downstream for 35 deg injection than for normal injection.

Conclusions

(i) For both 35 deg and 90 deg injection, an increase in the local heat transfer coefficient occurs as a result of injection. The increase is significant close to the injection holes. At larger distances downstream, the ratio h/h_0 tends toward unity.

(ii) The variation of the heat transfer ratio, h/h_0, is significant in the lateral direction until the injected jets begin to interact when the variation becomes small. Spanwise uniformity is reached closer to the injection holes for the higher injection angle.

(iii) At a given streamwise location both h/h_0 and $\bar{h}/h_0$ increase as M increases.

(iv) For jets injected at 35 deg, $\bar{h}/h_0$ can be as high as 1.35 at large blowing rates. For 90 deg injection, the corresponding value is 1.50. A realistic design of a film cooled component such as a turbine blade must be based on the heat transfer coefficient with injection; otherwise the life of the component will be overestimated.

(v) Normal injection results in a stronger interaction with the mainstream than 35 deg injection. Consequently, h/h_0 and $\bar{h}/h_0$ are initially higher for 90 deg injection than for 35 deg injection, and fall off more quickly with distance from the injection point. Far downstream, the effect of normal injection is much less than that of 35 deg injection.

Acknowledgments

The research reported here was carried out in the Department of Mechanical Engineering at the University of Nottingham with a grant from the Science and Engineering Research Council. The use of facilities and the financial support are gratefully acknowledged.

References

1 Metzger, D. E., Carper, H. J., and Swank, L. R., "Heat Transfer with Film Cooling Near Non-Tangential Injection Slots," ASME JOURNAL OF ENGINEERING FOR POWER, Vol. 90, 1968, pp. 157–164.

2 Choe, H., Kays, W. M., and Moffat, R. J., "The Superposition Approach to Film Cooling," ASME Paper No. 74-WA/HT-27, New York, 1974.

3 Metzger, D. E., Takeuchi, D. I., and Kuenstler, P. A., "Effectiveness and Heat Transfer with Full Coverage Film Cooling," ASME JOURNAL OF ENGINEERING FOR POWER, Vol. 95, 1973, pp. 180–184.

4 Ville, J. P., and Richards, B. E., "The Measurement of Film Cooling Effectiveness on Turbine Components in Short Duration Wind Tunnels," *AGARD CP 229*, Paper 34, 1977.

5 Liess, C., "Experimental Investigation of Film Cooling with Ejection from a Row of Holes for the Application to Gas Turbine Blades," ASME JOURNAL OF ENGINEERING FOR POWER, Vol. 97, Jan. 1975, pp. 21–27.

6 Eriksen, V. L., and Goldstein, R. J., "Heat Transfer and Film Cooling Following Injection Through Inclined Circular Holes," ASME *Journal of Heat Transfer*, Vol. 96, May 1974, pp. 239–245.

7 Metzger, D. E., and Fletcher, D. D., "Evaluation of Heat Transfer for Film Cooled Turbine Components," *Journal of Aircraft*, Vol. 8, No. 1, 1971, pp. 33–38.

8 Lander, R. D., Fish, R. W., and Suo, M., "External Heat Transfer Distribution on Film Cooled Turbine Vanes," *Journal of Aircraft*, Vol. 9, No. 10, 1972, pp. 707–714.

9 Jabbari, M. Y., and Goldstein, R. J., "Adiabatic Wall Temperature and Heat Transfer Downstream of Injection Through Two Rows of Holes," ASME JOURNAL OF ENGINEERING FOR POWER, Vol. 100, Apr. 1978, pp. 303–307.

10 Macleod, N., and Todd, R. B., "The Experimental Determination of Wall Fluid Mass-Transfer Coefficients Using Plasticised Polymer Surface Coatings," *Int. J. Heat Mass Transfer*, Vol. 16, 1973, pp. 485–503.

11 Hildebrand, B. P., and Haines, K. A., "Interferometric Measurements Using the Wavefront Reconstruction Technique," *Appl. Opt.*, Vol. 5, 1966, pp. 172–173.

12 Kapur, D. N., and Macleod, N., "Vapour Pressure Determination for Certain High-Boiling Liquids by Holography," *Ind. Eng. Chem.*, Prod. Res. Dev., Vol. 15, No. 1, 1976, pp. 50–54.

13 Hay, N., Lampard, D., and Saluja, C. L., "Application of the Swollen Polymer Technique to the Study of Heat Transfer on Film Cooled Surfaces," *7th International Heat Transfer Conference*, Munich, Vol. 4, 1982, pp. 503–508.

14 Macleod, N., "Holographic and ESPI Techniques for Mass Transfer Measurement and Heat Transfer Estimation," *International J. of Optics and Lasers in Engineering*, to be published.

15 Foster, N. W., and Lampard, D., "The Flow and Film Cooling Effectiveness Following Injection through a Row of Holes," ASME JOURNAL OF ENGINEERING FOR POWER, Vol. 102, No. 3, July 1980, pp. 584–588.

16 Kline, S. J., and McClintock, F. A., "Describing Uncertainties in Single Sample Experiments," *Mechanical Engineering*, 1953, pp. 3–8.

17 Knudsen, J. G., and Katz, D. L., *Fluid Dynamic and Heat Transfer*, McGraw-Hill, 1958, p. 487.

18 Rohsenow, W. M., and Hartnett, J. P., *Handbook of Heat Transfer*, McGraw-Hill, 1973, p. 8, 58.

19 Saluja, C. L., "Film Cooling from Rows of Discrete Holes," Ph.D. thesis, University of Wales Institute of Science and Technology, Cardiff, 1977.

20 Afejuku, W. O., Hay, N., and Lampard, D., "Measured Coolant Distributions Downstream of Single and Double Rows of Film Cooling Holes," ASME Paper No. 82-GT-144, 1982.

R. J. Goldstein

E. R. G. Eckert

H. D. Chiang

Department of Mechanical Engineering,
University of Minnesota,
Minneapolis, Minn. 55455

E. Elovic

General Electric Company,
Cincinnati, Ohio

Effect of Surface Roughness on Film Cooling Performance

An experimental investigation of film cooling on a rough surface has been performed using a mass transfer technique. Two injection geometries (one and two rows of holes) and six roughness patterns were used. The density of the injected gas was close to that of the free-stream air. The presence of roughness causes a decrease in the spanwise-averaged effectiveness for both injection geometries at low blowing rates, and an increase in the effectiveness for one-row injection at high blowing rates, but not for two-row injection. The results for two-row injection (with or without roughness) can be correlated by a parameter used to correlate slot-injection data. The influence of roughness pattern on the average effectiveness and on the lateral uniformity of the effectiveness is described.

Introduction

Film cooling has been widely used as a means of protecting solid surfaces exposed to high-temperature gas streams, especially in gas turbines. Past analytical and experimental studies, in general, assume a smooth wall surface. However, in the operation of gas turbines, the surface often becomes rough either by corrosion or by deposits from contaminants in the fuel or brought in with the atmospheric air. The effect of roughness on film cooling performance is thus of practical importance.

The present paper reports the results of film cooling measurements with discrete hole injection of air into an air stream flowing over a rough surface. A mass transfer technique is used to obtain the analogue of the adiabatic wall temperature. Helium is used as tracer gas in the secondary (injected) flow, and its concentration is determined by gas chromatography. In the reported results, the density of the injected gas is close to that of the mainstream air.

2 Apparatus

Measurements are taken in an open cycle wind tunnel with a 25cm-wide by 13cm-high test section. Mainstream air flows through a filter, a flow straightener, a series of three screens, and a 9-to-1 contraction section before entering the test section. After the test section, the air passes through a blower which discharges it into the atmosphere.

The injection system includes an orifice-metered air blower system to supply the air. Helium comes from a high-pressure cylinder and is regulated by capillaries. The air and helium flow through a mixing chamber and a plenum chamber before being injected into the mainstream. The air-helium mixture density is kept at 0.95 of the mainstream air density. A separate plate (removable) into which the jet holes are drilled is part of the test surface. It measures 24cm by 8cm (in flow direction) and sits on a 1cm step around its edges so that its lower open surface is 22cm by 6cm. The thickness of the plate is 1.9 cm.

The velocity of the main flow in the test section is either 30 or 45 m/s. The boundary layer on the test surface is "tripped" by a wire at the outlet of the contraction section; it is both turbulent and uniform across the width of the section. The displacement thickness at $X/D=0.0$ (measured in the absence of the injection holes) is 1.5 mm when the free-stream velocity is 45 m/s.

Two injection geometries are used – namely, one or two rows of injection holes. The injection holes are circular, $D=6.35$mm, and inclined by 35 deg to the mainstream flow. Eleven holes are arranged at three diameter centerline to centerline spacing across the span for the one-row case. For the two-row geometry, the staggered second row of ten holes is situated 2.6D upstream of the first row (Fig. 1).

Gas samples are taken through suction taps installed at specific locations along the test surface. A vacuum pump draws the gas through the taps. The gas flows through vinyl tubes to glass sampling loops which store the gas samples for later analysis in a gas chromatograph. The sampling process and the gas analysis procedure are similar to that used in reference [1]. Twenty-eight taps are arranged in four columns. The lateral positions of each of the four columns (e.g., Taps A-D, Fig. 1) are $Z/D=0.0$, 0.5, 1.0, and 1.5, respectively. The streamwise positions of the seven taps within each column are $X/D=4.7$, 8.7, 14.7, 20.7, 28.7, 38.7, and 50.7, respectively, for one-row injection, and are all smaller by $X/D = 0.7$ for two row injection, e.g., 4.0 instead of 4.7.

The surface roughness geometry was selected to simulate the roughness encountered on turbine blades. A blade with film cooling on both the suction and pressure sides was inspected for this purpose. The blade came from a turbine used in a relatively dirty environment. On the suction side,

Contributed by the Gas Turbine Division of THE AMERICAN SOCIETY OF MECHANICAL ENGINEERS and presented at the 29th International Gas Turbine Conference and Exhibit, Amsterdam, The Netherlands, June 4-7, 1984. Manuscript received at ASME Headquarters, December 27, 1983. Paper No. 84-GT-41.

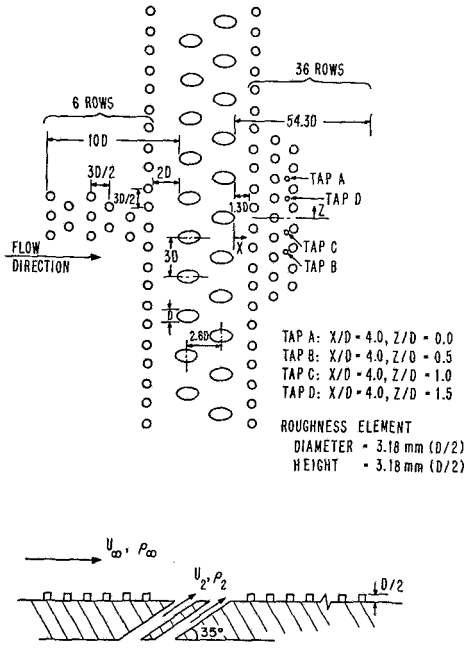

Fig. 1 Schematic of test plate for one roughness pattern (BH2H)

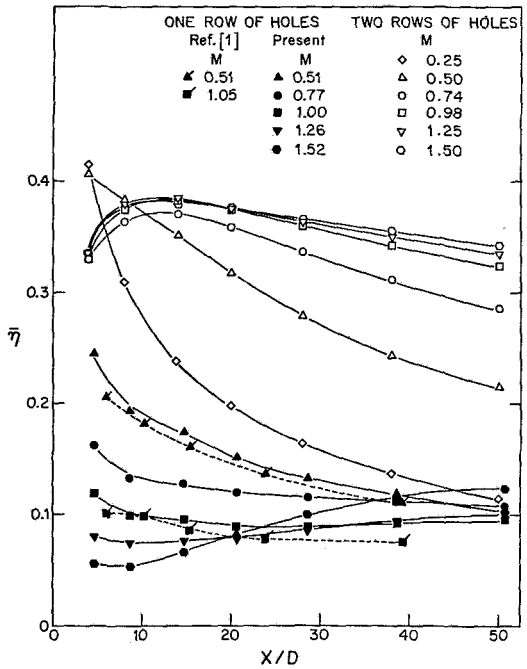

Fig. 2 Spanwise-averaged effectiveness as function of downstream position for smooth surface

roughenss was present upstream of the film cooling holes while, on the pressure side, there was roughness mainly downstream of the holes with some accumulation also occuring upstream. The height and spacing of the surface roughness were measured. A regular geometrically well-defined roughness pattern was designed to simulate the pattern found on the turbine blade.

Surface roughness in the tests is provided by cylindrical roughness elements with a diameter of 3.2mm ($D/2$) and a height of either 3.2mm ($D/2$) or 1.6mm ($D/4$) glued onto the test surface in a regular array. The roughness elements are in staggered rows with 1.5 D spacing between the rows and between individual elements in a row. Each row of roughness elements essentially covers the width of the tunnel. The height of the taller roughness elements ($D/2$) is modelled from the measurements of the inspected turbine blade section.

Six different roughness patterns are used – a combination of one of the two different-sized roughness elements placed in one of three different locations relative to the injection holes: roughness upstream only; downstream only; and both upstream and downstream. The upstream roughness has six rows of elements. The last row is 2D upstream of the upstream edge of the holes (the first row of holes in the two-row injection case). The downstream roughness is provided by 36 rows of elements, the first row is 2D downstream of the downstream edge of the injection holes (1.3D from the downstream edge of the second row of holes in the two-row case). A schematic of one of the six roughness patterns used in the present study is shown in Fig. 1. It is designated BH2H roughness. The notation of the roughness patterns is described in Appendix A.

3 Results

3.1 Effectiveness on a Smooth Surface. The film cooling effectiveness for a smooth surface was measured in the apparatus to provide a reference for the effect of surface roughness. Figure 2 shows the spanwise-averaged effectiveness, $\bar{\eta}$, as a function of the dimensionless downstream distance, X/D, for both one and two rows of injection holes. Some results from reference [1] are shown for comparison.

For two-dimensional film cooling (no variation of mainstream or injected flow across span), a film cooling parameter permits good correlation of the effectiveness data [2]. For the

Nomenclature

D = diameter of injection hole
M = blowing rate, $M = \rho_2 U_2 / \rho_\infty U_\infty$
Re = Reynolds number
U = mean velocity
X = distance downstream of trailing edge of downstream hole
Z = lateral position from centerline of downstream hole
η = local film cooling effectiveness
η_{max} = maximum value of η at a given Z
η_{min} = minimum value of η at a given Z
$\bar{\eta}$ = laterally-averaged film cooling effectiveness
ξ = a dimensionless parameter used in correlating two-dimensional film cooling data; defined in equations (1) and (2)
ζ = lateral smoothness parameter, $\zeta = (\eta_{max} - \eta_{min})/\bar{\eta}$ at a given X/D
μ = dynamic viscosity
ρ = density
$<\bar{\eta}>$ = area-averaged effectiveness, obtained by streamwise averaging of $\bar{\eta}$ between $4 \leq X/D \leq 50$
$<\bar{\eta}/\bar{\eta}_{smooth}>$ = streamwise averaging of $\bar{\eta}/\bar{\eta}_{smooth}$ between $4 \leq X/D \leq 50$ ($\bar{\eta}_{smooth}$ is $\bar{\eta}_{NO1H}$ or $\bar{\eta}_{NO2H}$ for one-row or two-row injection, respectively)

Subscripts

2 = secondary or injection flow
smooth = no surface roughness
∞ = mainstream flow

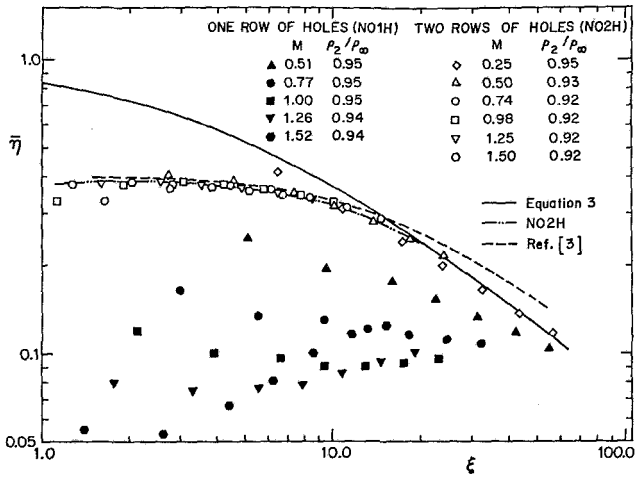

Fig. 3 Variation of spanwise-averaged effectiveness, $\bar{\eta}$, with film cooling parameter, ξ, for smooth surface

present study, this two dimensional parameter, ξ, is defined to be

$$\xi = \left(\frac{X}{D} + 1.909\right) \frac{6}{\pi M} \left(\frac{\mu_2}{\mu_\infty} \frac{\pi}{6} \mathrm{Re}_2\right)^{-1/4} \quad (1)$$

for two rows of injection holes [3], and

$$\xi = \frac{X}{D} \frac{12}{\pi M} \left(\frac{\mu_2}{\mu_\infty} \frac{\pi}{12} \mathrm{Re}_2\right)^{-1/4} \quad (2)$$

for one row of holes, where, in both cases, $\mathrm{Re}_2 = \rho_2 U_2 D/\mu_2$.

The variation of $\bar{\eta}$ with ξ for the present results is plotted in Fig. 3. Also plotted as a solid line on Fig. 3 is a theoretical prediction of two-dimensional film cooling adapted [2] from an analysis by Kutateladze and Leont'ev:

$$\eta = (1 + 0.249\ \xi)^{-0.8} \quad (3)$$

and a dashed line representing results presented in reference [3] for injection through two rows of holes with a smooth plane surface. A curve (NO2H) is also fitted to the two-row smooth surface data of the present study to be used in later comparisons.

From Fig. 3 one can see that the parameter ξ correlates film-cooling results for two rows of injection holes but does not correlate the data for one row of holes. With the two-row injection geometry, the interaction between the jets from the two staggered rows reduces the lateral nonuniformity. This interaction prevents the mainstream from flowing around and under individual jets and the rows of jets behave like a pseudo-two-dimensional sheet to the main flow. Even so at high blowing rates and/or small x (small ξ), the effectiveness is lower than that found with two-dimensional film cooling; the effectiveness at low blowing rate with the two staggered rows is comparable to that with a two-dimensional slot.

A characteristic of the discrete-hole injection geometry is the three-dimensional nature of the flow field and the resulting lateral nonuniformity in the effectiveness. A dimensionless lateral smoothness parameter, ζ, is defined at a given X/D by

$$\zeta = \frac{\eta_{\max} - \eta_{\min}}{\bar{\eta}} \quad (4)$$

The variation of ζ with X/D is presented in Fig. 4 for one and two-row injection geometries. The smaller value of ζ for the two-row geometry indicates a more uniform lateral distribution of effectiveness.

3.2 Influence of Roughness on the Average Effectiveness. Quantitative effects of the different roughness sizes and locations are investigated by comparing the effectiveness on

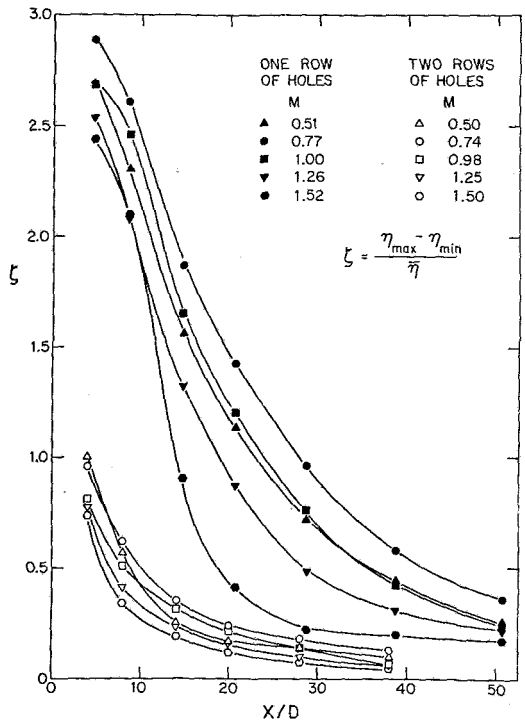

Fig. 4 Variation of lateral smoothness of effectiveness parameter, ζ, with downstream position for smooth surface

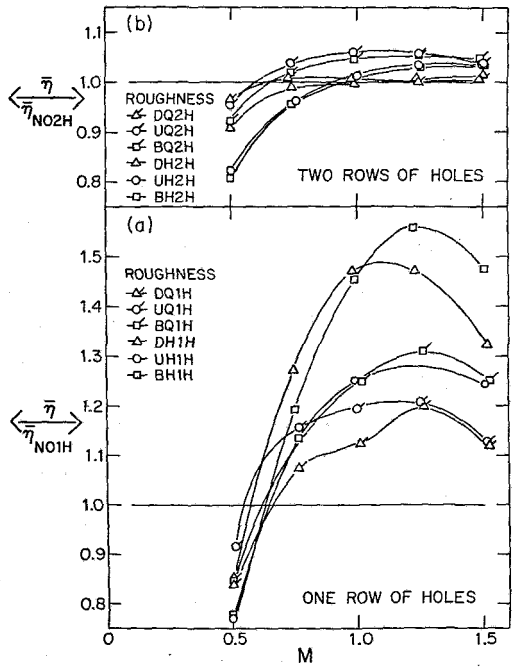

Fig. 5 Effect of roughness (relative to no roughness results) on area-averaged effectiveness as a function of blowing rate.

the rough surface to that on the smooth surface for the same injected flow. In general, the presence of roughness will affect the average effectiveness, the lateral distribution of the local effectiveness, the wall shear stress, and the heat transfer. The present investigation does not provide data for the examination of the last two factors. This section examines the effect of roughness on the average effectiveness. The effect of roughness on lateral variation of η is described in the next section.

The ratio of the average effectiveness with roughness to that with the smooth surface was calculated from the results

of the measurements. The variation of $\bar{\eta}/\bar{\eta}_{smooth}$ is relatively small, less than 30 percent over the entire range of X/D other than for the BH1H roughness at $M > 1.0$, which has a variation in $\bar{\eta}/\bar{\eta}_{smooth}$ of about 50 percent over the investigated range of X/D. This ratio ($\bar{\eta}/\bar{\eta}_{smooth}$) was averaged over the entire range of X/D measured ($4 \leq X/D \leq 50$). The resulting average quantity, $<\bar{\eta}/\bar{\eta}_{smooth}>$, is plotted as a function of the blowing rate, M, for different roughnesses in Figs. 5(a) and 5(b) for the two injection geometries. The presence of roughness causes a decrease in the effectiveness over that of the no-roughness runs for all roughness patterns at small blowing rates. At larger M, roughness can result in a significant improvement of the effectiveness for one row of injection holes, while for two rows of injection holes the improvement is minimal. These trends can be explained in the following way. For small M, the jet momentum is small and the injected flow remains attached to the wall. The presence of roughness induces more vigorous mixing between the mainstream and the secondary flows near the wall, decreasing the effectiveness due to greater dilution of the coolant. The situation is more complex at larger blowing rates. In the case of one row of holes, the high momentum of the secondary jets causes "blow-off" and the jets penetrate into the main flow away from the wall. The roughness causes more turbulent mixing and reduces the penetration of the secondary jets, thus improving the effectiveness. Note that the transition from a decreased to an increased effectiveness with roughness occurs at $M \sim 0.6$ for one row of holes; this roughly corresponds to the "blow-off" blowing rate for the density ratio, ρ_2/ρ_∞, used. With two rows of injection holes there is little improvement at higher M when roughness is present as the interaction between the staggered rows of jets already provides an almost continuous flow across the span, preventing "blow-off"; the effect of additional mixing caused by the presence of roughness is small.

With injection through a single row of holes, the effectiveness for all roughness patterns relative to that for no-roughness increases as M increases, reaches a maximum around $M = 1.25$, and decreases as M increases further. This maximum is primarily due to the minimum—around $M = 1.25$ (cf, Fig. 2 or 3)—of the area-averaged effectiveness, $<\bar{\eta}>$, for a smooth surface. The decrease in $<\bar{\eta}>$ with increasing M for a smooth surface in the range of $0.5 < M < 1.25$ is due to the "blow-off" of jets from the surface and the subsequent increase with M is due to the reattachment of the jets back to the wall by deflection from the main flow.

The effect of roughness element height ($D/2$ or $D/4$) can be observed on Fig. 5. For one row of holes, on a configuration-to-configuration basis, the taller roughness elements produce a bigger decrease in effectiveness relative to that of no-roughness case at $M < 0.6$ and generate a bigger improvement at $M > 0.6$ as compared to the shorter roughness elements. With the two-row geometry a similar influence is found (see Fig. 5(b)), at least at small M. Compared to the shorter roughness elements, the taller roughness elements cause greater mixing of the jets near the wall; at low M, this decreases the area-averaged effectiveness; at higher M, it will reduce the "blow-off" effect (for one-row-of-holes) and increase the area-averaged effectiveness.

The influence of roughness location (roughness downstream only "D," upstream only "U," and both upstream and downstream "B") can also be observed on Fig. 5. For the one-row geometry, the "B" configuration provides the largest improvement at large M, while the "U" configuration yields the smallest improvement. For moderate blowing rates, say $0.6 < M < 1.2$, the "B" configuration has a better improvement than the "U" configuration. However, DH1H now has the biggest improvement and DQ1H has the smallest improvement. At low M ($M < 0.6$), there is insufficient data to show any clear-cut effect of roughness location.

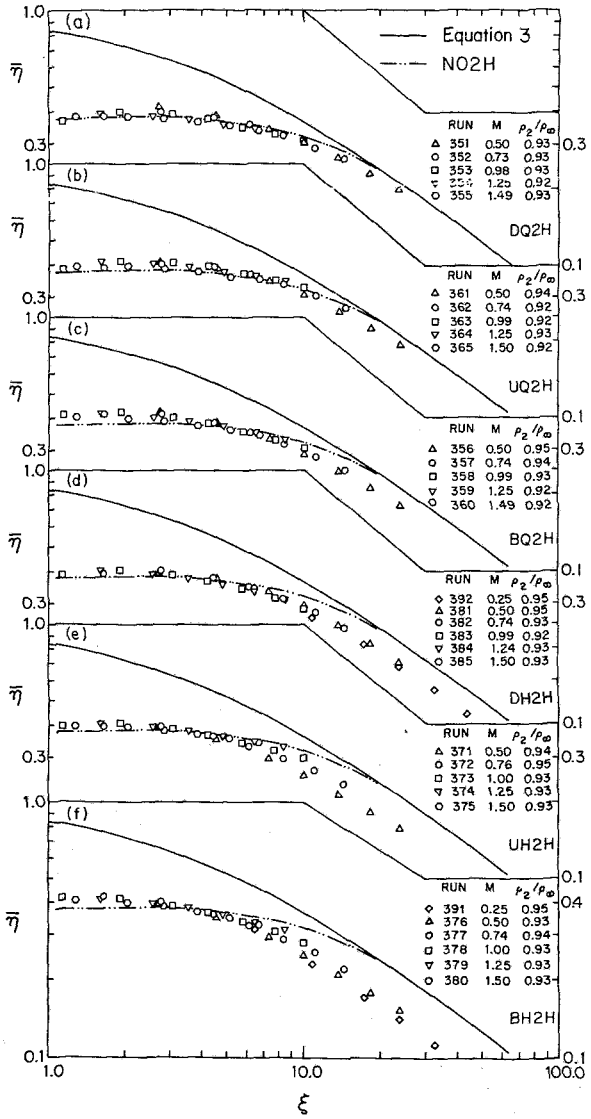

Fig. 6 Variation of spanwise-averaged effectiveness, $\bar{\eta}$, with film cooling parameter, ξ, for various roughness configuration with injection through two rows of holes.

Upstream roughness will increase the turbulent intensity in the approaching boundary layer, and downstream roughness will increase the mixing between the jets and the main flow. The effect of upstream roughness is less pronounced at large M where turbulent mixing is already vigorous; however, for the larger roughness height located upstream at small M, enough turbulence will be generated to have a big negative effect on the area-averaged effectiveness. The downstream roughness has a small effect at smaller M and produces different behaviors at larger M depending on the roughness sizes. Before the blown-off jets reattach to the wall ($0.6 < M < 1.2$), DH1H roughness produces the largest effectiveness and DQ1H the smallest; after reattachment ($M > 1.2$), both DH1H and DQ1H have an effect between that of the corresponding "U" and "B" configurations.

The above observations suggest that mixing between the jets and the mainflow (increased by downstream roughness) plays a more important role in reducing the "blow-off" phenomenon than approaching turbulent intensity (increased by upstream roughness) for the larger roughness size. For $0.6 < M < 1.2$, where the penetration of the jets is still small, having upstream roughness in addition to downstream roughness actually has an adverse effect—i.e., the im-

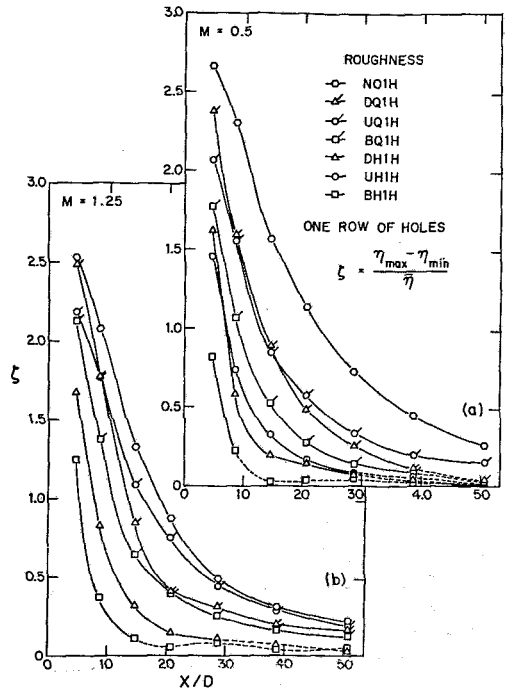

Fig. 7 Variation of lateral smoothness of effectiveness parameter, ζ, with downstream position for one-row injection with roughness

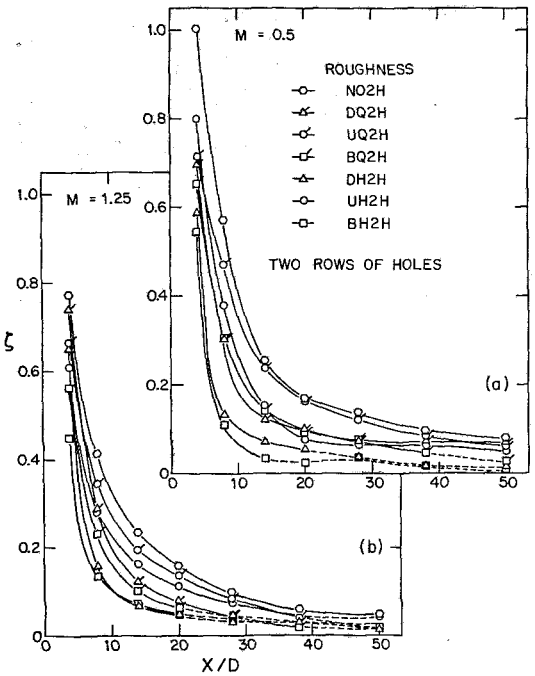

Fig. 8 Variation of lateral smoothness of effectiveness parameter, ζ, with downstream position for two-row injection with roughness.

provement in effectiveness is slightly less (BH1H vs DH1H). For $M > 1.2$, the jet momentum is high enough that both upstream and downstream roughnesses are needed for best reduction of "blow-off". With the shorter roughness elements, both the approaching turbulence level and the downstream mixing of jets and mainflow are moderate. In this case, having roughness elements upstream has a bigger effect than having them downstream for $0.6 < M < 1.2$; at $M > 1.2$, their individual effects are comparable.

With two-row injection, the effect of roughness can be investigated by using the parameter ξ. The variation of $\bar{\eta}$ with ξ for runs with two rows of holes is presented in Fig. 6. Figures 6a-f give results for DQ2H, UQ2H, BQ2H, DH2H, UH2H, and BH2H roughnesses, respectively. Also plotted on each of the figures is a curve which approximates the smooth surface (NO2H) results from Fig. 3. All the different roughness patterns can be correlated by ξ, suggesting a pseudo-two-dimensional behavior. The effect of roughness on effectiveness is minimal for $\xi < 6.0$, though, for some roughness patterns, there is a slight improvement over the no-roughness results. Small ξ corresponds to situations of high M and/or low X/D. For $\xi > 6.0$, UH2H and BH2H roughnesses (Figs. 6(*e*) and 6(*f*)) cause the biggest decrease in effectiveness; DQ2H and UQ2H (Figs. 6(*a*) and 6(*b*)) cause a small drop in effectiveness and, with BQ2H and DH2H (Figs. 6(*c*) and 6(*d*)), the decrease in effectiveness is moderate. The decrease in effectiveness is due to greater mixing of the injected flow with the mainstream when the roughness is present.

3.3 Effect of Roughness on Lateral Smoothness. The effect of roughness on the variation of η across the span can be assessed by comparison of ζ for various roughness types, as shown in Fig. 7 and 8 for one-row injection and two-row injection, respectively. Dotted lines indicate situations where the wall concentration profile can practically be considered as constant in the Z direction.

The presence of roughness results in a flatter profile as compared to the no-roughness case. As expected, the relative change is more pronounced for one row of holes since the wall concentration profile for NO2H is already relatively smooth. More mixing due to the presence of roughness causes the increased uniformity of the local effectiveness over the span of the surface. The taller roughness elements induce greater mixing and generate a flatter lateral distribution than the shorter roughness elements except perhaps for upstream roughness and two-row injection at small M and $X/D < 5.0$ (see Fig. 8(*a*)).

For one row of holes the "*B*" configuration gives the most uniform profile. The "*D*" and "*U*" configurations produce comparable results with the "*D*" configuration giving a slightly flatter lateral profile at large X/D, and the "*U*" configuration causing a somewhat more uniform distribution for small X/D. For two rows of holes the effectiveness is essentially uniform at X/D over 20.0; significant variations of effectiveness with Z occur for $X/D < 10.0$. Here the "*B*" configuration gives the flattest profile, with the "*D*" configuration next, and then the "*U*" configuration. The *UQ2H* configuration has almost the same lateral smoothness in effectiveness as does a smooth surface.

4 Conclusion

Surface roughness typical of that found on gas turbine blades exposed in a system operating in a relatively dirty environment can have a significant impact on film cooling performance – particularly with injection through a single row of holes. At low blowing rates, there is a decrease in the adiabatic wall effectiveness of the order of 10-to-20 percent over that compared to a smooth surface under similar conditions. However, at higher blowing rates, when the jets tend to lift-off from the surface, the film cooling performance is improved significantly, by as much as 40-to-50 percent under some conditions. This improvement follows from the greater turbulence and mixing with the rough surface, which tends to dissipate the injected flow and prevent it from penetrating as far into the mainstream. The effects are most pronounced with the largest roughness elements and generally also when the roughness is both upstream and downstream of the injection section. Although the general trends are similar with two rows of injection holes, the net effect is much smaller, particularly relative to the improvement that occurs at large blowing rates.

For injection through a single row of holes, a rough surface also produces a relatively uniform lateral distribution of film cooling effectiveness, as compared to that of a smooth surface. Similar trends were found with two rows of injection holes, although this injection system does not have a large lateral variation, even with a smooth surface. Lateral variation of effectiveness could be important in affecting temperature gradients and thermal stresses.

Care should be taken in interpretating the significant improvements and the magnitude of the effectiveness as well as the lateral smoothness of the effectiveness in terms of getting better film cooling performance with a rough surface. With such a surface, the magnitude of the heat transfer coefficient is expected to be larger than that of a smooth surface with or without film cooling. This would also, perhaps, point to the greater need of having film cooling when the surface is rough.

Acknowledgment

Financial support for this study by the Advanced Technology Program, Aircraft Engine Group, General Electric Company is gratefully acknowledged.

References

1 Pedersen, D. R., Eckert, E. R. G., and Goldstein, R. J., "Film Cooling with Large Density Differences Between the Mainstream and the Secondary Fluid Measured by the Heat-Mass Transfer Analogy," *Journal of Heat Transfer*, Vol. 99, 1977, pp. 620-627.

2 Goldstein, R. J., "Film Cooling," *Advance in Heat Transfer*, Vol. 7, p. 331 and p. 334. Edited by Irvine and Hartnett, New York: Academic Press, 1971.

3 Jabbari, M. Y., and Goldstein, R. J., "Adiabatic Wall Temperature and Heat Transfer Downstream of Injection Through Two Rows of Holes," ASME JOURNAL OF ENGINEERING POWER, Vol. 100, 1978, pp. 303-307.

APPENDIX

Classification of the Test System

In addition to the flow rates, parameters that were varied in the present test relate to the roughness pattern, the flow geometry, and the injected gas. To classify each series of tests, a four-character word is employed. This includes the following parameters:

1. roughness location;
2. type of roughness elements;
3. number of rows of holes; and
4. density ratio.

The first character designates the location of roughness used:

U = roughness elements upstream of injection hole only
D = downstream only
B = both upstream and downstream
N = no roughness

The second character designates the type of roughness elements employed (all elements had a diameter half that of the injection holes):

H = 3.2 mm height, equal to half the injection hole diameter (or $D/2$)
Q = 1.6 mm height, equal to one-quarter the injection hole diameter (or $D/4$)
0 = no roughness

The third character designates the injection geometry:

1 = one row of injection holes
2 = two rows of injection holes

The last character designates the injection gas density ratio:

H = density ratio 0.95, helium as tracer gas

EXAMPLE: Roughness type BH2H means density ratio 0.95, two rows of holes, roughness element of height D/2 placed both upstream and downstream of injection holes (see Fig. 1).

Film Cooling on a Gas Turbine Blade Near the End Wall

R. J. Goldstein

H. P. Chen

Mechanical Engineering Department,
University of Minnesota,
Minneapolis, Minn. 55455

The local film cooling effectiveness on a gas turbine blade with a row of discrete cooling jets has been measured using a mass transfer technique. Particular emphasis is placed on phenomena near the end wall of the blade. This region contains a horseshoe vortex system modified by a passage vortex. On the concave (pressure) surface the film cooling performance is not greatly altered by the presence of the end wall. On the convex surface of the blade the film cooling is essentially absent in a triangular region extending from near the region of peak curvature on the blade to its trailing edge. This unprotected region closely corresponds to the location of the passage vortex as indicated by flow visualization. The passage vortex sweeps away the injected coolant flow from the surface. Upstream of the unprotected area the injected flow is skewed toward the middle span of the blade. The influence of the end wall extends about one-half chord length up from the end wall in the present experiments.

Introduction

Over the last decade, the average temperature of combustion gas entering the first stage turbine in high performance aircraft gas turbines has increased from 1500K to 1750K; of this 250K increase, improved alloys contributed 65K while improved cooling contributed the rest [1]. In the next decade, the entry temperature in some turbine systems is expected to surpass 1900K, yet alloys generally must stay under 1300K [1]. To prevent high-temperature failure, further improvements in cooling methods such as film cooling, and internal convection and impingement heat transfer are required.

The present work is concerned with film cooling – a process in which a coolant injected along a surface exposed to a high temperature gas flow reduces the temperature of the boundary layer and hence the surface.

In studies of film cooling an adiabatic wall effectiveness is generally defined by:

$$\eta_{aw} = \frac{T_{aw} - T_r}{T_2 - T_r} \tag{1}$$

and the heat transfer is calculated from:

$$q = h(T_w - T_{aw}) \tag{2}$$

When η_{aw} and h are known, the local heat transfer can be calculated. Studies on full-coverage film cooling and transpiration cooling often use somewhat different definitions of heat transfer coefficient.

Early studies on film cooling on flat walls are reviewed in reference [2]. The effectiveness in two-dimensional incompressible film cooling mainly depends on the blowing rate, M, injection slot size, and the position downstream of injection. A heat sink model has been successfully used to analyze such a cooling system. For film cooling with injection through discrete holes, the local effectiveness also depends on the transverse position and the relative densities of the injected and mainstream fluids. A heat sink model for three-dimensional film cooling is mainly useful at low blowing rates and when there is not significant interaction among the injected jets. On gas turbine blades with discrete injection, the blade surface curvature and the two end walls make the problem more complex.

The influence of wall curvature on film cooling is most pronounced with injection through discrete holes [3, 4]. Measurements on a linear turbine cascade [4] show the importance of the curvature of the wall surface and the momentum flux of the injected jets relative to that of the mainstream. Thus, at low blowing rates (really, small momentum flux ratio, I), the film cooling effectiveness is better on a convex surface than on a flat plate, which, in turn, has better performance than a concave surface. This relative performance on surfaces of different curvature reverses at large momentum flux ratios. These differences are due to the influence of the pressure gradient normal to the surface and its effect on the curvature of the injected jets which can be distinct from the curvature of the mainstream. The influence of curvature on film cooling performance is considerably reduced with coolant injection through two rows of holes [5].

The present work is an experimental study of the influence of the end wall on film cooling of gas turbine blades using a single row of injection holes. In many gas turbines, the blade span is not large compared to the chord length, and a significant region on the blade is influenced by the end wall. Studies of the velocity field and heat transfer in the end wall region of a blade [6, 7, 8] show the complex flow in this region, which includes a horseshoe vortex system and a passage vortex in the region between two adjacent blades.

Contributed by the Gas Turbine Division of THE AMERICAN SOCIETY OF MECHANICAL ENGINEERS and presented at the 29th International Gas Turbine Conference and Exhibit, Amsterdam, The Netherlands, June 4-7, 1984. Manuscript received at ASME Headquarters, December 27, 1983. Paper No. 84-GT-42.

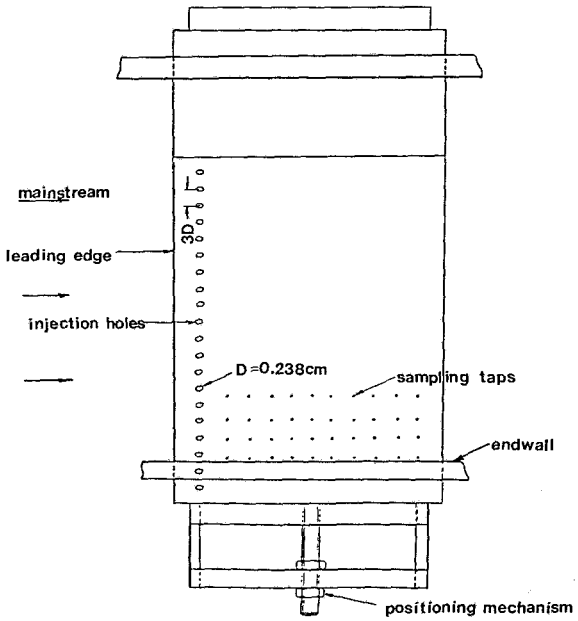

Fig. 1(a) Test blade – view of suction side

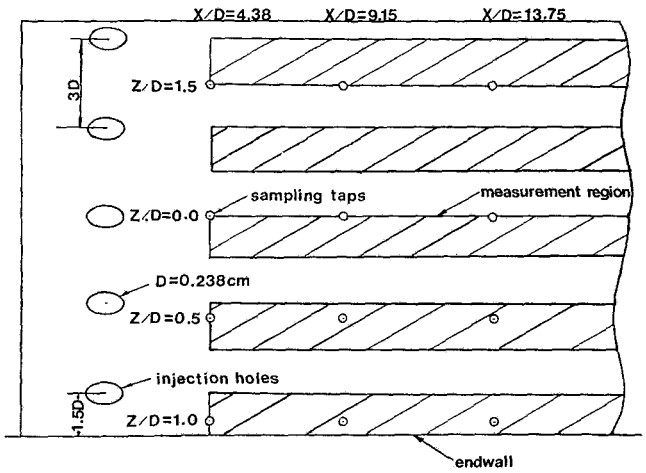

Fig. 1(b) Detail of test blade showing measurement region

Those studies are valuable in establishing the nature of the flow regime which helps explain experimental results of heat transfer and film cooling on the blades themselves.

Experimental System and Test Conditions

The experiments are conducted in a low velocity wind tunnel using a linear cascade of six turbine blades [4]. The inlet and outlet angles of the blade are 45.7 deg and 27.3 deg, respectively, and the angle of attack of the incoming flow is close to zero. The dimensions of the blade are enlarged several times over normal size with a chord length in the cascade of 16.9 cm. Four of the blades are solid. The two central ones are hollow, and are used to provide film cooling – on facing suction (convex) and pressure (concave) surfaces. The diameter of the injection holes is 2.38 mm; they are inclined at an angle 35 deg to the surface, and spaced three diameters apart. A mixture of air and helium is used as the injected fluid; the density is kept at approximately 0.96 that of the freestream. Blowing rates, M, of 0.5 on the convex surface and 0.8 and 1.55 on the concave surface are used. These three blowing rates correspond to values of I of, .26, .67, and 2.5, respectively.

The mass/heat transfer analogy is used to determine the film cooling effectivness. Instead of measuring an adiabatic temperature, the flow is essentially isothermal and the injected flow contains a tracer gas (helium in the present study). The concentration of the helium tracer gas is measured in samples drawn from near the wall through small (0.58 mm dia) sampling taps. As the concentration of helium in the mainstream is zero, the local impermeable wall effectiveness is the ratio of the helium concentration at the wall to that in the plenum which contains the injected fluid,

$$\eta_{iw} = C_{iw}/C_2 \tag{3}$$

The gas samples are collected during a run and later analyzed with a gas chromatograph utilizing a thermal conductivity cell. The sampling holes are distributed across the span at Z locations 0, 0.5, 1.0, and 1.5 diameters from the center of one of the injection holes, and at various positions downstream.

Figure 1 shows the positions of the holes and the sampling taps. The blade can be moved into or out of the end wall by moving it through a slot in the wall. Note that the four rows of sampling taps used are some distance apart. For a single positioning of the blade relative to the end wall, the measurements are taken for each row of sampling taps. These represent the regions between different injection holes. To get a consistent set of data for results between a given pair of holes (at fixed H/D) four different positionings of the blade must be used.

The lowest coolant hole was centered 1-1/2 diameters from the end wall. By moving the blade to somewhat more than a dozen different locations into or out of the end wall, a series of measurements can be taken which represent the area immediately below (i.e., toward the end wall) the lowest twelve

Nomenclature

$a_1 - a_2$ = attachment line, Fig. 5
C_{iw} = concentration of tracer at impermeable wall
C_2 = concentration of tracer in injected gas – usually measured in plenum
D = diameter of injection hole
h = heat transfer coefficient
H = distance along blade surface from end wall
M = blowing rate $\rho_2 U_2/\rho_\infty U_\infty$
I = momentum flux ratio $\rho_2 U_2^2/\rho_\infty U_\infty^2$
q = wall heat flow per unit time and area
R = density ratio ρ_2/ρ_∞
S_{S1} = saddle point, Fig. 5
$S_1 - S_2$ = separation line, Fig. 5
T = temperature
T_{aw} = adiabatic wall temperature
Tr = wall recovery temperature
T_w = wall temperature
T_2 = temperature of injected flow
U_2 = mean velocity in injection hole
U_∞ = mainstream velocity at injection hole location
X = distance downstream of downstream edge of injection holes
Z = transverse distance from center of injection hole to sampling hole; measured toward the end wall in present tests
α = angle between the injection hole centerline and local blade surface; 35 deg in present tests
η_{aw} = local adiabatic film-cooling effectiveness
η_{iw} = local impermeable -wall effectiveness
ρ_2 = density of injected flow
ρ_∞ = density of mainstream
δ_{99} = boundary layer thickness; distance from wall where velocity is 99 percent of free stream velocity

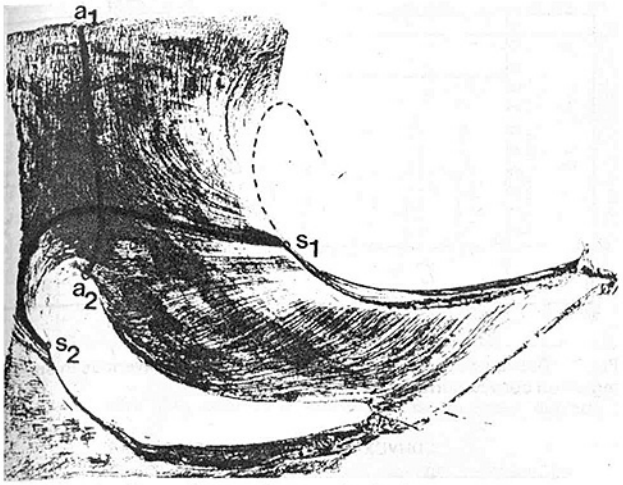

Fig. 2 Streamline tracks on endwall of gas turbine blade

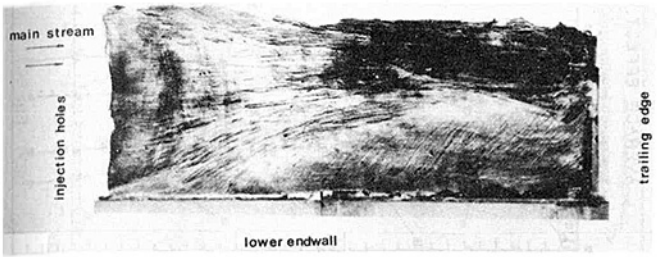

Fig. 3 Streamline tracks on convex surface of gas turbine blade

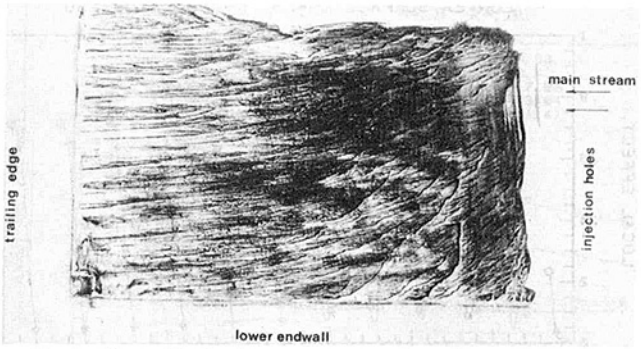

Fig. 4 Streamline tracks on concave surface of gas turbine blade

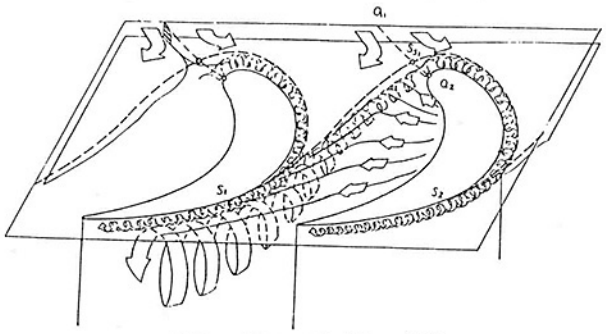

Fig. 5 Sketch of the flow near endwall of gas turbine blade

holes. The shaded areas show the regions over which the effectiveness can be measured. Note that these represent only one-half of the surface as the sampling taps were designed for a study in the central span of a blade where the flow is essentially symmetrical around an injection hole. This can be observed in the data (e.g., Fig. 6) where curves are drawn through the set of four data points which correspond to the position below each of the holes studied. These holes are positioned such that their centers are, 1-1/2 , 4-1/2, 7-1/2, ... and 37-1/2 diameters from the end wall.

As measurements are taken only over half of the area, there may be a slight error in the average effectiveness at different heights. In the case of essentially symmetric flow around a blade hole, this would not be important. However, in the end wall region, the flow is not symmetric; rather the jet is skewed either down toward the end wall or up toward the center of the span.

The mainflow velocity at the injection location is 19.8 m/s on the convex surface and 4.6 m/s on the concave surface. The flow of the mainstream approaching the blade cascade is approximately 11 m/s; the boundary layer of this flow on the end wall has a thickness, δ_{99}, of approximately 2 cm.

Flow Visualization

Flow near the end wall of a blade is studied using a mixture of fine carbon powder and oil spread on contact paper attached to the end wall and the blade surfaces. During exposure to the tunnel flow, the streamlines are traced on the paper. Figures 2, 3, and 4 show traces recorded on the end wall, convex surface, and concave surface, respectively. These results are in accord with those presented in reference [7], with a slight deviation on the concave surface. In the present study, skewing is observed of the flow over the concave surface with streamlines bent down toward the end wall. The flow phenomena can also be inferred from the present measurements of film cooling effectivness on the concave surface. The lines drawn on Fig. 2 are discussed below in the description of Fig. 5.

When a circular cylinder is exposed to a crossflow, the mainstream velocity near the front stagnation region decreases and the static pressure rises. In the three-dimensional region near the wall at the base of the cylinder, the velocity in the boundary layer is less than that in the mainstream. The result is a pressure gradient along the cylinder and a velocity component towards the wall which leads to a horseshoe vortex flow. Similarly, in the end wall region of a gas turbine blade, a horseshoe vortex system is formed, but the development of the flow is asymmetric. This is substantially due to the presence of a passage vortex, which, in turn, is due to the difference in pressure across the passage between two blades, with pressure being higher on the concave (pressure) side as compared to the convex (suction) side. Away from the end wall, this pressure difference is balanced by inertia forces as the flow curves around the blades. In the end wall region where the boundary layer is present, the inertia forces are not sufficient to overcome the pressure difference and a flow is established from the pressure side of one blade towards the suction side of the adjacent blade.

The passage vortex is shown in Fig. 5, along with the two legs of the horseshoe vortex formed around the blade (cf. reference [7]). A separation line, indicated by $S1 - S2$, is present in the boundary layer in front of a blade. The attachment line, $a1 - a2$, extends from the incoming flow to the front stagnation point. It intersects the separation line at the saddle point, S_{S1}. These lines are also drawn on the flow traces in Fig. 2. In front of the saddle point, the attachment line divides incoming flow entering the blade passage from that entering the adjacent passage. After the saddle point it divides the passage crossflow moving on to the convex surface of the neighboring blade from the flow moving around the leading edge of the blade onto the convex surface of the same blade. The leg of the horseshoe vortex formed on the pressure side of the blade is moved over towards the suction side of the adjacent blade by the passage vortex, which constantly feeds into the flow causing it to develop into a large vortex. The vortex that is formed initially on the suction side tends to

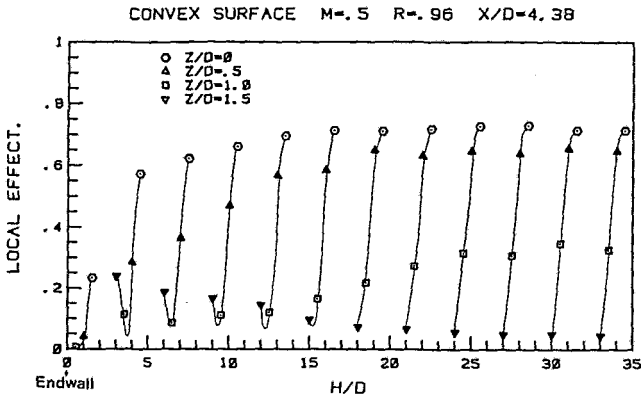

Fig. 6(a) Local film cooling effectiveness on convex surface at $M = 0.5$

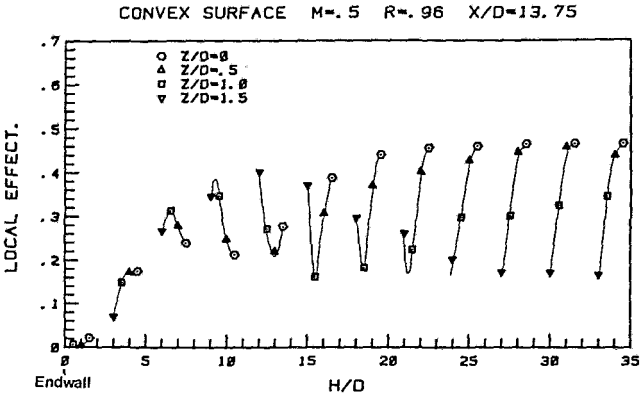

Fig. 6(b) Local film cooling effectiveness on convex surface at $M = 0.5$

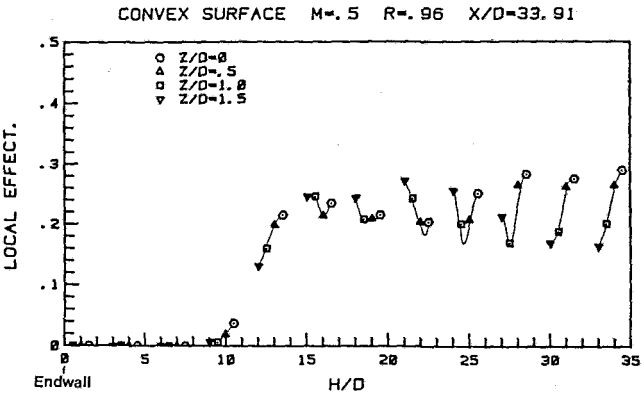

Fig. 6(c) Local film cooling effectiveness on convex surface at $M = 0.5$

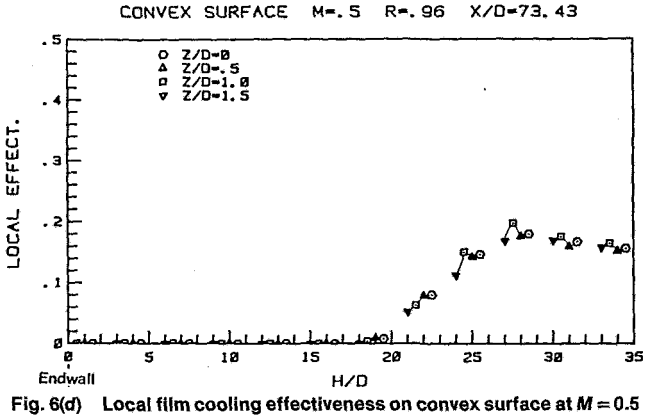

Fig. 6(d) Local film cooling effectiveness on convex surface at $M = 0.5$

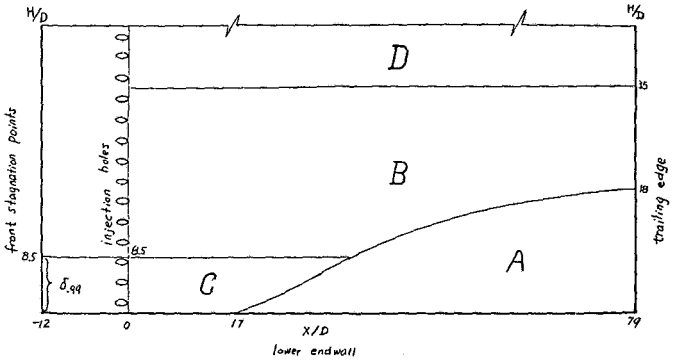

Fig. 7 Distribution range of local film cooling effectiveness in endwall region on convex surface of a blade

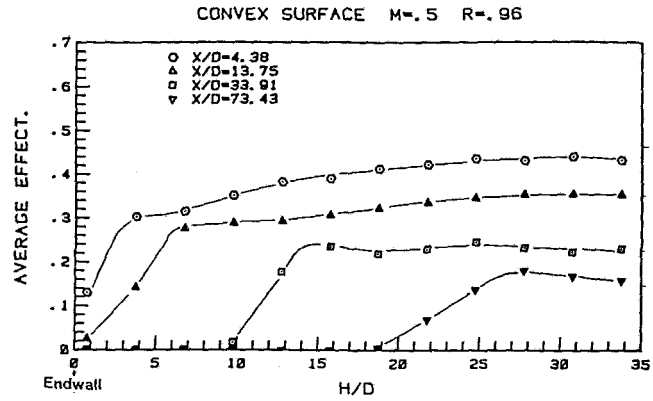

Fig. 8 Average film cooling effectiveness on convex surface at $M = 0.5$

diminish as it flows around the blade because of its opposite sense to that of the passage vortex. It finally becomes a small counter (corner) vortex or can be almost completely dissipated. The exact flow field in the end wall region depends on the position of the saddle point and the strength of the passage vortex which relate to the geometry of the blade cascade and incoming flow conditions, including angle of attack, incoming boundary layer thickness, and Reynolds number.

The passage vortex sweeps across the convex surface of the blade some distance from the stagnation region. The affected region on the blade appears to have a clear boundary and an almost triangular shape – in the present system, the trailing edge of the region is at an elevation of 4.3 cm above the end wall. Outside the triangular region, the streamlines near the convex surface are skewed toward the middle span of the blade (cf. Fig. 3). As Fig. 4 indicates, the streamlines by the concave surface are slightly inclined toward the end wall, apparently from the flow that enters into the passage vortex along the end wall. As the distance from the end wall increases, the skew of streamlines on both blade surfaces is reduced. Accurate determination of the flow direction near the blade surface is difficult, as gravity plays a role in the motion of the fluid on the contact paper. However, the general trends are clear in the region close to the passage vortex.

Impermeable Wall Effectiveness

Convex Surface. Figure 6 shows the local effectiveness on the convex surface of the blade. Note that the values of $Z/D > 0$ are all measured towards the end wall and as mentioned above, because of the limited number of sampling taps, only one-half of the region between any adjacent pair of injection holes is examined.

From the local measurements at a blowing rate of 0.5 and a density ratio of .96, different regions on the convex blade

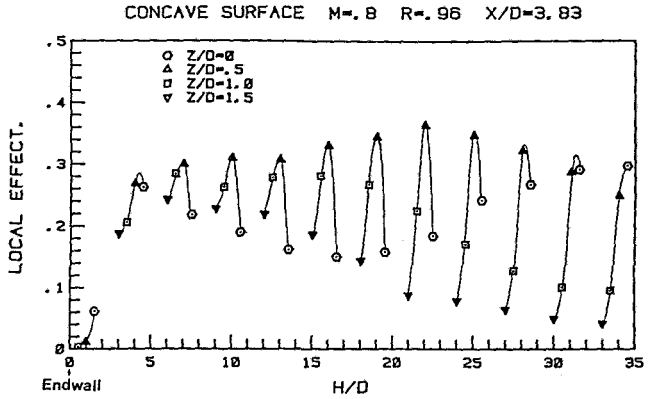

Fig. 9(a) Local film cooling effectiveness on concave surface at $M=0.8$

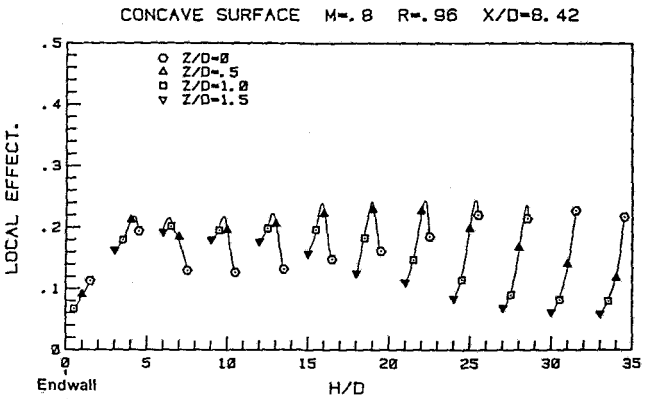

Fig. 9(b) Local film cooling effectiveness on concave surface at $M=0.8$

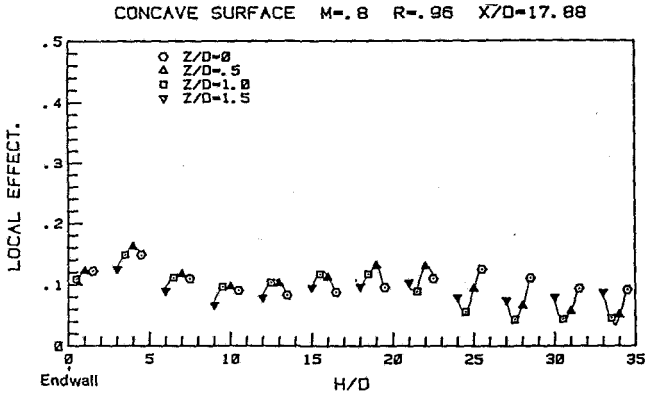

Fig. 9(c) Local film cooling effectiveness on concave surface at $M=0.8$

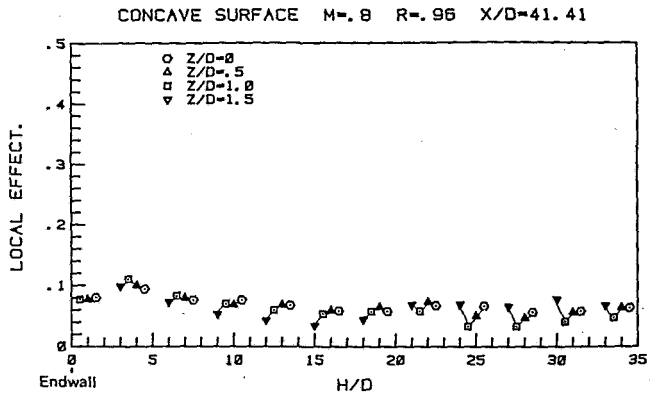

Fig. 9(d) Local film cooling effectiveness on concave surface at $M=0.8$

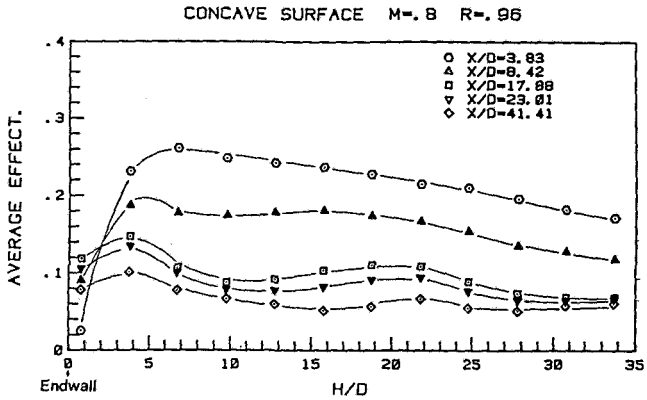

Fig. 10 Average film cooling effectiveness on concave surface at $M=0.8$

surface can be specified in terms of the local flow characteristics and film cooling performance. These areas are mapped out in Fig. 7. Region A is an unprotected region where the film coolant has essentially been stripped from the wall, or displaced by flow from the end wall; the size and shape of this region coincides closely with those of the passage vortex system determined in the visualization tests (cf. Fig. 3) and described in the section on flow visualization. If the end wall had been film cooled, perhaps some coolant might have flowed up into region A. Region B adjacent to this unprotected region is protected by the jets but the flow is skewed due to the presence of the passage vortex beneath region B; this results in a variation of local effectiveness which is not the same as in the two-dimensional flow region (Region D). Thus, where one might expect the maximum effectiveness to occur at a constant transverse position, for example at $Z/D=0$, in region B it occurs at different values of Z/D for different positions H, from the end wall. Region C, close to the end wall and near the injection holes is not strongly affected by the horseshoe vortex or the passage vortex which has not reached the suction surface here. However, the presence of the boundary layer on the end wall reduces the mainstream flow in the region of these injection holes giving an equivalent blowing rate or momentum flux ratio greater than that in the two dimensional flow region and, for the injection rate in the present study, a lower effectiveness.

The average effectiveness on the convex surface as a function of position from the end wall is shown in Fig. 8. These values are obtained by averaging the four points (at different Z/D) determined for each setting of the blade. Recall again, that Z is measured towards the end wall and the average is obtained for only half of the area between each pair of holes. The value of H/D corresponds to the average position, i.e. $Z/D=0.75$ for each setting. At X/D of 73.4, approximately 93 percent of the distance along the surface of the blade from the front stagnation line to the trailing edge of the blade, region A (cf. Fig. 7) extends out to H/D of approximately 18. The outline of region A can be inferred from Fig. 8. The average effectiveness in region B is not greatly different from that in the two dimensional region.

Concave Surface. On the concave surface of the blade, results are presented for two blowing rates, $M=0.8$ and $M=1.53$. For these conditions, values of local effectiveness are plotted on Figs. 9 and 11, and values of average effectiveness are shown on Figs. 10 and 12.

On the concave surface the film cooling effectiveness is not greatly altered by the presence of the end wall. There is an influence of the flow feeding into the passage vortex moving the injected flow, essentially skewing it, towards the end wall which changes the periodicity or phase of the local effectiveness relative to Z/D. The inclination of the streamlines

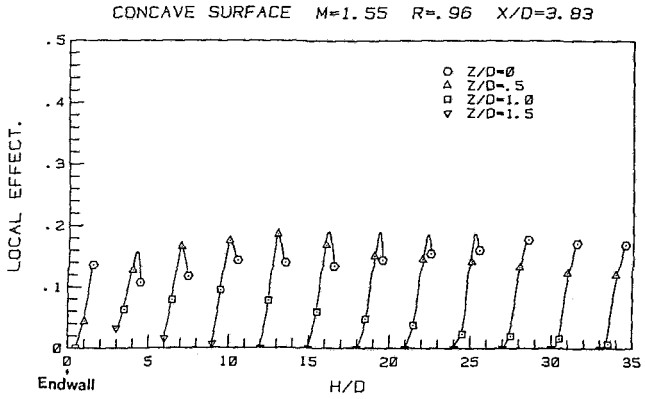

Fig. 11(*a*) Local film cooling effectiveness on concave surface at $M = 1.55$

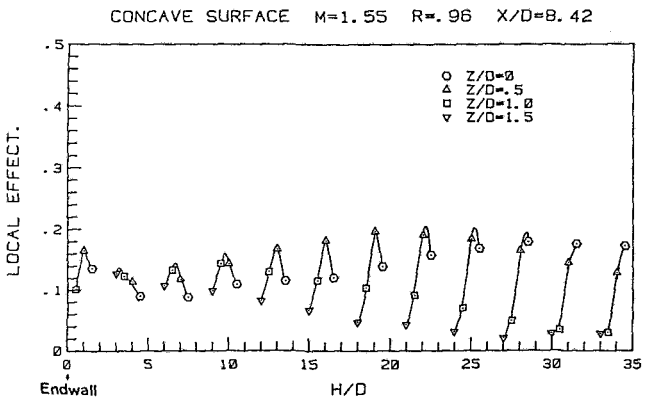

Fig. 11(*b*) Local film cooling effectiveness on concave surface at $M = 1.55$

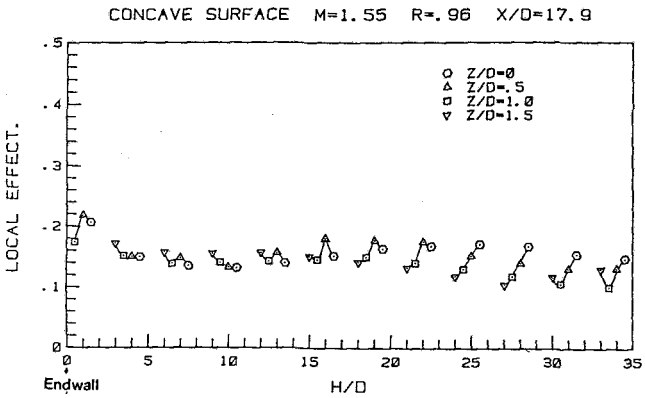

Fig. 11(c) Local film cooling effectiveness on concave surface at $M = 1.55$

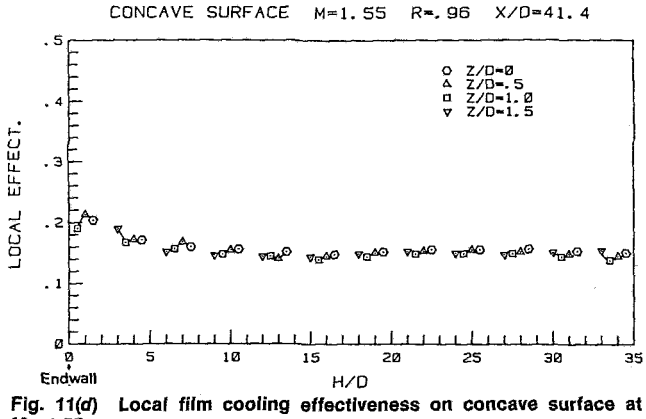

Fig. 11(*d*) Local film cooling effectiveness on concave surface at $M = 1.55$

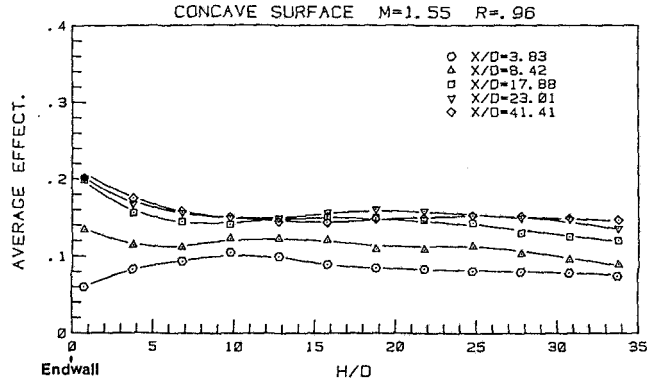

Fig. 12 Average film cooling effectiveness on concave surface at $M = 1.55$

is slight, compared to that on the convex surface. The difference in average effectiveness, relative to that in the two dimensional region, at small values H/D may be due to the presence of the boundary layer on the end wall and its effect on the local value of M or I, as well as the cross flow due to the fluid flowing into the passage vortex. In addition, the flow washing down the blade towards the end wall might result in a piling up of the film coolant near the end wall.

Conclusions

On the convex surface of a gas turbine blade there is a significant region close to the end wall over which the film cooling jets are essentially swept away from the surface by the presence of a passage vortex. This region commences some distance downstream of injection, near the location where the passage vortex reaches the convex surface. Above this region, away from the end wall, the film cooling jets are skewed changing the distribution of local effectiveness, but the average effectiveness is not greatly altered. Film cooling on the concave surface is not significantly affected by the end wall. In some regions it is improved over that in the central portion of the blade span, at least under the present test conditions.

The dimensions over which the influence of the end wall is felt on actual blades will depend on the geometry of the blades and the incoming flow conditions. Further studies are necessary to define the parameters that control the size of the unprotected region along the convex surface.

Acknowledgment

This study was conducted with support from the U.S. Air Force Office of Scientific Research. P. H. Chen was instrumental in the final preparation of this manuscript.

References

1 Hennecke, D. K., "Turbine Blade Cooling in Aeroengines," Von Karman Institute for Fluid Dynamics, Lecture Series 1982-02., and personal communication.

2 Goldstein, R. J., "Film Cooling," *Advances in Heat Transfer*, Vol. 7, Academic Press, New York and London, 1971, pp. 321–379.

3 Nicholas, J., and LeMeur, A., "Curvature Effect on a Turbine Blade Cooling Film," ASME Paper No. 74-GT-156, 1974.

4 Ito, S., Goldstein, R. J., and Eckert, E. R. G., "Film Cooling of a Gas Turbine Blade," ASME JOURNAL OF ENGINEERING FOR POWER, Vol. 100, July 1978, pp. 476–480.

5 Goldstein, R. J., Kornblum, Y., and Eckert, E. R. G., "Film Cooling Effectiveness on a Turbine Blade," to be published in *Israel Journal of Technology*.

6 Langston, L. S., Nice, L. M., and Hooper, R. M., "Three-Dimensional Flow within a Turbine Cascade Passage," ASME No. Paper 76-GT-50.

7 Langston, L. S., "Crossflows in a Turbine Cascade Passage," ASME Paper No. 80-GT-5, 1980.

8 Graziani, R. A., Blair, M. F., Taylor, J. R., and Mayle, R. E., "An Experimental Study of Endwall and Airfoil Surface Heat Transfer in a Large Scale Turbine Blade Cascade," ASME JOURNAL OF ENGINEERING FOR POWER, Vol. 102, Apr. 1980, pp. 257–267.

The Inverse Design of Internally Cooled Turbine Blades

S. R. Kennon
Graduate Research Assistant.

G. S. Dulikravich
Assistant Professor.

Department of Aerospace Engineering
and Engineering Mechanics,
University of Texas at Austin,
Austin, Texas 78712

A methodology is developed for the inverse design and/or analysis of interior coolant flow passage shapes in internally cooled configurations with particular applications to turbine cascade blade design. The user of this technique may specify the temperature (or heat flux) distribution along the blade outer fixed surface shape and the unknown interior coolant/blade interface. The numerical solution of the outer gas flow field determines the remaining unspecified blade outer surface quantity—surface heat flux if temperature was originally specified or vice versa. Along the unknown coolant flow passage shape the designer has the freedom to specify the desired temperature distribution. The hollow blade wall thickness distribution is then found from the solution of Laplace's equation governing the temperature field within the solid portion of the hollow blade, while satisfying both boundary conditions of temperature and heat flux at the fixed outer blade surface, and the specified temperature boundary condition on the evolving inner surface. A first order panel method, coupled with Newton's N-dimensional interation scheme, is used for the iterative solution of the unknown coolant/blade interface shape. Results are shown for a simple eccentrical bore pipe cross section and a realistic turbine blade cross section. The inverse design procedure is shown to be efficient and stable for all configurations that have been tested.

Introduction

Due to rising fuel costs, an impetus has arisen in the past decade for the design of highly efficient turbomachinery. The cost of large-scale testing of new designs has also escalated, making preliminary design using computational methods more attractive.

Internally cooled turbine blade design has traditionally been accomplished using various approximate and empirical techniques. The exterior gas flow is often assumed to be isentropic and the effects of rotation and three-dimensionality neglected. In addition, the turbine blade designer has no direct control of the detailed blade temperature distribution and has to live with whatever temperature distribution is found from expensive and time consuming experimental tests.

This paper describes an entirely new concept for the inverse design and analysis of internally cooled turbine blades. The technique allows the blade designer to specify the desired temperature or heat flux at each point on the turbine airfoil outer surface, using whatever criteria he chooses (thermal stress considerations, coolant flow availability, aerodynamic effects on the outer flow field, etc.). Potential savings from using this technique include the possibility of having higher turbine inlet temperatures and lower coolant flow rates. It is worth noting that existing internally cooled turbine blades can also be analyzed using this technique, and can possibly be redesigned for better performance.

Contributed by the Gas Turbine Division of THE AMERICAN SOCIETY OF MECHANICAL ENGINEERS and presented at the 29th International Gas Turbine Conference and Exhibit, Amsterdam, The Netherlands, June 4-7, 1984. Manuscript received at ASME Headquarters December 5, 1983. Paper No. 84-GT-7.

The Global Inverse Design Concept

The first step in this inverse design procedure is the specification of the blade outer surface temperature or heat flux distribution. The exterior flow is then solved using, say, a full potential [1] or Euler [2] code coupled with an appropriate boundary layer code [3]. Instead of this viscous/inviscid coupling, a Navier-Stokes equation solver [4] with appropriate turbulence modeling can be used. Regardless of what flow solver is used for the determination of the exterior compressible flow, the result will be the airfoil outer surface remaining quantity (temperature or heat flux) that was not specified. Alternatively, experimental data in the form of a Nusselt number distribution could be used with a specified surface temperature distribution to obtain the surface heat flux distribution. These flow field solutions can be obtained for two-dimensional cascades, quasi-three-dimensional cascades, or fully three-dimensional heat conduction problem in blade cross sections. Three-dimensional effects (radial heat flow) will be neglected, but it must be noted that this is not a limitation of the technique.

The dual boundary conditions of temperature and heat flux on the outer surface of the hollow airfoil and the temperature distribution alone on the unknown inner surface are then input to the solution of Laplace's equation for steady heat conduction in the solid portions of the hollow blade. This solution is accomplished by first determining an appropriate initial guess of the unknown coolant flow passage shape. The initial guess is based on the local one-dimensional heat conduction considerations. The temperature on the inner contour is then iteratively attained by reconfiguring the contour while at the same time satisfying the dual tem-

perature/heat flux outer surface boundary conditions. Note that the temperature and heat flux on the outer surface are satisfied separately; in other words, the boundary condition is not a standard linear combination of the two quantities. The calculated temperature distribution on the coolant/blade interface generally differs from the specified temperature, and Newton's iterative scheme is used to modify the inner contour and drive the temperature difference to within a given tolerance.

All two-dimensional solutions for the blade spanwise cross-sections can then be stacked up to determine the three-dimensional coolant flow passage shape. The coolant flow passage will now have a specified temperature and the obtained heat flux distribution on its surface. The heat flux alone will serve as an input to the solution of the coolant flow field. The solution of the coolant flow field using the heat flux boundary condition generally produces a different temperature distribution on the blade inner surface than the one that was initially specified. Thus, using the newly found temperature distribution on the coolant passage surface (or alternatively some combination of the new temperature and the one originally prescribed), a new coolant flow passage shape is found which satisfies the fixed blade outer surface dual boundary conditions. The process is repeated until a point is reached in which the blade inner surface temperature distribution calculated from the coolant flow field will match the temperature from the previous global iteration. Finally, the blade can be analyzed from structural considerations, including thermal stresses, and the entire process is repeated if the blade's structural integrity is not acceptable.

Coolant Flow Passage Shape Determination

Given the temperature and heat flux distributions on the outer surface, Ω_s, of a given turbine blade cross section (Fig. 1), the problem is to find the shape of the inner contour, Ω_c, that satisfies three specified boundary conditions: (*i*) the blade outer surface temperature, T_s; (*ii*) the blade outer surface heat flux, q_s; and (*iii*) the coolant/blade interface (inner contour) temperature, I_c. The solid portions of the hollow blade are assumed to be homogeneous and made of a material with a constant coefficient of heat conduction, λ. The heat flow is assumed to be steady and the temperature field in the material satisfies Laplace's equation

$$\lambda \nabla^2 \phi = 0 \tag{1}$$

where ϕ is the temperature. From potential theory, it is known that a solution to Laplace's equation can be found by superimposing a series of fundamental solutions. Since the final shape of the coolant flow passage can be highly irregular, depending on the temperature and heat flux boundary conditions, we decided to solve Laplace's equation using simple surface singularity distribution method. The technique described here utilizes straight panels with constant

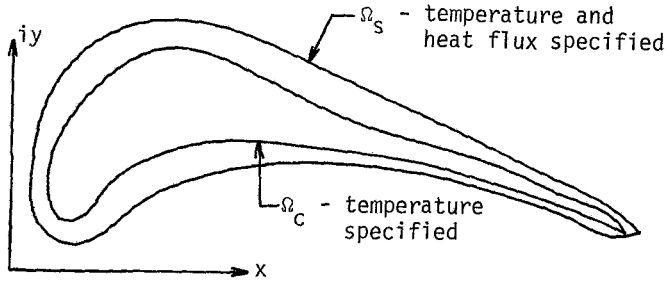

Fig. 1 Geometry and boundary conditions

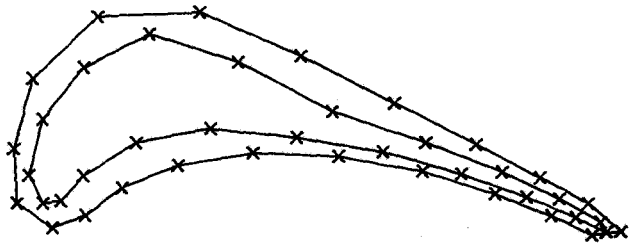

Fig. 2 Inner and outer contours discretized with panels

source (or sink) strength distributions to represent the heat flow between the outer, Ω_s, and inner, Ω_c, contours (Fig. 2). An initial guess for Ω_c is determined from one-dimiensional heat conduction using the temperature, T_s, and the heat flux, q_s, on the airfoil outer surface and the temperature, T_c, on the inner contour. The temperature induced at a point, z_o, by a panel of strength, K, is given by

$$\phi(z_o) = k \int \ln |z_o - z| \, ds \tag{2}$$

where the integration is performed along the panel. By replacing the outer (fixed) contour, Ω_s, with an equal number of straight panels (line segments), and denoting the strengths of these panels by k_{s_i} and k_{c_i}, respectively,

$$\phi(z_o) = \sum_{i=1}^{N} \{ k_{s_i} \int \ln |z_o - z| \, ds_i + k_{c_i} \int \ln |z_o - z| \, ds_i \} \tag{3}$$

for the temperature, ϕ, at any point, z_o, in the z-plane, where N is the number of panels on each contour. Also, from Fourier's heat conduction law the heat flux in the direction n at any point z_o is given by

$$-\lambda \frac{\partial \phi(z_o)}{\partial n} = -\lambda \sum_{i=1}^{N} \left\{ k_{s_i} \int \frac{\partial}{\partial n} \ln |z_o - z| \, ds_i + k_{c_i} \int \frac{\partial}{\partial n} \ln |z - z_o| \, ds_i \right\} \tag{4}$$

Nomenclature

i = complex number, $i = \sqrt{-1}$
I = temperature influence coefficient
J = heat flux influence coefficient
k = strength of a source or sink
N = number of panels on the inner and outer contours
q = specified heat flux
R = radius of curvature
s = arc length along a panel
T = specified temperature
x = x-coordinate of the z-plane
y = y-coordinate of the z-plane
z = coordinate in the complex plane $z = x + iy$
$\bar{z}$ = panel control point coordinate
$\hat{z}$ = panel end point coordinate
i,j,m,p = indices

Greek Symbols

ϕ = temperature
λ = coefficient of heat conduction
δ = distance measure
Ω = closed contour in the z-plane
ω = relaxation factor
α = optimal relaxation factor

Subscripts

s = blade surface
c = coolant/blade interface
o = particular point

Superscripts

n = iteration number
$\bar{}$ = panel control point
$\hat{}$ = panel end point

Satisfying the dual boundary conditions on Ω_s will give the values of k_{s_i} and k_{c_i}. The outer contour boundary conditions of temperature and heat flux are satisfied at the control points of the panels, $\tilde{z}_{s_i}$, defined as the average of the panel end points, $\hat{z}_{s_i}$ and $\hat{z}_{s_{i+1}}$. This procedure produces four $N \times N$ influence coefficient matrices that multiply the source and sink strengths as

$$\left[I_{s_{ij}}\right]\left\{k_{s_i}\right\}+\left[I_{c_{ij}}\right]\left\{k_{c_i}\right\}=\left\{T_{s_j}\right\} \tag{5}$$

$$\left[J_{s_{ij}}\right]\left\{k_{s_i}\right\}+\left[J_{c_{ij}}\right]\left\{k_{c_i}\right\}=-\frac{1}{\lambda}\left\{q_{s_j}\right\} \tag{6}$$

which can also be written as the $2N \times 2N$ partitioned matrix

$$\left[\begin{array}{c|c} I_{s_{ij}} & I_{c_{ij}} \\ \hline J_{s_{ij}} & J_{c_{ij}} \end{array}\right]\left\{\begin{array}{c} k_{s_i} \\ \hline k_{c_i} \end{array}\right\}=\left\{\begin{array}{c} T_{s_j} \\ \hline \dfrac{-q_{s_j}}{\lambda} \end{array}\right\} \tag{7}$$

Here, $I_{s_{ij}}$ and $I_{c_{ij}}$ denote the influence of the ith outer or inner panel on the control point of the jth outer panel, and $J_{s_{ij}}$ and $J_{c_{ij}}$ denote the influence of the ith outer or inner panel on the heat flux at the control point of the jth outer panel. Inverting equation (7) gives the values of k_{s_i} and k_{c_i}, which satisfy the dual boundary conditions on the outer contour, Ω_s. The inversion of equation (7) is performed using the method of Cholesky [5]. The temperature on the inner contour, ϕ_{c_j}, is then calculated using equation (2). This temperature will in general be different from the specified temperature T_{c_j}; therefore, a correction to the inner contour is calculated from Newton's method and is given by

$$\left[\frac{\partial\phi(\bar{z}^n_{c_j})}{\partial\bar{z}^n_{c_i}}\right]\left\{\Delta\bar{z}^n_{c_i}\right\}=\left\{T_{c_j}-\phi(\bar{z}^n_{c_j})\right\} \tag{8}$$

where the correction is defined by

$$\bar{z}^{n+1}_{c_i}=\bar{z}^n_{c_i}+\omega\Delta\bar{z}^n_{c_i} \tag{9}$$

and ω is the relaxation factor. The differentiation in Newton's method is determined analytically and is performed in the direction of the normal to the ith inner panel. The calculation of the derivative matrix requires the inversion of the $2N \times 2N$ matrix of equation (7); however, the LU decomposition of the matrix is stored from the solution for the panel strengths and thus can be used to determine the derivative matrix with negligible extra computation.

The relaxation factor, ω, is set equal to 1 for most of the iteration steps, but the existence of an optimal relaxation factor, α, is checked for at each iteration. After each iteration, the coordinates of the control points of the inner panels are changed by the calculated corrections, and so the new coordinates of the end points must be found. This is accomplished by noting that the contour is closed and that the control points are halfway between the end points with the result that

$$\hat{z}_{c_j}=(-1)^{j+1}\left\{2\sum_{i=1}^{j-1}(-1)^i\tilde{z}_{c_i}-\sum_{i=1}^{N}(-1)^i\tilde{z}_{c_i}\right\} \tag{10}$$

is the expression for the end points as a function of the control points. The existence of an optimal relaxation factor, α, can be shown by noting that certain positions of the control points produce a highly irregular contour, since the end points are calculated from a strict constraint that the control points are halfway between the end points. Thus α is the value of ω that minimizes this irregularity as ω varies from 0 to 1 and is given by

$$\alpha=\frac{-\frac{1}{2}\sum_{j}^{N}\sum_{m}^{N}\sum_{p}^{N}(\Delta\bar{x}^n_m\bar{x}^n_p+\Delta\bar{x}^n_p\bar{x}^n_m+\Delta\bar{y}^n_m\bar{y}^n_p+\Delta\bar{y}^n_p\bar{y}^n_m)\gamma_{mj}\gamma_{pj}}{\sum_{j}^{N}\sum_{m}^{N}\sum_{p}^{N}(\Delta\bar{x}^n_m\Delta\bar{x}^n_p+\Delta\bar{y}^n_m\Delta\bar{y}^n_p)\gamma_{mj}\gamma_{pj}} \tag{11}$$

where

$$\gamma_{ij}=\begin{cases}(-1)^{i+j} & \text{if } i<j\\ (-1)^{i+j+1} & \text{if } i>j\\ (-1)^{i+j+1}+1 & \text{if } i=j\end{cases} \tag{12}$$

The nonexistence of an optimal relaxation factor is evident when the α calculated from equation (11) is outside an acceptable range (α less than 0.2 or greater than 1.0).

The iterative procedure is concluded when the maximum error in satisfying the temperature boundary condition on the inner contour is below a certain tolerance. In the present work, 0.1 percent of the average specified temperature, T_{c_j}, was used as the convergence criterion.

Results

A computer program was developed to implement the inverse design procedure. Input to the program includes the airfoil outer contour coordinates, the outer surface temperature and heat flux distribution, and the inner contour temperature distribution. The program then calculates an initial guess for the wall thickness distribution from the one-dimensional heat conduction relations given by

$$\delta_i=R\left[1-\exp\left(\frac{\lambda T_{s_i}-T_{c_i}}{R\,q_{s_i}}\right)\right] \tag{13}$$

where δ_i is the normal distance from the ith outer panel, and R is the radius of curvature of the outer contour at the ith control point. As R goes to infinity, δ_i is calculated from the plane wall one-dimensional heat conduction equation.

$$\delta_i=\frac{-\lambda(T_{S_i}-T_{c_i})}{q_{s_i}} \tag{14}$$

The shape of the inner contour of the hollow airfoil is found iteratively.

Results for two cases are presented in this paper: a simple eccentrical bore pipe and a turbine cascade [6]. The eccentrical bore pipe is analogous to the buried cable problem and has an analytic solution [7] in which the isotherms are nonconcentric circles. Using the analytic solution to determine the heat flux on the outer surface and specifying constant temperatures on the outer surface on the pipe and on the unknown inner contour, the initial guess is postulated as shown in Fig. 3. After four iterations, the inner contour converged to the shape shown in Fig. 3.

The second test case is a transonic turbine cascade for which experimental data [6], in the form of Nusselt number distributions, were available (Fig. 4). Specified conditions were: constant 1500°F outer surface temperature; constant 1300°F coolant/blade interface temperature; turbine inlet temperature of 3100°F; and blade outer surface heat fluxes calculated from the given Nusselt number distribution. The blade was assumed to be made of a material with λ = 70 Btu/ft-°F. The initial guess calculated by our computer program is shown in Fig. 5 along with the final converged solution. The solution took four iterations to converge to within 0.1 percent of the specified inner wall temperature. Both test cases utilized 21 straight panels on both the inner and outer contours. The small iteration count for each case is due to the fact that the initial guesses were fairly close to the correct solution and that the optimum relaxation factor was

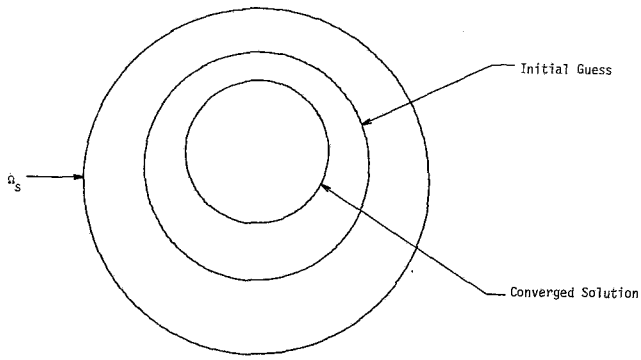

Fig. 3 Eccentrical bore pipe inverse design

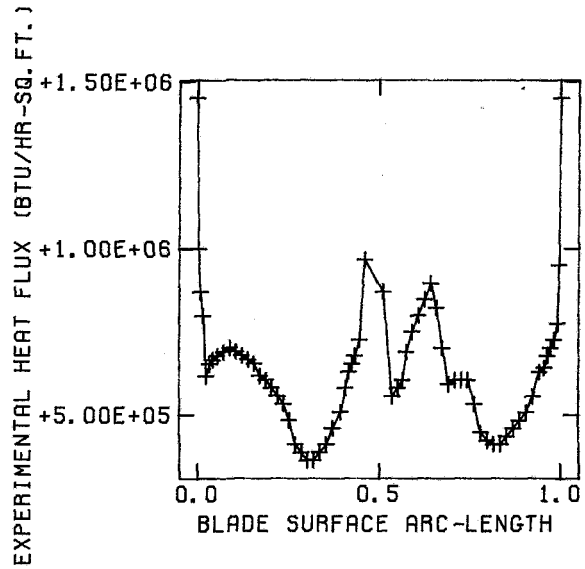

Fig. 4 Experimental heat flux distribution for MIT turbine blade [6]

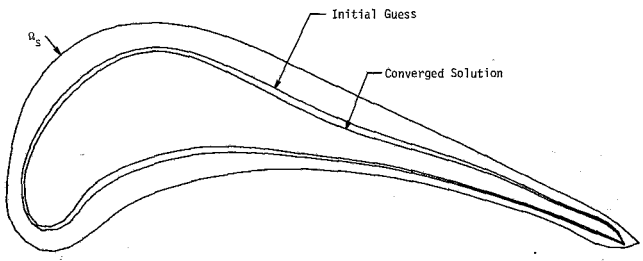

Fig. 5 MIT turbine blade inverse design [6]

used. Convergence displayed the usually expected quadratic convergence of Newton-type schemes. Approximately 10.0 cpu s on the CDC Cyber 170/750 were required for each iteration.

Future Research

There are many possibilities for extending the present method to more complex problems with increased accuracy. The panel method could be improved by using higher order curved panels and nonconstant panel singularity distributions [8]. A major extension of the method would be to make it fully three-dimensional by using quadrilateral elements in place of the outer blade surface (from hub to tip) and the unknown inner surface [9]. Most present turbine coolant flow passage designs include multiple holes and trailing edge coolant flow ejection; therefore, the present method could be extended to design and analyze these configurations. Transpiration cooled configurations could be designed and analyzed also since the coolant and heat flow through a porous medium has been shown by Siegel [10] to be derivable from a potential. One of the most intriguing applications for this method would be to attempt a multiple-point design of an entirely shock-free outer flow field [11] that could be maintained by varying the coolant flow rate. This shock-free design procedure would not entail any modification of the overall shape of the turbine blade. In addition, the method could be used to delay the onset of boundary-layer transition [12].

Summary

A procedure has been developed for the efficient design and analysis of coolant flow passage shapes in internally cooled configurations. The method is particularly applicable to turbine blade design but can also be used for the design of other configurations that utilize internal or external cooling such as missile cone tips, rocket nozzles, and internal combustion engines. The designer is able to specify both the temperature and heat flux at the turbine blade outer surface and the coolant/blade interface surface. The result of the design procedure is the shape of the interior coolant flow passage contour that satisfies all three of the above boundary conditions. When coupled with an appropriate flow solver, the method provides the gas turbine engine designer with an efficient tool for the preliminary design of coolant flow passages. The method is not limited to cascade design, but can be used for the fully three-dimensional design of coolant flow passages.

Acknowledgments

The authors would like to express their appreciation to E. McFarland of NASA Lewis Research Center, T. Booth of Garrett Turbine Engine Co., A. Wennerstrom and K. Mach of Wright Patterson Aeropropulsion Laboratory, and Dr. David Ives of Pratt and Whitney Aircraft Co. for their helpful comments and advice. This work has been supported by the Department of Aerospace Engineering and Engineering Mechanics at the University of Texas at Austin.

References

1 Dulikravich, D. S., "CAS2D-Fortran Program for Nonrotating, Blade-to-Blade, Steady, Potential Transonic Cascade Flows," NASA TP 1705, 1980.

2 Ni, Ron Ho, "A Multiple-Grid Scheme for Solving the Euler Equations," AIAA 81-1025R, 1982.

3 Gaughler, R. E., "Some Modifications to, and Operational Experience with, the Two-Dimensional, Finite-Difference, Boundary-Layer Code, STAN5," ASME 81-GT-89, 1981.

4 MacCormack, R. W., "A Numerical Method for Solving the Equations of Compressible Viscous Flow," AIAA 81-0110R, 1981.

5 Willems, N., and Lucas, W. M., Jr., *Matrix Analysis for Structural Engineers*. Prentice-Hall, Inc., Englewood Cliffs, N.J., 1968.

6 Hajjar, F. G., et al., "Aerodynamics and Heat Transfer of Transonic Turbine Blades at Off-Design Angles of Incidence," MIT Gas Turbine Laboratory Report.

7 Eckert, E. R. G., and Drake, R. M., Jr. *Analysis of Heat and Mass Transfer*. McGraw-Hill, New York, 1972.

8 McFarland, E., "Solution of Plane Cascade Flow Using Improved Surface Singularity Method," JOURNAL OF ENGINEERING FOR POWER, Vol. 104, July 1982.

9 Hess, J. L., and Smith, A. M. O., "Calculation of Potential Flow About Arbitrary Bodies," *Progress in Aeronautical Sciences*, Vol. 8, Pergamon Press, New York, 1966.

10 Siegel, R., and Snyder, A., "Heat Transfer in Cooled Porous Region with Curved Boundary," ASME *Journal of Heat Transfer*, Vol. 103, Nov. 1981.

11 Dulikravich, G. S., and Sobieczky, H., "Shockless Design and Analysis of Transonic Cascade Shapes," *AIAA Journal*, Vol. 20, No. 11, Nov. 1982, pp. 1572–1578.

12 Kahawita, R., and Meroney, R., "The Influence of Heating on the Stability of Laminar BoundaryLayers Along Concave Curved Walls," ASME 77-APM-4, 1977.

Boundary-Layer Transition and Separation Near the Leading Edge of a High-Speed Turbine Blade

H. P. Hodson[1]
Whittle Laboratory,
Cambridge University
Engineering Department,
Cambridge, England.

The state of the boundary layers near the leading edge of a high-speed turbine blade has been investigated, in cascade, using an array of surface-mounted, constant-temperature, hot-film anemometers. The measurements are interpreted with the aid of inviscid and viscous prediction codes. The effects of Reynolds number, compressibility, incidence, and free-stream turbulence are described. In all cases, the initial development of the boundary layers was extremely complex and, even at design conditions, separation and reattachment, transition and relaminarization were found to occur.

Introduction

The uncertainty associated with turbine blade-surface, boundary-layer predictions means that the designer is still dependent on data obtained by experiment. This is unfortunate, because the state of the blade surface boundary layers, that is, whether they are laminar or turbulent, separated or attached, affects both the aerodynamic performance and heat transfer characteristics of turbine blades. Because of this, there is still major requirement for steady-flow cascade data concerned with the development of blade-surface boundary layers and how they are affected by the large pressure gradients (favorable and adverse), the variable levels of free-stream turbulence, surface roughness and curvature, and the effects of compressibility and Reynolds number variations, all of which can be found in axial-flow turbines.

The leading edge region of the turbine blade surface is particularly important with regards to the boundary-layer development, not only because it is here that the heat transfer problems are often the most severe, but also because the initial development of the blade surface boundary layer can influence the behavior of the boundary layer over the remainder of the surface. Unfortunately, the usual problems associated with making boundary-layer measurements in high-speed cascades are also greatest in the leading edge region, since conventionally sized probes offer insufficient spatial resolution together with an often unacceptably high level of blockage. Fortunately, however, significant improvements in performance can often be made once the location, if any, of transition, separation, and reattachment are known. In view of this fact, a simple and cost effective technique, which involves the use of multielement surface mounted thin-films has been adapted by the author for use in the Transonic Cascade Facility of the Whittle Laboratory. This paper describes an investigation employing this technique.

Experimental Apparatus

The experimental results described in this paper were obtained in the Transonic Cascade Facility of the Whittle Laboratory [1]. This is a closed-circuit wind tunnel in which the Mach number ($M_2 < 1.62$) and the Reynolds number ($1 \times 10^5 < Re_2 < 13 \times 10^5$) can be varied independently. The facility is provided with a fully automated, computer-controlled traverse mechanism and data acquisition system. The blade-surface static pressures, for example, are measured using a Scanivalve system.

The cascade, itself, consisted of six blades which exhausted into a large plenum. Tailboards were not used because experience has shown that they are unnecessary. The blades under investigation were, in fact, turbine rotor root sections which operated at a nominal Reynolds number of 2.9×10^5 and at an exit Mach number of 0.71. Further details are provided in Table 1.

The initial development of the blade surface boundary layers has been investigated using an array of surface mounted thin-film anemometers. These multielement, hot-film gauges were deposited upon a thin (60 μm) and flexible

Table 1 Cascade information

Chord (mm)	55.88
Pitch-chord ratio	0.60
Inlet aspect ratio	1.715
Exit aspect ratio	1.818
Exit Mach no.	0.71
Exit Reynolds no. (chord based)	2.9×10^5
Inlet angle (deg from axial)	38.8
Exit angle (deg from axial)	−53.5
Inlet turbulence intensity (%)	0.5
Suction surface length (mm)	69.3
Pressure surface length (mm)	62.6
Stagger (deg)	−19.6

[1] Research Fellow, Girton College

Contributed by the Gas Turbine Division of THE AMERICAN SOCIETY OF MECHANICAL ENGINEERS and presented at the 29th International Gas Turbine Conference and Exhibit, Amsterdam, The Netherlands, June 4–7, 1984. Manuscript received at ASME Headquarters January 12, 1984. Paper No. 84-GT-179.

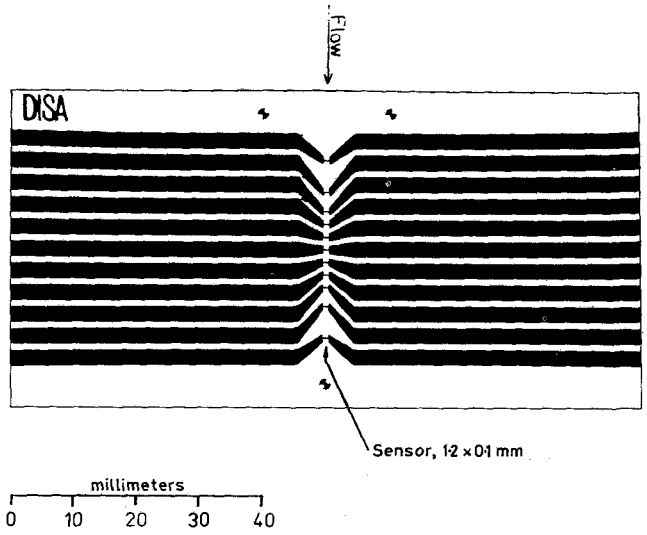

Fig. 1(a) Hot film instrumentation; multielement array

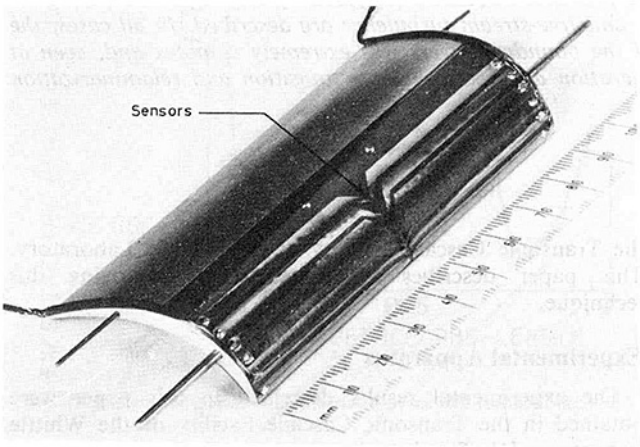

Fig. 1(b) Hot film instrumentation; instrumented blade

sheet of polyimide. An array is shown in Fig. 1(*a*). These gauges were specially manufactured by DISA of Denmark and are similar in construction to their single sensor Glue-On hot films.

The polyimide sheet, containing the hot-films, was glued to the blade surface using a low viscosity expoxy resin. The total thickness of the gauges and the adhesive was equal to 72 μm, which, as surface flow visualization confirmed, was small enough to not affect the flow around the leading edge. The flexibility of the polyimide sheet was, of course, a necessity if the blade profile was to be retained after fitting the gauges. An instrumented blade is shown in Fig. 1(*b*). Electrical connections were made by soldering enamel coated wires to the ends of the gauges. These wires were then connected, via 5 m lengths of coaxial cable and a multi-way rotary switch, to a single channel constant temperature anemometer.

The successful use of surface-mounted hot films in boundary layer investigations relies upon the similarity between the velocity profile adjacent to the wall and the temperature profile of the thermal boundary layer that is generated by the heated element. In such circumstances, the

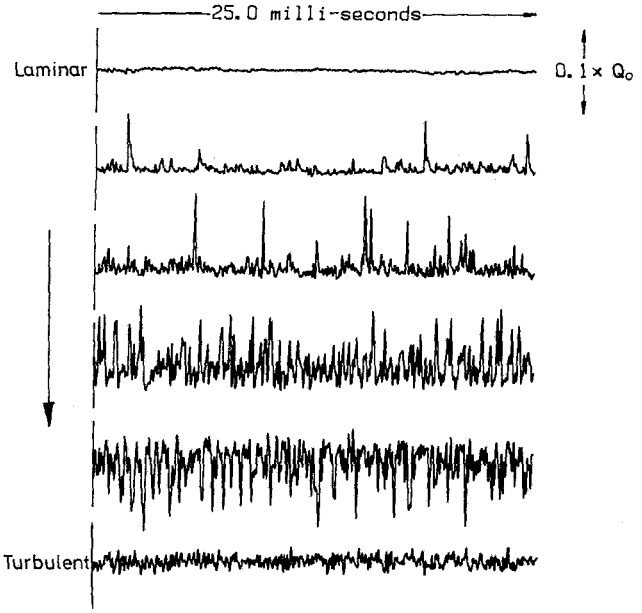

Fig. 2 Anemometer signals for a transitional boundary layer

relationship between the rate of heat transfer and the wall shear stress is of the form [2]

$$(Q - Q_s) = k\tau_\omega^{1/3}$$

where Q is the total instantaneous power dissipated by the film and Q_s is that lost to the substrate.

Unfortunately, Q_s is often much greater than $(Q - Q_s)$. It must, therefore, be accurately determined by calibration, a procedure which is both difficult and time consuming, even in incompressible flows. Fortunately, however, as in the case of a hot wire, the rate of heat lost to the substrate is approximately equal to the total rate (Q_o) measured under zero-flow conditions, and the net heat transfer rate $(Q - Q_o)$ has therefore been assumed to be proportional to the cube root of the wall shear stress. The effects of the small differences in sensor area, resistance, etc., upon the calibrations of the various sensors have been suppressed by reducing the data to the form of $(Q - Q_o)/Q_o$. Implicit in this method of data reduction is the assumption that the rates of heat transfer to the air and the substrate are similar functions of the same variables.

The surface mounted hot-film anemometer has a relatively high temporal resolution. Typically, their frequency response limit is in the range of 15-20 kHz, and they can therefore be used to investigate regions of the flow where unsteady phenomena are present. Natural transition is, of course, an unsteady process involving the intermittent formation of turbulent spots, which then grow to form a turbulent boundary layer that is also a region of unsteady flow, albeit different in character. Therefore, it is possible to identify the state of the boundary layer by examining the output signal of the hot-film anemometer. Figure 2 shows a series of typical output signals obtained within a boundary layer that underwent transition from laminar to turbulent flow.

With reference to Fig. 2, it should be noted that the level of

Nomenclature

k = calibration constant
M_2 = isentropic exit Mach number
Q = gross heat transfer rate
Q_0 = zero flow heat transfer rate
Q_s = heat transfer rate lost to substrate
Re_2 = isentropic exit Reynolds number (chord based)
s = percentage of surface distance
τ_w = wall shear stress

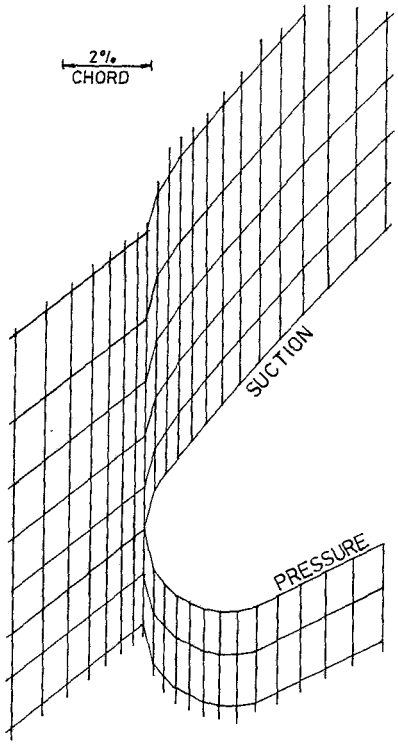

Fig. 3 Computational mesh in region of leading edge

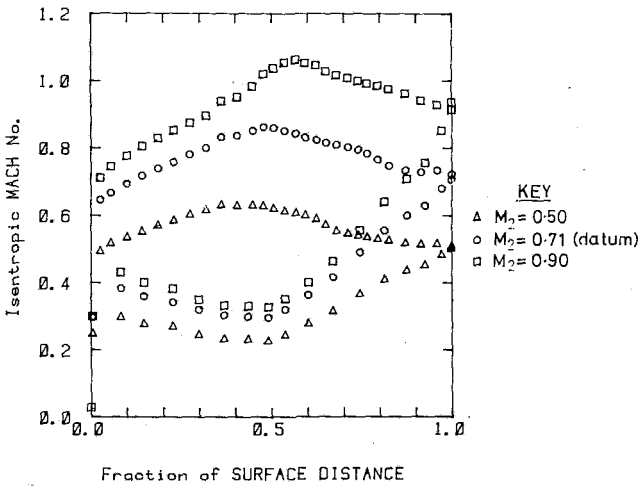

Fig. 4 Surface Mach number distributions at datum incidence, Reynolds number, and turbulence level

fluctuations within the transitional boundary layers is greater than in fully turbulent ones, because the change in shear stress that accompanies a change of state results in a change of heat transfer rate that is greater than that found in turbulent boundary layers.

The high-frequency data provided by the hot-films were digitized at the rate of 40 kHz before being stored in one of the laboratory's computers. In order to avoid Nyquist folding of these data, a low-pass, 10 kHz filter was used prior to acquisition.

Inviscid Prediction Technique

The blade surface Mach number distributions were predicted using the inviscid two-dimensional, time-marching method of Denton [3], which solves the Euler equations of motion in finite volume form.

For the purpose of the current investigation, the computational mesh in the region of the leading edge was much finer than would normally be used. An enlargement of this region is shown in Fig. 3. It should be noted that because the cascade is slightly flared (see Table 1) full agreement between the measurements and the prediction is not expected.

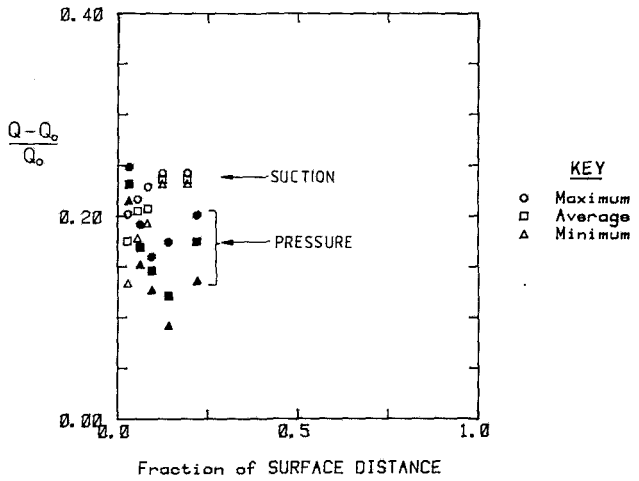

Fig. 5 Maximum, minimum, and mean rates of heat transfer measured at the datum conditions

Boundary Layer Prediction Technique

Predictions of the blade surface boundary layer development have been made using the code of Herbert and Calvert [4]. The measured, rather than the predicted blade-surface Mach number distributions were used as input data.

Because the boundary layer code was developed for use in compressor rather than turbine blade rows, the prediction of transition was not expected to be reliable. This fact does not, however, detract from the value of the predictions when they are used as an aid to interpreting the experimental data.

Results and Discussion

The initial development of the blade surface boundary layers has been investigated over a range of Mach numbers, Reynolds numbers, turbulence levels, and angles of incidence. The effects of independently varying each of these parameters, while the remainder are equal to the values given in Table 1, are described below.

The measured isentropic surface Mach number distribution for the datum condition is shown in Fig. 4. When plotted against surface length, as in this figure, the distribution takes the form of a roof-top design. On the suction surface, the Mach number increases rapidly from the stagnation point up to a value of 0.64 at 3 percent s. This is then followed by a less rapid, almost uniform increase up to a peak value of 0.88 at 48 percent s, after which the flow diffuses towards the trailing edge. On the pressure surface, the rapid acceleration around the leading edge is followed by a region of diffusion which ends at 49 percent s, from where the flow accelerates towards the trailing edge.

The measured maximum, minimum, and mean levels of heat transfer are presented in Fig. 5 for the datum conditions. The solid symbols correspond to the pressure surface measurements, while the open symbols refer to those on the suction surface. The maximum and minimum are shown, in addition to the mean rates of heat transfer, for two reasons. Firstly, this method of presentation provides an indication of both the magnitude and the symmetry of any fluctuations that might be present. Secondly, the surface-mounted hot film, like the hot wire, is insensitive to the sign of the flow vector. Therefore, in regions of unsteady separation, where the flow

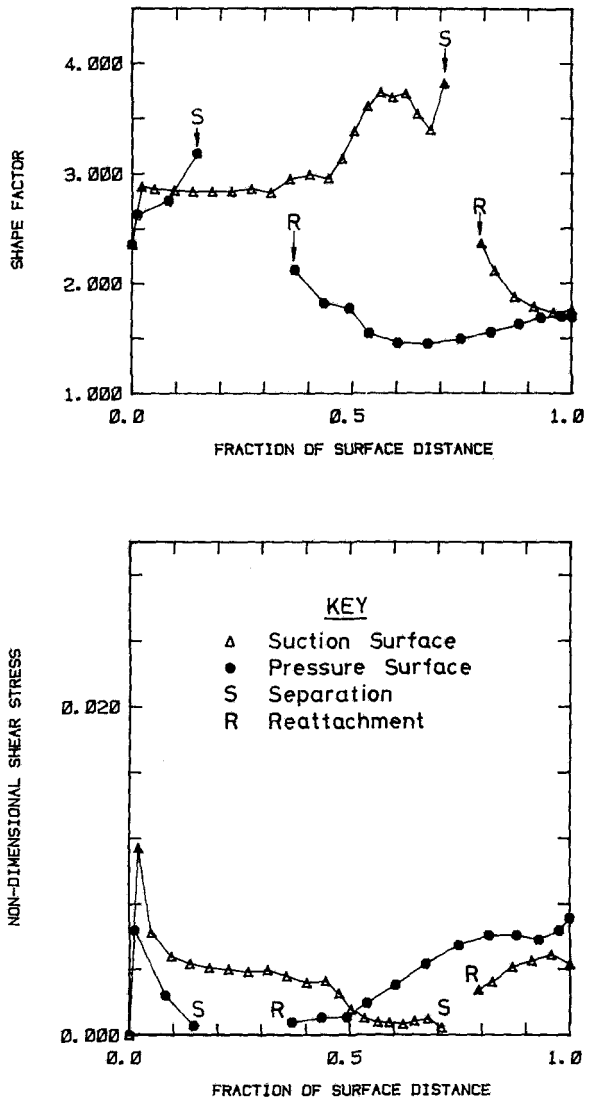

Fig. 6 Predicted shape factors and wall shear stresses for the blade surface boundary layers at the datum conditions

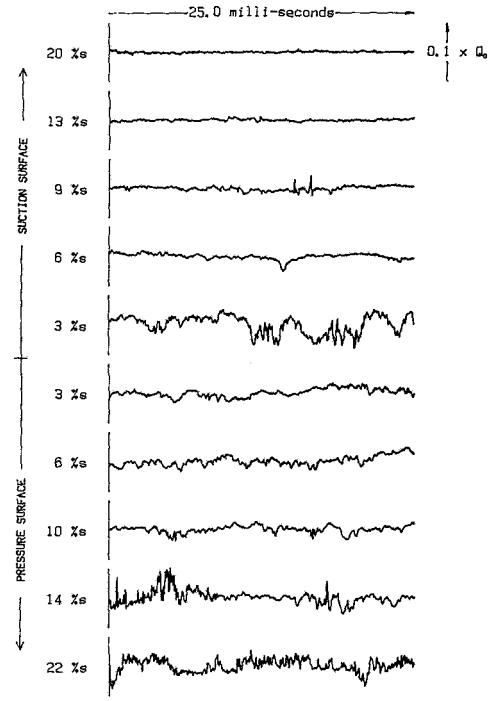

Fig. 7 Unsteady heat transfer signals at the datum conditions

direction is continually changing, it will be the minimum value of the heat transfer rate and not the mean which will indicate a zero value of the wall shear stress.

The measurements of Fig. 5 show that on the pressure surface, the heat transfer and, therefore, the wall shear stress, reduces in value from the leading edge to a minimum at 14 percent s. At this point, the difference between the maximum and minimum values has increased, indicating that the boundary layer has become more unsteady. As the shear stress rises beyond the minimum, the unsteadiness is seen to persist.

The pressure surface results of Fig. 5 may be compared with predicted values of the wall shear stress (nondimensionalized with respect to the exit dynamic pressure) which are shown in Fig. 6 for the datum conditions. It is predicted that on the pressure surface, the initially laminar boundary layer will separate at about 15 percent s, with turbulent reattachment occurring in the region of 35 percent. In view of this, it appears that the minimum value in the heat transfer measurements on this surface (Fig. 5) is coincident with a region of separated flow, and the rise in heat transfer that has occurred by 22 percent s must therefore be indicative of a reattached turbulent boundary layer.

It should be noted that the large, nonzero value of the minimum rate of heat transfer at 14 percent s on the pressure surface occurs, not because there is a large reversed wall shear stress within the bubble, but because there is an inequality between the measured heat transfer rate under zero-flow conditions (Q_o) and that which is actually lost to the substrate (Q_s). This fact serves to demonstrate the main weakness of the measurement technique, that is, its inability to detect regions of zero valued wall shear stress, and it is in such circumstances that the predictions are the most useful as an aid to data interpretation.

The output signals of the surface-mounted, hot-film anemometers often provide valuable transient information regarding the state of the boundary layers. The signals observed at the datum conditions are shown in Fig. 7. On the pressure surface, the first three signals contain relatively low-frequency fluctuations. At 14 percent s, however, the character of the signal has changed and the low-frequency fluctuations are interspersed with bursts of larger-amplitude, higher-frequency fluctuations that indicate the intermittent change from laminar to turbulent flow, where the shear stress is higher than in the laminar case. This generation of turbulence continues so that by 22 percent s, the signal is much more typical of a turbulent boundary layer that is interupted by the occasional presence of low shear stress regions of laminar flow.

The prediction (Fig. 6) stated that on the pressure surface at the datum conditions, separation occurs at approximately 15 percent s, which is near where the measured heat transfer ratio is at a minimum. Therefore, it must be concluded that the low-frequency fluctuations, which are present in the outputs of the first three pressure surface gauges, occur as a result of the diffusing boundary layer's inability to quench any disturbances which may naturally arise. Similar observations have been made by the author in other diffusing boundary layers (e.g., [5]). At 14 percent s, the transition to turbulent flow has already begun, which suggests that separation has in fact occured at a point between 10 and 14 percent s and not, as predicted, at 15 percent s. Interestingly, the rise in heat transfer which has occurred by 22 percent s (Fig. 5) indicates that reattachment has occurred, even though the boundary layer is not fully turbulent. Confirmation of the extent of the separation bubble has since been provided by an oil-and-dye

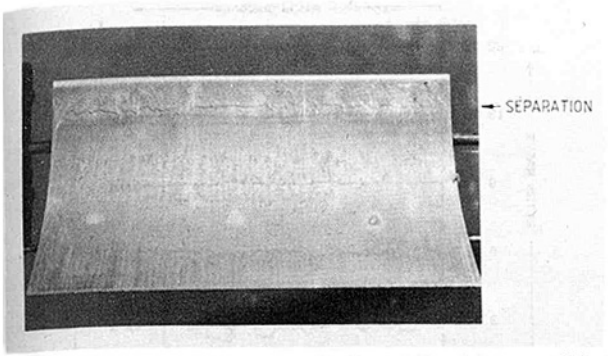

Fig. 8 Pressure surface flow visualization at the datum conditions (view normal to surface at separation point)

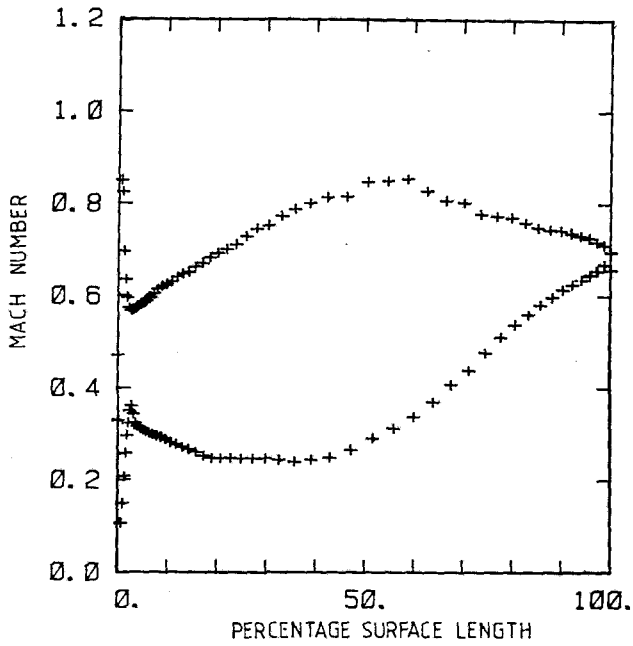

Fig. 9 Predicted two-dimensional Mach number distribution for the datum conditions

flow visualization technique, the results of which are photographed in Fig. 8. It was found that the bubble extended from 12 percent s to 20 percent s.

The incorrect prediction of the location of the pressure surface separation bubble is not unexpected, since the program was provided with relatively few data points in a region of rapidly changing boundary layer parameters. In fact, the actual amount of diffusion at the leading edge of the pressure surface is probably greater than that which is indicated by the measurements of Fig. 4. Evidence of this fact is contained within the predicted Mach number distribution of Fig. 9, where it should be remembered that because the prediction is only two-dimensional, the predicted inlet Mach numbers will be lower than those measured at the same exit conditions. The predictions show that initially, as a result of a small overspeed near the blend point at the leading edge of the pressure surface, the diffusion is much greater than that which is apparent from the measurements. This would, of course, result in an earlier than predicted separation of the boundary layer on the pressure surface.

On the pressure surface, qualitative agreement has been noted between the shapes of the measured wall shear stress (i.e., heat transfer) and the predicted values. On the suction surface, however, no such agreement is found and the predicted fall which occurs from 2–20 percent s is to be contrasted with the measured rise over the same part of the surface. The inviscid prediction (Fig. 9) provides an ex-

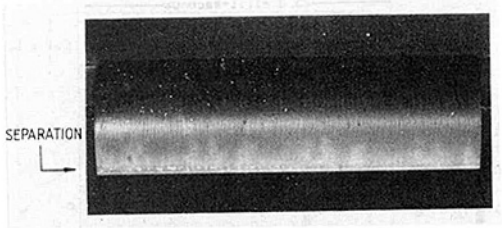

Fig. 10 Suction surface flow visualization at the datum conditions (view normal to surface at separation point)

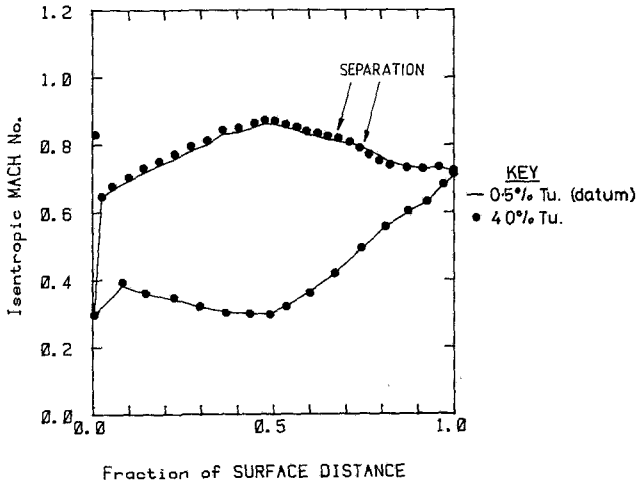

Fig. 11 Effect of free-stream turbulence on measured Mach number distributions

planation as to why there is this difference. It shows that there is an overspeed near the leading edge blend point of the suction surface. This was not detected in the cascade because of the positioning of the pressure tappings. As a result of this overspeed, the suction surface boundary layer experiences a rapid deceleration, which is severe enough to cause laminar separation and turbulent breakdown (see below). The magnitude of the wall shear stress is therefore extremely low in this region of separation. Whether reattachment occurs as a result of the transition or because of the reacceleration is not known. In either case, the length of the bubble will be extremely small and after reattachment, the wall shear stress will rise in the manner shown in Fig. 5. The existence of the suction surface leading edge separation bubble has since been confirmed by flow visualization (Fig. 10).

The effect of the leading edge overspeed upon the subsequent development of the suction surface boundary layer can be seen in the anemometer output signals of Fig. 7. These show that at 3 percent s, the boundary layer is very unsteady, with the regions of apparently turbulent flow being interspersed by periods where the flow fluctuates between characteristically laminar and turbulent states. As a result of the acceleration of the outerflow, this nearly turbulent boundary layer becomes relaminarized. The spikes which exist at 9 percent s denote, in fact, the reformation of turbulent spots within the virtually relaminarized boundary layer. At 13 percent s and beyond, no turbulent spots were observed and the boundary layer may be considered to be fully laminar. This relaminarization of the boundary layer, in the presence of the accelerating outer flow, was not unexpected, since the value of the acceleration parameter $\nu/u^2 \cdot du/ds$ was far greater than the value above which relaminarization is known to occur [6].

The effect of varying the exit Mach number on the surface Mach number distributions is shown in Fig. 4. The difference between the shapes of these plots is small in the vicinity of the leading edge and as a consequence, the nature of the boundary layer development is little changed. Because the differences

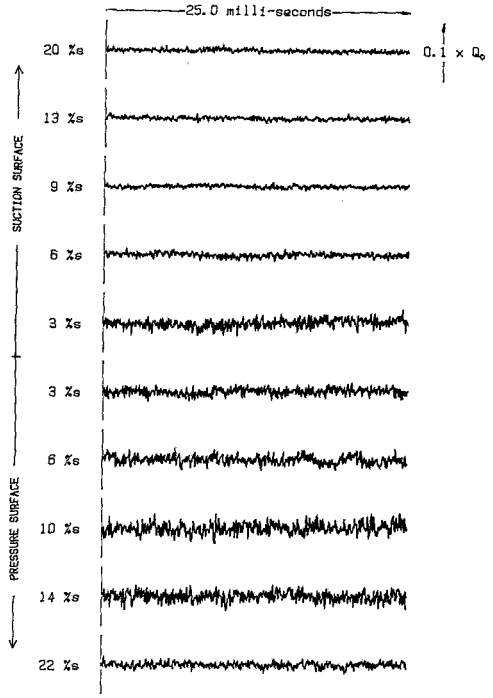

Fig. 12 Unsteady heat transfer signals at increased free-stream turbulence

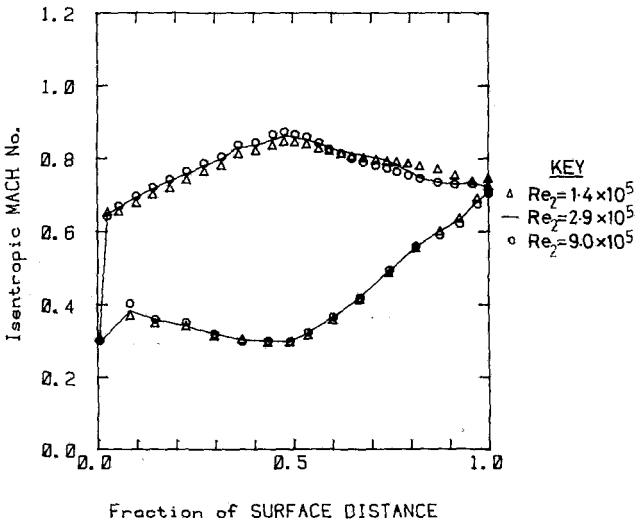

Fig. 13 Effect of Reynolds number on measured Mach number distribution

are small, no further results are presented concerning the effect of changing the exit Mach number.

The effect, upon the measured blade surface Mach numbers, of increasing the inlet free-stream turbulence intensity from 0.5 to 4.0 percent can be seen in Fig. 11. This comparison shows that in the regions where separation bubbles existed at the lower turbulence intensity (i.e. 3 percent on the suction surface; 14 percent s on the pressure surface), the Mach numbers, relative to those nearby, have been reduced. This indicates that the increased turbulence has, at the very least, significantly reduced the length of the separation bubbles. The Mach number distribution which corresponds to the higher turbulence level also confirms that a suction surface leading edge overspeed exists. The measurement of this overspeed was fortuitous, since it was not always possible to detect it, even when these same operating conditions were reestablished.

The overspeed was again found to bring about the formation of the leading edge separation bubble. Evidence of this came from both the mean heat transfer measurements and a surface-flow visualization experiment. The anemometer output signals that were obtained at the higher turbulence condition are shown in Fig. 12. The character of these signals is entirely different to those that are shown in Fig. 7 for the lower turbulence condition. Figure 12 shows that on the suction surface, the boundary layer is already turbulent by 3 percent s. This, therefore, suggests that the length of the separation bubble is reduced. Unfortunately, it also means that it is impossible to tell whether the boundary layer separates before or after transition. However, by specifying that transition occurred in the prediction before the diffusion, it was found that turbulent separation would not occur. Therefore, it must be assumed that the boundary layer, which was initially turbulent, was relaminarized as a result of the rapid acceleration before it undergoes separation and turbulent reattachment as a result of the ensuing diffusion. At the end of this diffusion, the boundary layer is again accelerated and relaminarization begins again. This second relaminarization can be seen in the output signals of Fig. 12, where the amplitude of the turbulent fluctuations decreases along the suction surface. In fact, the relaminarization continues up to peak suction with the result that, as Fig. 11 shows, laminar separation and turbulent reattachment occur in the region of 65 to 80 percent s.

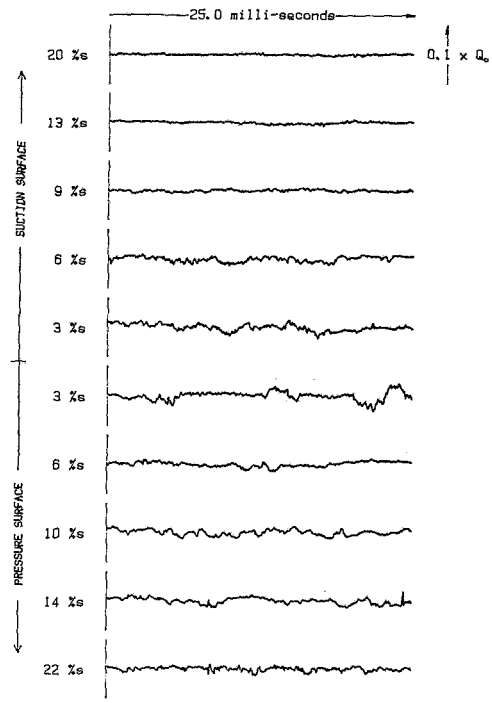

Fig. 14 Unsteady heat transfer signals at reduced Reynolds number (1.4×10^5)

On the pressure surface, at the higher level of free-stream turbulence, separation is prevented by the induced transition of the boundary layer. Therefore, the level of the fluctuations within the anemometer signals (Fig. 12) is similar to that near the leading edge of the suction surface.

The effect of decreasing the Reynolds number on the blade surface Mach number distributions is presented in Fig. 13. This shows that there is a relative increase in the Mach numbers in the regions where separation is expected to exist, implying that the separated regions are enlarged. This change is, of course, to be expected since at the lower Reynolds number, a boundary layer can withstand a region of diffusion for a greater length of the surface and that once separated, the onset of transition is delayed.

Confirmation of the existence of these changes is found in a comparison of the anemometer output signals obtained at the

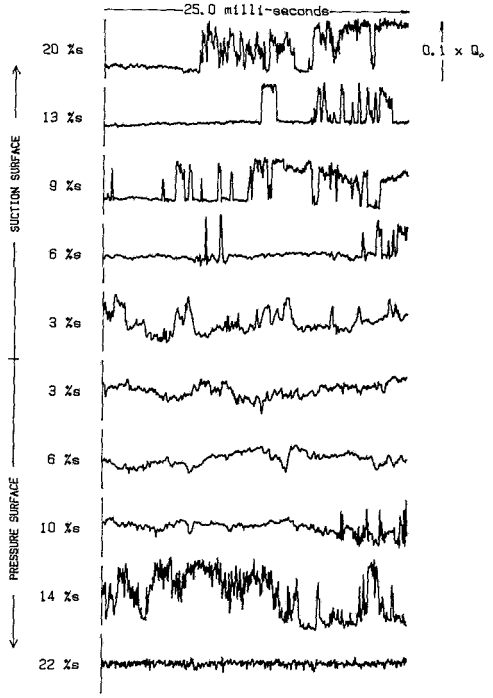

Fig. 15 Unsteady heat transfer signals at increased Reynolds number (9.0×10^5)

datum condition (Fig. 7) and at the reduced Reynolds number (Fig. 14). This shows that on the pressure surface, the amount of low-frequency unsteadiness is reduced at the lower Reynolds number and the process of transition cannot be seen, presumably because separation is delayed until about 22 percent s, which is where the minimum rate of heat transfer was found to occur and also, where the prediction stated it should occur. On the suction surface, reducing the Reynolds number causes an elongation of the separation bubble, which means that the signal is less unsteady at 3 percent s but, at the same time, it is more unsteady at 6 percent s. Beyond 6 percent s, however, the reduced Reynolds number means that relaminarization is more rapid than at the datum conditions and the fluctuations soon die away.

As one might expect, raising the chord-based Reynolds number has an effect opposite to that which results from a reduction. Figure 15 shows the hot-film output signals which were obtained at the higher Reynolds number. These signals show that the complete range of boundary layer phenomena, which can be found in two dimensional flows, exists at this operating condition. On the pressure surface, the increased Reynolds number means that the point of separation is closer to the leading edge. Indeed, the minimum shear stress occurred near 10 percent s, which corresponds to the location of the onset of transition shown in Fig. 15. The predictions confirmed that the location of separation should be nearer the leading edge and that the length of the separation bubble should be reduced. The results of Fig. 15 also show that full transition is complete by 22 percent s, the position at which reattachment was predicted.

On the suction surface, Fig. 15 shows that the development of the boundary layer at the higher Reynolds number is somewhat different to that which occurs at the datum conditions. The effect of the leading edge separation is still present, but relaminarization is not. Instead, there is a partial relaminarization between 3 and 6 percent s. However, the signal at 6 percent s also contains evidence that turbulent spots are beginning to form. These spots create a sudden increase in the heat transfer rate as they pass over the gauges, thereby creating the positive spikes which can be seen in the

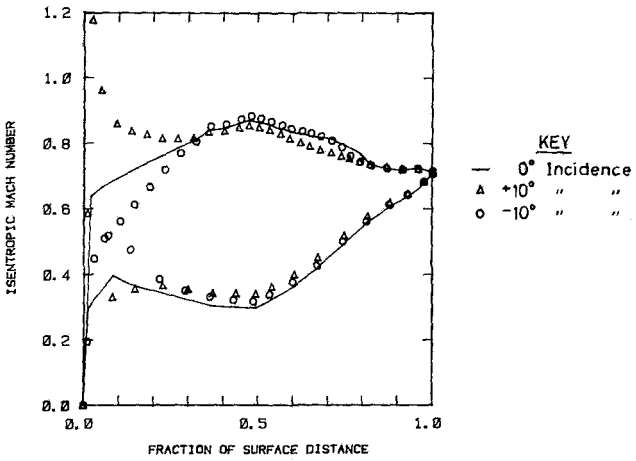

Fig. 16 Effect of incidence on measured Mach number distributions

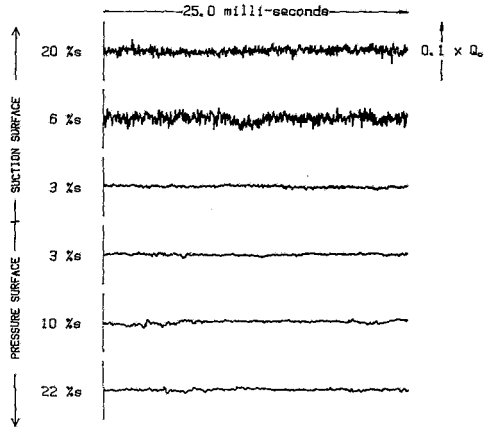

Fig. 17 Unsteady heat transfer signals at + 10 deg incidence

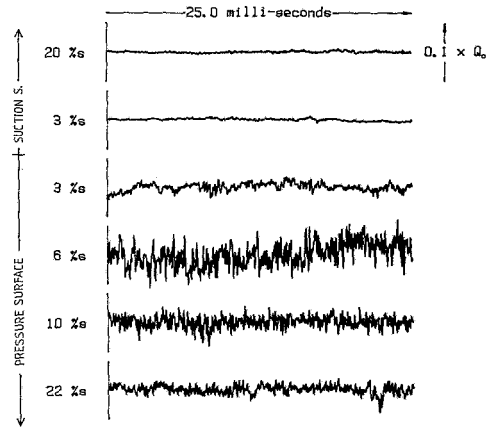

Fig. 18 Unsteady heat transfer signals at − 10 deg incidence

trace. As the boundary layer grows, more and more spots develop, which then coalesce to form an intermittently turbulent boundary layer. It should be noted that the length of the time scale in Fig. 15 is insufficient to enable an estimate of the intermittency to be made. However, by logging the signal for a great period of time (500 ms), it was found that by 20 percent s the boundary layer was turbulent for 45 percent of the time, which assuming a linear variation in intermittency, suggests that transition will not be complete until approximately 40 percent s. The length of the transition region

is, of course, considerable, because it exists in a region of rapidly increasing velocity. Evidence that full transition does in fact take place can be seen in Fig. 13, which shows that at the high Reynolds number, there is no separation bubble at the rear of surface.

The blade surface Mach number distributions that correspond to +10, 0, and −10 deg of incidence are presented in Fig. 16. This shows that increasing the incidence results in a much larger overspeed on the suction surface and a relieving of the diffusion on the pressure surface, whereas at negative incidence the Mach numbers over the leading portion of the suction surface are reduced and those on the pressure surface are increased.

The effect of increasing the incidence upon the development of the blade surface boundary layers is consistent with that expected. The selection of the anemometer output signals that are shown in Fig. 17 demonstrate this. They show that on the pressure surface, the boundary layer is laminar whereas on the suction surface, the initially laminar boundary layer separates after 3 percent s and then reattaches as a turbulent boundary layer before 6 percent s. It then continues to develop as a turbulent boundary layer, which does not, in fact, undergo relaminarization.

At negative incidence, the predicted and measured (see Fig. 18) boundary layers are both laminar on the suction surface. This agreement must be due to the absence of a leading edge overspeed on this surface, a fact which was later confirmed by surface-flow visualization. On the pressure surface, the boundary layer code predicted that laminar separation would occur at 10 percent s and that turbulent reattachment would occur at 20 percent s. In fact, the mean heat transfer measurements showed that the separation bubble began at approximately 3 percent s and that reattachment occurred before 6 percent s. This error in the prediction occurred, as in other similar cases, because insufficient data points were available in a region of rapidly changing boundary layer parameters.

Conclusions

The nature of the development of the blade surface boundary layers in the neighborhood of the leading edge of a high-speed turbine blade has been determined. The success of this investigation relied upon the acquisition of semi-quantitative boundary layer data, using surface-mounted hot films, which was then interpreted with the assistance of inviscid and viscous flow predictions.

At the design conditions, the use of this technique led to the discovery of a velocity overspeed at the leading edge of the suction surface. The deceleration which followed the overspeed resulted in the separation of the laminar boundary layer. The reacceleration, up to peak suction, which followed this deceleration then resulted in a relaminarization of the reattached turbulent boundary layer. On the pressure surface, at the same conditions, a separation bubble was also found to exist.

At off-design conditions, the development of the boundary layers was found to be consistent with the known effects of variable Mach and Reynolds numbers, free-stream turbulence, and incidence.

Acknowledgment

The author wishes to thank the members of the Whittle Laboratory who assisted in the work which is described in this paper, especially Dr. J-J Camus and Mr. R. G. Dominy. The support of Rolls-Royce Ltd., is gratefully acknowledged.

References

1 Gostelow, J. P., and Watson, P. J., "A Closed Circuit Variable Density Air Supply for Turbomachinery Research," ASME Paper No. 76-GT-62, 1976.

2 Bellhouse, B. J., and Schultz, D. L., "Determination of Mean and Dynamic Skin Friction, Separation and Transition in Low-Speed Flow With a Thin-Film Heated Element," *J.F.M.*, Vol. 24, No. 2, 1966, pp. 379–400.

3 Denton, J. D., "An Improved Time Marching Method for Turbomachinery Flow Calculation," ASME, Paper No. 82-GT-239.

4 Herbert, M. V., and Calvert, W. J., "Description of an Integral Method for Boundary-Layer Calculation in Use at N.G.T.E. With Special Reference to Compressor Blades," N.G.T.E. report M82019, July 1982, see also Calvert, W. J., "An Inviscid-Viscous Interaction Treatment to Predict the Blade-to-Blade Performance of Axial Compressors with Leading Edge Normal Shocks," ASME Paper No. 82-GT-135, 1982.

5 Hodson, H. P., "The Detection of Boundary Layer Transition and Separation in High-Speed Turbine Cascades," presented at 8th Int. Symp. on "Measurement Techniques in Transonic and Supersonic Flow," Aachen, Sept. 1983.

6 Jones, W. P., and Launder, B. E., "Some Properties of Sink-Flow Turbulent Boundary Layers," *J.F.M.*, Vol. 56, 1972, pp. 337–351.

B. T. F. Chung

M. M. Kermani

M. J. Braun

J. Padovan

Department of Mechanical Engineering,
The University of Akron,
Akron, Ohio 44325

R. C. Hendricks

NASA Lewis Research Center,
Cleveland, Ohio 44135

Heat Transfer in Thermal Barrier Coated Rods With Circumferential and Radial Temperature Gradients

To study the heat transfer in ceramic coatings applied to the heated side of internally cooled hot section components of the gas turbine engine, a mathematical model is developed for the thermal response of plasma-sprayed ZrO_2-Y_2O_3 ceramic materials with a Ni-Cr-AL-Y bond coat on a Rene 41 rod substrate subject to thermal cycling. This multilayered cylinder with temperature dependent thermal properties is heated in a cross-flow by a high velocity flame and then cooled by ambient air. Due to high temperature and high velocity of the flame, both gas radiation and forced convection are taken into consideration. Furthermore, the local turbulent heat transfer coefficient is employed which varies with angular position as well as the surface temperature. The transient two-dimensional (heat transfer along axial direction is neglected) temperature distribution of the composite cylinder is determined numerically.

Introduction

The thermal and corrosion protectant ceramic coatings applied to the heated side of engine components, such as combustors, seals, and blades of gas turbines, offer a potential improvement in efficiency through the use of higher operating gas temperature or less required cooling air. However, recent research [1, 2] has pointed to the fact that repeatedly subjecting a ceramic coating to high rates of initial heating can impose significant mechanical loads leading to delamination and component failure. Some simplified models [3] have shown that large thermal stresses may be induced during initial start up. In this connection, extensive research has been generated to determine the thermal and mechanical responses of the thermal barrier coating systems.

McDonald and Hendricks [1, 4] used a geometrically simple model to study the behavior of such composite structure subjected to thermal cycling. The specimen consists of a solid Rene 41 rod with a diameter of 1.3 cm coated with 0.13 mm Ni-Cr-AL-Y bond coat and 0.38 mm ZrO_2-Y_2O_3 ceramic. Eight such specimens in a rotating carousel were heated (1311°K) in cross-flow by a high speed of flame (M = 0.3) and then cooled by an air jet. The fuel was jet A-1. The condition of ceramic coating was determined by visual inspection. It was reported that the short cycle (4 min) greatly reduced the life of the ceramic coating in terms of time as compared with longer cycles (57 min). The failure occurred principally at the bond coat-ceramic coat junction. The authors performed the thermal stress calculation based on one-dimensional transient temperature distribution in the rod, i.e., the heat transfer analysis was based on the assumption that temperature gradient of the cylinder exists in radial direction only and the convective heat transfer coefficient is uniform along the circumferential direction. The same type one-dimensional heat transfer analysis was also employed in references [3, 5]. It appears that none of the previous investigations in this field considered the temperature variation along the angular direction; furthermore, very few earlier analyses included the gas radiation effect.

The purpose of this work is to investigate the effects of circumferential variation of heat transfer coefficient and gas radiation upon the temperature distribution in the multilayered solid cylinder. In reality, the convective heat transfer coefficient varies considerably with the angular position as well as the surface temperature which in turn is an unknown quantity.

Mathematical Model

Figure 1 depicts the cross section of the physical model under consideration. Essentially, the same geometry con-

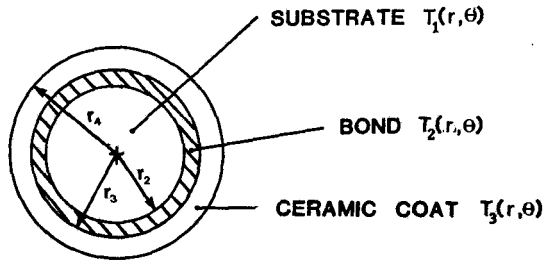

Fig. 1 Schematic of the model

Contributed by the Gas Turbine Division of THE AMERICAN SOCIETY OF MECHANICAL ENGINEERS and presented at the 29th International Gas Turbine Conference and Exhibit, Amsterdam, The Netherlands, June 4–7, 1984. Manuscript received at ASME Headquarters, January 12, 1984. Paper No. 84-GT-181.

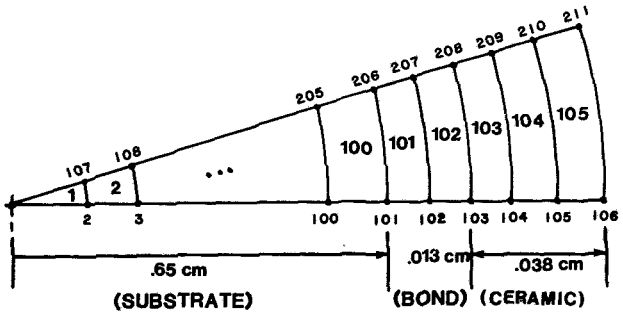

Fig. 2 Nodal and elemental arrangement of the two-dimensional model

sidered in references [1, 3] is examined. It is intended to determine the thermal response of ceramic ZrO_2-Y_2O_3 thermal barrier coatings over a Ni-Cr-AL-Y bond coat, both plasma-sprayed onto a solid Rene 41 rod substrate and subject to thermal shock. The governing heat transfer equations for the system can be written as

$$\nabla \cdot (k_i \nabla T_i(r,\theta,t)) = \rho_i c_i \frac{\partial T_i}{\partial t}(r,\theta,t)$$

$$\text{in } r_i < r < r_{i+1},\ t > 0 \text{ with } r_1 = 0 \qquad i = 1,2,3$$

where T_1, T_2, and T_3 refer to the temperature distributions of Rene 41, Ni-Cr-AL-Y, and Zr_2O_3-Y_2O_3, respectively, and r_2, r_3, and r_4 represent the interfaces at the substrate-bond, bond-ceramic, and ceramic-gas, respectively. The associated boundary and initial conditions are:

$$T_1(0,\theta,t) = \text{finite}$$

$$T_i(r_{i+1},\theta,t) = T_{i+1}(r_{i+1},\theta,t) \qquad i = 1,2$$

$$k_i \frac{\partial T_i}{\partial r}(r_{i+1},\theta,t) = k_{i+1} \frac{\partial T_{i+1}(r_{i+1},\theta,t)}{\partial r} \qquad i = 1,2$$

$$k_i \frac{\partial T_i}{\partial r}(r_{i+1},\theta,t) = h[T_g - T(r_{i+1},\theta,t)] + \sigma[\epsilon_g T_g^4 - \alpha_g T^4(r_{i+1},\theta,t)], \qquad i = 3$$

$$T_i(r,\theta,t) = T_i(r,\theta+2\pi,t) \qquad i = 1,2,3$$

$$T_i(r,\theta,0) = T_a \qquad i = 1,2,3$$

The thermal properties of each layer are temperature dependent and the heat transfer coefficient, h, is a function of angular position and surface temperature; T_a represents the initial temperature which is equal to the ambient temperature for the heating cycle and equal to T_g for the cooling cycle. The axial heat conduction has been neglected in this study, since the main objective here is to examine the circumferential heat transfer effect. Furthermore, the system is assumed to be symmetric between $0 \le \theta \le \pi$ and $\pi \le \theta \le 2\pi$. It should be pointed out that the present mathematical model is still greatly simplified with respect to the actual operating system mentioned in reference [1].

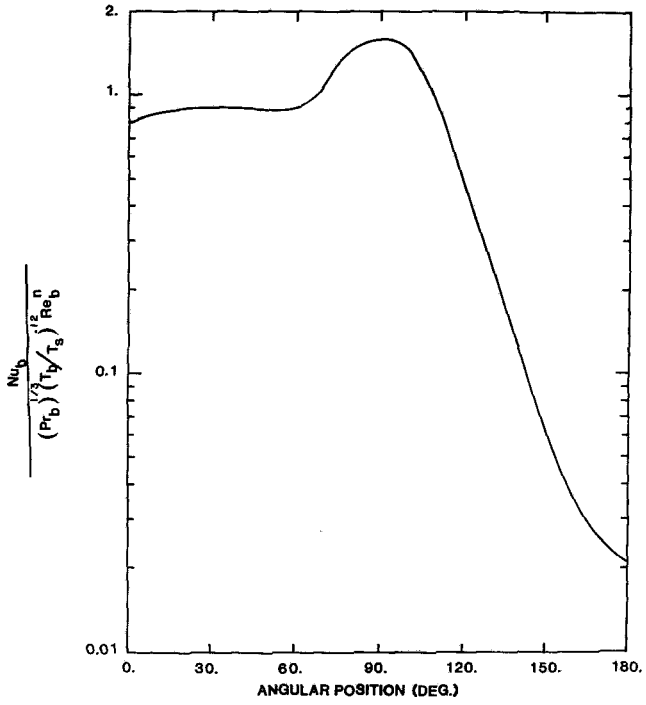

Fig. 3(a) Heat transfer coefficient correlation [7]

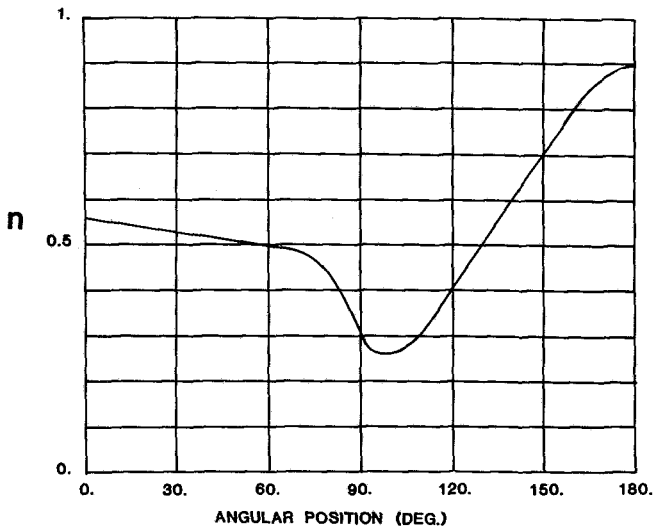

Fig. 3(b) Angular variation of the Re_b exponent n [7]

Due to inherently nonlinear nature of the problem, an analytical solution for the foregoing system is not feasible, therefore, a finite element technique is employed with the aid of the ADINAT program [6]. In ADINAT the isoparametric finite element discretization is utilized. The solution of the incremental heat transfer equation is achieved using Newton-

Nomenclature

c_p = heat capacity
h = heat transfer coefficient
k = thermal conductivity
M = Mach number
Nu = Nusselt number
Pr = Prandtl number
Re = Reynolds number
r = radius
t = time
T = temperature
T_a = initial temperature
T_b = bulk temperature
T_g = environment or gas temperature
T_s = surface temperature
θ = angular position
ρ = density
σ = Steffan-Boltzmann constant
ϵ_g = gas emissivity
α_g = gas absorptivity

Table 1 Thermophysical properties

Property	Temperature K°	Substrate Rene 41	Bond Coat NiCrALY	Ceramic Coat ZrO_2-Y_2O_3
Conductivity	283	.13848	.0577	.00721
	1352	.3346	.166	.0216
W/cm-K	1770	.41129	.208	.0273
Density	A11	.00782	.00698	.00567
Kg/cm^3				
Specific	283	406.	410.	491.
Heat	1367	544.	712.	670.
J/Kg-K	1770	596.	794.	737.

Raphson iteration and the transient analysis using a one-step α-family time integration scheme [6].

The number of time steps employed for this problem was 58. The time increments used were nonuniform. The following table illustrates the time steps and the corresponding time increments.

No. of time steps	3	20	8	5	8	14
Time increment (s)	0.1	0.2	0.5	1.0	2.0	5.0

A relative convergence criterion of 10^{-3} was used to terminate the iteration process of each time step.

Finite Element Discretization

The finite element mesh used in the present transient nonlinear two-dimensional problem contains rather large number of nodes due to geometry consideration. The aspect ratio of the element must be kept in a reasonable range (0.1 ~ 10) in order to obtain an accurate solution. Figure 2 shows a typical segment of nodal and elemental arrangement for one sector. In the present calculation, there are 3886 nodes and 3762 elements. The model considered here was only a semicircle in cross section of the rod, due to symmetry of the system. This semicircle was divided into 36 equal sectors. The four-node element was chosen in this study.

Heat Transfer Coefficient

It is important to have accurate information for the convective heat transfer coefficient between the air stream and the cylinder in order to obtain an accurate temperature distribution.

Convective heat transfer between a gas and a cylinder has been investigated extensively. However, reported measurements of local transfer coefficients are more limited in range and considerable disagreement is noted between the results of the various investigators. The widely accepted correlation proposed by Churchill and Brier [6] was adopted in the present analysis. Figure 3(*a*) shows their proposed variation of $Nu_b/[(Pr_b)^{1/3}Re^n b\ (T_b/T_s)^{0.12}]$ versus angular position θ. The exponent, n, on Reynolds number also depends on the angular position and this relationship is shown in Fig. 3(*b*). The subscripts b and s denote the condition at the bulk stream and on the surface, respectively.

The properties of the flame were taken to be air properties at 1311°K and the atmospheric pressure. The flow conditions and thermal properties of the gas at the heating and cooling processes are as follows:

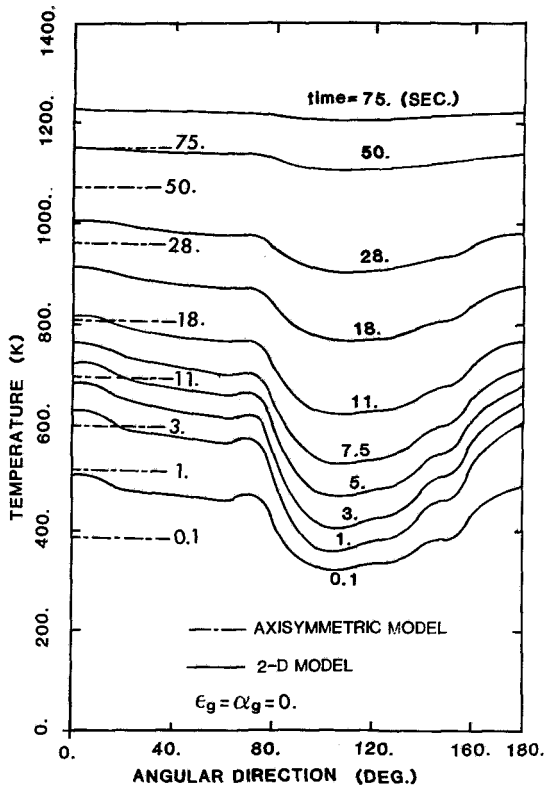

Fig. 4 Ceramic surface temperature versus angular position at various times with $\epsilon_g = 0$

Heating process:	Cooling process:
$T_b = 1311°K$	$T_b = 290°K$
$\nu_b = 2.006 \times 10^{-3}$ ft^3/s	$\nu_b = 0.18 \times 10^{-3}$ ft^3/s
$k_b = 0.07907$ w/m-K	$k_b = .01977$ w/m-K
$Re_b = 1.59 \times 10^4$	$Re_b = 1.77 \times 10^5$
$Pr_b = 0.7502$	$Pr_b = 0.72$

Note that the surface temperature is not known a priori for the present problem.

Thermophysical Properties

The thermophysical properties of substrate, bond coat and the ceramic coatings are available in the literature. They are given in Table 1 at various temperatures. To evaluate these properties at the temperatures other than those shown in Table 1, linear interpolation was applied.

Results and Discussion

In this study the results of heating and cooling of each cycle are considered separately. The rod initially at the room temperature of 290°K is subjected to a high heat flux with an equivalent environment temperature of 1311°K. After reaching the steady state condition at a temperature of 1311°K, the rod is cooled by an air jet at 290°K until the equilibrium condition is reached.

Heating Case. The contribution of gas radiation depends on the properties such as the mean beam length, combustion gas composition and the partial pressure of water vapor and carbon dioxide. Since the detailed information is not available at the present stage, we will perform a parametric study by considering three different cases: $\epsilon_g = \alpha_g = 0$, $\epsilon_g = \alpha_g = 0.5$ and $\epsilon_g = \alpha_g = 1.0$, where the first case corresponds to pure convective boundary condition.

Figure 4 illustrates the variation of temperature with respect

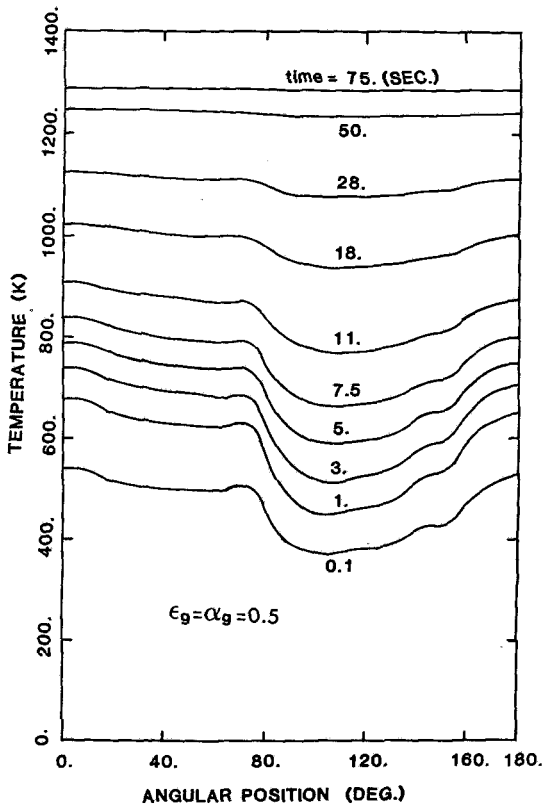

Fig. 5 Ceramic surface temperature versus angular position at various times with $\epsilon_g = 0.5$

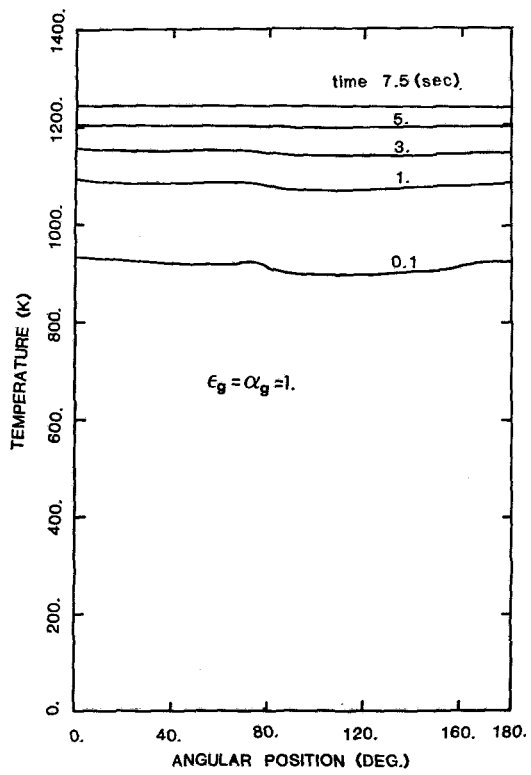

Fig. 6 Ceramic surface temperature versus angular direction at various times with $\epsilon_g = 1.0$

to angular position on the ceramic surface. Radiation is not included for these axisymmetric calculations. For comparison purposes, the temperature history for an axisymmetric model [1, 3] is also shown in Fig. 4. In this model, the variation of heat transfer coefficient in the angular direction was neglected and the following correlation for the heat transfer coefficient was employed [7]:

$$\mathrm{Nu}_b = 0.60\,\mathrm{Pr}_b^{1/3}\mathrm{Re}_b^{1/2}(T_b/T_s)^{0.12}$$

It can be seen from this graph that at the smaller times the temperatures for axisymmetric case are close to the corresponding average temperatures for nonaxisymmetric case. As the time increases the axisymmetric model tends to underpredict the average surface temperatures.

Figures 5 and 6 show the variation of temperature with respect to angular position when the gas radiation is taken into account with gas emissivity being 0.5 and 1.0, respectively. As is seen, the system reaches the steady state much faster as the gas emissivity increases. In addition, the two-dimensional effect becomes insignificant at extremely high gas emissivity. This fact is further observed from Fig. 7 in which the temperature is plotted against time with angular position and gas emissivity as parameters. The figure clearly demonstrates that when the radiation is considered, the system reaches equilibrium temperature rather fast as opposed to the case of heating by pure convection. It is also observed that at the initial stage of the heating period there exists a large temperature gradient along the circumferential direction. This gradient becomes smaller as the gas emissivity is increased.

It is noted that a few local maxima and minima exist on the curves shown in Figs. 4 and 5. On the angular direction there are five local maxima/minima in temperature. These points are identical for the cases with and without radiation. They are at angular positions of 0, 65, 105, 145, and 180 degrees. Figure 7 shows the temperature history of the ceramic coating surface at these five angular positions. The importance of the

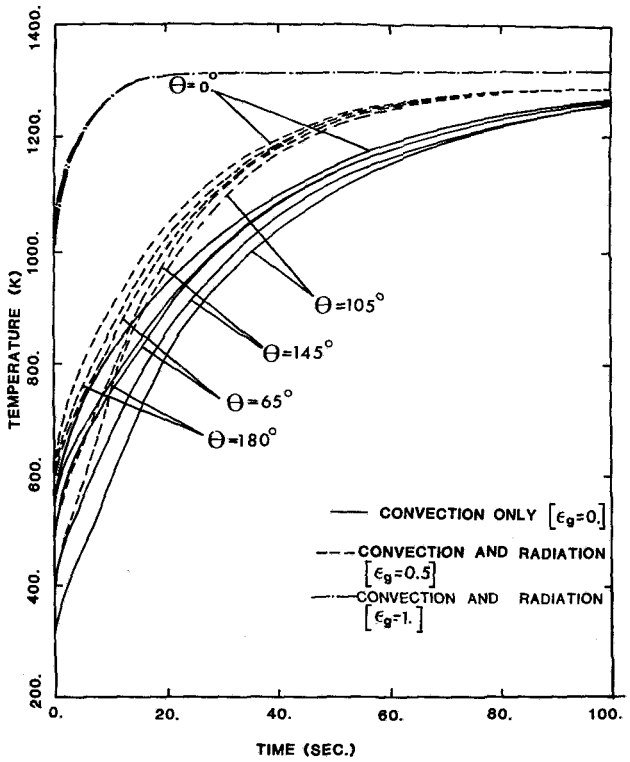

Fig. 7 Surface temperature histories for five angular positions; heating case

gas radiation becomes clear when the gas emissivity is in the order of 0.5. The radiation effect yields a higher rate of temperature change and hence creates a more severe thermal shock. Consequently, a shorter time is required for the system to reach the steady state.

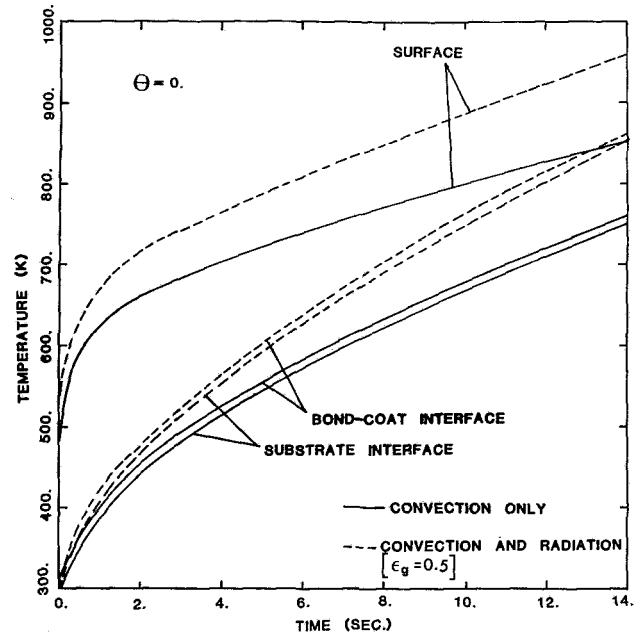

Fig. 8 Interfacial temperature histories during first 14 seconds of heating for angular position $\theta = 0$

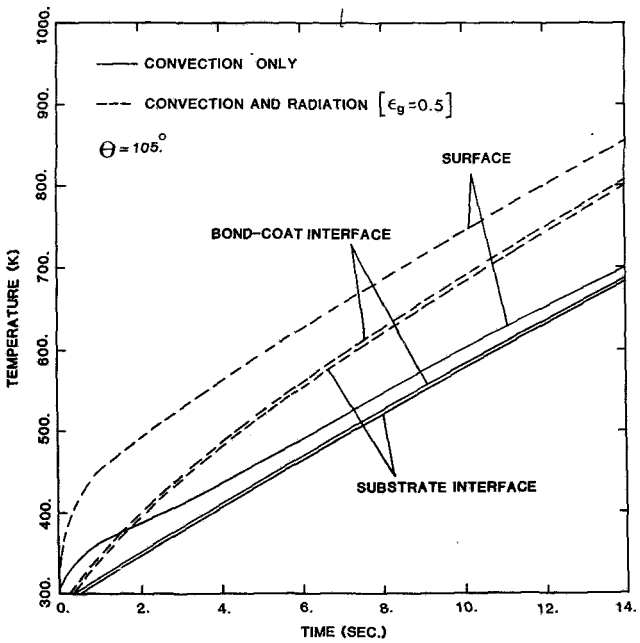

Fig. 9 Interfacial temperature histories during first 14 seconds of heating for angular position $\theta = 105$ deg

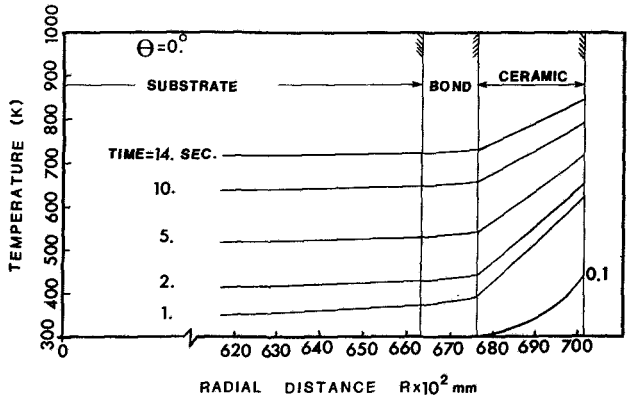

Fig. 10 Temperature distribution in radial direction at angular position $\theta = 0$ deg

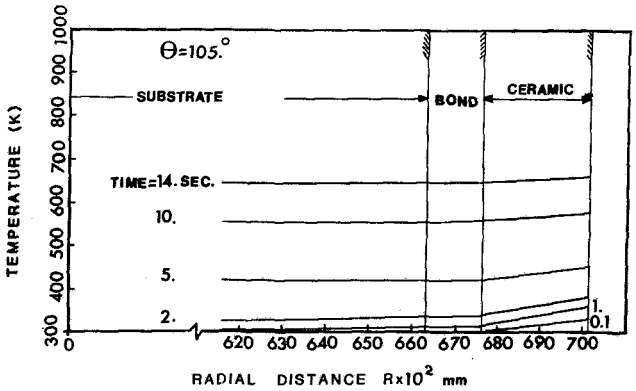

Fig. 11 Temperature distribution in radial direction at angular position $\theta = 105$ deg

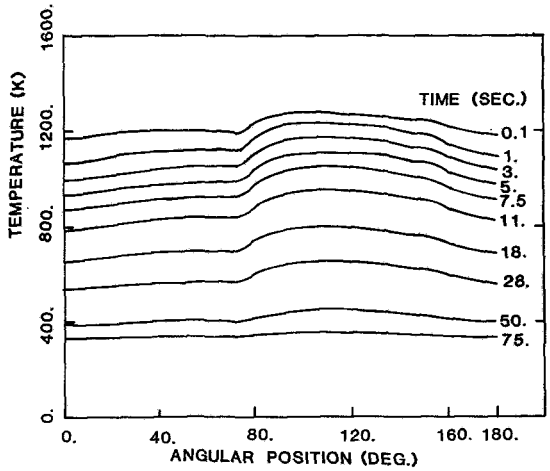

Fig. 12 Variation of surface temperature in angular direction for the case of cooling

Since the temperature gradient is extremely large at the initial stage of the heating process, the first few seconds of the application of the thermal load is important from the thermal stress point of view. Figures 8 and 9 show the temperature history of the first 14 seconds after the application of the thermal load. Both figures illustrate the temperature history at three different positions in radial direction. They are at the ceramic surface, bond-coat interface, and bond-substrate interface. Figure 8 represents the stagnation position of the cylinder, i.e., $\theta = 0$ deg. It is found that the most severe temperature rise occurs at the stagnation point. The effect of radiation is observed from the dashlines for which the gas emissivity and absorptivity are set equal to 0.5. The same trends of heat transfer characteristics are found for positions $\theta = 65$, 145, and 180 deg. At a given time, the lowest temperature is found in the vicinity of the angular position of 105 degrees from the stagnation point. Figure 9 illustrates the temperature history of the three interfaces at this angular position. It is seen that there exists a much smaller temperature gradient in ceramic layer as compared to that of other locations. Furthermore, the radiation appears to cause a larger temperature gradient within the ceramic layer at this angular position. Figures 10 and 11 illustrate the temperature variation along the radial direction at certain times and at two angular locations $\theta = 0$ and $\theta = 105$ deg, respectively. Radiation is not included here. As is anticipated, the temperature gradients in the ceramic are much more severe than that in the substrate.

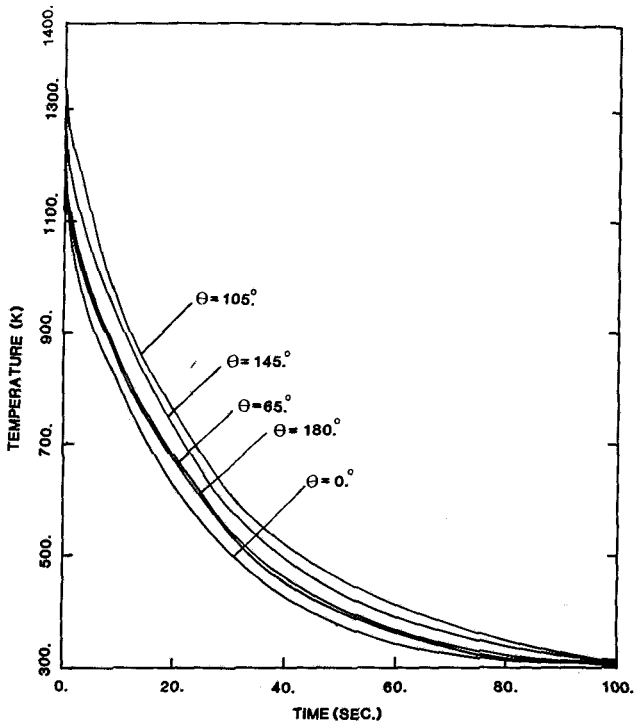

Fig. 13 Temperature history curve for five angular positions; cooling case

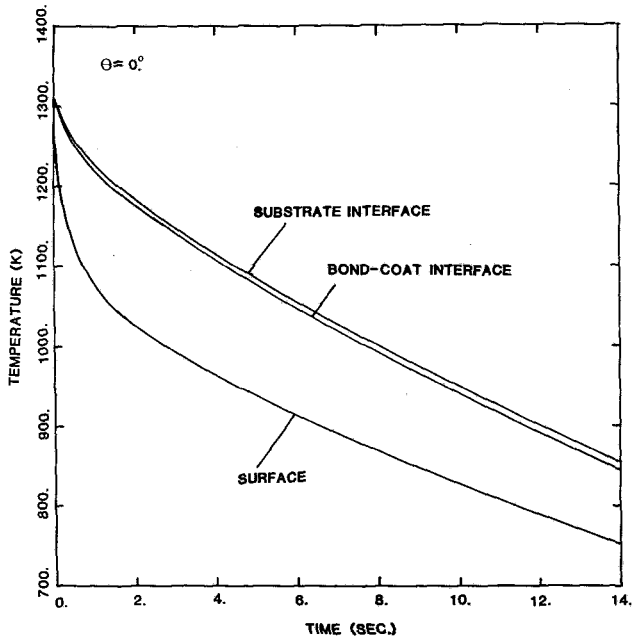

Fig. 14 Interfacial temperature histories during first 14 seconds of cooling for angular position θ = 0 deg

Cooling Case. A cooling process starts after four minutes of heating of the specimen. At this moment the temperature of the cylinder has practically reached a uniform temperature of 1311°K according to our numerical calculations. The cylindrical rod is then cooled by an air jet at a temperature of 290°K. The same correlation for heat transfer coefficient in the heating case is used. Assuming that the air is dry, the gas radiation becomes negligibly small for the cooling. Figure 12 shows the variation of temperature in the circumferential direction at different times. As is expected, the local maxima/minima angular positions are the same as in the heating case. Figure 13 illustrates the surface temperature

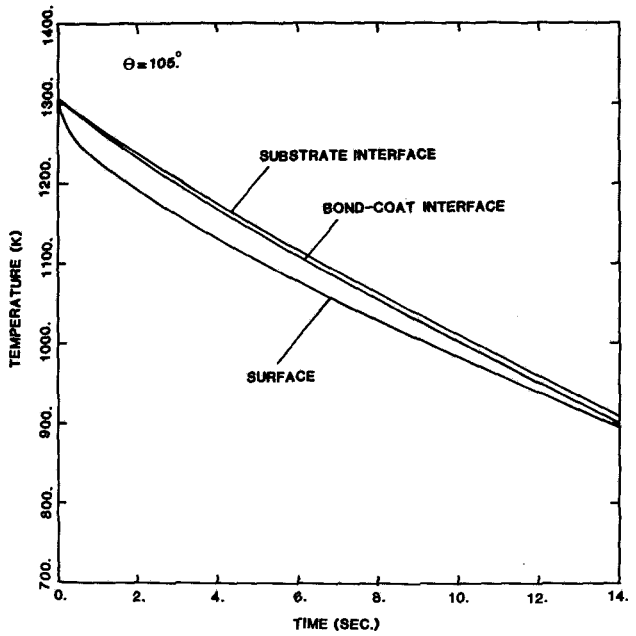

Fig. 15 Interfacial temperature histories during first 14 seconds of cooling for angular position θ = 105 deg

histories during the cooling of these five positions. Figures 14 and 15 show the temperature variations at each layer during the first 14 seconds of the cooling process for angular positions θ = 0 and θ = 105, respectively. Again, similar to the case of heating the temperature gradient within the ceramic layer is rather large except near the angular position of 105 degrees.

Conclusion

The thermal response of plasma-sprayed ZrO_2-Y_2O_3 ceramic materials with a Ni-Cr-AL-Y bond coat on a solid Rene 41 rod substrate subject to thermal shock is studied. In particular, the effects of circumferential variation of heat transfer coefficient and gas radiation are investigated, a case for which none of the previous analyses in this field have considered. Due to the temperature dependent thermal properties in each layer and the nonlinear nature of the imposed boundary conditions, the present problem was solved numerically using a finite element technique. The temperature distribution of the composite cylindrical specimen was presented for both heating and cooling processes. It was found that in either case, the temperature changes most from its equilibrium state at the stagnation point (θ = 0 deg) and changes least at θ = 105 degrees. Similarly, at a given time the maximum temperature gradient across the ceramic occurs at θ = 0 deg while the minimum temperature gradients at θ = 105 deg. However a severe angular temperature gradient is observed in the vicinity of θ = 90 deg.

The effect of gas radiation upon temperature distribution becomes significant as the gas emissivity and absorptivity are in the order of 0.5. The radiation effect yields a higher rate of temperature change and hence creates a more severe thermal shock. Also, a shorter time is required for system to reach the steady state.

The circumferential heat transfer is found to be significant as is evidenced from the large temperature variations along the angular direction. However for combustion gases with extremely high emissivity and absorptivity, the heat transfer effect along angular direction becomes insignificant, con-

sequently, the simplified one-dimensional axisymmetric model will suffice.

Comparison of temperature history was also made between the two-dimensional and the previous one-dimensional models under a pure convection. Our numerical computations reveal that the earlier one-dimensional analysis tends to underpredict the average temperature at larger time.

The final objective of the present project is to develop an understanding of where and why the TBC will spall. The objective cannot be achieved until the thermal stress analysis is completed. However, it is anticipated that the present two-dimensional thermal model will enhance and improve the predictions of the thermal stresses of the system.

Acknowledgments

The work was supported by NASA Lewis Research Center under the grant NAG-3-265.

References

1 McDonald, G., and Hendricks, R. C., "Effect of Thermal Cycling on ZrO_2-Y_2O_3 Thermal Barrier Coatings," *Thin Solid Films*, Vol. 73, 1980, pp. 491–496.

2 Hendricks, R. C., McDonald, G., and Poolos, A. P., "Prolonging Thermal Barrier Coated Specimen Life by Thermal Cycle Management," NASE TM-81742, 1981.

3 Hendricks, R. C., McDonald, G., Mullen, R. L., Braun, M. J., Chung, B. T. F., and Padovan, J., "Thermomechanical Loading of Multilayered Cylindrical Geometries in Thermal Cycling from 300 to 1300 K," *Proceedings ASME-JSME Thermal Engineering Joint Conference*, Vol. 3, 1983, pp. 329–341.

4 Hendricks, R. C., and McDonald, G., "Assessment of Variations in Thermal Cycle Life Data of Thermal Barrier Coated Rods," *Thin Solid Films*, Vol. 74, 1981.

5 Taylor, C. M., and Bill, R. C., "Thermal Stresses in Plasma-Sprayed Ceramic Gas Path Seal," *J. Aircraft*, Vol. 16, No. 4, 1979, pp. 239–246.

6 Bathe, K. J., "ADINAT—A Finite Element for Automatic Dynamics Incremental Non-Linear Analysis of Temperature," Rept. #82448-5, 1978, M.I.T., Cambridge, Mass.

7 Churchill, S. W., and Brier, J. E., "Convective Heat Transfer from a Gas Stream at High Temperatures to a Circular Cylinder Normal to the Flow," *Chemical Engineeirng Progress Symposium Series*, Vol. 51, 1955, pp. 57–66.

Acoustic Emission Evaluation of Plasma-Sprayed Thermal Barrier Coatings

C. C. Berndt
NASA-Lewis Research Center,
Cleveland, Ohio, 44135
Fellow of the Joint Institute
for Aerospace Propulsion
and Power with Cleveland State
University

Acoustic emission techniques have recently been used in a number of studies to investigate the performance and failure behavior of plasma-sprayed thermal barrier coatings. Failure of the coating is a complex phenomena, especially when the composite nature of the coating is considered in the light of possible failure mechanisms. Thus it can be expected that both the metal and ceramic components (i.e., the bond coat and ceramic overlay) of a composite thermal protection system influence the macroscopic behavior and performance of the coating. The aim of the present work is to summarize the "state-of-the-art" in terms of this initial work and indicate where future progress may be made.

Introduction

Plasma-sprayed thermal barrier coatings may be used to improve the efficiency and utility of gas turbine engines [1–4]. Their main advantage lies with a low thermal diffusivity and conductivity [5, 6] which is representative of a ceramic material. Usual methods of characterization for thermal barrier coatings include burner rig tests which simulate the high heat flux conditions that these coatings experience during their service life. These tests are destructive and indicate the relative number of thermal cycles that substrate/coating systems endure. However, it is expected that failure of the thermal protection system is progressive, since cracking and crack growth have been observed prior to ultimate failure, and thus catastrophic failure occurs at some stage when there is a transformation from the microcrack to a macrocrack network. Acoustic emission (AE) techniques have recently been used to examine failure characteristics of plasma-sprayed thermal barrier coatings.

Comprehensive reviews of AE methodology already exist [7–10]. The essential thrust in materials characterization has been to relate an AE response – either rise time [11], amplitude distribution [11–20], count rate magnitude [21, 22], events [19], accumulative counts [10, 22–24], or energy [25, 26] – to a materials parameter such as crack growth or interaction, oxidation, and other measurements of materials durability and performance. The most elementary analysis examines qualitative trends drawn out by the accumulative AE counts that occur above a specific threshold voltage.

Acoustic emission methods have been used, with respect to plasma spray coating technology, in two distinct research areas. The major assumption is that the AE response is related to the cracking behavior. It is well known that elastic energy is emitted during cracking processes, and this is expected to be fundamentally related to cracking mechanisms. However, it is very difficult to analyze an extremely large volume of data that may be generated in a few microseconds. Therefore, the data are usually averaged in some manner during the time frame of experimentation. The "count rate" parameter is one such measurement. It is derived from the frequency that a signal exceeds a particular threshold voltage during a specific time interval. It should be remembered that the initial studies were carried out on thermal barrier coatings of interest at that time and were based on Al_2O_3 and TiO_2 ceramics.

Experimental Details

The AE investigations which have been related to properties of plasma-sprayed coatings are summarized in Table 1 [27–37]. Very brief comments about the test methods and AE results are included in this table. Two areas of applied research have been investigated. These are the determination of mechanical properties (i.e., indentation and tensile adhesion tests) and the coating response to thermal environments. These methods may be used with X-ray diffraction and scanning electron microscopy to characterize the chemical composition and failure processes. A major aim has been establishing a data base for mechanistic studies, and much exploratory work has evolved. An important thrust has been to understand how the original powder formulation and substrate processing parameters change the coating integrity and AE response. For example, powders may be produced by fusing, sintering, spray drying, or composite methods to give a variety of particle morphologies and size distributions. Also the substrate surface may be prepared by various methods, such as preheat conditioning or grit blasting, prior to coating deposition. Examples from both research areas are detailed below.

Mechanical Testing. This area includes indentation and tensile adhesion tests. The early experiments of Safai et al. [27] were carried out on plasma-sprayed and flame-sprayed

Contributed by the Gas Turbine Division of THE AMERICAN SOCIETY OF MECHANICAL ENGINEERS and presented at the 29th International Gas Turbine Conference and Exhibit, Amsterdam, the Netherlands, June 4–7, 1984. Manuscript received at ASME Headquarters February 9, 1984. Paper No. 84-GT-292.

Table 1 Acoustic emission studies on thermal barrier coatings

Reference and Coatings Studied[1]	Type of Test	AE Parameter Examined
(27) Al_2O_3 (f), Al_2O_3-13% TiO_2, Al_2O_3, Al_2O_3-40% TiO_2	-indentation	- total AE counts
(28) Al_2O_3, Al_2O_3-2.5% TiO_2, TiO_2, Al_2O_3-13% TiO_2, Al_2O_3-40% TiO_2	- furnace testing to 475-520°C	- accumulative AE counts
(29) unknown	- cooling of specimen - bending of coating attached to substrate	- accumulative AE counts - effect of deposition parameters i.e., current, air pressure, preheating
(30) stainless steel, 7% YSZ NiCrAlY (ht)	- tensile adhesion tests	- accumulative AE counts - sensitive strain tests of coatings
(31) 8% YSZ (ht)	- tensile adhesion tests	- accumulative AE counts - count rate distributions
(32) 20% MSZ (ht)	- tensile adhesion tests	- accumulative AE counts - average AE count
(33) NiAl-20% Al_2O_3, NiAl-40% Al_2O_3 NiAl-40% ZrO_2, NiAl-50% ZrO_2	- bending tests	- count rate observation - examination of RMS
(34) 8% YSZ	- tensile adhesion tests	- analysis of count rate distributions
(35) Al_2O_3, 20% YSZ, TiO_2, 7% CSZ, NiCrAl	- thermal tests	- accumulative AE counts
(36) 12% YSZ, NiCrAlZr (ht)	- thermal tests	- accumulative AE counts - processing effects - count rate analysis - bond coat effects
(37) 12% YSZ (ht)	- thermal tests	- accumulative AE counts - count rate analysis - sequential failure of coatings

(1) (ht) indicates that some coatings were heat treated, (f) indicates that the coating was flame sprayed. All the other coatings were plasma-sprayed.
YSZ indicates yttria stabilized zirconia, MSZ is magnesia stabilized and CSZ is calcia stabilized. Weight percentages are used.

ceramic coatings and are pertinent to the study of thermal barrier coatings. A summary of their results is shown in Table 2 and reveals an inverse correlation between total AE counts measured during hardness testing and the tensile adhesion strength. The AE data have the additional advantage of conveying information about fracture mechanisms within the coating. Thus the flame-sprayed coating displayed noise levels almost one order of magnitude in excess of the most adherent coating. It was suggested that the coating porosity played a significant role as centers for noise activity. It is clear then, from this initial study, that a propensity for crack evolution and mobility as measured by AE during indentation tests, also correlates to a lower adhesion strength. This research has not been actively pursued with respect to the field of thermal barrier coatings. However, a modified technique, which incorporates attaching a transducer to a scribe and then scratch-testing coatings, has been successful [41–43] in the routine assessment of adhesion characteristics of coatings.

Monitoring of AE during tensile adhesion tests permits direct comparison of the mechanical properties to the noise level and intrinsic character of the coating. A summary of AE and bond strength data is presented in Table 3 and shows that the total AE count is proportionately related to the tensile adhesion bond strength of the coating. In other words, coatings which released a high amount of elastic energy prior to ultimate tensile failure also exhibited a high bond strength. This relation holds even if the different experimental arrangements of these studies are considered. It should be further noted that the bond strengths and the accumulative AE count data show a wide scatter for nominally replicate coatings. This variation may be related to either real changes in actual processing conditions (i.e., the plasma deposition parameters or changes in the substrate) or to factors associated with the preparation of the tensile adhesion test specimen and testing methods. For example, a low measurement of bond strength may result from imperfect specimen preparation where fine peripheral cracks have been introduced into the specimen. It has also been demonstrated, from the mechanical testing of coatings, that high count rates may be associated with cracking around fine topographic features on the surfaces of individual particles while low count rates can be related to interlamellar failure [31, 34].

Thermal Tests. It is difficult to correlate the various thermal cycling experiments due to the different AE equipments used in these investigations. In one case, an "Acoustic Emission Technology Corporation" system was used [27, 28, 30–33, 35], whereas the other workers used a "Dunegan/Endevco 3000 series" system [36, 37].

The first area [28] of investigation concerns the high-temperature response of plasma-sprayed Al_2O_3, Al_2O_3 with either 2.5, 13, or 40wt percent TiO_2 and TiO_2 coatings which were heated up to 520°C. This initial work revealed how the accumulative AE changed for the various coatings and qualitatively related the response to the cracking morphology that was observed by scanning electron microscopy. An important result was the relative effect of the weight percentage of TiO_2 in an Al_2O_3 -TiO_2 powder mix. It was found that a coating manufactured from a two-component system displayed less noise than coatings formed from each individual component. This was interpreted as less cracking within the coating and therefore enhanced durability. However a major shortcoming of this preliminary work, and one that is common with all AE analyses, is in *quantitatively* assessing the AE information to give crack densities and distributions.

Another AE study has been carried out during the thermal cycling of Al_2O_3, TiO_2, ZrO_2-7wt percent CaO, and ZrO_2-20wt percent Y_2O_3 coatings [35]. In some cases, a NiCrAl bond coat was also used. It was found that the total AE count (count rate was not examined) changed with respect to temperature and that these trends could be correlated to the coating integrity. The extent of cracking within the coating

during thermal cycling was reflected by the character of AE activity in the temperature regime of experimentation. These tests showed that the bond coat acted as a compliant layer between the substrate and the ceramic coating. For example, the initial thermal cycles of a bond-coated specimen may show more counts than a specimen coated only by a ceramic. However, it was demonstrated that the total count of the bond-coated sample decreased on repeated thermal cycling, and this indicated that the bond coat may arrest cracks and thereby improve coating integrity.

A more recent study differed from the previous work by examining the count rate distribution as well as the accumulative counts. The count rate was considered as distinguishing between different cracking phenomena. Coatings of ZrO_2-12wt percent Y_2O_3 were tested by heating to 1200°C and cooling to room temperature over a cycle period of 10 hrs [36, 37]. The magnitude of the count rates were then compared to establish the nature of the major failure mechanism. Thus the most predominant count rate that contributed to the total accumulative count could be discerned; and this was termed the "peak count rate." However, the temperature or time sequence nature of the data is lost in using this method to analyse the AE data. One way of finding the influence of temperature on the count rate is to calculate an average temperature from the measured count rate. This method is an approximation because it is based on establishing an "average independent parameter" from the "measured dependent value." On the other hand these results gave insights into: (*i*) the relative distribution of the count rate phenomena; and (*ii*) the influence of temperature with regard to crack growth. The main emphasis is that the effect of temperature on the AE response from the coating can be studied. Other more rigorous analyses are currently being developed.

Discussion

Cracking Processes. Several considerations and assumptions of the AE method are detailed below. A basic premise is that the AE is related to cracking processes within the specimen. The AE generated from other processes, such as phase transformations, is negligible since the heat treatment times are very short. However, noise may be generated from oxidation processes and, more importantly, from the effects of oxide growth on the coating structure.

It is argued that the count rate parameter may have significance in regards to cracking processees. It is certain that many different cracking events are integrated for any specific count rate value and each of these events may generate their own characteristic AE count rate. On the other hand, there are many variables associated with cracking; for example, the number of cracks, the size of cracks, the distribution of cracks, and how all of these relate to crack growth. High count rates arise from an increase in crack initiation and/or growth, and they were not randomly distributed with respect to the temperature. It has been shown that a particular count rate interval contributes a significant proportion of the total counts and that the count rate value and its share is dependent on the coating formulation and deposition technique. It is possible to relate the peak count rate to the temperature at which AE events occur but no rigorous analysis presently exists.

It has been pointed out previously that acoustic emission during any sampling period is dependent on both the number of cracks and growth of cracks. Thus it is conceivable that two sets of contrasting conditions (large growth of a few cracks or small growth of many cracks) may give rise to the same count rate. This is a crucial problem to reconcile because it relates to the mechanism of cracking. Therefore the "count rate" does not indicate the kinetic processes of crack interaction. It is reasonable to assume that identical deformation processes are occurring throughout the coating and therefore the relative effects can be examined at different temperatures. In the same manner, different coatings may be compared by their different AE responses. With regard to these assumptions, the experimental data can be related in a semiquantitative manner to cracking behavior.

It is important to distinguish between the terms "extent of cracking" and "cracking mechanisms." The extent of cracking refers to the crack growth, and this is quantified directly by the total number of AE counts. However, the rate at which these counts occur identifies whether cracking occurs via lamellar, translamellar or through bond coat and substrate interactions (or any other processes which generate noise) and this is termed the cracking mechanism.

Mechanical Tests. Tensile adhesion tests are primarily carried out to ascertain materials properties of coatings [44, 45]. Several critiques have already pointed out the limitations of this test technique with respect to the important material properties of the coating [46, 47]. The modes of failure are broadly classified into two types: (*i*) cohesive when failure occurs entirely through the coating, and (*ii*) substrate-interfacial where failure occurs at the interface between the coating and the substrate. Failure may also occur near the bond coat-ceramic coating interface and this is often termed adhesive failure. Mixed modes of failure may occur in the same specimen and therefore characterization of the bond strength by a single number is too simplistic. Also, such data do not contribute to an understanding of fundamental coating properties and do not give insight into failure mechanisms.

However, the count rate parameter may present further insights into cracking phenomenon and rate activated processes. For example, the count rate distributions of samples subjected to tensile adhesion tests, in some instances, displayed bimodal distributions [31, 34]. The nature of this distribution could be directly correlated to the fine topographic detail on the fracture surface. This, in turn, resulted from a powder consisting of the coalescence of many fine particles (produced by a sintering process) instead of using the ball-milled product of the fused powder. Therefore, in the foregoing example, the count rate was a more sensitive measurement than the accumulative counts and could be related to the cracking mechanism.

Any detailed analysis of the failure mechanisms of coatings must correlate the count rate distribution to the coating microstructure and bond strength data. Other workers [22, 25] have used AE methods to characterize the bond strength of organic adhesives that were tested by the lap shear technique. An interesting result was that faulty preparation of joints that resulted in low bond strengths could also be detected by greater amounts of emission at relatively low loads. This is analogous to work carried out on plasma-sprayed coatings, and thus very high count rates observed during the initial loading may represent a different cracking mechanism. The magnitude represents either: (*i*) the nucleation of new cracks, or (*ii*) the growth and interaction of the existing cracks. Therefore, the physical processes which account for the monomodal distributions of increasing count rate are crack formation and growth.

It should be pointed out that the AE response from indentation and tensile adhesion tests show inverse behavior. For example, the AE counts are a maximum for the most adherent coatings, as measured by bond strength determinations (Table 3), but are a minimum for the same coating during indentation tests (Table 2). The change in AE response occurs due to the nature of both test methods. The tensile adhesion test is an endurance test ending with catastrophic failure of the specimen. On the other hand, indentation tests yield a result when the fracture resistance of the test material

Table 2 Acoustic emission and mechanical tests for plasma-sprayed coatings (1)

Coating (2)	AE counts (10^3)	Strength (MPa)	Hardness (R_c)
Al_2O_3 (f)	308	4.4 (3)	40
Al_2O_3 (p)	139	6.9 (4)	60
Al_2O_3-13% TiO_2 (p)	85	15.5	63
Al_2O_3-40% TiO_2 (p)	39	27.6	61

(1) Strength data from sources as indicated, otherwise from reference 38. AE data from reference 27.
(2) (f) is flame sprayed, (p) is plasma sprayed.
(3) reference 39.
(4) reference 40.

Table 3 AE studies and tensile adhesion tests of plasma-sprayed coatings (1)

Reference and Coating (2)	Bond strength (MPa) mean	s.d. (3)	Total AE mean	s.d.
(30) Stainless steel	54.2	8.5 (5)	61,300	42,636
7% YSZ	25.8	6.9 (5)	10,670	5,630
7% YSZ (ht)	19.2	2.8 (5)	8,530	2,856
7% YSZ + NiCrAlY	54.8	--- (2)	40,575	-----
7% YSZ + NiCrAlY (ht)	59.5	9.4 (3)	36,025	16,743
(31) 8% YSZ	34.5	3.3 (6)	51,270	26,851
8% YSZ (ht)	12.9	6.9 (4)	6,528	4,232
(32) 20% MSZ	18.2	2.3 (4)	7,320	3,326
20% MSZ (ht)	22.3	3.4 (3)	14,073	7,112

(1) Different AE equipment has been used for these experiments.
(2) YSZ indicates yttria stabilized zirconia and MSZ is magnesia stabilized. Weight percentages are used. (ht) indicates that coatings were heat treated in argon at 1200°C.
Note that the original powder morphologies differ.
(3) Standard deviation. Values in brackets indicate the number of tests.

balances a predetermined force. Therefore, in the latter case, minimum AE response indicates the more durable material.

Thermal Cycling. The AE data of thermal cycling experiments can be regarded in the same fashion as the bond strength measurements. The thermal tests examined the influence of the bond coat and substrate heat treatment on the AE character of the coating, whereas the strength measurements concentrated on effects arising from powder morphology and heat treatment of the coating. Incorporation of a bond coat, in the case of thermal cycling, decreases the absolute value of the peak count rate, while the number of counts which occur over these intervals increases. This relationship is observed regardless of the substrate conditioning treatments. The inference is that many small cracking events occur (rather than fewer large cracks) when the bond coat is used. Such failure mechanisms as microcracks have a beneficial effect of dissipating energy and increasing the fracture toughness [48] of materials.

Heat treatment of the substrate immediately prior to coating deposition also changed the AE response during thermal cycling. Coatings that were deposited onto preheated substrates showed evidence of cracking at higher temperatures during cooling than coatings sprayed under optimal conditions. This clearly demonstrates the application of AE methods to follow, in situ, thermally activated cracking processes. It was also possible to examine the sequence of coating failure during thermal cycling. In this case, the analysis of the AE data is quite complex, since the prior cracked structure of the coating influences the AE response. There is also the matter of dissociating new crack activity with cracking phenomenon that result from crack edges rubbing against each other. This will to a certain extent mask newly occurring fracture processes from detection.

Future Studies. Initial work on coating evaluation via AE studies has shown promise as a characterization technique for the fracture behavior of plasma-sprayed thermal barrier coatings. Further work is aimed at precisely quantifing the count rate and crack growth (or kinetic) aspects of coating failure. It will be necessary to characterize the different failure modes of the coating/substrate system, that is, the interlamellar and translamellar failures of the ceramic and bond coat components. A more fundamental analysis of coating behavior is to examine the unprocessed AE signal. An analysis of this nature is difficult to carry out but is expected to lead to a detailed understanding of cracking mechanisms.

Conclusions

The present work reviews experiments carried out during thermal cycling and tensile adhesion tests of plasma-sprayed coatings which were simultaneously monitored for acoustic emission. In this way the progressive failure of coatings can be ascertained.

The mechanical studies have been based on tensile adhesion tests and show that adhesion strength is related to the accumulated AE counts. Thus coatings that fail at a high tensile stress also exhibit a high AE count. More detailed analysis related the count rate distribution, with respect to time, to the fracture morphology.

The AE data indicate that the thermal cycling performance of plasma-sprayed coatings that have been prepared under different conditions can be distinguished by their AE spectra. The spectrum can be described in terms of either accumulative counts or total counts for a specific count rate interval. The latter method enables dissociation of the peak count rate, which is expected to be related to the cracking mechanism. It was also established how these phenomena changed with respect to temperature.

Acknowledgments

The author wishes to thank Prof. H. Herman and Mr. R. Shankar of the Laboratory for Surface Science and Technology at the State University of New York at Stony Brook for discussions and provision of facilities. This work has been supported by NASA-Lewis Research Center (Surface Protection Section) under grant numbers NAG 3-164 and NCC 3-27.

References

1 Stepka, F. S., Liebert, C. H., and Stecura, S., "Summary of NASA Research on Thermal Barrier Coatings," SAE *Transactions*, Vol. 86, 1977, pp. 1487–1499.

2 Miller, R. A., Levine, S. R., and Hodge, P. E., "Thermal Barrier Coatings for Superalloys, Superalloys—1980," Pub. ASM, 1980, pp. 473–480.

3 Levine, S. R., Miller, R. A., and Stecura, S., "Improved Performance Thermal Barrier Coatings," *Proc. NACE Int. Conf. on High-Temperature Corrosion*, edited by R. A. Rapp, Pub. NACE, 1983, pp. 621–627.

4 Levine, S. R., Miller, R. A., and Hodge, P. E., "Thermal Barrier Coatings for Heat Engine Components," *SAMPE Quart.*, Vol. 12, Oct. 1980, pp. 20–26.

5 Sevcik, W. R., and Stoner, B. L., "An Analytical Study of Thermal Barrier Coated First Stage Blades on a JT9D Engine," NASA-Lewis CR-135360, Jan. 1978.

6 Elchinger, M. F., Martin, C., and Fauchais, P., "Measure of the Diffusivity of Ceramic Materials Either Sintered or Sprayed by Means of a Flash Method With a Positive or Negative Pulse," *Rev. Int. Hautes Temper. Refract.*, Vol. 16, 1979, pp. 317–330.

7 Lord, A. E., Jr., "Acoustic Emission," *Physical Acoustics*, Vol. 11, 1975, pp. 289–353, edited by W. P. Mason and R. N. Thurston, Academic Press, 1975.

8 Vary, A., "Ultrasonic Measurement of Materials Properties," *Research Techniques in Nondestructive Testing*, Vol. 4, 1980, pp. 159–204, edited by R. S. Sharp, Academic Press, 1980.

9 Liptai, R. G., Harris, D. O., and Tatro, C. A., ed. *Acoustic Emission*, ASTM STP 505, Pub. ASTM Philadelphia, Pa., 1972.

10 Wadley, H. N. G., Scruby, C. B., and Speake, J. H., "Physical Examination of Metals," *Int. Met. Rev.*, Vol. 25, No. 2, 1980, pp. 41–64.

11 Rodgers, J., "Wave-Shape Analyses of AE Trends, in "Acoustic Emission Trends," *Pub. Acoustic Emission Technology Corp.*, Vol. 3, No. 1, 1982.

12 Curtis, G., "Acoustic Emission—Spectral Analysis of Acoustic Emission," *Non-Destr. Test.*, Vol. 7, No. 4, 1974, pp. 82–91.

13 Cuthrell, R. E., and Randich, E., "The Embrittling Effects of Hydrogen on a Variety of Inorganic Materials as Indicated by Acoustic Emission," *J. Mater. Sci.*, Vol. 14, 1979, pp. 2563–2566.

14 Guild, F. J., Phillips, M. G., and Harris, B., "Acoustic Emission Studies of Damage in GRP," *NDT Int.*, Vol. 13, No. 10, 1980, pp. 209–218.

15 Hill, R., and Stephens, R. W. B., "Simple Theory of Acoustic Emission—Consideration of Measurement Paremeters," *Acustica*, Vol. 31, 1974, pp. 224–230.

16 Holt, J., Goddard, D. J., and Palmer, I. G., "Methods of Measurement and Assessment of the Acoustic Emission Activity from the Deformation of Low Alloy Steels," *NDT Int.*, Vol. 14, No. 4, 1981, pp. 49–58.

17 Peapell, P. N., and Topp, K., "Acoustic Emission—An Analytical System for Research and Teaching," *Metall. and Mater. Techn.*, Vol. 14, No. 1, 1982, pp. 21–24.

18 Pollack, A. A., "Acoustic Emission-2; Acoustic Emission Amplitudes," *Non-Destr. Test.*, Vol. 6, No. 5, 1973, pp. 264–269.

19 Stone, D. E. W., and Dingwall, P. E., "Acoustic Emission Parameters and Their Interpretation," *NDT Int.*, Vol. 10, No. 4, pp. 51–62.

20 Woodward, B., "Identification of Acoustic Emission Source Mechanisms by Energy Spectrum Analysis," *Ultrasonics*, Vol. 14, No. 11, 1976, pp. 249–255.

21 McKinney, K. R., Chaskelis, H. H., and Freiman, S. W., "Prediction of Flaw Sizes From Acoustic Emission Measurements in Ceramics," *Am. Ceram. Soc.*, Vol. 59, No. 7&8, 1976, pp. 369–370.

22 Hill, R., "The Use of Acoustic Emission for Characterising Adhesive Joint Failure," *NDT Int.*, Vol. 10, No. 4, 1977, pp. 63–72.

23 Ashary, A., Meier, G. H., and Pettit, F. S., "Acoustic Emission of Oxide Cracking," *High-Temperature Protective Coatings*, edited by S. C. Singhal, ASM, 1982, pp. 105–119.

24 Drouillard, T. F., and Glenn, T. G., "Production Acoustic Emission Testing of Braze Joints," *Review of Progress in Quantitative Nondestructive Testing*, edited by D. O. Thompson and D. E. Chimenti, Plenum Press, 1982, pp. 485–489.

25 Curtis, G. T., "Acoustic Emission Energy Relates to Bond Strength," *Non-Destr. Test.*, Vol. 8, No. 5, 1975, pp. 249–257.

26 Dickinson, J. T., Snyder, D. B., and Donaldson, E. E., "Electron and Acoustic Emission Accompanying Oxide Coating Fracture," *Thin Solid Films*, Vol. 72, 1980, pp. 223–228.

27 Safai, S., Herman, H., and Ono, K., "Acoustic Emission Study of Thermally-Cycled Plasma-Sprayed Oxide Coatings," *9th. Int. Thermal Spraying Conf.*, The Hague, 19–23 May, 1980, Nederlands Instituut voor Lasteniek, 1980, pp. 129–132.

28 Safai, S., Herman, H., and Ono, K., "Acoustic Emission Study of Thermal-Sprayed Oxide Coatings," *Am. Ceram. Soc. Bull.*, Vol. 58, No. 6, 1979, p. 624.

29 Steffens, H. -D., and Crostack, H. -A., "Non-Destructive Testing of Thermally Sprayed Coatings," *9th. Int. Thermal Spraying Conf.*, The Hague, 19–23 May, 1980, Nederlands Instituut voor Lasteniek, 1980, pp. 120–128.

30 Shankar, N. R., Berndt, C. C., and Herman, H., "Characterization of the Mechanical Properties of Plasma-Sprayed Coatings," *Mater. Sci. Res.*, Vol. 15, edited by D. R. Rossington, R. A. Condrate and R. L. Snyder, Plenum Press, 1983, pp. 473–490.

31 Shankar, N. R., Berndt, C. C., and Herman, H., "Failure and Acoustic Emission Response of Plasma-Sprayed ZrO_2-8wt% Y_2O_3 Coatings," *Ceram. Eng. Sci. Proc.*, Vol. 3, No. 9–10, 1982, pp. 772–792.

32 Shankar, N. R., Berndt, C. C., and Herman, H., "Structural Integrity of Thermal Barrier Coatings by Acoustic Emission," *10th. Int. Thermal Spraying Conf.*, Essen, 2–6 May, 1983, Pub. DVS (German Welding Soc.), 1983, pp. 41–45.

33 Berndt, C. C., et al., "Fire Barrier Coatings for Protection of Aluminum Structures," ibid, pp. 182–186.

34 Berndt, C. C., "Behavior of Plasma-Sprayed Coatings," *Ultrastructure Processing of Ceramics, Glasses and Composites*, Gainesville, Fla., edited by L. L. Hench and D. R. Ulrich, J. Wiley and Sons, 1984, pp. 524–532.

35 Shankar, N. R., et al., "Acoustic Emission From Thermally Cycled Plasma-Sprayed Oxides," *Am. Ceram. Soc. Bull.*, Vol. 62, No. 5, 1983, pp. 614–619.

36 Berndt, C. C., and Herman, H., "Failure During Thermal Cycling of Plasma-Sprayed Thermal Barrier Coatings," *Thin Solid Films*, Vol. 108, No. 4, 1983, pp. 427–437.

37 Berndt, C. C., "Studies on Plasma-Sprayed Thermal Barrier Coatings," NATO Advanced Study Institute, Les Arcs, France, July 3–15, 1983, edited by S. C. Singhal and R. Kossowski, Plenum Press, in press.

38 Metco Plasma-Spraying Tables, Pub. Metco Inc., Westbury, N.Y.

39 Lyashenko, B. A., et al., "Strength of Adhesion between Plasma-Sprayed Coatings and the Base Metal," *Soviet Powder Metall. and Metal Ceram.*, Vol. 8, 1969, pp. 331–334.

40 Wilms, V., and Herman, H., "Plasma Spraying of Al_2O_3 and Al_2O_3-Y_2O_3, *Thin Solid Films*, Vol. 39, 1976, pp. 251–262.

41 Hinterman, H. E., "Tough-Hard Composite Materials—Interface—Coating Relationships," *Annals CIRP*, Vol. 31, 1982, pp. 435–440.

42 Laeng, P., and Steinmann, P. A., "Adhesion Testing of Hard CVD Coatings Using the Scratch Test," *8th Int. Conf. on CVD*, edited by J. M. Blocker, Jr., G. S. Vuillard, and G. Wahl, Electrochem. Soc., Pennington, N.J., 1981, pp. 723–736.

43 Perry, A. J., Laeng, P., and Steinmann, P. A., "Scratch Test Adhesion of TiC Deposited Industrially by Chemical Vapor Deposition on Steel," *Thin Solid Films*, Vol. 96, No. 1, 1981, pp. 45–51.

44 "Standard Method of Test for Adhesion or Cohesive Strength of Flame-Sprayed Coatings," ASTM, C 633–69, The American Society for Testing and Materials.

45 Davies, D., and Whittaker, J. A., "Methods of Testing the Adhesion of Metal Coatings to Metals," *Met. Reviews*, Vol. 12, 1967, pp. 15–26.

46 Berndt, C. C., and McPherson, R., "The Adhesion of Plasma Sprayed Ceramic Coatings to Metals," *Mater. Sci. Res.*, Vol. 14, 1981, pp. 619–628.

47 Mittal, K. L., "Adhesion Measurement of Thin Films," *Electrocomponent Sci. and Tech.*, Vol. 3, 1976, pp. 21–42.

48 Pompe, W., et al., "Increased Fracture Toughness of Brittle Materials by Microcracking in an Energy Dissipative Zone at the Crack Tip," *Mater. Sci. Letters*, Vol. 13, 1978, pp. 2720–2723.

Effect of Pressure on Heat Transfer to a Particle Exposed to a Thermal Plasma

Xi Chen
Engineering Thermophysics Division,
Department of Engineering Mechanics,
Tsinghua University,
Beijing 100084,
People's Republic of China

E. Pfender
Heat Transfer Division,
Department of Mechanical Engineering,
University of Minnesota,
Minneapolis, Minn. 55455

This study is concerned with the effect of reduced pressure on heat transfer to particulate matter injected into a thermal plasma. Reduced pressures in conjunction with the high temperature in a thermal plasma lead to a strong increase of the mean free path in the plasma, and therefore, the Knudsen effect plays an important role in this situation. Based on the heat-conduction-potential jump approach, calculated data are presented for small spherical particles, typical for applications in plasma processing (for example, plasma spraying) and in plasma chemistry. The Knudsen effect severely reduces the heat flux to a particle, even for larger particles (up to 100 μm) at reduced pressures. For small particles (<10 μm) this effect is even felt at atmospheric pressure.

Introduction

Although several aspects of heat transfer to a particle immersed into an atmospheric-pressure thermal plasma have been studied [1-12], a quantitative assessment of the effect of pressure on heat transfer remains still to be done. This paper addresses this problem.

Heating of particles in a thermal plasma at reduced pressures is of increasing interest in connection with plasma spraying in soft vacuum. There is no doubt that heat transfer to a particle will be substantially reduced as the pressure is lowered. In a typical soft-vacuum plasma spray arrangement, particles will be heated under variable pressure as they travel along their trajectories.

Since the pressure is still high close to the nozzle exit of the plasma spray gun, the initial part of the trajectory of an injected particle will be particularly important for heat transfer.

The effect of pressure on heat transfer to a particle is due to:

1 The change of composition and the change of thermophysical properties of the plasma (ionization-recombination and/or dissociation-recombination are pressure-dependent)

2 The increased mean free path length of gaseous particles at reduced pressures, which implies [10] that the Knudsen effect will play an important role at reduced pressures.

It will be shown in a later part of this paper that the effect of pressure on heat transfer due to the change in plasma composition and properties is of less importance compared to the Knudsen effect. Therefore, this paper will be primarily concerned with a quantitative analysis of the Knudsen effect on heat transfer to small particles. The heat-conduction-potential jump approach developed in a previous paper [10] will be employed in this analysis; i.e., validity of the calculated results will be restricted to the temperature jump region applicable to relatively small values of the Knudsen number, but beyond values for which the continuum approach would be valid. Further analysis considering larger values of the Knudsen number will be reserved for a subsequent paper.

The time intervals required for the different steps of particle heating (heating of solid phase, melting of the solid phase, heating of the liquid phase and evaporation) will change compared to atmospheric pressure conditions. The time periods needed for the different steps of particle heating can be readily calculated using a method described in [8]. Therefore, this aspect will not be included in this paper.

Assumptions

The following assumptions are employed in this study:

1 The particle is exposed to a uniform plasma in local thermodynamic equilibrium (LTE).

2 The heat transfer process is steady.

3 There is no relative motion between the particle and the plasma. As recently shown [12, 13], the contribution of convection to particle heat transfer is negligible, even for relative velocities between a particle and the plasma in the order of 100 m/s.

4 The particle is assumed to be spherical.

5 Radiation from and to the particle is neglected.

6 The surface temperature of the particle is assumed to be uniform.

7 The Knudsen number is sufficiently small so that the heat-conduction-potential jump approach [10] is applicable.

These assumptions are identical to those used in the previous analysis [10], with the exception of an additional assumption concerning the plasma pressure. The effects of different types of thermal plasmas, on evaporation, on

Contributed by the Gas Turbine Division of THE AMERICAN SOCIETY OF MECHANICAL ENGINEERS and presented at the 29th International Gas Turbine Conference and Exhibit, Amsterdam, The Netherlands, June 4-7, 1984. Manuscript received at ASME Headquarters February 6, 1984. Paper No. 84-GT-287.

radiation and on forced convection, were studied in [7, 8, 10, 12]; therefore, these effects on heat transfer will not be included in the present paper. All calculations will be restricted to an argon plasma and a nonevaporating particle with a uniform and constant surface temperature (1000 K).

Calculation Procedure

The calculation procedure, including the Knudsen effect, has been described to some detail in a previous paper [10] without considering changes of the thermophysical properties of an argon plasma with pressure.

Neglecting the Knudsen effect, the specific heat flux, q_{oc}, to a particle of radius r_s may be expressed by [7]

$$q_{oc} = (S_\infty - S_s)/r_s \tag{1}$$

where S_∞ and S_s denote the heat-conduction-potentials at ambient plasma temperature (T_∞) and at the surface temperature of a particle (T_W), respectively.

When the Knudsen effect is taken into account, the following heat-conduction-potential jump exists at the particle surface

$$S_g - S_s = z^* \left(\frac{dS}{dr}\right)_s \tag{2}$$

Subscript "g" expresses the jump condition at the particle surface, z^* is the jump distance of the heat-conduction-potential derived in [10] as

$$z^* = \left(\frac{2-a}{a}\right)\left(\frac{\gamma}{1+\gamma}\right)\frac{4\bar{k}}{\rho_s \bar{v}_s \bar{C}_p} \tag{3}$$

or

$$z^* = \left(\frac{2-a}{a}\right)\left(\frac{\gamma}{1+\gamma}\right)\frac{2}{\mathrm{Pr}_s}\lambda^* \tag{4}$$

In these equations, a is the thermal accomodation coefficient, γ is the specific heat ratio, ρ_s, Pr_s, and $\bar{v}_s$ are the gas density, the Prandtl number and the average molecular speed at the actual surface temperature (T_w) of a particle, respectively. The coefficients $\bar{k}$ and $\bar{C}_p$ are the average values of the thermal conductivity and of the specific heat taken between the actual surface temperature (T_w) and the surface temperature under jump conditions (T_g), respectively. These coefficients may be expressed by

$$\bar{k} = \int_{T_w}^{T_g} k dT/(T_g - T_w) = (S_g - S_s)/(T_g - T_w) \tag{5}$$

$$\bar{C}_p = \int_{T_w}^{T_g} C_p dT/(T_g - T_w) = (h_g - h_s)/(T_g - T_w) \tag{6}$$

In equations (5) and (6), S_g and h_g are the heat conduction potential and the specific enthalpy corresponding to T_g, respectively.

The ratio of heat fluxes to a particle with and without accounting for the Knudsen effect has been derived as [10]

$$\frac{q_o}{q_{oc}} = \frac{1}{1 + (z^*/r_s)} \tag{7}$$

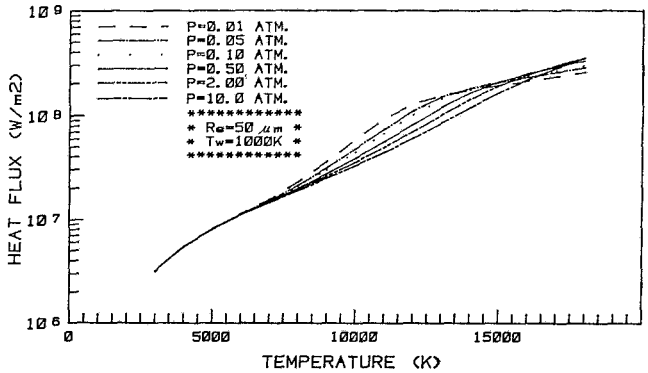

Fig. 1 Specific heat fluxes without Knudsen effect q_{oc} at different plasma temperatures and pressures (r_s = 50 microns)

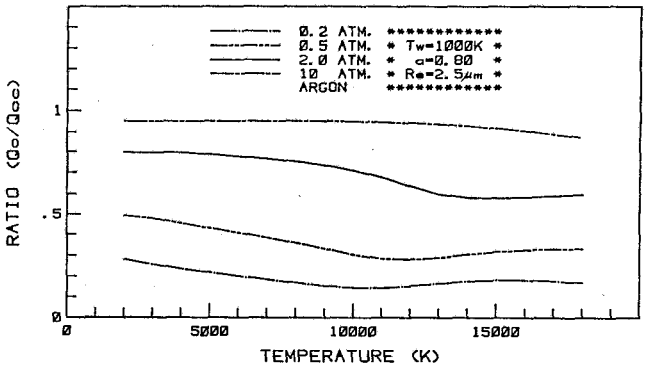

Fig. 2 Ratio of heat fluxes with and without Knudsen effect versus plasma temperature for r_s = 2.5 microns.

This ratio can be treated as a correction factor due to the presence of the Knudsen effect. Equation (7) shows that the Knudsen effect always reduces the heat flux to particle (q_o). If the Knudsen effect is negligible, i.e., if the Knudsen number becomes very small (e.g., smaller than 10^{-3}), then $z^* \to 0$ and $q_o \to q_{oc}$.

The quantity λ^* in equation (4) is defined as

$$\lambda^* = \frac{2\bar{k}}{\rho_s v_s \bar{C}_p}\mathrm{Pr}_s \tag{8}$$

and may be treated as an effective mean free path-length of gaseous particles within the temperature interval from T_w to T_g under plasma conditions. Correspondingly, an effective Knudsen number under plasma conditions may be defined as

$$\mathrm{Kn}^* = \frac{\lambda^*}{2r_s} \tag{9}$$

where ($2r_s$) is the diameter of the particle. It is obvious that both λ^* and Kn^* increase at reduced pressures due to the decrease of the gas density (ρ_s).

Nomenclature

- a = thermal accomodation coefficient
- C_p = specific heat at constant pressure
- h = specific enthalpy
- k = thermal conductivity
- Kn^* = effective Knudsen number
- Pr_s = Prandtl number at T_w
- q_o = specific heat flux with Knudsen effect
- q_{oc} = specific heat flux without Knudsen effect
- r = radial coordinate from particle center
- r_s = particle radius
- S = heat conduction potential
- T = absolute temperature
- T_w = actual surface temperature of particle
- v_s = average molecular speed at T_w
- z^* = jump distance of heat conduction potential
- γ = specific heat ratio
- λ^* = effective mean free path length
- ρ_s = density at T_w

Subscripts

- g = under jump condition
- s = at particle surface
- ∞ = ambient condition

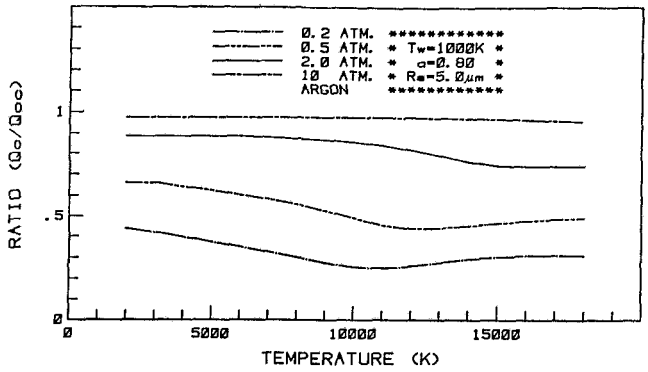

Fig. 3 Ratio of heat fluxes with and without Knudsen effect versus plasma temperature for r_s = 5 microns

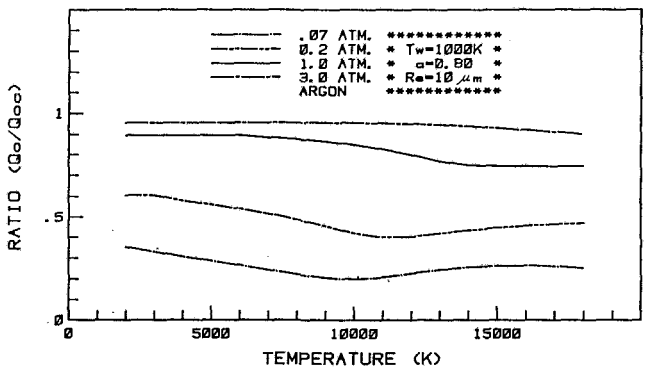

Fig. 4 Ratio of heat fluxes with and without Knudsen effect versus plasma temperature for r_s = 10 microns

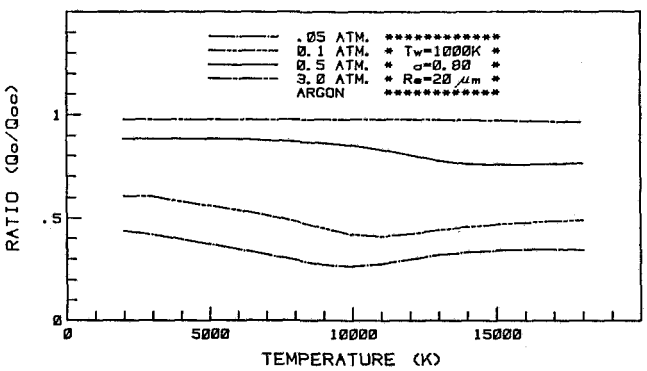

Fig. 5 Ratio of heat fluxes with and without Knudsen effect versus plasma temperature for r_s = 20 microns

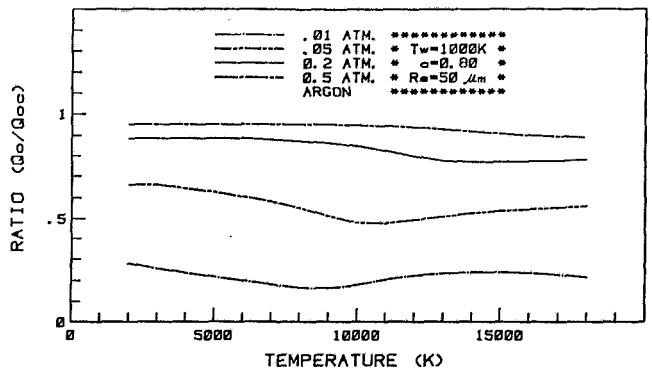

Fig. 6 Ratio of heat fluxes with and without Knudsen effect versus plasma temperature for r_s = 50 microns

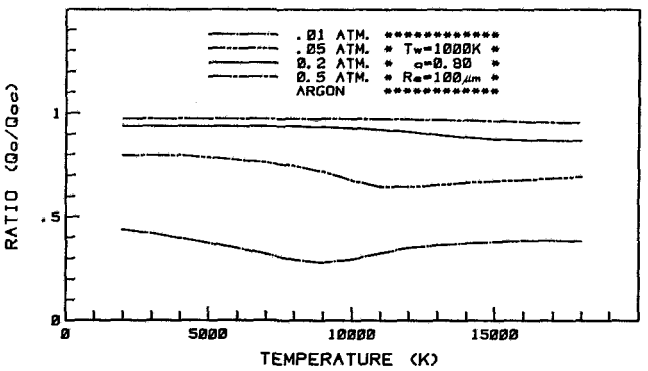

Fig. 7 Ratio of heat fluxes with and without Knudsen effect versus plasma temperature for r_s = 50 microns

As described in [10], the calculation procedure requires an iteration starting from a guess value of the jump temperature at the particle surface (T_g). The argon properties at different pressures used in this study are calculated by using a program given in [14]. From the calculated thermal conductivity, specific heat, specific enthalpy, and heat conduction potential as a function of the plasma temperature and pressure, $\bar{k}$ and $\bar{C}_p$ can be derived by using equations (5) and (6). Substituting the values of $\bar{k}$ and $\bar{C}_p$ into equation (3), z^* is obtained and the heat flux ratio can be calculated from equation (7). Since the specific heat flux without accounting for the Knudsen effect, q_{oc}, has been given by equation (1), the heat flux with the Knudsen effect, q_o, and hence $(dS/dr)_s = q_o$, are determined. Thus, $S_g - S_s$ is obtained from equation (2) by using the calculated values of z^* and $(dS/dr)_s$. Correspondingly, T_g can be found from the known relation between the heat conduction potential, S, and the plasma temperature, T, for a given pressure. If this calculated value of T_g is different from the guess value, it will be used as a new guess value for T_g. This iteration process is repeated until a convergent value for T_g is obtained. All the other interesting quantities such as the jump distance, z^*, the heat flux ratio, q_o/q_{oc}, the effective mean free path length, λ^*, and the effective Knudsen number, Kn^*, can also be obtained by this iteration process.

Results and Discussions

For a single particle exposed to an argon plasma, the calculated heat flux as a function of plasma temperature and pressure is shown in Fig. 1, without accounting for the Knudsen effect. In spite of a drastic change in plasma pressure (from 0.01 to 10 atm), the variation of the heat flux remains relatively small, especially for plasma temperatures below 7000 K. At these temperatures, the heat flux does not depend on pressure because ionization becomes negligible at such low temperatures. As the plasma temperature is raised to a value around 10,000 K, the specific heat flux q_{oc} will increase with decreasing pressure as shown in Fig. 1. This fact is associated with the equilibrium composition of the plasma, which shifts towards higher degrees of ionization at reduced pressures. This, in turn, increases the thermal conductivity and the heat conduction potential correspondingly. Actual experience in plasma spraying reveals, however, the opposite trend; i.e., heating of particles becomes more difficult at reduced pressures. As mentioned earlier, the Knudsen effect will exert a dominating influence on heat transfer, causing a severe reduction of the heat fluxes with decreasing pressure.

Since the heat flux without the Knudsen effect (q_{oc}) is in-

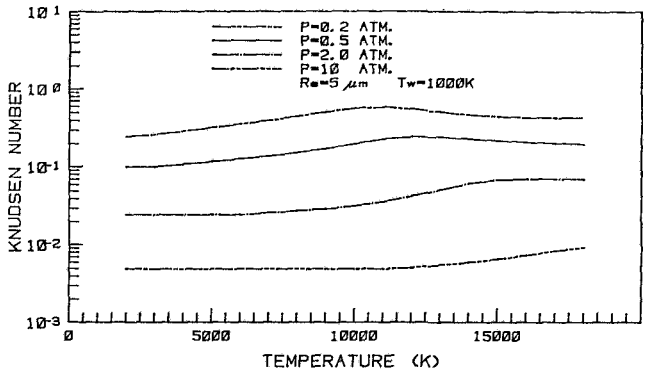

Fig. 8 Variation of effective Knudsen number with plasma temperature and pressure for r_s = 5 microns

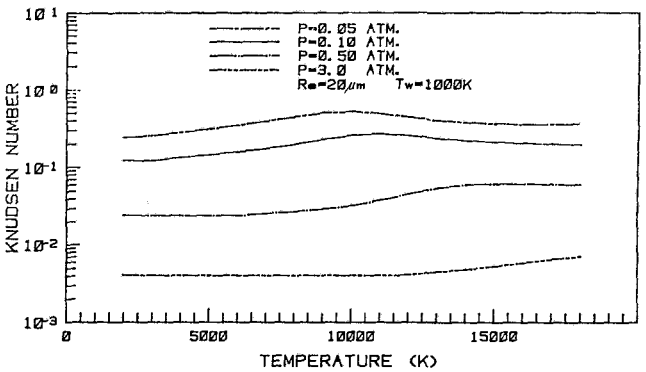

Fig. 9 Variation of effective Knudsen number with plasma temperature and pressure for r_s = 20 microns

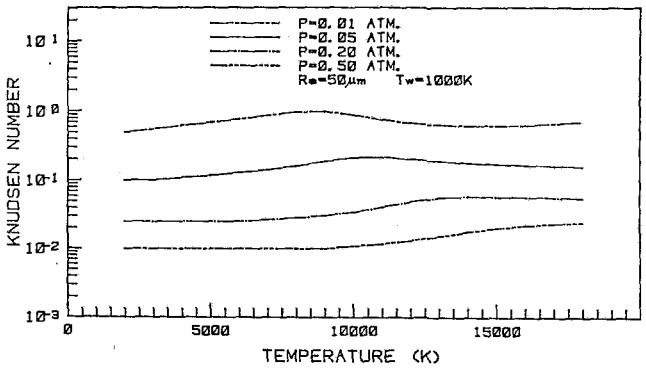

Fig. 10 Variation of effective Knudsen number with plasma temperature and pressure for r_s = 50 microns

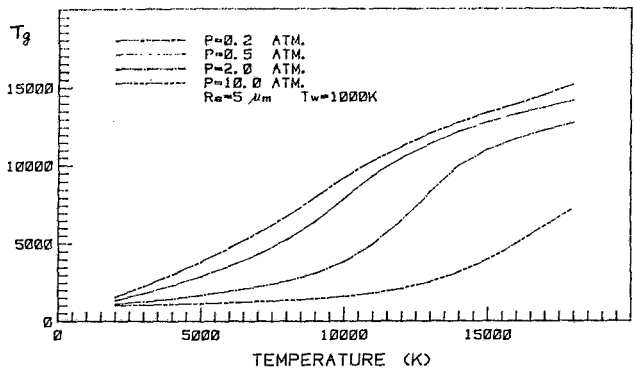

Fig. 11 Variation of the calculated values of T_g with plasma temperature and pressure for r_s = 5 microns

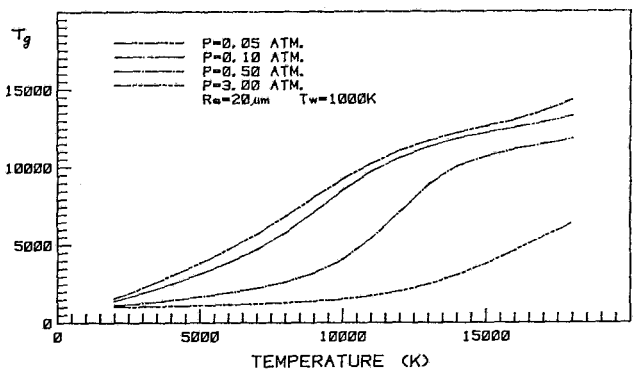

Fig. 12 Variation of the calculated values of T_g with plasma temperature and pressure for r_s = 20 microns

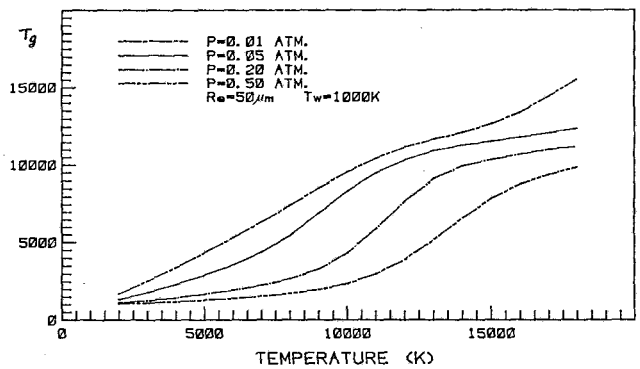

Fig. 13 Variation of the calculated values of T_g with plasma temperature and pressure for r_s = 50 microns

versely proportional to the particle radius according to equation (1), the calculated results shown in Fig. 1 may be easily extended to other particle radii for the specified pressure range from 0.01 to 10 atm.

Calculated results of the heat flux ratio with and without the Knudsen effect are shown in Figs. 2–7 for particles with radii of 2.5, 5, 10, 20, 50, and 100 μm, respectively. Since q_{oc} is known from equation (1) or Fig. 1, the effect of pressure on the specific heat flux with the Knudsen effect can be deduced readily from the results of the heat flux ratios presented in Fig. 2–7. The value of the thermal accomodation coefficient has been taken as 0.8 throughout all the calculations of this paper according to [10].

An examination of these results shows that for smaller particles, the Knudsen effect is pronounced, even at higher pressures. Figure 2 shows, for example, that the Knudsen effect for a particle with a radius of 2.5 μm is appreciable even for pressures as high as 2 atm. Figure 3 shows the corresponding results for a particle radius of 5 μm. The heat flux ratios shift to higher values compared to the results of Fig. 2; but even for 2 atm, the Knudsen effect is not negligible for this particle size.

Figure 4 refers to a particle radius of 10 μm and pressures from 3 atm down to 0.07 atm. For pressures above 1 atm, the Knudsen effect losses its significance for this particle size, but there is a strong effect on heat transfer for pressures below 1 atm. This is even more pronounced in Fig. 5, which considers a particle radius of 20 μm and a pressure range from 3 atm down to 0.05 atm.

Finally, Fig. 6 and 7 consider subatmospheric pressures only, ranging from 0.5 down to 0.01 atm and particle radii of 50 μm and 100 μm, respectively. For both particle sizes, the

Knudsen effect becomes negligible for pressures exceeding 0.5 atm. There is, however, a more than 70 percent reduction of heat transfer at 0.01 atm for particles of 50 μm radius (Fig. 6) and the corresponding reduction is more than 50 percent for particles of 100 μm (Fig. 6) and the corresponding reduction is more than 50 percent for particles of 100 μm (Fig. 7).

All the data shown in Figs. 2 to 7 are restricted to the pressure range in which the heat conduction potential jump approach [10] is applicable. Therefore, the pressure range in Figs. 4–7 is shifted to lower values as the particle size increases. For cases in which the plasma pressure is lower than the minimum values indicated in Figs. 2–7, a free-molecular flow approach or an approach valid for the transition region will be needed.

For three typical values of the particle radius (r_s = 5, 20, and 50 μm), the calculated effective Knudsen numbers Kn* are shown in Figs. 8–10.

For the specified particle sizes and pressure ranges in Figs. 8–10, the effective Knudsen numbers cover a range from approximately 4.10^{-3} to almost 1. Comparisons of Fig. 8 and 3, of Fig. 9 and 5, and of Fig. 10 and 6 reveal that the Knudsen effect will be appreciable as soon as the effective Knudsen number exceeds values around 10^{-2}.

The particle surface jump temperatures, T_g, are plotted in Fig. 11–13 as a function of the plasma temperature for the same parameters used in Fig. 8–10, respectively. For situations in which the Knudsen effect becomes pronounced, the jump temperature, T_g, differs appreciably from the actual surface temperature, T_w, of the particle. In fact, as shown in Figs. 11–13, the jump temperature may approach the plasma temperature, T_∞, for the most extreme cases covered in this study (Kn* > 0.1).

Conclusions

This study of the effect of pressure on heat transfer to a particle exposed to a thermal plasma is based on the so-called "heat conduction potential jump approach." The main conclusions deduced from this study are as follows:

1 For small particles with radii typical for applications in plasma chemistry and plasma processing, the effect of pressure on heat transfer is governed by the Knudsen effect. The contribution due to the variations of thermophysical properties with pressure is of less importance.

2 Considering a particle of given size, the Knudsen effect becomes important as soon as the effective Knudsen number exceeds values of approximately 10^{-2}, and in this regime heat transfer to a particle decreases with decreasing pressure. This finding may impose severe limitations on the type of materials and the particle sizes which can be processed in plasmas at reduced pressures.

3 Although the results presented in this paper are restricted to argon plasmas and particle surface temperatures of 1000 K, the same trend is expected for other types of plasmas and for varying particle surface temperatures.

4 Flow effects (convection) are neglected in this paper because of the small Reynolds numbers experienced in plasma processing of small particles. According to the results of previous studies [12, 13], the findings presented in this paper apply also for heat transfer to particles immersed into a flowing plasma.

5 The assumption of LTE used in this study may require modifications, especially for situations with very low pressures (< 0.1 atm). These modifications require information on the plasma itself, including its mode of generation (field-free plasmas, arcs, RF-discharges etc.).

Acknowledgments

This work has been supported in part by the National Science Foundation under grant NSF/CPE 8200628 and in part by the Ministry of Education, PRC (for Xi Chen).

References

1 Bonet, C., "Thermal Plasma Processing," *Chem. Engng. Prog.*, Vol. 72, 1976, p. 63.

2 Yoshida, T., and Akashi, K., "Practicle Heating in a Radio-Frequency Plasma Torch," *J. Appl. Phys.*, Vol. 48, 1977, p. 2252.

3 Boulos, M. I., "Heating of Powders in the Fire-Ball of an Inductive Plasma," IEEE *Trans. Plasma Sci.*, Vol. 4, 1978, p. 93.

4 Fiszdon, J. K., "Melting of Powder Grains in a Plasma Flame," *Int. J. Heat Mass Transfer*, Vol. 22, 1979, p. 749.

5 Sayegh, N. N., and Gauvin, W. H., "Numerical Analysis of Variable Property Heat Transfer to a Single Sphere in High-Temperature Surroundings," *AIChE Journal*, Vol. 25, 1979, p. 522.

6 Raykalin, N. N., Uglov, A. A., Iokhov, Yu. N., and Gnedovets, A. G., "Properties of Heating of Submicron Metal Particles in a Hot Gas," *High Temperature*, Vol. 19, 1981, p. 404.

7 Chen, Xi, and Pfender, E., "Heat Transfer to a Single Particle Exposed to a Thermal Plasma," *Plasma Chemistry and Plasma Processing*, Vol. 2, 1982, p. 185.

8 Chen, Xi, and Pfender, E., "Unsteady Heating and Radiation Effects of Small Particles in a Thermal Plasma," *Plasma Chemistry and Plasma Processing*, Vol. 2, 1982, p. 291.

9 Lee, Y. C., "Trajectories and Heating of Particles Injected Into a Thermal Plasma," Master's thesis, Department of Mechanical Engineering, University of Minnesota, 1982.

10 Chen, Xi, and Pfender, E., "Effect of the Knudsen Number on Heat Transfer to a Particle Immersed Into a Thermal Plasma," *Plasma Chemistry and Plasma Processing*, Vol. 3, 1983, p. 97.

11 Bourdin, E., Fauchais, P., and Boulos, M., "Transcient Heat Conduction Under Plasma Conditions," *Int. J. Heat Mass Transfer*, Vol. 26, 1983, p. 567.

12 Chen, Xi, and Pfender, E., "Behavior of Small Particles in a Thermal Plasma Flow," *Plasma Chemistry and Plasma Processing*, Vol. 3, No. 3, 1983, p. 351.

13 Chen, Xi, Lee, Y. C., and Pfender, E., "The Importance of Knudsen and Evaporation Effects on Modeling in Thermal Plasma Processing," *Proc. of the 6th Internat. Symp. on Plasma Chemistry*, Vol. 1, 1983, p. 51; Université de Sherbrooke and McGill University, Montreal/Canada.

14 Hsu, K. C., "A Self-Consistent Model for the High Intensity Free-Burning Argon Arc," Ph.D. dissertation, Department of Mechanical Engineering, University of Minnesota, 1982.

Vibration Characteristics of the HPOTP (High-Pressure Oxygen Turbopump) of the SSME (Space Shuttle Main Engine)[1]

D. W. Childs
Professor.

D. S. Moyer
Graduate Research Assistant.

Mechanical Engineering Department,
Texas A&M University,
College Station, Texas 77843

A review is presented of various rotordynamic problems which have been encountered and eliminated in developing the current flight engines and of continuing subsynchronous problems which are being encountered in developing a 109 percent power level engine. The basic model for the HPOTP, including the structural dynamic model for the rotor and housing and component models for the liquid and gas seals, turbine-clearance excitation forces, and impeller-diffuser forces, are discussed. Results from a linear model are used to examine the synchronous response and stability characteristics of the HPOTP, examining bearing load and stability problems associated with the second critical speed. Various seal modifications are examined and shown to have favorable consequences with respect to bearing reactions and stability. Differences between linear and nonlinear model results are discussed and explained in terms of simple models. The transient nonlinear model is used to demonstrate forced subsynchronous motion similar to that observed in test data for models which are lightly damped but stable. The subsynchronous motion results from bearing clearance nonlinearities. Simulation results indicates that synchronous bearing loads can be reduced but that subsynchronous motion is not eliminated by seal modifications.

Introduction

The SSME (Space Shuttle Main Engine) has been under development by Rocketdyne Division of Rockwell International since the early 1970s. The George C. Marshall Space Flight Center has administered the program development for NASA. The SSME is designed to operate at the following three conditions:

MPL (Minimum Power Level):	$\omega = 20{,}900$ cpm
RPL (Rated Power Level):	$\omega = 28{,}200$ cpm
FPL (Full Power Level):	$\omega = 30{,}380$ cpm

At RPL, the turbines develop approximately 1.71×10^7 watts (22,900 hp). FPL is 109 percent of RPL. RPL performance is adequate for the equatorial orbits which have been flown to date; however, polar orbits require FPL performance. *This paper concerns various rotordynamics problems related to the HPOTP (High-Pressure Oxygen Turbopump) which were eliminated in developing a reliable RPL engine and new problems which are being encountered in developing FPL performance.*

As compared to more conventional turbomachinery, liquid-rocket-engine turbopumps present the following distinctive rotordynamics development problems:

(*a*) The units operate in ball bearings which are lubricated with the cryogenic fluid being pumped. The bearings themselves provide virtually no damping.

(*b*) Because of the extraordinarily low viscosity of liquid oxygen and liquid hydrogen, neither fluid can be effectively used in a squeeze film damper. Moreover, the presence of these cryogenic fluids precludes the use of other fluids in conventional dampers or elastomeric dampers.

(*c*) Oxygen-compatible motion transducers are under development; however, they are not currently available. Moreover, a typical turbopump design presents severe difficulty in access to the rotating assembly for relative motion measurements, particularly when access for motion measurements was not a consideration in the initial design. Vibration data for the SSME turbopumps have largely been confined to the output of accelerometers mounted on the housing. For most of the development period of the HPOTP, there has been no speed probe pickup and no once-per-revolution phase mark from the shaft to use in data analysis.

The calculated linear critical speeds for the current nominal HPOTP are at approximately 12,500 (208 Hz.) and 32,500

[1] The work reported herein was supported in part by NASA Contract NAS8-34505 from the George C. Marshall Space Flight Center.

Contributed by the Gas Turbine Division of THE AMERICAN SOCIETY OF MECHANICAL ENGINEERS and presented at the 29th International Gas Turbine Conference and Exhibit, Amsterdam, The Netherlands, June 4–7, 1984. Manuscript received at ASME Headquarters December 19, 1983. Paper No. 84-GT-31.

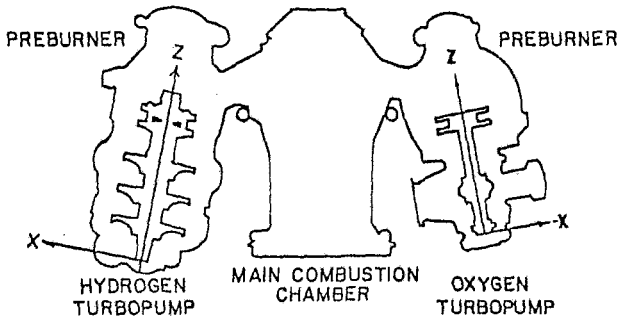

Fig. 1 SSME powerhead component arrangement and local coordinate systems

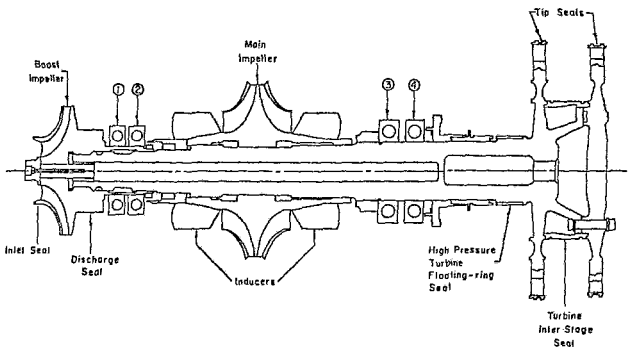

Fig. 2 HPOTP rotating assembly

cpm (540 Hz.) These calculated values are for complete housing-rotor models, including seals, clearance-excitation forces, gyroscopic coupling, etc. The undamped, zero-running-speed, rotor-housing modes associated with the first and second critical speeds are illustrated in Fig. 3. The modeshape associated with the first critical speed primarily involves overhung motion of the turbine with relatively small amplitudes at the bearings and main impeller. The modeshape associated with the second critical speed involves large amplitudes at the main impeller and bearings with small amplitudes at the turbine.

Initial vibration problems with the HPOTP involved motion associated with the first critical speed. Synchronous and subsynchronous (at approximately 200 Hz.) motion was excessive. This problem was remedied by changing the turbine interstage seal from a stepped-labyrinth configuration to a convergent taper seal with a honeycomb stator and a smooth rotor. This change was implemented based on the beneficial consequences of a similar change in the pump interstage seals of the HPFTP (High-Pressure Fuel Turbopump) [1].

The second problem associated with the HPOTP involved subsynchronous vibrations at approximately 400–420 Hz. This motion tended to initiate when the running speed reached the appropriate excitation frequency, and persisted as subsynchronous motion when the running speed was increased. A failure and explosion of the HPOTP occurred in a test run when the running speed first traversed the maximum-amplitude frequency range and then was reduced to and remained at the now synchronous frequency. The failure was attributed to an inadequate bearing-carrier design which caused unequal load sharing of the bearings. Subsequently, redesigned bearing carriers eliminated the "400 Hz." subsynchronous motion. The general feeling was that the new bearing carrier designs caused a more equal load sharing and maintained the correct axial bearing preloads, thus realizing the "expected" radial stiffness of the bearings and elevated the rotor second critical speed.

The bearing-carrier redesign was sufficient to yield a reliable pump for RPL operations; however, demonstration of FPL capability has been impeded by repeated occurrence of subsynchronous motion in the 450–500 Hz. frequency range. The incidence of this motion rarely occurs during initial operation at higher power levels, but tends to develop after an accumulation of time and develops more rapidly with higher synchronous vibration levels. However, once a unit begins to "whirl," it will repeatedly whirl, generally with progressively increasing severity. The frequency of the subsynchronous motion is sometimes at a fixed fraction of running speed ranging from 88 to 95 percent. This "tracking" characteristic is in marked contrast to the earlier "400 Hz." phenomenon where the whirl-frequency of the subsynchronous motion remained constant, relatively independent of running speed.

Post-run inspection of turbopumps has revealed that, although the balls in some bearings, primarily bearing 2, appear to be unblemished, their diameters have in fact, been reduced by as much as 0.17 mm in some cases. The cause of this dimensional attrition is unknown, but has been ascribed to either excessive radial loads or the absence of radial loads which leads to skidding.

The analysis results which have been completed to date and are reported herein do not provide a complete or comprehensive explanation for the measured dynamic characteristics of the HPOTP; however, they do provide answers for the following questions:

(*a*) What are the linear dynamic characteristics of the *nominal* turbopump model with respect to critical-speed locations, bearing reactions, predicted housing accelerometer levels, and predicted onset speeds of instability?

(*b*) How can the linear dynamic characteristics be improved by feasible, physical modification of the HPOTP seals?

(*c*) What causes the subsynchronous motion?

(*d*) From a rotordynamics viewpoint, what are the principal problems experienced by the HPOTP?

(*e*) What improvements are possible with the HPOTP?

The following section briefly describes the structure and components of the rotordynamic model, with the succeeding section describing the results of linear and nonlinear analysis.

The Rotordynamics Model

Structural Dynamics Model. The structural-dynamics model of the rotor and the housing form the basic framework of the turbopump model. Both the housing and rotor structural dynamics models used here were developed by Rocketdyne. A general three-dimensional, finite-element approach was used to model the HPOTP housing without the rotor. A lumped parameter model was developed for the rotor using beam structural elements and lumped masses and inertias. The rotordynamics model uses modes from the housing model (without the rotor) and free-free rotor modes.

Bearings. The bearings are the structural elements which tie the rotors and housings together. As illustrated in Fig. 2, there are two sets of bearings. The net load from each set is transmitted through a plate-cylinder structure to the housing. The bearings in a bearing set are axially preloaded against each other, but are not designed to accept axial thrust loads from the turbopumps. A balance-piston arrangement at the discharge of the main impeller absorbs axial thrust, and radial clearances are provided at the bearing outer faces to allow the bearings to slip axially without developing excessive axial loads.

Experience and limited test data [2] for the SSME bearings indicate a nominal stiffness of approximately 8.76×10^7 N/m. This is approximately one-half of the values predicted by A. B. Jones-based analysis [3].

The radial clearances provided at the bearings to permit axial motion provides an *essential* "dead-band" nonlinearity. The clearance values used in this study are

$$\delta_P = 0.0127 \text{ mm}, \ \delta_T = 0.0127 \text{ mm} \tag{1}$$

where P and T denote pump and turbine bearings.

Liquid Seals. Liquid wear-ring seals are provided at the inlet and discharge of the boost impeller. The current inlet seal is a stepped labyrinth design with four cavities. The current discharge seal is a three segment, stepped seal. Each constant-radius seal segment has a series of circumferential grooves.

Experience and limited test data [4] have shown that labyrinth or serrated seals of the type currently employed on the impeller inlet and discharge yield stiffness and damping coefficients which are substantially smaller than corresponding values for smooth constant clearance seals. Replacing the current grooved boost-impeller, wear-ring seals with plain annular seals has the potential for a beneficial increase in stiffness and damping in the HPOTP. In fact, as the following discussion explains, various additional possibilities exist for optimizing seals.

The force-motion model for liquid seals has the form

$$-\begin{Bmatrix} F_X \\ F_Y \end{Bmatrix} = \begin{bmatrix} K & k \\ -k & K \end{bmatrix} \begin{Bmatrix} X \\ Y \end{Bmatrix} + \begin{bmatrix} C & c \\ -c & C \end{bmatrix} \begin{Bmatrix} \dot{X} \\ \dot{Y} \end{Bmatrix} + \begin{bmatrix} M & m \\ -m & M \end{bmatrix} \begin{Bmatrix} \ddot{X} \\ \ddot{Y} \end{Bmatrix}$$

In this model (X, Y) are the components of the *relative* motion between the rotor and housing. Black et al. [5, 6] were responsible for most of the analytical developments related to the analysis of seals leading to the definition of stiffness, damping, and added-mass coefficients. His analysis demonstrates that the "cross-coupled" stiffness coefficient, k, arises solely due to fluid rotation within the seal. As a fluid element proceeds axially along an annular seal, shear forces at the rotor accelerate or decelerate the fluid tangentially until an axsymptotic value is reached. For a seal with the same directionally homogeneous surface-roughness treatment on the rotor and the housing, the average asymptotic tangential velocity is $R\omega/2$, where R is the seal radius and ω is the rotor running speed.

The cross-coupled stiffness coefficient k acts in opposition to the direct damping coefficient C to destabilize rotors. Hence, steps which can be taken to reduce the net fluid rotation within a seal will improve rotor stability by reducing k. The following two steps are currently under consideration for providing more net damping to the HPOTP rotating assembly:

(*a*) If the *inlet* tangential velocity can be reduced, the high axial velocities in a cryogenic seal are such that the fluid may proceed through a seal without substantially increasing its tangential velocity. An antivortex web has been proposed at the inlet to the boost-impeller inlet seal to reduce the inlet tangential velocity and yield a reduced k. This practice has been followed previously for the labyrinth seals of high-pressure compressors.

(*b*) Von Pragenau [7] has recently demonstrated that the asymptotic tangential velocity can be modified if a different surface roughness is used for the rotor and stator elements. Rough rotor/smooth stator and smooth rotor/rough stator combinations yield higher and lower asymptotic values, respectively. Von Pragenau calls the rough stator/smooth rotor configuration a "damper seal" because of its enhanced stability characteristics. The roughness has the additional potential benefit of reducing leakage. Damper seal configurations are presently under consideration for both the inlet and discharge seals of the boost impeller.

Liquid seal coefficients for the boost impeller seals were calculated based on analysis by Childs [8]. Current analyses yield finite-length solutions for constant-clearance or convergent-tapered seals with different but directionally homogeneous surface roughness treatments on the rotor and stator.

Gas Seals. The HPOTP turbines are shrouded, and single-cavity tip seals are provided to reduce leakage between the turbine shroud and the stator. The interstage seal between the turbines uses a honeycomb stator element with a smooth rotor and inlet anti-vortex ribs to reduce the inlet tangential velocity component. A floating-ring shaft seal is provided at the turbine discharge to restrict leakage of the hot turbine gases towards the lox within the pump. The flow across this seal is choked.

Seal coefficients calculations used in the study are based on the analyses of Nelson [9]. The analyses apply to constant-clearance or convergent taper geometries, account for the development of tangential velocity within the seals, and different but directionally-homogeneous surface roughness on the rotor and stator.

Turbine Clearance Excitation Forces. Clearance-excitation forces are developed by turbines due to the dependency of local efficiency on local clearances. The destabilizing force is modeled by

$$\begin{Bmatrix} F_X \\ F_Y \end{Bmatrix} = \begin{bmatrix} 0 & k_T \\ -k_T & 0 \end{bmatrix} \begin{Bmatrix} X \\ Y \end{Bmatrix}; \quad k_T = \frac{\beta T}{D_p H} \tag{3}$$

where T is the turbine torque, D_p is the average pitch diameter of the turbine blades, H is the average height, and β defines the change in turbine efficiency due to uniform changes in clearance. Again, the components (X, Y) of equation (3) define the displacement of the turbine relative to the housing. Thomas initially identified this destabilizing phenomenon [10], while Alford [11] subsequently and independently developed the same model. Test results for shrouded turbines have yielded values for β on the order of 0.6 [12].

Impeller-Diffuser Forces. A test program has been under way at the California Institute of Technology for some time to measure the static and dynamic forces experienced by a pump impeller in either a volute or a vaned diffuser. Chamieh et al. [13] have defined the following model on the basis of static measurements of an impeller within a vaned diffuser:

$$-\frac{1}{\rho A_2 V_2^2} \begin{Bmatrix} F_X \\ F_Y \end{Bmatrix} = \begin{bmatrix} K^* & k^* \\ -k^* & K^* \end{bmatrix} \begin{Bmatrix} X/R_2 \\ Y/R_2 \end{Bmatrix} = \begin{bmatrix} -2.0 & 0.7 \\ -0.7 & -2.0 \end{bmatrix} \begin{Bmatrix} X/R_2 \\ Y/R_2 \end{Bmatrix} \tag{4}$$

where R_2 is the impeller radius, ρ is the fluid density, $V_2 = R_2\omega$ is the impeller tip velocity, and $A_2 = 2\pi R_2 b_2$ is the exit flow area. Note that the direct-stiffness coefficient in equation (4) is negative, i.e., the impeller-diffuser force causes a reduction in rotor stiffness. From equation (4), the dimensional impeller-diffuser coefficients are defined by

$$\bar{K} = K^* \frac{\rho A_2 V_2^2}{2R_2} = K^*(\pi \rho b_2 R_2{}^2)\omega^2$$
$$\bar{k} = k^*(\pi \rho b_2 R_2{}^2)\omega^2 \tag{5}$$

Analysis Procedures and Results

Introduction. The radial clearances which are provided at the outer races of the bearings to permit axial slipping and

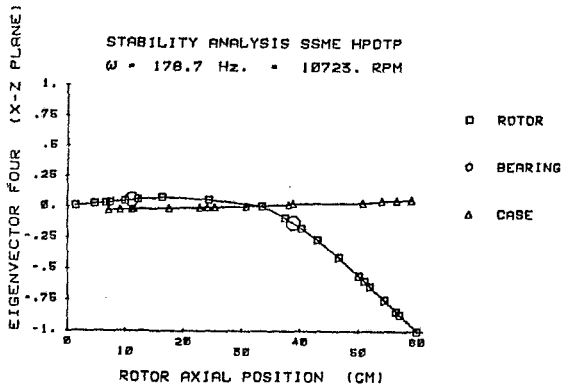

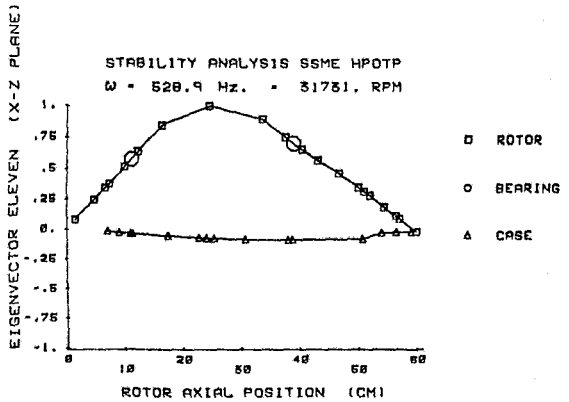

Fig. 3 Undamped, zero-running-speed, rotor-housing modes associated with the first and second critical speeds

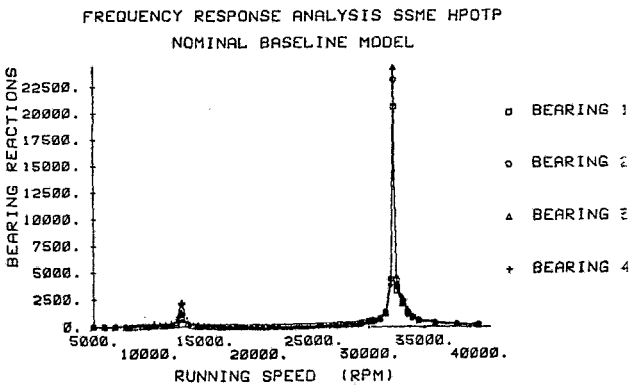

Fig. 4 Bearing reactions for the nominal linear model with speeds out of 40,000 cpm

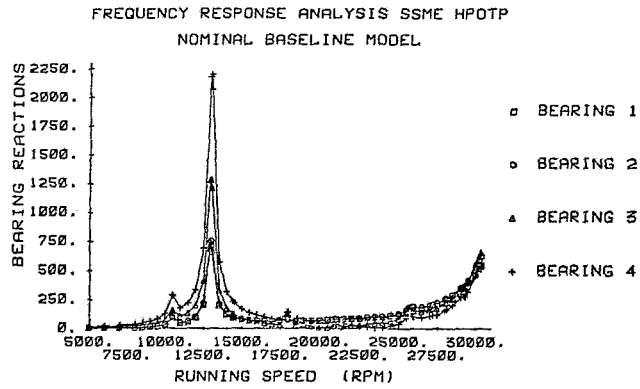

Fig. 5(a) Bearing reactions for the nominal linear model for speeds from 5000 cpm to FPL

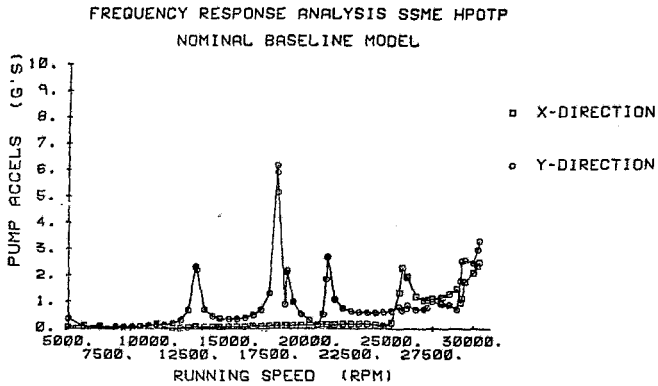

Fig. 5(*b*) Pump accelerometer levels in the *X-Z* and *Y-Z* planes

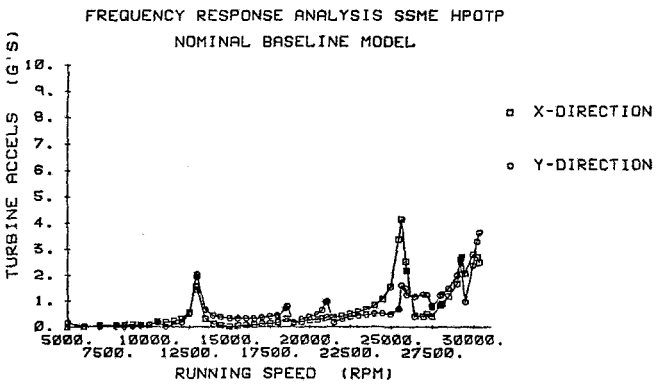

Fig. 5(*c*) Turbine accelerometer levels in the *X-Z* and *Y-Z* planes

prevent the bearings from absorbing axial loads provide the essential nonlinearity in a rotordynamics model for the HPOTP. If these "deadband" clearances are eliminated, the resultant model is basically linear. As the following sections demonstrate, the results of linear and nonlinear analysis differ substantially, but linear analysis remains an efficient procedure for general characterization of the turbopump's rotordynamics.

Linear Analysis Procedures and Results.

Rotordynamic Characteristics of the Nominal Model. The analysis procedure used here is basically the same as that outlined in [1]. Modal coordinates based on the zero-running-speed coupled rotor-housing modes are used. Gyroscopic coupling and forces due to seals, turbine clearance-excitation, the interaction of impellers and diffusers, damping, etc., couple the modal coordinates via modal stiffness, damping, and inertia matrices. The onset speed of instability for a turbopump configuration is defined by calculating the complex eigenvalues of the system dynamic matrix at various speeds. Synchronous-response amplitudes of bearing reactions and acceleration levels of accelerometers mounted on the turbopump housing due to imbalance are calculated.

For the purposes of the present discussion, the *nominal linear model* is defined as having bearing stiffness on the order of 8.76×10^7 N/m ($.5\times10^6$ lbs/in.). Calculated seal coefficients are based on the dimensions of seals currently used in the turbopump. The clearance-excitation force coefficient at the turbines use a β of 0.6.

An inspection of the modeshapes of Fig. 3 indicates that the clearance-excitation force at the turbine represents the dominant destabilizing excitation force for motion associated with the first critical speed. Following the initial "400 Hz." subsynchronous vibration problem, the suggestion was made [15] that impeller-diffuser-interaction forces provided the principal destabilizing mechanism for motion associated with

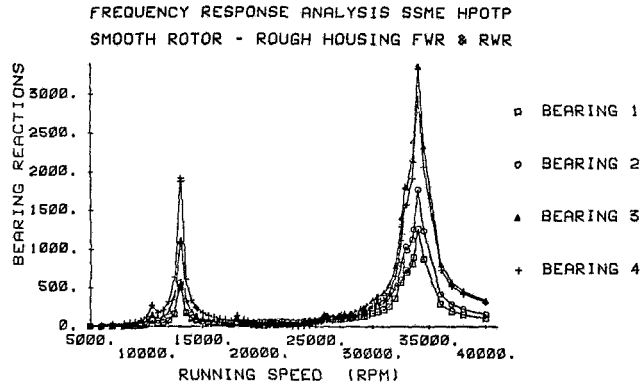

Fig. 6 Bearing reactions for the nominal model with "damper" seal coefficients for the boost-impeller inlet and discharge seals

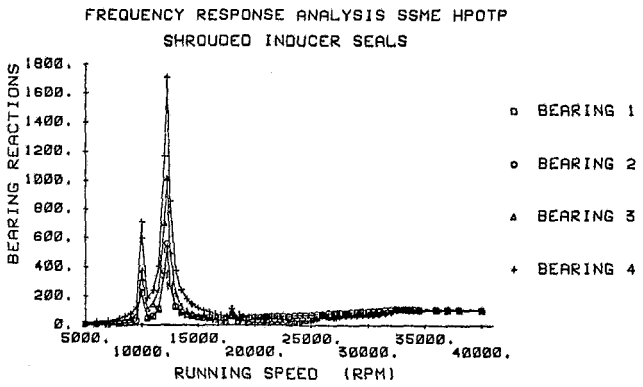

Fig. 7 Bearing reactions for the model with seal with coefficients for a shrouded impeller

the second critical speed. The published cross-coupling coefficients of equation (4) certainly supported this view. If the nominal model includes the stiffness coefficients of equation (4), the OSI (Onset Speed of Instability) is only 17,200 cpm. However, the stability is very sensitive to damping, and the addition of 875 Ns/m (5.0 lb. s/in.) at the main impeller with no bearing damping elevates the OSI to 30,480 cpm. The whirl frequency at OSI is 536 Hz. These concentrated damping coefficients act to restrain relative motion between the rotor and housing. The foregoing damping value is used in the nominal linear model.

Figure 4 illustrates the bearing reactions for running speeds from 5000 to 40,000 cpm. The first and second critical speeds are clearly evident, with the second critical speed clearly having little or no damping. Figure (*a*) illustrates the same results for speeds from 5000 cpm to FPL. Figure 5 (*b*) and (*c*) illustrate predicted acceleration levels for accelerometers mounted on the housing at the pump and turbine ends of the turbopump. Clearly, FPL is quite near the predicted second critical speed. Also, while the bearing reactions are responsive to the "rotor" critical speeds, the housing accelerometer levels may respond more sharply to rotor-housing combined modes. This is particularly true for the first critical speed at approximately 12,500 cpm. However, the predicted accelerometer levels are quite responsive to motion associated with the "rotor" second critical speed at approximately 32,500 cpm.

The above analysis supports the following conclusions with respect to the dynamic characteristics of the HPOTP:

(*a*) Response. The proximity of the second critical speed to FPL is a continuing cause for concern with respect to excessive bearing loads. Even modest losses of bearing stiffnesses are sufficient to drop the second critical speed into the operating range.

(*b*) Stability. Based on the prior "400 Hz." experience with this turbopump, the second critical speed appears to be lightly damped and subject to instability.

Table 1 Linear OSI, whirl frequency, and predicted bearing reactions at FPL

Configuration	OSI (cpm)	Whirl freq. (Hz.)	Bearing reactions at FPL (lbs) 1	2	3	4
Nominal	30,480	536	553	635	667	548
Nominal with damper boost-impeller seals	36,350	576	251	349	513	411
Nominal with shrouded-inducer seals	59,950	315	80	85	57	58

Seal Modifications to Improve Rotordynamic Response and Stability. The preceding material demonstrated the relevant dynamic characteristics of the HPOTP with respect to response and stability. The present section deals with predicted improvements in rotordynamic response due to the following seal modifications:

(*a*) Replace the current inlet and discharge seals of the boost impeller with "damper" seals using a rough stator and smooth rotor. Test results at Texas A&M University of proposed damper seal and smooth seals flight candidates show a substantial reduction in leakage due to roughness and slight increases in direct stiffnesses and net damping.

(*b*) Replace the current unshrouded inducers with shrouded inducers and use the outer surfaces of the shrouded inducer to develop seal forces.

Figure 6 illustrates the bearing reactions which result for choice (*a*), and a comparison of this result with the nominal-model results of Fig. 5(*a*) indicates a sharp reduction in bearing reactions. Moreover, the OSI is increased moderately. Table 1 provides a summary of the results for both the nominal results and the seal modifications cited above and demonstrates that the damper seals yield a predicted reduction in bearing loads on the order of 37 percent and an increase of the predicted OSI to 36,350 rpm.

Figure 7 illustrates the results for the shrouded inducer configuration. Stated briefly, the second critical speed is simply eliminated for this configuration, and the OSI is much greater than FPL.

An assessment of the results presented in Figs. 6, 7 and Table 1 supports the following general conclusions:

(*a*) Modification of the boost impeller seals has the potential for significantly reducing bearing reactions at FPL as compared to the nominal model. However, the second critical speed remains only slightly above FPL and any loss of bearing stiffness will drop the second critical speed into the operating range.

(*b*) The damper-seal modification yields a predicted increase of the OSI by 19 percent.

(*c*) The shrouded-inducer design eliminates both the second critical speed and the stability problem.

Nonlinear Analysis Procedures and Results. As noted previously, the bearing "dead-band" clearances provide the essential nonlinearity in the HPOTP model. The bearing clearances interact with the effects of side loads and bearing deadbands to yield significantly different results for a nonlinear model than those predicted by linear models.

Figure 8 illustrates the analytical model used by Yamamoto [16] to investigate the influence of bearing clearances on rotordynamic response in the absence of side loads. For zero bearing clearances, the model of Fig. 8 reduces to a simple Jeffcott model with viscous external damping. Figure 9 illustrates the response characteristics for a progressive in-

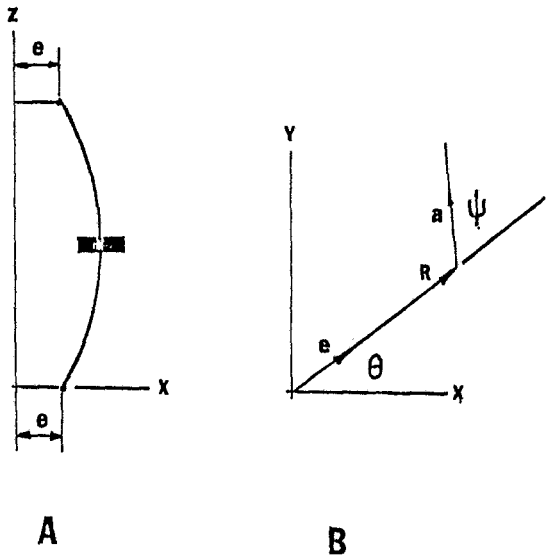

Fig. 8 Yamamoto's model for synchronous response with bearing clearance

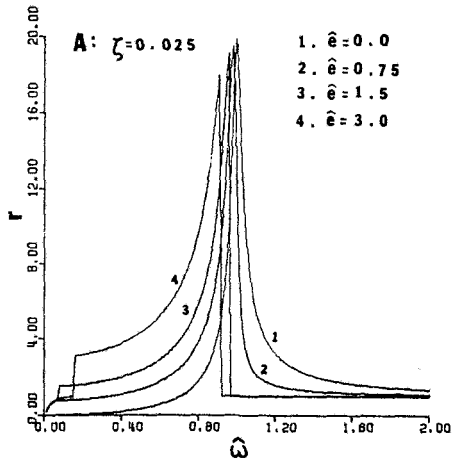

Fig. 9 Synchronous-response characteristics for Yamamoto's model with increasing bearing clearances

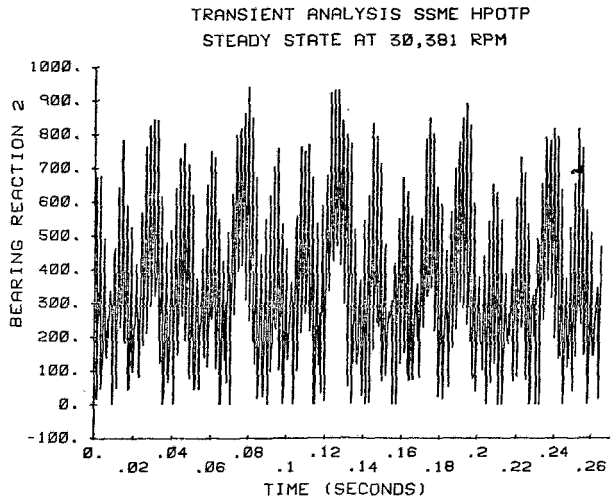

Fig. 10(a) Bearing 2 reaction magnitude versus time at FPL for the nominal nonlinear model

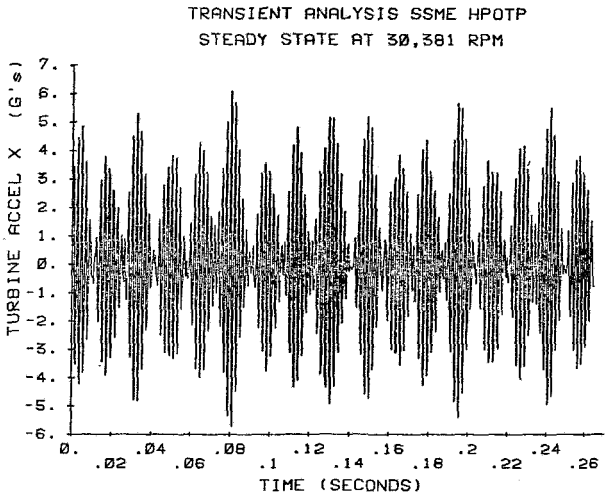

Fig. 10(b) Turbine X-Z plane acceleration magnitude versus time for the nominal nonlinear model

crease in the ratio of bearing clearance to imbalance eccentricity $\hat{e}=e/a$. The results are for a damping ratio of 2.5 percent. The results of Fig. 9 indicate that the speed location of maximum bearing reactions is reduced by increasing $\hat{e}$. Moreover, the drop in amplitude for speeds above the maximum bearing-load can be precipitous. The response characteristics of Fig. 9 can give rise to "jump" phenomena with the synchronous vibration level jumping either up or down for very small changes in running speed. Flight data for the HPOTP have demonstrated sudden step increases in accelerometer levels.

From these results, one would anticipate that bearing clearances could easily drop the peak-bearing-load running speed location associated with the second critical speed into the operating range. In fact, parametric studies of the bearing clearances clearly confirm this result [15]. They also confirm the peak-bearing-load speeds can be reduced below FPL for sufficiently large clearances. Hence for a given running speed, a nonlinear model with bearing clearances can yield either substantially larger or smaller bearing reactions than the linear model.

The nonlinear model was verified by comparison to results from the linear model, e.g., the second-critical-speed location at 32,500 cpm was obtained for zero bearing clearances. Figure 10 illustrates the bearing 2 reaction magnitude and turbine acceleration signals at FPL for the nominal model with the bearing clearances of equation (1). Observe the "clipping" of the bearing reaction magnitudes in Fig. 10(*a*), which results from motion through the bearing deadband. Motion in and out of the deadband results as a combination of static displacement due to the impeller and turbine side loads and elliptical orbits due to imbalance. Bearing clipping generates a nearly periodic impulsive loading at the bearings that excites the beating motion which is evident in the accelerometer signal prediction of Fig. 10(*b*). Spectrum analysis results of the accelerometer signals at FPL and two higher speeds are provided in Fig. 11, and reveal a subsynchronous signal at 26,500 cpm (443 Hz). Both the synchronous and subsynchronous signals are observed to decrease as the running speed increases. Observe that the frequency of the subsynchronous motion is consistent with frequencies observed in test data as opposed to the linear predictions of 520 Hz. The linear model corresponding to the result of Fig. 10 is lightly damped but stable. The nonlinear model remains in a limit cycle motion with subsynchronous components until the destabilizing force components at the main impeller are increased to 250 percent of their nominal values, but then diverge exponentially. Based on these observations, the subsynchronous component of Fig. 11 is deemed to be the result of bearing nonlinearities and not the result of an instability. However, the nonlinear subharmonic motion can only be developed for light rotor damping.

The subsynchronous motion of Figs. 10 and 11 arises at

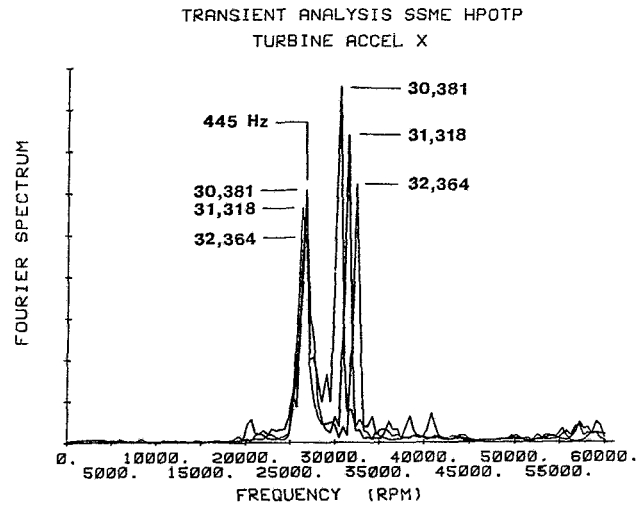

Fig. 11 Turbine X-Z plane acceleration spectra at FPL and higher speeds for the nominal nonlinear model

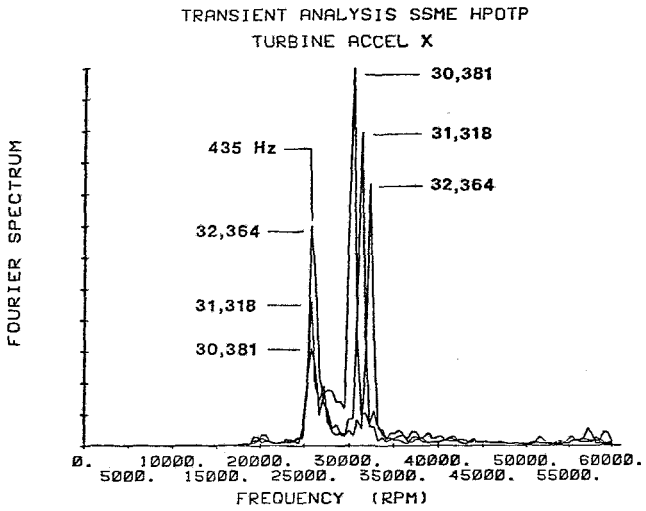

Fig. 12 Turbine X-Z plane acceleration spectra at FPL and higher speeds for nonlinear model number 2

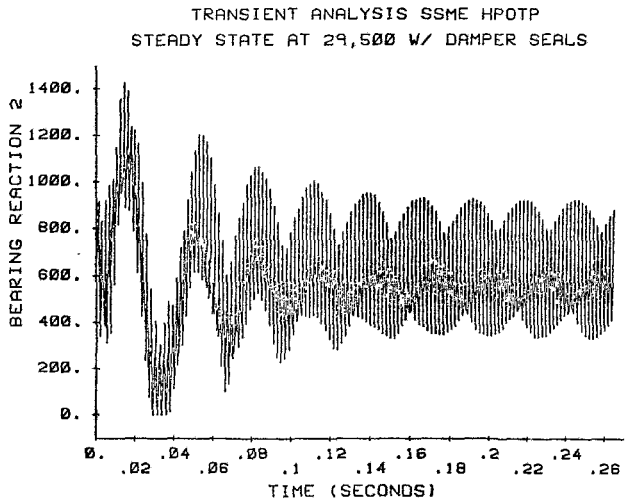

Fig. 13 Bearing 2 reaction magnitude at 29,500 cpm for the nominal nonlinear model with damper seals at the boost impeller

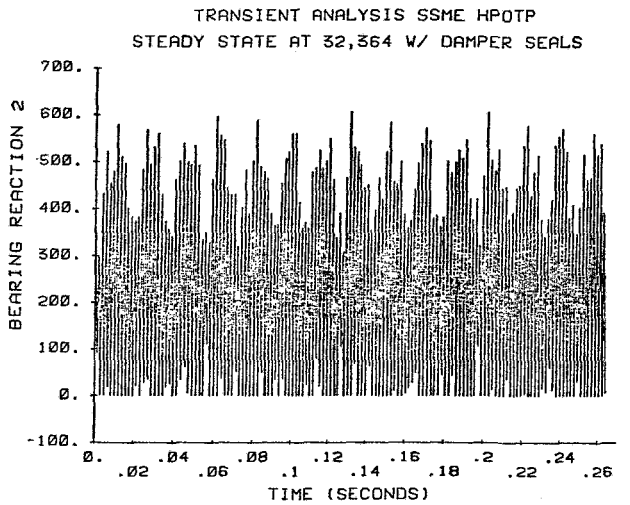

Fig. 14 Bearing 2 reaction magnitude at above FPL for the nominal nonlinear model with damper seals at the boost impeller

speeds above the maximum synchronous response speed predicted by Yamamoto's model in Fig. 9. This statement is supported by the results in Fig. 12, which shows the bearing 2 reaction magnitude predictions at 29,450 cpm.

A second nonlinear model configuration which yielded a substantial subsynchronous vibration component was obtained by doubling both the imbalance magnitudes and the destabilizing force coefficients at the main impeller, adding damping at the bearing (350 Ns/m or 2 lb s/in), and increasing the damping at the main impeller to 2625 Ns/m (15 lb s/in). This configuration is predicted to be linearly stable at FPL. Spectral analysis results for this configuration at FPL and two higher speeds are presented in Fig. 12. In this case, the subsynchronous component increases with running speed, while the synchronous component decreases.

The response characteristics of a nonlinear model including bearing clearances is sensitive to many parameters including bearing clearances, imbalance magnitudes, side load magnitudes, damping coefficients, destabilizing force magnitudes, etc., and a study including a systematic variation of all these parameters would be helpful. However, the simulation results of Figs. 10–12 are sufficient to support the following conclusions:

(*a*) The subsynchronous motion which is evident in these results can be obtained due to bearing-clearance nonlinearities for a linearly-stable but lightly damped model.

(*b*) A whirl frequency of subsynchronous motion at 440 Hz is predicted by the nonlinear model as compared to 520 Hz for the linear model. This whirl frequency reduction results solely from the bearing clearances and does not require any stiffness reduction in the model at the bearings or elsewhere.

(*c*) As predicted by Yamamoto [16] and earlier simulations [15], bearing clearances can drop the peak-vibration running speed into the operating range, and these synchronous vibration loads would appear to pose a more serious threat to bearing lifetime than the subsynchronous motion.

The following options are being pursued to improve the dynamic characteristics of the HPOTP:

(*a*) Units are being prepared for tests which include a stiffened rotor, damper seals at the boost impeller, and a modified turbine interstage seal.

(*b*) Although attractive from a dynamics viewpoint, the shrouded inducer design poses serious manufacturing problems and also raises concerns with respect to cavitation performance. Pending resolution of these problems, no tests of this configuration are presently scheduled.

Figure 13 illustrates simulation results for the nominal nonlinear model with damper seals at 29,500 cpm. Observe the sharp reduction in synchronous bearing loads. This reduction is due to (*a*) load sharing by the seals and (*b*) in-

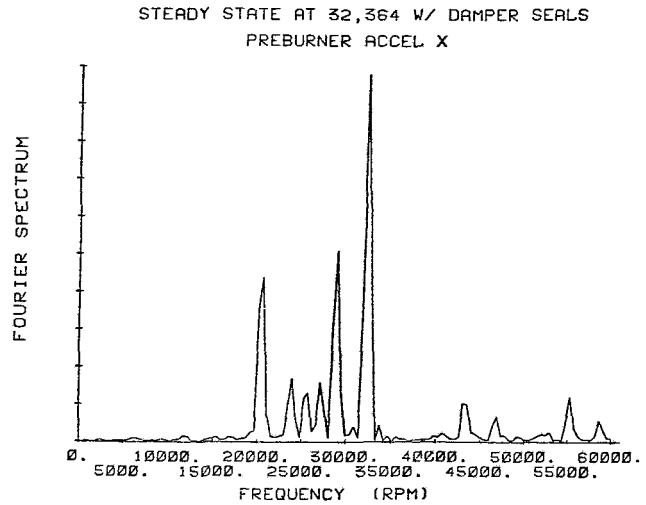

Fig. 15 Preburner *X-Z* accelerometer spectrum at FPL for the nominal nonlinear model with damper seals at the boost impeller

creases in damping that, according to Yamamoto's predictions, lower the peak bearing reaction amplitudes. Figure 14 illustrates the bearing reaction above FPL. Observe that clipping of the bearing loads due to motion in and out of the deadband has actually increased. The corresponding accelerometer spectrum is given in Fig. 15 and demonstrates a rich spectrum of subsynchronous components. The damper seals increase bearing-reaction clipping by opposing the side load and moving the rotor towards the center of the bearing clearances. The model is setup with the seal and bearing centers coincident radially. In an actual engine, some lack of concentricity can be expected which might counteract the seals centering action.

An inspection of Figs. 13–15 support the following conclusions with respect to implementation of the damper seals:

(*a*) In accordance with the linear predictions of Fig. 6, a marked reduction in synchronous bearing loads is predicted.

(*b*) Motion in and out of the bearing clearances is increased with a consequent increase in bearing-reaction-magnitude clipping and an increase in subsynchronous motion.

If current bearing distress is the result of excessive synchronous loads, seal modification should be very beneficial. However, if the bearing problems are associated with unloading and ball skidding, seal modifications will be counter-productive.

Conclusions

Linear and nonlinear analyses of the HPOTP support the following conclusions:

(*a*) By linear predictions, the second critical speed is only slightly above the FPL running speed and is lightly damped. Even a modest loss of bearing stiffness is sufficient to drop the second critical speed into the operating range and yield a prediction of excessive bearing loads.

(*b*) Based on prior test experience, the HPOTP appears to be lightly damped.

(*c*) The subsynchronous motion that is evident in test results can be obtained in a nonlinear model due to bearing clearances. Motion in and out of the deadband clearances excites subharmonic motion for a stable but lightly damped model.

(*d*) A whirl frequency of subsynchronous motion at 440 Hz is predicted by the nonlinear model which is consistent with test results but at odds with a linear prediction of 520 Hz. This whirl frequency reduction results solely from the bearing clearances, and does not require any stiffness reduction in the model at the bearings or elsewhere.

(*e*) Bearing clearances can drop the peak-vibration running speed into the operating range yielding a prediction of excessive bearing loads.

(*f*) Incorporation of damper seals into the boost impeller seals markedly reduces predicted synchronous bearing loads, but increases bearing-reaction clipping and subsynchronous motion at FPL.

Acknowledgments

Discussions with Robert Beatty concerning a parallel investigation at Rocketdyne were very helpful to the authors.

References

1 Childs, D. W., "The Space Shuttle Main Engine High-Pressure Fuel Turbopump Rotordynamic Instability Problem," ASME JOURNAL OF ENGINEERING FOR POWER, Vol. 100, Jan. 1978, pp. 48–57.

2 Beatty, R. F., and Rowan, B. F., "Determination of Ball Bearing Dynamic Stiffness," *Proceedings, Second Workshop on Rotordynamic Instability Problems in High-Performance Turbomachinery*, NASA CP 2250.

3 Jones, A. B., "A General Theory for Elastically Constrained Ball and Radial Roller Bearings Under Arbitrary Load and Speed Conditions," ASME *Journal of Basic Engineering*, Vol. 82, No. 2, June 1960, pp. 309–320.

4 Black, H. F., and Cochrane, E. A., "Leakage and Hybrid Bearing Properties of Serrated Seals in Centrifugal Pumps," Paper G5, 6th International Conference in Fluid Sealing, Munich, German Federal Republic, 27 Feb.–2 Mar. 1973.

5 Black, H. F., and Jensen, D. N., "Effects of High-Pressure Ring Seals on Pump Rotor Vibrations," ASME Paper No. 71-WA/FE-38, Winter Annual Meeting, Washington, D.C., 1971.

6 Black, H. F., Allaire, P. E., and Barrett, L. E., "The Effect of Inlet Flow Swirl on the Dynamic Coefficients of High-Pressure Annular Clearance Seals," Ninth International Conference on Fluid Sealing, BHRA Fluid Sealing Conference, Leeuwenhorst, The Netherlands, Apr. 1981.

7 von Pragenau, G. L., "Damping Seals for Turbomachinery," NASA TP-1987, Mar. 1982.

8 Childs, D. W., "Finite-Length Solutions for Rotor-dynamic Coefficients of Turbulent Annular Seals," ASME *Journal of Lubrication Technology*, Vol. 105, pp. 437–445, July 1983.

9 Nelson, C. D., "The Rotordynamic Coefficients of High-Pressure Annular Gas Seals," accepted for presentation at the 1984 ASME Gas Turbine Conference.

10 Thomas, J. J., "Instabilie Eigenschwingungen von Turbine Laufern, angefacht durch die Spaltstromungen Stopfbushsen un Beschaufelungen, *AEG-Sonderdruch*, 1958.

11 Alford, J., "Protecting Turbomachinery From Self-Excited Rotor Whirl," ASME JOURNAL OF ENGINEERING FOR POWER, Oct. 1965, pp. 333–343.

12 Hauck, L., "Measurement and Evaluation of Swirl-Type Flow in Labyrinth Seals," NASA CP 2250, Rotordynamic Instability Problems in High-Performance Turbomachinery, Proceedings of a workshop held at Texas A&M University, 10–12 May 1982.

13 Chamieh, D. S., Acosta, A. J., Brennen, C. E., Caughey, T. K., and Franz, R., "Experimental Measurement of Hydrodynamic Stiffness Matrices for a Centrifugal Pump Impeller," NASA CP 2250 Rotordynamic Instability Problems in High Performance Turbomachinery, Proceedings of a workshop held at Texas A&M University, 10–12 May 1982.

14 Acosta, A. J., Brennen, C. A., Caughey, T. K., and Jerg, B., "Measurement of Impeller-Inducer Rotor Forces for Evaluation of Dynamic Coefficients," presented at the ASME Applied Mechanics, Bioengineering, and Fluids Engineering Conference, 20–22 June 1983.

15 Childs, D. W., "Rotordynamics Analysis for the HPOTP (High Pressure Oxygen Turbopump) of the SSME (Space Shuttle Main Engine), "an Interum Progress Report for NASA Contract NAS8-31233, Department of Mechanical Engineering, The University of Louisville, 15 Sept. 1979.

16 Yamamoto, T, "On the Critical Speeds of a Shaft," *Memoirs of the Faculty of Engineering*, Nagoga University, Vol. 6, No. 2, 1954.

Rolling Element Bearing Monitoring Using High Gain Eddy Current Transducers

R. G. Harker

J. S. Hansen

Bently Nevada Corporation,
Minden, Nevada 89423

A technique is described which provides early detection of rolling element bearing failure through direct observation of the bearing outer race with a high-gain eddy current probe. Data is presented that compares REBAM™ – Rolling Element Bearing Activity Monitor – to traditional monitoring approaches that employ case mounted velocity and acceleration transducers. Generally, the REBAM approach simplifies the analysis of bearing condition because of its proximity to the bearing and its insensitivity to extraneous vibration sources due to the relative mounting approach employed. A summary of field results is presented and its suitability to high speed gas turbine monitoring is discussed.

Introduction

The concept of measuring deflections of a rolling element bearing outer race was first accomplished by the use of strain gages attached to the outer race. Because of the obvious problems of attaching the strain gage for permanent installation (as the race sometimes slowly precesses), a major improvement to this concept was made by the United States Department of the Navy. They conducted laboratory studies using nontouching fiber optic sensors to detect microinch deflections of the outer race that occur during bearing operation. It was concluded from these studies that this technique provided a means of observing not only rotor and bearing related motions, but also could act as a detection device for internal bearing flaws [1–3].

As an alternative to the fiber optic sensor, Bently Nevada Corporation developed a very high gain displacement transducer using field proven and industry accepted nontouching eddy current proximity technology (Fig. 1). This eddy current sensor exceeds the fiber optic sensor in electrical performance, and unlike the fiber optic sensor, it is not susceptible to calibration changes due to the optical properties in the gap being modified by dirt or contaminants found in normal industrial environments.

To better assess the applicability of this concept as a general rolling element bearing technique, three parallel test phases were chosen:

1 Laboratory tests at several bearing manufacturers' research and development facilities

2 Tests at a leading pump manufacturer on a 600-hp single stage centrifugal process pump

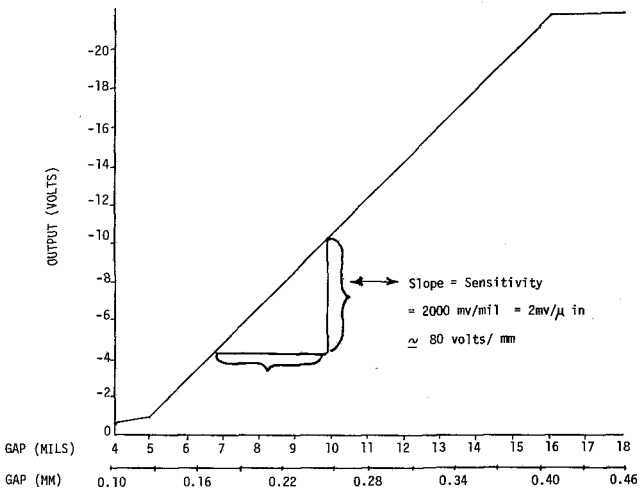

Fig. 1 High-gain eddy current system output voltage change with gap

3 Field trial tests on a diverse selection of rotating equipment which utilize rolling element bearings.

The results from one of the bearing manufacturer's tests are presented, along with the results from the pump test. An overview of the ongoing field trial program is also provided.

Although this technology is in its infancy, significant advantages over existing monitoring methods have already been established which justify continuing development effort.

An understanding of the operational characteristics of this methodology and of contrasting techniques provides insight into these advantages.

The Concept of Observing the Back of the Outer Race

A high-gain eddy current proximity transducer is mounted through the bearing housing observing the external surface of

Contributed by the Gas Turbine Division of THE AMERICAN SOCIETY OF MECHANICAL ENGINEERS and presented at the 29th International Gas Turbine Conference and Exhibit, Amsterdam, The Netherlands, June 4–7, 1984. Manuscript received at ASME Headquarters December 19, 1983. Paper No. 84-GT-25.

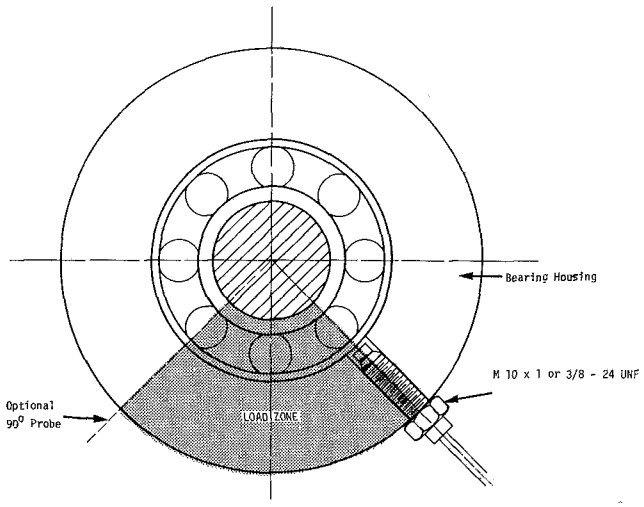

Fig. 2 Typical probe mount

the bearing outer race (Fig. 2, Probe Installation). The outer race of a rolling element bearing deflects minutely as a function of the force applied during bearing operation. As a rolling element passes the observed area, it deflects the outer race toward the probe, causing a proportional change in the signal level. This deflection is in the range of 50–500 microinches and is easily measured by the high-gain eddy current transducer (Fig. 1). Under typical operating conditions, the signal of a good bearing observed on an oscilloscope displays few or no spikes of significant amplitude, but instead shows smooth, low-frequency components characteristic of normal rotor motion, (1×, 2×, etc.) superimposed on the internal rolling element passage motion (RP×).

Under conditions where an internal bearing flaw is present, high-frequency "spikes" of significant amplitude occur. The primary spike frequencies observed by a displacement transducer lie between 20 and 200 times the rotational speed of the machine (Fig. 3, Good Bearing and Bad Bearing).

The high-frequency flaw-related signals are separated from the lower-frequency rotor-related signals through the use of an electronic filter (Fig. 4). This high-pass filtering improves the effective signal-to-noise ratio, permitting even small flaws to be detected. Pictured in Fig. 4 is a comparison of the flaw-related (high-pass filtered) signals from a good bearing and from an identical bearing with a small (.002 sq. in., 1.2 sq. mm) flaw. The bad bearing to good bearing peak-to-peak ratio in this case is well in excess of 2, which indicates a level change significant enough to warrant further investigation. An oscilloscope observation of the high-pass filtered signal provides the positive indication of bearing damage in an early stage.

Observation of the rotor-related signal from a bearing is achieved by selectively low-pass filtering the signal. This low-pass filtered signal shows a primary roller passage component (RP×) for both good and bad bearings. This component results from a force imposed on the outer race by the passage of rolling elements. Each upward peak occurs as a rolling element passes in line with the eddy current sensor. The forces transferred from the rotor through the rolling elements to the outer race cause a deflection of the race and thus a corresponding output change from the eddy current sensor. A simple tool, such as an oscilloscope, is normally sufficient to characterize rolling element bearing condition with this method of monitoring. A review of the entire signal spectrum may be helpful to determine the presence of particular frequencies of interest. A radial ball bearing, installed on a 3600 rpm single-stage pump, is used as an example (Fig. 5).

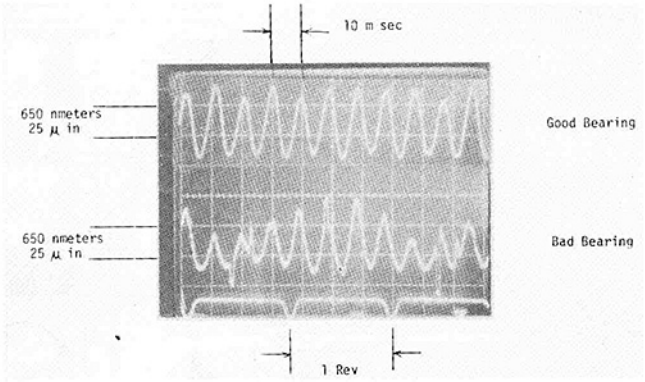

Fig. 3 Unfiltered oscilloscope signals for good and bad bearings

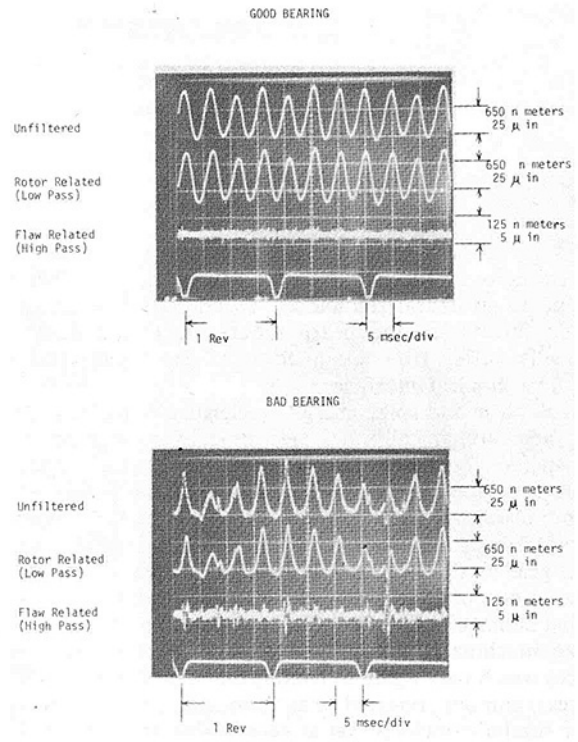

Fig. 4

The frequencies occurring below rotative speed (1×) may be indicative of rotor system instability mechanisms such as seal whirl. Bearing cage defects also may produce subsynchronous frequencies, as the rotational speed of the cage is approximately 0.4 times shaft rotative speed. Events that appear at rotative speed (1×) can indicate imbalance or excessive clearance. An out-of-round inner race or shaft may also cause a 1× component. A significant 2× component is often found if a loose bearing fit exists. An "egg shaped" inner race can produce a 2× component. A monitor can warn of changes beyond normal levels, thus providing early warning of conditions which could lead to machine damage. A component corresponding to vane passage is normally observed at the bearing outer race, as well as on the pump support structure.

Internal bearing flaws or roughness generate spectral components between 20× and 200× the shaft rotative speed. Within this frequency band, support structure resonances may exist. Case mounted transducers will respond at these frequencies requiring bearing-related frequency components to be "sorted-out" from these extraneous signals using high resolution spectrum analyzers. The eddy current method

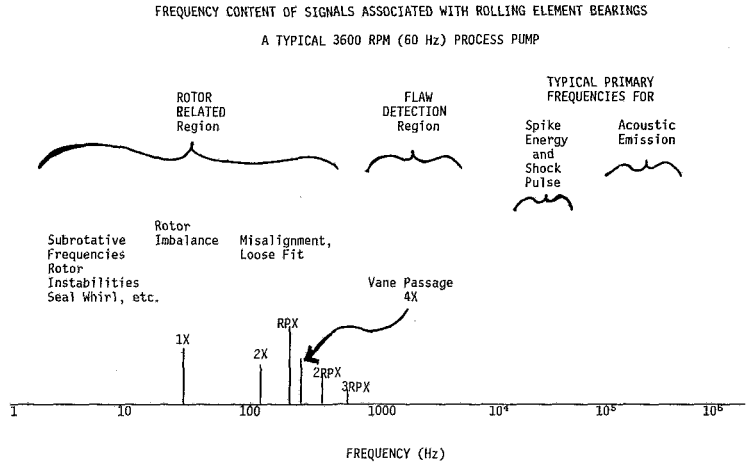

1. As a general rule, the higher the frequency of the signal, the more strongly it will be attenuated by any intervening medium between the source of the signal and the sensor.
2. Case measurements are generally subject to interference from nearby gear clash, pump cavitation, steam throttling, oil ring slingers, etc.
3. Eddy Current Proximity System directly observes the bearing "action."
4. Housing motion is "ignored" in the relative measurement techniques used by the Eddy Current Proximity System.

Fig. 5

provides a relative output signal equal to the motion between the bearing outer race and support structures, so it does not respond to structural resonances. In addition, the sensor is located directly at the bearing outer race and does not physically suffer from attenuation of the signals through several mechanical interfaces.

Shock pulse and spike energy accelerometer-based systems are tuned mechanically and electronically to monitor high frequencies, typically 25–100 KHz. Although spectral components due to bearing flaws may be found in this range, it is not always possible to resolve them from other inherent sources of high frequency activity such as cavitation, oil ring noise, gear clash, or steam throttling. To ensure that an increase in output from these systems originates from internal bearing damage, a knowledge of the operating characteristics of the machine is normally necessary to eliminate signal sources which may relate to routine machine behavior. Other devices commonly referred to as "acoustic emission" operate under similar principles, yet at even higher frequencies. It is imperative that all these type devices mate closely to the machine casing to avoid attenuation of the signal through the mounting interface.

A characteristic of high-frequency, case-mounted transducer systems is a tendency to not always increase in response as bearing damage progresses. This may be because the high-frequency signals are caused by the rubbing of subsurface microscopic interfaces as rollers pass over the regions where the metal structure is in the earliest stage of failure. To the unaided eye, the bearing is still in perfect condition at this point. When the distressed metal actually shears, dislodging metal particles into the bearing, the microscopic interface is destroyed and the corresponding amplitude of the high frequency signals is reduced. In contrast, the eddy current proximity system is sensitive only after visible damage has occurred and the bearing failure is in progress. The eddy current system will then show increases in the amplitude and frequency of the spikes in the *flaw detection* region.

Manufacturer's Test Stand Findings

As an initial effort to qualify the performance of the eddy current approach to rolling element bearing monitoring, the system was installed on an endurance test stand at a major bearing manufacturer (Fig. 6). The 35 mm bore 207 ball

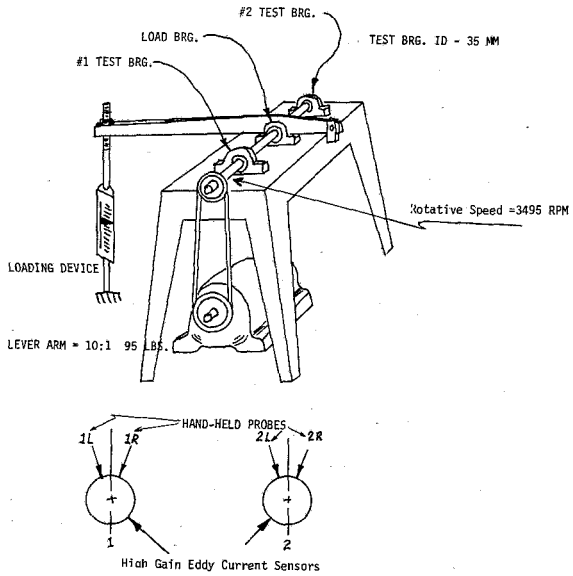

Fig. 6 Test stand

bearing was subjected to a load of 1020 Kg (2244 lb.) corresponding to an L_{10} of 128 hrs. The grease lubricated bearing was run at a constant speed of 3000 rpm and an air temperature of 21°C ± 2°C. The motor driven endurance test stand was wired to shut down when the bearing monitoring system response increased by 20 percent above the ambient level. Approximately 150 hrs after the test began, the response increased by roughly a factor of 2. Disassembly of the bearing under test revealed that a flaw 1.5 mm × 0.7 mm (1/16 in × 1/32 in) had developed and was responsible for the increase. Tests were conducted simultaneously using several commercially available flaw detection systems in parallel with the eddy current system. The results are presented in Fig. 7. The first test was a series of four loads corresponding to average bearing lives of 13.5 years to 9.5 days. The bearing was also checked at an extremely heavy load which further degraded the bearing. The results of these tests are represented by the histogram data (Fig. 7). The general conclusion indicated by

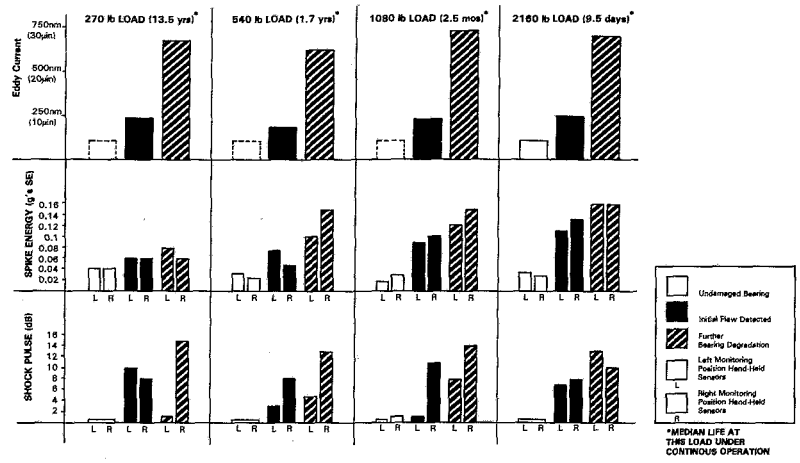

Fig. 7 Measured response under varying load and flaw severity of three flaw detection systems

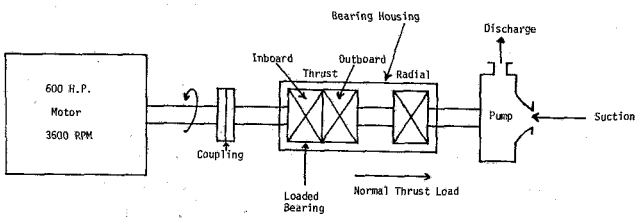

Fig. 8 Single-stage centrifugal pump

this preliminary test is that the eddy current method shows a considerably larger change ratio as failure of the bearing progresses. In some cases, the other systems actually registered decreases in output as the bearing condition worsened.

Tests on a Commercial Pump

The bearing test stand results were encouraging, but tests on an actual machine were required to assure that the technology was suited for monitoring industrial rotating equipment.

This phase of the testing involved actual installation on a widely used centrifugal pump. A schematic of this pump is shown in Fig. 8. The pump tested was of the single-stage overhung process type.

The pump was installed in a test loop, permitting load and flow conditions to be varied over the operational range. The casing and bearings were fitted with a broad collection of transducers (see Fig. 9), including case mounted acclerometers and velocity pickups. Radial displacement of the bearing outer races was monitored with high-gain eddy current probes. Spring loaded thermocouples provided continuous temperature indication of the bearing outer race surface. Commercially available spike energy, shock pulse, and acoustic emission bearing monitoring systems were installed and monitored throughout the course of the tests.

Comparative results of one of the tests is displayed in Fig. 10. Shown is the relative response of two identical bearings, one in perfect operating condition and the other with an inner race flaw. The principal finding was that the case mounted instruments, including shock pulse, spike energy, and acoustic emission units, did not respond in this situation to the inner face flaw.

The eddy current system experienced a significant increase corresponding to a response ratio of 1.6 to 4.3, depending on load and flow conditions. The cause of the level increase was verified by analyzing the phase relationship of the flaw signal to the Keyphasor signal (see Fig. 11). The large spikes led the

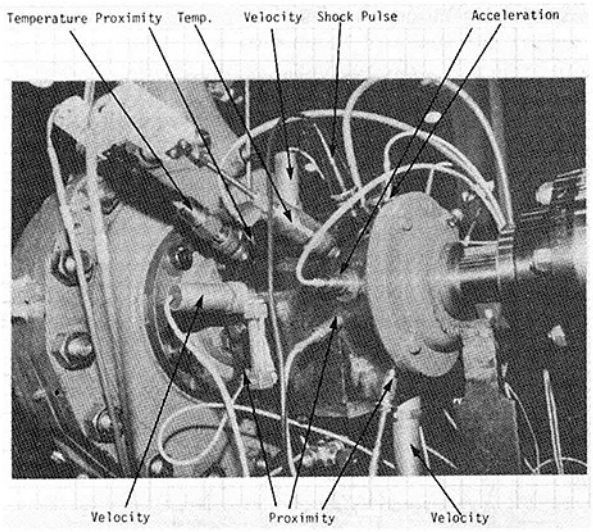

Fig. 9 Acoustic emission sensor hidden from view; spike energy probe was hand-held.

Keyphasor by approximately 70 deg corresponding to the inner race flaw striking a rolling element near the eddy current sensor being monitored.

These results provided further evidence that this new technology has certain advantages over case mounted transducer systems.

Field Trial Programs

The last phase of "proof testing" was to measure system performance on actual rotating machinery in a field environment. The goals of this ongoing program are:

1 To determine applications that best suit this technology
2 To optimize system performance in those applications
3 To measure and document system performance
4 To summarize the information on system performance for general reference

The applications were selected to provide a broad base of information. They include:

1 *A Diammonium Phosphate (DAP) Granulator in the Fertilizer Industry.* A bearing supporting one of the trunnion rolls exhibited an abbreviated life when standard load/life computations were applied. The plant engineer believed the failures were the result of a large asymmetric loading of the

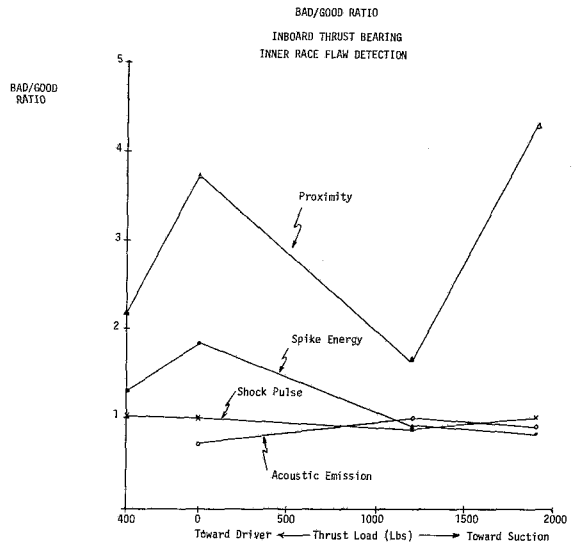

Fig. 10

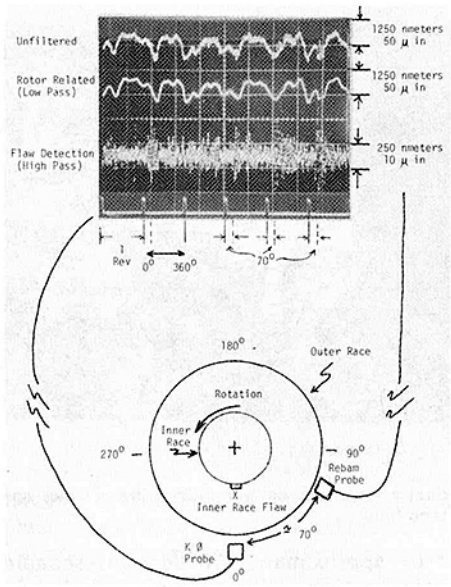

Fig. 11

trunnion bearing due to an uneven distribution of the material within the granulator barrel. Attempts to monitor this application using case mounted accelerometers had been futile because of the very low speed of the trunnion shaft (40 rpm). The eddy current system was employed because of its good sensitivity to low-frequency, rotor-related events as well as to high frequency effects.

2 *A Coal Pulverizer in the Power Generation Industry.* A mean time to failure of roughly 3 months existed on the radial support bearings. The 400-mm (16-in.) shaft typically would shear near the radial bearing. The customer was primarily interested in the rotor-related information as in the first case cited.

3 *A 1500-hp Pit Pump in the Phosphate Mining Industry.* This service is very severe with occasional case velocities in excess of 5 in. per second. Upon initial installation, an abnormally large clearance was detected by the eddy current system in the radial bearing nearest the impeller. The 225-mm (9-in.) shaft sheared within 12 hrs of this observation, destroying the entire bearing housing.

4 *A Large Vertical Salt Bath Pump for a Plasticizer Reactor.* The customer was unable to detect any problems using conventional case mounted instruments, although bearing failures occurred on a frequent basis, often within 12 hrs of making the measurements.

5 *Support Bearings for the Bull Gear in a Large Industrial Compressor.* The journal bearings formerly used as the support for the bull gear had been replaced with rolling element bearings to minimize wear of the pinion gears. It was believed that by minimizing bull gear movement by using a rolling element bearing, tooth wear would be significantly reduced. The eddy current system was installed primarily because of its rotor-related frequency response capability.

6 *Thrust Bearing on a Small Steam Turbine.* The eddy current system was installed on the thrust bearing located at the outboard end of a small steam turbine. The turbine operates at 5500 rpm and acts as the driver for an ethane compressor at 22,000 rpm through a speed increaser. Approximately 2 months after installation, the system detected a surge in the compressor and provided an immediate response of twice the signal level observed under normal conditions.

7 Other applications under study include a small screw-type plant air compressor, a centrifuge, a circulating water pump, a boiler feed pump, a cryogenic pump, several small (25–40 hp) electric motors, and a gearbox.

Presently, the performance of the system in these applications is being documented in a participative effort with the equipment owners. The technology is still in its infancy, but it continues to prove its value, suitability, and reliability for the industrial environment.

References

1 Hirschfeld, F., and Philips, G. J., "Rotating Machinery Bearing Analysis," *Mechanical Engineering*, July 1980.

2 Philips, G. J., "Bearing Performance Investigation Through Speed Ratio Measurements," *Proceedings of the 33rd Annual Meeting of ASLE*, Dearborn, Mich., 17–20 April 1978, Vol. 22, No. 4, Oct. 1979, pp. 307–314.

3 "The Fiber Optic Bearing Monitor," ISA publication, 1982, ISBN: 0-87664-689-5.

4 Bently, D. E., Hansen, J. S., Howard, F., and Modarelli, J., "REBAM™—A Technical Review," Bently Nevada Corporation Publication #130583, May 1983.

S. C. Kaushal
Scientist,
G.T.R.E.,
Bangalore, India

V. A. Kumar
Scientist,
N.A.L.,
Bangalore, India

K. Lakshmikantan
Scientist,
G.T.R.E.,
Bangalore, India

Experimental Analysis of Damper Behavior of Squeeze Film Dampers for Gas Turbine Engines

This paper discusses the experimental evaluation of performance of squeeze film dampers without centralizing retaining springs. Rotor amplitudes in the damper plane and damping coefficient have been considered to assess the system performance. Tests were conducted on two damper configurations that were to go in the rotor assembly of a certain gas turbine engine. Land width and film thickness were varied, and experiments were conducted for different values of excitation frequency, oil supply pressure, and unbalance. The test program showed that the parameters are to be individually optimized to obtain better overall performance in the damper systems without centralizing springs. The damper configurations subjected to severe dynamic conditions due to unbalance on overhung mass were also experimentally analyzed.

Introduction

The current trend of turbomachine design of higher speeds implies that the rotor has to cross over or sometimes operate near the critical speed range associated with large vibration amplitudes and transmitted forces. The squeeze film concepts have been successfully applied in recent gas turbine designs by Rolls Royce [1], General Electric [2], and Pratt and Whitney to reduce these vibration amplitudes. Of the various configurations in which the squeeze film dampers have found practical applications, a major difference exists between those in which the rotor is held centrally by retaining springs or flex bars in the bearing plane, and those in which the rotor is allowed to find its own position in the clearance circle. The latter configuration without the retaining springs has the practical advantage of design simplicity and space saving, and therefore this design has been favored in the number of gas turbines that have recently been developed.

Parametric studies of squeeze film dampers have been made by a number of investigators [4, 6, 7], where the system analyzed contained flex bars. The effect of metallic end seal without centralizing springs [3] and the influence of O-rings with flex bars [5] have also been studied. But the need to optimize the individual parmeters in damper configurations without flex bars has not been reflected.

The objective of this experimental program is to study the influence of geometric parameters on the performance of squeeze film dampers without centralizing retaining springs. The study was restricted to two parameters: i.e., the squeeze film thickness and land width, because these parameters could be controlled without resorting to major design alterations in engines. The aim of this study was to investigate if the individual parameters could be optimized to obtain better overall performance.

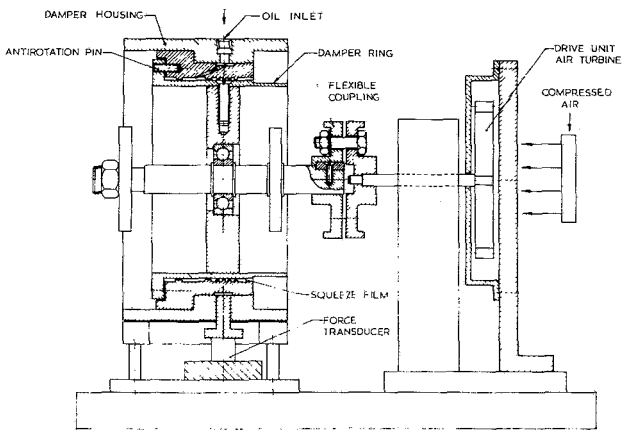

Fig. 1 Schematic diagram—squeeze film damper rig

Many investigators have observed that a small misalignment at bearing supports seriously affects the system performance. Experimental work of Buske [8] shows that the hydrodynamic pressure pattern in a bearing is very sensitive to misalignment. Piggot [9] has observed that a misalignment as small as 0.05 mm in 300 mm length can reduce the safe load carrying capacity of a journal bearing by 40 percent. Lund and Orcutt [10] observed that the whirl orbit amplitude for the rotor system with out of line unbalance is higher than the amplitude of similar system subjected to in-line unbalance. This holds true at each plane along the shaft axis, including the bearing supports.

Based on these observations, it was felt that the overhung unbalance, which could be a possible cause of misalignment at

Contributed by the Gas Turbine Division of THE AMERICAN SOCIETY OF MECHANICAL ENGINEERS and presented at the 29th International Gas Turbine Conference and Exhibit, Amsterdam, The Netherlands, June 4–7, 1984. Manuscript received at ASME Headquarters December 16, 1983. Paper No. 84-GT-8.

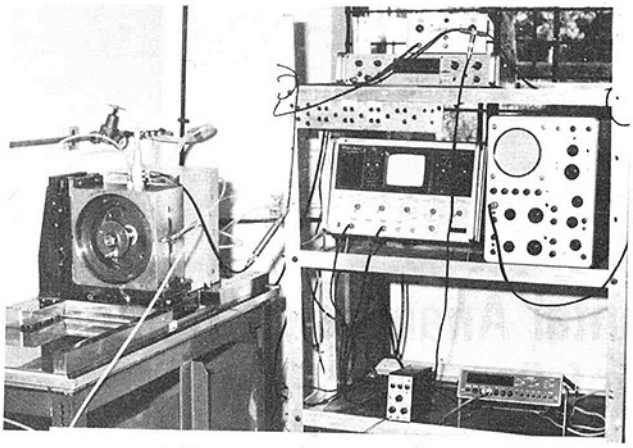

Fig. 2 Photographic view of test rig

the damper plane, would result in severe dynamic conditions. Therefore, it was also the objective of this program to investigate the effect of the overhung unbalance on damper behavior.

Experimental Facility and Instrumentation

The test facility consists of a horizontal rotor coupled to an air turbine through a flexible coupling to isolate transmission of vibration from the air turbine to the damper system. The damper assembly consists of an outer damper ring mounted on a rolling element bearing, and the rotation of the damper ring being prevented by the antirotation pins. The source of excitation of the damper ring was a pure rotating force, and this was achieved by introducing eccentric mass on two circular disks mounted on either side of the damper ring and equidistant from it. The rig schematic is shown in Fig. 1, and the photographic view of the rig is shown in Fig. 2.

The quantitative values of damping coefficient were calculated by using the equation $B = F \sin/\omega X$ [4]. The different parameters, like excitation frequency, damper displacement, transmitted force, and the phase relation between the displacement and the transmitted force, were directly measured. Noncontacting type of proximity pickup was used to measure the damper sleeve displacement and the pickup was calibrated before each set of experiments to study the drift in calibration. Since the tests were conducted without centralizing flex bars, the damper ring was free to rest on the housing under static conditions. Therefore, the nominal upward shift in the axis of the damper ring was measured to obtain damper displacement from the mean position under dynamic conditions. The calibration constants were available, since the probe had already been calibrated for different initial air gaps. A separate eddy current probe, mounted on the air turbine housing, was used to measure the rotational speed. Piezo-electric force transducer was used to measure the force transmitted to the structure. All the signals were recorded in a multichannel tape recorder for further signal processing and analysis. The time-averaging technique was used to obtain noise-free averaged signals for force and amplitude, and these signals were then cross correlated to obtain phase angle between the two averaged signals. The schematic of the rig instrumentation is shown in Fig. 3.

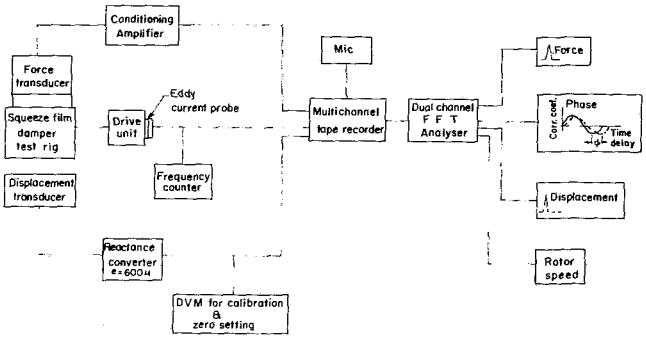

Fig. 3 Instrumentation layout

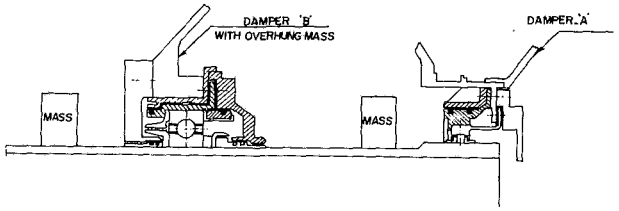

Fig. 4 Bearing supports and squeeze film dampers cross section

Experimental Investigation and Test Description

It has been earlier shown that the performance gain could be achieved by introducing the centralizing flex bars and the metallic end seals in squeeze film dampers [3]. The damping performance could be further improved by optimizing any of the following parameters:

(*a*) Film thickness or damper clearance, C
(*b*) Damper land width, L
(*c*) Diameter, D, at which oil film is located
(*d*) Oil viscosity

For a gas turbine application, it may not always be possible to introduce centralizing flex bars due to space restriction, and the damper diameter could only be increased to a very limited extent. Experimental investigation here therefore was restricted to study the effect of squeeze film thickness and land width for damper configuration without centralizing flex bars.

The purpose of this experimentation was not only to improve the damper performance but also to investigate the contribution of the individual parameters in overall performance improvement. In other words, for a particular value of one parameter, say film thickness, the land width may require optimization to get the best damping performance.

It has also been shown that the damper supporting the overhung mass is subjected to severe dynamic conditions due to unbalance on the overhung mass. In fact, this condition was simulated in the rig to study the effect of increase in land width in one of the damper configurations.

The tests were carried out on two damper systems supporting the LP rotor of a gas turbine engine shown in Fig. 4. The damper details are shown in Fig. 5(*a*), and the damper components are shown in Fig. 5(*b*). The effect of land width and film thickness on damper performance was investigated for damper "A", and based on these tests, the damper "B" parameters were fixed. In actual application the damper "B"

Nomenclature

B = damping coefficient, N-s/m
C = squeeze film thickness, m
D = damper ring dia, m
F = maximum value of transmitted force, N
L = damper land width, m
X = maximum value of damper ring amplitude, m
ω = excitation frequency, s^{-1}
φ = phase angle between damper ring vibration and force transmitted, deg
μ = oil viscosity, N-s/m^2

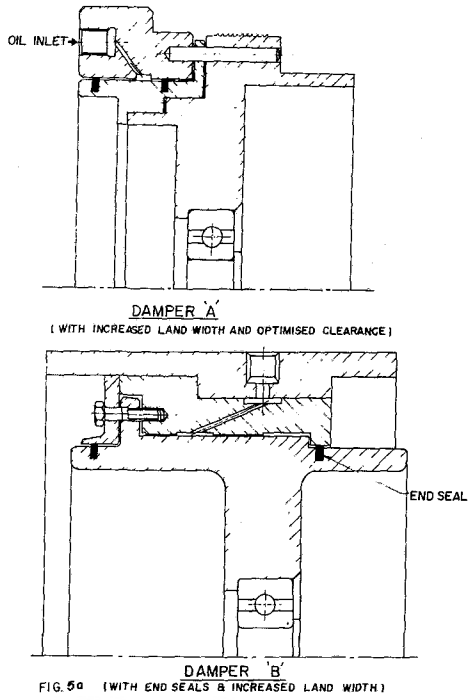

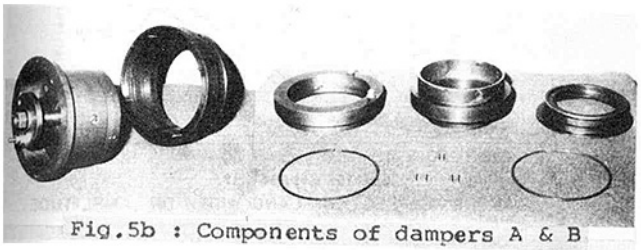

Fig. 5

supports the overhung mass. The effect of increase in land width was studied on damper "B" simulating the unbalance on overhung mass. The oil supply pressure and unbalance were simulated to obtain direct performance comparisons. The tests with a particular damper geometry were repeated to confirm the reliability of experimental data. The force and amplitude signals were time averaged in frequency domain to eliminate the noise. Typical signals are shown in Fig. 6(*a*). The oil-film breakdown leading to metal to metal contact was observed when the damper configuration was subjected to high excitation force due to large unbalance at higher rotational speeds. The amplitude signal corresponding to the film breaking phenomenon is shown in Fig. 6(*b*). It was observed that once the film breaks or the instability sets in, it always persists despite the increase in oil supply pressure.

Test Results and Discussions

The critical speed of the test rotor as a function of support stiffness was evaluated, and it was found that there was no appreciable change in critical speed within the stiffness range observed experimentally. The first bending critical speed was of the order of 72.2 Hz. A similar observation was made experimentally which can be seen as amplitude peaks at around 70 Hz in Figs. 8, 9, and 10. It was possible to eliminate these peaks substantially by suitably modifying the damper geometries.

Damper "A"

(*a*) *Effect of Squeeze Film Thickness.* The damper configuration "A," with metallic end seals and end seal gap optimally located with respect to oil supply ports [3], was

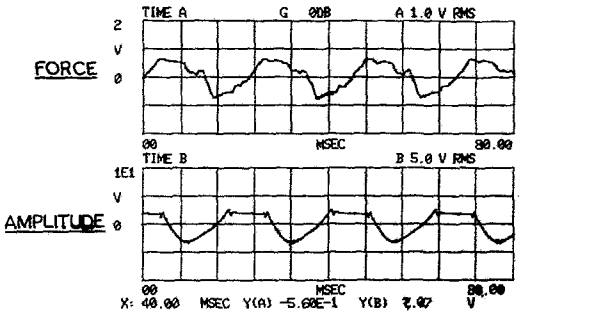

RECORDED FORCE & AMPLITUDE SIGNAL (OIL FILM BREAKING)
DAMPER 'B' - 58 Hz - OIL PRE. 280 kPa (WITHOUT END SEALS)
FIG. 6a

DAMPER 'A' - OIL FILM BREAKING
65 Hz - OIL FILM THICKNESS - 250 μ
OIL PRESSURE - 280 kPa

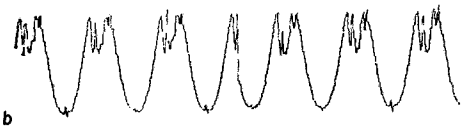

FIG. 6b
RECORDED AMPLITUDE SIGNAL FOR DAMPER 'A'

Fig. 6

tested for film thickness of 90 μm, 150 μm, and 500 μm. The land width expressed in terms of L/D ratio has been maintained as 0.082. The effect of film thickness on damper performance is shown in Fig. 7. The lowest film thickness of 90 μm gives the best performance up to a speed range of 45 Hz, beyond which the oil film breaks for all oil supply pressures. The film thickness of 500 μm gives the worst performance and again the film breaks after 63 Hz. From this trend, it was concluded that a film thickness between these two extremes could be optimized for improved performance. For $L/D = 0.082$, the film thickness of 250 μm seems to be giving a better performance as compared to the one with 150 μm thickness. No film breaking phenomenon was observed in case of 250 μm and 150 μm film thickness values, but the tests were stopped at 80 Hz and 70 Hz, respectively, due to rough running of the rig.

(*b*) *Effect of Increased Land Width.* The film thickness of 150 μm and 250 μm were tested for increased land width ($L/D = 0.15$). The effect of increased land width on damper performance is shown in Fig. 8. There is a considerable reduction in damper amplitude for 150 μm, as well as for the 250 μm film thickness, but the film thickness of 150 μm gives better overall damper performance. On the average the damping coefficient has shown the increasing trend, and it has been possible to cover the speed range up to 90 Hz for the damper configuration with film thickness of 150 μm and the increased land width corresponding to $L/D = 0.15$. This was the maximum speed that could be attained in the present rig set up.

It may be noted that the film thickness of 250 μm gives better performance when the land width corresponds to $L/D = 0.082$, and subsequently when the land width is increased ($L/D = 0.150$), the film thickness of 150 μm gives better performance. The results clearly indicate that the geometric parameters in a damper configuration without the centralizing springs have to be optimized individually to obtain better overall performance.

Damper "B"

With the test conducted on damper "A," as datum, the film thickness of 125 μm was optimized for this configuration and tests were conducted for two land widths, i.e., L/D = 0.085 and 0.182. The land width to diameter ratio has been restricted to less than 0.2, because of the limitation imposed by the particular application. The effect of land width on damper performance for an unbalance of 0.018 Nm is shown in Fig. 9, and these results could be summarized as follows:

(*a*) For the damper configuration without end seals, increase in land width has shown marked reduction in damper amplitude, thereby indicating that the land width plays an important role in improving the damper performance.

(*b*) For damper configuration with end seals, increase in land width has not shown further reduction of damper amplitude; however, there is an increase in damping coefficient. It amounts to an improvement in the overall performance of the damper.

Effect of an Unbalance on Overhung Mass. The improvement in performance due to increased land width has been directly brought out in Fig. 10. This damper configuration supports an overhung rotor mass in engine application, and it was observed that the damper oil film is subjected to severe dynamic conditions when unbalance is introduced on overhung mass (refer to Fig. 10). The damper configuration with end seals and L/D = 0.085 experience a film breakdown at about 63 Hz when an unbalance of 0.014 Nm was introduced at overhung mass. Under similar

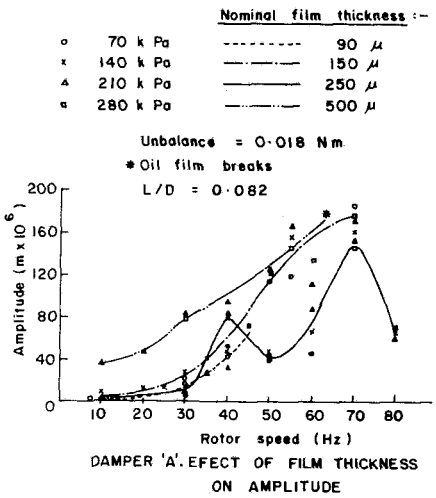

Fig. 7 Optimization of film thickness for damper "A" (unbalance = 0.018 Nm)

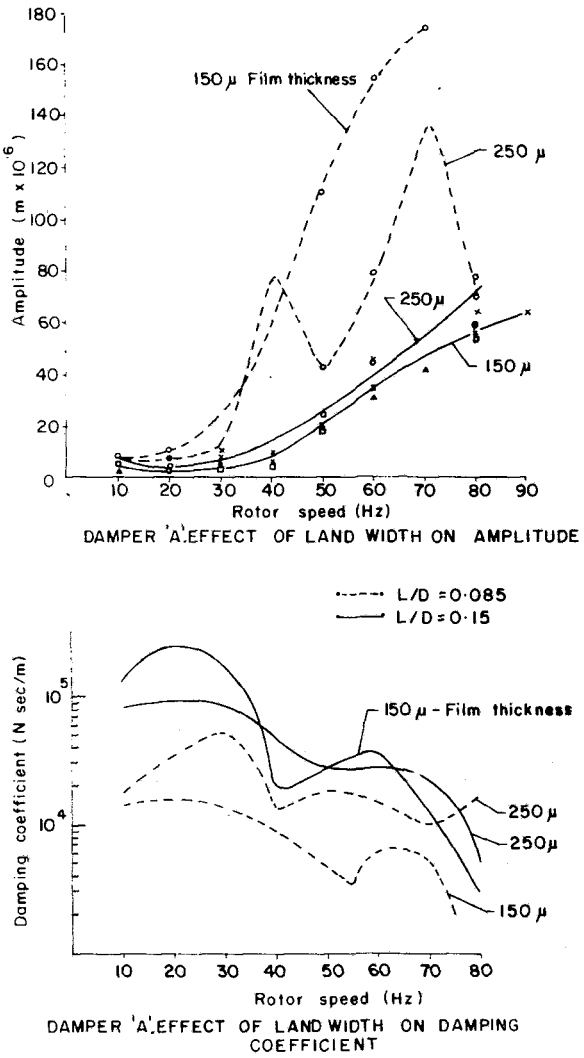

Fig. 8 Effect of land width on damper "A"

Table 1 Comparison of Damping Coefficients

Damping configuration			Damping coefficient, N s/m		
Type	L/D	C microns	Theoretical	Experimental	Remarks
A	0.082	500	0.05×10^4	0.3 to 0.5 $\times 10^4$	ref. Fig. 7
A	0.082	250	0.43×10^4	0.5 to 5.5 $\times 10^4$	ref. Fig. 7
A	0.082	150	1.97×10^4	0.4 to 6.8 $\times 10^4$	ref. Fig. 7
A	0.082	90	9.14×10^4	2.0 to 13 $\times 10^4$	ref. Fig. 7
A	0.15	150	3.06×10^4	3 to 23 $\times 10^4$	ref. Fig. 8
A	0.15	250	0.86×10^4	3 to 10 $\times 10^4$	ref. Fig. 8
B	0.085	125	1.32×10^4	1.9 to 7 $\times 10^4$	ref. Fig. 9
B	0.182	125	8.79×10^4	4 to 10 $\times 10^4$	ref. Fig. 9

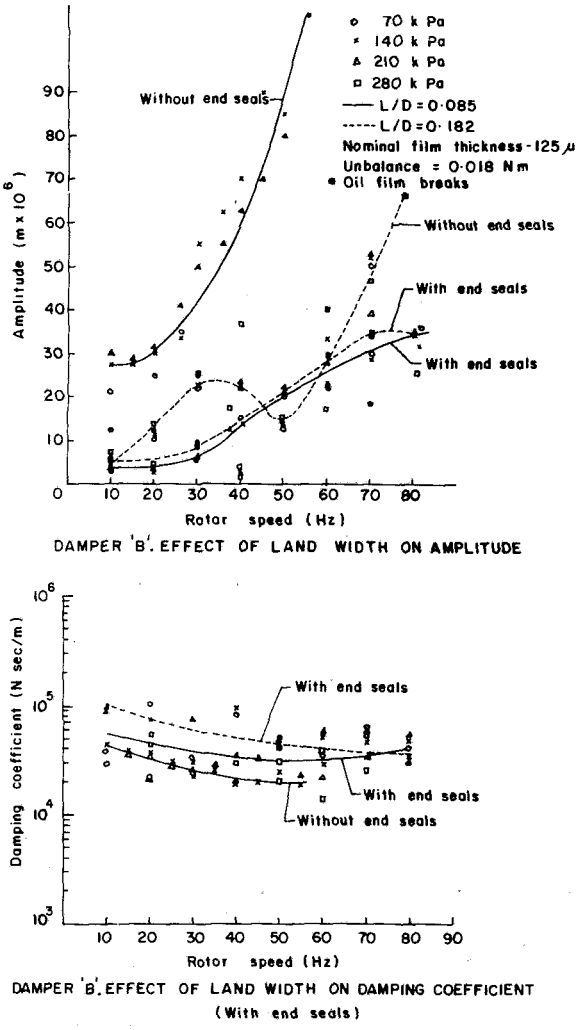

Fig. 9 Effect of end seals and land width on damper "B" (unbalance = 0.018 Nm)

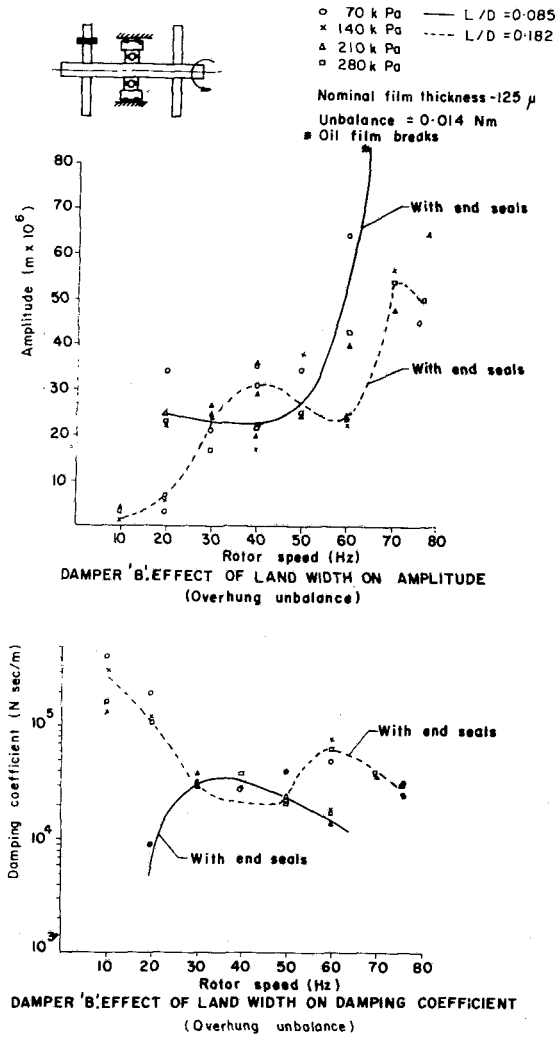

Fig. 10 Damper "B": performance with unbalance on overhung mass

operating conditions, the rotor could go up to 80 Hz speed without any film breakdown when the land width was increased to $L/D = 0.182$. In other words, the damper configuration with increased land width could withstand higher excitation force due to unbalance.

The experimental values of damping coefficients were compared with the theoretical values estimated using the equation (4).

$$B = \mu L \left(\frac{D}{2C}\right)^3 12\pi \left[1 - \frac{\tan h\,(L/D)}{(L/D)}\right]$$

The results, as tabulated in Table 1, show that theoretical values of damping coefficients are generally lower than the experimentally determined values. This was also observed in experimental work reported in [4, 11].

Conclusions

The effect of land width, film thickness, and oil supply pressure on the performance of squeeze film dampers without centralizing springs has been experimentally studied.

The land width and film thickness is to be individually optimized to obtain better overall performance. Under severe dynamic conditions, when end seals are used, land width plays a very significant role in attenuating the vibration amplitude.

Increase in oil supply pressure within the range tested seem to improve the damping performance. But, in the event of failure of squeeze film, any increase in oil supply pressure does not seem to relieve the situation.

Acknowledgment

The authors gratefully acknowledge with thanks, Mr. M. Ananda for his assistance in conducting the experiments.

References

1 "The Rolls Royce RB-211—Three Shaft Turbofan Engine," *Aircraft Engineering*, April 1968, p. 22.

2 Magge, N., "Philosophy, Design, and Evaluation of Soft Mounted Engine Rotor System," *Journal of Aircraft*, April 1975, p. 318.

3 Kumar, V. A., Kaushal, S. C., and Lakshmikantan, K., "Experimental Investigation on the Role of Flex Bars and Metallic End Seals in Squeeze Film Dampers," 6th ISABE, Paris, June 1983.

4 Thomson, K. K., and Anderson, H., "Experimental Investigation of a Simple Squeeze Film Damper," ASME Paper No. 73-DET-101.

5 Kumar, V. A., "Influence of O-rings on the Behaviour of Damping Coefficient in a Squeeze Film Mounted Ball Bearing," 5th ISABE, Bangalore, India, Feb. 1981.

6 Tonneson, J., "Experimental Parametric Study of a Squeeze Film Bearing," ASME *Journal of Lubrication Technology*, Apr. 1976.

7 Kumar, V. A., and Paranjpe, P. A., "Experimental Evaluation of Damping Coefficient in Squeeze Film Mounted Ball Bearings," 4th ISABE, Fla., Apr. 1979.

8 Buske, A., "Influence on Bearing Design on Load Carrying Capacity and Safety of Bearings," Stahl Eisen, 1951, p. 71.

9 Pigott, R. J. S., "Bearing and Lubrication Bearing Troubles Traceable to Design can be Avoided by Engineering Studies," *Mech. Engineering*, 1942, p. 64.

10 Lund, J. W., and Orcutt, F. K., "Calculations and Experiments on the Unbalance Response of a Flexible Rotor," ASME *Journal of Engineering for Industry*, Nov. 1967.

11 Sharma, R. K., and Botman, M., "Experimental Study of Steady-State Response of Oil Film Dampers," ASME Paper No. 77-DET-33.

W. N. Shade
Chief Design Engineer,
Centrifugal Compressors.
Mem. ASME

D. E. Hampshire
Supervisor,
Research and Development.
Mem. ASME

Cooper Energy Services,
Mount Vernon, Ohio 43050

An Experimental Investigation of Oil-Buffered Shaft Seal Flow Rates

An experimental investigation was conducted to identify an optimum oil-buffered shaft seal for use on centrifugal compressors, with the primary objective being minimal seal oil exposure to process gases that cause seal oil degradation or are toxic. Types of seals tested included smooth bore cylindrical bushings, spiral groove cylindrical bushings, radial outward-flow face seals, and radial inward-flow face seals. The influence of shaft speed, gas pressure, seal oil differential pressure, oil bypass flow rate, and oil supply temperature on process side seal oil flow rate was determined. The investigation revealed some surprising relationships between seal oil flow rates and the escape of process gas.

Introduction

Shaft seals are required in centrifugal compressors to prevent the leakage of process gas from the pressurized gas cavity to atmosphere. The seals must function satisfactorily over the entire compressor operating range, including start-up and shut-down. Depending upon the process variables and the type of gas to be sealed, labyrinths, carbon rings, bushings, or contact seals may be used separately or in combination to effect the desired sealing. In centrifugal compressors for natural gas service, the oil buffered smooth bore cylindrical bushing seal has been an accepted type of seal for many years in hundreds of applications [1]. Compared to other types of oil-buffered seals, smooth bore bushings are less sensitive to dirt damage, are not affected by axial movement of the rotor shaft, and are not significantly influenced by rotor shaft vibration. As a result, long operating life is a primary advantage of this type of seal [2, 3].

Although there are variations in oil-buffered smooth bore bushing seal designs between manufacturers [2–7], a common design employs a double-seal arrangement at each end of the compressor shaft, as shown in Fig. 1. The steel-babbitt or steel-aluminum seal rings float on an oil film from oil supplied between the rings at a pressure differential of 0.35–1.03 bar (5–15 psi) above the process gas pressure. Oil flows across the atmospheric, or low-pressure, seal with a differential pressure that is equal to process gas pressure plus 0.35–1.03 bar (5–15 psi). This oil flow is collected in an atmospheric drain and returned to the oil sump for reuse. Oil flowing across the process side, or high-pressure, seal into an internal drain cavity prevents process gas leakage from the compressor to atmosphere. Oil collected in the high-pressure seal drain cavity is saturated with process gas and typically drains into a trap and a degasser for separation of the gas from the oil before the oil returns to the sump for reuse. The outward flow through the low-pressure bushing seal is not exposed to process gas and is therefore not subject to contamination.

In applications where the process gas is toxic or causes degradation of the seal oil, the oil from the high-pressure seal oil drain is either discarded or subjected to one or more types of reclamation processes. In many cases, the reclamation simply involves increasing the holding time in the degasser so that the gas can separate out of solution. Particularly in North Sea installations, seal oil contamination with aromatic and aliphatic hydrocarbons of C_4 to C_{16} have caused rapid deterioration of the oil viscosity and flash point [8–12]. The further use of seal oil thus contaminated could be extremely hazardous and would also lead to expensive downtime should the reduced viscosity cause a bearing, seal, or gear failure. If the contaminant is hydrogen sulfide, the risk of sulfide stress corrosion is markedly increased. Although a process involving heating, vacuum degassing, and filtration has been developed to successfully reclaim the contaminated oil, the comparatively high oil flow rates of smooth bore cylindrical bushing seals (as much as 70 times a comparable face seal [7]) remain a concern in many applications of this nature.

To identify an acceptable alternative to the traditional process side smooth bore bushing seal for centrifugal compressors in natural gas applications, many types of oil-buffered seal designs were considered. Important objectives in selection of an alternate seal design included:

1 Total containment of process gas
2 Maximum high-pressure seal oil flow rate not to exceed 19 l/day (5 US GPD)
3 Process side seal to be usable in conjunction with conventional smooth bore bushing on atmospheric side, to replace the traditional two-bushing arrangement
4 Design retrofittable to existing compressors with minimal component modifications and oil system revisions
5 Ease of maintenance
6 Minimum service life of two years
7 Minimal cost increase

Three types of alternative process side seals were selected for evaluation, along with the conventional smooth bore

Contributed by the Gas Turbine Division of THE AMERICAN SOCIETY OF MECHANICAL ENGINEERS and presented at the 29th International Gas Turbine Conference and Exhibit, Amsterdam, The Netherlands, June 4–7, 1984. Manuscript received at ASME Headquarters December 18, 1984. Paper No. 84-GT-9.

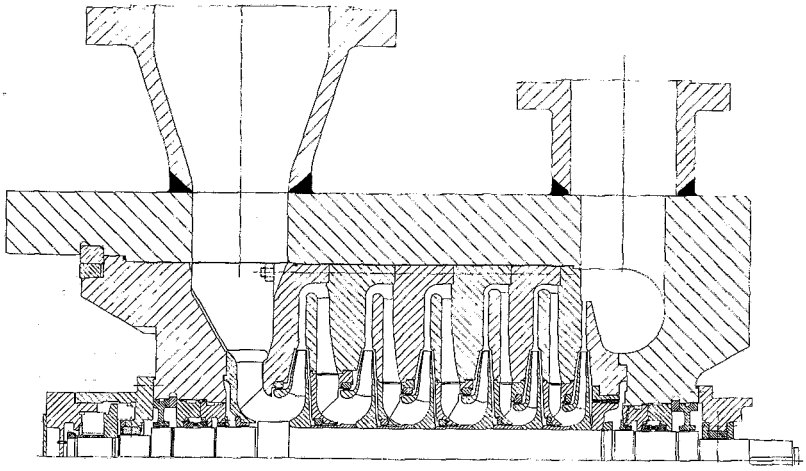

Fig. 1 Typical Cooper-Bessemer centrifugal compressor

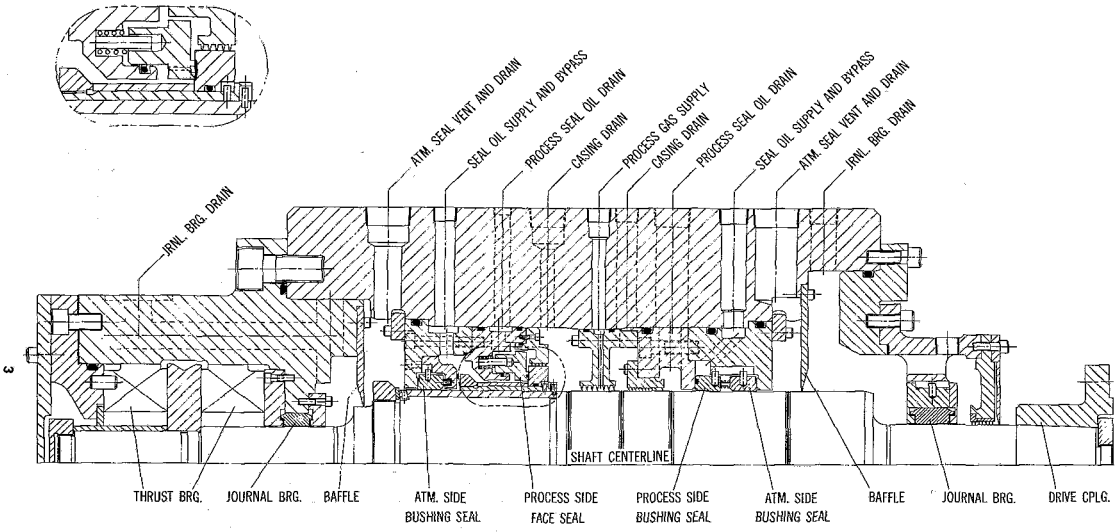

Fig. 2 Seal test rig cross section showing conventional cylindrical smooth-bore bushing seal assembly and radial outward-flow face seal assembly

bushing in a test rig (see Fig. 2) especially built to simulate an intermediate size Cooper-Bessemer RCB barrel compressor. The seal types included:

- Spiral groove cylindrical bushing seal
- Radial inward-flow face seal
- Radial outward-flow face seal, two designs

Tests were planned to determine the influence of shaft speed, process gas pressure, seal oil differential pressure, oil bypass flow rate, and oil supply temperature on seal oil flow rate for each seal configuration. The results of these tests, as well as some surprising trends regarding leakage of process gas, are reported in this paper.

Description of Seals Tested

Smooth-Bore Cylindrical Bushing Seal. The test rig shown in Fig. 2 contained two sets of shaft seals surrounding an internal pressurized cavity similar to a beam style compressor arrangement. Conventional double smooth-bore bushing seals were used on the drive end of the rig throughout the test. Some baseline data were collected from these seals as various other seal arrangements were evaluated in the free end of the rig.

A cross section of the double smooth-bore bushing seal arrangement used in the testing is shown on the right end of the test rig in Fig. 2. Freedom of radial movement is inherent in the design, and motion in this plane occurs during start-ups as the shaft journals rise in their bearings and in response to equalizing pressures from within the flow annulus.

Hydraulic pressure acting on the exposed surfaces of the floating bushing exerts sufficient axial force to prevent leakage past the lapped sealing face adjacent to the housing. The process side seal may contain a viton O-ring in the sealing face as a further precaution against leakage of seal oil or process gas across the face. Four coil springs, located by dowel pins, are provided to keep the bushings placed against the housing sealing faces until sufficient hydraulic pressure is applied. Each bushing contains a radial dowel that loosely engages a slot in the housing bore to prevent rotation.

Seal oil at 0.35–1.03 bar (5–15 psi) above the process gas pressure is supplied into an annulus around the housing. Oil

Nomenclature

ΔP = seal oil bypass pressure-process gas pressure, bar (psi)
Q_g = gas loss, kg/day (lb/day)
Q_{gv} = gas loss, 1/day (ft^3/day)
Q_o = seal oil flow rate, 1/day (US gpd)

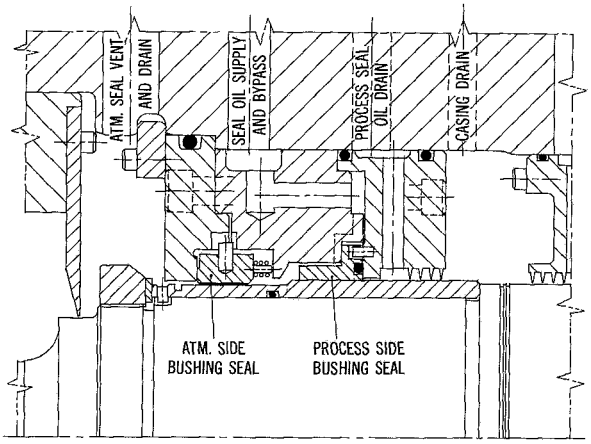

Fig. 3 Spiral groove cylindrical bushing seal assembly

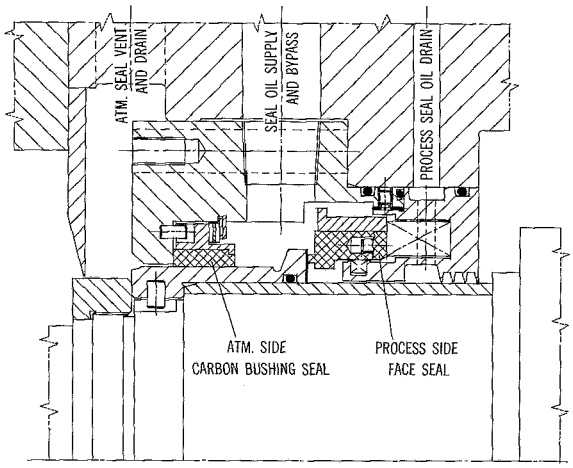

Fig. 4 Radial inward-flow face seal assembly

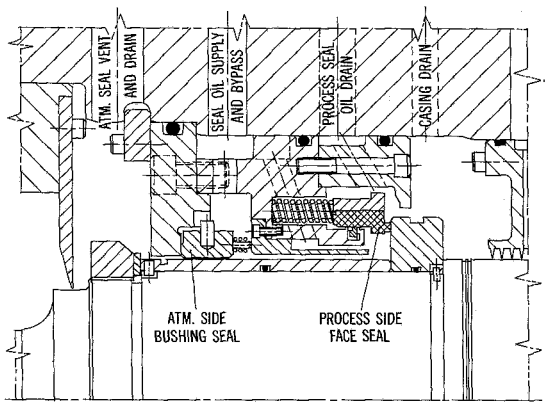

Fig. 5 Alternate radial outward-flow face seal assembly

flows from the annulus toward the outer perimeter of the process side bushing through four drilled holes. This oil cools the outside of the process bushing before flowing through the annular clearance of each seal, with most of the oil flowing through the atmospheric side bushing and a relatively small amount flowing through the process bushing into drains which have been discussed previously. Excess oil flowing through the housing exits through a bypass port, carrying away some of the heat generated by the shearing of the oil film in the bushing bores.

The smooth-bore cylindrical bushings tested were of mild steel with a tin-based babbitt bore lining. The nominal bore diameter was 139.7 mm (5.5 in.), and the active length was 20.6 mm (0.812 in.). Actual diametral clearances of the bushings tested included 0.102 mm (.004 in.), 0.137 mm (.0054 in.), and 0.160 mm (.0063 in.).

Spiral Groove Cylindrical Bushing Seal. The spiral groove cylindrical bushing seal shown in Fig. 3 has most of the inherent advantages of the smooth bore bushing, but has significantly lower oil flow rates. Oil is supplied into the housing at a pressure sufficient to maintain the bypass oil flowing out of the housing at 0.35–1.03 bar (5–15 psi) above the process gas pressure. For improved cooling, the oil is forced through a series of radial grooves and annuli around the entire outer perimeter of the process side bushing and into the cavity between the two bushing seals. One-third to two-thirds of this oil passes on through the assembly and out the bypass port. Most of the remainder flows through the atmospheric side bushing, and only a small amount flows across the bore of the process side bushing. The atmospheric side bushing is a conventional smooth-bore bushing.

The bore of the steel/tin-babbitt process side bushing is 28.5 mm (1.122 in.) long with a nominal diameter of 142.2 mm (5.60 in.). One-third of the bore on the oil side of the bushing is smooth with a diametral clearance of 0.130 mm (0.0051 in.). The two-thirds of the bore closest to the gas side contains three tapered spiral grooves machined in a manner that causes a pumping action counter to the normal flow of seal oil across the bore.

The process bushing seal face contains a viton O-ring that seats against a mating Teflon coated housing surface. The bushing shoulder, the housing recess, and the O-ring groove are sized to adequately preload the O-ring until oil pressure is applied.

Radial In-Flow Face Seal. A face seal is a mechanical seal consisting of a rotating collar, or runner, and a nonrotating carbon seal ring. Contact between the collar and the seal ring is maintained by calibrated springs and a small, carefully designed, closing force resulting from unbalanced hydraulic pressure acting on the exposed surfaces of the seal ring.

The carbon seal ring is suspended so that it may float in an axial and, to a lesser extent, in a radial direction, enabling it to compensate for displacement of the collar due to rotor vibration, thermal expansion, or misalignment of the shaft. An elastic seal, such as an O-ring, usually comprises the secondary sealing element between the seal ring and the stationary mounting. This element is designed to offer minimum resistance to motion of the seal ring. Maintenance of parallelism and flatness between the mating surfaces of the collar and the seal ring is vital to the effectiveness of this type of seal. The seal ring is geometrically contoured to maintain dimensional stability and surface flatness during operation. Axial pins engage the housing to prevent rotation of the carbon seal ring.

The radial in-flow face seal is the most common type of face seal. Figure 4 shows a cross section of the seal tested. Seal oil is introduced at a pressure of 2.41–3.45 bar (35–50 psi) above process gas pressure into the space between the process side carbon face seal and the atmospheric side bushing seal, which happens to be a steel/carbon bushing for this arrangement. Since there is no bypass flow in this particular design, the atmospheric bushing is sized to flow sufficient oil to keep the face seal cool by drawing supply oil over it. Oil is forced radially inward between the 147.6-mm (5.81-in.)-dia carbon sealing face and the hardened collar by the 2.41–3.45 bar (35–50 psi) pressure differential opposed by the centrifugal pumping action of the rotating collar. As a result, the face seal is held off the rotating collar by a narrow film of oil which leaks across the face and collects in an internal drain

cavity. The carbon face seal is reinforced by an outer steel ring. The secondary seal is of Teflon construction. Fourteen Inconel springs are used to hold the face seal carbon against the collar.

Radial Out-Flow Face Seal. The radial outward-flow face seal differs from the radial inward-flow face seal primarily in the direction of oil flow across the sealing face. Since the radial outward-flow face seal takes advantage of the centrifugal pumping action of the rotating collar, the differential pressure required is more consistent with that required by conventional bushing seals. This is an important system consideration when retrofitting of existing compressors is desired. Two radial outward-flow face seal designs were evaluated.

The first design, shown in the left side of Fig. 2, requires seal oil at a supply pressure sufficient to maintain a bypass pressure of 0.35–1.03 bar (5–15 psi) above the process gas pressure. Oil is introduced into an annular cavity between the process side face seal and the conventional atmospheric side smooth-bore bushing seal. A small amount of seal oil flows parallel to the shaft and under the carbon face seal. The pumping action of the rotating collar and the pressure differential cause a thin film of oil to flow between the carbon sealing face and the collar. This oil is collected in a high-pressure drain cavity similar to the other types of seals. One-third to one-half of the remaining supply oil flows across the atmospheric side bushing to a drain, with the balance flowing out the bypass port. Both of these flows carry heat away from the cartridge.

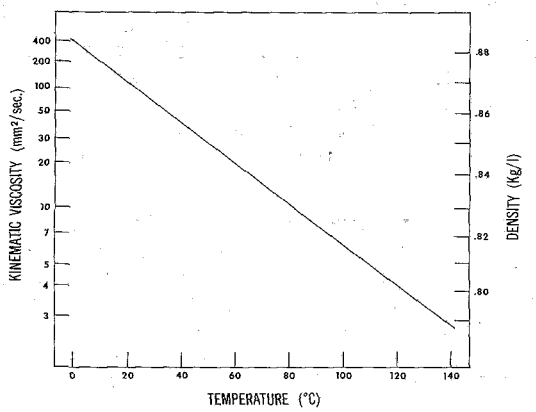

Fig. 6 Test oil viscosity—temperature and density—temperature relationships

The carbon seal ring is reinforced by an outer stainless steel ring. The 171.5 mm (5.76 in.) carbon sealing face is divided into two sections by a circumferential groove in the face. The outer section is a continuous surface, but the inner section is divided into 31 pads, some of which are slightly tapered to provide hydrodynamic lift for start-up and low-speed operation. The relief between each pad contains a bleed hold running axially through the carbon ring. The secondary seal is a viton O-ring backed-up by a Teflon lip seal. Eighteen stainless steel compression springs keep the carbon seated against the collar.

The other radial outflow face seal design, shown in Fig. 5, has several significant differences from the one just described. By the manufacturer's specification, seal oil is required at a pressure sufficient to maintain 1.03–2.07 bar (15–30 psi) above process gas pressure at the bypass port. Also in this design, fresh oil is ducted through a series of annular passages past the process side face seal as it flows to the conventional atmospheric side smooth bore bushing and the bypass. Further significant differences include a completely continuous single carbon sealing face, a Teflon secondary seal assembly, and the use of 20 compression springs to seat the carbon against the collar.

Experimental Apparatus/Technique

Test Stands. The testing was conducted on two different test rigs. The main rig, shown in Fig. 2, simulated a typical beam style compressor seal arrangement. The drive train consisted of a 522 kW (700 hp) 3575 rpm electric motor, a clutch/brake unit to provide variable speed, and a 3.0 ratio speed-increasing gear-box. The drive train is shown in Fig. 8. The test rig rigid shaft was supported at each end by radial tilt pad journal bearings with a five-pad, double-acting, tilt pad thrust bearing on the free end. The rig housing, shown in Fig. 9, consisted of a one-piece forged casing capable of 138 bar (2000 psi) working pressure.

An oil schematic for the main test rig is shown in Fig. 7. Oil from the tank was pumped by two rotary pumps connected in parallel. One pump was rated 136 l/min (36 gpm) at 3.4 bar (50 psi) with 880 mm^2/s (4000 sus) viscosity oil. The other pump was rated 204 l/min (54 gpm) at 5.9 bar (85 psi) with 880 mm^2/s (4000 sus) viscosity oil. From the pumps, the oil traveled through two shell and tube heat exchangers used to

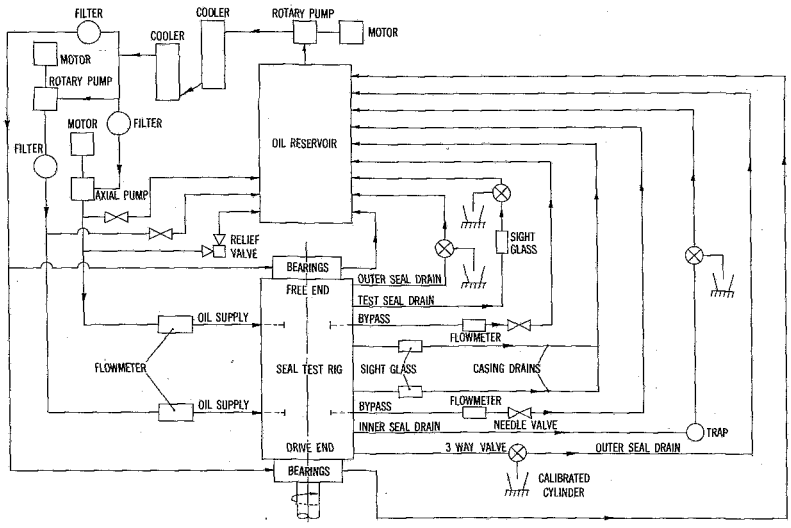

Fig. 7 Test rig oil system schematic

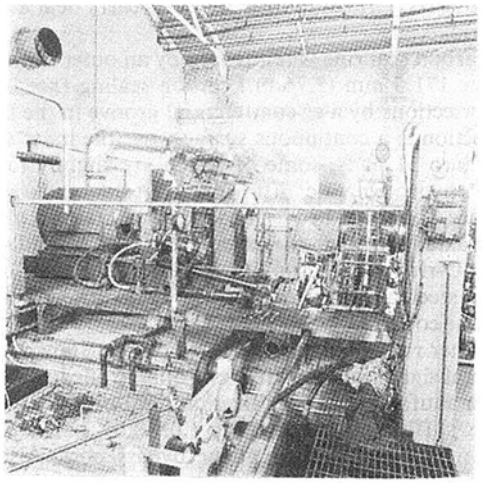

Fig. 8 Main test rig drive train

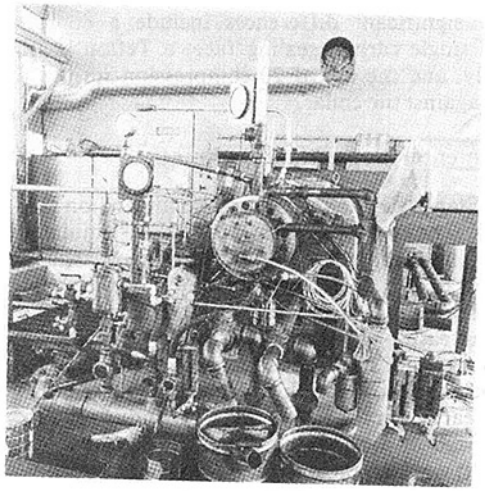

Fig. 9 End view of main test rig

maintain the desired supply temperature. From the heat exchangers, the oil split three ways. One portion went to a 10-micron filter and on to the test rig bearings at 2.1 bar (30 psig). A second portion of oil went to a rotary pump, rated 69 l/min (18.3 gpm) at 59 bar (1000 psi) with 13.6 mm^2/s (70 sus) viscosity oil, then through a 5-micron filter and on to the drive end bushing seals. The third portion of oil flowed through a 10-micron filter to a variable stroke, axial pump rated 117 l/min (31 pgm) at 221 bar (3200 psi) with 13.6 mm^2/s (70 sus) viscosity oil, and then to the primary test seal and free end outer bushing seal. All drains from the test rig were piped back to the oil tank.

The test oil was a 150 sus turbine oil. Significant oil characteristics are shown in Fig. 6.

All testing was performed with nitrogen gas. An external volume bottle was added to the system to provide gas loss measurement capability.

The gas was contained by two seals on the main test rig; the primary test seal and the inner smooth bore bushing seal on the drive end. The separate oil supply and bypass piping allowed the seals at either end of the rig to be controlled independently. This arrangement permitted the operating conditions to be held constant at one end of the rig, while varying conditions at the other end. System gas loss measurements provided relative values for the seals and determined trends of gas loss as conditions were varied.

The second test rig was an overhung unit with the test seal at the outboard location. The rig was driven by a 150-kW (200

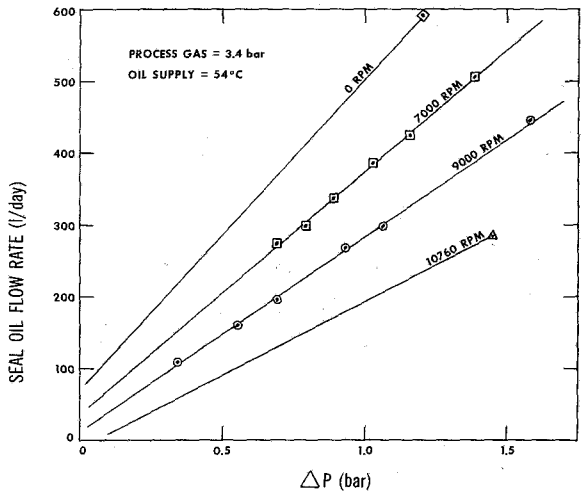

Fig. 10 Process side smooth bore cylindrical bushing seal oil flow as a function of shaft speed and differential pressure

hp) d-c motor, belt-connected to a jack shaft, with a 9.7 ratio speed-increasing gearbox. The unit was capable of variable speed operation up to 19,000 rpm. The shaft bearings consisted of radial tilt pad journal bearings near each end of the shaft and a double-acting tilt pad thrust bearing near the driven end. Due to the overhung configuration, significant thrust loading was developed. This loading was balanced by an oil cavity contained by bushing seals of different diameters. The thrust loading limited the operating gas pressure to 59 bar (850 psi). Independent oil systems supplied the test seal and the thrust balancing seals.

The gas was contained by only the test seal in the second test rig. Measured system gas loss was therefore attributed entirely to the test seal.

Operating Technique. After assembly, each seal was tested without rotation to insure proper alignment and secondary sealing. Proper assembly was verified if there was no measurable system gas loss and, for the face seals, no oil leakage. Static tests were conducted with gas pressures from 3.4 bar (50 psig) to 121 bar (1750 psi) and bypass oil to gas differential pressures, ΔP, from 0 bar (0 psi) to 2.4 bar (35 psi).

Once a test point was established (speed, gas pressure, ΔP, oil supply temperature, and bypass flow), three successive readings were taken to insure stabilized conditions. During the test, the casing drains inboard of the inner seal drains were monitored to insure no mixing of the inner seal oil flows.

Instrumentation/Measurement Technique. Temperatures, pressures, and flows were measured at the oil supply, oil bypass, inner seal drain, outer seal drain, and gas supply. Each of the above measurement locations was in the piping immediately outside of the casing. Various intermediate oil temperatures inside the casing were measured depending on the seal tested. Metal temperatures were measured in the babbitt of the smooth-bore bushing seals. Bearing pressures and temperatures were monitored as were horizontal, vertical, and axial shaft vibrations. Axial position and speed of the test rig shaft were also measured.

The gas pressure was measured with either a bourdon-type pressure gage or a digital pressure transducer depending on the pressure level. Other pressures of significance were determined with differential pressure gages referenced to gas pressure. All gages were periodically calibrated with a deadweight tester.

Temperatures were measured with type "T" (copper-constantan) thermocouples.

Flows were measured by several methods. Supply oil flows

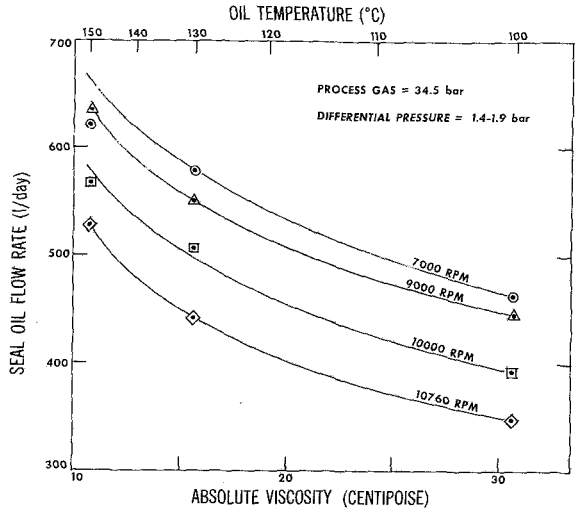

Fig. 11 Process side smooth bore cylindrical bushing seal oil flow as a function of oil absolute viscosity and oil supply temperature

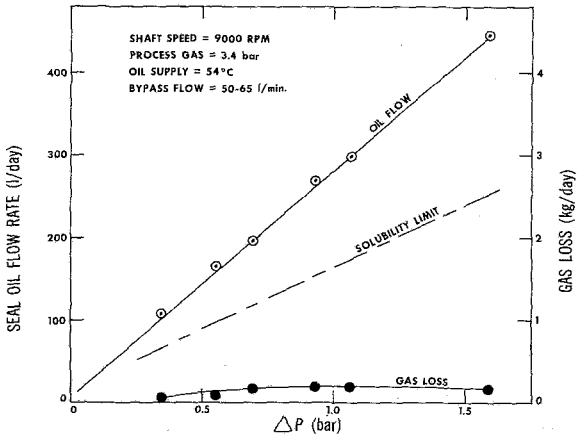

Fig. 12 Process side smooth-bore cylindrical bushing seal oil flow and gas loss as functions of differential pressure

and bypass oil flows were measured with turbine flowmeters that were calibrated with the test oil at operating conditions. Seal flows were determined by collecting the oil for a specified period of time (2–20 min). The oil weight or volume was measured and converted to a flow rate.

System gas loss was found by measuring the pressure decay of the gas volume, .01 m^3 (640 $in.^3$). The time for the gas pressure to drop 1–2 percent was measured and used with the pressure drop and temperature to calculate the amount of gas loss. The range of test times was 7 to 180 s. Several gas loss measurements were taken and averaged for each test point.

Test rig shaft speed was measured with a 30 tooth gear, magnetic pick-up, and digital counter. Axial vibration and position were sensed at the free end of the shaft, and horizontal and vertical shaft vibrations were sensed between the drive end journal bearing and the coupling hub using proximity probes.

Solubility of nitrogen in the test oil was determined with a degasser and a soap bubble gage. Inner seal oil flow was directed through a degasser where the oil flow rate and gas volume were determined. The degasser consisted of a 152-mm (6-in.)-dia pipe with 12 plates arranged to force the oil/gas mixture to flow over 6 of the plates. The gas could escape out the top of the degasser, while the clean oil was flowing out the end. The soap bubble gage consisted of a glass tube with the capability to form a soap bubble in the bottom of the tube. The gas drove the soap bubble up the calibrated tube. The

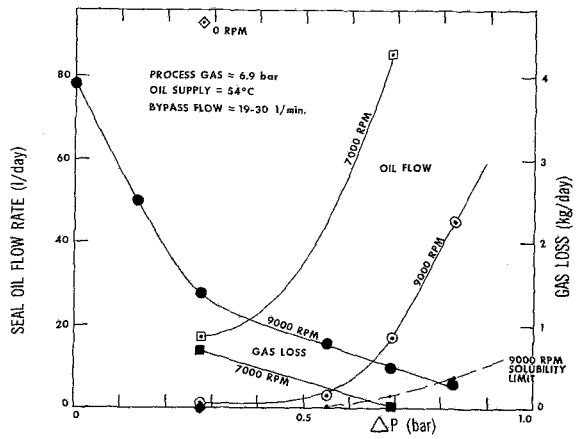

Fig. 13 Process side spiral-groove cylindrical bushing seal oil flow and gas loss as functions of shaft speed and differential pressure

time required for the soap bubble to move a specified distance was measured and used to calculate the gas flow. The oil flow was determined with a calibrated cylinder and a stopwatch.

Discussion of Results

The initial test plan was to determine the influence of operating conditions on the oil flow rates of various seal designs. Key variables were shaft speed, process gas pressure, ΔP, oil supply temperature, and bypass oil flow rate. The measured ΔP is representative of the differential pressure across the seal; the measured value is determined outside the test rig and includes a portion of the pressure drop across the seal cartridge. The seal cartridge pressure drop varied from 0.2–2.1 bar (3–30 psi), depending on the seal configuration and operating conditions. While determining the above oil flow characteristics, unexpected gas loss levels and trends were discovered.

Solubility of Gas in Oil. A small quantity of process gas loss is inherent in oil-buffered shaft seals due to the solubility of gas into the oil. Analysis of the seal oil degasser data yielded the following results

Shaft Speed, RPM	9000		
Gas Pressure, bar (PSI)	3.4 (50)		
Bypass Flow, l/min. (GPM)	64 (17)		
Oil Temperature, °C (°F)	54 (130)		
△P, bar (PSI)	1.6 (22.5)	1.1 (16)	0.9 (13)
Seal Flow, l/day (GPD)	452 (119)	317 (84)	262 (69)
Gas Loss, l/day (ft^3/day)	138 (4.9)	92 (3.2)	75 (2.6)
Solubility Constant, Q_{gv}/Q_o	.31	.29	.29

The measured solubility constant, Q_{gv}/Q_o, agrees very well with published solubility constants for nitrogen in oil of similar viscosity as the test oil [13, 14]. Per the reports, the solubility constant varies directly with pressure and increases slightly as temperature increases.

All testing was conducted with nitrogen as the test gas. Natural gas was not tested, but published results of tests on natural gas compressor seals conclude that there is very little difference between nitrogen and natural gas with respect to gas loss values [4]. However, a general ASTM standard suggests that the solubility constant of methane, the major

constituent in most natural gas mixtures, is about 65 percent higher than nitrogen [14].

Smooth-Bore Cylindrical Bushing Seal. The effect of shaft speed and ΔP on the seal oil flow rate of smooth-bore cylindrical bushing seals is shown in Fig. 10. Seal oil flow rate has a linear dependency on the ΔP and decreases with increasing rotor shaft speed.

The measured smooth-bore bushing seal oil flow rates vary inversely with the cube root of the absolute viscosity of the oil. For example, increasing seal oil supply temperature from 30°C (100°F) to 66°C (150°F) changes the absolute viscosity of the oil from 30.6 centipoise to 10.7 centipoise and results in an oil flow increase of $\sqrt[3]{30.6/10.7}$ or 42 percent. Figure 11 shows this variation of oil flow with oil viscosity and supply temperature for various speeds.

Results indicate that smooth-bore cylindrical bushing oil flow rates are independent of process gas pressure and bypass flow rate over the ranges tested. Process gas pressure was varied from 3.4 bar (50 psi) to 103 bar (1500 psi) and bypass flow was varied from 42 1/min (11 gpm) to 79 1/min (21 gpm).

The gas loss characteristic of the smooth-bore bushing seal is shown in Fig. 12. The measured gas loss is significantly below the level anticipated by solubility of the gas into the oil. The solubility limit was calculated from the oil flow and the measured solubility constant.

Spiral-Groove Cylindrical Bushing Seal. The influence of shaft speed and ΔP on the spiral-groove cylindrical bushing seal oil flow and gas loss is shown in Fig. 13. Like the smooth-bore bushing, oil flow decreases with increasing shaft speed. However, the relationship is much more dramatic for the spiral-groove bushing. The spiral-groove bushing oil flow varies exponentially with the ΔP. Figure 13 also shows that gas loss does not increase with increased oil flow. Therefore, gas loss cannot be entirely attributed to solubility. In reality, the gas loss increases as oil flow decreases, so that decreasing ΔP and increasing shaft speed cause the gas loss from the spiral groove bushing to increase.

The impact of process gas pressure on oil flow and gas loss is shown in Fig. 14. Oil flow is virtually independent of gas pressure, but gas loss is significantly affected.

Varying bypass flow rates between 19 1/min (5 gpm) and 57 1/min (15 gpm) has little effect on gas loss; however, test results show a linear relationship between process side seal oil flow rate and bypass flow rate.

Varying oil supply temperature between 38°C (100°F) and 66°C (150°F) has little impact on gas loss, but does influence oil flow. Increasing oil temperature increases the oil flow, but the trend is not the same as the cubic relationship found for the smooth-bore bushing.

Figures 15 and 16 show the effect of the spiral grooves on oil flow and gas loss. The only significant difference in the two seals tested was the three tapered spiral grooves covering two-thirds of the seal length towards the gas side. Figure 15 shows that the spiral grooves significantly reduce oil flow. Figure 16 shows the gas loss trends due to the spiral grooves. With process gas pressures above 6.9 bar (100 psi), the spiral grooves increase gas loss; with process gas pressures below 6.9 bar (100 psi) and ΔP's above 0.6 bar (9 psi), the spiral grooves have no effect on gas loss. The level of the gas loss is slightly above the expected solubility gas loss for the same bushing without spiral grooves. With ΔP's below 0.6 bar (9 psi), the spiral groove bushing gas loss increases significantly above its solubility gas loss level.

Further testing of the standard spiral groove bushing and two modified versions was conducted on the second test rig. One modification was the addition of a circumferential groove at the transition of the spiral grooves to the smooth bore portion of the seal. The other modification was to replace the 70 durometer O-ring secondary seal with a 50 durometer O-ring. Testing the standard spiral-groove bushing in the second test rig provides verification that the test rig does not influence the results. Testing at 34.5 bar (500 psi), comparable oil flow and gas loss rates were obtained in both

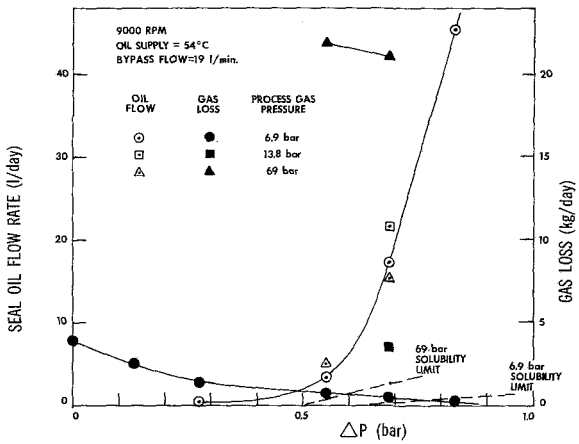

Fig. 14 Process side spiral-groove cylindrical bushing seal oil flow and gas loss as functions of process gas pressure and differential pressure

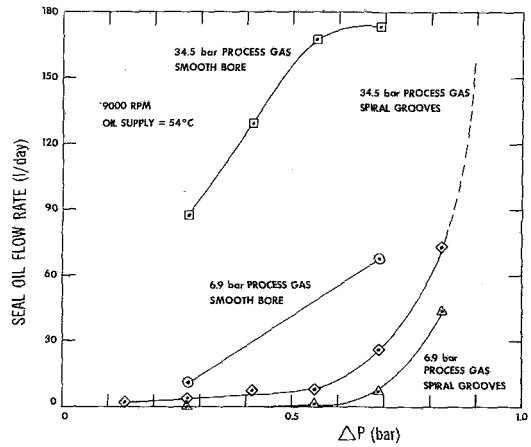

Fig. 15 Effect of spiral grooves on cylindrical bushing seal oil flow as a function of process gas pressure and differential pressure

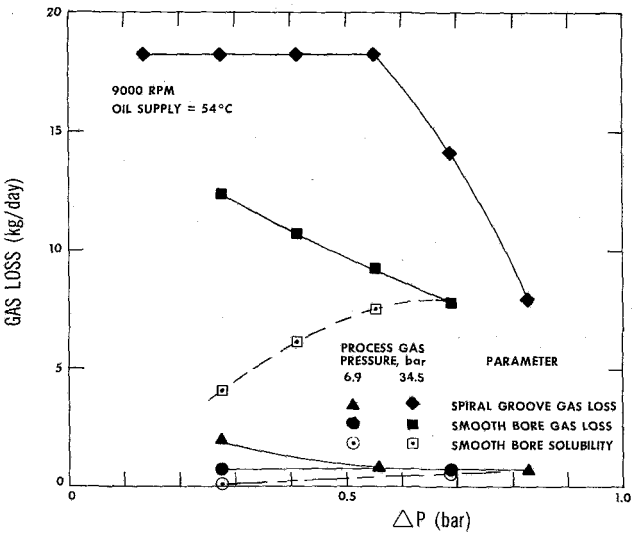

Fig. 16 Effect of spiral grooves on cylindrical bushing seal gas loss as a function of process gas pressure and differential pressure

rigs. At 6.9 bar (100 psi), the second rig obtained significantly lower oil flow and significantly higher gas loss than the main rig. Although the levels were different, the trends remained the same.

The circumferential groove causes a slight increase in oil flow and a slight decrease in gas loss, with no change in the trends. The gas loss trend remains contrary to solubility. Changing the O-ring from 70 durometer to 50 durometer causes a slight increase in both oil flow and gas loss with no change in trends.

Radial Inward-Flow Face Seal. The radial inward-flow face seal requires a higher differential pressure than the other types of seals, making it more complex to retrofit. Consequently, it was not part of the original test program. However, as the gas loss trends of the other types of low leakage seals became apparent, a limited evaluation of this widely used type of seal was conducted in the second test rig. The data from this seal provide a benchmark for comparison with the other seal designs. Test results are listed below.

Gas loss trends were not established, since the overall gas loss level was very small. Gas loss and oil flow rates appeared to be independent of shaft speed.

ΔP, bar (PSI)	2.4 (35)	
Oil Temperature, °C (°F)	54 (130)	
Gas Pressure, bar (PSI)	6.9 (100)	34.5 (500)
Oil Flow, l/day (GPD)		
@ 7000 RPM	--	4.7 (1.3)
@ 9000 RPM	5.7 (1.5)	6.8 (1.8)
@ 11000 RPM	--	4.5 (1.2)
Gas Loss, Kg/day (lb/day)	.12 (.27)	.46 (1.01)
Solubility, Kg/day (lb/day)	.06 (.13)	.24 (.52)

Radial Outward-Flow Face Seals. Two radial outward-flow face seal designs were tested. The first design tested is shown in Fig. 5. Oil flows for this seal were unstable and high. For example, at operating conditions of 10,760 rpm, 54°C (130°F) oil supply temperature, 6.9 bar (100 psi) process gas pressure, 57 l/min (15 gpm) bypass flow, and 1.0 bar (15 psi) ΔP, oil flow rates vary from 98 l/day (26 gpd) to 212 l/day (56 gpd). No reason for the unstable operation was found, so testing was stopped and the seal returned to the vendor. Investigations by the vendor resulted in modifications to the secondary seal but no further testing has been conducted.

The second design is shown in the left end of the test rig in Fig. 2. The variation of oil flow and gas loss as functions of shaft speed, and ΔP is shown in Fig. 17. More data scatter was experienced with the radial outward-flow face seal than with the other process side seals.

Contrary to the bushing seal trend, the oil flow of the radial outward-flow face seal increases with increasing speed. The gas loss level is near solubility expectations at high ΔP's, but deviates rapidly as ΔP decreases. The effect of process gas pressure is shown in Fig. 18. As in the other process side seals, oil flow is independent of the process gas pressure, but gas loss, on both a mass and volume basis, increases with increasing process gas pressure.

For an increase in oil supply temperature, the oil flow of the second design decreased. This trend is attributed to the influence of temperature on the hydrodynamic lift coefficient. The oil flow was also influenced directly by bypass flow rate.

A major concern with the second design is the high oil temperature immediately upstream of the face seal interface. The oil supply to the seal is forced through a small annulus. Typical temperatures at the inlet to the face seal are

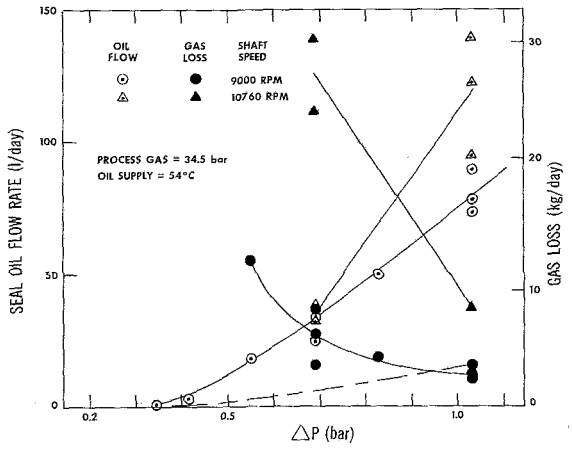

Fig. 17 Radial outward-flow face seal oil flow and gas loss as functions of shaft speed and differential pressure

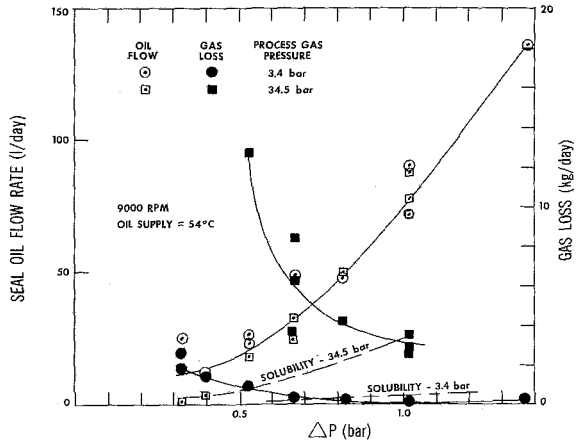

Fig. 18 Radial outward-flow face seal oil flow and gas loss as functions of process gas pressure and differential pressure

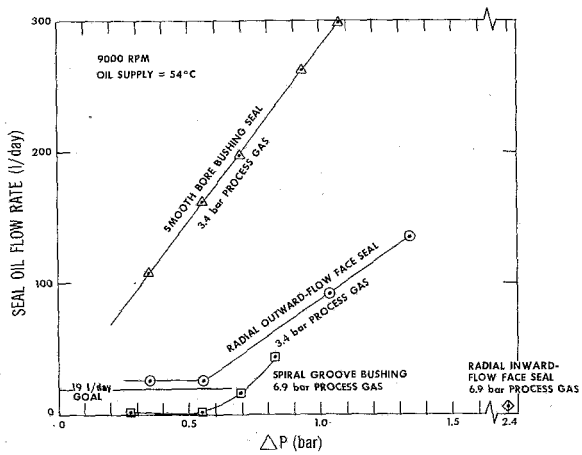

Fig. 19 Comparison of oil flow as a function of differential pressure for process side seal configurations

127–138°C (260–280°F). After only 185 hr of running, carbon deposits were found on the face seal ring and on the collar. A modification to enlarge the annulus for improved oil cooling has been conceived but not tested.

Conclusions

Seal Oil Flow Rates. Minimal seal oil flow is desirable where reclamation of contaminated drain oil is a cost prohibitive solution. Figure 19 compares the seal oil flow rate versus ΔP for the process side seals that were tested. The

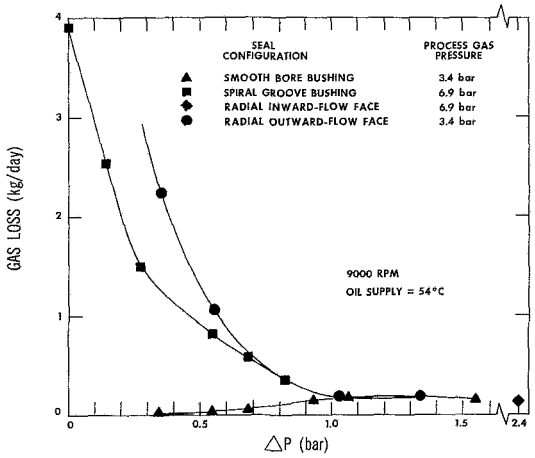

Fig. 20 Comparison of gas loss at low process gas pressure for process side seal configurations

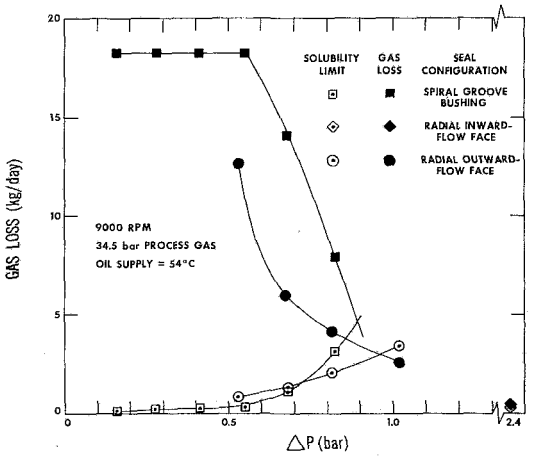

Fig. 21 Comparison of gas loss at 34.5 bar process gas pressure for process side seal configurations

comparison is made at 9000 rpm, which is a typical design speed for this size of seal, and at relatively low process gas pressures. Process side seal oil flow rates are virtually independent of process gas pressure but do vary with speed. As can be seen in Fig. 19, the process side seals with flow rates that meet the objective of 19 1/day (5 gpd) are the spiral groove bushing seal, operated with a ΔP of less than 0.70 bar (10 psi), and the radial inward-flow face seal. In fairness to the smooth bore bushing seal, the seal for which data are included herein had a relatively large diametral clearance of 0.137 mm (.0054 in.). Field experience with smooth bore bushing seals of this diameter shows that flow rates as low as 95 1/day (25 gpd) are achievable with clearances of .08–0.10 mm (.003–.004 in.), and a ΔP of about 0.4 bar (5.8 psi). The oil flow rate of the radial outward-flow face seal is only slightly above the 19 1/day (5 gpd) objective at 9000 rpm at ΔP's below 0.55 bar (8 psi). The conclusions drawn from Fig. 19 must be tempered by the gas loss behavior of each of the seals.

Gas Loss. The primary function of the process side seal is to contain the process gas within the compressor. Therefore, gas loss is a measure of seal deficiency. A comparison of gas loss versus ΔP for the various seals tested is shown in Figs. 20 and 21. Figure 20 compares the gas loss for process gas pressures of 3.4 bar (50 psi) and 6.9 bar (100 psi). Both the smooth-bore bushing seal and the radial inward-flow face seal have minimal gas loss, less than 0.2 kg/day (0.4 lb/day). With ΔP's above 1.03 bar (15 psi), the spiral-groove bushing seal and radial outward-flow face seal also have gas loss of less than 0.2 kg/day (0.4 lb/day), but as pointed out in Fig. 19, have oil flow rates considerably above 19 1/day (5 gpd).

Figure 21 compares the gas loss and solubility limits for the various seals at a process gas pressure of 34.5 bar (500 psi). Again, the radial inward-flow face seal has the minimum gas loss, with the spiral-groove bushing seal and the radial outward-flow face seal approaching the minimal gas loss level only at high ΔP's. No gas loss data were obtained for the smooth-bore bushing seal at low ΔP's and 34.5 bar (500 psi) gas pressure.

A small quantity of gas loss is inherent due to the solubility of gas into the oil. Gas loss attributable to solubility varies with the oil flow rate; however, of the seals tested, only the smooth-bore bushing seal has a gas loss trend that is consistent with solubility (increasing gas loss with increasing oil flow). Using the quantity of gas loss due to solubility as the allowable level of gas loss, the minimum oil flow rate and gas loss obtainable with each seal, along with the required ΔP, at 9000 rpm are:

PROCESS GAS = 3.4-6.9 bar (50-100 PSI)

Seal Type	Qo		Qg		△P	
	l/day	(GPD)	kg/day	(lb/day)	bar	(PSI)
Smooth bore bushing	95	(25)	0.2	(0.4)	0.35	(5.0)
Spiral groove bushing	34	(9)	0.3	(0.7)	0.79	(11.5)
Radial inward-flow face	6	(1.5)	0.12	(0.3)	2.4	(35)
Radial outward-flow face	41	(11)	0.3	(0.7)	0.75	(10.9)

PROCESS GAS = 34.5 bar (500 PSI)

Seal Type	Qo		Qg		△P	
	l/day	(GPD)	kg/day	(lb/day)	bar	(PSI)
Smooth bore bushing	--		--		--	
Spiral groove bushing	107	(28)	4.7	(10)	0.88	(12.8)
Radial inward-flow face	7	(1.8)	0.5	(1)	2.4	(35)
Radial outward-flow face	71	(19)	3.2	(7)	0.98	(14.2)

The tabulated smooth-bore bushing seal loss is the actual measured value, since the actual gas loss was always less than the solubility limit. The radial inward-flow face seal gas loss is also the actual measured value, which is twice its gas loss due to solubility level, but small with respect to the gas loss of the other seals.

The oil flow and gas loss of the spiral-groove bushing seal and radial outward-flow face seal are extremely sensitive to operating conditions. A small change in operating conditions for these seals will dramatically increase either oil flow or gas loss. The sensitivity of the radial inward-flow face seal to deviations in operating conditions was not determined.

Using the gas loss due to solubility as the acceptance criterion, the preceding tables show that only the radial inward-flow face seal satisfies the 19 1/day (5 gpd) objective. With this criterion, there is a stong probability that all of the gas loss is through the drain oil. If this is the case, it can be separated from the oil by some type of degassing process. If, however, the gas loss is greater than the solubility limit, then some gas is leaking across the seal into the bypass oil, as was confirmed during the testing program. When this situation occurs, there is little opportunity for the entrained gas to diffuse out of the oil, since normal seal oil reservoir retention times are as short as 8 min. [15]. Published test results [4] of a 368-mm (14.5-in.) oil-buffered shaft seal operating at 3600 rpm and 3.65 bar (53 psi) gas pressure reported measured gas loss of 1.4–2.5 kg/day (3–5.5 lb/day). The same report stated that the gas loss acceptance limit was 181 kg/day (400 lb/day). Compared to this limit, all of the seals tested perform very well.

In order to obtain another benchmark for evaluating the significance of the measured gas loss levels, North Seal oil degradation data [10] were considered. Cootes [10] reported

that new oil contained about .01 percent C_4–C_{16} content and that severely degraded oil contained 1.26 percent. The exact concentration where the oil becomes unacceptable was not reported, but for discussion purposes it is assumed herein that a 0.1 percent concentration of C_4–C_{16} constituents is all that can be tolerated. Cootes's process gas contained 2.65 percent of C_4–C_{16} by weight. Taking the spiral groove bushing data from Figs. 13 and 14 for a 0.7 bar (10 psi) ΔP resulting in 19 l/day (5 lb/day) oil flow, the gas loss values are 0.5 kg/day (1.1 lb/day) with 6.8 bar (100 psi) gas pressure, of which 0.2 kg/day (0.4 gpd) is from solubility. For a 378-L (100-gal) reservoir, it would take 36 days for the reservoir to be contaminated to a 0.1 percent concentration of C_4–C_{16} if the drain oil is decontaminated before return to the reservoir. When this same exercise is carried out for the 34.5 bar gas pressure, however, the contamination time drops all the way to 1 day. When it is considered that two of these seals are present in most compressors, the significance of this gas loss into the bypass oil becomes very apparent.

Seal Retrofit Capability. A major objective of the program was to identify a low flow seal that could be adapted to existing compressor systems with minimal change to the existing hardware. Many seal oil systems use a differential regulator that maintains a ΔP of 0.35–1.03 bar (5–15 psi) for smooth-bore bushing seals. In this range of ΔP's, the spiral-groove bushing seal and the radial outward-flow face seal appear to have limited acceptability because of comparatively high gas loss. The radial inward-flow face seal requires a minimum ΔP of 2.4 bar (35 psi). Therefore, a differential regulator change will be required to retrofit it into any smooth-bore bushing installation. In addition, many process compressors have seal oil systems that rely on an overhead tank instead of a differential regulator. Normally these tanks are mounted above the compressor at sufficient elevation to provide a ΔP of only 0.35–0.5 bar (5–7 psi). This differential pressure would not be adequate for any of the low flow seals tested, so that the seal oil system would require some modifications to operate with them.

With respect to retrofit of the shaft and surrounding seal housing, the spiral-groove bushing seal woud require no modifications. However, both face seals would need a shoulder to precisely locate the rotating collar along with sleeves, nut, and a locking system to permit assembly and maintain relative positioning of the carbon seal and the rotating collar. Refer to the various cross sections, Figs. 2–5, to see the various types of modifications required.

All of the process side seal designs are usable with a smooth-bore bushing on the atmospheric side of the double-seal arrangement.

Seal Life and Maintenance. The testing was not of sufficient duration to determine the service life of the various low flow seals. Extensive field operating experience with smooth-bore bushing seals shows that these seals have long service lives due to their minimal susceptibility to dirt, misalignment, and shaft vibration problems. With the exception of the Teflon coating on the seal housing, the design of the spiral-groove bushing seal is such that it should have a life expectancy similar to that of the smooth-bore bushing. Servicing of these seals is relatively simple when compared to face seals.

The face seals are expected to have shorter life than the bushing seals because of increased susceptibility to damage by dirt, misalignment, shaft axial motion, and shaft radial vibration [16]. The carbon seal must be flat within a few light bands. The axial position of the rotating collar relative to the carbon seal must be maintained typically within 2.5 mm (0.1 in.) and the flatness and squareness of the shaft shoulder that mates with the rotating collar must be within .0025 mm (.0001 in.). Face seal manufacturers usually hedge when quoting life estimates because of sensitivity to seal operating factors that are beyond their control. One to three years is often mentioned as typical life expectancy. Numerous parts are included in the face seal assembly and manufacturers typically recommend on-site replacement and factory repair of the entire assembly when servicing is necessary.

The smooth-bore bushing seal and some types of face seals are independent of shaft rotational direction. However, the spiral-groove bushing seal and the radial outward-flow face seal shown in Fig. 2 are dependent on rotational direction. For these types of seals, different seal rings are needed for each end of the compressor and care must be taken not to intermix them.

Seal Costs. The smooth-bore bushing seal is the simplest and least expensive of the seals. All of the other seals discussed herein (the spiral-groove bushing seal, and radial inward-flow face seal, and the radial outward-flow face seal) are roughly six times the OEM cost of a smooth-bore bushing seal assembly. The complexity of the other types of seals and the cost of the carbon ring for the face seals largely account for this cost differential. When field conversion from smooth-bore bushings to one of the other types is desired, the additional costs of seal oil system conversion must be considered.

All or some of the cost differential between smooth-bore bushing seals and the other types may be recoverable from the reduced cost of oil reclamation and replacement in installations where oil contamination or degradation occur.

Recommendations

For applications where exposed oil flow rates are not critical or where oil reclamation is a cost-effective alternative, the smooth-bore bushing seal represents the best selection. Low maintenance, simplicity, long life, and low cost are its major advantages. Certainly, in clean gas applications, there would be no strong incentive to consider other types of seals.

For applications with a process gas suction pressure of 6.9 bar (100 psi) or below, the spiral-groove bushing seal should reduce oil flow to 30–40 percent of the smooth bore bushing seal. This seal can be used at higher gas pressures than 6.9 bar (100 psi) if higher ΔP's are used to control gas leakage; however, this will likely result in oil flow rates that are 60–80 percent of the smooth-bore bushing. Despite the higher cost, there would appear to be a number of comparatively low-pressure applications where this seal would be preferred.

In situations where oil flow rate and gas loss must be minimized, the radial inward-flow face seal, in conjunction with a steel-babbitt atmospheric side bushing, may be the best selection. However, the increased maintenance, shorter service life, higher initial cost, and complexity of this seal should be carefully weighed against smooth-bore bushings accompanied by an oil reclamation process, to find the most cost-effective solution.

Based on the results of testing up to this point in time, the radial outward-flow face seal needs further development before it could be considered an acceptable seal for compressors requiring sealing surface speeds of 50 m/s (164 ft/s), or more.

While not studied as part of this test program, the dry gas face seal [17] is an interesting concept worthy of further study. The main attraction of this seal is that it totally eliminates the need for a seal oil system [18]. Although it would solve the oil contamination problems of oil-buffered seals, it has all the maintenance, life, and initial cost concerns of the other face seals. In addition, a small amount of process gas, typically 30–60 kg/day (66–132 lb/day) [17], must be vented off to a safe atmosphere when the seal is operating.

Acknowledgments

The authors would like to thank the management of Cooper Energy Services for permission to publish this paper and numerous fellow employees for their assistance and support. Particular thanks is extended to F. W. Fetters and C. Van-Winkle for their conscientious and meticulous testing efforts.

References

1 "Centrifugal Compressor Installation List," Cooper Energy Services.

2 "Dynamic Sealing: Theory and Practice," Koppers Company, Inc., Form 899, Sept. 1976, pp. 16–25.

3 Buchter, H. H., *Industrial Sealing Technology*, Wiley, 1979, pp. 124–125, 207–230, 382–383, 396–402.

4 Kaufman, H. N., and Raimondi, A. A., "Tests of Natural Gas Compressor Seals," *Lubrication Engineering*, Vol. 39, No. 5, May 1983, pp. 306–317.

5 Scheel, L. F., "New Ideas on Centrifugal Compressors," *Compressor Handbook*, Gulf Publishing Co., 1969, pp. 30–34.

6 *Shaft Seals*, Stein Seal Company.

7 Gartman, H., *DeLaval Engineering Handbook*, McGraw-Hill, 1970, pp. 6.80–6.83.

8 Williams, L., "Contamination of Compressor Seal Oil," Bowser Filtration, Ltd., Aug. 1982.

9 "Compressor Seal Oil Purification Plant," Bowser Filtration, Ltd.

10 Cootes, L., "Contamination of Centrifugal Process Gas Compressor Lube Oil and Seal Oil Systems by Hydrocarbon Condensate," ASME Paper No. 81-GT-182.

11 Simnett, A. D., "Problems Experienced During and After Installation of Gas Compression in UK Southern North Sea," ASME Paper No. 83-GT-21.

12 "Natural Gas Reinjection," Royal Lubricants Co., Inc., June 1983.

13 "Solibility of Nitrogen in Various Liquids," *Industrial and Engineering Chemistry*, Vol. 23, No. 5, May 1931.

14 "Estimation of Solubility of Gases in Petroleum Liquids," *ASTM Standard D-2779-69*.

15 *Lubrication, Shaft Sealing, and Control Oil Systems for Special-Purpose Applications*, American Petroleum Institute Standard 614, Sept. 1973, p. 4.

16 Abar, J. W., "Failures of Mechanical Face Seals," *Engineering Fluid Sealing*, Crane Packing Co., 1979, pp. 265–277.

17 Sedy, J., "Improved Performance of Film-Riding Gas Seals Through Enhancement of Hydrodynamic Effects," ASLE Paper No. 78-LC-38-1.

18 Sloan, M., Martin, J., and Morales, P., "Natural Gas Transmision: NOVA's Energy Conservation Program," *Energy Processing/Canada*, Jan.–Feb. 1983.

K. Jimboh
Manager,
Aero-Engine and Space
Development Group

H. Aono
Deputy Manager,
Research and Development Department.

T. Chikata
Group Leader,
Research and Development Department.

Y. Hagiwara
Engineer,
Research and Development Department.

K. Nakasu
Researcher,
Research Institute.

T. Hoshino
Researcher,
Research Institute.

Ishikawajima-Harima Heavy
Industries, Co., Ltd.,
Tokyo, Japan

Thrust Load Measurement on Aero-Engine Bearing

Aero-engine bearings operate in an extraordinarily high speed range (high DN number) and severe conditions. It is especially necessary to measure and adjust the bearing thrust load in the engine development phase, but it is very difficult to measure the thrust load accurately, because bearings and bearing housings are subjected to elevated temperature and oil environment. Open space permitted for installation of thrust measurement transducers is small and limited around the bearing housing. We tried to measure the thrust load by applying "Unit Cells," which are installed between bearing and bearing housing. "Unit Cells" which have been specially designed to measure the bearing thrust load are very small and temperature-compensated load cells. We have been successful in measuring the actual thrust load using the above "Unit Cells," both in the steady-state and transient condition. Repeatability and hysteresis of the data have been satisfactory. We have established the effect of seal clearance on the thrust load by the measurement. We also have obtained the dynamic characteristics of the thrust load versus rotor speed in low bypass fan engines. Procedure and obtained data are presented in detail.

Introduction

The current aero-engine is required to be light in weight, with high performance and low-level fuel consumption. In an aero-engine's development phase, the structural integrity program associated with the bearings has been very important and is becoming even more important for high-performance engines of today. Aero-engine bearings operate in high DN number (more than 10^6) because aero-engine rotors are lightweight and operate in a high speed range. Therefore, the consideration of the bearing life is one of the problems associated with engine development, and it is especially necessary to adjust the bearing thrust load in engine development. But it is not easy to measure the bearing thrust load accurately, because bearing and bearing housings are subjected to elevated temperature and oil environment. Open space permitted for installation of any transducers is small and limited around the bearing housing.

In the early phase, several methods have been investigated in our laboratory. These are, for example:

- Thrust-ring method: Measure the bending strain on the thrust-ring installed in the bearing support.
- Modified bearing support method: Measure the bending strain on the modified bearing support.

However, the bearing thrust load was never measured to our satisfaction using the foregoing methods. We thought that the reasons were the following:

- The strain output versus thrust load was not sufficiently large.
- The strain drift due to elevated temperature was considerably larger than the strain to be measured.
- The static instability condition in which the load transducers were supported between bearing and support structure at more than three contact points was not desirable for thrust load measurement.

Therefore, the following new approach has been investigated and evaluated.

Measurement Approach. To make the measurement of bearing thrust load on a low bypass fan engine as shown in Fig. 1, "Unit Cells," which are very small and temperature-compensated load cells, have been specially designed. "Unit Cells" are required to have a capability by which the thrust

Contributed by the Gas Turbine Division of THE AMERICAN SOCIETY OF MECHANICAL ENGINEERS and presented at the 29th International Gas Turbine Conference and Exhibit, Amsterdam, The Netherlands, June 4–7, 1984. Manuscript received at ASME Headquarters December 18, 1983. Paper No. 84-GT-10.

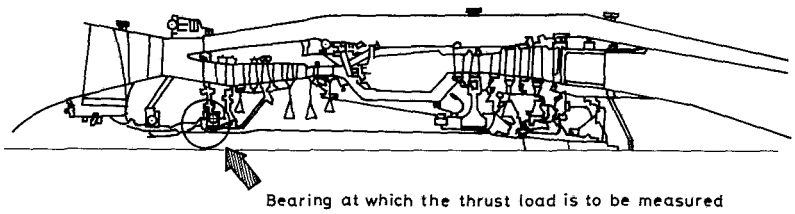

Fig. 1 Typical assembly of low bypass fan engine

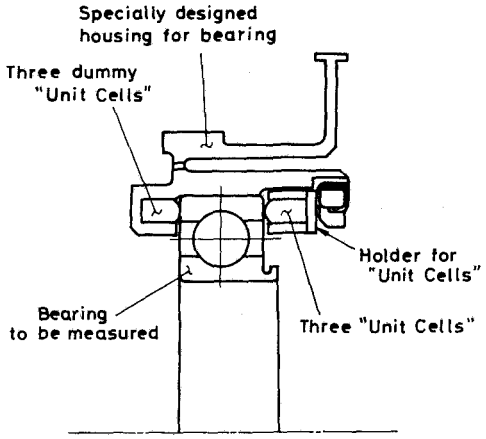

Fig. 2 Schematic installation of bearing and "unit cells"

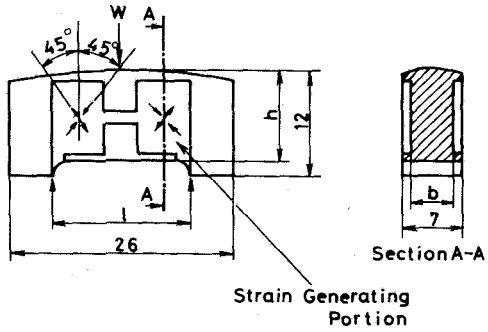

Fig. 3 Structure of "unit cells"

load can be measured up to 9.8 KN under approximately 433 K ambient temperature. Six "Unit Cells" are installed between bearing and bearing housing as shown in Fig. 2. Three "Unit Cells" which are installed rearward of the bearing are used for acquiring the data. Another three dummy "Unit Cells," which are installed forward of the bearing, are used for adjusting the same stiffness as the active "Unit Cells." To obtain the data of the thrust load, the following calibration tests are necessary before commencement of the engine testing: (*i*) static load test; (*ii*) temperature characteristics test. Relationships between load and output strain of "Unit Cells" are determined by the static load test. Thermal output of "Unit Cells" are also determined by the temperature characteristics test. As the result of these calibration tests, the bearing thrust load can be measured in an operating engine and these "Unit Cells" which were subjected to the calibration test were assembled to the engine. The data were expected to be obtained both in the steady-state and transient condition.

Description of "Unit Cells"

Basic Design. Because open space permitted for installation of thrust measurement transducers is small and limited around the bearing housing, transducers are required to be small at all costs. Moreover, the following considerations must be taken into account for design of "Unit Cells":

(*i*) To possess sufficient structural strength against the estimated load.

(*ii*) To obtain sufficient strain sensitivity for the expected load.

(*iii*) To possess sufficient durability in oil and elevated temperature environment.

Consequently, we have considered that the outer dimensions 26 mm^W × 12 mm^H × 7 mm^t of the "Unit Cell" as shown in Fig. 3 are satisfactory for installation of the "Unit Cells" between bearing and bearing housing.

Structural Design. It is predicted that the estimated maximum thrust load will be approximately 9.8 KN and that the estimated pre-torque load will be approximately 19.6 KN. Accordingly, we considered that the maximum capability of the transducer is approximately 29.4 KN. It is essential that the thrust load of the bearing should be measured by three transducers on three support points in order to maintain the support condition of static stability. Therefore, it is sufficient that one transducer, that is a "Unit Cell," should have a capability of maximum 9.8 KN load. The basic structure of the "Unit Cell" is illustrated in Fig. 3 (W = 9.8 KN; l = 16 mm; b = 5 mm; h = 10 mm; $E = 2.1 \times 10^5 N/mm^2$; σy = more than 883 MPa). The material of "Unit Cells" is nickel-chromium-molybdenum steel. From this model,

$$(\sigma b)\max = \frac{3Wl}{2bh^2} \text{ and } \tau\max = \frac{3W}{4bh} \tag{1}$$

$$\sigma\max \leqq \sqrt{(\sigma b)^2\max + 3(\tau\max)^2} = 539\ \text{MPa} \tag{2}$$

we can find and confirm that σmax is sufficiently lower than σy of material.

Nomenclature

b = thickness of "Unit Cell"
E = Young's modulus
F = thrust load
Fu = load on "Unit Cells" due to thrust load
G = elastic coefficient of shear
h = height of "Unit Cell"
l = length of "Unit Cell"
Po = preload by nut tightening
t max = maximum temperature
W = load
ϵf = strain at rated output
ϵs = strain of strain-generating portion on "Unit Cell"
ϵt = maximum output strain of "Unit Cell"
$\epsilon t(\max)$ = maximum thermal output of "Unit Cell" at temperature t(max)
σmax = maximum equivalent stress
$\sigma(b)\max$ = maximum bending stress
σy = yield strength
τmax = maximum shear stress

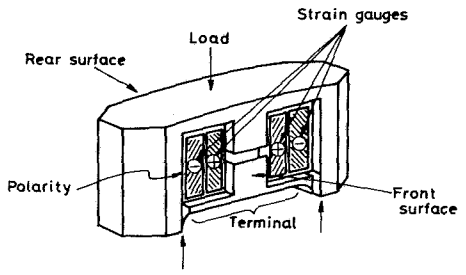

Fig. 4 Strain gage application on "unit cell"

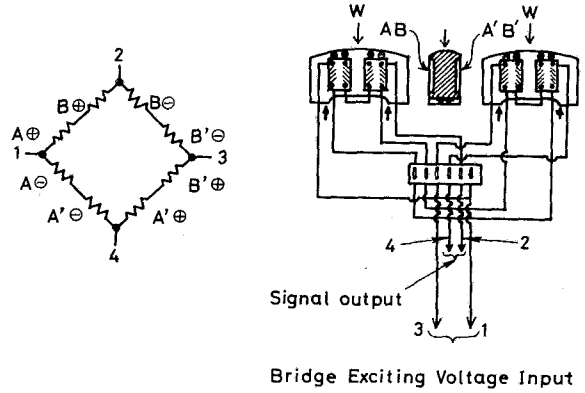

Fig. 5 Bridge circuit

Strain Characteristics. Strain gages are positioned at the strain-generating portion of the "Unit Cell" in order to detect the strain whose direction is 45 deg to the loading direction. A fourfold increase of sensitivity is expected due to the constitution of the bridge circuit with each strain gage. In this bridge circuit, the maximum strain output is predicted to be approximately 3660 micro-strain under 9.8 KN load as following.

$$\epsilon S = \frac{\tau \max}{2G} \tag{3}$$

$$\epsilon T = 4\epsilon S = \frac{2\tau \max}{G} \tag{4}$$

At $W = 9.8$ KN from equation (1) and $G = 80.4$ KN/mm^2

$$\epsilon T = 3659 \times 10^{-6} \tag{5}$$

we have concluded that the expected strain value is sufficient to acquire the data and is within an acceptable limit for strain gages.

Durability. The most important point for the "Unit Cells" design is to prevent the bearing from failure even if the strain gage, adhesive or any coating material is pealed off. Then the following countermeasures are considered:

(*i*) The area to which the strain gages are to be attached must be a lower level (concave) surface than the surface of the "Unit Cells."

(*ii*) Heat-resisting and oil-resisting resin is to be poured into the concave area after being strain-gaged.

(*iii*) Stainless film is to be placed over the "Unit Cells" surface to prevent the resin from dropping out.

(*iv*) The clearance between the "Unit Cells" and the holder is to be less than 0.05 mm, in order to prevent the bearing from failure even if the stainless film is pealed off.

(*v*) Wiring slots for strain gaging and terminal are to be arranged.

The maximum oil temperature at engine testing is estimated to be 433 K. A heat-resisting strain gage, no-creep adhesive, and high performance coating are selected for "Unit Cells" application.

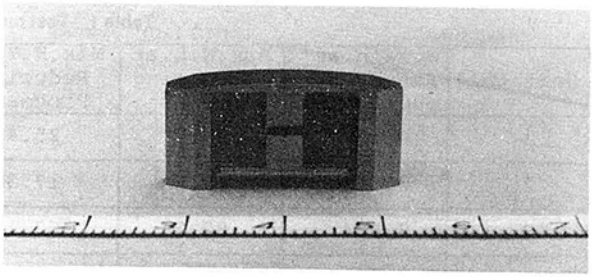

Fig. 6 Overview of "unit cell"

Effect of Surface Roughness. The concave area of the strain-generating portion as shown in Fig. 4 has been manufactured by using the electric discharge machine (EDM), because the conventional machining process is not applicable. It has been found that the roughness of the surface machined by EDM is approximately 20 μmp-p, but a surface roughness of approximately 2 μmp-p is required for strain gaging. Then, after EDM, electrolytic grinding and paper grinding are applied for the concave area of the "Unit Cells."

Bridge Circuit Between Strain Gages. Eight strain gages were attached on each "Unit Cell" as shown in Fig. 4. That is, four strain gages were attached on each side of the surface (front and rear), and two strain gages in each concave area. In order to take an average of the output from each strain gage, the bridge circuit as shown in Fig. 5 was formed among strain gages. As the resistance of each strain gage is approximately 350 Ω, the resistance of the above bridge is approximately 700 Ω. We think that 700 Ω resistance is desirable for signal conditioning, because the signal to noise ratio will be improved and error will be reduced. When we measure the bearing thrust load in the engine, three "Unit Cells" are going to be applied on each bearing. Therefore, a combination of three "Unit Cells" is also to be considered. The combination/distribution switch box is accommodated for signal acquisition. Not only the individual output of each "Unit Cell," but also the combination output of three "Unit Cells" is obtained. We think that this combination output is efficient for measuring the thrust load. A photograph of strain gaged "Unit Cells" is shown in Fig. 6.

Calibration Test for "Unit Cells"

Calibration test for the "Unit Cells" is composed of the following static load test and the temperature characteristics tests:

Static Load Test. The tensile/compressive machine is applied for this test and the load range to be tested is up to 9.8 KN. The static load test was carried out on the following two cases: (*i*) test for individual "Unit Cell"; (*ii*) test for combination of three "Unit Cells" (combination cell). The characteristics of "Unit Cells" are evaluated based on the following equation and Fig. 7.

$$\text{Nonlinearity (N.L)} = \frac{Ln(\max)}{\epsilon f} \times 100(\%.\text{R.O}) \tag{6}$$

$$\text{Hysteresis (H.Y)} = \frac{Hy(\max)}{\epsilon f} \times 100(\%.\text{R.O}) \tag{7}$$

$$\text{Repeatability (R.E)} = \frac{\text{Re}(\max)}{\epsilon f} \times 100(\%.\text{R.O}) \tag{8}$$

$$\text{Temperature Influence (T.I)} = \frac{\epsilon t(\max)/\epsilon f}{t_{\max}} \times 100(\%.\text{R.O/K}) \tag{9}$$

Table 1 Test result of individual "Unit Cells"

Unit Cell	Strain at Rated Output (9.8KN)	Max.N.L at Increasing Process	Max.H.Y at Reducing Process	N.L.	H.Y	R.E	T.I	Accuracy
1	3,587	16.3	25.4	0.45	0.71	0.81	4.1×10^{-3}	2.11
2	3,592	15.6	17.3	0.43	0.48	0.79	-3.0×10^{-3}	1.64
3	3,684	82.2	-67.1	2.23	-1.82	1.53	-4.44×10^{-3}	3.78
Average	3,621	-	-	-	-	-	-	2.51

Table 2 Test result of Combination Cell

Load Point	Strain at Rated Output (9.8KN)	Max.N.L at Increasing Process	Max.H.Y at Reducing Process	N.L	H.Y	R.E	T.I	Accuracy
O	1,200	3.7	10.0	0.31	0.83	0.16	1.1×10^{-3}	1.02
A	1,210	3.7	13.8	0.31	1.14	0.28	"	1.31
H	1,190	4.1	10.0	0.34	0.84	0.19	"	1.04
I	1,207	3.2	11.9	0.27	0.99	0.17	"	1.15
N	1,194	3.8	10.3	0.32	0.86	0.19	"	1.05
C	1,210	3.3	11.6	0.27	0.96	1.31	"	1.72
J	1,209	-4.7	12.5	-0.36	1.03	0.40	"	1.26
G	1,195	3.4	11.4	0.28	0.95	0.48	"	1.20
M	1,197	8.7	8.7	0.73	0.73	0.77	"	1.38

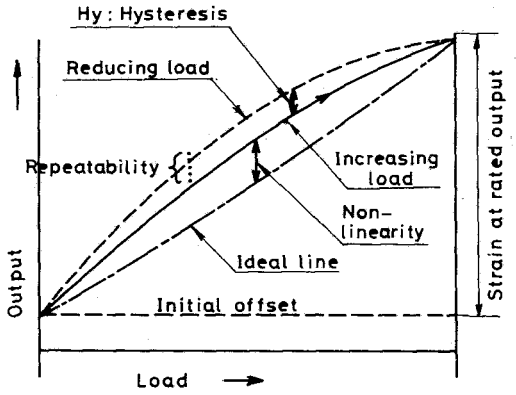

Fig. 7 Curve for calibration

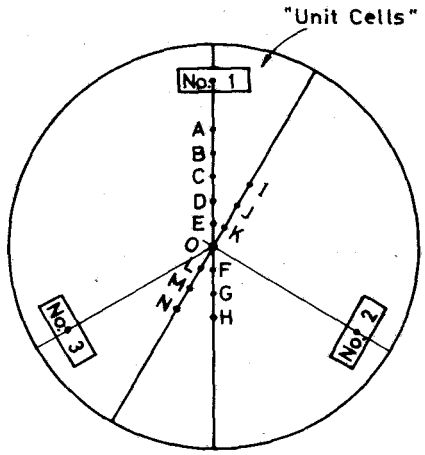

Fig. 8 Various loading points at offset loading test

Accuracy

$$=\sqrt{(\text{N.L})^2+(\text{H.Y})^2+(\text{R.E})^2+(\text{T.I}\times t\max)^2} \quad (10)$$

R.O; Rated ouput

Test for Individual "Unit Cell." Three "Unit Cells," which are to be installed between the bearing and bearing housing at engine testing, were subjected to the static load test, and the test result is shown in Table 1. Table 1 indicates that the average value of the rated strain output is fairly consistent with the theoretical value as shown in equation (5), and that the average error is approximately 2.5 percent. We think that the above test result is reasonable and the "Unit Cell" is applicable for measuring the thrust load.

Test for Combination Cell. The Combination Cell is a load-cell in which three "Unit Cells" are accommodated and which should be installed on the bearing housing. The Combination Cell was subjected to the offset loading test in which the load was put on at various axial loading points as shown in Fig. 8, and the test result is shown in Table 2. Table 2 indicates that the accuracy is independent of the position of the loading point and that the error is less than approximately 1.7 percent. We think that the foregoing test result of the Combination Cell is better than expected, and that the Combination Cell is an appropriate tool to measure the bearing thrust. A photograph of the bearing subassembly installed in the Combination Cell is shown in Fig. 9.

Temperature Characteristics Test. An electric oven is applied for this test and the temperature range to be tested is from room temperature to 433 K. The temperature drift at zero load point was obtained on Combination Cell as shown in Fig. 10. According to Fig. 10, it is found that the maximum thermal output at up to 433 K on Combination Cell is -18 micro-strain, and the temperature influence of zero load point

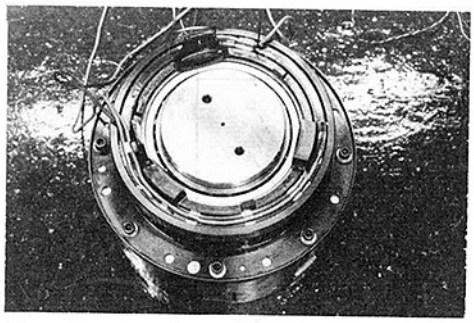

Fig. 9 View of bearing subassembly accommodating "unit cells"

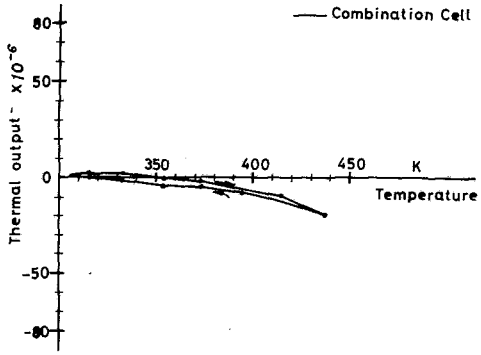

Fig. 10 Temperature characteristics of "unit cell"

is 1.1×10^{-3} percent R.O/K. We think that the temperature influence of strain output on the Combination Cell is negligible and that the Combination Cell is suitable for measuring the thrust load at elevated temperature.

Test Results

In engine testing, three "Unit Cells" and three dummy "Unit Cells" were installed as shown in Fig. 2, and the pretorque load was loaded on the all "Unit Cells." Then, the load which is to be worked on the "Unit Cells" is half the thrust load to be measured (as shown in equations (11) and (12) and Fig. 11). From the balance of force

$$F + (Po - Fu) = Po + Fu \tag{11}$$

$$Fu = \frac{F}{2} \tag{12}$$

The bearing subassembly as shown in Fig. 2 was subjected to the static load test again and the relation between the thrust load and output strain of the "Unit Cells" was obtained as shown in Fig. 12. Accordingly, it was confirmed that the relation between the thrust load and output strain is fairly consistent with the result of the static load test in the Combination Cell. Therefore, it was also confirmed that the effect of preload on the "Unit Cells" is negligible. The temperature of the holder of the "Unit Cells" and the bearing outer-race was measured in engine testing, too, in order to confirm that the temperature of "Unit Cells" should be kept within the limited temperature, that is, less than 433 K. In measuring the actual bearing thrust load of the running engine, the steady-state data and the transient data were acquired and evaluated, respectively.

Steady-State Data. The output strain signal from the "Unit Cells" is amplified and displayed by the digital static strain meter in the process of steady-state data acquisition. The result of measured data during engine running test is shown in Fig. 13. In the process of data acquisition in Fig. 13, the engine was operated at several specified rotating speeds and its revolution was maintained constant at each speed.

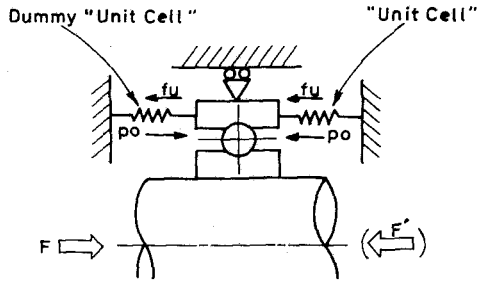

Fig. 11 Model of thrust load measurement

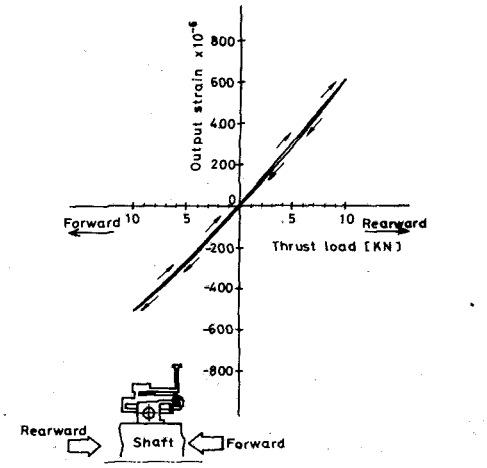

Fig. 12 Characteristics between thrust load and output strain from combination cell installed in the bearing subassembly

According to Fig. 13, it is found that the variation of the measured thrust load versus engine revolution is reasonable and that the temperature of the "Unit Cells" holder and bearing outer-race is less than 433 K. It is also found that the thrust load at 20,200 rpm is 8.04 KN, and its direction is forward on engine. Therefore, we think that the measured thrust load as shown in Fig. 13 is satisfactory and reliable data. Though the thrust load of 8.04 KN at 20,200 rpm is tolerably consistent with the predicted value in engine initial design phase, the 8.04 KN thrust load is large in value considering the bearing life. To make the life of the bearing longer, it is necessary to reduce the thrust load on the bearing. Then, two steps of modification in the seal clearance and bleed hole size were carried out as shown in Fig. 14, and the thrust load on the bearing was measured, respectively.

- Test No. 1: Original design
- Test No. 2: Two kinds of seal clearance reduced
- Test No. 3: Bleed hole size increased and another seal clearance reduced

The data of the measured thrust load for each test case as shown in Fig. 15 indicate that the variation of the measured thrust load versus engine revolution has a qualitatively similar tendency in each test case and that the thrust load has been reduced due to each of the above modifications. Consequently, the thrust load on the bearing could be adjusted to 1.96 KN at 21,000 rpm (corrected speed).

Transient Data. The output strain signal from the "Unit Cells" is amplified and recorded by the dynamic signal conditioner and X-Y recorder. The results of the measured data in Tests No. 1 and 3 are shown in Figs. 16 and 17, respectively. In the process of data acquisition, shown in Figs. 16 and 17, the engine was operated under the condition of sudden acceleration and sudden deceleration. According to Figs. 16 and 17, it is found that the thrust load versus engine

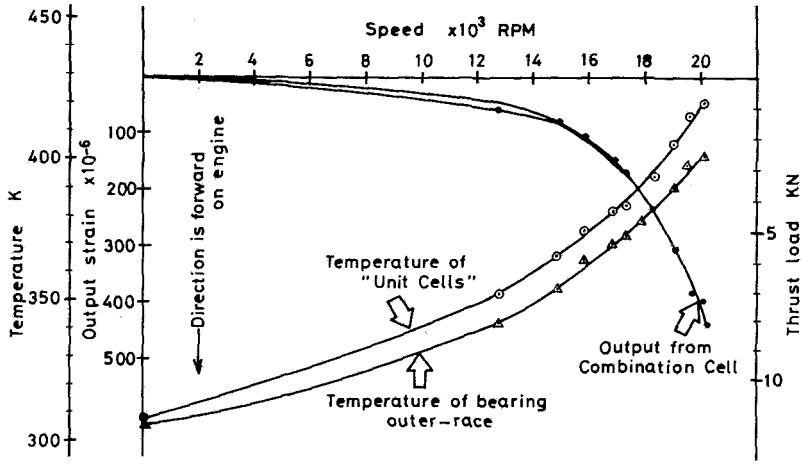

Fig. 13 Measured data during engine running test at steady state

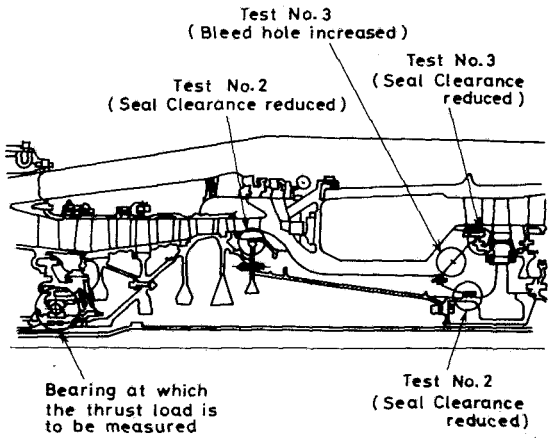

Fig. 14 Modifications for reducing bearing thrust load

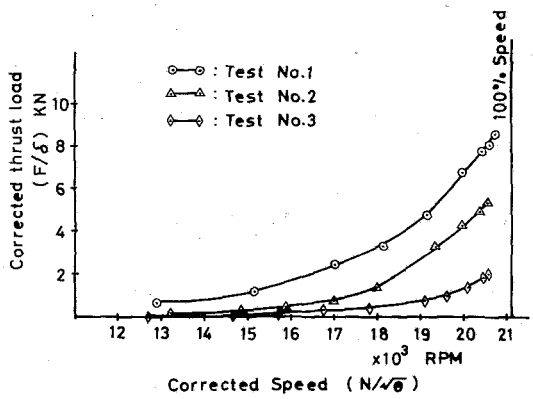

Fig. 15 Measured thrust load for three test cases

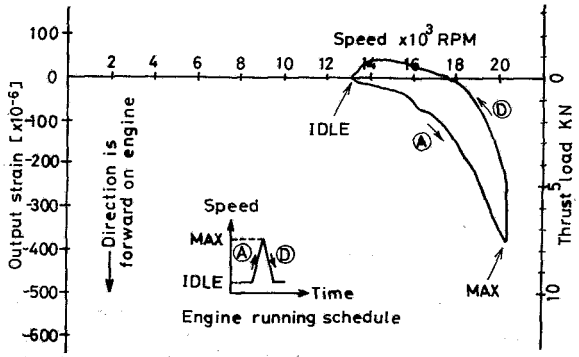

Fig. 16 Measured thrust load at sudden acceleration and deceleration in Test no. 1

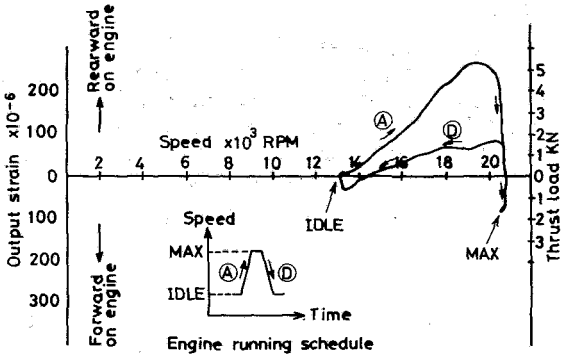

Fig. 17 Measured thrust load at sudden acceleration and deceleration in Test no. 3

revolution indicates the hysteresis characteristics and that the value of the thrust load at maximum revolution is fairly consistent with steady-state data. It is especially interesting that the hysteresis characteristics under Test No. 1 is an inversion of the hysteresis characteristics under Test No. 3 between the process of sudden acceleraton and deceleration. We think that the hysteresis discrepancy between the data of original design (Test No. 1) and data of the modified one (Test No. 3) depends on the dynamic characteristics of the secondary air system.

Concluding Remarks

By means of "Unit Cells," which are very small and specially designed load cells, we have been successful in measuring the actual thrust load during engine testing at steady-state and transient condition. Based on the measured thrust load, we have proved the effect of several modifications which aimed at reduction of the bearing thrust load, and we have reduced the bearing thrust load practically. Also, we have obtained the dynamic characteristics of the thrust load versus rotor speed during the sudden acceleration and deceleration of a low bypass fan engine.

References

1 Merritt, U. V., "Direct Measurement of Bearing Thrust Loads Using Strain Gages," AiResearch Manufacturing Company of Arizona, Workshop, 1978 SESA Spring Meeting.

2 Nicholls, D. W., "Applications of Strain Gages in Gas Turbine Testing," Garrett Corporation AiResearch Manufacturing Division, Western Regional Strain Gage Committee, 1972 SESA Spring Meeting.

J. C. MacBain
Aero Propulsion Laboratory
(AFWAL/POTA),
Wright Patterson AFB, Ohio 45433

R. E. Kielb
Structural & Mechanical Technology
Division,
NASA Lewis Research Center,
Cleveland, Ohio 44135

A. W. Leissa
Department of Engineering Mechanics,
Ohio State University,
Columbus, Ohio 43210

Vibrations of Twisted Cantilevered Plates—Experimental Investigation

The experimental portion of a joint government/industry/university research study on the vibrational characteristics of twisted cantilevered plates is presented. The overall purpose of the research study was to assess the capabilities and limitations of existing analytical methods in predicting the vibratory characteristics of twisted plates. Thirty cantilevered plates were precision machined at the Air Force's Aero Propulsion Laboratory. These plates, having five different degrees of twist, two thicknesses, and three aspect ratios representative of turbine engine blade geometries, were tested for their vibration mode shapes and frequencies. The resulting nondimensional frequencies and selected mode shapes are presented as a function of plate tip twist. The trends of the plate natural frequencies as a function of the governing geometric parameters are discussed. The effect of support compliance on the plate natural frequency and its impact on numerically modeling twisted plates is also presented.

Introduction

An in-depth knowledge of the resonant modes and frequencies of turbomachinery blading is essential in order to ensure long-life structurally sound blades. Blade failures due to high cycle fatigue resulting from resonant vibrations can be quite costly, both in terms of safety and maintenance in military and civilian turbine engines. Accurate analytical, numerical, and experimental methods for analyzing the vibratory characteristics of blading are essential to avoid destructive resonant conditions. Towards this end, a joint government/industry/university research effort was carried out to assess the accuracy of state-of-the-art finite element methods, lumped parameter (beam) models, and shell models in computing the natural frequencies and mode shapes of turbomachinery blading.

Numerical results for the resonant frequencies and mode shapes of twisted blades have been available for more than four decades by means of one-dimensional (beam) analysis. As blade designs evolved, having lower aspect ratios, it became necessary to develop two- and three-dimensional analytical models and associated computer programs to analyze the resulting platelike vibrational characteristics. Most of these programs are based upon finite elements and some have been available for more than a decade.

In spite of long and intensive development of these analytical tools, considerable differences exist in some of the numerical results, especially when significant pretwist and low aspect ratio are involved. The joint research effort was initiated to address these problems. The work consisted of numerically computing the mode shapes and natural frequencies of a series of twisted cantilever plates using the best available one-dimensional beam analyses, two- and three-dimensional finite element codes, and shell analysis codes and comparing the results to accurate experimental results and with each other. To concentrate on the most significant aspects of the problem, the initial part of the study was limited to a series of thirty nonrotating twisted cantilever plates having rectangular cross sections. Each plate had a given degree of twist, aspect ratio, and thickness as described below in detail. The geometric parameters involved span a range typical of today's turbomachinery blading.

A total of sixteen government, industry, and university participants carried out the numerical analysis of the plates. Because of the comprehensiveness of the study and the vast amount of data resulting from it, the present paper will address only the experimental portion of the twisted plate analysis. An in-depth comparison of the numerical results and a summary of both the experimental and analytical results will be addressed in two later papers [1, 2].

Mechanical and Material Properties of the Twisted Plate

Thirty cantilevered plates were machined from 7075-T6 cold drawn aluminum bar stock. The bar stock was from a single lot and, in its unmachined form, was a long cylindrical section having a 2.25-in. (5.72-cm) dia. The 2.25-in. (5.72-cm) bar was first machined on a lathe into cylinders having a 2.00 in. (5.08 cm) length by 2.25-in. (5.72-cm)-dia base interfacing with a 2.00-in. (5.08-cm)-dia cylinder of length 2.00 in. (5.08 cm), 4.00 in. (10.16 cm) or 6.00 in. (15.24 cm). The 2.00-in.-dia cylinders were then machined on a programmable milling machine to generate the twisted plates. The coordinates for the machining operation were generated using equations [1–3]. The coordinates, x, y, and z are in the direction of the plate span, chord, and depth, respectively, and are shown in Fig. 1.

Contributed by the Gas Turbine Division of THE AMERICAN SOCIETY OF MECHANICAL ENGINEERS and presented at the 29th International Gas Turbine Conference and Exhibit, Amsterdam, The Netherlands, June 4–7, 1984. Manuscript received at ASME Headquarters January 6, 1984. Paper No. 84-GT-96.

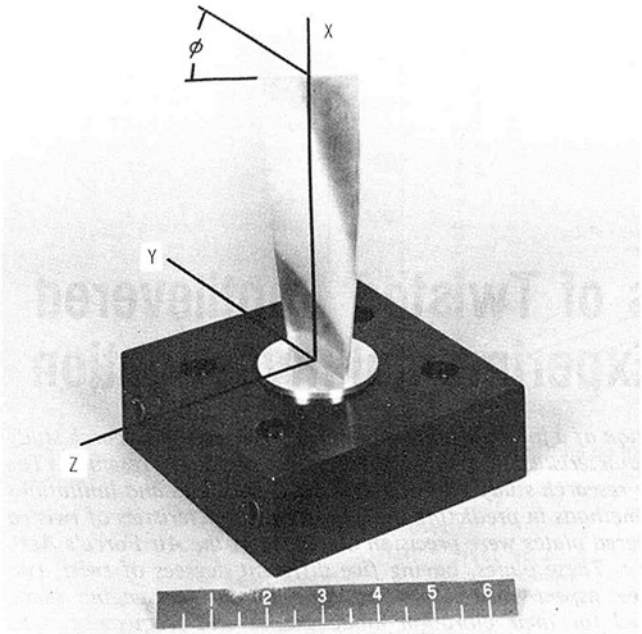

Fig. 1 Twisted cantilevered plate in holding fixture (a/b = 3, b/h = 20, ϕ = 60 deg)

$$x_i = \left(i - \frac{1}{2}\right)\Delta \tag{1}$$

$$y_R = \frac{b}{2} + c = -y_L \tag{2}$$

$$Z_{L,R} = \mp\left(\frac{b}{2} + c\right)\text{Tan}\,\phi_i + \left(r + \frac{h}{2}\right)\frac{1}{\cos\phi_i} \tag{3}$$

$$i = 1,2,3 \ldots n$$

where:

Δ = width of cut
n = a/Δ, number of cuts
ϕ_i = $(x_i/a)\,\phi$, ϕ-tip twist
c = arbitrary distance to make $y_{L,R}$ constant
r = radius of end mill
a = plate length
b = plate width
h = plate thickness
L,R = subscripts denoting initial and final position of chordwise cut, respectively.

The x, y, z coordinates were put on paper tape for use in the milling operation. Based on equations [1–3], it can be seen that each cross section of the twisted plate in the y–z-plane forms a rectangle having a width, b, and a height, h.

The thirty plates were machined so as to cover a representative spectrum of geometric parameters relevant to turbomachinery blading. The geometric parameters covered were:

Aspect ratio (a/b) = 1, 2, 3
Tip twist (ϕ) = 0, 15, 30, 45, and 60 deg
Thickness ratio (b/h) = 5, 20

The width, b, was held constant at 2.00 in., so that the physical length, a, of the specimens was 2, 4, or 6 in. in order to achieve the desired aspect ratio. Further, 15 plates were machined to a nominal thickness of 0.100 in. (.254 cm) and the remaining 15 to a nominal thickness of 0.400 in. (1.016 cm) in order to achieve the thickness ratios of 20 and 5, respectively. One of the finished plates is shown in Fig. 1 (a/b = 3, b/h = 20, ϕ = 60 deg). The finished nominal length and width of the plates were accurate to ±.001 in. It is noted, however, that the narrow sides of the plates in the spanwise (z) direction were not machined flat but, rather, were left having the curvature of the original 2.00-in.-dia cylinder. This contributed, at most, an increase in the plate mass of 1.3 percent in the worst case (h = .400 in.) over one that had flat sides and is thus considered to be negligible. The resulting normal thickness of each of the finished plates varied slightly from the nominal thickness of 0.100 in. and 0.400 in. The average thickness, h, for each of the specimens based upon micrometer measurements (accurate to ±0.0001 in.) is given in Table 1.

Table 1 Average plate thickness, h (in.)

Aspect Ratio	Nominal h (in)	Tip Twist, ϕ 0°	15°	30°	45°	60°
1	.100	.102	.100	.106	.103	.104
	.400	.401	.404	.406	.407	.409
2	.100	.104	.104	.104	.102	.102
	.400	.403	.403	.407	.400	.398
3	.100	.100	.107	.108	.104	.106
	.400	.402	.399	.403	.404	.404

The mass density of the 7075-T6 aluminum was computed by weighing a block of the material on a balance scale. The block measured 4.005 in. × 1.005 in. (±.002 in.). Its mass was measured to be 368.8 gm (±0.05 gm). This yields a mass density of 2.61×10^{-4} lbm/in.^{3}, accurate to within ±0.7 percent.

The modulus of elasticity of 7075-T6 aluminum can vary appreciably from one lot to another. For example, under static loading, 7075-T6510 extruded aluminum typically has a modulus of elasticity measured at 10.48×10^6 psi in the longitudinal direction under tensile loading and 10.71×10^6 psi in the same direction under compressive loading [3]. Hence a specific measurement of the modulus of elasticity of 7075-T6 aluminum used in these tests was called for.

The measurement for the modulus of elasticity was carried out at M.I.T.'s Department of Aeronautics and Astronautics by Professor E. F. Crawley, using a unique test apparatus for measuring the fundamental frequency and modal damping of free-free beams [4]. Two specimens of the 7075-T6 aluminum were sent to M.I.T. for testing. The specimens were long, slender beams measuring 12.00 in. × 0.952 in. × 0.102 in. Using the M.I.T. apparatus, the fundamental frequency of the specimens were measured. Knowing the nondimensional frequency for a free-free beam to be

$$\lambda = \omega\sqrt{\frac{\rho A a^4}{EI}} = 22.3734 \tag{4}$$

and the dimensions and mass density of the beam, equation (4) could be used to compute the modulus of elasticity, E. The use of simple beam theory in this calculation is justified since the length-to-depth ratio (a/h) is 117.6 and the length-to-width ratio (a/b) is 12.6. Further, the value of λ = 22.3734, based on simple beam theory is an upper bound on the "actual" nondimensional value. Hence, solving for E

provides a lower bound on the modulus of elasticity. The resulting value for E was computed to be 10.34×10^6 psi ($\pm .5$ percent). This value is based on a free-free beam fundamental frequency of 144.87 Hz (accurate to 4.5 significant digits). The principal advantage of this type of test for the modulus of elasticity is that boundary conditions, and the difficulties encountered in defining their fixity, do not play a role in the test.

The final material property to be defined is Poisson's ratio, ν. Its value was taken from [5] as $\nu = .3$.

The material properties for the 7075-T6 aluminum specimens are summarized in Table 2.

An estimate of the error introduced in computing the nondimensional frequency, λ, based upon the accuracies of the properties given in Table 2 can be gained as follows. The nondimensional frequency is

$$\lambda = \omega a^2 \sqrt{\frac{12\rho(1-\nu^2)}{Eh^2}} \tag{5}$$

In equation (5), let the terms in the numerator (a and ρ) have some positive error and those in the denominator (E and h) have some negative error. Thus equation (5) becomes

$$\lambda = \omega a^2 (1+e_1)^2 \sqrt{\frac{12\rho(1+e_2)(1-\nu^2)}{E(1-e_3)h^2(1-e_4)^2}}$$

or

$$\lambda = \omega a^2 \left[\frac{12\rho(1-\nu^2)}{Eh^2}\right]^{1/2} \cdot \left[\frac{(1+e_1)^4(1+e_2)}{(1-e_3)(1-e_4)^2}\right]^{1/2} \tag{6}$$

Define the error term Er as

$$Er = \left[\frac{(1+e_1)^4(1+e_2)}{(1-e_3)(1-e_4)^2}\right]^{1/2} \tag{7}$$

The worst case would be a plate having $a = 2$ in. and $h = .1$ in., i.e., errors e_1, and e_4 will have their greatest effect. Thus from Table 2

$$\begin{aligned} e_1 &= \frac{.001}{2} = .0005 \quad \text{(length)} \\ e_2 &= .007 \quad \text{(density)} \\ e_3 &= .005 \quad \text{(modulus)} \\ e_4 &= \frac{.001}{.1} = .01 \quad \text{(thickness)} \end{aligned} \tag{8}$$

Thus equation (7) becomes

$$Er = \left[\frac{(1.0005)^4(1.007)}{(.995)(.99)^2}\right]^{1/2} = 1.017 \tag{9}$$

We see that, at most, a 1.7 percent error in frequency will be incurred based upon the material property and geometric tolerances.

Experimental Test Setup, Procedure and Results

The thirty twisted plates were tested at the Aero Propulsion Laboratory's Turbo Structures Research Laboratory (TSRL) using holographic interferometry. The application of holographic interferometry to study vibrating objects is an ideal method of experimentally determining the object's resonant modes and frequencies. It is particularly useful for vibration analysis because the object under study is not physically contacted, can be of any shape, and the final result consists of a full-field picture of the vibratory object's displacement. For a more in-depth treatment of the technique, the reader is referred to the text by Collier et al. [6].

To carry out the vibration survey on each specimen, the cylindrical base of the twisted plate was first clamped in a holding fixture (see Fig. 1). The holding fixture consisted of two steel blocks (6 in. × 4 in. × 1.75 in.) each having a half-cylindrical hole, slightly undersized relative to the twisted plate base, machined from one of its long sides. The two blocks were clamped around the base of the twisted plate and drawn together by two 3/8-16 bolts tightened to 150 in.-lb. The holding fixture was then bolted to a 1-ton vibration isolation table using four 1/4-20 bolts (125 in.-lb torque). The twisted plate was excited to resonance using either a siren or piezoelectric crystal attached to the holding fixture. The choice of exciter was dependent upon the amount of energy needed to excite a given mode shape. Typically, the crystal was used to excite the higher modes of vibration.

Table 2 Material properties of twisted plates

Mass density, $\rho = 2.61 \times 10^{-4}$ lbm/in.^{3} ($\pm .7$ percent)
Modulus of elasticity, $E = 10.34 \times 10^6$ psi ($\pm .5$ percent)
Poisson's ratio, $\nu = 0.3$
Dimensional tolerances, ± 0.001 in.

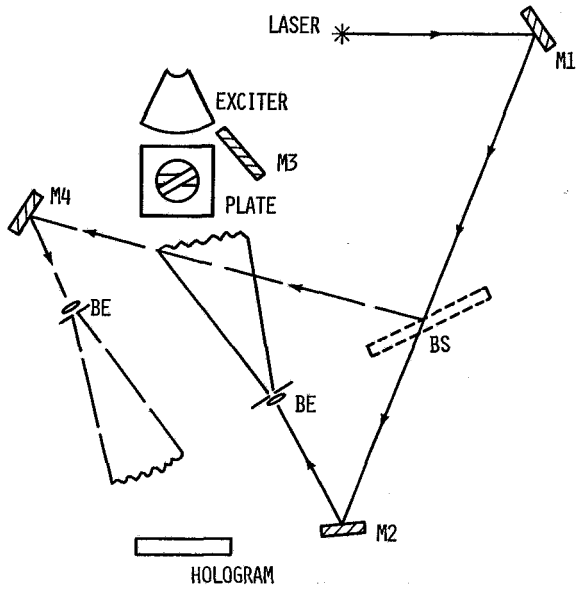

Fig. 2 Experimental setup for carrying out holographic vibration tests: M1, M2, M3, M4—mirrors; BE—beam expander; BS—beam splitter

A schematic of the experimental set-up is shown in Fig. 2. This is a typical off-axis holographic arrangement. The laser used for the tests was a 2-W Argon-ion (Spectra-Physics 166-09). One item that is different from the usual experimental setup is mirror M3. Mirror M3 is not used to direct the laser beam in the test set-up but, rather, is used to view the side of the twisted plate, a view that is approximately perpendicular to the front view of the plate. Hence, in the presentation of experimental results given below, the reader will see two views of each mode shape. The left-hand view is the plate displacement normal to the viewer. The right-hand mode shape in the same photograph is the displacement of the plate in a plane parallel to the hologram plane, i.e., displacement orthogonal to the left-hand photograph. In this way, the "edgewise" modes or modes in the plate's stiff direction could be observed. The extensional modes, however, were not detected by this set-up. These modes involve stretching along the symmetry axis in the spanwise direction. The first ten to twelve resonant modes and frequencies were experimentally determined for each of the twisted plates. In the case of the plates having an aspect ratio of 1 and thickness ratio of 5, only the first six modes of vibration were able to be excited. In order to minimize "observer error" in recording the resonant frequencies, at least two test runs were made by different technicians on each plate. The repeatability of the fixture

Table 3 Nondimensional frequency as a function of tip twist (a/b = 3, b/h = 20)

a/b=3, b/h=20 (6 in. x 2 in. x 0.1 in. plates)

MODE			TIP TWIST, ϕ (DEGREES)				
	Name	m/n	0	15	30	45	60
1	1B	0/0	3.31	3.29	3.28	3.31	3.22
2	1T	1/0	19.53	19.64	23.48	28.20	32.22
3	2B	0/1	20.71	20.64	18.00	15.97	14.07
4	1E	--	58.2	57.7	57.9	64.7	73.3
5	3B	0/2	58.46	51.52	46.03	47.22	47.59
6	2T	1/1	62.28	64.02	71.47	82.57	93.85
7	3T	1/2	113.2	114.5	123.2	136.4	150.9
8	4B	0/3	114.9	112.5	112.1	108.8	107.9
9	4T	1/3	176.5	175.9	184.0	194.7	201.7
10	5B	0/4	188.0	183.5	183.4	178.5	175.7
11	1C	2/0	206.4	200.6	202.9	200.4	201.8

Table 4 Nondimensional frequency as a function of tip twist (a/b = 3, b/h = 5)

a/b=3, b/h=5 (6 in. x 2 in. x 0.4 in. plates)

MODE			TIP TWIST, ϕ (DEGREES)				
	Name	m/n	0	15	30	45	60
1	1B	0/0	3.21	3.19	3.20	3.18	3.21
2	1T	1/0	18.39	18.42	18.63	18.86	19.28
3	2B	0/1	19.88	19.63	21.15	21.82	22.47
4	3B	0/2	53.89	52.25	50.47	47.37	44.96
5	2T	1/1	56.97	57.00	57.55	58.10	58.92
6	2E*	--	62.35	60.56	61.16	62.88	65.67
7	3T	1/2	100.4	99.91	100.9	100.3	102.0
8	4B	0/3	101.8	105.8	99.22	97.53	93.54
9	4T	1/3	148.0	152.0	150.4	150.1	150.5
10	1C	2/0	--	183.1	--	--	--

*1E mode not observed

Table 5 Nondimensional frequency as a function of tip twist (a/b = 2, b/h = 20)

a/b=2, b/h=20 (4 in. x 2 in. x 0.1 in. plates)

MODE			TIP TWIST, ϕ (DEGREES)				
	Name	m/n	0	15	30	45	60
1	1B	0/0	3.44	3.28	3.33	3.40	3.23
2	1T	1/0	13.87	15.02	23.96	19.58	28.69
3	2B	0/1	20.70	19.50	16.16	18.59	13.74
4	2T	1/1	44.73	46.52	65.41	56.45	75.02
5	1E	--	50.44	57.41	63.14	62.04	63.20
6	3B	0/2	57.68	51.53	48.47	51.40	44.70
7	3T	1/2	86.32	86.46	102.97	97.24	110.75
8	1C	2/0	90.16	887.21	90.66	93.86	87.06
9	4B	0/3	113.0	109.9	110.1	114.7	103.5
10	--	2/1	121.8	118.2	125.2	126.7	128.2
11	4T	1/3	142.5	140.7	152.0	151.3	154.0
12	--	2/2	168.1	163.8	172.1	173.2	175.1

Table 6 Nondimensional frequency as a function of tip twist (a/b = 2, b/h = 5)

a/b=2, b/h=5 (4 in. x 2 in. x 0.4 in. plates)

MODE			TIP TWIST, ϕ (DEGREES)				
	Name	m/n	0	15	30	45	60
1	1B	0/0	3.10	3.13	3.13	3.09	3.08
2	1E	--	9.44	10.92	9.99	10.27	9.37
3	1T	1/0	12.53	12.72	12.94	13.21	13.67
4	2B	0/1	18.63	19.09	19.22	20.15	20.07
5	2E	--	35.55	38.02	35.77	36.64	38.71
6	2T	1/1	39.54	40.00	40.26	40.60	41.27
7	3B	0/2	48.17	49.69	48.33	50.72	47.47
8	3T	1/2	--	72.22	--	--	--

clamping conditions was also checked. The resonant frequencies were found to be repeatable to within 0.5 percent. In addition to recording the resonant frequencies, the mode shapes were also recorded for all plates having 0 and 60 deg twist. The resulting frequencies and some of the modes are given below. The reader is referred to [7] for the complete set of photographs of the modes for the flat and 60 deg twisted plates.

Tables 3–8 give the nondimensional frequencies for the experimentally determined modes for each of the twisted plate specimens. The plate modes are denoted in terms of their commonly known names, such as "2B" for second bending, "3T" for third torsion, or "1C" for first chordwise bending. Modes which are predominately edgewise bending are identified as 1E, 2E, etc. The modes are also denoted in terms of the classical plate nomenclature, m/n. "m" refers to the number of nodal lines across the plate width or chord and "n" refers to the number of nodal lines along the plate length or span, not counting the nodal line at the fixed base of the plate. Each table presents the nondimensional frequencies of a set of twisted plates having a given aspect ratio (a/b) and thickness ratio (b/h) for the five cases of tip twist (0, 15, 30, 45, and 60 deg). Modes are arranged in order of their frequencies for the untwisted ($\phi = 0$ deg) plate.

Figures 3–8 present the nondimensional frequencies from Tables 3–8 in graphical format as a function of tip twist. Some general trends can be seen from a look at the tables and

Table 7 Nondimensional frequency as a function of tip twist ($a/b = 1$, $b/h = 20$)

a/b=1, b/h=20 (2 in. x 2 in. x .1 in. plates)

MODE		TIP TWIST, ϕ (DEGREES)				
Name	m/n	0	15	30	45	60
1 1B	0/0	3.32	3.05	3.13	2.96	2.84
2 1T	1/0	7.80	9.39	13.09	17.09	20.15
3 2B	0/1	19.85	17.97	16.90	14.51	12.36
4 1C	2/0	26.07	24.28	25.26	25.47	25.47
5 2T	1/1	28.37	27.94	31.27	34.50	36.96
6 1E	--	36.63	38.94	39.16	38.24	39.48
7 --	2/1	49.71	47.45	49.94	54.91	56.93
8 3B	0/2	56.84	53.01	54.13	48.39	46.73
9 --	3/0	59.3	60.7			
10 --	1/2	64.7	58.4			

Table 8 Nondimensional frequency as a function of tip twist ($a/b = 1$, $b/h = 5$)

a/b=1, b/h=5 (2 in. x 2 in. x .4 in. plates)

MODE		TIP TWIST, ϕ (DEGREES)				
Name	m/n	0	15	30	45	60
1 1B	0/0	2.93	2.85	2.81	2.76	2.59
2 1E	--	4.06	5.48	6.03	6.91	8.81
3 1T	1/0	6.75	7.00	6.89	7.22	7.40
4 2B	0/1	13.87	13.00	13.14	13.84	12.41
5 2T	1/1	21.49	--	--	--	--
6 1C	2/0	22.23	21.83	21.16	20.92	--

corresponding curves. With increasing twist, for thinner plates ($b/h = 20$):

1 Torsional frequencies show a marked increase.

2 Flapwise bending frequencies decrease; for the fundamental frequency (i.e., first flapwise bending, 1B) the decrease becomes more significant as the aspect ratio (a/b) decreases.

3 Edgewise bending frequencies increase; the increase becomes less significant as the aspect ratio decreases.

4 Chordwise bending frequencies are not significantly affected.

For thicker plates ($b/h = 5$) the aforementioned effects are typically less strongly present. Figures 9–11 show the family of mode shapes excited for three plate specimens having (*a*) $a/b = 3$, $b/h = 20$, $\phi = 60$ deg; (*b*) $a/b = 1$, $b/h = 20$, $\phi = 0$ deg; and (*c*) $a/b = 1$, $b/h = 20$, $\phi = 60$ deg. Recall that the "mirror" image on the right-hand side of each photograph shows the edgewise displacement of the plate. This will only be of interest, of course, when the plate has some degree of twist to it. The photographs of the modes were taken from time-average holograms. The fringes in the photographs represent a contour map of the plate's displacement normal to the viewer. The whitest fringes are node lines.

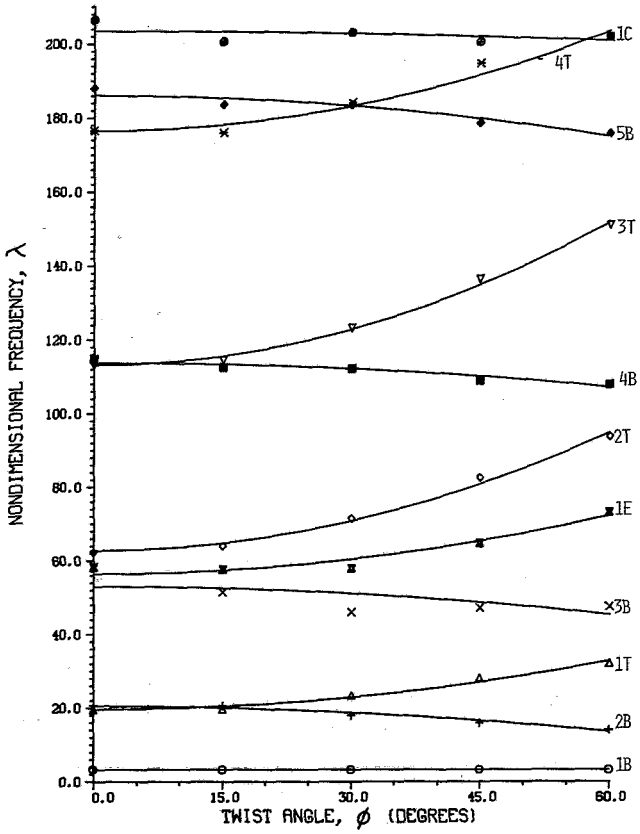

Fig. 3 Experimental nondimensional frequency as a function of tip twist ($a/b = 3$, $b/h = 20$)

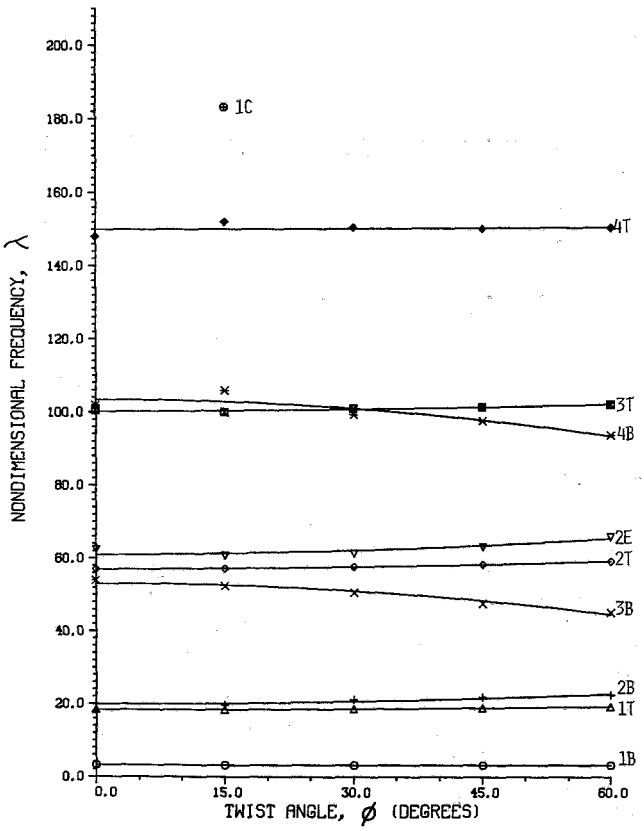

Fig. 4 Experimental nondimensional frequency as a function of tip twist ($a/b = 3$, $b/h = 5$)

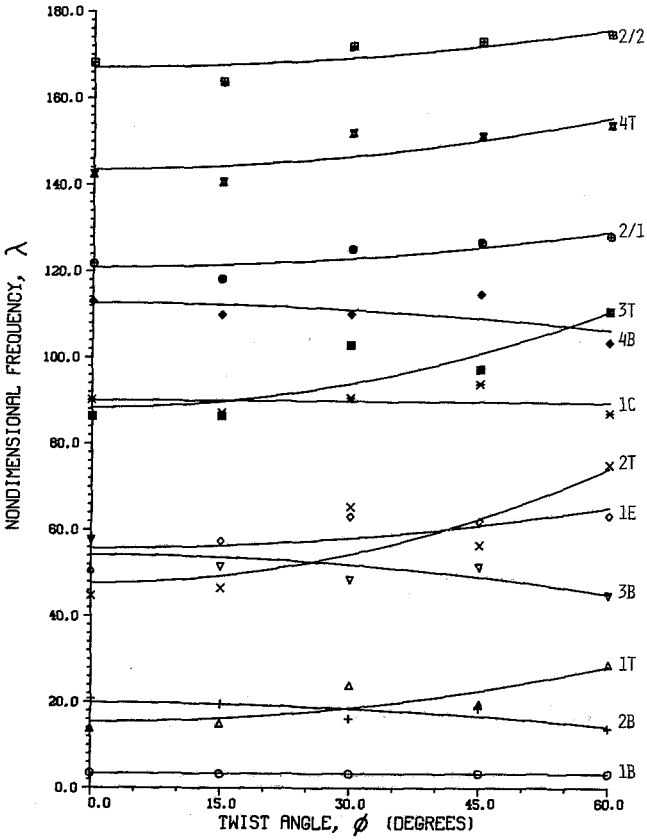

Fig. 5 Experimental nondimensional frequency as a function of tip twist ($a/b = 2, b/h = 20$)

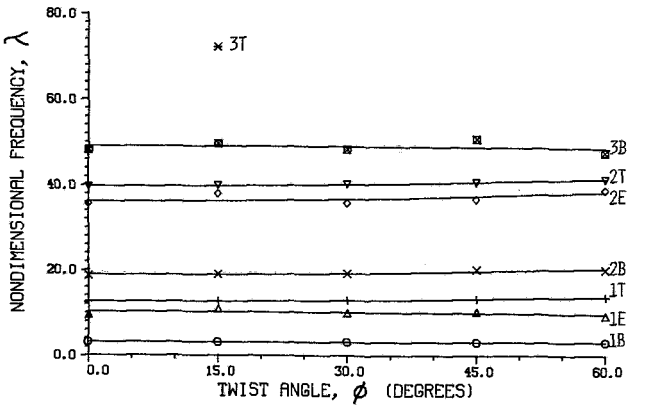

Fig. 6 Experimental nondimensional frequency as a function of tip twist ($a/b = 2, b/h = 5$)

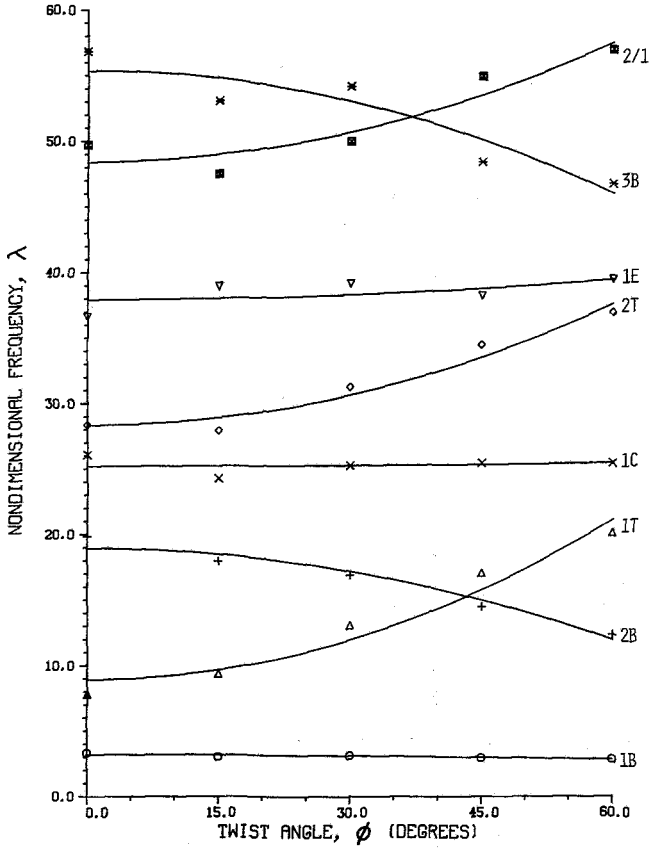

Fig. 7 Experimental nondimensional frequency as a function of tip twist ($a/b = 1, b/h = 20$)

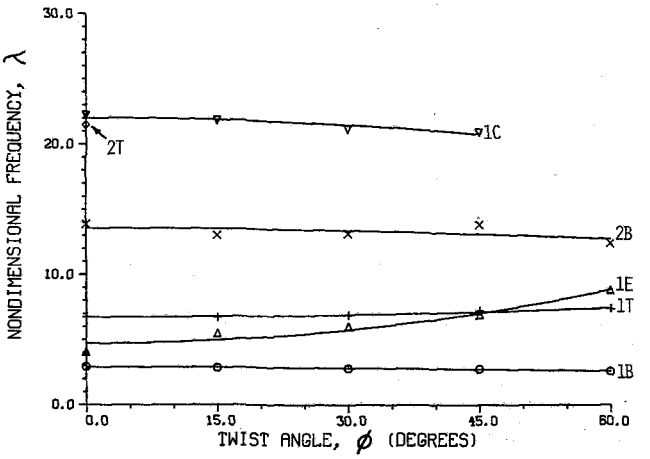

Fig. 8 Experimental nondimensional frequency as a function of tip twist ($a/b = 1, b/h = 5$)

Effect of Support Compliance on Test Results

Support compliance can have a significant effect on natural frequencies of cantilever plates and beams [8, 9]. This effect is especially significant for the lower modes of plates and beams having small length to depth ratios ($a/h < 15$) and can lead to relatively large differences between experimentally and analytically determined resonant frequencies. Table 9 shows the fundamental frequency for each of the six cantilever flat plates ($\phi = 0$ deg) used in the experimental tests along with the fundamental frequencies of four flat plates having length to depth ratios of 5, 15, 40, and 60 obtained using finite element analysis [7]. The nondimensional frequencies, given in the first column of the "Experimental" section in Table 9 are taken from Tables 3–8. The first column of nondimensional frequencies in the "Finite Element" section in Table 9 are taken from [7] and are part of the finite element study mentioned in the introduction. They are also nondimensionalized using equation (5). The two sets of data, normalized to the fundamental frequency from simple beam theory (discussed below), are shown as a function of length to depth ratio in Fig. 12. It is evident from the figure that the experimentally determined frequency decreases with increasing length to depth ratio at a much greater rate than the fundamental frequency computed using the finite element models.

Probably the largest contributing factor causing the experimental frequency to diverge from that determined analytically as the length to depth ratio decreases is support compliance or flexibility in the rotational degree of freedom

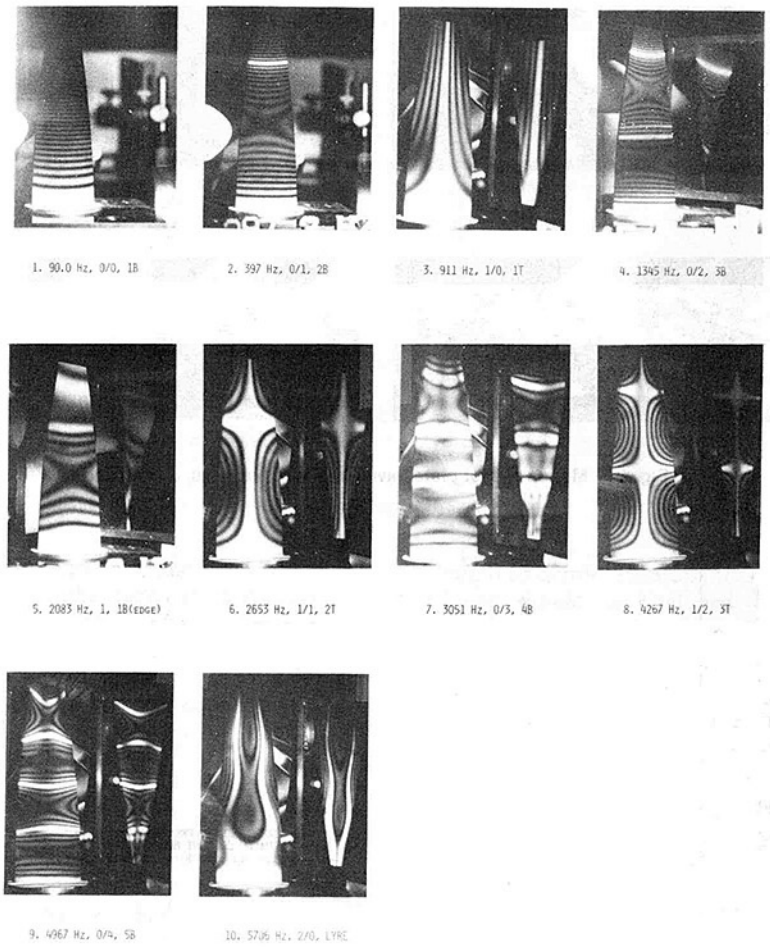

Fig. 9 Modes 1-10 for plate having $a/b = 3, b/h = 20, \phi = 60$ deg

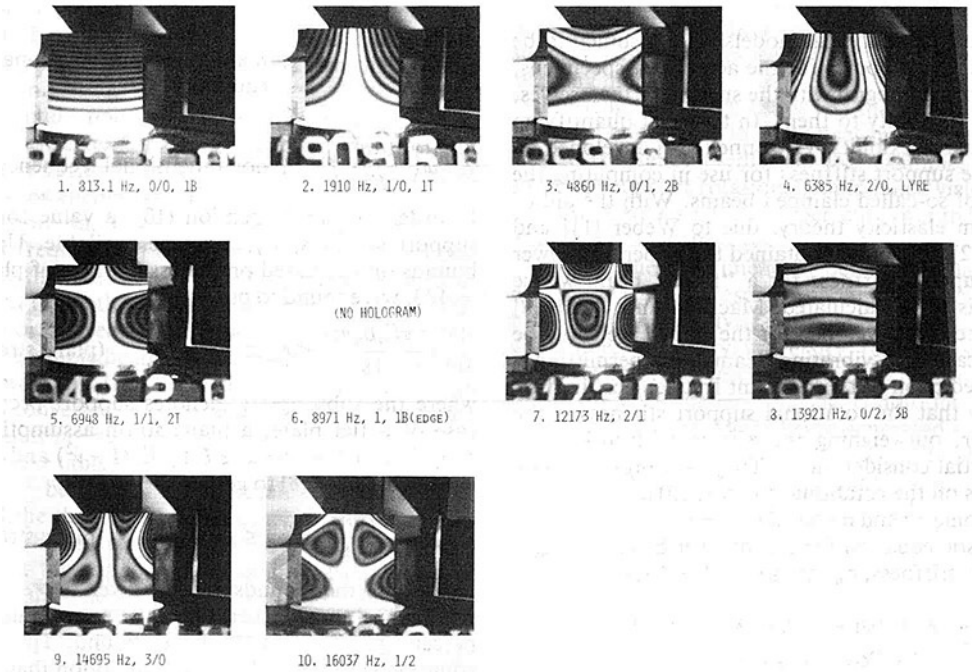

Fig. 10 Modes 1-10 for plate having $a/b = 1, b/h = 20, \phi = 0$ deg

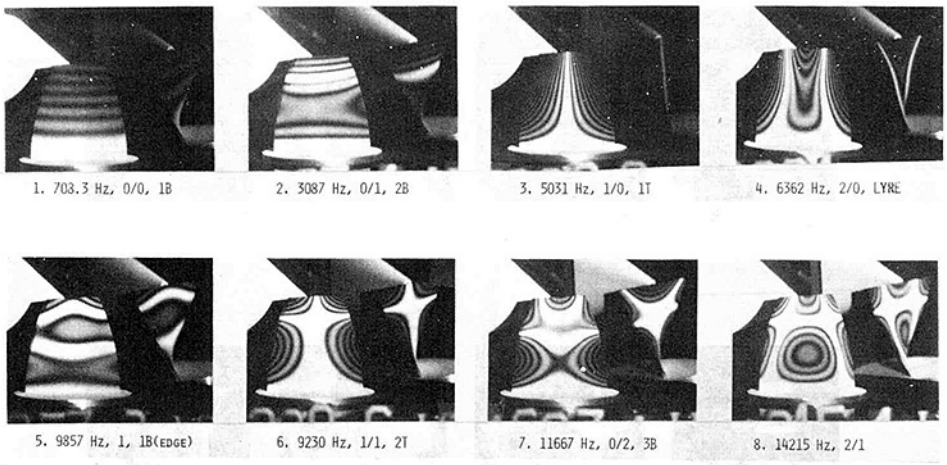

Fig. 11 Modes 1-8 for plate having $a/b = 1$, $b/h = 20$, $\phi = 60$ deg

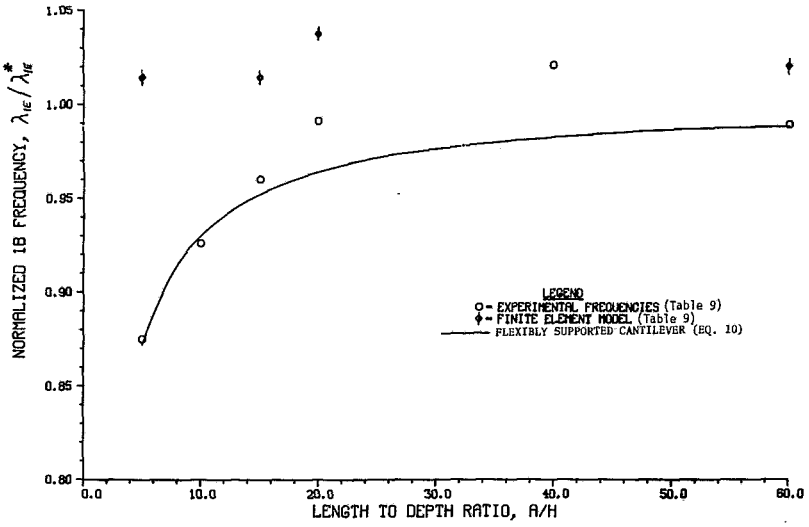

Fig. 12 Normalized first bending frequency as a function of length to depth ratio, a/h ($\lambda^*_{1E} = 3.516$)

[8, 9]. While all of the analytical models were assumed to be rigidly supported, the supports for the actual test specimens, having been machined integral with the specimens themselves, have an inherent flexibility to them. In terms of quantifying the effect of support flexibility, O'Donnell [10] developed an expression for the support stiffness for use in computing the static deflection of so-called clamped beams. With the aid of some results from elasticity theory, due to Weber [11] and Muskhelishvili [12], O'Donnell obtained the upper and lower bounds on the support stiffness for a "fixed" beam whose static deflection is to be calculated. MacBain and Genin [8] showed how the results developed for the static case could be extended to the case of a vibrating beam, thus permitting a more accurate prediction of the resonant frequencies. In their paper, they show that the rotational support stiffness is the controlling factor, outweighing the effects of translational stiffness and inertial considerations. They also present upper and lower bounds on the rotational support stiffness in terms of the support geometry and material properties.

The characteristic equation for a cantilever beam having a rotational support stiffness, r_m, at its so-called "fixed" end is

$$R = \frac{\lambda^{1/2}(\text{Sin}\,\lambda^{1/2}\,\text{Cosh}\,\lambda^{1/2} - \text{Cos}\,\lambda^{1/2}\,\text{Sinh}\,\lambda^{1/2})}{1 + \text{Cos}\,\lambda^{1/2}\,\text{Cosh}\,\lambda^{1/2}} \tag{10}$$

where:

$$R = \frac{r_m a}{EI}, \quad \text{nondimensional rotational end fixity}$$

$$\lambda = \omega\left(\frac{\rho A a^4}{EI}\right)^{1/2}, \quad \text{nondimensional frequency}$$

In order to utilize equation (10), a value for the rotational support stiffness, r_m, must be available. Upper and lower bounds on r_m, based on the assumption of plane stress and $\nu = 1/3$, were found to be

$$\frac{\pi E_s b_s h_s^2}{18} \le r_m \le \frac{\pi E_s b_s h_s^2}{15.25} \quad \text{(plane stress)} \tag{11}$$

where the subscript, s, denotes support properties. For the case of a flat plate, a plane strain assumption is more appropriate and we replace E by $E/(1-\nu^2)$ and ν by $\nu/(1-\nu)$ in equation (26) of [8] to get

$$\frac{\pi E_s b_s h_s^2}{16.04} \le r_m \le \frac{\pi E_s b_s h_s^2}{13.77} \quad \text{(plane strain)} \tag{12}$$

Note that the bounds on r_m given by equation (12) are relatively close together with the upper bound being only 15 percent greater than the lower bound. The lower bound in equation (12) is based on the assumption that the linear stress distribution occurring in the beam also occurs at the beam-

Table 9 Flat plate fundamental frequency as a function of length to depth ratio

Length/Depth	Non-Dimensional Frequency					
	Experimental			Finite Element†		
a/h	λ_1	λ_{1E}	$\lambda_{1E}/\lambda^*_{1E}$	λ_1	λ_{1E}	$\lambda_{1E}/\lambda^*_{1E}$
5	2.93	3.07	.873	3.400	3.564	1.014
10	3.10	3.25	.924	--	--	--
15	3.21	3.37	.958	3.399	3.563	1.013
20	3.32	3.48	.990	3.475	3.643	1.036
40	3.44	3.60	1.024	--	--	--
60	3.31	3.47	.987	3.419	3.584	1.019
00	--	3.516	1	--	3.516	1

†NASTRAN, (Cosmic), CTRIA2 elements, consistent mass (Ref 5, Report A)

support interface. The upper bound in equation (12) is based on a solution assuming that the beam-support interface remains plane after deformation. The reader is referred to [8] for details.

If we now consider the support stiffness, r_m, to take on a value midway between the bounds given in equation (12), we have

$$r_m = \frac{\pi E_s b_s h_s^2}{14.90} \tag{13}$$

Then the nondimensional rotational fixity becomes

$$R = \left(\frac{\pi E_s b_s h_s^2}{14.90}\right)\left(\frac{a}{EI}\right) \tag{14}$$

For equal support and beam properties, as in the present case, equation (14) becomes

$$R = 2.530\left(\frac{a}{h}\right) \tag{15}$$

It is seen from equation (15) that the nondimensional rotational end fixity is a function only of the beam length to depth ratio, a/h. It should be noted that for a severely twisted plate or for a turbine blade, the use of equation (15) should be treated cautiously in that one is deviating from the assumption of plane strain.

The fundamental nondimensional frequency, λ_1, in equation (10) was determined for various values of the rotational support stiffness, R, given by equation (15), based on the aspect ratios encompassed by the twisted plate study. Since its derivation was based on simple beam theory, the nondimensional frequency in equation (10) differs from that in Tables 3-8 by the factor $(1-\nu^2)^{1/2}$. λ_1 is shown as a function of the length to depth ratio, a/h, as the solid line in Fig. 12. It has been normalized to the value of λ_1 for an infinitely rigid support, the simple beam fundamental frequency of $\lambda^*_{1E} = 3.516$. Accordingly, the nondimensional frequencies in Table 9 were converted to an equivalent simple beam frequency by multiplying them by $1/(1-\nu^2)^{1/2}$. They are denoted as λ_{1E} in the table.

A comparison betweeen the normalized experimental frequencies and the theoretical curve generated by equations (10) and (15) shows reasonably close agreement and demonstrates that the support plays an increasingly greater role for small length to depth ratios. Note that the normalized finite element results based on a rigid support assumption are relatively insensitive to length to depth ratio, their average value being slightly greater than the simple beam frequency, $\lambda^*_{1E} = 3.516$. One can see from Fig. 12 that, as a general rule, for length to depth ratios less than 15, the effects of support flexibility should be included to insure that computed frequencies are within 5 percent of actual values.

Discussion and Conclusion

This paper has presented the results of tests determining the mode shapes and natural frequencies of 30 twisted cantilever plates having a range of geometries representative of turbomachinery blading. The nondimensional frequencies and modes shapes were determined for the first 10 to 12 vibration modes of each of the twisted plates. The nondimensional frequencies were presented as a function of tip twist, ϕ, for each of the plate geometries. Typically, the torsional frequencies show a marked increase with respect to tip twist. The flapwise bending frequencies decrease with increasing tip twist although the rate of decrease is less marked than the rate of increase for the torsional modes. The first flapwise bending mode, for example, is relatively insensitive to twist, showing only slight decrease as the tip twist is increased. For the thicker plates ($b/h = 5$), the effect of twist was less significant than for the thinner plates ($b/h = 20$).

As the length to depth ratio (a/h) decreases, the effect of support flexibility plays an increasingly greater role on the natural frequency, especially for the flapwise fundamental bending mode.

For length to depth ratios less than 15, support compliance should be included in analytical models to insure more accurate frequency prediction. For example, for $a/h = 10$, the effect of support rotational compliance yields a fundamental bending frequency that is 7 percent lower than the comparable simple beam frequency.

Finally, the experimentally determined natural frequencies and mode shapes presented herein will be compared with the numerical and analytical findings resulting from the joint government/industry/university research study on twisted plates. The bench test frequencies will also be compared to those obtained under rotating conditions. These data are currently (January 1983) being generated in spin pit tests at the NASA Lewis Research Center, Cleveland, Ohio. The foregoing results and correlations with the bench test frequencies will be forthcoming in two later papers.

Acknowledgment

The authors wish to express their appreciation for the excellent technical support provided by Mr. Bruce E. Tavner of the US Air Force Wright Aeronautical Laboratories Aero Propulsion Laboratory in carrying out the vibration tests on the twisted plates.

References

1 Kielb, R. E., Leissa, A. W., and MacBain, J. C., "Vibrations of Twisted Cantilevered Plates," forthcoming in *International Journal of Numerical Methods in Engineering*.

2 Leissa, A. W., MacBain, J. C., and Kielb, R. E., "Vibrations of Twisted Cantilevered Plates," forthcoming in *Journal of Sound Vibration*.

3 Kaufman, J. G., Brownhill, D. J., Davis, R. E., and Babilon, C. F., "New Data on the Modulus of Elasticity of Aluminum Alloys," *Journal of Materials*, Vol. 6, No. 4, 1970, pp. 1001–1016.

4 Mohr, D. G., and Crawley, E. F., "Empirical Measurements of Material Damping of Aluminum and Graphite/Epoxy in Free-Fall with Tuneable Excitation," MIT Space Systems Laboratory Report 11-82, June 1982.

5 *Metals Handbook—Properties and Selection of Metals*, Vol. 1, ASM, 8th ed.

6 Collier, R. F., Burckhardt, C. B., and Lin, L. H., *Optical Holography*, Academic Press, New York, 1971, pp. 420–453.

7 Kielb, R. E., Leissa, A. W., MacBain, J. C., and Carney, K. S., "Phase I Final Results—Joint Research Effort on Vibrations of Twisted Plates," NASA-RP 1983; (in preparation).

8 MacBain, J. C., and Genin, J., "Natural Frequencies of a Beam Considering Support Characteristics," *Journal of Sound and Vibration*, Vol. 27, No. 2, 1973, pp. 197–206.

9 Beglinger, V., Bolleter, U., and Locher, W. E., "Effects of Shear Deformation, Rotary Inertia, and Elasticity of the Support on the Resonance Frequencies of Short Cantilever Beams," JOURNAL OF ENGINEERING FOR POWER, Vol. 98, Jan. 1976, pp. 79–87.

10 O'Donnell, W. J., "The Additional Deflection of a Cantilever Due to the Elasticity of the Support," *Journal of Applied Mechanics*, Vol. 27, 1960, pp. 461–464.

11 Weber, C., "The Deflection of Loaded Gears and the Effect of Their Load Carrying Capacity," Department of Scientific and Industrial Research, London: Sponsored Research, Germany, Report No. 3, pt. 1, 1953.

12 Muskhelishvili, N. I., *Some Basic Problems of the Mathematical Theory of Elasticity*, P. Noordhoff, Ltd., Groninger-Holland, 4th ed., 1963, p. 467.

A Blade Loss Response Spectrum for Flexible Rotor Systems

M. Alam
Graduate Student.

H. D. Nelson
Professor.

Mechanical and Aerospace Engineering,
Arizona State University,
Tempe, Ariz. 85287

A shock spectrum procedure is developed to estimate the peak displacement response of linear flexible rotor-bearing systems subjected to a step change in unbalance (i.e., a blade loss). A progressive and a retrograde response spectrum are established. These blade loss response spectra are expressed in a unique nondimensional form and are functions of the modal damping ratio and the ratio of rotor spin speed to modal damped whirl speed. Modal decomposition using complex modes is utilized to make use of the unique feature of the spectra for the calculation of the peak blade loss displacement response of the rotor system. The procedure is applied to three example systems using several modal superposition strategies. The results of each are compared to true peak displacements obtained by a separate transient response program.

Introduction

The transient response of multilevel flexible rotor-bearing systems due to a step change in unbalance (i.e., blade loss) is a matter of considerable concern to engine analysts/designers. This type of severe loading may cause large amplitude displacements relative to the support structure, large shock loads at the intershaft and support bearings, and/or large internal forces in the rotating assemblies. It is, of course, essential to clearly understand the system dynamic characteristics for this kind of loading so that appropriate design parameters may be selected.

The ability to analyze large-order rotor system time transient responses has existed for some while, and several computer codes using a variety of approaches (e.g., [4–9]) have been written and successfully utilized. All of these programs typically require long and expensive computer runs and, therefore, are not always popular for preliminary design studies. A procedure that would allow the analyst to study response characteristics without the necessity of running a separate time transient for each parameter change is certainly desirable.

In 1933, M. A. Biot [1] suggested a method for determining the resistance of buildings to earthquakes. He obtained the response of a series of damped single degree of freedom systems due to the shock loading and noted the peak response. A plot of the peak response versus the undamped natural frequency for various values of the damping ratio is defined as the shock response spectrum. Biot's concept of a shock response spectrum has evolved into a popular design tool for structural dynamicists. This present procedure, such as outlined by Clough and Penzien [2], is restricted to symmetric systems with proportional damping. The equations of motion for these systems are decoupled by utilizing the orthogonality property of the undamped system modes. The analysis can then proceed toward obtaining the generalizaed time history of each mode due to the shock loading or, alternately, to obtaining the peak response of each mode by the shock spectrum approach. The peak physical coordinate responses are then determined by superposing the peak modal responses usually in a root sum square sense.

Rotor dynamic systems, in contrast to usual aerospace and civil engineering structures, are not symmetric. The presence of gyroscopic effects and general bearing properties renders the equations of motion nonsymmetric for typical rotor dynamic systems. The use of modal decomposition for this nonsymmetric case requires the use of complex right and left vectors such as outlined by Fawzy [10], Nordman [11], and others. A biorthogonality property of these complex vectors is used to decouple the system equations. In this work, the shock spectra concept has been generalized to accommodate nonsymmetric systems for the specific application of a blade loss loading. Blade loss response spectra are defined and utilized to estimate the peak response of each precessional mode. The physical coordinate responses are then approximated by superposing the precessional model responses using a variety of strategies.

A paper of particular note on blade loss dynamics is the work of Kirk and Hibner [3]. In their work, the response characteristics due to a blade loss for a single-mass rotor on isotropic supports is studied in considerable detail. They include plots of the peak displacement response of the rotor versus the rotor spin speed for three separate dynamic magnification factors. A family of these curves constitutes what this present paper refers to as a blade loss response spectrum. In their case, the spectrum is restricted to a single-mass rotor with isotropic supports. More general multiple degree of freedom flexible rotor systems cannot be directly treated using their spectrum; however, they do suggest how it may be used in a qualitative sense for more complicated

Contributed by the Gas Turbine Division of THE AMERICAN SOCIETY OF MECHANICAL ENGINEERS and presented at the 29th International Gas Turbine Conference and Exhibit, Amsterdam, The Netherlands, June 4–7, 1984. Manuscript received at ASME Headquarters December 19, 1983. Paper No. 84-GT-29.

configurations. The primary motivation for this present work was the paper by Kirk and Hibner, and the product is a generalization of their original contribution.

Mathematical Development

The matrix equation of motion of a discretized linear rotor-bearing system with a step change in rotating unbalance force is of the form

$$\mathbf{M}\ddot{\bar{q}}+\mathbf{C}\dot{\bar{q}}+\mathbf{K}\bar{q}=\bar{Q}u \tag{1}$$

The various arrays in equation (1) are defined in detail in the Nomenclature. The unbalance force vector in equation (1) is a very sparse vector with the only nonzero terms associated with the translational coordinates at the blade loss station, l. These two force components, as illustrated in Fig. 1, are

$$\begin{Bmatrix} Q_X \\ Q_Y \end{Bmatrix} = \mu\epsilon_l\Omega^2\left[\begin{Bmatrix} \cos\phi_l \\ \sin\phi_l \end{Bmatrix}\cos\Omega t+\begin{Bmatrix} -\sin\phi_l \\ \cos\phi_l \end{Bmatrix}\sin\Omega t\right] \tag{2}$$

and are assembled into $\bar{Q}$ in the usual manner to provide a system unbalance force vector of the form

$$\bar{Q}=\bar{Q}_c\cos\Omega t+\bar{Q}_s\sin\Omega t \tag{3a}$$

$$=\bar{Q}_p e^{+j\Omega t}+\bar{Q}_r e^{-j\Omega t} \tag{3b}$$

where: $\bar{Q}_p = (\bar{Q}_c - j\bar{Q}_s)/2$, $\bar{Q}_r = (\bar{Q}_c + j\bar{Q}_s)/2$

It is convenient, although not necessary, to write equation (1) in the state form.

$$A\dot{\bar{y}}+\mathbf{B}\bar{y}=(\bar{Y}_p e^{+j\Omega t}+\bar{Y}_r e^{-j\Omega t})u \tag{4}$$

where

$$\mathbf{A}=\begin{bmatrix} \mathbf{O} & \mathbf{M} \\ \mathbf{M} & \mathbf{C} \end{bmatrix} \qquad \mathbf{B}=\begin{bmatrix} -\mathbf{M} & \mathbf{O} \\ \mathbf{O} & \mathbf{K} \end{bmatrix} \tag{5}$$

$$\bar{y}=\begin{Bmatrix} \dot{\bar{q}} \\ \bar{q} \end{Bmatrix} \qquad \bar{Y}_p=\begin{Bmatrix} \bar{O} \\ \bar{Q}_p \end{Bmatrix} = \bar{Y}_r^*$$

The coupled state equation, equation (4), may be decoupled using the modal expansion (e.g., [11]).

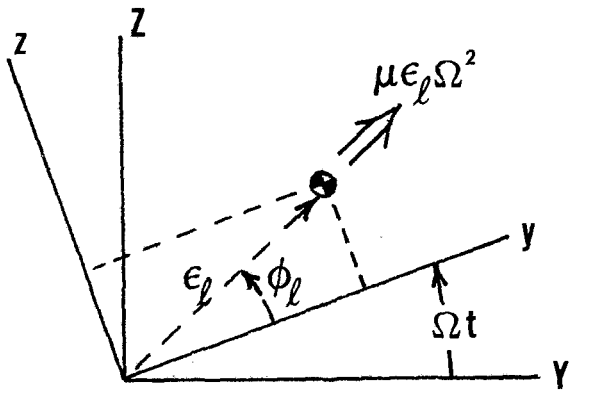

Fig. 1 Blade loss unbalance force at station l

$$\bar{y}=\sum_{i=1}^{2n}\bar{y}_i\eta_i \tag{6}$$

which expresses the physical state in terms of the state right vectors, $\bar{y}_i$, and associated complex modal coordinates, η_i. By utilizing biorthogonality relations, which also require the state left vectors, $\bar{z}_i$, the decoupled equations are typically

$$\dot{\eta}_i-\lambda_i\eta_i=(P_i^p e^{+j\Omega t}+P_i^r e^{-j\Omega t})u \tag{7}$$

$$i=1,2,\ldots,2n$$

The complex coefficients:

$$P_i^p=\frac{\bar{v}_i^T\bar{Q}_p}{N_i} \quad \text{and} \quad P_i^r=\frac{\bar{v}_i^T\bar{Q}_r}{N_i} \tag{8}$$

are defined as the progressive and retrograde modal participation factors, respectively, for the ith complex mode.

It is assumed at this point that the systems to be considered are all underdamped so that the state eigenvalues and vectors appear in complex conjugate pairs. The solution of equation (7), for zero initial conditions, is then

$$\eta_i(t)=P_i^p R_i^p(t)+P_i^r R_i^r(t) \tag{9}$$

with:

Nomenclature

$\mathbf{A},\mathbf{B}$ = system state matrices
c = isotropic damping coefficient
c_{YY},c_{ZZ} = Y,Z direct damping coefficients
$\mathbf{C}$ = system gyroscopic plus dissipation matrix (asymmetric)
j = imaginary element, $\sqrt{-1}$
k = isotropic stiffness coefficient
k_{YY},k_{ZZ} = Y,Z direct stiffness coefficients
$\mathbf{K}$ = system stiffness plus circulation matrix (asymmetric)
l = blade loss station number
$\mathbf{M}$ = system mass matrix (symmetric)
n = system degrees of freedom
N_i = modal norm
P_i^p,P_i^r = progressive, retrograde modal participation factors
$\bar{q}$ = system displacement vector
$q_s^{(k)}$ = kth element of $\bar{q}_{\max}$, using strategy s (s = 1,2,3,4)
$\bar{Q}$ = system unbalance force vector
$\bar{Q}_c,\bar{Q}_s$ = cosine, sine components of $\bar{Q}$
$\bar{Q}_p,\bar{Q}_r$ = progressive, retrograde components of $\bar{Q}$
R_i^p,R_i^r = progressive, retrograde modal blade loss response functions
S_i^p,S_i^r = nondimensional forms of R_i^p, R_i^r
t = time
u = unit step function
u_{ki} = kth element of $\bar{u}_i$
$\bar{u}_i,\bar{v}_i$ = right, left displacement eigenvectors
V_i,W_i = Y,Z translations at station i
$\bar{y}$ = state vector
$\bar{y}_i,\bar{z}_i$ = right, left state eigenvectors
$\bar{Y}$ = state force vector
$\bar{Y}_p,\bar{Y}_r$ = progressive, retrograde components of $\bar{Y}$
ξ_i = damping ratio, $\sigma_i/\bar{\omega}_i$
η_i = complex modal coordinate
λ_i = eigenvalue, $-\sigma_i+j\omega_i$
$\mu\epsilon_l$ = blade loss unbalance amplitude, station l
ρ_i = speed ratio, Ω/ω_i
σ_i = damping coefficient
ϕ_l = blade loss unbalance angle, station l
Φ_p,Φ_r = progressive, retrograde blade loss response spectrum
ω_i = damped whirl frequency, $\bar{\omega}_i\sqrt{1-\xi_i^2}$
$\bar{\omega}_i$ = undamped whirl frequency
Ω = blade loss spin speed

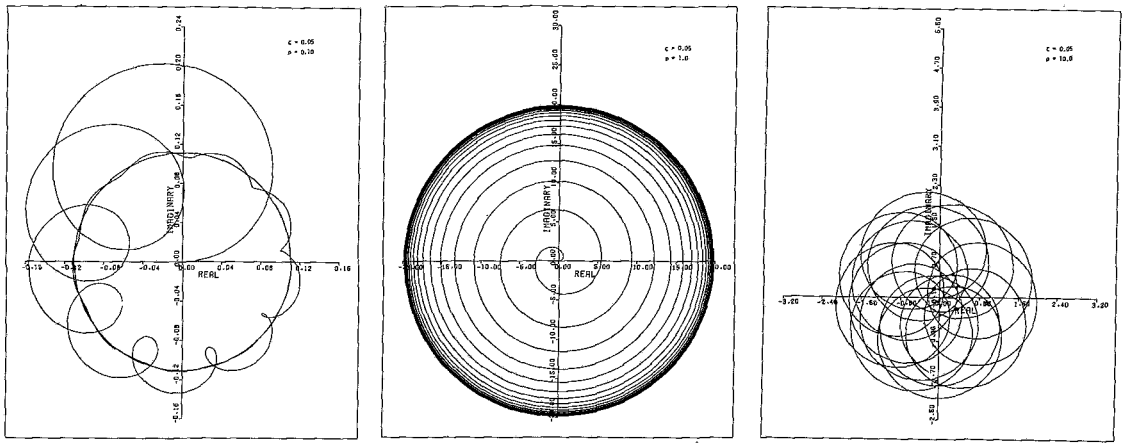

Fig. 2 Typical progressive blade loss response functions

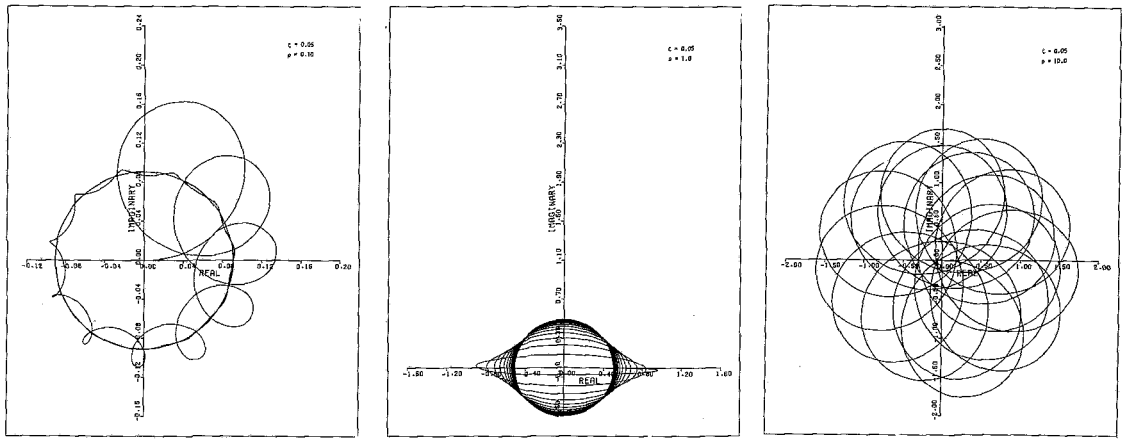

Fig. 3 Typical retrograde blade loss response functions

$$R_i^p(t) = \frac{e^{+j\Omega t} - e^{\lambda_i t}}{(+j\Omega - \lambda_i)} \tag{10a}$$

$$R_i^r(t) = \frac{e^{-j\Omega t} - e^{\lambda_i t}}{(-j\Omega - \lambda_i)} \tag{10b}$$

defined as the progressive and retrograde modal blade loss response functions respectively for the ith complex mode.

It is convenient to define a nondimensional form of modal blade loss response functions as given by equation (11) below

$$S_i^p(t) = \Omega R_i^p(t) \tag{11a}$$

$$S_i^r(t) = \Omega R_i^r(t) \tag{11b}$$

Plots of these complex progressive and retrograde functions, with time as a parameter, are shown in Figs. 2 and 3, respectively, for example values of the damping ratio, ξ, and spin ratio, ρ. All of the responses approach circular motion as $t \to \infty$.

Equation (9) provides the complex modal transient response for mode i and the state physical coordinate response is obtained from the right vector expansion of equation (6), which is repeated below.

$$\bar{y} = \begin{Bmatrix} \dot{\bar{q}} \\ \bar{q} \end{Bmatrix} = \sum_{i=1}^{2n} \begin{Bmatrix} \lambda_i \ \bar{u}_i \\ \bar{u}_i \end{Bmatrix} \eta_i \tag{6}$$

The upper half of equation (6) yields the velocity response of the system and the lower half yields the displacement response. As $t \to \infty$, the transient response approaches the steady synchronous unbalance response due to the blade loss rotating unbalance.

As stated in the introduction, it may be adequate in preliminary design studies to simply know the peak responses due to the blade loss loading rather than the detail of the time transients. To this end, the following procedure is proposed for the purpose of defining a blade loss response spectrum. The absolute value of the kth typical physical coordinate displacement, u_{ki}, for the ith mode from equations (6, 9, and 11) satisfies the triangle inequality

$$|u_{ki}\eta_i| \le \frac{1}{\Omega}|P_i^p S_i^p u_{ki}| + \frac{1}{\Omega}|P_i^r S_i^r u_{ki}| \tag{12}$$

If the maximum absolute amplitudes of the blade loss response functions are used in equation (12), the following inequality exists

$$|u_{ki}\eta_i|_{\max} \le \frac{1}{\Omega}[|P_i^p||S_i^p|_{\max} + |P_i^r||S_i^r|_{\max}]|u_{ki}| \tag{13}$$

The set of maximum amplitudes of the nondimensional blade loss response functions, $S^p(t)$ and $S^r(t)$, are defined as the progressive and retrograde blade loss response spectrum, respectively. The subscript has been dropped since the form of the nondimensional functions is the same for each mode. Thus

$$\Phi_p(\rho,\xi) \triangleq |S^p(t)|_{\max} \tag{14a}$$

$$\Phi_r(\rho,\xi) \triangleq |S^r(t)|_{\max} \tag{14b}$$

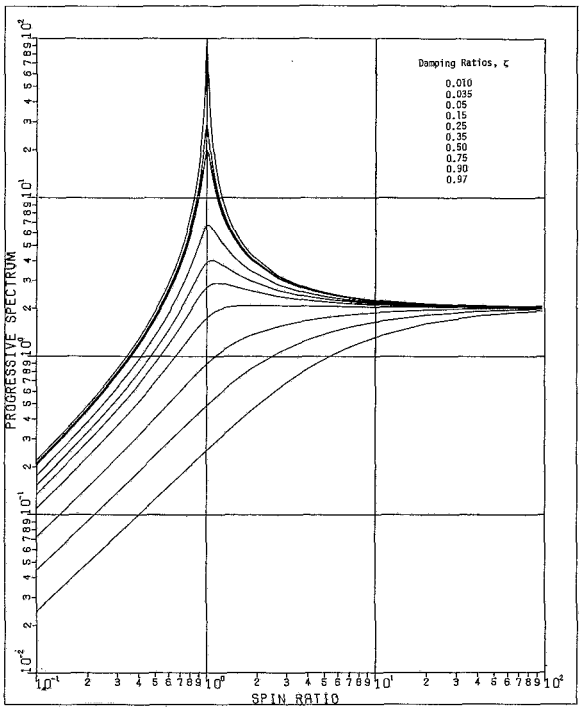

Fig. 4 Progressive blade loss response spectrum

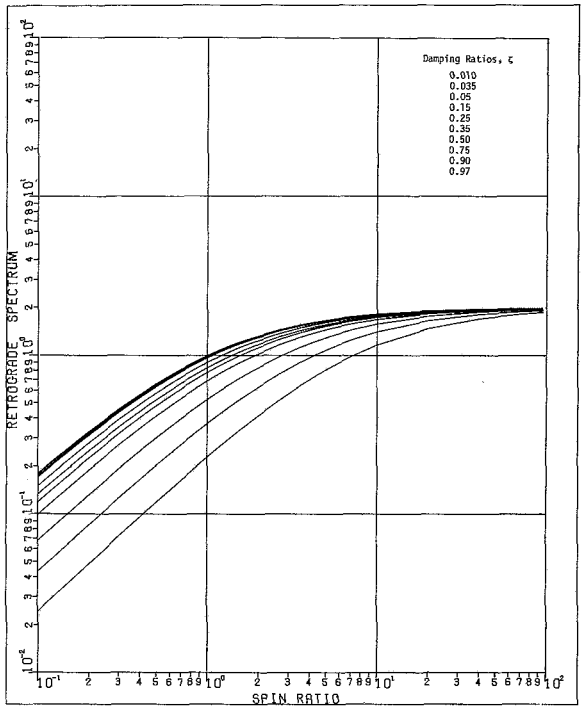

Fig. 5 Retrograde blade loss response spectrum

The spectra associated with the definitions of equation (14) are shown in Figs. 4 and 5. The progressive spectra have a peak in the vicinity of $\rho = 1$, while the retrograde spectra do not possess this dynamic magnification characteristic. Both spectra approach 2.0 for large values of the spin ratio. By utilizing the definitions of equation (14), the inequality of equation (13) may be written as

$$|u_{ki}\eta_i|_{\max} \le \frac{1}{\Omega}[|P_i^p|\Phi_p(\rho_i,\xi_i) + |P_i^r|\Phi_r(\rho_i,\xi_i)]|u_{ki}| \tag{15}$$

Equation (15) provides the maximum possible amplitude contribution to the kth element of the physical coordinate response due to the ith complex mode. The peak displacement response of the rotor system may then be estimated by combining the contributions from each complex mode. Since absolute values of the responses has been introduced, all of the relative phase between the modal responses is lost. A variety of superposition strategies can be defined, and four possibilities are suggested below

1 Absolute Value Sum (AVS):

$$q_1^{(k)} \triangleq \frac{1}{\Omega}\sum_{i=1}^{2N}[|P_i^p|\Phi_p(\rho_i,\xi_i) + |P_i^r|\Phi_r(\rho_i,\xi_i)]|u_{ki}| \qquad 2N \le 2n \tag{16}$$

2 Root Sum Square (RSS):

$$q_2^{(k)} \triangleq \frac{1}{\Omega}\sqrt{\sum_{i=1}^{2N}[|P_i^p|\Phi_p(\rho_i,\xi_i) + |P_i^r|\Phi_r(\rho_i,\xi_i)]^2|u_{ki}|^2} \qquad 2N \le 2n \tag{17}$$

3 RSS/AVS Combination 1:

$$q_3^{(k)} \triangleq \frac{1}{\Omega}\sqrt{\sum_{i=1}^{2L}[|P_i^p|\Phi_p(\rho_i,\xi_i) + |P_i^r|\Phi_r(\rho_i,\xi_i)]^2|u_{ki}|^2} + \frac{1}{\Omega}\sum_{m=1}^{2M}[|P_m^p|\Phi_p(\rho_m,\xi_m) + |P_m^r|\Phi_r(\rho_m,\xi_m)]|u_{km}|$$

$$2L + 2M \le 2n \qquad 0.5 \le \rho_m \le 1.5 \qquad \rho_i < 0.5 \text{ or } \rho_i > 1.5 \tag{18}$$

4 RSS/AVS Combination 2:

$q_4^{(k)}$ = Same form as equation (18) (19)

$$2L + 2M \le 2n \qquad \rho_m \le 2.0 \qquad \rho_i > 2.0$$

The first strategy is simply the sum of the peak absolute responses from each of the complex modes and is the most conservative approach that can be taken. The peak predictions obtained by this approach will always be higher than the true peaks but may be too high for normal usage. The second strategy is the most popular for shock spectra methods in symmetric structures and generally provides a prediction that is conservative. This cannot be assured, however, as will be evident in the results presented for the example systems. The third and fourth strategies combine some of the features of the first two strategies. For method 3, the sum of the absolute values are used if the spin ratio at blade loss is within a neighborhood of a resonance, i.e., $0.5 \le \rho \le 1.5$. All other mode contributions are included in a root sum square sense. For method 4, the same philosophy as in method 3 is used, except that the absolute sum is used for modes with $\rho \le 2$ and all other modes are included in the root sum square sense. The cutoff values of ρ for strategies 3 and 4 are arbitrary and the values used here are simply one set of arbitrary choices.

In all of the superpositions listed above, the summation has been on the complex modes. The modes appear in complex conjugate pairs however, and the conjugate mode contributes exactly the same amount to the maximum amplitude response as the mode itself. Since a complex mode and its conjugate combine to form a real precessional mode, the summations in

equations (16–19) can be interpreted as summations over the precessional modes.

The number N in strategies 1 and 2 represents the number of precessional modes that the analyst wishes to use. As with other types of modal analyses, the higher frequency modes have a lesser and usually negligible effect on the sum total. The number M in strategies 3 and 4 represents all precessional modes that are in the spin ratio range for the absolute value sum, and the number L represents the number of precessional modes that the analyst wishes to use in the root sum square contribution. Usually all low frequency modes would be included and the high frequency modes would be truncated at a value of the analyst's choice.

Applications

A computer subroutine to implement the foregoing procedures has been developed and included in the finite element based computer program ARDS (*A*nalysis of *R*otor *D*ynamic *S*ystems), which was developed previously under NASA LeRC Grant NAG 3-6. The progressive and retrograde blade loss response spectra are generated one time and are stored in a tabular form for table lookup during the actual

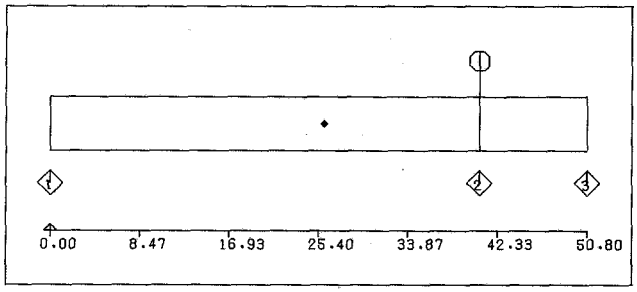

Fig. 6 Rotor 1 configuration

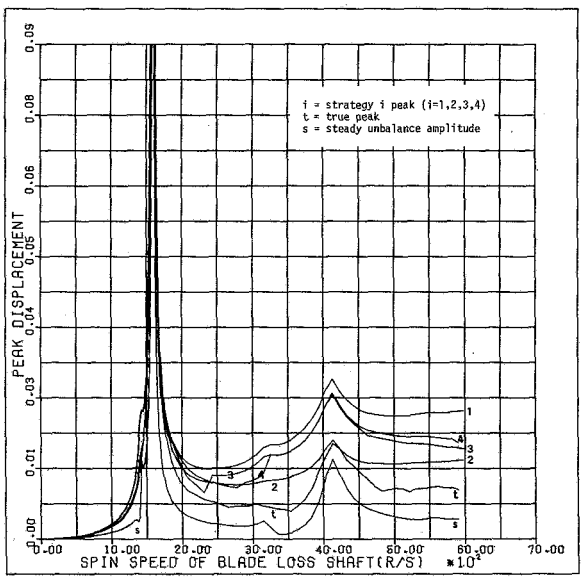

Fig. 7 V_2 peak displacement, Rotor 1

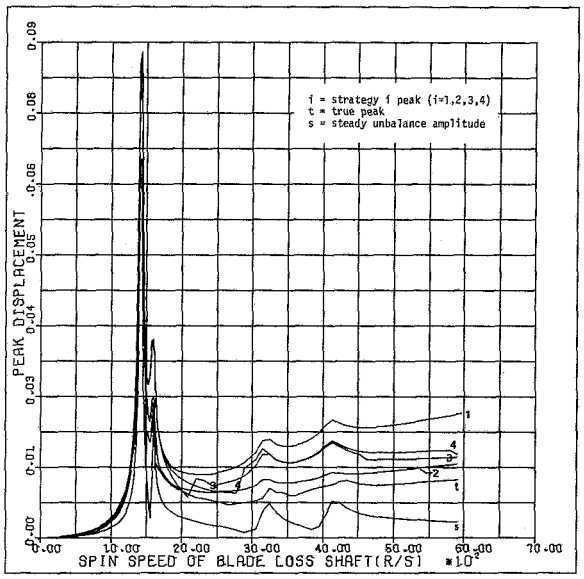

Fig. 8 W_2 peak displacement, Rotor 1

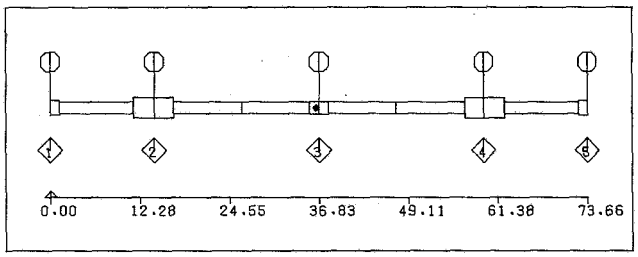

Fig. 9 Rotor 2 configuration

Table 1 Rotor 2 physical properties[a]

Stn no.	Subel. no.	Length (cm)	Radius (cm)	Mass (kg)	Diametral inertia (kg-cm^2)	Polar inertia (kg-cm^2)
1	1	1.245	1.0035	2.921	0.	0.
	2	10.135	0.7940			
	3	2.845	1.3970			
2	1	2.667	1.3970	3.393	143.2	281.7
	2	9.335	0.7940			
	3	9.334	0.7940			
	4	1.270	0.8435			
3	1	1.270	0.8435	0.848	0.	0.
	2	9.334	0.7940			
	3	9.335	0.7940			
	4	2.667	1.3970			
4	1	2.845	1.3970	3.393	143.2	281.7
	2	10.135	0.7940			
	3	1.245	1.0035			
5				2.785	0.	0.

[a] $E = 20.69\ 10^6$ N/cm^2 $\rho \doteq 0$ for subelements

analysis. The system eigenvalues and modes are also stored at three different spin speed sets, and a quadratic curve fit is used to determine their values at the analysis spin speeds.

Three example systems are analyzed to study the validity of the proposed procedure. The peak responses were determined for typical system physical coordinates, using the four superposition strategies suggested above, and the results were also compared to the true peak values obtained by a transient response subroutine contained in the program ARDS. The steady-state response associated with the blade loss unbalance is also shown for comparison.

Example 1. The rotor system used in the initial test is a single-shaft rotor consisting of a uniform shaft, 50.8 cm length and 2.54 cm radius, with a single concentrated disk, located 40.64 cm from station 1, as illustrated in Fig. 6. The uniform shaft has an elastic modulus of 20.69×10^6 N/cm^2 and a volume mass density of 8304 kg/m^3. The mass of the concentrated disk at station 2 is 4.9035 kg with a polar and diametral inertia of 271.2 kg-cm^2 and 135.6 kg-cm^2, respectively. The rotating assembly is connected to a rigid base by two identical orthotropic supports at stations 1 and 3. The direct stiffnesses in the Y- and Z-directions are k_{YY} = 437,815 N/cm and k_{ZZ} = 262,689 N/cm. The corresponding direct damping coefficients are c_{YY} = 8.76 N-s/cm and c_{ZZ} = 5.25 N-s/cm.

A blade loss is simulated at station 2, resulting in a cg eccentricity of 0.254 mm. Plots of peak values of V and W displacements at station 2 versus the blade loss spin speed are shown in Figs. 7 and 8, respectively. The first three forward critical speeds are 1,550, 4,100, and 11,500 R/S and the first three backward critical speeds are 1,400, 3,200, and 5,450 R/S.

Example 2. The rotor configuration used in example 2 is identical with the blade loss test rig developed by United Technologies, Inc., under NASA Contract NAS3-18523. Details on the rotor configuration, shown in Fig. 9, are included in [12] and are also listed in Table 1.

A blade loss resulting in a cg eccentricity of 0.081491 mm is simulated at station 2. The rotor is supported at stations 1 and 5 by two identical isotropic supports with a stiffness of k = 4,550 N/cm and a damping coefficient of c = 0.65 N-s/cm. Plots of the peak V displacement at stations 1 and 2 versus the blade loss spin speed are shown in Figs. 10 and 11, respectively. For this system, the first two undamped forward critical speeds are 157 and 309 R/S.

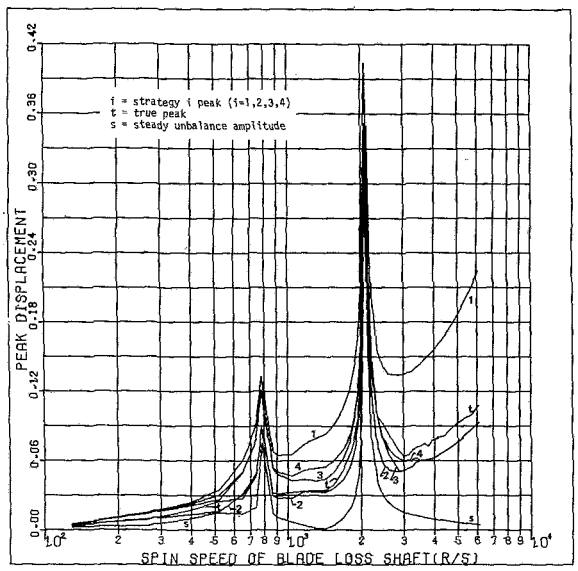

Fig. 10 V_1 peak displacement, Rotor 2

Example 3. The rotor configuration of example 3 is a dual-shaft system as shown in Fig. 12, and was previously analyzed in [13] using component mode synthesis. The two rotors are interconnected by an intershaft bearing between station 4 of shaft 1 and station 10 of shaft 2. Rotor (1,2) is

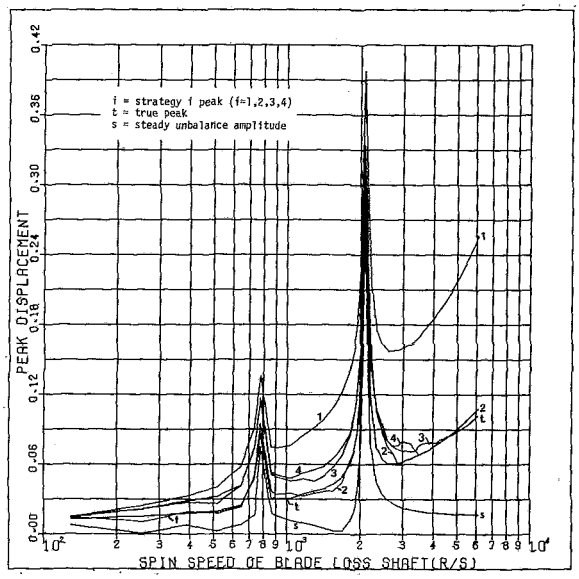

Fig. 11 V_2 peak displacement, Rotor 2

Table 2 Rotor 3 subelement data[a]

Shaft	Element	Subel.	Length (cm)	Inner radius (cm)	Outer radius (cm)
1	1	1	7.62	0.	1.524
	2	1	8.89	0.	1.524
		2	8.89	0.	1.524
	3	1	7.62	0.	1.524
		2	7.62	0.	1.524
	4	1	5.08	0.	1.524
	5	1	5.08	0.	1.524
2	7	1	5.08	1.905	2.54
	8	1	7.62	1.905	2.54
		2	7.62	1.905	2.54
	9	1	5.08	1.905	2.54

[a] $E = 20.69\ 10^6$ N/cm^2, $G = E/2.6$, $\rho = 8304$ kg/m^3

Table 3 Rotor 3 concentrated disk data

Shaft	Station	Mass (kg)	Polar inertia (kg-cm^2)	Diametral inertia (kg-cm^2)
1	2	4.904	271.2	135.6
	5	4.203	203.4	101.7
2	8	3.327	146.9	73.4
	9	2.277	97.2	48.6

Table 4 Rotor 3 bearing data

Shaft	Station (a)	Station (b)[a]	Stiffness (N/cm)	Damping (N-s/cm)
1	1	0	262,795	35.0
	4	10	87,598	26.3
	6	0	175,197	35.0
2	7	0	175,197	17.5

[a] 0 – denotes a connection to the rigid base

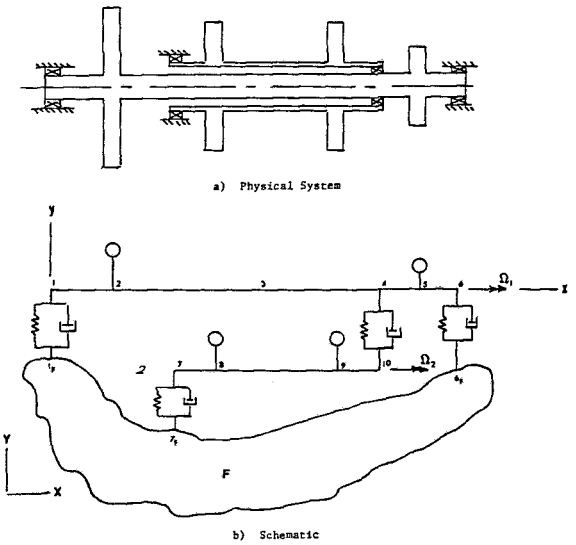

Fig. 12 Rotor 3 configuration

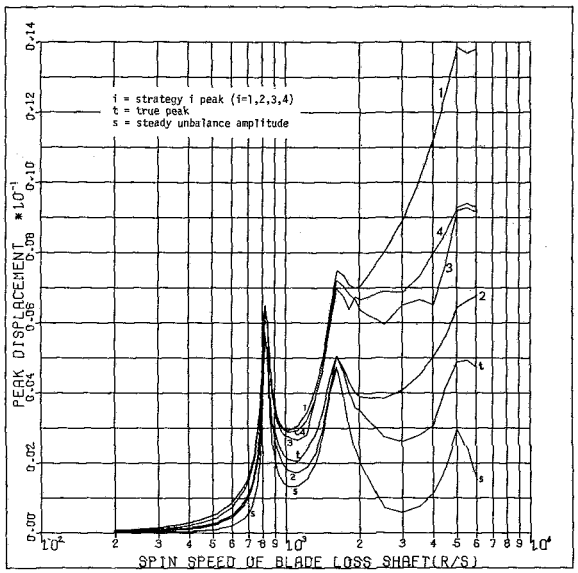

Fig. 13 V_1 peak displacement, Rotor 3

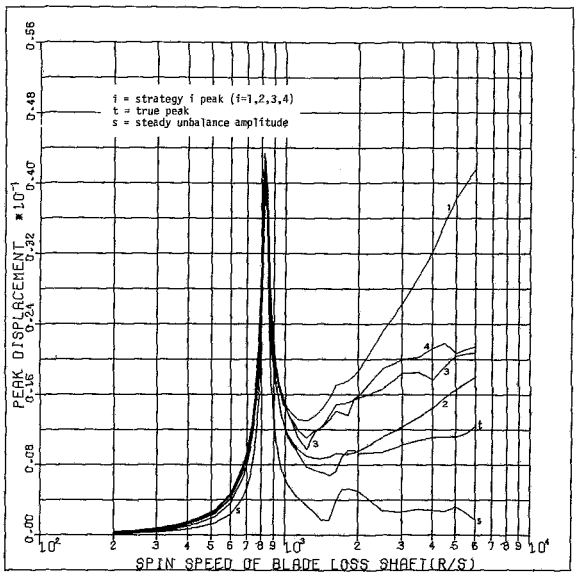

Fig. 14 V_4 peak displacement, Rotor 3

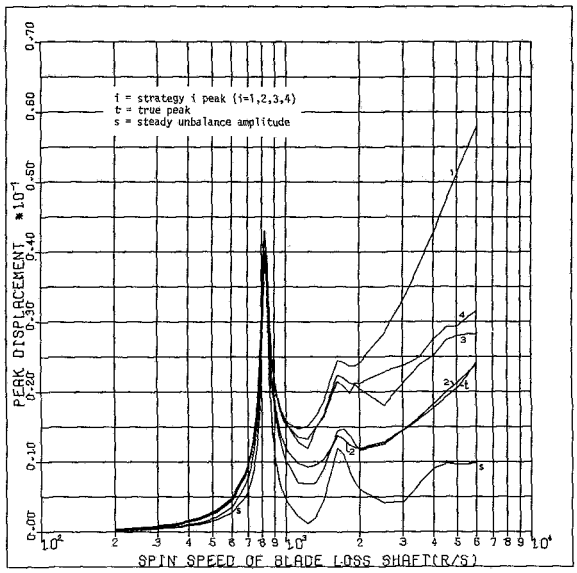

Fig. 15 V_9 peak displacement, Rotor 3

modeled as a (6,4) station, (24,16) degree of freedom, (5,3) element assembly with station locations as indicated in Fig. 12.

Details of the rotor configuration are listed in [13] and also in Tables 2 and 3.

The rotor assemblies are supported on a rigid foundation by isotropic damped bearings with properties listed in Table 4.

A blade loss is simulated at station 9 resulting in a cg eccentricity of 0.254 mm. Plots of the peak V displacement at stations 1, 4, and 9 versus the blade loss spin speed are shown in Figs. 13, 14, and 15, respectively.

Results and Conclusions

The three example systems, previously described, were analyzed using the blade loss response spectrum approach, and the predicted peak responses were compared with true peak responses obtained by using a separate transient analysis program. The results show that the proposed spectrum approach has considerable potential for preliminary blade loss design studies. In general, the analysis results show the same qualitative characteristics for all three systems analyzed.

The peak response prediction using the sum of the absolute values (AVS) of each complex mode contribution is always conservative. This strategy provides reasonable results in the neighborhood of critical speeds with large dynamic magnification, but yields predictions that are typically two to three times larger than the true peaks at other speeds. The root sum square (RSS) superposition strategy appears to be the most logical one to use. A review of all the results presented shows that this approach is generally conservative with predictions that are nominally less than 20 percent larger than the true peaks. The RSS strategy, however, may yield predictions which are lower than the true peaks in some speed ranges so an appropriate factor of safety should be utilized.

The third and fourth strategies (RSS/AVS), which combine AVS and RSS contributions, are less conservative than strategy 1 (AVS) and are more conservative than strategy 2 (RSS). In the examples studied, the peak responses obtained using the RSS/AVS approaches were generally larger than the true peaks; however, this characteristic cannot be assured. There does not appear to be any real advantage in using an

RSS/AVS strategy since the RSS approach with a suitable factor of safety would yield essentially the same results.

The procedure proposed in this work is based on linear analysis. In view of the severe nature of a blade loss transient, one should certainly question the suitability of a linear analysis assumption. Since the intent in this procedure, however, is for preliminary design studies, it is hoped that this linear model can still be used to advantage. The proof of this statement, of course, can only be provided by correlation with test data.

The proposed spectrum approach for predicting peak blade loss response appears to be a promising design/analysis tool. The peak response characteristics of a system can be predicted for an entire speed range using a small amount of computation time compared with time transient analyses. The peak response predictions using all of the proposed superposition strategies should be requested for any analysis, since the added computation time is trivial. It appears, however, that that the RSS superposition strategy with an appropriate factor of safety is the most logical one to use. Final design studies, of course, should be verified by system time transient analyses.

For the examples presented, the spectrum approach required approximately 1/20 of the CPU time compared to the time transient method. This ratio can vary a considerable amount depending on system size and mode selection, but an order of magnitude savings in CPU time is a reasonable expectation for most systems.

Acknowledgment

The work presented in this paper was supported in part by NASA Grant NAG 3-6 under the coordination of D. P. Fleming and A. F. Kascak.

References

1 Biot, M. A., "Theory of Elastic Systems Vibration under Transient Impulse With an Application to Earthquake-Proof Building," *Proceedings of the National Academy of Sciences*, Vol. 19, 1933, pp. 262–268.

2 Clough, R., and Penzien, J., *Dynamics of Structures*, McGraw-Hill, New York, 1975.

3 Kirk, R. G., and Hibner, D. H., "A Note on Blade Loss Dynamics of Rotor-Bearing Systems," ASME *Journal of Engineerng for Industry*, Vol. 98, No. 2, May 1976, pp. 497–504.

4 Kirk, R. G., and Gunter, E. J., "Nonlinear Transient Analysis of Multi-Mass Flexible Rotors—Theory and Applications," NASA CR-2300, 1973.

5 Lund, J. W., "Linear Transient Response of a Flexible Rotor Supported in Gas Lubricated Bearings," ASME Paper 75-Lub-40, 1975.

6 Childs, D. W., "A Rotor-Fixed Modal Simulation Model for Flexible Rotating Equipment," ASME *Journal of Engineering for Industry*, Series B, Vol. 96, No. 2, May 1974, pp. 659–669.

7 Dennis, A. J., Eriksson, R. H., and Seitelman, L. H., "Transient Response Analysis of Damped Rotor Systems by the Normal Mode Method," ASME Paper 75-GT-58, 1975.

8 Nelson, H. D., and Meacham, W. L., "Transient Analysis of Rotor-Bearing Systems Using Component Mode Synthesis," ASME Paper 81-GT-110, 1981.

9 Gallardo, M. J., et al., "Blade Loss Transient Dynamics Analysis," Three Volumes, NASA CR-NAS3-22053, General Electric Co., June 1981.

10 Fawzy, I., and Bishop, R. E. D., "On the Dynamics of Linear Non-Conservative Systems," *Proceedings of the Royal Society of London*, A., Vol. 352, 1976, pp. 25–40.

11 Nordman, R., "Schwingungsberechnung von nichtkonservativen Rotoren mit Hilfe von Links und Rechtseigenvectoren," VDI-Berichte Nr. 269, 1976.

12 Buono, D. F., Schlitzer, L. D., Hall, R. G., III, and Hibner, D. H., "Transient Dynamics of a Flexible Rotor with Squeeze Film Dampers," NASA CR-3050, September, 1978.

13 Glasgow, D. A., and Nelson, H. D., "Stability Analysis of Rotor-Bearing Systems Using Component Mode Synthesis," ASME *Journal of Mechanical Design*, Vol. 102, No. 2, Apr. 1980, pp. 352–359.

J. H. Griffin
Associate Professor,
Department of Mechanical Engineering,
Carnegie-Mellon University,
Pittsburgh, Pa. 15213

A. Sinha
Assistant Professor,
Department of Mechanical Engineering,
The Pennsylvania State University,
University Park, Pa. 16802

The Interaction Between Mistuning and Friction in the Forced Response of Bladed Disk Assemblies

This paper summarizes the results of an investigation to establish the impact of mistuning on the performance and design of blade-to-blade friction dampers of the type used to control the resonant response of turbine blades in gas turbine engines. In addition, it discusses the importance of friction slip force variations on the dynamic response of shrouded fan blades.

1 Introduction

This paper discusses the influence of mistuning on the forced response of bladed disk assemblies in which the blades are linked by either of two types of friction elements, turbine blade friction dampers or part span shrouds. Mistuning refers to variations in the dynamic properties of the system that, even when small, can significantly alter its dynamic response and cause the blades' amplitudes to vary widely within the same assembly [1-12]. The amount of relative motion between adjacent blades can significantly affect how friction elements behave, since for small motions they may only deform elastically while for larger motions they may slip and dissipate energy. As a result, mistuning that induces random variations in blade amplitudes may also affect how such nonlinear elements should be designed. If the system is tuned, then all blades respond with the same amplitude to a uniform external excitation. In this instance, the system's response can be shown to be the same as that of an equivalent single blade model with a blade to ground damper whose dynamic behavior can be relatively easily calculated to provide a "tuned system theory" of response. The main objective of this paper is to investigate to what extent solutions to mistuned disks differ from such a theory.

Blade to blade friction dampers provide links between vibrating points on adjacent blades (Fig. 1). They transmit loads through friction contacts which dissipate energy when slip occurs. They have been used for years by the designers of jet engines to reduce turbine blade resonance. When a bladed disk exhibits large resonant stresses that differ significantly from blade to blade the designer needs to know how to design a damper to correct the problem. Specifically, what value of friction slip load will reduce the amplitude of the high-response blade the most and how much reduction will he get? This study focuses on these two concerns by comparing optimized values of slip load and amplitude reduction calculated from models of mistuned rotors with those predicted by tuned system theory to find out if friction dampers for mistuned rotors need to be designed differently than for their tuned counterparts.

Part span shrouds are pieces of metal which protrude from the sides of the airfoils. As the engine rpm increases they are brought into contact with shrouds from neighboring blades by centrifugal forces that tend to untwist the air foils (Fig. 2). Their primary purpose is to restrict vibratory motion and raise the natural frequencies of otherwise low-frequency fan blades, thus increasing the aeroelastic stability of the stage. Like turbine blade dampers, part span shrouds provide a friction interface between adjacent blades. However, analyzing their structural response is more complicated for a number of reasons. Because the friction interface is not parallel to the direction of vibratory motion, the normal load on the interface (and consequently the friction slip load) can vary dynamically as a function of time. Also, since the shroud

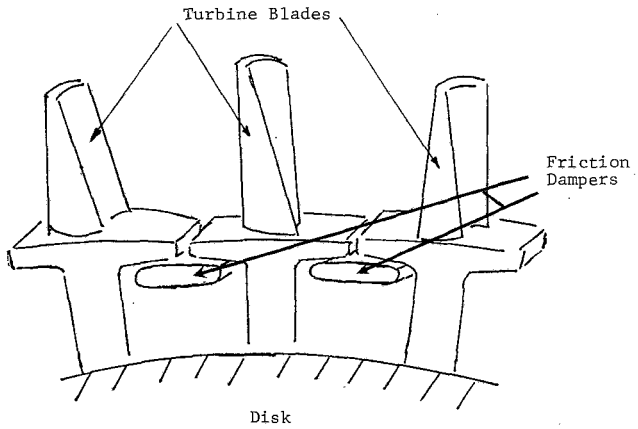

Fig. 1 Schematic of blade-to-blade friction dampers

Contributed by the Gas Turbine Division of THE AMERICAN SOCIETY OF MECHANICAL ENGINEERS and presented at the 29th International Gas Turbine Conference and Exhibit, Amsterdam, The Netherlands, June 4-7, 1984. Manuscript received at ASME Headquarters January 9, 1984. Paper No. 84-GT-139.

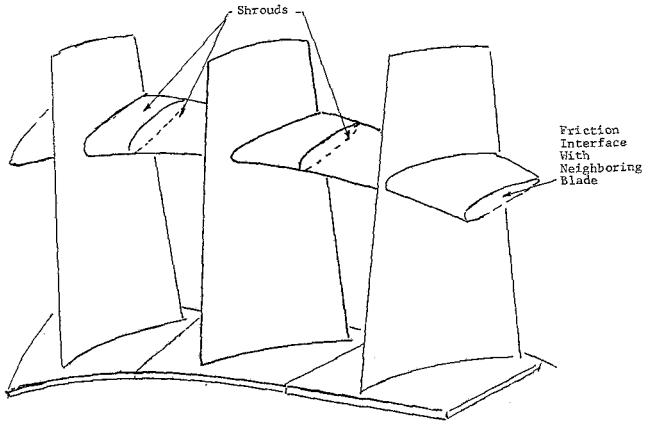

Fig. 2 Schematic of shrouded fan blades

contact points are relatively high on the blades, the nonlinear effects can greatly alter the mode shape of the blades' response. And, lastly, because the static component of the shroud contact pressure depends on the way the shrouds interlock with each other, minor variations in the shrouds' and blades' dimensions can cause significant differences in slip load from interface to interface. As a result of these types of complexities, the development of analytical procedures for predicting the dynamic response of shrouded fan stages is still in its infancy, and it is not possible at this time to focus on the same type of design concerns as for friction dampers. This paper considers the case of tight shrouds and small motions for which the first two aforementioned complications are less significant. As a result, relatively simple dynamic models can be used to examine the third factor, i.e., whether mistuning induced by slip load variations is an important consideration in predicting the dynamic response of these systems and how it compares to other more traditional sources of blade mistuning. That variations in slip loads can induce variations in blade amplitudes in these types of systems has been demonstrated in a recent paper by Muszynska and Jones [14].

The spring/mass model used to represent the bladed disk is an extension of that used for single blade dynamics in [13] and in some respects is less complex than that developed by Muszynska and Jones [14, 15]. It has the added feature of directly modeling the modal stiffness of the nonlinear element which was found to be an important factor in predicting the response of blade to ground turbine blade dampers [13]. The steady-state response for this stage model is calculated in a manner analogous to that used in [13–18]. For first-order steady response, this procedure is equivalent to the alternate methods described in [19–21]. The accuracy of this approach has been verified both by the authors of this paper [16, 22] and by Plunkett [23] by comparing steady-state solutions determined from it with "long time" transient solutions independently calculated using finite difference methods.

First, the spring/mass model of the stage and the procedure for calculating the steady-state solution are given. Then, a model of a single blade is presented that has the same dynamic behavior as that of a tuned system. Based on this model, simple expressions are provided for calculating the optimum friction slip load and the associated reduction in amplitude that would occur if the system were tuned. Next, the results for a number of simulations of mistuned bladed disks with friction dampers are given and compared with predictions from this tuned system theory. Last, simulations of a shrouded stage with both friction slip load variations and blade mistuning are presented.

2 Model Description and Method of Solution

In the rotor stage model depicted in Fig. 3, m_i and k_i are the modal mass and stiffness, respectively of the ith blade. The

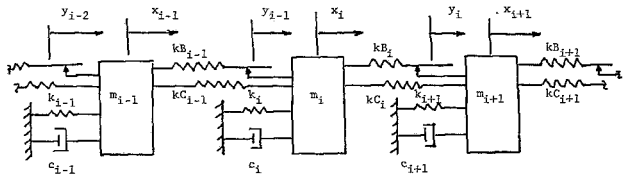

Fig. 3 Spring/mass model of rotor stage

mechanical coupling between the blades due to the disk's flexibility is represented by the springs with stiffness kC_i. In such a model the mass's displacement, x_i, is proportional to the ith blade's motion in the corresponding mode, e.g., first bending. The stiffness of the ith nonlinear element is represented by kB_i, and it slips when it is deformed to the point that it transmits a force of magnitude FS_i. Other sources of damping such as those caused by aerodynamic forces are represented by the viscous dampers attached to each blade. The external force represents a Fourier component of a particular engine order excitation and, as a result, is sinusoidal in time and differs only in phase from blade to blade. Such excitation which can be caused by the wakes induced by static upstream structures or by circumferential variations in fuel distribution, is one of the principal types found in jet engines.

The governing equation of motion for the ith mass may be written as

$$m_i\ddot{x}_i + (k_i + kC_i + kC_{i-1} + kB_i + kB_{i-1})x_i + C_i\dot{x}_i = (kC_i + kB_i)x_{i+1} + (kC_{i-1} + kB_{i-1})x_{i-1} + kB_i(y_i - x_{i+1}) - kB_{i-1}(y_{i-1} - x_i) + f_o\cos(\omega t + \psi_i) \quad (1)$$

where, $i = 1,2,3, \ldots, N$, and N is the number of blades. In equation (1), because of circular symmetry, $(i+1)$ is taken as 1 if $i = N$ and $(i-1)$ as N if $i = 1$. The nonlinear aspect of the problem is embedded in the terms y_i, $i = 1,2,3, \ldots, N$, the displacements of the nonlinear elements at the slip joints. The system is linear if the system is fully stuck ($y_i = x_{i+1}$) or fully slipping ($y_i = x_i$). For intermediate cases, the response is nonlinear and can be calculated approximately in the following manner [13–18].

Assume that the steady-state response is harmonic, i.e.,

$$x_i = A_i\cos(\omega t + \phi_i) \quad (2)$$

where $i = 1,2, \ldots, N$. Equation (2) implies that

$$x_i - x_{i+1} = Ar_i\cos(\omega t + \phi r_i) \quad (3)$$

where by using the appropriate trigonometric identities the relative amplitude and phase, Ar_i and ϕr_i, can be expressed in terms of A_i and ϕ_i.

The nonlinear terms, $(y_i - x_{i+1})$, $i = 1,2, \ldots, N$, are expanded in a Fourier series and only the terms with the fundamental frequency are retained. The expansion of the nonlinear terms is represented as

$$y_i - x_{i+1} = a_i\cos(\omega t + \phi r_i) + b_i\sin(\omega t + \phi r_i) \quad (4)$$

where from [18]

$$a_i = Ar_i(\pi - \theta_i + 0.5\sin 2\theta_i)/\pi \quad (5)$$

and

$$b_i = Ar_i \cdot (\sin^2\theta_i)/\pi \quad (6)$$

where

$$\theta_i = \cos^{-1}(1 - 2FS_i/(kD_i \cdot Ar_i))$$
$$FS_i = \text{slip load} \quad (7)$$

Substituting (2) and (3) into the governing system of differential equations (1), the method of harmonic balance requires that the coefficients of the sine and cosine terms be

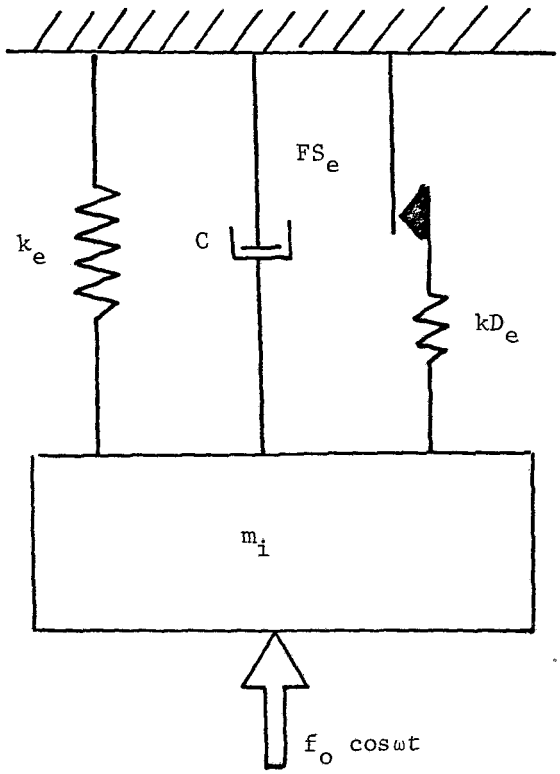

Fig. 4 SDOF model equivalent to tuned rotor

independently equated. This results in $2N$ nonlinear algebraic equations that can be solved numerically with standard subroutines [24] to find N amplitudes and N phases. Solutions calculated using this approximate approach were compared with "long time solutions" from transient numerical solutions of the governing equations and were found to agree quite well.

3 Equivalent Single Degree of Freedom System (SDOF) for a Tuned Disk

In this paper, the system is said to be "tuned" if the dynamic properties of the disk, blades, and nonlinear elements are uniform throughout the structure. If, in addition, the excitation is the same except for a constant phase difference, ψ, between blades, then the amplitudes of the blades on the disk will be identical and have the same value as that of the SDOF system depicted in Fig. 4. The dynamic properties of the equivalent system are [18]

$$k_e = k_i + 4kC_i \sin^2(\psi/2) \tag{8}$$

$$kD_e = 4 \cdot kB_i \cdot \sin^2(\psi/2) \tag{9}$$

$$FS_e = FS_i \cdot 2 \cdot \sin(\psi/2) \tag{10}$$

Physically, the SDOF system responds in the following manner. If the slip load, FS_e, is sufficiently large, no slip occurs and the system resonates at the stuck natural frequency, $((k_e + kD_e)/m_i)^{1/2}$. If the slip load is zero, the system behaves as if the nonlinear element was not present and resonates at the free natural frequency, $(k_e/m)^{1/2}$. For intermediate values of FS_e, the nonlinear element slips and dissipates energy. Under these circumstances, the frequency at which it most strongly vibrates, ω_{res}, lies between the free and stuck natural frequencies, and its amplitude of vibration at ω_{res}, A_{res}, is lower. An objective in this type of analysis is to establish the optimum value of slip load, $FS_{e(opt)}$, which for a given level of excitation will minimize A_{res} (Fig. 6). A second goal is to calculate how much the vibration will be reduced under these circumstances, i.e., calculate R, where

Table 1 Nominal values of modal parameter (SI units)

m_i	=0.0114	kB_i	=18,900
k_i	=430,000	c_i	=1.381
kC_i	=45,430	f_o	=1.0

$$R = \frac{\text{Maximum Amplitude } FS_e = FS_{e(\text{opt})}}{\text{Resonant Amplitude } FS_e = 0} \tag{11}$$

The single degree of freedom system was analyzed in [13]. If the following dimensionless notation is introduced

$$\epsilon = kD_e/(k_e + kD_e) \tag{12}$$

$$\zeta = c/(2\, m_i (k_e + kD_e))^{1/2} \tag{13}$$

$$\chi = 2\pi\zeta/\epsilon \tag{14}$$

then it is found in [13] that reasonable approximations for the optimum slip load and the amplitude reduction factor are

$$(FS_e)_{\text{opt}} \cong \frac{1}{2} f_o \pi/(1+\chi) \tag{15}$$

and

$$R \cong \chi/(1+\chi) \tag{16}$$

for the small value of ϵ and ζ typically found in bladed disk structures.

From (10) and (15), the optimum slip load in the blade to blade system is approximately

$$FS_{i(\text{opt})} \cong \frac{1}{4} f_o \pi/[(1+x) \cdot \sin(\psi/2)] \tag{17}$$

Equations (16) and (17) will be used to approximate amplitude reduction and optimum slip load based on tuned system theory.

4 Simulation of Mistuned Bladed Disks With Friction Dampers

In this section, a study of mistuned bladed disks with friction dampers is reported. Blade-to-blade dampers have been used for years by the designers of gas turbine engines to reduce the vibratory stresses in turbine stages. They are pieces of metal that rest on the inboard side of the blade platforms (Fig. 1) and are held in place by the centrifugal force caused by engine rotation. Dampers hold the blades apart until the vibratory forces "squeezing" the dampers become larger than the slip load, that is, the centrifugally induced contact force multiplied by the coefficient of friction. When this value is exceeded, a damper slips and dissipates energy.

Dampers of this type are characterized dynamically by two features: (*i*) a nearly constant slip load, FS_i, for all dampers on the assembly and (*ii*) relatively small modal stiffness, kB_i. The slip load is constant because the contact pressure in the friction joint is proportional to the mass of the damper which does not vary significantly. As a result, the slip load, FS_i, is set to the same value, FS, for all of the simulations reported in this section. Second, since the modal displacement of the platform is usually small, the modal stiffness of the damper (which is proportional to the platform modal displacement squared [13]) is small compared with the modal stiffness, k_i, of the blade. It should be noted that neither of these faces is true in the case of part span shrouds reported in section 5.

The nominal values of mass, stiffnesses, viscous damping, and amplitude of excitation used in the simulation are given in Table 1 and are representative of a high-pressure turbine stage. The model is consistent with those used in [6] and [13].

The results of three types of studies are summarized in this section: (*i*) a baseline study on the influence of alternate mistuning, (*ii*) the influence of changing various model parameters on the response of a randomly mistuned 8-bladed disk, and (*iii*) a study of five randomly mistuned 8-bladed

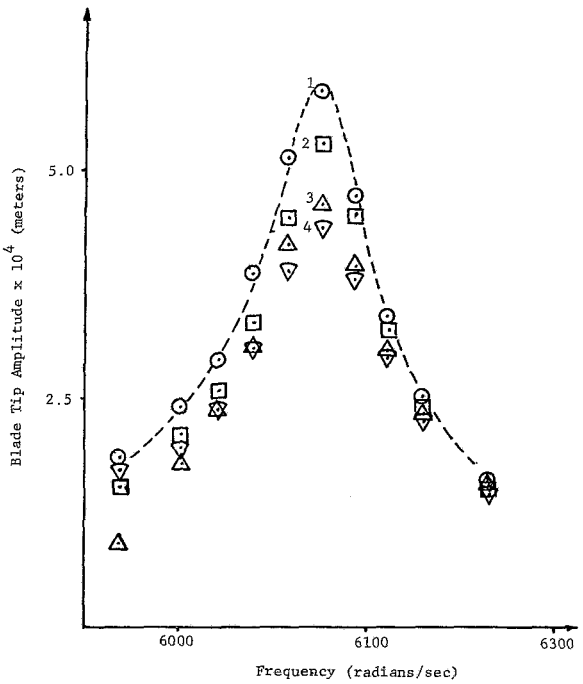

Fig. 5 Response of blades for $FS = 1.95$

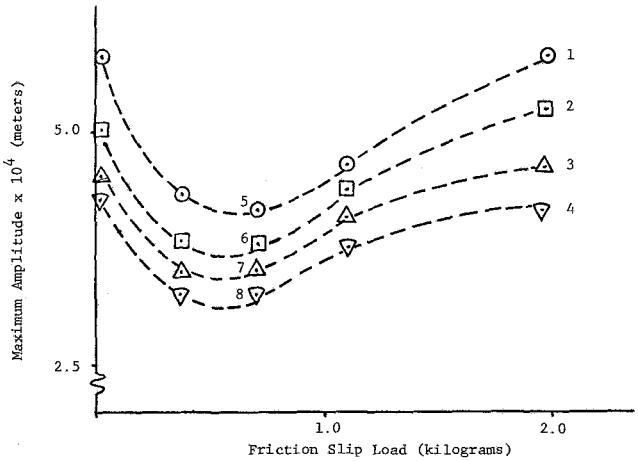

Fig. 6 Maximum response as a function of slip load, FS

disks the objective of which was to investigate the behavior of a distribution of blade amplitudes as well as the behavior of the highest response blade on any of the disks. For each of these cases, the amplitude reduction factor for the highest responding blade on the disk and an estimate of optimum value of slip load for the high response blade are reported and compared with values from tuned system theory, i.e., equations (16) and (17). The objective of this comparison is to establish to what extent the behavior of the blade most likely to fail, the high response blade, can be predicted and optimized by tuned system theory. Before these studies are discussed, an example of how the data were generated is given.

A model of an 8-bladed disk with random mistuning was constructed by varying the blade modal stiffness k_i around the disk (Disk 1 of Table 4). The stiffnesses were randomly selected from the statistical distribution described in [6], which was developed to reflect actual blade frequency data. The slip load, FS, in the model was fixed and the forced response of the system calculated over a frequency range that included the highest response of the system. For a case of a high slip load, the response of four representative blades is

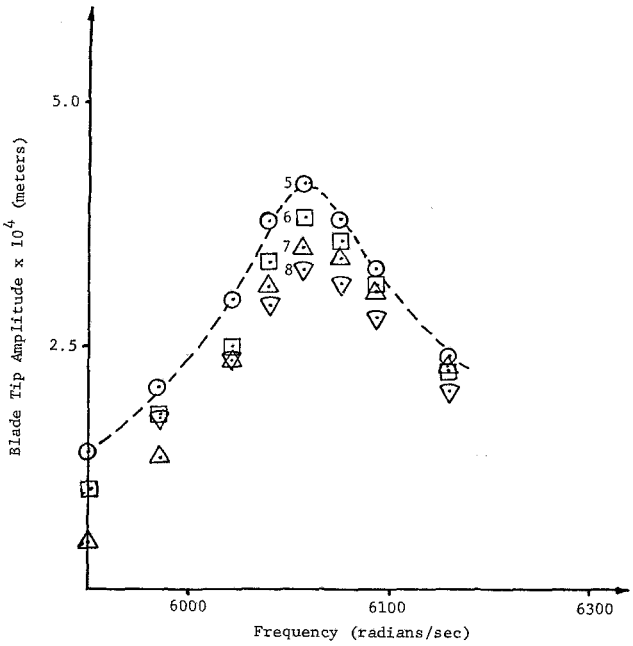

Fig. 7 Response of blades for $FS = 0.7$

Table 2 Summary of results for alternate mistuning

# of blades		6		8		12
$\Delta k/k_i$(%)	R	$FS_{(opt)}$	R	$FS_{(opt)}$	R	$FS_{(opt)}$
0	0.62	0.5-0.7	0.74	0.4-0.6	0.85	0.4-0.6
6.3	0.58	0.5-0.7	0.73	0.4-0.6	0.82	0.4-0.6
12.6	0.58	0.5-0.7	0.70	0.4-0.65	0.83	0.4-0.6
25.2	0.54	0.5-0.7	0.65	0.4-0.65	0.77	0.4-0.6
Eqs. (16,17)	0.60	0.63	0.72	0.57	0.82	0.56

depicted in Fig. 5. The values of maximum blade response, points 1, 2, 3, and 4, were noted and plotted on Fig. 6 as the peak response associated with the slip load, 1.95. The forced responses of the same blades for a slip load of 0.7 are depicted in Fig. 7 and the points of peak response, designated as 5, 6, 7, 8 are indicated. Figure 6 is typical of all such curves calculated in that near the optimum value of slip load the response is relatively flat. As a result, for a reasonable amount of computational effort the amplitude reduction ratio could be calculated relatively precisely while the optimum values of slip load could only be estimated to within approximately 20 percent. Because of the flatness of the curve, this resolution was judged adequate since anywhere within this range of FS the amplitude would not vary significantly.

In the case of alternate mistuning, identical high-frequency blades and identical low-frequency blades are placed in an alternating pattern around the disk. In this instance, the forced response of the bladed disk is characterized by only two amplitudes, that of the high- and of the low-frequency blades. The results for 6, 8, and 12 bladed disks with different amounts of mistuning are summarized in Table 2. Δk is the difference in stiffness between the blades. In all cases, the phase angle of the excitation is equal to $2\pi/N$, which corresponds to a first-order excitation. Under this type of excitation, increasing the number of blades is merely a device for decreasing the average interblade phase angle of the response. The results of Table 2 indicate that the influence of interblade phase angle is correctly accounted for by tuned system theory. It also indicates that the amount of alternate mistuning has little influence on either the amplitude reduction factor or the optimum slip load. This is an interesting result, since if it is assumed that interblade phase angle of the response is a constant equal to that of the excitation, variations in amplitude from blade to blade would

Table 3 Summary of results for randomly mistuned 8-bladed disk

$\frac{kC}{kC_{BL}}$	$\frac{C}{C_{BL}}$	$\frac{kB}{kB_{BL}}$	$\frac{\Delta\psi}{\Delta\psi_{BL}}$	$\frac{SDk}{SDk_{BL}}$	$FS_{(opt)}$	$FS_{opt}^{(tuned)}$	R	R^{tuned}
1	1	1	1	1	0.42-0.76	0.58	0.71	0.72
2	1	1	1	1	0.38-0.68	0.56	0.71	0.73
1	0.5	1	1	1	0.72-1.30	0.90	0.57	0.56
1	1	2	1	1	0.65-1.08	0.89	0.54	0.56
1	1	1	2	1	0.50-0.80	0.61	0.47	0.45
1	1	1	3	1	0.50-0.80	0.56	0.33	0.34
1	1	1	4	1	0.50-0.80	0.53	0.28	0.31
1	1	1	1	4	0.32-0.60	0.58	0.75	0.72

Table 4 Blade stiffnesses $\times 10^{-3}$

Disk No.	Blade number 1	2	3	4	5	6	7	8
1	433	445	437	427	432	413	424	428
2	421	424	429	441	452	427	430	416
3	429	426	422	430	430	439	429	435
4	451	425	432	417	418	432	434	431
5	423	426	429	420	425	452	428	436

Table 5 Ratios of slip loads

	Shroud number 1	2	3	4	5	6
Ratio	0.166	0.986	0.389	0.316	0.789	0.039

result in very different optimum slip load values for high response blades [25]. The simulations reported in this study indicate that while the phase difference between every second blade is $2 \cdot (2\pi/N)$, the phase jump is not equally distributed on both sides of a given blade, and this unequal phase shift manages to compensate for amplitude variations. As a result, it is observed that for alternate mistuning tuned system theory provides a reasonable estimate both of how much the amplitude will be reduced and at what value of slip load the damper is optimized.

The second case investigates the influence of model parameters on the dynamic response of a randomly mistuned 8-bladed disk. The results, summarized in Table 3, require a few comments for clarity. Modal parameters are ratioed to their baseline values of Table 1. *SDK* is the sample standard deviation of the blade stiffnesses, k_i, the baseline value in this case is 9350. Table 3 indicates that in every case simulated tuned theory approximated the dynamic behavior of the worst blade on the disk relatively well.

Third, the dynamic responses were calculated for five independently constructed randomly mistuned bladed disks having the blade stiffnesses indicated in Table 4. The results for all 40 blades are summarized by the distributions depicted in Fig. 8. It is interesting to note that the distribution of the blades when the dampers are active is more compact than when they are stuck even though there is more mechanical coupling under the latter conditions. Tuned theory predicts that the amplitude reduction ratio, R, should be 0.72 and that the dampers should be optimized at a slip load of 0.57. In fact, the worst blade on any of the disks had an R value of 0.69 and an optimum value of slip load between 0.5 and 0.8.

In summary, for the cases of mistuning studied, equations (16) and (17), which were developed from tuned system theory, provide a reasonable estimate of to what extent the amplitudes of high response blades can be reduced by friction dampers as well as at what value of slip load the system is optimized.

5 Simulation of a Mistuned Bladed Disk With a Part Span Shroud

The blades on fan stages with part span shrouds are connected by nonlinear structural elements that are in several important respects quite different from the turbine blade

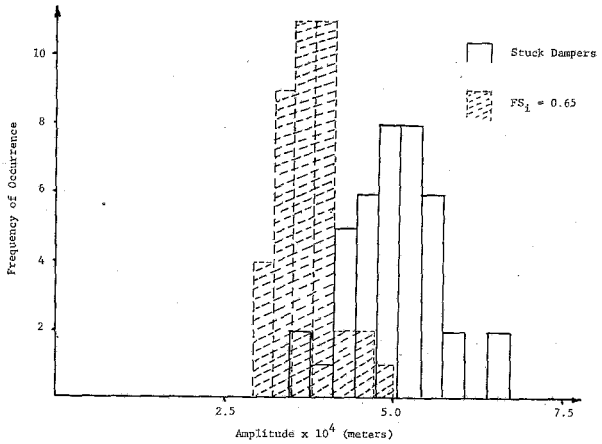

Fig. 8 Amplitude distributions for stuck and optimized dampers

dampers discussed in the last section. Their slip load can vary significantly from one shroud interface to another. Second, the modal stiffness, k_i, of the shrouds is significantly larger and, as a result has more impact on the dynamic response. Last, because of the nature of the shroud geometry, the contact pressure across the friction interface may have a dynamic component as well as a static value and as a result the slip load can vary dynamically during a cycle.

Shrouded fan blades are designed to take advantage of the blade untwist that occurs with increased engine rpm. The shrouds are angled metal protrusions on the airfoil whose surfaces make contact with those of the neighboring blade as the airfoil sections rotate. Because of minor variations in blade geometries, a blade will come in contact first with only one of its neighbors, preferentially loading that contact surface. Since the slip load for that friction interface is proportional to the contact pressure they can vary widely from shroud interface to shroud interface. This effect will be simulated by varying FS_i from element to element in the model. The ratios of FS_i used in the 6-bladed disk are given in Table 5. Their average value is varied to represent changes in shroud tightness.

Second, because the shrouds are physically stiffer than the friction dampers and because they are located at a more outboard position on the blade, their modal stiffnesses are greater than that of the turbine blade dampers. This effect is modeled by using significantly larger values of kB_i (kB_i = 93,500) than in the case of the turbine blades of section 4. A second effect of stiff shrouds is that the mode shape of the blades changes significantly from when they are fully slipping to when they are fully stuck. A single-mode model of the blade can correspond to either the fully slipping modal values of mass, stiffness, etc., or the fully stuck values [13] and, in fact, if these two sets of modal properties do not differ very much (the case for many turbine blades with friction dampers) either expansion provides an accurate quantitative model over the full range of possible slip loads. However, this is not the

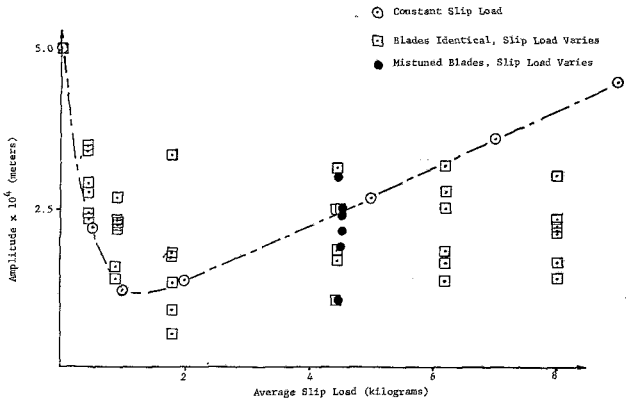

Fig. 9 Response of a stage with part span shrouds

case for shrouds, and consequently, the results of this section are quantitatively correct only over a limited range of slip load, and either underestimates the nonlinear effects if the stuck modal values are used or overestimates them if the free values are used.

Last, as the blades vibrate their relative motion alters the normal load on the shroud interface and causes the slip load to vary dynamically during the cycle. This is true for shrouds but not turbine blade dampers because for shrouded fan blades the blade's motions are not parallel to the plane of the friction interface (which they are in the case of most turbine blade dampers). Consequently, the model used in this study which does not take variable slip load into account is quantitatively correct only for small motions in systems with high centrifugally induced normal loads, since in these cases the percentage error in neglecting the dynamic variation in slip load is small. For this reason and because of the problem associated with changes in mode shape that were discussed in the last paragraph, the results discussed in this section for the simple spring-mass friction model should be considered similar to that of a shrouded fan only if the modal parameters used are the same as for a fan stage with stuck shrouds and then only for high values of slip load.

The simulations discussed in this section were inspired by the outcome of recent experiments performed on "tuned" and "mistuned" shrouded fan stages at the United Technologies Research Center in East Hartford, Connecticut. A set of blades were tuned in the sense that each blade had very similar natural frequencies. When tested as an assembly, however, they exhibited just as wide a scatter of responses as did the purposely mistuned disk. Srinivasan [26] deduced that this must be caused by uncontrolled variations in slip load. The objective of this section is to see to what extent this type of result can be reproduced analytically.

Unless noted, modal parameters were the same as those given in Table 1. Three cases were calculated: (*i*) a baseline tuned system, (*ii*) a system which is tuned except for random variations in slip load, (*iii*) a system with blade mistuning and with random variations in slip load. Cases (*ii*) and (*iii*) were meant to roughly correspond to Dr. Srinivasan's experiments. The results for a 6-bladed disk are presented in Fig. 9. The dashed line linking the open circles is the response of a perfectly tuned system. The squares represent the amplitudes of the six blades when the slip load varies in a random fashion from shroud to shroud. In this plot, the ratios of slip loads around the disk are kept constant (Table 5) and the average value, *FS*, is varied over a range of values. In this case, it is clear that tuned system theory provides only a gross estimate of the actual response of this type of mistuned system. *FS* equal to 4.5 was taken as representative of a relatively tight shroud such as might be found in practice and random variations in k_i were introduced as well. The amount of stiffness mistuning incorporated was approximately the same as that used in the randomly mistuned turbine blade model of the previous section and would induce an amplitude scatter of roughly 50 percent if the system was linear. The results are indicated by the solid circles in Fig. 9. Several results are worth noting. Most of the blade amplitudes changed very little, less than 10 percent, when blade mistuning was introduced, with only one blade changing significantly (43 percent increase). In fact, what would be thought of as increasing mistuning resulted in a lower value of amplitude on the highest responsing blade. These data would tend to corroborate Dr. Srinivasan's experience in that the key parameter in shrouded fan blade mistuning may not be variations in individual blade frequencies but variations in shroud contact pressures.

6 Conclusions

Studies were conducted in which the response of mistuned bladed disks with blade to blade friction dampers and the response of mistuned fan stages with part span shrouds were simulated.

In the case of friction dampers, the amplitude reduction ratio and the optimum value of friction slip force for the worst blade on the disk were calculated for a variety of situations and did not differ significantly from those calculated from tuned system theory, equations (16) and (17). This suggests that from a practical point of view mistuning may not need to be directly considered in their design. It probably does need to be considered indirectly, however, in correctly establishing the generalized force (f_o in Fig. 3) acting on the stage [6]. This inference is based only on the limited simulations discussed in this paper and needs to be confirmed by more extensive studies of this type which represent a wider variety of hardware configurations.

In the simulation of a fan stage with part span shrouds, it was found that mistuning induced by variations in shroud slip loads could dominate the response of the system to such an extent that adding conventional blade mistuning had little effect on the dynamic behavior of the assembly and, in fact, caused the response of the worst blade on the disk to slightly decrease in amplitude.

7 Acknowledgments

The authors wish to thank Mr. Brian Van Mook for his help in performing some of the many numerical simulations that were the basis for data presented in this paper. The authors also wish to thank Dr. A. V. Srinivasan for his stimulating remarks concerning his recent experimental results. This work was supported by NASA Grant NAG-3-231.

References

1 Wagner, J. T., "Coupling of Turbomachine Blade Vibrations Through the Rotor," ASME JOURNAL OF ENGINEERING FOR POWER, Vol. 89, Oct. 1967, pp. 502-513.

2 Armstrong, E. K., and Stevenson, R. E., "Some Practical Aspects of Compressor Blade Vibration," *Journal of the Royal Aeronautical Society*, Vol. 64, No. 591, Mar. 1960, pp. 117-130.

3 Whitehead, D. S., "Effect of Mistuning on the Vibrations of Turbomachine Blades Induced by Wakes," *Journal of Mechanical Science*, Vol. 8, No. 1, Mar. 1966, pp. 15-21.

4 Edwins, D. J., "The Effects of Detuning Upon the Forced Vibrations of Bladed Disks," *Journal of Sound Vibration*, Vol. 9, 1969, pp. 65-79.

5 Ewins, D. J., "A Study of Resonance Coincidence in Bladed Disks," *Journal of Mechanical Engineering Science*, Vol. 12, No. 5, 1970.

6 Griffin, J. H., and Hoosac, T. M., "Model Development and Statistical Investigation of Turbine Blade Mistuning," to be presented at the 9th Biennial Design Conference on Mechanical Vibration and Noise, Dearborn, Michigan, Sept. 1983.

7 Dye, R. C. F., and Henry, T. A., "Vibration Amplitudes of Compressor

Blades Resulting from Scatter in Blade Natural Frequencies," ASME JOURNAL OF ENGINEERING FOR POWER, Vol. 91, 1969, p. 182.

8 Ewins, D. J., "Vibration Characteristics of Bladed Disk Assemblies," *Journal of Mechanical Engineering Sciences*, Vol. 15, No. 3, 1973.

9 Srinivasan, A. V., and El-Bayoumy, L. E., "The Effect of Mistuning on Rotor Blade Vibration," *AIAA Journal*, Vol. 13, April 1975, pp. 460–464.

10 Huang, Wen-hu, "Vibration of Some Structures With Periodic Random Structures," *AIAA Journal*, Vol. 20, No. 7, July 1982.

11 Sogliero, G., and Srinivasan, A. V., "Fatigue Life Estimates of Mistuned Blades Via a Stochastic Approach," *AIAA Journal*, Vol. 18, No. 3, pp. 318–323.

12 Kaza, K. R. V., and Kielb, R. E., "Effects of Mistuning on Bending-Torsion Flutter and Response of a Cascade in Incompressible Flow," AIAA Paper No. 81-0532 presented at the AIAA Dynamics Specialists Conference, Atlanta, Ga., Apr. 8–10, 1981 (DOE/NASA/1028-29; NASA TM-81674); scheduled for publication in the *AIAA Journal*, Aug. or Sept. 1982.

13 Griffin, H. J., "Friction Damping of Resonant Stresses in Gas Turbine Engine Airfoils," ASME JOURNAL OF ENGINEERING FOR POWER, Apr. 1980, Vol. 102, pp. 329–333.

14 Muszynska, A., and Jones, D. I. G., "On Tuned Bladed Disk Dynamics: Some Aspects of Friction Related Mistuning," *Journal of Sound and Vibration*, Vol. 86, No. 1, 1983, pp. 107–128.

15 Muszynska, A., and Jones, D. I. G., "A Parametric Study of Dynamic Response of a Discrete Model of Turbomachinery Bladed Disk," ASME 81-DET-137, presented at the Design Engineering Technical Conference, Sept. 20–23, 1981, Hartford, Conn.

16 Sinha, A., and Griffin, J. H., "Effects of Static Friction on the Forced Response of Frictionally Damped Turbine Blades," ASME Paper No. 83-GT-155, presented at the 28th International Gas Turbine Conference, Phoenix, Ariz., Mar. 27–31, 1983.

17 Sinha, A., and Griffin, J. H., "Friction Damping of Flutter in Gas Turbine Engine Airfoils," *Journal of Aircraft*, Vol. 20, No. 4, Apr. 1983, p. 372.

18 Sinha, A., and Griffin, J. H., "Effects of Friction Dampers on Aerodynamically Unstable Rotor Stages," AIAA Paper No. AIAA-83-0848-CP, presented at the 24th Annual SDM Conference, Lake Tahoe, May 1983.

19 Timoshenko, S., and Young, D. H., "Systems With Nonlinear and Variable Spring Characteristics," *Vibration Problems in Engineering*, 3d ed., Van Nostrand, New York, 1964, pp. 163–168.

20 Caughey, T. K., "Sinusoidal Excitation of a System with Bilinear Hysteresis," ASME *Journal of Applied Mechanics*, Vol. 27, Dec. 1960, pp. 640–643.

21 Chikwendu, S. C., and Kevorkian, J., "A Perturbation Method for Hyperbolic Equations with Small Nonlinearities," SIAM *Journal of Applied Mathematics*, Vol. 22, No. 2, Mar. 1972, pp. 235–258.

22 Menq, C., and Griffin, J. H., "A Comparison of Transient and Steady-State Finite Element Analyses of the Forced Response of a Frictionally Damped Beam," to be presented at the 9th Biennial Design Conference on Mechanical Vibration and Noise, Dearborn, Mich., Sept. 1983.

23 Plunkett, R., *Damping Applications for Vibration Control*, AMD-Vol. 38, (edited by P. J. Torvik), ASME, New York, 1980, pp. 65–74.

24 IMSL Library Reference Manual, 9th ed., Vol. 4, INSL, Inc.

25 Griffin, J. H., "An Analytical Comparison of Blade-to-Blade and Blade-to-Ground Dampers for Use in Gas Turbine Engines," *Proceedings of the Eight Canadian Congress of Applied Mechanics*, 1981, p. 405.

26 Srinivasan, A. V., "private communications."

Transient Thermal Stresses in a Reinforced Hollow Disk or Cylinder Containing a Radial Crack

Renji Tang[1]

F. Erdogan

Lehigh University,
Department of Mechanical Engineering
and Mechanics,
Bethlehem, Pa. 18015

In this paper, the transient thermal stress problem in a hollow cylinder or a disk containing a radial crack is considered. It is assumed that the cylinder is reinforced on its inner boundary by a membrane which has thermoelastic constants different than those of the base material. The transient temperature, thermal stresses, and the crack tip stress intensity factors are calculated in a cylinder which is subjected to a sudden change of temperature on the inside surface. The results are obtained for various dimensionless parameters and material constants. The special cases of the crack terminating at the cylinder-membrane interface and of the broken membrane are separately considered and some examples are given.

1 Introduction

Cracking due to thermal stresses arises in many practical applications particularly when sudden changes occur in the environmental temperature. Suddenly cooled glass plates and containers are generally the familiar examples for the phenomenon. The problem may also be quite important in such structural components as the pressure vessels, piping, and hollow circular disks subjected to thermal transients. In these structures the actual problems are usually very complicated three-dimensional crack problems. Under thermal shock, a part-through crack may initiate or an existing part-through crack may propagate in axial or circumferential as well as in the thickness direction. However, if the crack driving force due to mechanical stresses is sufficiently small, then because of the self-equilibrating nature of the thermal stresses and of the fracture toughness gradient, the growth of the crack in thickness direction is generally arrested. A clear demonstration of this process may be seen in the results reported in [1], where it was observed that in relatively thick-walled hollow circular glass cylinders suddenly cooled from inside an axial initial crack penetrated into the cylinder wall only partially but propagated axially along the entire length of the cylinder. It is clear that in such problems the corresponding plane strain or plane stress solutions may provide very useful bounds for the actual part-through crack problem.

The axisymmetric problem for a thick-walled cylinder containing a part-through circumferential crack and subjected to transient thermal stresses was considered in [2]. In this paper we consider the corresponding plane strain or plane stress problem for a hollow circular cylinder that contains a radial crack. To simulate the cladding (in, for example, nuclear pressure vessels), it is assumed that the cylinder is reinforced on the inside boundary by a (thin) membrane. The results found may also be applicable to other composite cylinders or disks in which the thickness of the inner cylinder or ring is relatively very small.

In solving the problem, it is assumed that the material is linear, the thermo-mechanical constants of the cylinder and the reinforcing membrane are independent of temperature, the bending stiffness of the reinforcing membrane and all thermoelastic coupling effects are negligible, and the transient thermal stress problem may be treated as a quasi-static, time-dependent problem, that is, all inertia effects may be neglected. Previous studies on dynamic thermoelasticity indicate that this last assumption, which simplifies the analysis of the problem quite considerably, would not cause any significant changes in the results (see, for example, [3] and [4]). Since the problem is linear, the solution of the crack

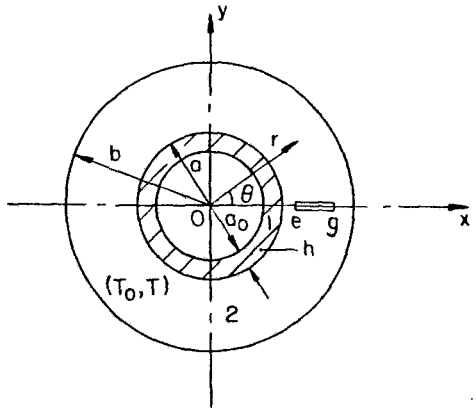

Fig. 1 The geometry of the reinforced cylinder containing a radial crack

[1] Visiting Scholar. Permanent address: Associate Professor, Department of Mathematics and Mechanics, Lanzou University, China.

Contributed by the Gas Turbine Division of THE AMERICAN SOCIETY OF MECHANICAL ENGINEERS and presented at the 29th International Gas Turbine Conference and Exhibit, Amsterdam, The Netherlands, June 4–7, 1984. Manuscript received at ASME Headquarters January 9, 1984. Paper No. 84-GT-148.

problem due to thermal stresses and to all other sources of loading may be considered separately. Also, the solution of the crack problem under thermal stresses may be obtained in two steps. The first would be the calculation of time-dependent thermal stresses in an uncracked reinforced cylinder under given temperature and stress boundary conditions. Then the second step would be the solution of an isothermal crack problem in which the self-equilibrating crack surface tractions equal and opposite to that obtained in the first solution are the only external loads. The complete solution may be obtained by adding these last two solutions to the other isothermal results. Needless to say, in thermal stress, as well as in the isothermal problems, the important information that is useful in fracture considerations is contained in the perturbation solutions.

2 The Thermal Stresses

Referring to Fig. 1 for notation, let the temperatures in reinforcing and main cylinders be T_1 and T_2, respectively. If we assume that the crack surfaces are well-insulated, then T_1 and T_2 would be functions of radial coordinate r and the time t only. Let T_0 be the initial temperature of the composite cylinder and the temperature changes θ_1 and θ_2 be defined by

$$\theta_1(r,t) = T_1(r,t) - T_0, (a_0 < r < a, 0 \le t) \tag{1}$$

$$\theta_2(r,t) = T_2(r,t) - T_0, (a < r < b, 0 \le t) \tag{2}$$

In the case of uncracked cylinders, the problem is axisymmetric, the shear stresses are zero, and the relevant displacement and stress components may be expressed as follows (see, for example, [5])

$$u_{ri}^T(r,t) = \frac{1+\nu_i}{1-\nu_i}\frac{\alpha_i}{r}\int_{a_i}^{r}\theta_i(\rho,t)\rho d\rho + C_{1i}r + \frac{C_{2i}}{r} \tag{3}$$

$$\sigma_{ri}^T(r,t) = -\frac{\alpha_i E_i}{1-\nu_i}\frac{1}{r^2}\int_{a_i}^{r}\theta_i(\rho,t)\rho d\rho + \frac{E_i}{1+\nu_i}\left(\frac{C_{1i}}{1-2\nu_i} - \frac{C_{2i}}{r^2}\right) \tag{4}$$

$$\sigma_{\theta i}^T(r,t) = \frac{\alpha_i E_i}{1-\nu_i}\frac{1}{r^2}\int_{a_i}^{r}\theta_i(\rho,t)\rho d\rho - \frac{E_i\alpha_i}{1-\nu_i}\theta_i(r,t) + \frac{E_i}{1+\nu_i}\left(\frac{C_{1i}}{1-2\nu_i} + \frac{C_{2i}}{r^2}\right) \tag{5}$$

where $i=1,2$,

$a_i = a_0, a_0 < r < a$, for $i=1$

$a_i = a, a < r < b$, for $i=2$

α_i, E_i, and ν_i are the standard thermoelastic constants of the materials, u_{ri}^T is the radial displacement, and the unknown constants C_{1i} and C_{2i} are determined from the following boundary and continuity conditions

$$\sigma_{r1}^T(a_0,t) = 0; \sigma_{r2}^T(b,t) = 0 \tag{6a,b}$$

$$u_{1r}^T(a,t) = u_{2r}^T(a,t); \sigma_{r1}^T(a,t) = \sigma_{r2}^T(a,t) \tag{7a,b}$$

Thus, from (3), (4), (6), and (7), it can be shown that

$$C_{11} = \frac{1-2\nu_1}{a_0^2}\frac{\Delta_1}{\Delta_0}; C_{12} = \frac{\Delta_1}{\Delta_0};$$

$$C_{21} = \frac{\alpha_2(1+\nu_2)(1-2\nu_2)B}{(1-\nu_2)b^2} + \frac{1-2\nu_2}{b^2}\frac{\Delta_2}{\Delta_0};$$

$$C_{22} = \frac{\Delta_2}{\Delta_0} \tag{8a-d}$$

where

$$\Delta_0 = -\frac{E_2(a^2-b^2)[(1-2\nu_1)a^2+a_0^2]}{(1+\nu_2)a_0^2a^4b^2} + \frac{E_1(a^2-a_0^2)[(1-2\nu_2)a^2+b^2]}{(1+\nu_1)a_0^2a^4b^2};$$

$$\Delta_1 = -\frac{E_2(a^2-b^2)}{(1-\nu_1)(1-\nu_2^2)a^4b^4}\cdot[-(1+\nu_1)(1-\nu_2)\alpha_1 b^2 A + (1-\nu_1)(1+\nu_2)(1-2\nu_2)\alpha_2 a^2 B] + \frac{[\alpha_2E_2a^2(1-\nu_1)B + \alpha_1E_1b^2(1-\nu_2)A][(1-2\nu_2)a^2+b^2]}{(1-\nu_1)(1-\nu_2)a^4b^4};$$

$$\Delta_2 = \frac{[(1-2\nu_1)a^2+a_0^2][\alpha_2E_2a^2(1-\nu_1)B + \alpha_1E_1b^2(1-\nu_2)A]}{(1-\nu_1)(1-\nu_2)a_0^2a^4b^2} + \frac{E_1(a^2-a_0^2)}{(1-\nu_1^2)(1-\nu_2)a_0^2a^4b^2}\cdot[(1+\nu_1)(1-\nu_2)\alpha_1b^2A - (1-\nu_1)(1+\nu_2)(1-2\nu_2)\alpha_2a^2B];$$

$$A = \int_{a_0}^{a}\theta_1(r,t)r\,dr; B = \int_{a}^{b}\theta_2(r,t)r\,dr \tag{9a-e}$$

It should be noted that the expressions (3-5), (8), and (9) are valid for the case of plane strain only. For "disk" problems, which may be approximated by generalized plane stress, E_i and ν_i should be replaced by $E_i(1+2\nu_i)/(1+\nu_i)^2$ and $\nu_i/(1+\nu_i)$, respectively.

To obtain the temperature distributions θ_1 and θ_2, the following diffusion equations must be solved under given initial and boundary conditions

$$\nabla^2\theta_i(r,t) = \frac{1}{D_i}\frac{\partial\theta_i(r,t)}{\partial t}, (i=1,2) \tag{10}$$

where $a_0 < r < a$ for $i=1$, $a < r < b$ for $i=2$ and D_1 and D_2 are the respective coefficients of diffusivity. A particular problem of interest is the sudden cooling of the composite cylinder from inside which is initially under a homogeneous temperature T_0. Thus, if it is assumed that for $t>0$ the cylinder wall $r=a_0$ is maintained at a constant temperature T_{a0} and the outer surface $r=b$ is insulated, (10) must be solved under

$$\theta_1(r,0) = 0, (a_0 < r < a) \tag{11}$$

$$\theta_2(r,0) = 0, (a < r < b) \tag{12}$$

$$\theta_1(a,t) - \theta_2(a,t); k_1\frac{\partial}{\partial r}\theta_1(a,t) = k_2\frac{\partial}{\partial r}\theta_2(a,t), (0 < t) \tag{13a,b}$$

$$\theta_1(a_0,t) = \theta_{a0}H(t); \frac{\partial}{\partial r}\theta_2(b,t) = 0 \tag{14a,b}$$

where

$$\theta_{a0} = T_{a0} - T_0, \tag{15}$$

k_1 and k_2 are the coefficients of heat conduction and $H(t)$ is the Heaviside function. By using the Laplace transforms, the solution of (10) subject to (11-14) may be obtained as follows

$$\frac{\theta_1(r^*,t^*)}{\theta_{a0}} = 1 - \sum_{1}^{\infty}\frac{2e^{-\lambda_n^2t^*}}{a^*\lambda_nH^*(\lambda_n)}[\kappa_0\beta Z_{00}(a^*\lambda_n, r^*\lambda_n)Z_{11}(\beta a^*\lambda_n, \beta\lambda_n) + Z_{01}(\beta a^*\lambda_n, \beta\lambda_n)Z_{01}(r^*\lambda_n, a^*\lambda_n)], \tag{16}$$

$$\frac{\theta_2(r^*,t^*)}{\theta_{a0}} = 1 + \frac{4}{\pi} \sum_1^\infty \frac{Z_{01}(\beta r^* \lambda_n, \beta\lambda_n)\, e^{-\lambda_n^2 t^*}}{a^{*2}\lambda_n^2 H^*(\lambda_n)} \tag{17}$$

where the cylinder functions and the dimensionless quantities are defined by

$$Z_{ij}(x,y) = J_i(x)\, Y_j(y) - Y_i(x) J_j(y), (i,j = 0,1) \tag{18}$$

$$r^* = r/b, a_0^* = a_0/b, a^* = a/b, t^* = D_1 t/b^2,$$

$$\beta = (D_1/D_2)^{1/2}, \kappa_0 = k_2/k_1 \tag{19}$$

$$\begin{aligned} H^*(\lambda_n) = {} & \kappa_0 \beta^2 Z_{00}(a_0^* \lambda_n, a^* \lambda_n)[Z_{01}(\beta a^* \lambda_n, \beta\lambda_n) \\ & - \frac{1}{a^*} Z_{01}(\beta\lambda_n, \beta a^* \lambda_n)] \\ & + Z_{01}(\beta a^* \lambda_n, \beta\lambda_n)[-Z_{00}(a_0^* \lambda_n, a^* \lambda_n) \\ & + \frac{a_0^*}{a^*} Z_{11}(a_0^* \lambda_n, a^* \lambda_n)] \\ & - \beta\kappa_0 Z_{11}(\beta\lambda_n, \beta a^* \lambda_n)[-Z_{01}(a_0^* \lambda_n, a^* \lambda_n) \\ & + \frac{a_0^*}{a^*} Z_{01}(a^* \lambda_n, a_0^* \lambda_n)] \\ & + \beta Z_{01}(a_0^* \lambda_n, a^* \lambda_n)[-Z_{11}(\beta\lambda_n, \beta a^* \lambda_n) \\ & + \frac{1}{a^*} Z_{00}(\beta\lambda_n, \beta a^* \lambda_n)] \end{aligned} \tag{20}$$

λ_n are the roots of

$$\begin{aligned} & \beta\kappa_0 Z_{00}(a_0^* \lambda_n, a^* \lambda_n) Z_{11}(\beta\lambda_n, \beta a^* \lambda_n) \\ & + Z_{01}(\beta a^* \lambda_n, \beta\lambda_n) Z_{01}(a_0^* \lambda_n, a^* \lambda_n) = 0 \end{aligned} \tag{21}$$

and J_n and Y_n are the Bessel functions of first and second kind, respectively.

The thermal stresses in the composite cylinder without the crack may be obtained by substituting from (16) and (17) into (4) and (5). For example, the hoop stresses $\sigma_{\theta 1}$ and $\sigma_{\theta 2}$ that are needed in the solution of the crack problem are found to be

$$\sigma_{\theta 1}^T(r^*,t^*) = \frac{\alpha_1 E_1 \theta_{a0}}{1-\nu}\left[\frac{F_i(r^*)}{r^{*2}} - \frac{\theta_1(r^*,t^*)}{\theta_{a0}} + \frac{r^{*2} + a_0^{*2}}{r^{*2}} S_1\right] \tag{22}$$

$$\sigma_{\theta 2}^T(r^*,t^*) = \frac{\alpha_2 E_2 \theta_{a0}}{1-\nu}\left[\frac{F_2(r^*)}{r^{*2}} - \frac{\theta_2(r^*,t^*)}{\theta_{a0}} + F_2(1) + \frac{\alpha_1(1+r^{*2})}{\alpha_2 r^{*2}} S_2\right] \tag{23}$$

where

$$\begin{aligned} F_1(r^*) = {} & \int_{a_0^*}^{r^*} \frac{\theta_1(r^*,t^*)}{\theta_{a0}} r^* dr^* = \frac{r^{*2} - a_0^{*2}}{2} \\ & - \sum_1^\infty \frac{2e^{-\lambda_n^2 t^*}}{a^* \lambda_n^2 H^*(\lambda_n)} \\ & \cdot \{\kappa_0 \beta Z_{11}(\beta a^* \lambda_n, \beta\lambda_n)[r^* Z_{01}(a^* \lambda_n, r^* \lambda_n) \\ & - a_0^* Z_{01}(a^* \lambda_n, a_0^* \lambda_n)] \\ & + Z_{01}(\beta a^* \lambda_n, \beta\lambda_n)[r^* Z_{11}(r^* \lambda_n, a^* \lambda_n) \\ & - a_0^* Z_{11}(a_0^* \lambda_n, a^* \lambda_n)]\}, \end{aligned}$$

$$\begin{aligned} F_2(r^*) = {} & \int_{a^*}^{r^*} \frac{\theta_2(r^*,t^*)}{\theta_{a0}} r^* dr^* = \frac{r^{*2} - a^{*2}}{2} \\ & + \frac{4}{\pi} \sum_1^\infty \frac{e^{-\lambda_n^2 t^*}}{\beta a^{*2} \lambda_n^3 H^*(\lambda_n)} \\ & \cdot [r^* Z_{11}(\beta r^* \lambda_n, \beta\lambda_n) - a^* Z_{11}(\beta a^* \lambda_n, \beta\lambda_n)], \end{aligned}$$

$$\begin{aligned} S_1 = {} & \frac{[(1-2\nu)a^{*2} + 1]\left[\frac{\alpha_2 E_2}{\alpha_1 E_1} a^{*2} F_2(1) + F_1(a^*)\right]}{(a^{*2} - a_0^{*2})[(1-2\nu)a^{*2} + 1] - \frac{E_2}{E_1}(a^{*2} - 1)[(1-2\nu)a^{*2} + a_0^{*2}]} \\ & + \frac{\frac{E_2}{E_1}(a^{*2} - 1)[F_1(a^*) - (1-2\nu)\frac{\alpha_2}{\alpha_1} a^{*2} F_2(1)]}{(a^{*2} - a_0^{*2})[(1-2\nu)a^{*2} + 1] - \frac{E_2}{E_1}(a^{*2} - 1)[(1-2\nu)a^{*2} + a_0^{*2}]}, \end{aligned}$$

$$\begin{aligned} S_2 = {} & \frac{[(1-2\nu)a^{*2} + a_0^{*2}]\left[\frac{\alpha_2 E_2}{\alpha_1 E_1} a^{*2} F_2(1) + F_1(a^*)\right]}{(a^{*2} - a_0^{*2})[(1-2\nu)a^{*2} + 1] - \frac{E_2}{E_1}(a^{*2} - 1)[(1-2\nu)a^{*2} + a_0^{*2}]} \\ & + \frac{(a^{*2} - a_0^{*2})\left[F_1(a^*) - (1-2\nu)\frac{\alpha_2}{\alpha_1} a^{*2} F_2(1)\right]}{(a^{*2} - a_0^{*2})[(1-2\nu)a^{*2} + 1] - \frac{E_2}{E_1}(a^{*2} - 1)[(1-2\nu)a^{*2} + a_0^{*2}]} \end{aligned} \tag{24a-d}$$

and, for simplicity, it is assumed that $\nu_1 = \nu_2 = \nu$.

If one further assumes that $E_1 = E_2 = E$ as well as $\nu_1 = \nu_2 = \nu$ (i.e., that the elastic constants but not the thermal coefficients of the two cylinders are the same), then the expressions for hoop stresses are further simplified and become

$$\sigma_{\theta 1}^T(r,t) = \frac{E}{1-\nu}\frac{1}{r^2}\left\{\frac{r^2+a_0^2}{b^2-a_0^2}\left[\alpha_1\int_{a_0}^{a}\theta_1(r,t)\,rdr + \alpha_2\int_a^b\theta_2(r,t)\,rdr\right] + \alpha_1\int_{a_0}^{r}\theta_1(r,t)\,rdr - \alpha_1 r^2\theta_1(r,t)\right\} \tag{25}$$

$$\sigma_{\theta 2}^T(r,t) = \frac{E}{1-\nu}\frac{1}{r^2}\left\{\frac{r^2+a_0^2}{b^2-a_0^2}\left[\alpha_1\int_{a_0}^{a}\theta_1(r,t)\,rdr + \alpha_2\int_a^b\theta_2(r,t)\,rdr\right] + \alpha_1\int_{a_0}^{a}\theta_1(r,t)\,rdr + \alpha_2\int_a^r\theta_2(r,t)\,rdr - \alpha_2 r^2\theta_2(r,t)\right\} \tag{26}$$

If the thickness $a-a_0$ of the inner cylinder is indeed very small, then the analysis given in this section may be simplified quite considerably by using the indentities

$$Z_{00}(x,x)=0, Z_{11}(x,x)=0, Z_{01}(x,x)=-\frac{2}{\pi x} \tag{27}$$

In this case, the characteristic equation (21) giving the roots λ_n may be approximated by

$$Z_{01}(\beta a^*\lambda_n, \beta\lambda_n)=0 \tag{28}$$

An interesting special case of the thermal shock problem under consideration would be the yielding of the inner cylinder that may occur if the step change θ_{a0} in the inner wall temperature is sufficiently high. The limiting value $\theta_F=\theta_{a0}$ that corresponds to the yielding of the membrane cladding may be obtained from (22) by letting

$$\sigma_{\theta 1}^T(a^*,+0)=\sigma_F \tag{29}$$

where σ_F is a measure of the yield condition of the material (e.g., the flow stress).

For the very thin inner cylinder previously mentioned, it can be shown that

$$H^*(\lambda_n)\cong\frac{2\beta}{\pi a^*\lambda_n}\left[Z_{11}(\beta\lambda_n,\beta a^*\lambda_n)-\frac{1}{a^*}Z_{00}(\beta\lambda_n,\beta a^*\lambda_n)\right], \quad F_1(a^*)\cong 0, \theta_1(a^*,t^*)\cong\theta_{a0} \tag{30}$$

and from (29), we find

$$\theta_F = -\frac{(1-\nu)\sigma_F}{\alpha_1 E_1} \tag{31}$$

3 The Crack Problem

The thermal stress problem for a composite cylinder containing an axial crack in a radial plane (Fig. 1) may now be solved by using the equal and opposite of the hoop stress given by (23) as the crack surface traction. As shown in [6], this problem must be solved under the following boundary conditions

$$\sigma_{rr}(b,\theta,t)=0; \sigma_{r\theta}(b,\theta,t)=0, (0\le\theta\le 2\pi, 0<t) \tag{32a,b}$$

$$\sigma_{rr}(a,\theta,t)-\lambda\sigma_{\theta\theta}(a,\theta,t)=0, (0\le\theta<2\pi, 0<t) \tag{33}$$

$$\sigma_{r\theta}(a,\theta,t)+\lambda\frac{\partial}{\partial\theta}\sigma_{\theta\theta}(a,\theta,t)=0, (0\le\theta<2\pi, 0<t) \tag{34}$$

$$\sigma_{\theta\theta}(r,+0,t)=\sigma_{\theta\theta}(r,-0,t)=-\sigma_{\theta 2}^T(r,t), (e<r<g, 0<t) \tag{35a}$$

$$u_\theta(r,0,t)=0, (a<r<e, g<r<b, 0<t) \tag{35b}$$

where σ_{ij}, $(i,j=r,\theta)$ and u_θ are the stresses and the circumferential displacement in cylinder 2 for the perturbation problem and

$$\lambda=\begin{cases}\left(1-\dfrac{a_0}{a}\right)E_1/E_2, & \text{for plane stress}\\ \left(1-\dfrac{a_0}{a}\right)\dfrac{aE_1(1-\nu_2^2)}{aE_2(1-\nu_1^2)+(a-a_0)E_1\nu_2(1+\nu_2)}, & \text{for plane strain}\end{cases} \tag{36}$$

By using the model to treat a cracked cylinder reinforced by a membrane developed in [6], the present transient thermal stress problem may be reduced to the following integral equation

$$\int_e^g\frac{f(\rho,t)}{\rho-r}d\rho+\int_e^g k(r,\rho)f(\rho,t)\,d\rho=\frac{\pi(1+\kappa)}{2\mu}\sigma_{\theta 2}^T(r,t), \quad (e<r<g, 0<t) \tag{37}$$

where $\kappa=3-4\nu_2$ for plain strain, $\kappa=(3-\nu_2)/(1+\nu_2)$ for plane stress, $\mu=E_2/2(1+\nu_2)$, and the unknown function f and the kernel k are defined by

$$f(r,t)=\frac{\partial}{\partial r}[u_\theta(r,+0,t)-u_\theta(r,-0,t)], (e<r<g) \tag{38}$$

$$k(r,\rho)=-\frac{1}{2}\left\{-\frac{\beta_2}{r^2}+2\gamma_0+\frac{2\gamma_1}{r^3}+6\delta_1 r + \sum_{n=2}^{\infty}[\alpha_n r^{n-2}+\beta_n(n+2)r^n+\gamma_n r^{-(n+2)}+\delta_n(n-2)r^{-n}]\right\} \tag{39}$$

$$\beta_0=\frac{2(1-\lambda)a^2}{a^2(1-\lambda)-b^2(1+\lambda)}\left(\rho-\frac{b^2}{\rho^2}\right),$$

$$\gamma_0=\frac{1}{a^2(1-\lambda)-b^2(1+\lambda)}\left[-(1+\lambda)\rho+\frac{a^2(1-\lambda)}{\rho}\right],$$

$$\gamma_1=\frac{a^4(1-3\lambda)}{a^4(1-3\lambda)-b^4(1+\lambda)}\left[-\frac{3\rho^2}{2}+b^2+\frac{b^4}{2\rho^2}\right],$$

$$\delta_1=\frac{1}{a^4(1-3\lambda)-b^4(1+\lambda)}\left[-\frac{3(1+\lambda)\rho^2}{2}+b^2(1+\lambda)+\frac{a^4(1-3\lambda)}{2\rho^2}\right],$$

$$\alpha_n=b^{-2(n-1)}\rho^{n-1}-(n-1)b^2\frac{c_n}{c_0}-b^{-2(n-1)}\frac{d_n}{c_0},$$

$$\gamma_n=\frac{1}{1+\lambda}\left[-a^{2(n+1)}\rho^{-(n+1)}(1-2\lambda n-\lambda)-a^2(1+n-n\lambda-\lambda)\frac{d_n}{c_0}+a^{2(n+1)}(1-2n\lambda-\lambda)\frac{c_n}{c_0}\right],$$

$$c_0=n^2(1+2\lambda+\lambda^2)a^{-2}b^2-2(n^2-1)(1-\lambda^2)-[1+2n\lambda+(2n-1)\lambda^2]a^{-2n}b^{2n}-[1-2n\lambda-(2n+1)\lambda^2]a^{2n}b^{-2n}+n^2(1-2\lambda-3\lambda^2)a^2b^{-2},$$

$$
\begin{aligned}
c_n = &\{(1-n^2)(1-\lambda^2)-[1-2n\lambda-(2n+1)\lambda^2]a^{2n}b^{-2n}\\
&+n^2(1-2\lambda-3\lambda^2)a^2b^{-2}\}\rho^{-(n+1)}\\
&+\{(2+n-n^2)(1-\lambda^2)b^{-2}\\
&-(2+n-n^2)(1+\lambda)^2a^{-2}\}\rho^{-(n-1)}\\
&+\{(1+n)[1+2n\lambda-(1-2n)\lambda^2]a^{-2n}-[(1+n)\\
&-(n^2+1)\lambda^2]b^{-2n}\}\rho^{n-1}+\{(2+n)(1+\lambda)^2a^{-2}b^{-2n}\\
&-(2+n)[1+2n\lambda-(1-2n)\lambda^2]a^{-2n}b^{-2}\}\rho^{n+1},\\
d_n = &\{-(1-n)[1-2n\lambda-(1+2n)\lambda^2]a^{2n}\\
&+(1-n)(1-\lambda^2)b^{2n}\}\rho^{-(n+1)}\\
&-\{(2-n)(1+\lambda)^2a^{-2}b^{2n}-(2-n)[1-2n\lambda\\
&-(1+2n)\lambda^2]a^{2n}b^{-2}\}\rho^{-(n-1)}+\{n^2(1+\lambda)^2a^{-2}b^2\\
&+(1-n^2)(1-\lambda^2)-[1-2n\lambda\\
&-(1+2n)\lambda^2]a^{2n}b^{-2n}\}\rho^{n-1}\\
&+\{(2-n-n^2)(1+\lambda)^2a^{-2}\\
&-(2-n-n^2)(1-\lambda^2)b^{-2}\}\rho^{n+1}
\end{aligned}
\tag{40}
$$

From (35*b*) and the definition of f as given by (38), it is seen that the integral equation (37) must be solved under the following single-valuedness condition

$$\int_e^q f(r,t)\,dr=0 \tag{41}$$

The singular integral equation may easily be solved by using the technique described, for example, in [7]. If the crack is fully embedded in cylinder 2 (i.e., if $a<e<g<b$), then the solution of (37) is of the form

$$f(r,t)=\frac{F(r,t)}{[(r-e)(g-r)]^{1/2}},(e<r<g,0<t) \tag{42}$$

where F is a bounded unknown function. In order to have a solution such as (42), it is, of course, assumed that the combination of mechanical and transient thermal hoop stresses in the neighborhood of the crack are predominantly tensile. Otherwise the crack may close at one or both ends and (42) would not be valid. If part of the crack lies in a region of compressive hoop stress, then the crack surfaces may close smoothly and the location of the related crack tip would be unknown. In this case, the unknown crack tip location is determined from the cusp condition that requires that the corresponding stress intensity factor be zero and the problem may be solved by using the technique described in [8]. After solving (37), the Mode I stress intensity factors at the crack tips e and g may be determined from

$$k_1(e,t)=\frac{2\mu}{1+\kappa}\lim_{r\to e}\sqrt{2(r-e)}f(r,t)=\frac{2\mu}{1+\kappa}\frac{F(e,t)}{\sqrt{(g-e)/2}} \tag{43}$$

$$k_1(g,t)=-\frac{2\mu}{1+\kappa}\lim_{r\to g}\sqrt{2(g-r)}f(r,t)=-\frac{2\mu}{1+\kappa}\frac{F(g,t)}{\sqrt{(g-e)/2}} \tag{44}$$

In the special case of the inner crack tip touching the reinforcing membrane (i.e., for $e=a$), it was shown analytically in [6] that at this crack tip the derivative f of the crack surface displacement is bounded. Physically, this follows from the fact that since the membrane has no bending stiffness, when the crack touches it, it would form a kink. In this case, the solution of (37) is of the form

$$f(r,t)=\frac{F(r,t)}{(g-r)^{1/2}},(a=e<r<g,0<t) \tag{45}$$

where the bounded function F is determined by following the technique used in [6].

In the other special case in which the external loads are sufficiently high so that the membrane is fully yielded (if, for example, $\theta_{a0}>\theta_F$ and no mechanical loading is present), the problem may be treated as an "edge crack" problem and the yielding membrane may be replaced by constant tensile tractions on the crack surface. In this case, too, the only relevant stress intensity factor is that at the crack tip $r=g$.

Finally, there is the case of the broken membrane in which the problem may be treated as an edge crack problem.

4 Results and Discussion

Some calculated results giving the transient temperature and thermal stress distributions obtained from (16), (17), and (26) are shown in Figs. 2–5. In (16) and (17), 50 terms are used

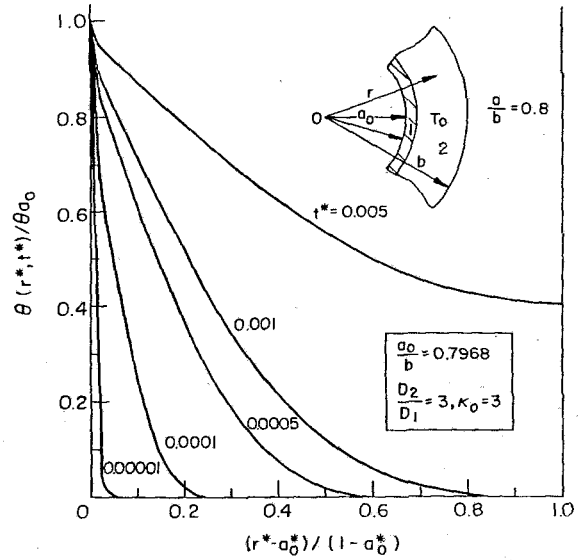

Fig. 2 Transient temperature distribution in a hollow composite cylinder due to a sudden change θ_{a0} in the inner surface temperature ($(a-a_0)/(b-a)$ = 0.016)

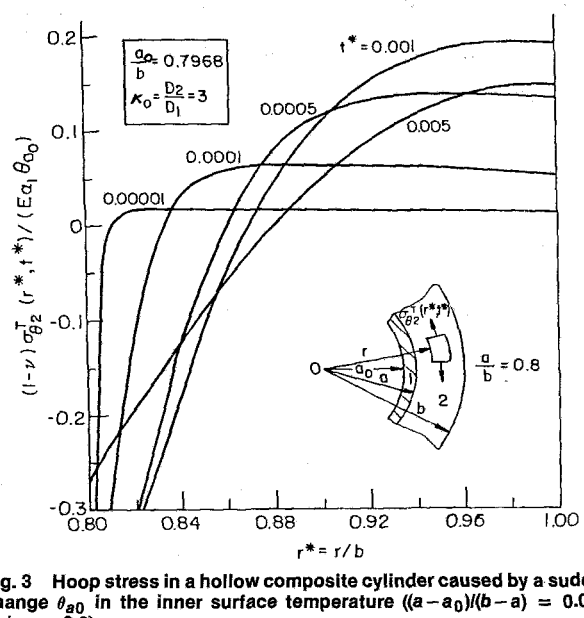

Fig. 3 Hoop stress in a hollow composite cylinder caused by a sudden change θ_{a0} in the inner surface temperature ($(a-a_0)/(b-a)$ = 0.016, α_2/α_1 = 0.8)

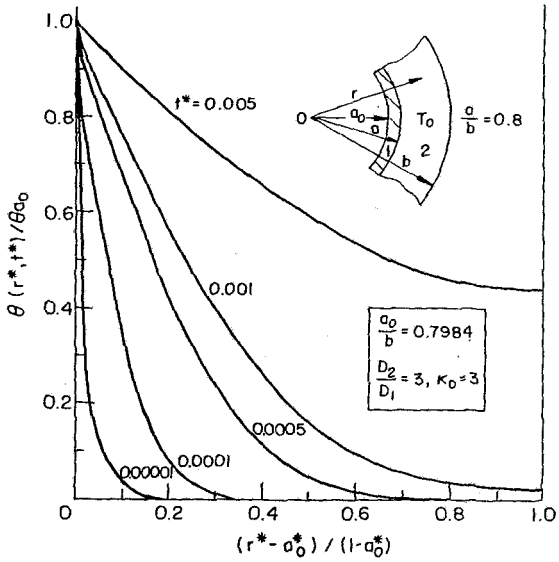

Fig. 4 Transient temperature distribution in a hollow composite cylinder due to a sudden change in the inner surface temperature ($(a-a_0)/(b-a) = 0.008$)

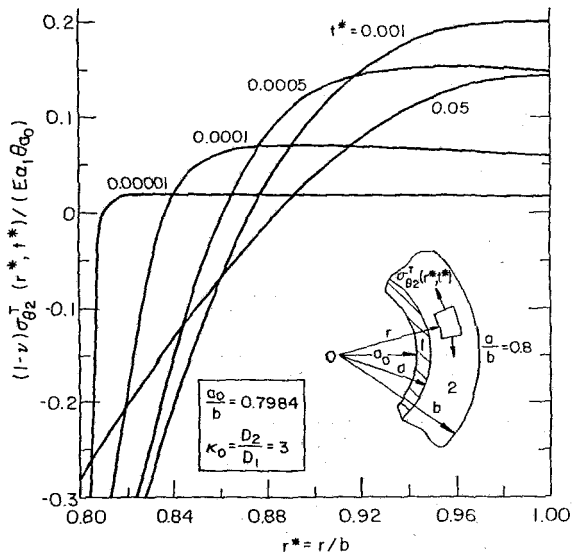

Fig. 5 Hoop stress in a hollow composite cylinder caused by a sudden change in the inner surface temperature ($(a-a_0)/(b-a) \approx 0.008$, $\alpha_2/\alpha_1 = 0.8$)

in the series to calculate the temperatures which proved to be quite sufficient. The results are calculated by varying dimensionless quantities defined by (19). In these calculations it is assumed that for the two cylinders the elastic constants are equal ($E_1 = E_2 = E$, $\nu_1 = \nu_2 = \nu$) but the thermal constants are different ($D_1 \neq D_2$, $k_1 \neq k_2$) and the composite cylinder is under a state of plane strain. Figures 2–5 show the temperature and the hoop stress distribution for two different clad thicknesses ($(a-a_0)/(b-a) = 0.016$ and 0.008). Referring to (15) note that for sudden cooling from inside θ_{a0} is negative resulting in tensile stresses at and near the inner boundary (Figs. 3 and 5). For an embedded crack ($a<e<g<b$), the corresponding stress intensity factors are shown in Tables 1 and 2. The tables show the normalized stress intensity factors which are defined by

$$k_1(e,t) = \lim_{r\to e} \sqrt{2(e-r)}\,\sigma_{\theta\theta}(r,0,t), \bar{k}(e) = \frac{k_1(e,t)}{k_0} \tag{46}$$

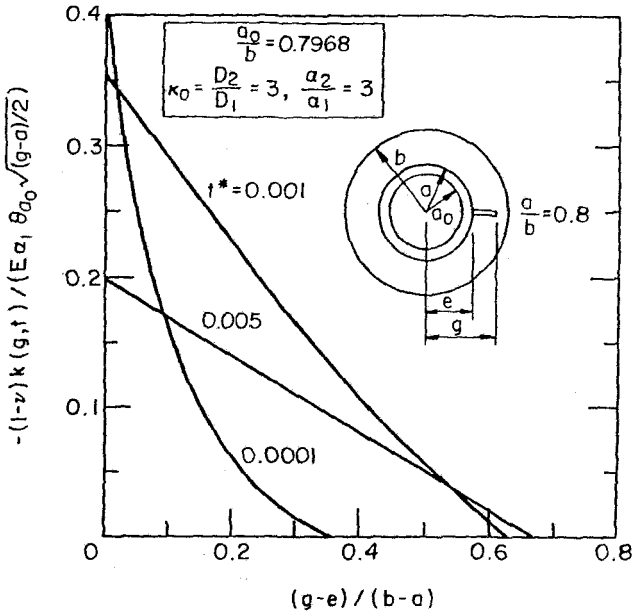

Fig. 6 The normalized stress intensity factor $\bar{k}(g) = -k(g,t)/E\alpha_1\theta_{a0}\sqrt{(g-e)/(2/(1-\nu)}$ in a reinforced cylinder that contains a crack terminating at the reinforcement-cylinder interface and that is subjected to a sudden change in the inner surface temperature ($E_1 = E_2 = E$, $\nu_1 = \nu_2 = \nu$, $(a-a_0)/(b-a) = 0.016$, the case of plane strain)

$$k_1(g,t) = \lim_{r\to g} \sqrt{2(r-g)}\,\sigma_{\theta\theta}(r,0,t), \bar{k}(g) = \frac{k_1(g,t)}{k_0} \tag{47}$$

$$k_0 = -\frac{E_2\alpha_1\theta_{a0}}{1-\nu_2}\sqrt{(g-e)/2} \tag{48}$$

Note that for longer crack lengths the outer tip $r=g$ of the crack would be in the compression zone and consequently the related stress intensity factor becomes negative.

In the case of the inner crack tip terminating at cylinder-reinforcement interface, the stress intensity factor at the outer tip $r=g$ is shown in Fig. 6. It may again be observed that as g increases the stress intensity factor $k_1(g,t)$ decreases and eventually becomes negative. In these calculations, too, it is assumed that $E_1 = E_2 = E$, $\nu_1 = \nu_2 = \nu$.

The effect of modulus ratio $E_1/E_2 = E^*$ on the transient thermal stress $\sigma_{\theta 2}^T$ in the main cylinder is shown in Fig. 7 for the case of plane strain and in Fig. 8 for plane stress. The figures show the results at a fixed time $t^* = D_1 t/b^2 = 0.0005$ and for $\alpha_2/\alpha_1 = 0.8$, $\nu_1 = \nu_2 = 0.3$, $D_2/D_1 = 3$ and $k_2/k_1 = 3$. Tables 3 and 4 show the corresponding normalized stress intensity factors for an embedded crack. The results for the crack touching the membrane and for the broken membrane (i.e., for the edge crack) are given in Table 5. Note that for the broken membrane case generally the stress intensity factors are considerably higher.

Tables 1–4 and Fig. 6 clearly show that an internal crack in a cylinder undergoing thermal shock at the inner boundary would always tend to propagate towards the inside wall, it may be arrested at the cylinder-reinforcement boundary if the reinforcement material is sufficiently tough, and under thermal shock alone it is not possible for the crack to propagate through the entire wall thickness of the cylinder. The tables also show that, generally for a given crack geometry the stress intensity factors first increase and, after going through a maximum, start decreasing with increasing time. This behavior, as well as the fact that for relatively long cracks the stress intensity factors at the two crack tips may have opposite signs, is suggested by the thermal stress profiles shown in Figs. 3, 5, 7, and 8.

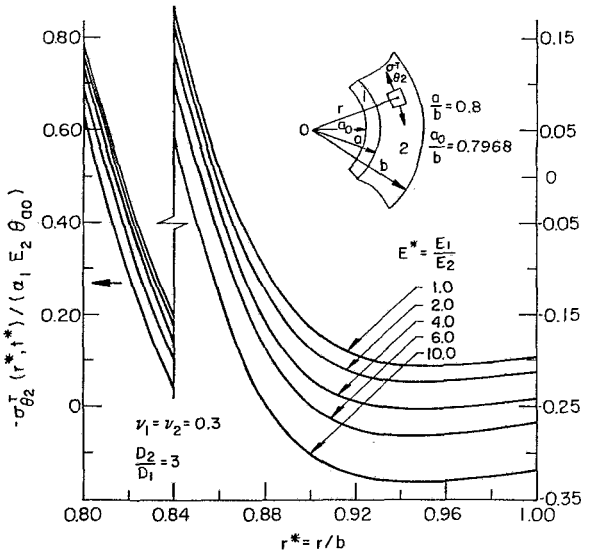

Fig. 7 The influence of the modulus ratio E_1/E_2 on the distribution of hoop stress in a composite cylinder undergoing a sudden change in the inner surface temperature ($t^* = D_1 t/b^2 = 0.0005$, $(a-a_0)/(b-a) = 0.016$, $e/b = 0.81$, the case of plane strain)

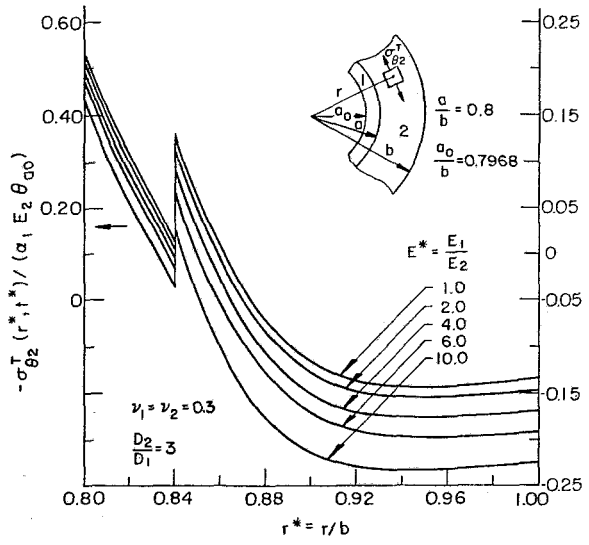

Fig. 8 The influence of the modulus ratio E_1/E_2 on the distribution of hoop stress in a composite cylinder undergoing a sudden change in the inner surface temperature ($t^* = D_1 t/b^2 = 0.0005$, $(a-a_0)/(b-a) = 0.016$, $e/b = 0.81$, the case of plane stress)

Table 1 Normalized stress intensity factors for an embedded crack in a reinforced cylinder subjected to transient thermal stresses ($a_0/b = 0.7968$, $a/b = 0.8$, $k_2/k_1 = 3$, $D_2/D_1 = 3$, $\alpha_2/\alpha_1 = 0.8$, $e/b = 0.84$, $E_1 = E_2$, $\nu_2 = \nu_2$)

$\frac{g-e}{b-a}$	t*=0.0005		t*=0.001		t*=0.005	
	$\bar{k}(e)$	$\bar{k}(g)$	$\bar{k}(e)$	$\bar{k}(g)$	$\bar{k}(e)$	$\bar{k}(g)$
0.05	0.11258	0.07698	0.16846	0.13549	0.11857	0.10180
0.10	0.09617	0.03173	0.15356	0.09109	0.11120	0.07845
0.20	0.06695	-0.03653	0.12573	0.01508	0.09707	0.03509
0.30	0.04130	-0.08115	0.09912	-0.04545	0.08270	-0.00419
0.40	0.01857	-0.10986	0.07337	-0.09284	0.06770	-0.03938
0.50	-0.00189	-0.13062	0.04836	-0.13134	0.05204	-0.07128

Table 2 Normalized stress intensity factors for an embedded crack in a reinforced cylinder subjected to transient thermal stresses ($a_0/b = 0.7968$, $a/b = 0.8$, $k_2/k_1 = 3$, $D_2/D_1 = 3$, $\alpha_2/\alpha_1 = 0.8$, $e/b = 0.84$, $E_1 = E_2$, $\nu_2 = \nu_2$)

$\frac{g-e}{b-a}$	t*=0.0005		t*=0.001		t*=0.005	
	$\bar{k}(e)$	$\bar{k}(g)$	$\bar{k}(e)$	$\bar{k}(g)$	$\bar{k}(e)$	$\bar{k}(g)$
0.05	0.13677	0.09793	0.18877	0.15414	0.12371	0.10688
0.10	0.11899	0.04822	0.17328	0.10742	0.11642	0.08352
0.20	0.08715	-0.02784	0.14430	0.02677	0.10247	0.04005
0.30	0.05893	-0.07845	0.11639	-0.03816	0.08822	0.00057
0.40	0.03376	-0.11135	0.08916	-0.08943	0.07328	-0.03486
0.50	0.01106	-0.13495	0.06259	-0.13114	0.05764	-0.06692

Table 3 The effect of the modulus ratio E_1/E_2 on the stress intensity factors in a reinforced cylinder, $k_n = -k_1/\alpha_1 E_2 \theta_{a0} \sqrt{(g-e)/2}$, $a_0/b = 0.7968$, $a/b = 0.8$, $e/b = 0.81$, $t^* = DT/b^2 = 0.0005$, $\alpha_2/\alpha_1 = 0.8$, $k_2/k_1 = 3$, $D_2/D_1 = 3$, $\nu_1 = \nu_2 = 0.3$, the case of plane strain

$\frac{g-e}{b-a}$	$E_1/E_2 = 1$		$E_1/E_2 = 2$		$E_1/E_2 = 6$		$E_1/E_2 = 10$	
	$k_n(e)$	$k_n(g)$	$k_n(e)$	$k_n(g)$	$k_n(e)$	$k_n(g)$	$k_n(e)$	$k_n(g)$
0.05	0.57556	0.49535	0.55469	0.47486	0.48101	0.40217	0.41844	0.34024
0.10	0.55370	0.39808	0.53000	0.37589	0.45059	0.29988	0.38554	0.23669
0.15	0.53438	0.31039	0.50762	0.28680	0.42198	0.20803	0.35420	0.14377
0.20	0.51465	0.23159	0.48504	0.20706	0.39366	0.12643	0.32335	0.06143
0.25	0.49342	0.16180	0.46139	0.13673	0.36513	0.05505	0.29263	-0.01036
0.30	0.47052	0.10099	0.43654	0.07569	0.33636	-0.00639	0.26207	-0.07195

Table 4 The effect of the modulus ratio E_1/E_2 on the stress intensity factors in a reinforced cylinder, $k_n = -k_1/\alpha_1 E_2 \theta_{a0} \sqrt{(g-e)/2}$, $a_0/b = 0.7968$, $a/b = 0.8$, $e/b = 0.81$, $t^* = Dt/b^2 = 0.0005$, $\alpha_2/\alpha_1 = 0.8$, $k_2/k_1 = 3$, $D_2/D_1 = 3$, $\nu_1 = \nu_2 = 0.3$, the case of plane stress

$\frac{g-e}{b-a}$	$E_1/E_2 = 1$		$E_1/E_2 = 2$		$E_1/E_2 = 6$		$E_1/E_2 = 10$	
	$k_n(e)$	$k_n(g)$	$k_n(e)$	$k_n(g)$	$k_n(e)$	$k_n(g)$	$k_n(e)$	$k_n(g)$
0.05	0.40280	0.34667	0.38800	0.33217	0.33564	0.28058	0.29124	0.23668
0.10	0.38732	0.27847	0.37022	0.26256	0.31276	0.20793	0.26620	0.16285
0.15	0.37362	0.21700	0.35405	0.19996	0.29130	0.14295	0.24263	0.09703
0.20	0.35965	0.16179	0.33784	0.14402	0.27048	0.08554	0.22017	0.03924
0.25	0.34468	0.11292	0.32100	0.09474	0.25002	0.03562	0.19862	-0.01068
0.30	0.32858	0.07035	0.30344	0.05204	0.22987	-0.00710	0.17791	-0.05312

Table 5 The effect of E_1/E_2 on the normalized stress intensity factor $k_n(g)$ for a crack touching the membrane cylinder interface and for a fully broken membrane, $k_n(g) = -k_1(g,t)/E_2\alpha_1\theta_{a0}\sqrt{(g-a)}$, $a_0/b = 0.7968$, $a/b = 0.8$, $e/a = 1$, $t^* = D_1 t/b^2 = 0.005$, $k_2/k_1 = 3$, $D_2/D_1 = 3$, $\nu_1 = \nu_2 = 0.3$, $\alpha_2/\alpha_1 = 0.8$, the case of plane strain

$\frac{g-e}{b-a}$	Crack touching the membrane			broken membrane-edge crack	
	$E_1/E_2=1$	$E_1/E_2=2$	$E_1/E_2=10$	$E_1/E_2=1$	$E_1/E_2=2$
0.10	0.23866	0.22678	0.15943	0.39231	0.39201
0.20	0.20237	0.18697	0.11076	0.35107	0.34859
0.30	0.16164	0.14404	0.06290	0.32931	0.32314
0.40	0.11804	0.09940	0.01651	0.31389	0.30323
0.50	0.07348	0.05484	-0.02742	0.29972	0.28361
0.60	0.02973	0.01190	-0.06839	0.28100	0.25851
0.70	-0.01222	-0.02881	-0.10741	0.24839	0.21943

Acknowledgments

This work was supported by NSF under the Grant MEA-8209083, NASA-Langley under the Grant NGR 38-007-011 and was completed by the second author at the Fraunhofer-Institut für Werkstoffmechanik in Freiburg while he was the recipient of an Alexander von Humboldt Senior U.S. Scientist Award.

References

1 Stahn, D., and Blauel, J. G., "Experimentelle Untersuchungen zur Rissausbreitung in Glashohlzylindern unter Thermoschockbelastung," *Vortrag XI*, Int. Glaskongress Prag, Sammelband II, 1977, pp. 435–445.

2 Nied, H. F., and Erdogan, F., "Transient Thermal Stress Problem for a Circumferentially Cracked Hollow Cylinder," *Journal of Thermal Stresses*, Vol. 6, 1983, pp. 1–14.

3 Sternberg, E., and Chakravorty, J. G., "On Inertia Effects in a Transient Thermoelastic Problem," ASME *J. Appl. Mech.*, Vol. 26, 1959, pp. 503–508.

4 Sternberg, E., and Chakravorty, J. G., "Thermal Shock in an Elastic Body with a Spherical Cavity," *Q. Appl. Math.*, Vol. 17, 1959, pp. 205–220.

5 Timoshenko, S., and Goodier, J. N., *Theory of Elasticity*, McGraw-Hill, 1951.

6 Tang, Renji, and Erdogan, F., "Stress Intensity Factors in a Reinforced Thick-Walled Cylinder," *Int. J. Engng. Science*, Vol. 22, 1984, (to appear).

7 Erdogan, F., "Mixed Boundary Value Problems in Mechanics," *Mechanics Today*, edited by S. Nemat-Nasser, Vol. 4, 1978, pp. 1–86.

8 Bakioglu, M., and Erdogan, F., "Crack-Contact and the Free-End Problem for a Strip under Residual Stress," ASME *J. Appl. Mech.*, Vol. 44, 1977, pp. 41–44.

Observations on the Interaction of High Mean Stress and Type II Hot Corrosion on the Fatigue Behavior of a Nickel Base Superalloy

J. M. Allen
Westinghouse Combustion Turbine Systems Division,
Concordville, Pa. 19331

G. A. Whitlow
Westinghouse Research and Development Center,
Pittsburgh, Pa. 15235

A study measuring the effects of a molten sulfate/chloride salt on the creep/fatigue behavior of a nickel base turbine blade superalloy, Udimet 720, at 1300°F (704°C) is described. Cyclic stress–cycles to failure (S-N) curves were generated at high mean stress levels, with mean stress, maximum stress, or the ratio of minimum to maximum stress (R ratio) held constant. In salt, it was found that when maximum stress is above the yield, with the cyclic component 20 percent of the maximum, failure occurs by stress corrosion fatigue in orders of magnitude less time than for corresponding loading conditions in air. It is significant, from a failure analysis point of view, that fatigue fracture is intergranular in these circumstances. Similar fatigue behavior may be expected for other nickel base alloys, however, at substantially lower maximum stresses inasmuch as Udimet 720 exhibits superior short time rupture strength, i.e., resistance to this form of stress corrosion, over the other blade alloys evaluated in this environment.

Introduction

The impact of a molten sulfate/chloride salt at 1300–1350°F (704–732°C) on the stress rupture (SR), low cycle fatigue (LCF), and high cycle fatigue (HCF) properties of nickel base alloy Udimet 720 was recently reported [1–4]. In these tests, corrosion produced by the laboratory environment duplicated, in an accelerated fashion, the Type II hot corrosion attack frequently observed on combustion turbine blades retrieved from service [5, 6], and it significantly affected the mechanical properties. With respect to cyclic stress-environmental interaction, at the HCF end of the fatigue spectrum the endurance limit was reduced by a factor of about three, and transgranular fatigue fracture initiating at corrosion pits was observed [1, 2]. In the LCF regime, reductions of 95 and 28 percent in the respective ductility and strength coefficients in the Coffin-Manson and Basquin relationships between cyclic strain and life were noted, as well as a predominantly intergranular mode of fracture at high cyclic strains [3]. The SR investigation, which included four high temperature nickel base superalloys in addition to Udimet 720, showed that rupture life is increasingly diminished as stress is increased above a threshold of about 60 ksi (413 MPa), and that while the reduction in SR life for the Udimet 720 material was significant, the effect was much greater for the other alloys evaluated [4].

Table 1 Chemistry (wt %) and heat treatment of Udimet 720

Ni	Cr	Co	Ti	Mo	Al	W	Zr	C	B
55	18	15	5	3	2.5	1.4	.04	.035	.035

- Solution 4h at 2135°F (1168°C), air cool (AC).
- Stabilize 4h at 1975°F (1079°C), AC.
- Age 24h at 1550°F (843°C), AC.
- Final age 16h at 1400°F (760°C), AC.

Table 2 Tensile properties of Udimet 720

Temperature		UTS		.2% YS		Elong.	RA
(°F)	(°C)	(ksi)	(MPa)	(ksi)	(MPa)	(%)	(%)
70	21	159	1096	124	854	6.3	5.2
1200	649	181	1247	111	765	14.4	13.0
1400	760	153	1054	110	758	23.7	30.5

The HCF study described previously [1] was subsequently extended to include testing designed to measure the effect of the salt environment on the creep/fatigue behavior of Udimet 720. This entailed generating fatigue stress-cycles to failure (S-N) curves at a high R ratio (minimum to maximum stress) and at high mean stresses where mean stress or maximum stress in the cycle is held constant. The purpose of these tests was twofold: to quantify the reduction in fatigue properties from the interaction of high mean stress and Type II hot corrosion, and to document fracture morphology, which could be useful in failure analyses. In this paper, a detailed presentation of results from the fatigue study of Udimet 720

Contributed by the Gas Turbine Division of THE AMERICAN SOCIETY OF MECHANICAL ENGINEERS and presented at the 29th International Gas Turbine Conference and Exhibit, Amsterdam, The Netherlands, June 4–7, 1984. Manuscript received at ASME Headquarters January 9, 1984. Paper No. 84-GT-149.

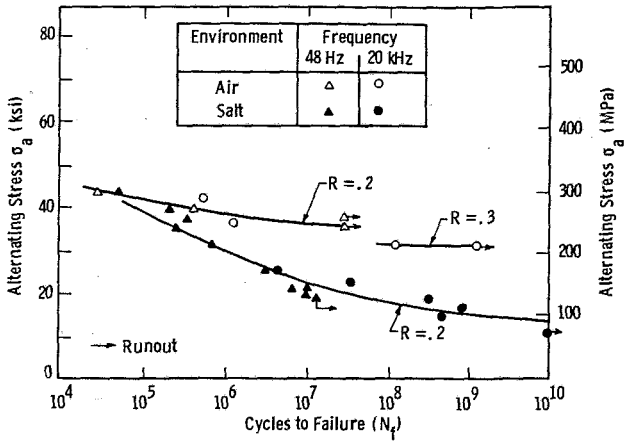

Fig. 1 Effects of environment and frequency of cycling on the HCF strength of Udimet 720 at 1300°F (704°C) and $R = .2$ to .3 [1]

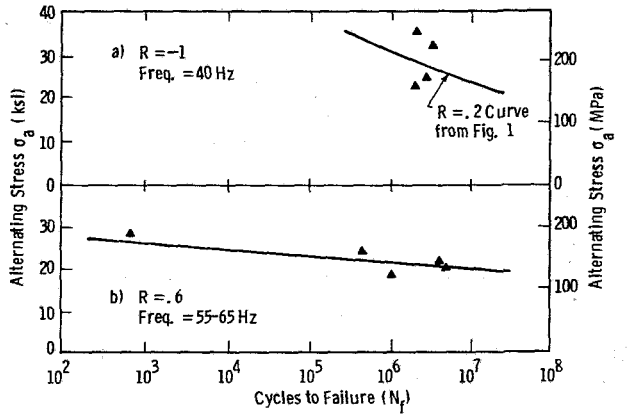

Fig. 2 HCF strength of Udimet 720 in salt environment at 1300°F (704°C) for $R = -1$ and .6

at high mean stress is given, with emphasis on the effect the salt environment has on fracture morphology and the practical implications therefrom.

Material and Experimental Procedure

High-frequency, high mean load fatigue tests were conducted on the wrought nickel base superalloy Udimet 720[1]. Chemical composition, heat treatment, and tensile properties are given in Tables 1 and 2. Conventional, load controlled, axial fatigue tests, in the frequency range 40–65 Hz, were carried out at 1300°F (704°C) using a .25-in.-(6.35-mm)-dia by .75-in.-(19.1-mm)-gage length specimen [1].

Testing was performed in two environments, viz., air and a molten salt. The salt environment was provided by a 60/40 mole fraction mixture of $Na_2SO_4/MgSO_4$ [with a melting point of approximately 1220°F (660°C)] containing 1 weight percent NaCl. The salt was contained in a stainless steel cup integral with the bottom grip of the fatigue unit. The cup was filled to a level coincident with the midpoint of the specimen gage length, and at temperature a thin film of liquid salt covered a small portion of the upper half of the gage length by capillary action. This simulates the deposition of such films on turbine airfoils that occurs when these contaminants are present in the fuel and air. At 1300°F (704°C), this environment produces the Type II form of hot corrosion attack [5, 6], which occurs in the temperature range 1100–1400°F (593–760°C).

[1] Trademark of Special Metals Corporation

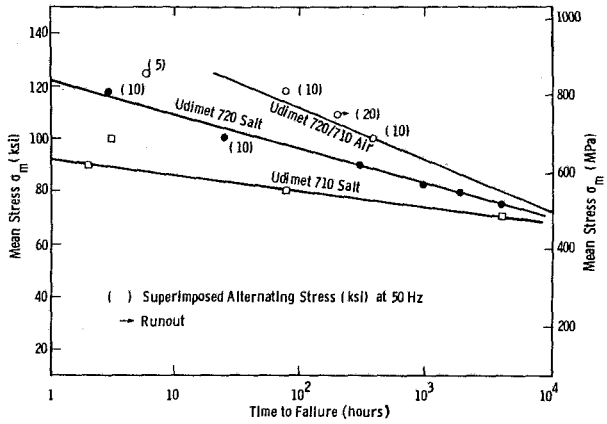

Fig. 3 Effect of salt environment and low alternating stress on stress rupture of Udimet 710 and 720 alloys at 1300°F (704°C)

Results

Results from the moderate R ratio (.2–.3) HCF tests reported earlier [1,2] are reproduced in Fig. 1 for reference purposes. Figure 1 shows that fatigue strength is independent of cyclic frequency, in the range 48Hz–20KHz for both environments and that a reasonably definite endurance limit in the salt environment is not reached in 10^7 to 10^8 cycles as it is in air. A runout at 10^{10} cycles was obtained at 12 ksi (83 MPa), which in conjunction with the trend of the S-N curve through the failure points suggests that this may be below the cyclic stress threshold for transgranular crack propagation from corrosion pits produced by the salt [1]. Thus the endurance limit in salt ($>10^{10}$ cycle fatigue strength) appears to be about one-third of that in air ($>10^7$ cycle fatigue strength).

Figure 2 displays results from four tests in the salt environment at zero mean load ($R = -1$) and five data points obtained in the salt environment at high mean loads ($R = .6$). Although the fully reversed ($R = -1$) stress amplitudes ranged from 23 to 36 ksi (158 to 248 MPa), failure occurred in a narrow range, 1.96 to 3.2×10^6 cycles. These data illustrate the large scatter often encountered in the aggressive salt environment. It is interesting to note that this cluster of data centers fairly well on the $R = .2$ curve, also shown in Fig. 2(*a*), showing that there is little effect of mean stress from $R = -1$ to $R = .2$ on 10^6 to 10^7 cycle fatigue strength. For cyclic lives $\sim 10^7$, the effect is minimal for R ratios up to at least .6, as evidenced by the data in Fig. 2(*b*). However, there is a substantial R ratio effect at higher maximum stresses. For example, the 10^4 cycle fatigue strength at $R = .6$, Fig. 2(*b*), is one-half that at $R = .2$, Fig. 1. Maximum tensile stress in the fatigue cycle is approximately the same in both instances.

The 10^{10} cycle fatigue strength was not determined for R ratios $> .2$ in air or salt, but in salt it is obviously not more than the 12 ksi (83 MPa) measured at $R = .2$. For high values of mean stress ($R = .82$ to .85) it was found that cyclic stresses of this magnitude can be superimposed, at 50 Hz, without affecting creep life [2]. This is shown in Fig. 3, where several failures obtained at low alternating to mean stress ratios are plotted with the SR data previously reported [4] for Udimet 720 in the air and salt environments. It can be seen that when the mean stress from these creep/fatigue tests is plotted against time to failure the points very nearly fall on the SR lines.

To determine the transition from the fatigue to creep mode of failure with a minimum number of tests, testing was conducted such that alternating stress was varied while the maximum or mean stress was held constant following the approach adopted in a similar study [7]. The results, shown in Figs. 4 and 5, are supplemented with data obtained by interpolation from Figs. 1 and 2(*b*). These points aided in

Table 3 Creep/fatigue life and fracture appearance of Udimet 720 in air and salt environments

Mean Stress		Cyclic Stress		Life and Fracture Appearance in Air			Life and Fracture Appearance in Salt		
(ksi)	(MPa)	(ksi)	(MPa)	Cycles	Hours	% Transgranular	Cycles	Hours	% Transgranular
125	861	5	35	1.1×10^6	6.11	0.0			
119	820	10	69	1.4×10^7	77.80	7.2	4.9×10^5	2.720	0
119	820	20	138	2.7×10^4	.18	11.8			
100	689	10	69	6.9×10^7	383.00	10.9	4.4×10^6	24.400	0
100	689	30	207	1.6×10^7	87.80	17.5			
112	772	28	193				7.8×10^2	.004	<1
96	661	24	165				4.1×10^5	2.090	<1
84	579	21	145				4.8×10^6	24.200	8

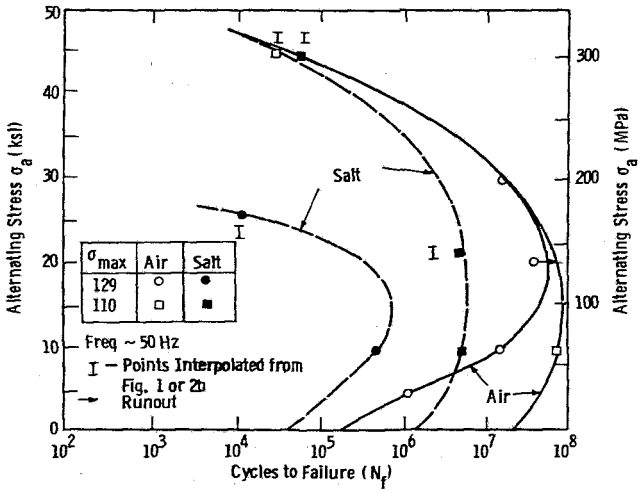

Fig. 4 Effect of environment on creep/fatigue strength of Udimet 720 at 1300°F (704°C) and constant maximum stress

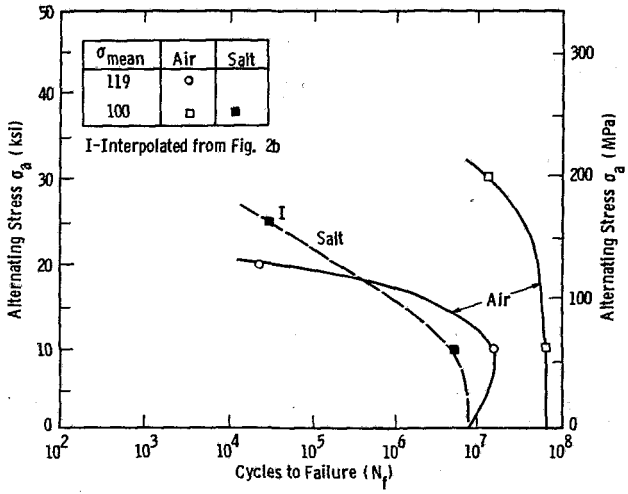

Fig. 5 Creep/fatigue strength of Udimet 720 in air and salt under constant mean stress at 1300°F (704°C)

drawing the upper or fatigue dominated portion of the curves in Figs. 4 and 5. The lower, creep-dominated segments of the curves were drawn to intersect the cycles to failure axis at the number of cycles equivalent to the life obtained by extrapolating the SR line, Fig. 3, to the appropriate mean stress. The resulting rupture times, in seconds, were multiplied by a frequency of 50 Hz to obtain the equivalent cycles to failure for the zero alternating stress case.

From the data curves presented in Figs. 1-5, well-defined modified Goodman diagrams at 1.5×10^7 cycles to failure can be constructed for both environments, and these are shown in Fig. 6.

Fractographic information gleaned from the broken specimens is summarized in Table 3 for both air and salt environments, and in Fig. 7 typical micrographs of some of the fractures are shown. The classical transgranular fatigue initiation area is evident in some cases, while in others the fracture surface is essentially 100 percent intergranular.

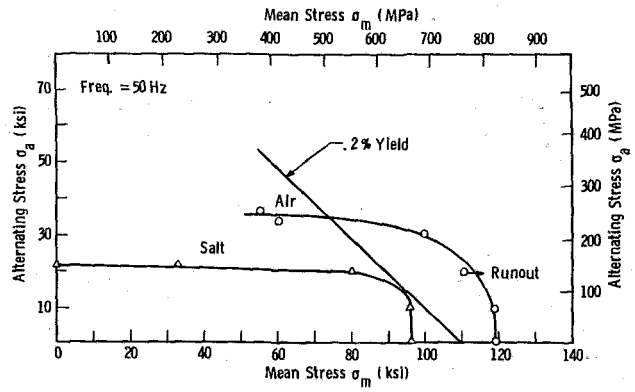

Fig. 6 Modified Goodman diagrams (1.5×10^7 cycles) for Udimet 720 in air and salt at 1300°F (704°C)

Discussion

It is well known that tensile mean stress reduces fatigue strength. As mean stress approaches the rupture strength, time-dependent damage also enters into the failure process as implied in Figs. 3-6. The inversion of the S-N curves in Fig. 4 is attributable to the dominant mode of failure changing from fatigue to stress rupture as the alternating stress is reduced while holding the maximum stress constant [7]. Figure 5 demonstrates this transition in failure mechanism more clearly inasmuch as the component governing stress rupture, the mean stress, is held constant.

It can be seen that, in air, adding a 10 ksi (69 MPa) alternating component to a steady component of 119 ksi (820 MPa) does not significantly alter life at a cycling rate of 50 Hz. However, superimposing an alternating stress of 20 ksi (138 MPa) on the 119 ksi (820 MPa) mean stress decreases life by a factor of approximately 400, clearly indicating a changeover to fatigue-dominated failure. Reducing the mean stress to 109 ksi (751 MPa) while maintaining the alternating component at 20 ksi (138 MPa) resulted in a runout (no failure), Fig. 4, at a time in excess of that nominally required to cause stress rupture at this level of mean stress, Fig. 3. Increasing the cyclic stress to 30 ksi (207 MPa), but holding the maximum constant, changes the controlling mode of failure back to fatigue, as shown in Figs. 4, 5, and 6.

Fracture appearance information on most of the broken specimens is given in Table 3. Note that the sample that failed in air at 119 ksi (820 MPa) mean stress and 20 ksi (138 MPa)

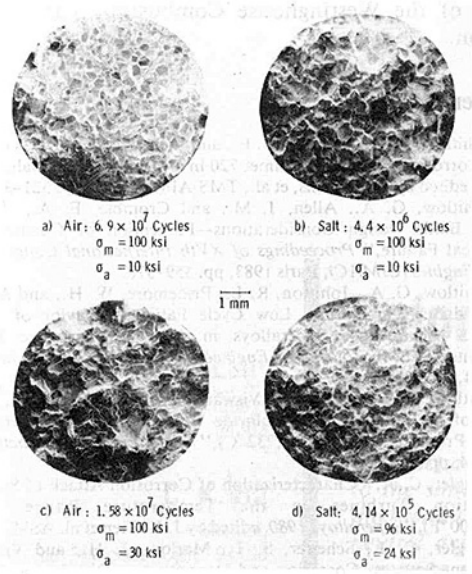

Fig. 7 Typical fracture surfaces for Udimet 720 in air and salt environments under creep/fatigue loading conditions at 1300°F (704°C)

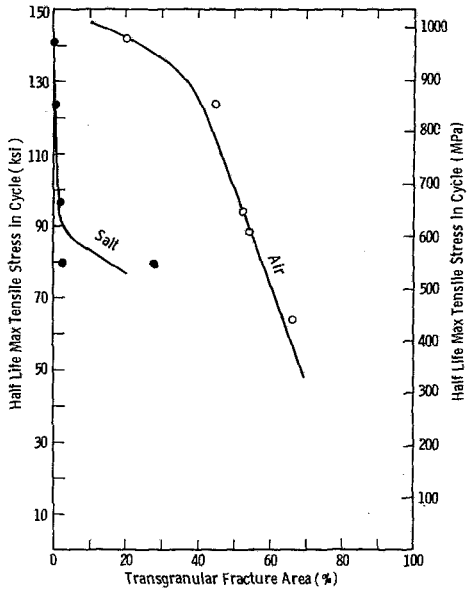

Fig. 8 Effect of maximum tensile stress on fracture appearance of Udimet 720 in LCF, 1 cpm, 1350°F (732°C), $R \sim -1$, as a function of test environment [3]

alternating stress, from fatigue, exhibited a fracture surface that was approximately 12 percent transgranular. The specimen loaded to the same mean stress but a lower alternating stress [10 ksi (69 MPa)] in air fractured when the transgranular area was approximately 7 percent of the cross section. The latter case is interesting in that, despite the fairly strong evidence of fatigue, life was essentially the same as for simple stress rupture at the same mean load. This was also true for the 100 ksi (689 MPa)/10 ksi (69 MPa) mean to alternating case, where the transgranular thumbnail, Fig. 7(*a*) (7 o'clock position), is approximately 11 percent of the total fracture area. The reason this kind of behavior may occur was provided by Ellison and Sullivan [8], who showed that at high static stress intergranular creep cracking initiates very early, in less than one-half the time to rupture, and that ±10 ksi (69 MPa) cyclic stress can propagate cracks a few grain diameters in size in a transgranular fashion. Under their test conditions (Udimet 700 alloy in air at 1400°F (760°C), 70 to 80 ksi (482 to 551 MPa) ±10 ksi (69 MPa)) propagation was accelerated by the low alternating stress, while for the aforementioned tests this was not the case.

In the sulfate/chloride environment superimposing a 50 Hz, 10 ksi (69 MPa) alternating stress on mean stresses of 100 ksi and 119 ksi (689 and 820 MPa) did not affect SR life either, Figs. 4 and 5. In these circumstances SR life is only about 6 and 4 percent of that for the corresponding loading conditions in air, Fig. 3, due to the corrosion assisted stress rupture phenomenon previously described [4] for Udimet 720 and four other nickel base alloys. Thus it is not surprising that these fractures are completely intergranular, Table 3 and Fig. 7(*b*). Increasing the alternating component to approximately 25 ksi (172 MPa) on the mean stress of 100 ksi (689 MPa) induces failure by fatigue in orders of magnitude less time, Fig. 5, but the fracture is still greater than 99 percent intergranular, Table 3 and Fig. 7(*d*); conversely for these loading conditions in air the fracture would be expected to be approximately 16 percent transgranular, based on interpolation of the fracture areas shown in Figs. 7(*a*), 7(*c*), and Table 3. This indicates that when the maximum stress is high enough – above the yield in this case – and the R ratio is around .6, not only will failure occur rapidly by fatigue, but the fracture could be entirely intergranular. This is significant because intergranular fracture is usually interpreted to denote time-dependent, as opposed to cycle-dependent, failure in post-mortem fractographic analyses.

A review of fractographic data from the LCF study of [3] reveals that similar behavior occurred at high maximum stress in those tests. The relationship between transgranular fracture area and maximum tensile stress is shown in Fig. 8, in which the stresses plotted are midlife tensile peaks obtained under fully reversed strain control conditions ($R \sim -1$) at 1 cpm frequency of cycling. Note that in air fracture areas are greater than 25 percent transcrystalline for cyclic stresses of ±140 ksi (965 MPa) and lower. In the salt environment, however, transgranular fracture area approaches zero at cyclic stresses above the yield [>110 ksi (758 MPa)].

In practice, stresses high enough to cause this kind of failure behavior in Udimet 720 should not be encountered. However, it probably can occur at substantially lower maximum stresses for other turbine blade alloys. This projection is based on the fact that stress rupture life at high levels of stress for the four other nickel base alloys evaluated in the salt environment is much more severely degraded than it is for Udimet 720 [4]. For example, the 1-hr stress rupture strength of Udimet 710 is about 30 ksi (207 MPa) less than it is for Udimet 720 in the salt environment, Fig. 3. In air, mechanical properties (stress rupture, tensile, and LCF) for the two alloys have been shown to be essentially the same [3, 4]. Thus it is conceivable that some alloys in certain combustion turbine environments could experience intergranular high-frequency fatigue failure if design values of vibratory and maximum steady stress are based on mechanical properties obtained in a clean air environment, and it can, therefore, be considered a possible mode of failure in the analysis of blades exhibiting intergranular fracture initiation in the presence of this form of corrosion.

In summary, a distinct difference in fatigue behavior has been observed at high mean loads in the salt environment. In [1], it was shown that HCF strength at modest levels of mean stress is reduced by a localized or pitting type corrosion, from which transgranular fatigue failure initiates at lower than anticipated values of nominal cyclic stress. At high values of mean stress, this study revealed that fatigue failure can occur by a stress corrosion mechanism that becomes increasingly deleterious as maximum tensile stress in the cycle exceeds a certain level. Intergranular fatigue fracture was observed in cycles where maximum stress exceeds the yield and alternating stress is 20 percent of the maximum.

Conclusions

- At certain combinations of alternating and high mean stress, failure occurs by stress corrosion fatigue. This was observed when cyclic stress is 20 percent of the maximum and the maximum exceeds the yield. Failure occurs in orders of magnitude less cycles than for corresponding loading conditions in air, and fatigue fracture morphology becomes intergranular.
- Based on comparative short-time stress rupture tests of several alloys in air, it is anticipated that similar fatigue behavior may occur at substantially lower maximum stresses for many of the nickel base alloys; e.g., Udimet 710, whose mechanical properties are almost identical to those for Udimet 720 in air, has a 1-hr rupture strength 30 ksi (207 MPa) less than it is for Udimet 720 in the salt environment.
- At modest levels of mean stress, HCF strength is reduced by a localized or pitting type corrosion, from which transgranular fatigue fracture initiates. Notably, the endurance limit is reduced to approximately one-third of that in air, and it is not evident until about 10^{10} cycles are accumulated.

Acknowledgments

The authors gratefully acknowledge the support of their many colleagues, especially W. H. Pridemore, who performed the HCF-high mean load tests, and the technical and financial support of E. A. Crombie, S. T. Scheirer and A. J. Scalzo of the Westinghouse Combustion Turbine Systems Division.

References

1 Whitlow, G. A., Willertz, L. E., and Tien, J. K., "Effects of Frequency on the Corrosion Fatigue of Udimet 720 in a Molten Sulfate Salt," *Ultrasonic Fatigue*, edited by J. M. Wells, et al., TMS-AIME, 1982, pp. 321–332.

2 Whitlow, G. A., Allen, J. M., and Crombie, E. A., "Combustion Turbine Blade Design Considerations—Prevention of Corrosion Assisted Mechanical Failure," *Proceedings of XVth International Congress on Combustion Engines (CIMAC)*, Paris 1983, pp. 559–578.

3 Whitlow, G. A., Johnson, R. L., Pridemore, W. H., and Allen, J. M., "Intermediate Temperature, Low Cycle Fatigue Behavior of Coated and Uncoated Nickel Base Superalloys in Air and Corrosive Sulfate Environments," ASME *Journal of Engineering Materials and Technology*, Vol. 106, 1984, pp. 43–49.

4 Whitlow, G. A., Beck, C. G., Viswanathan, R., and Crombie, E. A., "The Effects of a Liquid Sulfate/Chloride Environment on Superalloy Stress Rupture Properties at 1300°F (732°C)," *Metallurgical Transaction A*, Vol. 15A, 1984, pp. 23–28.

5 Spengler, C. J., "Characterization of Corrosion Attack of Superalloys in Combustion Turbines in the Temperature Range 600–760°C (1100–1400°F)," *Superalloys 1980*, edited by J. K. Tien et al. ASM, New York.

6 Spengler, C. J., Scheirer, S. T., Marlow, J. H., and Vitello, J. J., "Corrodant Sources, Corrosion and Deposition in Distillate and Heavy Oil Fired Turbines," *Proceedings of the 2nd Conference on Advanced Materials for Alternative Fuel-Capable Heat Engines*, edited by J. W. Fairbanks, and J. Stringer, EPRI Report RD-2369-SR, May 1982, pp. 4-53–4-72.

7 Fritzemeier, L. G., Paulson, R. R., Luton, M. J., and Tien, J. K., "S-N Curve Inversion of a Nickel-Base Superalloy at Elevated Temperature," *Scripta Metallurgica*, Vol. 16, 1982, pp. 115–116.

8 Ellison, E. G., and Sullivan, C. P., "The Effect of Superimposed Fatigue on the Creep Behavior of the Nickel-Base Alloy Udimet 700," ASM *Transactions*, Vol. 60, 1967, pp. 88–98.

J. H. Lau[1]
Hewlett-Packard Laboratory,
Palo Alto, Calif. 94303

C. K. Hu
Bechtel,
San Francisco, Calif. 94103

Deformation of Curved Bars With Creep

An exact analysis is presented for the creep deformation of a curved bar subjected to the simultaneous actions of bending moment and axial force. Dimensionless interaction curves and charts, which relate the variables, axial force, location of neutral axis, maximum stress and strain rate, bending moment, and change in curvature rate, are also provided for engineering practice convenience. The constitutive relationship of the curved bar is described by the Prandtl-Nadai Creep Law.

Introduction

Modern technological progress demands the use of materials in load-carrying members (e.g., curved bars) at increasingly higher stresses for a long period of time. Furthermore, most of the curved bars, particularly in fields of gas turbine [1, 2], jet propulsion, oil refinery, chemical process, and power systems, must be designed to carry their loads at elevated temperatures in order to increase the thermodynamic efficiency. Therefore, as recommended by ASME Boiler and Pressure Vessel Code [3], the effect of creep strains on stresses must be assessed.

There is no other type of mechanical behavior that has had a greater number of empirical formulas proposed to represent it than has creep (see [4–7] for listing). In general, different formulas are good for different materials. For metal components, most design charts and formulas have been derived from the power creep law [8, 9] or the hyperbolic sine law proposed by Prandtl [10] and Nadai [11–13]. A detailed discussion of these two creep relations has been given by McVetty [14]. For wrought 18 percent Cr, 8 percent Ni steel tested at 1500°F, the hyperbolic sine law has been shown to fit the empirical data better than the power creep law; however, the hyperbolic sine law has not been used as much as the power creep law [15] on account of its greater mathematical complexity.

Some useful design charts and insight for elbows subjected to creep deformation have been given by Spence and Boyle [16–21]. Most of their results were based on the power creep law or dealt with the case of pure bending. In the present paper, the load-deformation behavior of bending of curved beams with circular cross sections in the presence of axial force (Fig. 1) is studied. The beam material is assumed to have identical tensile and compressive stress-strain rate relations, and to obey the Prandtl-Nadai creep law. The derivation is based on the assumption of Winkler's theory of curved beams, which stated that the cross sections are inextensional and that they remain plane and normal to the centroidal axis. Useful results are presented in the form of dimensionless curves and charts. The use of these charts is illustrated by example problems.

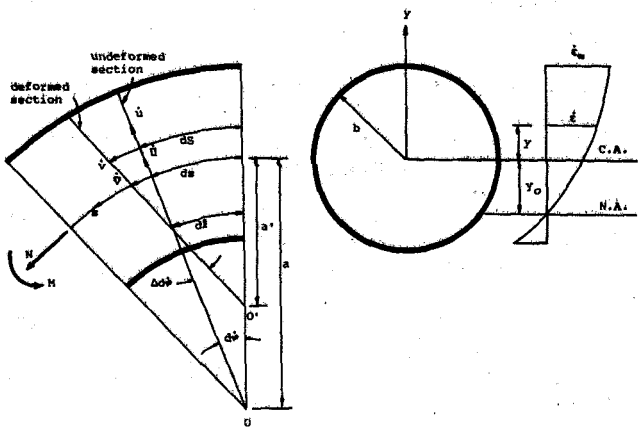

Fig. 1 Creep deformations of a curved beam

Analysis

Kinematics of Deformation. Based on Winkler's theory [22–24], the linearized radial and circumferential components of displacement rate, $\dot{u}$ and $\dot{v}$, at a distance y from the centroidal axis can be shown as

$$\dot{u} = \dot{\bar{u}} \tag{1}$$

$$\dot{v} = \left(1 + \frac{y}{a}\right)\dot{\bar{v}} - y\frac{d\dot{\bar{u}}}{ds} \tag{2}$$

where $\dot{\bar{u}}$ and $\dot{\bar{v}}$ are the radial and circumferential components of displacement rate of a particle on the centroidal axis. Since the cross sections are assumed to be inextensional, y is invariant under the deformation. The positive senses of $\dot{u}$, $\dot{v}$, $\dot{\bar{u}}$, $\dot{\bar{v}}$, and y are shown in Fig. 1. The arc length element of a fiber at distance y from the centroidal axis, dS, is related to the arc length element measured on the centroidal axis, ds, by

$$dS = \left(1 + \frac{y}{a}\right)ds \tag{3}$$

[1] Formerly with Bechtel

Contributed by the Gas Turbine Division of THE AMERICAN SOCIETY OF MECHANICAL ENGINEERS and presented at the 29th International Gas Turbine Conference and Exhibit, Amsterdam, The Netherlands, June 4–7, 1984. Manuscript received at ASME Headquarters January 12, 1984. Paper No. 84-GT-176.

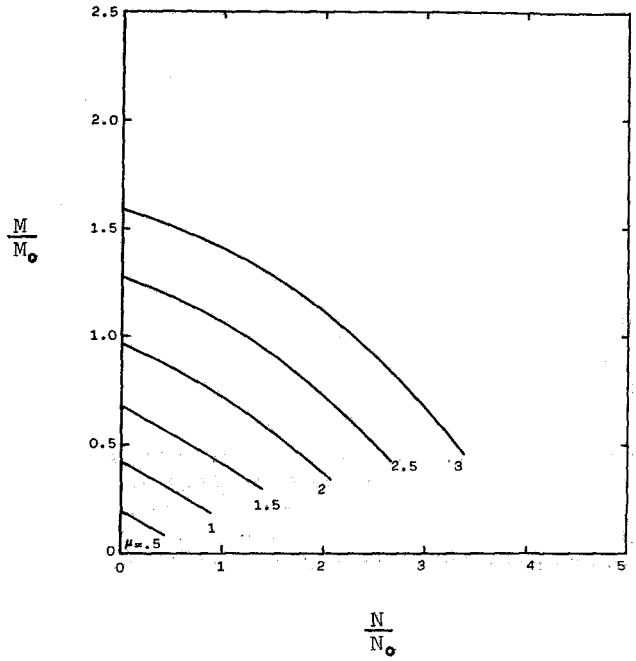

Fig. 2 Dimensionless bending moment and axial force interaction curves ($\gamma = 0$)

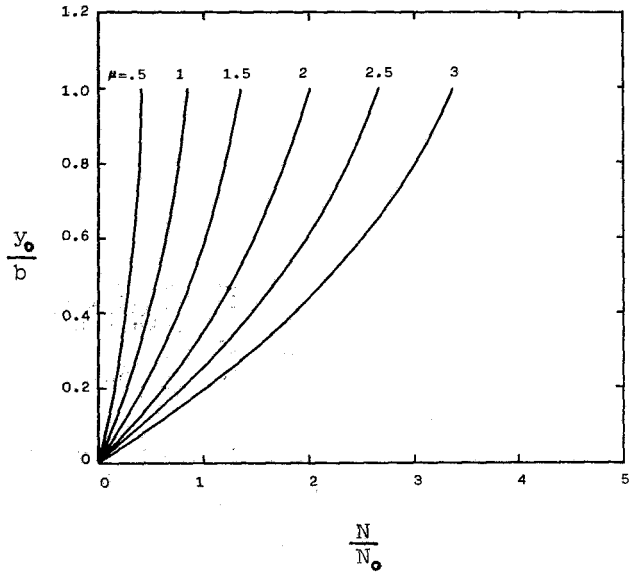

Fig. 3 Neutral axis location ($\gamma = 0$)

where a is the radius of curvature of the undeformed centroidal axis.

The circumferential strain rate of a fiber at distance y from the centroidal axis, $\dot{\epsilon}$, is given by Fig. 1 as

$$\dot{\epsilon} = \frac{d\dot{v}}{dS} + \frac{\dot{u}}{a+y} \tag{4}$$

Substituting equations (1–3) into equation (4), we have

$$\dot{\epsilon} = \frac{d\dot{v}}{ds} + \frac{1}{a+y}\left(\dot{u} - ay\frac{d^2u}{ds^2}\right) \tag{5}$$

At the extreme fiber, $y = b$, the maximum circumferential strain rate, $\dot{\epsilon}_m$, is

$$\dot{\epsilon}_m = \frac{d\dot{v}}{ds} + \frac{1}{a+b}\left(\dot{u} - ab\frac{d^2\dot{u}}{ds^2}\right) \tag{6}$$

At the neutral axis, $y = -y_0$, the circumferential strain rate is zero, i.e.,

$$0 = \frac{d\dot{v}}{ds} + \frac{1}{a-y_0}\left(\dot{u} + ay_0\frac{d^2\dot{u}}{ds^2}\right) \tag{7}$$

where y_0 defines the location of the neutral axis. Solving equations (6) and (7) yields

$$\dot{u} + a\frac{d\dot{v}}{ds} = \frac{b(1+\gamma)y_0}{(b+y_0)\gamma}\dot{\epsilon}_m \tag{8}$$

$$\frac{d\dot{v}}{ds} - a\frac{d^2\dot{u}}{ds^2} = \frac{b(1+\gamma)}{(b+y_0)\gamma}\dot{\epsilon}_m \tag{9}$$

and equation (5) becomes

$$\dot{\epsilon} = \frac{(1+\gamma)(y/b+y_0/b)}{(1+\gamma\, y/b)(1+y_0/b)}\dot{\epsilon}_m \tag{10}$$

where

$$\gamma = \frac{b}{a} \tag{11}$$

has been substituted.

Constitutive Equation. The Prandtl-Nadai Creep Law is given by the average uniaxial stress-strain rate relation

$$\sigma = \sigma_0 \sinh^{-1}\left(\frac{\dot{\epsilon}}{\dot{\epsilon}_0}\right) \tag{12}$$

where σ_0 and $\dot{\epsilon}_0$ are material constants [11, 12, 13, 25, 26]. For design purposes, it is convenient to introduce the "stress parameter," μ, such that

$$\sigma_m = \mu\sigma_0 \tag{13}$$

in which σ_m is the maximum circumferential stress occurring at the extreme fiber, where the maximum circumferential strain rate is

$$\dot{\epsilon}_m = \dot{\epsilon}_0 \sinh(\mu) \tag{14}$$

Consequently, the circumferential strain rate and stress distribution are, respectively

Nomenclature

a = radius of curvature of the undeformed centroidal axis
a' = radius of curvature of the deformed centroidal axis
b = radius of curved bars
F,E = complete elliptic integrals of the first and second kinds
M = bending moment
M_0 = equation (22)
N = axial force
N_0 = equation (21)
S = arc length of a circumferential fiber of the deformed curved bar with ordinate y
s = arc length on the centroidal axis
$\dot{u},\dot{v}$ = radial and circumferential components of displacement rate of a particle with initial coordinates (y, S)
$\dot{\bar{u}},\dot{\bar{v}}$ = radial and circumferential components of displacement rate of a particle on the centroidal axis. $\dot{\bar{u}}$ and $\dot{\bar{v}}$ are functions of s alone.
$\sigma_0,\dot{\epsilon}_0$ = material constants
$\sigma\ \dot{\epsilon}$ = circumferential stress and strain rate
$\sigma_m,\dot{\epsilon}_m$ = maximum circumferential stress and strain rate
y_0 = location of the neutral axis
γ = equation (11)
μ = equation (13)
$\dot{\Delta}d\phi$ = angle of rotation rate
$\dot{\Delta}\psi$ = change in curvature rate

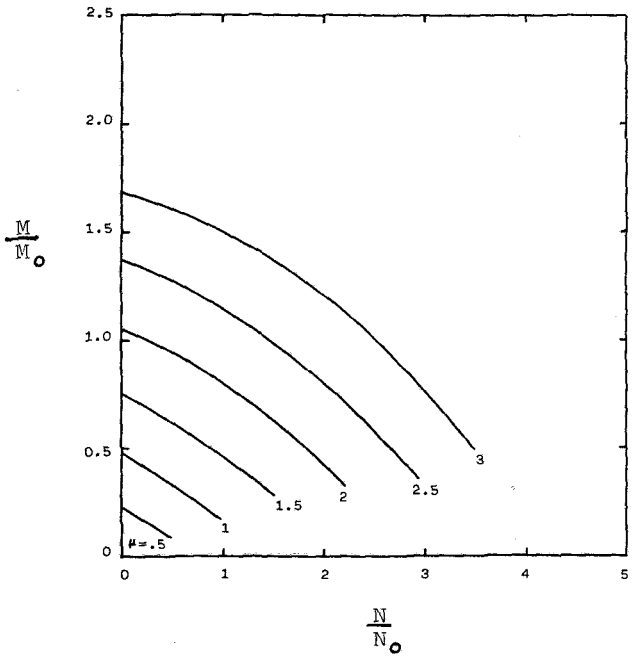

Fig. 4 Dimensionless bending moment and axial force interaction curves ($\gamma = .2$)

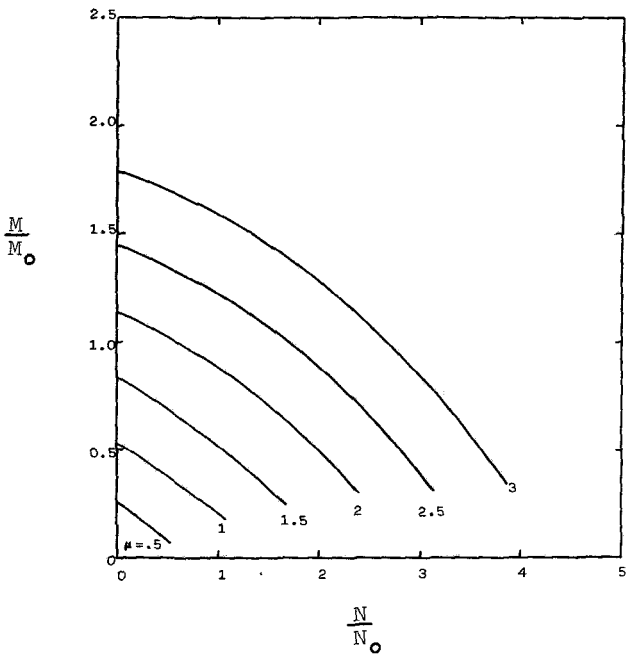

Fig. 6 Dimensionless bending moment and axial force interaction curves ($\gamma = .4$)

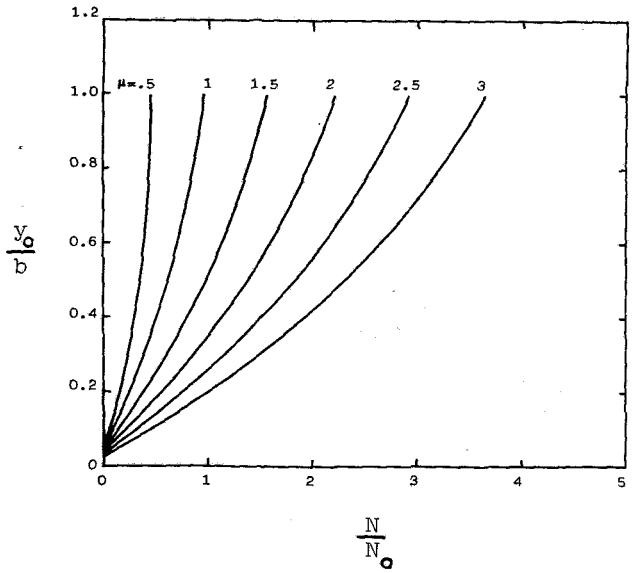

Fig. 5 Neutral axis location ($\gamma = .2$)

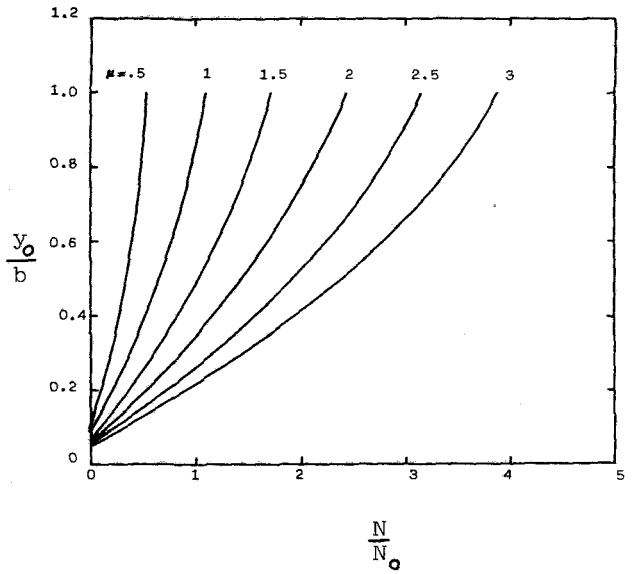

Fig. 7 Neutral axis location ($\gamma = .4$)

$$\dot{\epsilon} = \frac{b(1+\gamma)(y+y_0)\dot{\epsilon}_0}{(b+\gamma y)(b+y_0)} \sinh(\mu) \tag{15}$$

and

$$\sigma = \sigma_0 \sinh^{-1}\left[\frac{(1+\gamma)(y+y_0)b}{(b+\gamma y)(b+y_0)} \sinh(\mu)\right] \tag{16}$$

Equilibrium Equations. The net tension, N, and the bending moment, M, about the centroidal axis of the cross section are (the positive senses of N and M are shown in Fig. 1), respectively

$$N = \int \sigma \, dA \tag{17}$$

and

$$M = \int \sigma \, y \, dA \tag{18}$$

Substituting equation (16) into equations (17) and (18), we have

$$\frac{N}{N_0} = \int_{-b}^{b} \left(1 - \frac{y^2}{b^2}\right)^{1/2} \sinh^{-1}\left[\frac{(1+\gamma)(y+y_0)b}{(b+\gamma y)(b+y_0)} \sinh(\mu)\right] dy/b \tag{19}$$

and

$$\frac{M}{M_0} = \int_{-b}^{b} \left(\frac{y}{b}\right)\left(1 - \frac{y^2}{b^2}\right)^{1/2} \sinh^{-1}\left[\frac{(1+\gamma)(y+y_0)b}{(b+\gamma y)(b+y_0)} \sinh(\mu)\right] dy/b \tag{20}$$

where

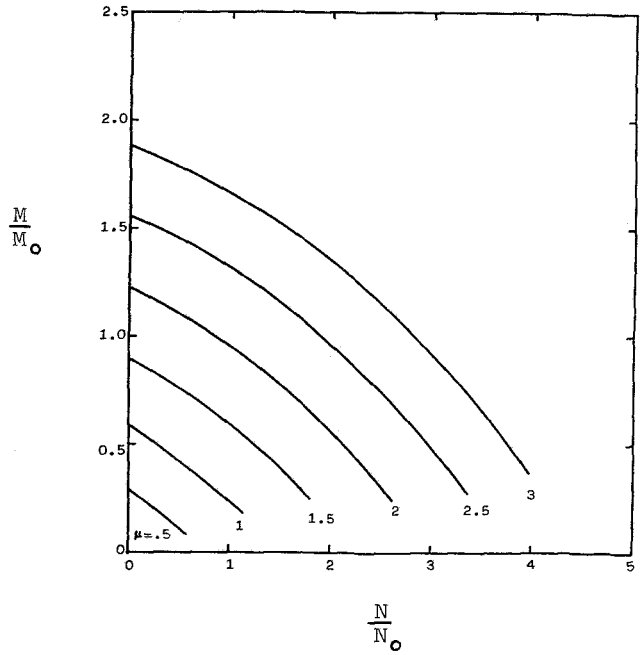

Fig. 8 Dimensionless bending moment and axial force interaction curves ($\gamma = .6$)

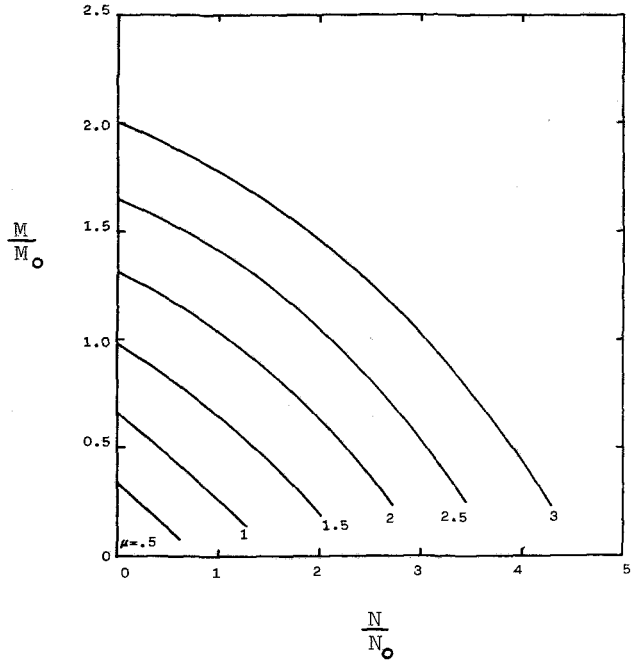

Fig. 10 Dimensionless bending moment and axial force interaction curves ($\gamma = .8$)

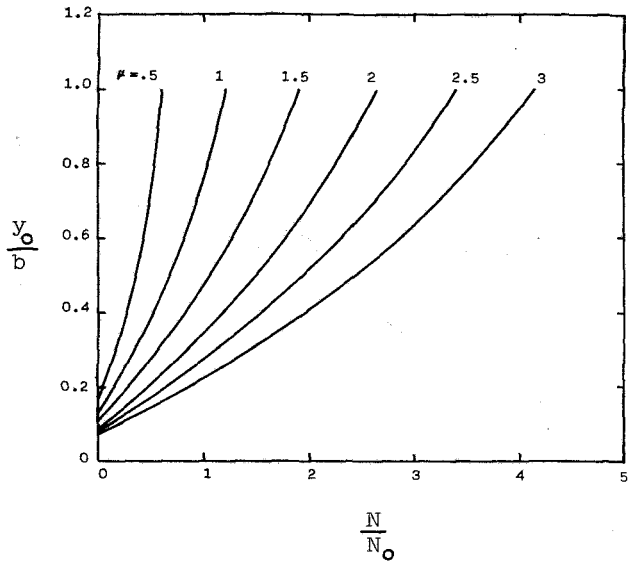

Fig. 9 Neutral axis location ($\gamma = .6$)

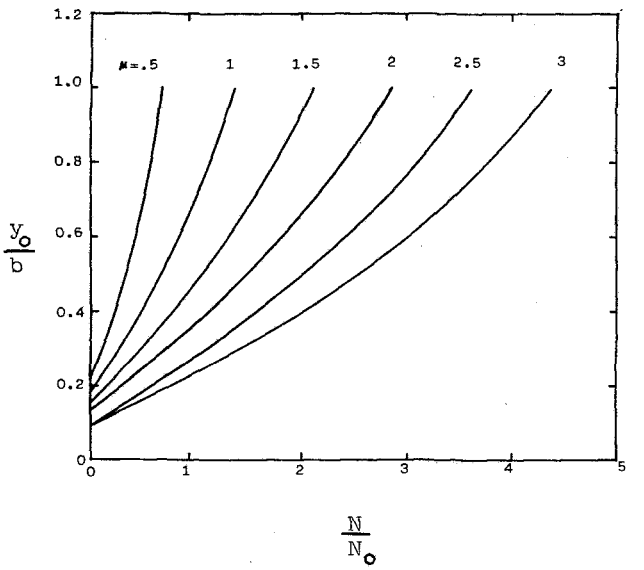

Fig. 11 Neutral axis location ($\gamma = .8$)

$$N_0 = 2b^2\sigma_0 \tag{21}$$

and

$$M_0 = 2b^3\sigma_0 \tag{22}$$

have been substituted. Simpson's rule [27] with 180 equal intervals is employed to evaluate the integrals in equations (19) and (20). Numerical results are plotted in Figs. 2–11 for a wide range of values of μ, γ, M, N, and y_0. The case of $\gamma = 0$ corresponds to a straight beam.

For a straight beam subjected to pure bending, $N = 0$ and equation (20) becomes

$$\frac{M}{M_0} = \int_{-b}^{b} \left(\frac{y}{b}\right)\left(1-\frac{y^2}{b^2}\right)^{1/2} \sinh^{-1}\left[\frac{y}{b}\sinh(\mu)\right] dy/b$$

The above integral can be integrated exactly into closed form

$$\frac{M}{M_0} = \frac{2}{9k}\left[F - 2E + \frac{2(F-E)}{k^2}\right]$$

where

$$k = \frac{\sinh(\mu)}{[1+\sinh^2(\mu)]^{1/2}} < 1$$

and F and E are the complete elliptic integrals of the first and second kinds, respectively. The values of M/M_0 for $\mu = 0.5$, 1, 1.5, 2, 2.5, and 3 are shown in Fig. 2. It is obvious that the difference between the exact closed-formed solutions and the numerical integration solutions is invisible.

Deflection of Curved Bars.

Refer to Fig. 1, where we have

$$dl = (a' - y_0)(\dot{\Delta}d\phi + d\phi) \tag{23}$$

and

$$dl = (a - y_0)d\phi \tag{24}$$

where $\dot{\Delta}d\phi$ is the angle of rotation rate of a plane from its

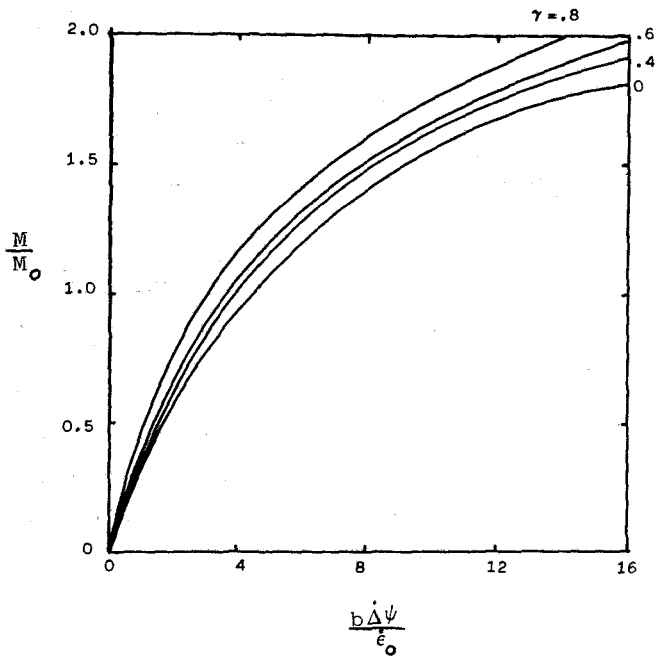

Fig. 12 Moment-curvature relations

undeformed position to the deformed position, and it is related to the centroidal axis displacement rate components, $\dot{u}$ and $\dot{v}$, by the following expression

$$\frac{\dot{\Delta} d\phi}{d\phi} = \frac{d\dot{v}}{ds} - a\frac{d^2\dot{u}}{ds^2} \tag{25}$$

a' is the radius of curvature of the deformed curved beam with the center of curvature at $0'$, and can, in view of equations (9, 11, 14, 23, 24, 25), be written as

$$a' = \frac{b + y_0 + (1+\gamma)\dot{\epsilon}_0 y_0 \sinh(\mu)}{\gamma(b+y_0) + b(1+\gamma)\dot{\epsilon}_0 \sinh(\mu)} b \tag{26}$$

The change in curvature rate, $\dot{\Delta}\psi$, is defined by

$$\dot{\Delta}\psi = \frac{1}{a'} - \frac{1}{a} \tag{27}$$

Substituting equation (26) into equation (27) leads to

$$\frac{b\dot{\Delta}\psi}{\dot{\epsilon}_0} = \frac{(1+\gamma)(b-\gamma y_0)\sinh(\mu)}{b + [1+(1+\gamma)\dot{\epsilon}_0 \sinh\mu] y_0} \tag{28}$$

Since $1 >> (1+\gamma)\dot{\epsilon}_0 \sinh\mu$, equation (28) becomes

$$\frac{b\dot{\Delta}\psi}{\dot{\epsilon}_0} = \frac{(1+\gamma)(b-\gamma y_0)\sinh(\mu)}{b+y_0} \tag{29}$$

Thus for a given γ, M, and N, the values of μ and y_0 can be determined by the charts provided in Figs. 2–11, and the change in curvature rate may be obtained by equation (29) for the applied loads. Figure 12 shows the dimensionless moment-curvature relations for $N = 0$, $\gamma = 0$, 0.4, 0.6, and 0.8.

Example Problems

Problem 1.

Given $\gamma = 0.6$, $M/M_0 = 0.6$, and $N/N_0 = 1.9$. Find σ, $\dot{\epsilon}_m$, and y_0/b.

Solution. From Fig. 8, with $M/M_0 = 0.6$ and $N/N_0 = 1.9$, we have $\mu = 2$, and from Fig. 9 with $N/N_0 = 1.9$ and $\mu = 2$, we have $y_0/b = 0.65$. From equation (16), we have the following stress distribution

$$\sigma = \sigma_0 \sinh^{-1}\left[\frac{3.517(0.65 + y/b)}{1+0.6y/b}\right]$$

The maximum strain rate can be obtained from equation (14) as

$$\dot{\epsilon}_m = 3.627\dot{\epsilon}_0$$

Problem 2.

Given $\gamma = 0.4$, $M/M_0 = 1.2$, and $\mu = 2.5$. Find N/N_0, y_0/b, and $\dot{\epsilon}$.

Solution. From Fig. 6 with $M/M_0 = 1.2$ and $\mu = 2.5$, we have $N/N_0 = 1.125$. From Fig. 7 with $\mu = 2.5$ and $N/N_0 = 1.125$, we have $y_0/b = 0.3$. The strain rate distribution is given by equation (15) as

$$\dot{\epsilon} = \frac{6.516(0.3 + y/b)}{1+0.4y/b}\dot{\epsilon}_0$$

Problem 3.

Given a 180 deg curved bar with $\gamma = 0.8$ subjected to a pure bending moment of $M/M_0 = 1.5$. Determine the deflection rate, $\dot{\delta}$, across the diameter.

Solution. The deflection rate across the diameter is

$$\dot{\delta} = 2(a - a') \tag{30}$$

Substituting equation (26) into equation (30), in view of equations (28) and (29), it can be shown that

$$\frac{\dot{\delta}}{a\dot{\epsilon}_0} = \frac{2}{\gamma}\frac{b\dot{\Delta}\psi}{\dot{\epsilon}_0} \tag{31}$$

In the present case ($\gamma = 0.8$, $M/M_0 = 1.5$), Fig. 12 yields $b\dot{\Delta}\psi/\dot{\epsilon}_0 = 6.74$. Thus we have $\dot{\delta}/a\dot{\epsilon}_0 = 16.85$, where a is the radius of curvature of the undeformed centroidal axis, $\dot{\epsilon}_0$ is the material constant.

Conclusions

Based on small deformation theory, an exact analysis has been presented for the bending of curved beams with Prandtl-Nadai creep law in the presence of axial force. Useful curves and charts that relate the variables, axial force, location of neutral axis, bending moment, maximum stress and strain rate, and change of curvature rate have also been provided for a wide range of conditions. The use of these charts has been illustrated by examples for determining the stress and strain rate distribution, resultant axial force and bending moment, and deflection. The accuracy of the present results has been demonstrated by comparing with closed-form solutions for the pure bending of a straight beam.

It is noted that the results presented here can also be applied to nonstationary creep, provided that the material constants σ_0 and $\dot{\epsilon}_0$ are generated from the average isochronous stress-strain diagram [28–30] and the strain rate component is changed to strain component.

References

1 Boyce, P. M., *Gas Turbine Engineering Handbook*, Gulf Publishing Company, Houston, 1982.

2 Frost, F. P., "Some Practical Examples of Creep in Metal Components and the Resulting Design Problems," *Creep of Engineering Materials*, edited by C. D. Pomeroy, Mechanical Engineering Publications, Ltd., London, 1978.

3 ASME Boiler and Pressure Vessel Code, Section III, Division 1, "Class One Components in Elevated Temperature Services," 1977.

4 Boresi, A. P., and Sidebottom, O. M., TAM Report No. 347, Department of Theoretical and Applied Mechanics, University of Illinois, Urbana, Ill. 1971.

5 Lin, T. H., *Theory of Inelastic Structures*, John Wiley & Sons, New York, 1968.

6 Findley, W. N., Lai, J. S., and Onaran, K., *Creep and Relaxation of Nonlinear Viscoelastic Materials*, North-Holland, 1976.

7 Boyle, J. T., and Spence, J., *Stress Analysis for Creep*, Butterworth & Co., Ltd., 1983.

8 Norton, F. H., *The Creep of Steel at High Temperature*, McGraw-Hill, New York, 1922.

9 Bailey, R. W., "Utilization of Creep-test Data in Engineering Design," *Proc. Inst. Mech. Engrs.*, Vol. 131, 1935, London, pp. 131–350.

10 Prandtl, L., "Ein Gedankenmodell zur kinetischen Theorie der festen Korper," *ZAMM*, Vol. 8, 1928, pp. 85–196.

11 Nadai, A., "The Influence of Time Upon Creep, The Hyperbolic Sine Law," *S. Timoshenko Anniversary Volume*, Macmillian, New York, 1938, p. 155.

12 Nadai, A., *Theory of Flow and Fracture of Solids*, 2d ed., McGraw-Hill, New York, 1950.

13 Nadai, A., "The Creep of Metals Under Various Stress Conditions," *Von Karman Anniversary Volume*, California Institute of Technology, 1941, pp. 237–257.

14 McVetty, P. G., "Creep of Metals at Elevated Temperature—The Hyperbolic Sine Relations between Stress and Creep Rate," ASME *Transactions*, Vol. 65, 1943, p. 761.

15 Hult, J., *Creep in Engineering Structures*, Blaisdell Pub. Co., London, 1966.

16 Spence, J., "Creep Analysis of Smooth Curved Pipes under In-plane Bending," *Journal of Mechanical Engineering Science*, Vol. 15, 1973, pp. 252–265.

17 Spence, J., "Stationery Creep Stresses for Elliptical Cross-Section Pipe Bends Subject to In-plane Bending," ASME *Journal of Pressure Vessel Technology*, Vol. 96, 1974, pp. 162–170.

18 Spence, J., and Boyle, J. T., "An Analysis for Out-of-plane Bending on Curved Pipes in Creep: Development of Method and Design Factors," International Working Group of Fast Reactors, Specialists Meeting on High Temperature Structural Design Technology, Champion, Pa., Apr., 1976.

19 Boyle, J. T., and Spence, J., "The Nonlinear Analysis of Pressurized Curved Pipes," *Proceedings of the 3rd International Conference on Pressure Vessel Technology*, Tokyo, pt. 1, 1977, p. 121.

20 Boyle, J. T., and Spence, J., "The Flexibility of Curved Pipes in Creep," ASME *Journal of Pressure Vessel Technology*, Vol. 99, 1977, pp. 444–453.

21 Boyle, J. T., and Spence, J., "Generalized Structural Models in Creep Mechanics," *Creep in Structures*, edited by A. R. S. Ponter and D. R. Hayhurst, Springer-Verlag, New York, 1981.

22 Timoshenko, S., *Strength of Materials*, pt. 1, 3d ed., Robert E. Krieger Pub. Co., Huntington, N.Y.

23 Novozhilov, V. V., *Foundations of the Nonlinear Theory of Elasticity*, Graylock Press, Rochester, N.Y., 1953.

24 Langhaar, H. L., Boresi, A. P., and Carver, D. R., "Energy Theory of Buckling of Circular Elastic Rings and Arches," *Proceedings of the 2nd. U.S. National Congress of Applied Mechanics*, June 1954, pp. 437–443.

25 Nadai, A., and McVetty, P. G., "Hyberbolic Sine Chart for Estimating Working Stresses of Alloys at Elevated Temperatures," ASTM, *Proceedings*, Vol. 43, 1943, pp. 734–745.

26 Nadai, A., "On the Creep of Solids at Elevated Temperatures," *Journal of Applied Physics*, Vol. 8, 1937, p. 418.

27 McCalla, T. R., *Introduction to Numerical Methods and FORTRAN Programming*, John Wiley & Sons, New York, 1967.

28 Smith, J. O., and Sidebottom, O. M., *Inelastic Behavior of Load-Carrying Members*, John Wiley & Sons, New York, 1965.

29 Robotnov, Y. N., *Creep Problem in Structural Members*, North-Holland, 1969.

30 Kraus, H., *Creep Analysis*, John Wiley & Sons, New York, 1980.

A Simplified Method for Elastic-Plastic-Creep Structural Analysis

A. Kaufman
National Aeronautics and Space Administration,
Lewis Research Center
Cleveland, Ohio 44135

A simplified inelastic analysis computer program (ANSYMP) was developed for predicting the stress-strain history at the critical location of a thermomechanically cycled structure from an elastic solution. The program uses an iterative and incremental procedure to estimate the plastic strains from the material stress-strain properties and a plasticity hardening model. Creep effects can be calculated on the basis of stress relaxation at constant strain, creep at constant stress or a combination of stress relaxation and creep accumulation. The simplified method was exercised on a number of problems involving uniaxial and multiaxial loading, isothermal and nonisothermal conditions, dwell times at various points in the cycles, different materials, and kinematic hardening. Good agreement was found between these analytical results and nonlinear finite element solutions for these problems. The simplified analysis program used less than 1 percent of the CPU time required for a nonlinear finite element analysis.

Introduction

The drive toward better performance and fuel economy and aircraft gas turbine engines has resulted in higher turbine inlet temperatures, pressure ratios, and rotor speeds. These more severe operating conditions have subjected the hot section components to thermomechanical load cycles that induce significant inelastic strains and eventual fatigue cracking. It has become increasingly difficult to design reliable components to meet both the engine life and performance requirements. Improvements in the durability of these components depend on accurate structural analysis and life prediction. Life prediction methods have been under development by the NASA Lewis Research Center and other organizations [1–4]. Application of these methods requires knowledge of the temperature-stress-strain history at the critical crack initiation location of the structure.

The primary structural parameters of interest for life prediction purposes are generally the total strain range and the mean cyclic stress. For most practical cases, the critical location and the total strain range can be satisfactorily obtained from an elastic analysis [3–5]. However, in cases involving purely mechanical load cycling, creep, or large plastic strains, an elastic analysis may not be adequate to determine the total strain range. Mean stresses for hot section components, as well as multiaxial and thermomechanical fatigue specimens, must be calculated from some type of nonlinear analysis. The accuracy of the solutions is largely dependent on the adequacy of the material properties and the creep-plasticity models used in the analysis.

Nonlinear finite element analysis is being increasingly used for calculating inelastic structural response. However, nonlinear methods are not feasible for use as a component design tool because of the high computing costs associated with the iterative and incremental nature of the inelastic solutions. Computing costs are further increased by the presence of high thermal gradients and geometrical irregularities, such as cooling holes, which necessitate three-dimensional analyses. Three-dimensional, nonlinear finite element analyses are prohibitively time consuming and expensive to conduct in the early design stages for combustor and turbine structures.

To improve the design of hot section components, it is necessary to develop simpler and more economical methods for representing structural behavior under cyclic loading. Development of life prediction methods would also benefit from a simplified analysis method for determining the structural behavior of multiaxial and thermomechanical fatigue specimens.

This study was conducted to develop a fully automated simplified analytical procedure for estimating the stress-strain history of a thermomechanically loaded structure subject to cyclic inelasticity. A computer program (ANSYMP) was created to predict the cyclic-stress-strain history at the critical location of a structure from a calculated elastic solution or one constructed from strain measurements at the critical location. An incremental and iterative procedure estimates the plastic strains from the material stress-strain properties and a plasticity hardening model. Creep options are incorporated into the program on the basis of stress relaxation at constant strain, creep at constant stress or a combination of stress relaxation and creep accumulation.

Analytical predictions from the simplified method were compared with nonlinear finite element solutions from the MARC computer program [6] for a number of problems. Initial development of the program was based on a strain-

Contributed by the Gas Turbine Division of THE AMERICAN SOCIETY OF MECHANICAL ENGINEERS and presented at the 29th International Gas Turbine Conference and Exhibit, Amsterdam, The Netherlands, June 4–7, 1984. Manuscript received at ASME Headquarters, January 12, 1984. Paper No. 84-GT-191.

controlled uniaxial problem with cyclic stress-strain and creep properties for Inconel 718 alloy. Verification of the simplified procedure was conducted using test problems involving an Inconel 718 benchmark notch specimen that was load cycled in an experiment designed to verify structural analysis methodologies [7] and a double-edge wedge specimen that had been thermally cycled in fluidized beds [8]. A kinematic hardening model was used for all of these problems. In [5] a MARC elastic-plastic analysis using a kinematic hardening model gave excellent agreement with the experimental results for the benchmark notch specimen under continuous mechanical load cycling. Cyclic stress-strain and creep properties for IN 100 alloy [5] were used in the analyses for the wedge specimen problem. Variations of these three problems, including imposed creep dwell times at different points in the cycles, were exercised with both the ANSYMP simplified analysis program and the MARC program. Verification of the simplified analysis procedure was made on the basis of how well it was able to duplicate the stress-strain hysteresis loops from MARC elastic-plastic-creep analyses of these problems.

Analytical Procedure

A simplified inelastic procedure was developed for calculating the stress-strain history at the critical fatigue location of a structure subjected to cyclic thermomechanical loading. The fundamental assumption in this procedure is that the inelastic region is local and is constrained from redistribution by the surrounding elastic material. It follows from this assumption that the total strain history at the critical location can be defined by an elastic solution. Justification for the assumption of elastic constraint of local inelasticity can be found in [3–5], where structural analyses of combustor liners, air-cooled turbine blades, and wedge fatigue specimens have shown that the total strain ranges from elastic and nonlinear solutions are in close agreement. A corollary to this assumption is that the elastic loading and unloading segments of the effective stress-equivalent total strain hysteresis loops constructed from an elastic-plastic analysis will be parallel to the elastic hysteresis loop. This is demonstrated by comparing the nonlinear and elastic hysteresis loops in [5].

The basic problem in developing the simplified analytical procedure was to characterize the yield surface in terms of the total strain obtained from an elastic analysis or strain measurements. Classical plasticity theory characterizes the yield surface by a yield condition to describe yielding under multiaxial stress states and by a hardening model to establish the location of the yield surface during cycling. The simplified procedure was set up to accommodate itself to any yield criterion or hardening model. The only requirements are that the elastic input data be consistent with the yield criterion and that the appropriate material properties be used in conjunction with the hardening model.

In this study, all of the analyses were performed with a kinematic hardening model. A representation of a cyclic stress-strain curve by a bilinear kinematic hardening model is illustrated in Fig. 1. The loci of the tips of the cyclic curves is described by the equation

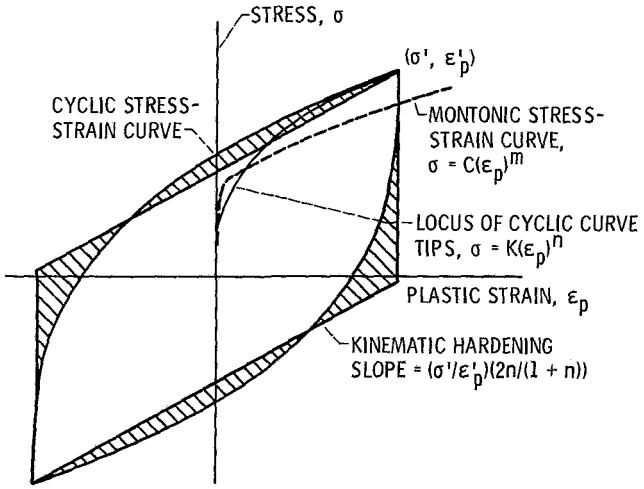

Fig. 1 Representation of stress-strain curves

$$\sigma = K(\epsilon_p)^n \tag{1}$$

The work hardening slope for the kinematic hardening model was determined from energy considerations to give the same strain energy, as indicated by the enclosed area in Fig. 1, as the actual stress-strain curve. This work hardening slope will be defined by

$$m = (\sigma'/\epsilon_p')(2n/(1+n)) \tag{2}$$

and the initial yield point, $\Delta\sigma_{yi}$, by

$$\Delta\sigma_{yi} = \sigma' - m(\epsilon_p') \tag{3}$$

The yield stress shift ($\Delta\sigma_y$) due to load reversal under kinematic hardening is

$$\Delta\sigma_y = 2(\sigma_y - m(\epsilon_p)) = 2(\sigma_{yi}) \tag{4}$$

Creep characteristics of the material were incorporated into the program in the power law

$$\epsilon_c = (\sigma/A)^B t^C \tag{5}$$

A strain-hardening law [9] was used to accumulate creep strain under changing stress. Any of three creep options can be selected; (*i*) stress relaxation at constant strain, (*ii*) cumulative creep at constant stress, and (*iii*) a combination of (*i*) and (*ii*).

Most nonlinear computer programs use the von Mises yield criterion and incremental plasticity theory. Implicit in the von Mises yield criterion is the conversion of the total strain from a uniaxial stress-strain curve to modified equivalent total strain, as discussed in [9]. The modified elastic equivalent total strain corresponds to the uniaxial total elastic strain multiplied by $2(1 + \nu)/3$. This relationship must be taken into account for multiaxial problems in applying strain results from elastic finite element analyses or strain measurements as

Nomenclature

A,B,C = temperature-dependent constants in creep power law, equation (5)
E = modulus of elasticity
K,n = temperature-dependent constants in stress-strain equation, equation (1)
m = kinematic work hardening slope (Fig. 1)
t = time
$\Delta\sigma_y$ = yield stress shift due to load reversal
ϵ_c = creep strain
ϵ_p = plastic strain
ϵ_p' = maximum plastic strain in cycle (Fig. 1)
ϵ_t = total strain
σ = stress
σ_y = current yield stress
σ_{yi} = initial yield stress
σ' = maximum stress in cycle (Fig. 1)
ν = Poisson's ratio

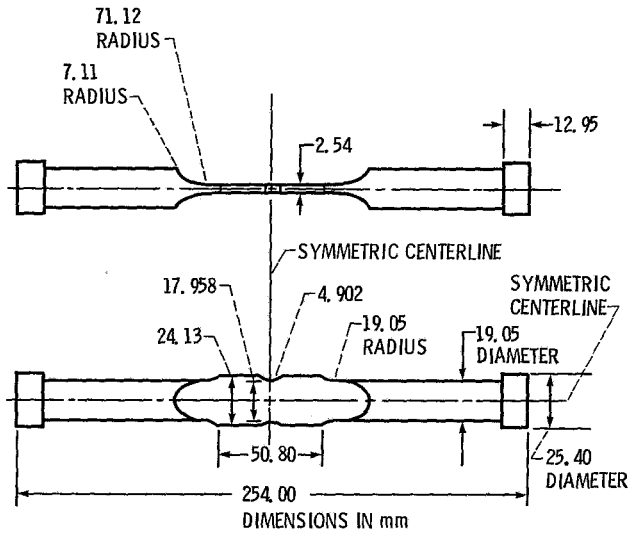

Fig. 2 Benchmark notch specimen (K_t = 1.9)

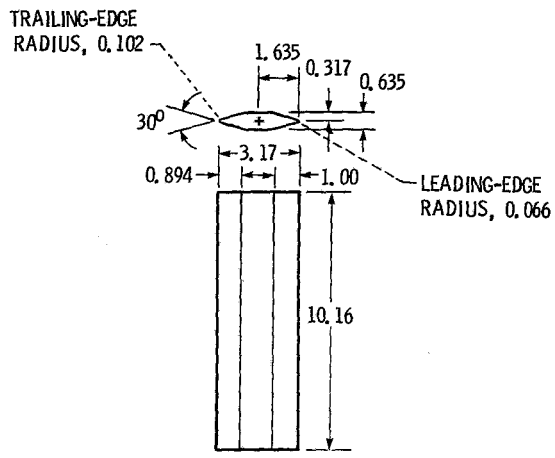

Fig. 3 Double-edge wedge. (All linear dimensions in centimeters.)

input for the simplified inelastic analysis. Both elastic and nonlinear finite-element analyses for this study were conducted with the MARC computer program. The elastic solutions computed from MARC for input into the simplified analysis method were automatically obtained in terms of von Mises effective stresses and modified equivalent total strains.

The elastic input data are subdivided into a sufficient number of increments to define the stress-strain cycle. Dwell times are specified for increments which require creep analysis. The increments are analyzed sequentially to obtain the cumulative plastic and creep strains and to track the yield surface. An iterative procedure is used to calculate the yield stresses for increments undergoing plastic straining. First, an estimated plastic strain is assumed for calculating an initial yield stress from the stress-strain properties and the simulated hardening model. Second, a new plastic strain is calculated as

$$\epsilon_p = \epsilon_t - \epsilon_c - \sigma_y/E \tag{6}$$

The yield stress is then recalculated using the new plastic strain. This iterative procedure is repeated until the new and previous plastic strains agree within a tolerance 1 percent.

A FORTRAN IV computer program (ANSYMP) was created to automatically implement the simplified analytical procedure. The program consists of the main executive routine, ANSYMP, and four subroutines, ELAS, YIELD, CREEP, and SHIFT. The incremental elastic data and temperatures are read into subroutine ELAS. Material stress-strain properties as a function of temperature and a simulated hardening model are incorporated in subroutine YIELD and the creep characteristics are incorporated in subroutine CREEP. Subroutine SHIFT is required to update the temperature effects on the yield stress shift. SHIFT also serves the function of deciding the future direction of the yield surface under nonisothermal conditions by determining the relation of future to past thermal loading.

The ANSYMP program is available from the Computer Software Management Information Center (COSMIC), University of Georgia, Athens, Ga. 30602 under LEW 14011. A flow chart of the program and sample input and output data are presented in [10].

The calculational scheme initially follows the effective stress-equivalent strain input data from subroutine ELAS until the occurrence of initial yielding. The stress-strain solution then proceeds along the yield surface as determined from the stress-strain properties in subroutine YIELD. At each increment during yielding the stress shift (difference between new yield stress and stress predicted from elastic analysis) from the original input data is calculated. Elastic load reversal is signaled when the input stress is less than the yield stress from the previous increment. During elastic unloading, the stresses are translated from the original elastic analysis solution by the amount of the calculated stress shift. Reverse yielding occurs when the stress reaches the reverse yield surface as determined from the hardening model incorporated in subroutine YIELD. Again, the solution follows the yield surface until another load reversal is indicated when the stress based on the shifted elastic solution is less than the yield stress. The elastic response during load reversal is obtained by translating the original elastic solution according to the new stress shift calculated during reversed yielding. The stress-strain response for subsequent cycles is computed by repeating this procedure of identifying load reversals, tracking reverse yield surfaces and translating the original elastic solution during elastic loading and unloading. Creep computations are performed for increments involving dwell times using the creep equation and strain hardening rule incorporated in subroutine CREEP. Depending on the nature of the problem, the creep effects are determined on the basis of one of the three options provided in the subroutine.

The computer program was verified by conducting simplified analyses for a series of three problems and comparing the results to those from MARC nonlinear analyses. The first of these problems was a simulation of a uniaxial specimen subjected to strain cycling under isothermal conditions. Variations of this problem were run with no creep dwell times and with dwell times at minimum and intermediate total strain levels. A kinematic hardening model was used with cyclic stress-strain and creep properties for Inconel 718 alloy obtained from [7]. Nonlinear and elastic MARC analyses of this problem were performed by using a single 20 node, three-dimensional element. The MARC solutions for the uniaxial problem were computed for the centroid of the single solid element model. The second problem considered was a mechanically load-cycled benchmark notch specimen shown in Fig 2. This specimen was tested under isothermal conditions as part of a program to provide controlled strain data for constitutive model verification [7]. A MARC analysis of this problem using kinematic hardening demonstrated excellent agreement with expermental data in [5]. A number of variations were run with both the MARC and ANSYMP programs. These variations included dwell times at maximum, minimum, and intermediate total strains and dwell times at increments where tensile yielding occurred. The simplified analysis of the benchmark notch problem used the kinematic hardening model and cyclic stress-strain and data for Inconel 718 alloy. The third problem was an IN 100 double-edge wedge specimen that was thermally cycled in the

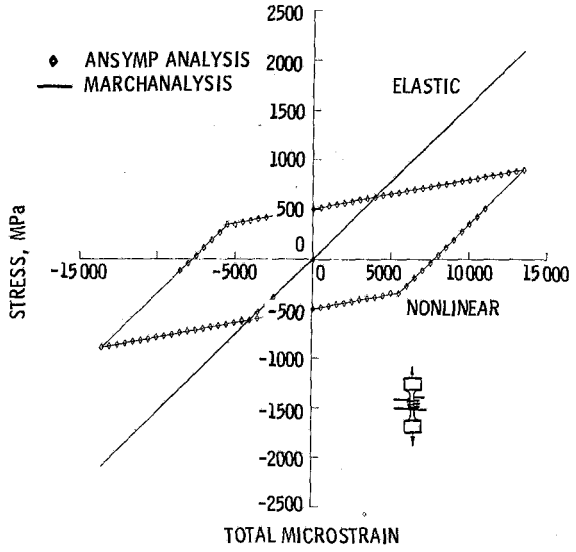

(a) No creep dwell time.

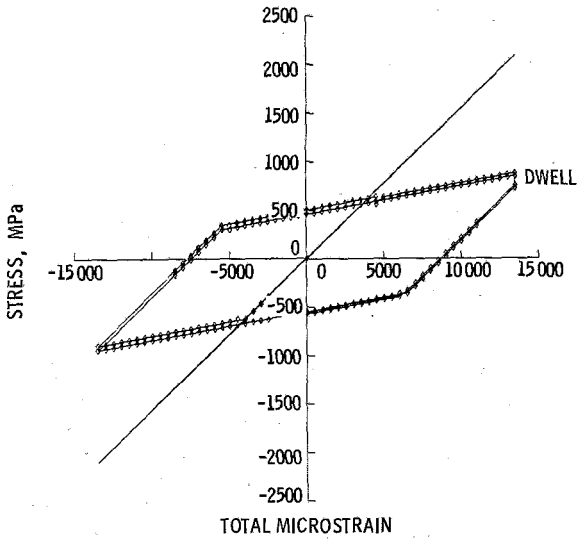

(b) Dwell time at maximum strain.

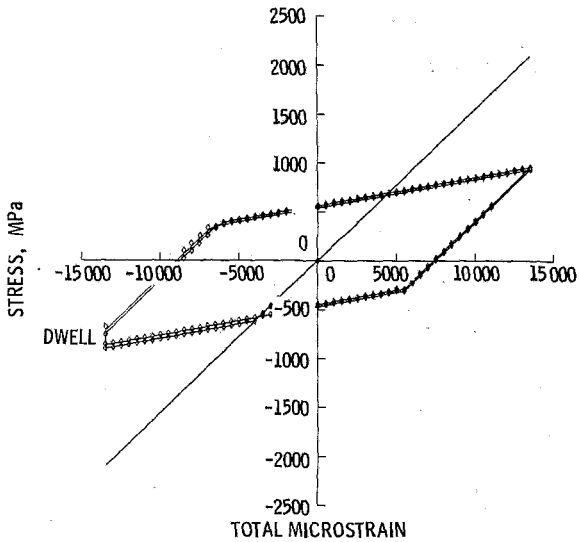

(c) Dwell time at minimum strain.

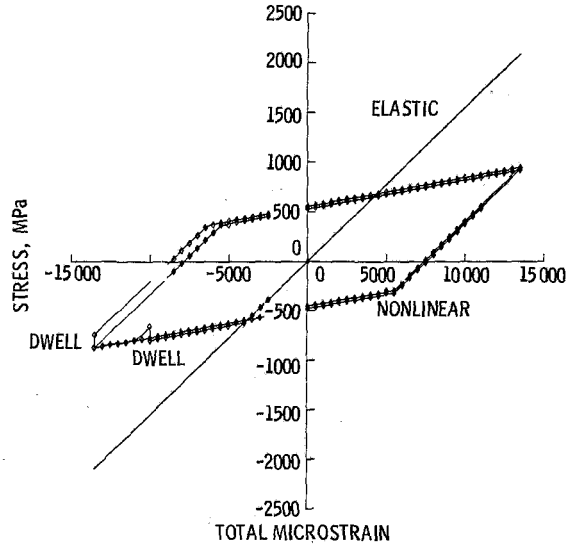

(d) Dwell times at minimum and intermediate strains.

Fig. 4 Comparison of ANSYMP and MARC analysis results for uniaxial problem

fluidized bed facility described in [8]. This problem provides a nonisothermal case for evalating the computer program. Both the MARC and ANSYMP analyses used the kinematic hardening model and the IN 100 cyclic stress-strain and creep properties reported in [5]. The geometry of the double-edge wedge specimen is illustrated in Fig. 3. The wedge problem was analyzed without dwell times and with dwell times at maximum and minimum total strain levels. The MARC solutions shown for the benchmark notch and wedge specimens were computed at the closest Gaussian integration point to the critical crack initiation location.

The material properties and kinematic hardening models were coded into subroutines YIELD, SHIFT, and CREEP. The program input initially involves specification of the number of increments of elastic input data, number of increments with dwell times, number of subincrements the dwell times are to be subdivided for creep calculations, the selected creep option and a pointer that refers to the type of problem to be solved and the set of material properties to be used in the analysis. The temperature, stress and total strain for the elastic solution is then listed for each increment. The elastic input data were repeated a second time to conduct the simplified analyses for two cycles for all the problems considered in this study. Finally, the dwell times are specified for those increments where creep calculations are to be performed. The output includes an echo of the parameters and the increment dwell times. For each increment, the temperature, stress, and the total, plastic and creep strains are listed. The output lists double the increments that were specified for the input because the stress-strain solution is printed for the beginning and end of each dwell increment.

Discussion of Analytical Results

The results of the simplified elastic-plastic-creep analyses of the uniaxial, benchmark notch, and wedge specimen cases are discussed herein. Comparisons are made with MARC inelastic solutions. Stress-strain cycles used for comparison purposes are in terms of effective stresses and equivalent total strains based on the von Mises yield criterion. The discussion is based on the critical location in the specimen where fatigue cracking would start.

Uniaxial Problem. The uniaxial problem was used for the basic development of the simplified approach and computer program. Since the loading was strain-controlled, the

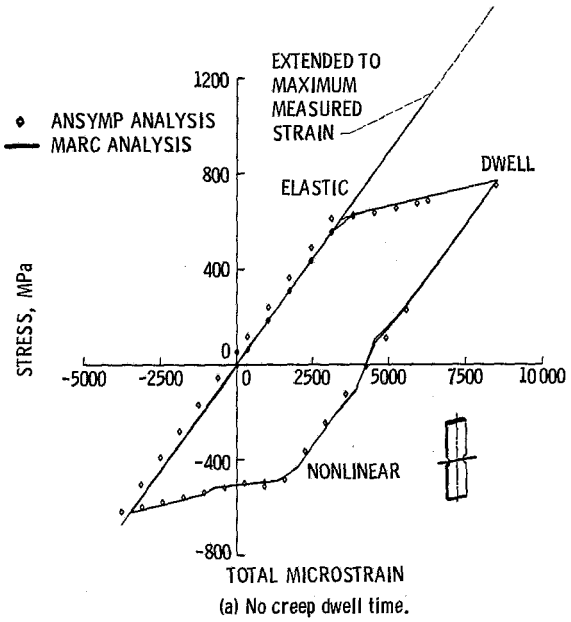

(a) No creep dwell time.

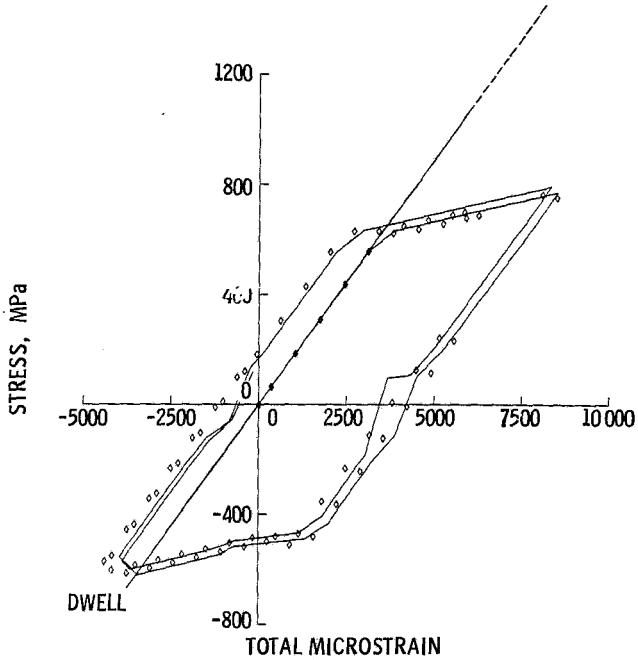

(c) Dwell time at minimum strain - creep option 3.

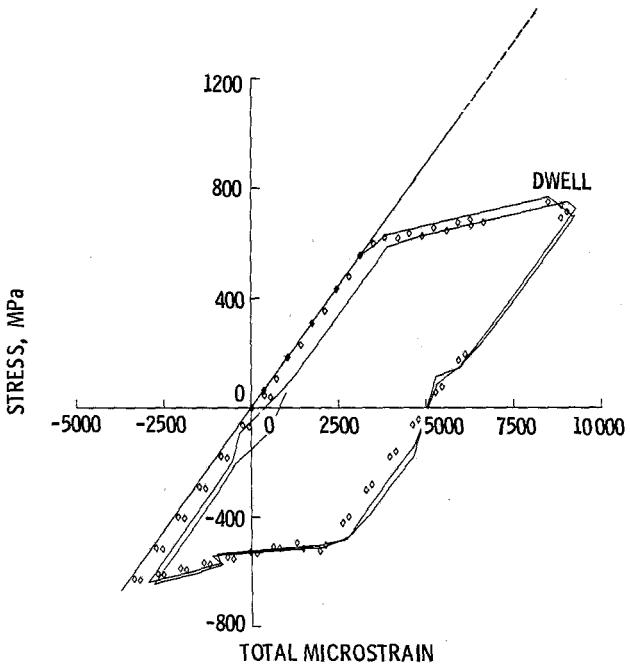

(b) Dwell time at maximum strain - creep option 3.

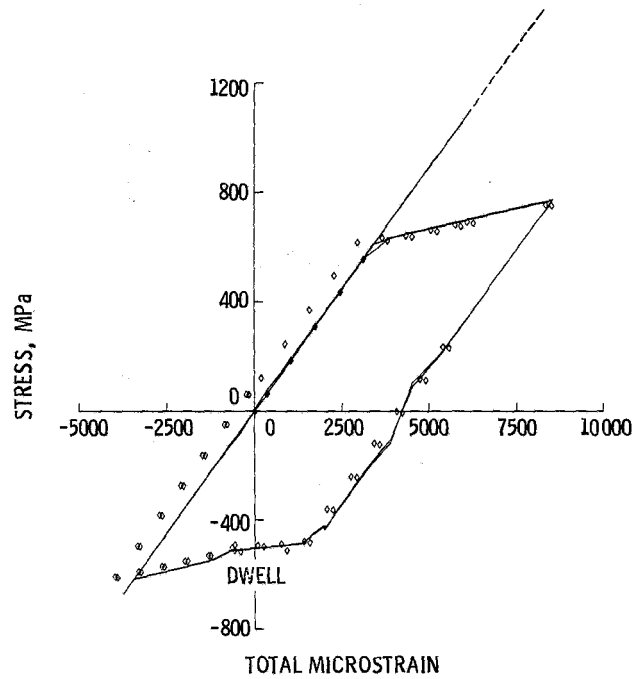

(d) Dwell time at intermediate strain - creep option 3.

Fig. 5 Comparison of ANSYMP and MARC analysis results for benchmark problem

maximum and minimum total strains were identical for the MARC elastic and nonlinear finite-element solutions. Also the effect of creep dwell time at any increment was to cause stress relaxation under constant total strain.

Four variations of the uniaxial problem were considered in this study. These were initial compressive loading without creep dwell times (Fig. 4(*a*)), dwell time at maximum strain (Fig. 4(*b*)), dwell time at minimum strain (Fig. 4(*c*)), and dwell times at minimum and intermediate strains (Fig. 4(*d*)). A constant temperature 649°C was assumed during the strain cycling. Creep option (*i*) (stress relaxation at constant strain) was used for all the creep computations.

A comparison of the stress-strain cycles obtained from the simplified and MARC elastic-plastic-creep analyses is shown in Fig. 4. Agreement between the ANSYMP and MARC nonlinear solutions is seen to be excellent for all the uniaxial cases.

Benchmark Notch Problem. The benchmark notch test was conducted by mechanical load cycling at a constant temperature of 649°C. A mechanically loaded structure, especially where the peak strain occurs at a discontinuity, is most likely to violate the basic assumption of the simplified approach that strain redistribution is prevented by containment of the local plastic region by the surrounding elastic material. The computed total strain range from the MARC elastic-plastic analysis was 20 percent greater than that ob-

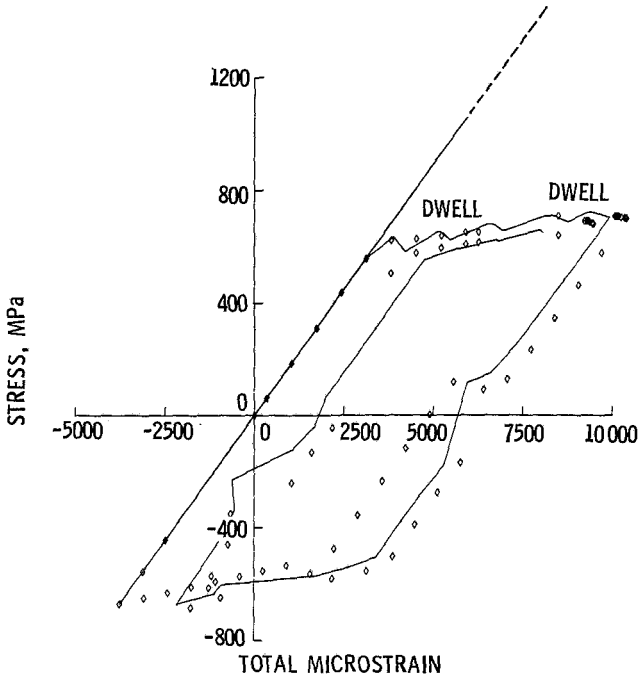

(e) Dwell times at tensile yield strains - creep option 3.

Fig. 5 Concluded

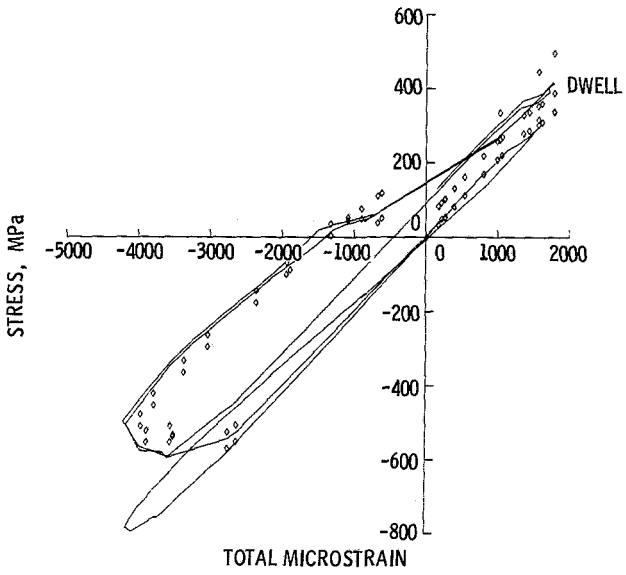

(b) Dwell time at maximum strain - creep option 3.

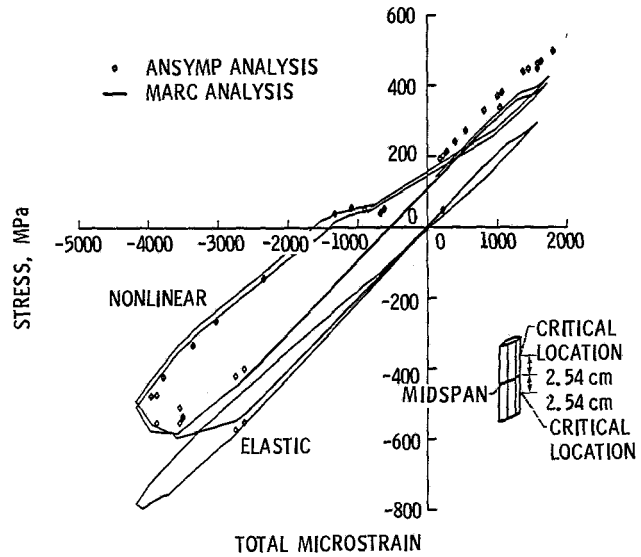

(a) No creep dwell time.

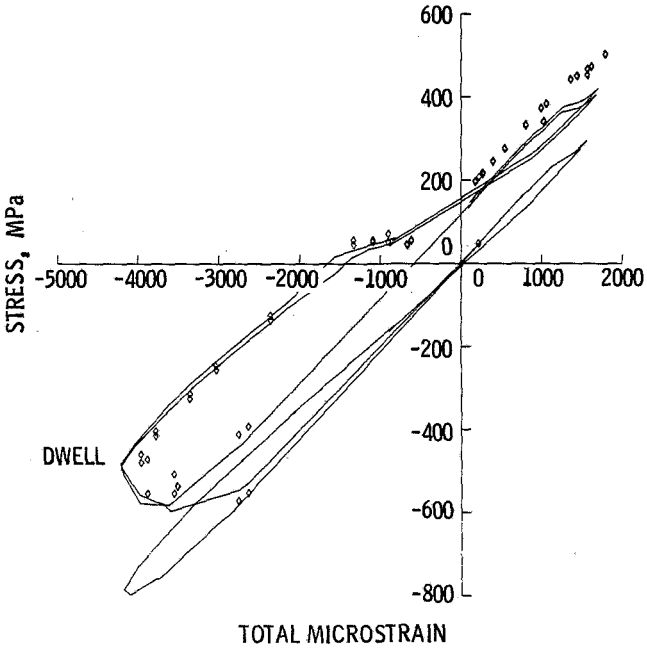

(c) Dwell time at minimum strain - creep option 3.

Fig. 6 Comparison of ANSYPM and MARC analysis results for wedge problem

tained from the MARC elastic analysis. This foreshortening of the elastic strain range would cause the simplified procedure to truncate the stress-strain hysteresis loop. Therefore, the elastic solution was constructed from strain measurements obtained at the notch root in [7]. When the elastic solution was extended to be consistent with the measured notch root strain, the agreement between the simplified and MARC elastic-plastic stress-strain hysteresis loops was excellent as demonstrated in Fig. 5(*a*). Both the ANSYMP and MARC elastic-plastic analyses gave stable stress-strain hysteresis loops for the second cycle. Further work has since been done to develop Neuber corrections for adjusting the elastic solution in this type of problem. The extended elastic strain range was used for all analyses of the benchmark notch problem in this study.

In Fig. 5 comparisons are shown of simplified and nonlinear finite-element analytical results for benchmark notch cases involving dwell times at maximum strain (Fig. 5(*b*)), at minimum strain (Fig. 5(*c*)), at intermediate strain in compressive yield (Fig. 5(*d*)) and at all increments involving tensile yielding (Fig 5(*e*)). ANSYMP analyses were performed using all three creep options for each of benchmark cases. The creep analyses using option 3 (combined stress relaxation and creep accumulation) gave the most consistent agreement with the MARC nonlinear finite-element solutions. This would indicate that creep option 3 should be used in most cases other than strain controlled problems.

In terms of cycle mean stresses, the simplified procedure gave results more compatible with MARC elastic-plastic analyses than were possible from an elastic solution. The mean stresses from the simplified and MARC elastic solutions

were 68 and 223 megapascals, respectively, compared to 77 megapascals for the MARC elastic-plastic solution. The application of creep dwell times did not significantly alter the cycle mean stresses. The ANSYMP analyses of the benchmark notch problem used less than 1 percent of the central processor unit (CPU) time required by the MARC nonlinear analyses.

Wedge Specimen Problem. The double-edge wedge specimen provided a nonisothermal case for evaluation of the simplified procedure and the operation of the ANSYMP program. Because of the incremental temperature changes, the elastic solution was no longer linear as for the isothermal uniaxial and benchmark notch cases.

In Fig. 6(*a*), the stress-strain hysteresis loops calculated from the ANSYMP simplified procedure and MARC elastic-plastic analyses are compared for two thermal cycles without dwell times. Reasonably good agreement is shown between the ANSYMP and MARC stress-strain hysteresis loops in Fig. 6(*a*). The mean stress for the second MARC stress-strain cycle was 55 megapascals. The simplified procedure predicted a mean stress of 20 megapascals compared to −201 megapascals for the elastic solution.

These analyses were repeated with dwell times imposed at the maximum strain level. As shown in Fig. 6(*b*), the predicted ANSYMP solution for this case was not in good agreement with the MARC nonlinear stress-strain cycles. This was due to the extreme sensitivity of creep computations to small variations in stress. The maximum tensile stresses predicted from ANSYMP for the elastic-plastic case (Fig. 6(*a*)) were not accurate enough to use for creep calculations. Better agreement between ANSYMP and MARC elastic-plastic-creep solutions is shown in Fig. 6(*c*) for dwell times applied at the minimum strain level of the cycle. This is due to the better agreement between ANSYMP and MARC stress predictions in compressive yield shown in Fig. 6(*a*).

Summary of Results

A simplified analysis procedure was developed for calculating the stress-strain history at the critical location of a thermomechanically cycled structure. A FORTRAN IV computer program, ANSYMP, was created to implement this procedure. The general conclusions and observations that were drawn from the evaluation of the method are as follows:

1. The predicted stress-strain response showed good to excellent agreement with elastic-plastic finite element analysis solutions using the MARC program.
2. The predicted creep response showed generally good agreement with comparable MARC analytical results. However, the accuracy of the creep calculations was very sensitive to variations in the calculated effective stresses from the MARC solution for the elastic-plastic case without creep. The creep option averaging the effects of stress relaxation at constant stress and cumulative creep at constant total strain demonstrated the most consistent agreement with MARC creep computations except for strain-controlled problems.
3. Mean cyclic stress predictions were in considerably better agreement with MARC nonlinear analysis results than mean stresses obtained from elastic solutions.
4. Nonlinear stress-strain histories were computed from the ANSYMP program with less than 1 percent of the CPU time required by the MARC program.
5. The accuracy of the simplification process is problem dependent. Strain redistribution adversely affects the solution accuracy. This is most likely to occur with mechanical load cycling at regions of high strain gradients. Neuber type corrections are being developed to account for strain redistribution under applied mechanical loading.

References

1 Halford, G. R., and Saltsman, J. F., "Strainrange Partitioning—A Total Strain Range Version," NASA TM-83023, 1983.

2 Hirschberg, M. H., and Halford, G. R., "Use of Strainrange Partitioning to Predict High-Temperature Low-Cycle Fatigue Life of Metallic Materials," NASA TN D-8072, 1976.

3 Moreno, V., "Combustor Liner Durability Analysis," PWA-5684-19, Pratt & Whitney Aircraft Group, East Hartford, CT., 1981. (NASA-CR-165250).

4 McKnight, R. L., Laflen, J. H., and Spamer, G. T., "Turbine Blade Tip Durability Analysis," R81AEG372, General Electric Co., Cincinnati, Ohio, 1981. (NASA-CR-165268).

5 Kaufman, A., "Evaluation of Inelastic Constitutive Models for Nonlinear Structural Analysis," *Nonlinear Constitutive Relations for High Temperature Appilcations*, NASA-CP-2271, 1983.

6 *MARC General Purpose Finite Element Analysis Program; User Manual*, Vols. A and B, MARC Analysis Research Corporation, Palo Alto, 1980.

7 Domas, P. A., et al., "Benchmark Notch Test for Life Prediction," R82AEB358, General Electric Co., Cincinnati, Ohio, 1982. (NASA-CR-165571).

8 Bizon, P. T., and Spera, D. A., "Comparative Thermal Fatigue Resistances of Twenty-Six Nickel and Cobalt-Base Alloys," NASA TN D-8071, 1975.

9 Mendelson, A., *Plasticity; Theory and Application*, Macmillan, New York, 1968.

10 Kaufman, A., "Development of a Simplified Procedure for Cyclic Structural Analysis," NASA TP-2243, 1983.

D. W. Cameron
Rolls-Royce Research Fellow,
Department of Mechanical Engineering,
University of Toronto,
Toronto, Ontario M5S 1A4

R. H. Jeal
Chief Materials Engineer,
Rolls-Royce, Ltd., Aeroengine Division,
Derby, England DE2 8BJ

D. W. Hoeppner
Cockburn Professor of Engineering Design and Director,
Structural Integrity, Fatigue, and Fracture Laboratories,
Department of Mechanical Engineering,
University of Toronto,
Toronto, Ontario M5S 1A4

SEM Investigations of Fatigue Crack Propagation in RR 58 Aluminum Alloy

Aluminum alloy RR 58 (AA 2618) has been viewed during exposure to cyclic loading, which is applied using a load frame inserted into a scanning electron microscope. Thus observation of surface interactions of the material microstructure with a propagating crack is feasible. Photomicrographs and (for the purposes of analysis and presentation) dynamic, real-time video-recordings used to document the processes will be displayed and the nature of the observations presented in relation to existing physical understanding of fatigue. Some additional ideas will be included based on the results presented herein.

Introduction

The scanning electron microscope provides great facility for viewing the surfaces of conductive materials and has provided many important contributions to our understanding of their nature. Using this instrument to view the surface of a cyclically loaded specimen in a "real-time" mode enhances our knowledge of a materials response to this stimulus. The level of observation is typically several grain diameters as the crack propagates through the unique pseudo-continua of each specimen. This particular point is brought forward to obviate discussion of the usefulness of macroscopic continuum descriptors (e.g., stress, stress intensity, etc.) in characterizing events at the microstructural level, where discontinuous, inhomogeneous, and anisotropic elements are inherently present in some statistically varying format. A description of material response must be predicated on some observed event(s), whether it be the result of extended surveillance of the active process(es) that are not inherently measurable or by analysis of numerical data of some type (given that it is physically consistent with the details to be portrayed). The approach taken in this investigation is the former: attempting to document the surface response of a material's microstructure as a fatigue crack progresses through it. This then leads to a conceptual view of material's behavior that is essentially nonnumeric in nature yet is just as valid as an arithmetic statement of a "response." The key word above is nature – an understanding of the natural philosophy of materials without immediate recourse to a representation of "numbers."

Experimental Technique

The apparatus used is described in other places in further detail [1] and consists of a load frame of 1.8kN capacity, a portion of which is inserted into the viewing chamber of a SEM. This servohydraulically controlled device has the capability of applying alternating loads of positive R ratio to maximum capability at typically employed frequencies in the range of 0.1–30 Hz. A view of this equipment is seen in Fig. 1 for ease of reference. Specimen geometries of varying types have been employed, but current experiments have been employing a sample shape as shown in Fig. 2. The reduced section (noted as A-A in the figure) is rectangular in cross section, having the nominal dimensions 1-mm × 4-mm. The test article is prepared using standard mechanical polishing techniques on one of the broad surfaces of the gage length and notched using a jeweller's saw at approximately midlength to

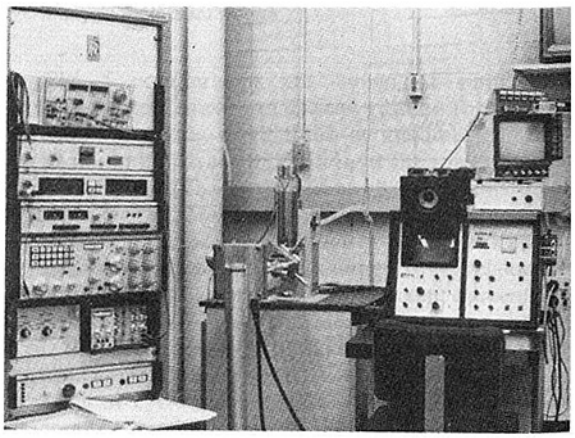

Fig. 1 SEM – load frame experimental apparatus including control equipment

Contributed by the Gas Turbine Division of THE AMERICAN SOCIETY OF MECHANICAL ENGINEERS and presented at the 29th International Gas Turbine Conference and Exhibit, Amsterdam, The Netherlands, June 4–7, 1984. Manuscript received at ASME Headquarters January 18, 1984. Paper No. 84-GT-205.

minimize the area initially requiring observation for the detection of a cracklike discontinuity. Etching is performed using appropriate reagents to delineate extant microstructural features and to allow the effect of those features on crack propagation to be observed.

The material employed in this investigation is RR58 (AA2618). It was developed originally in the 1940s as a high-temperature aluminum alloy for sheet and forging applications [2, 3]; it is a precipitation hardenable material with the evolved nominal composition 2.2 Cu-1.5 Mg-1 Fe-1 Ni-0.18 Si-0.07Ti. The complexity of the alloying generates increased microstructural stability and uniformity of precipitation from the intermetallics $FeNiAl_9$ and Al_2CuMg (S phase) for improved high-temperature properties (creep). As with all aluminum alloys, this material also contains a great number of included objects of varying composition, which the industry euphemistically refers to as constituent particles. Finish polishing was conducted using a MgO paste (MgO with distilled water), following a six micron diamond rough polishing operation. This produced a reasonable surface quality that was then etched to reveal discernable microstructural elements. The features thus revealed were predominantly grain and subgrain boundaries as well as providing some relief to the constituent particles and etching some of them out as the matrix around them was dissolved. This essentially describes the bulk of the features to be seen in the photomicrographs. The material was obtained from a section of the centrifugal impeller from a Dart aero-engine. No specific orientations of the test articles with respect to the component were requested or maintained. They were deemed unnecessary considering the nature of this journey into the world of conceptual mechanics of materials.

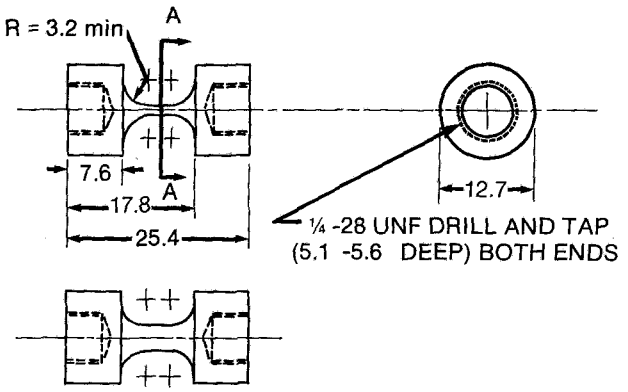

Fig. 2 Typical test coupon geometry. Usually tested after notching at the gage length center with a jeweller's saw. (Note: most dimensions in millimeters.)

Experimental "Results"

This section is devoted to the presentation of photomicrographs obtained during the testing of two notched samples, both were tested using a maximum net section stress of 200 MPa with a R ratio of 0.5. The pictures were obtained using the secondary electron image presented on the high

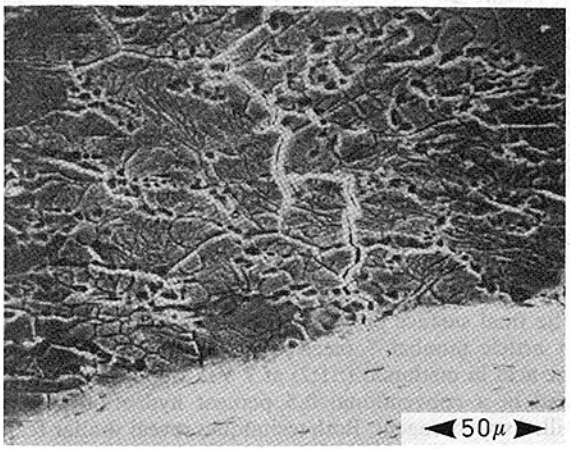

Fig. 3 Specimen RR58 number 7 at 185,000 cycles. Note grain boundaries, subgrains, etched out particles and crack.

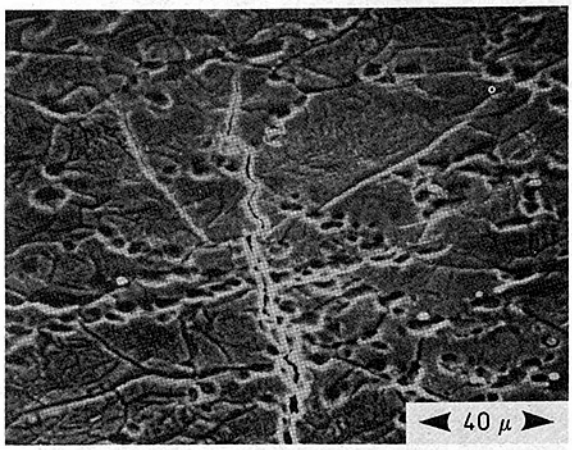

Fig. 4 Crack tip region at 230,000 cycles in RR58 number 7. Separate branching cracks are evident.

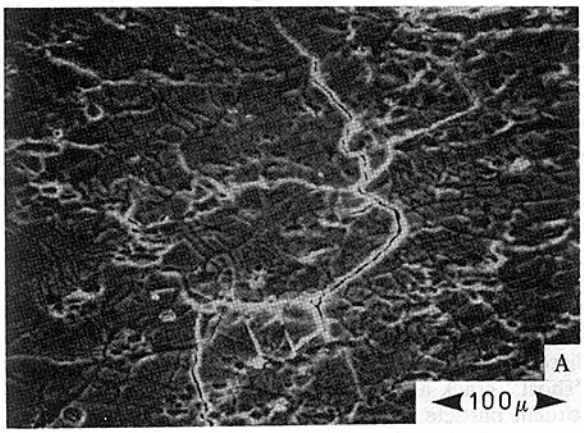

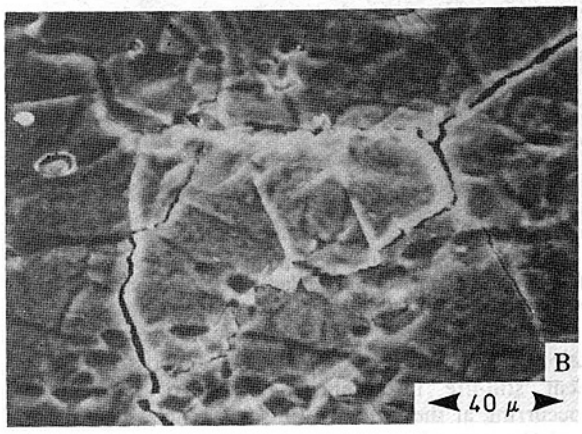

Fig. 5 Now at 320,000 cycles RR58 number 7 shows multiple cracks in (*a*) and mixed cracking at the marked direction change in (*b*)

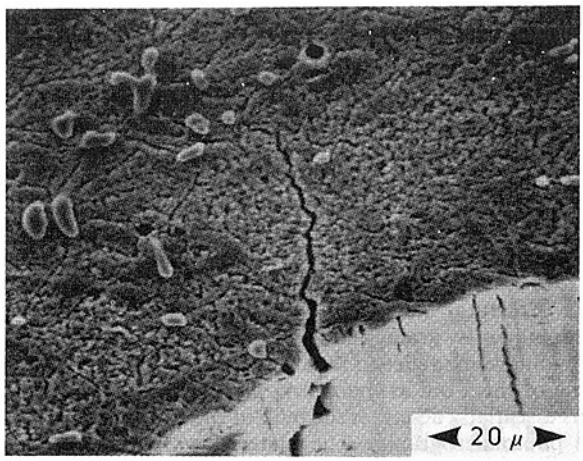

Fig. 6 "Early" crack region at 20,000 cycles for RR58 number 9. The change in etchant provides a different appearance of the microstructure.

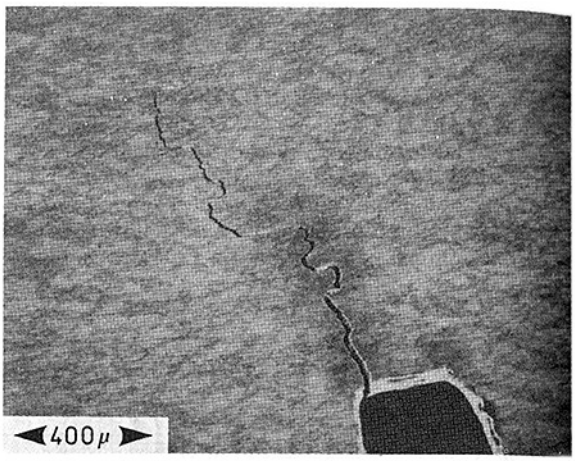

Fig. 9 A "macro" view at 700,000 cycles of RR58 number 9. Directional changes and fretting debris again obvious.

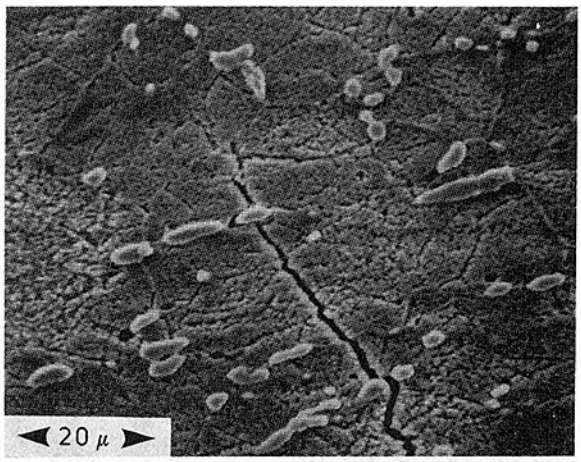

Fig. 7 At 200,000 cycles the crack tip region shows particle matrix separation at the discontinuity in RR58 number 9

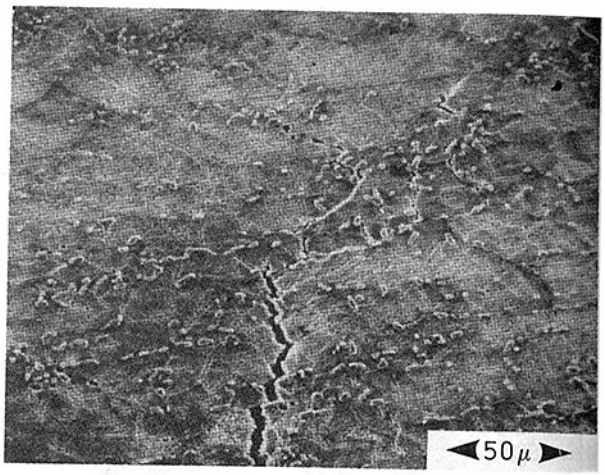

Fig. 10 Diffuse and unlinked cracks/fissures appear at 707,350 cycles in article number 9 of RR58. Note the apparent influence of inclusion fields in some areas.

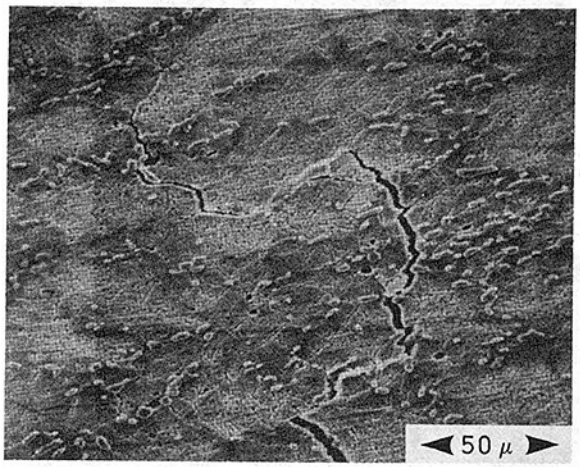

Fig. 8 Changes in crack path direction are evident in coupon number 9 of RR58 at 600,000 cycles. Note the fretting debris at microstructural interference points along the crack.

resolution CRT of the ISI Alpha 9 microscope. They represent "still-life" instantaneous portraits of the events that were occurring at the time. Testing frequencies varied from 0.2 to 33 Hz, depending on whether real-time viewing, "run-up" cycles, or strictly visual monitoring was being performed.

The final surface preparation of each sample is different. Test article number 7 received an electrolytic treatment of nitric acid in methonal (::1:2) at 7 V. Coupon number 9 was etched in a conventional 0.5 percent hydrofluoric acid in distilled water reagent. Both techniques reveal similar features but are obviously quite different in appearance.

Figure 3 presents a relatively early view of specimen number seven. Grains and subgrains are easily seen, along with the crack that has propagated several grain diameters into the material at this point. Using this preparation, the constituent particles have "etched out" and, by and large, only pits remain to show their original locations. The remaining photographs (Figs. 4 and 5) display other regions at various other times during testing (total specimen life 481748 cycles). These reflect a tendency toward intergranular/interboundary propagation, although some areas of transgranular propagation are evident. Note that branching and occasional radical direction changes are present.

The change in etchant effected a marked alteration in the appearance of RR58 article number 9 (Figs. 6–10). As an example instance, the constituent particles are present and stand out on the surface: the grain boundaries also are easily discerned. Again the first photomicrograph (Fig. 6) shows a "short" crack as it propagates from the notch root. A constituent particle adhering to one side of the open crack, but pulled out from the other, is shown in Fig. 7. Changes in crack direction are obvious in Fig. 8 and the emergence of

fretting debris from interfering crack faces should also be noted. This also is reflected in Fig. 9, which shows a more "macroscopic" view toward the end of life (716720 cycles to failure by separation). In the last micrograph, diffuse cracking can be observed both in terms of branching and discontinuities that appear to lead the traceably contiguous crack.

Observations

Of primary importance here is the concept that microstructure does control what is happening at a local level and thus must have the potential for effecting changes in macroscopic property responses (although these influences may not be detectable). Granted that these are inherently visual arguments, they carry the weight of observation (with some interpretation) for enhancing our view of materials response to cyclic loading.

These experiments have shown several distinct points to support these ideas. They can be essentially summarized as:

1 Microstructural features are crack-path and rate-controlling, but no consistent discernable patterns have emerged.
2 Irregular crack paths are observed with interboundary propagation seeming dominant.
3 Crack branching and diffuse cracking may occur generating multiple operational singularities within a region.

These observations stimulate reflection on the basic assumptions present in most of the crack modelling techniques typically employed in fracture or life prediction methodologies. The presence of diffuse cracking or crack branching is not represented by a singular crack tip. All specimens tested have shown deviations from crack linearity (i.e., propagation not perpendicular to the loading axis), which implies something other than the macroscopic Mode I response characteristics may be controlling. These two points are used only as examples and not to disparage a technology which has proven so useful. Nonetheless, the authors encourage that assumptions be explicitly acknowledged and demonstrated to be consistent with the response of the material involved and its analytical representation. Of particular concern in this regard is the relative scale of analysis. "At what point do continuum models break down?" is the question to be answered!

A Further Note

As mentioned in the abstract, dynamic videorecordings are employed as a means of documentation for the events that are observed. While not having the resolution of the "still" photomicrographs, the real-time video tapes offer the best means for establishing the conceptual link to material response in that they portray directly the evolution of events. Much remains to be improved upon in the technique, and tape editing would markedly enhance its already powerful effect. It is indeed unfortunate that this written record cannot more adequately reflect the phenomena observed. Given this limitation, however, the reader is encouraged to think of the possibilities that might be encountered as a crack propagates through a spatially and time-varying microstructure. Obviously a great challenge awaits.

Acknowledgments

The authors would like to thank the Rolls-Royce Aeroengine Division, Derby, England for their continued support and stimulation. The University of Toronto also has been instrumental in aiding the effort as well as the Natural Sciences and Engineering Research Council of Canada. A special acknowledgment is given Janet Lambert for her usual help in typing the manuscript and Fraser Smith for his consistent assistance in proofreading and other duties.

References

1 Cameron, D. W., and Hoeppner, D. W., "A Servohydraulic Controlled Load Frame for SEM Fatigue Studies," *International Journal of Fatigue*, Vol. 5, No. 4, Oct. 1983, pp. 225–229. Butterworth Scientific, Ltd., Journals Division, Guildford, U.K.

2 Polmear, I. J., *Light Alloys, Metallurgy of the Light Metals*, 1st ed., Ch. 3, Edward Arnold and American Society for Metals, U.S.A., 1982, pp. 80, 81.

3 Taylor, T. A., "Recent Developments in Materials for Gas Turbines," *Proceedings of the Institution of Mechanical Engineers*, London, Vol. 153, 1946, pp. 505–512.

Journal of Engineering for Gas Turbines and Power

Discussion

Effect of New Blade Cooling System With Minimized Gas Temperature Dilution on Gas Turbine Performance[1]

I. G. Rice.[2] The authors are to be commended on their paper, which links blade cooling methods with combined-cycle efficiency. The industrial gas turbine industry should continue to reexamine old as well as new cooling methods in light of overall combined-cycle efficiency. The industry should also keep abreast with the new emerging manufacturing techniques such as (*i*) casting both nozzle vanes and rotating blades in two halves and fusion-bonding the two halves together (NASA E^3 engine program), (*ii*) fabricating the blading with a thin outer shell bonded to ribs of an inner, strong casted core providing cooling flow channels (Westinghouse/EPRI program) (*iii*) applying thermal barrier ceramic coating to the pressure side of the vanes and blades as currently being done by Rolls-Royce on their RB-211-535 E4 engines, and (*iv*) the more recent method of rapid solidification by plasma deposition (RSPD), a low-pressure spray method to form finished thin-walled superalloy laminate parts being developed by General Electric. New manufacturing techniques on the horizon, when fully perfected and made cost effective, will make it possible to further reevaluate blade cooling for industrial gas turbines and combined cycles.

The authors define gas turbine firing temperature early in the paper as "combustor exit average gas temperature" which cyclewise favors internal convection cooling of the nozzle vanes with (*a*) cooling air, (*b*) humidified precooled air, (*c*) steam, or (*d*) water. The results and conclusions of their study depend to a great extent on the definition of firing temperature as related to turbine inlet temperature.

There are two other definitions of firing temperature appearing in the literature where considerable coolant, either air or steam, is used first for internal convection/impingement cooling followed by external film cooling. The discharge of the coolant to the main gas stream creates a different situation requiring special considerations. A second definition of turbine inlet temperature therefore evolved, which can be stated as the average total temperature of the mixture of the combustion gas and the nozzle vane coolant where total temperature is the theoretical impact temperature of the gas and coolant fully mixed before expansion. The third definition is referred to as "turbine rotor inlet temperature," which is the average total temperature of the combustion gas and the nozzle vane coolant mixture with respect to the rotating blades and which takes into consideration the fact that the blades are running away from the gas stream, so to speak, with a blade velocity about 50 to 60 percent of that of the gas stream. The impact temperature the blades realize is thus lower than the full total impact temperature relative to the nozzle vane. To compensate for the nozzle exit mixture temperature a term, "overfiring" has been used for the combustor which can increase incrementally upwards of some 200°F (111°C), as confirmed by Fig. 11 of the authors' paper.

The third definition seems to be more appropriate for nozzle vane film cooling and is often used by aircraft engine engineers. This definition, however, denotes that complete mixing of the coolant with the combustion gas takes place as both pass through the nozzle vane channels. Equation (10) of the authors' paper would be applicable in this case, but since only partial mixing actually takes place, particularly for trailing edge cooling, the nozzle vane wake is at a noticeably lower temperature than the core flowing through the central part of the vane channels. This wake flows crosswise to the rotating blade channels where more complete mixing takes place as the mixture imparts its energy as it passes through these blade channels. Therefore, this discusser questions the use of equation (10) in relation to velocity energy conversion by rotating blades and downstream reaction if present.

The authors' use of equation (9) in their paper assumes α to be the typical 180 deg impact point exit and the 30 deg downstream exit to the gas stream, respectively, of the film cooling nose showerhead weep holes and the downstream body weep holes. Impingement cooling is generally used in conjunction with weep hole film cooling wherein the static pressure is dissipated by impingement and the heated coolant is then allowed to "weep" to form a film. Appreciable potential expansion velocity energy is lost in the process. If the exit velocity of the coolant through the little round holes is too great, the coolant will blow right through the boundary layer causing turbulence, and there will be no protective heat barrier film created. Here lies a dilemma for present-day film cooling.

The validity and acceptance of either definition two or three as appropriate can be related to the combustor itself wherein there is always primary, secondary, and tertiary air used in the process of raising, sculpturing, and tempering the near stoichiometric flame. The nozzle vane nose (leading edge) coolant rejection at a place where the velocity is still low (about Mach .1) and the static pressure is high can be considered as merely quadrivial cooling air – air used to film cool the vane leading edges which is no different in principle than tertiary cooling air used to film cool the combustor liner.

There is another film cooling method not presently used for blading. This method is being used for wings of airplanes and is known as the process of full coverage tangential "blowing." Although it might possibly be used for air coolant it can be readily applied very effectively with steam where a higher pressure as needed is available than that of the fixed compressor discharge. Slot exit velocities equal to or greater than the main stream velocity at lines of entry can be achieved

[1] By K. Kawaike, N. Kobayashi, and T. Ikeguchi, published in the October 1984 issue of the ASME JOURNAL OF ENGINEERING FOR GAS TURBINES AND POWER, Vol. 106, No. 4, pp. 756–764.

[2] Consultant, Spring, Texas, Fellow, ASME.

to conserve velocity energy and help stabilize the boundary layers. The new manufacturing techniques will make this approach of slot "blowing" a viable contender. However, today's state-of-the-art manufacturing techniques can be used for steam cooling with only minor modifications without using full slot blowing. Regarding steam blade cooling, references [1–7] are given.

The first stage nozzle exit velocity for a given exit Mach number depends upon the inlet pressure and inlet temperature. The same is true with respect to the coolant's inlet temperature and pressure at its entrance to the main gas stream. The gas follows a near constant entropy expansion. The nose cooling air or steam has much more driving force than trailing edge coolant flow. The core flow between adjacent vanes has more enthalpy drop and thus exists at a higher velocity. The authors do not consider variations in exit velocity or distinguish between nose and trailing edge coolant.

Considering steam as the coolant, pumping loss calculated by equation (12) can be reduced because considerably less coolant steam is required to cool the rotating blades than that required by the already heated cooling air in the proposed arrangement of the authors. Further, disk and seal frictional drag factors can be reduced by using steam due to steam's lower viscosity.

There is another factor that affects expansion velocity and nozzle vane design and that factor is the circumferential temperature profile encountered. A multiple "can" type combustor (assumed to be the type applied by the authors with reference to Fig. 1) has high temperature spikes down the center of each can. The annular circumferential exit profile must be considered as well as radial profile. Oftentimes where "can" type combustors are used the nozzle vanes that are subjected to the temperature spikes will burn or develop trailing edge warp whereas the other vanes on either side exposed to the lower temperature will not so deteriorate. Therefore experience indicates that the nozzle vane cooling design must be based on the temperature spike and not the average circumferential temperature. The annular combustor with a greater number of fuel nozzles and no radial wall restrictions has a far superior circumferential temperature profile as is well known. A discussion of vane and blade cooling should include the combustor system employed.

In closing, this discusser does not believe there is any appreciable gain, if any gain at all, in combined-cycle efficiency when considering the second or third definition of firing temperature and the application of formulas (9) and (10). Also it is not known or proven that nozzle vanes can operate at 1400°C combustor outlet temperature by applying internal convection/impingement air cooling only without relying on external film cooling. Further, it is not known if pure steam, indeed a far superior coolant to air, can provide adequate nozzle vane cooling using internal convection/impingement cooling only without the benefit of external film cooling for combustor outlet temperatures above 1200°C. The authors might like to comment on any rig tests that have been run and the data obtained in support of their conclusions.

This discusser does compliment the authors on taking a step forward toward reevaluating blade cooling with respect to combined-cycle efficiency and suggests that a similar evaluation be made for steam cooling to include both the simple cycle and reheat cycle gas turbines.

References

1 Rice, I. G., "Steam-Cooled Blading in a Combined Reheat Gas Turbine/Reheat Steam Turbine Cycle: Part I, Performance Evaluation," ASME Paper No. 79-JPGC-GT-2.

2 Rice, I. G., "Steam-Cooled Blading in a Combined Reheat Gas Turbine/Reheat Steam Turbine Cycle: Part II, Design Considerations," ASME Paper No. 79-JPGC-GT-3.

3 Rice, I. G., "The Reheat Gas Turbine With Steam-Blade Cooling—A Means of Increasing Reheat Pressure, Output and Combined Cycle Efficiency," ASME JOURNAL OF ENGINEERING FOR POWER, Vol. 104, Jan. 1982.

4 Rice, I. G., and Jenkins, P., "Comparison of the HTTT Reheat Gas Turbine Combined Cycle With the HTTT Nonreheat Gas Turbine Combined Cycle," ASME JOURNAL OF ENGINEERING FOR POWER, Vol. 104, Jan. 1982.

5 Rice, I. G., "The Integrated Gas/Steam Nozzle With Steam Cooling: Part I, Application," ASME Paper No. 84-GT-134.

6 Rice, I. G., "The Integrated Gas/Steam Nozzle With Steam Cooling: Part II, Design Considerations," ASME Paper No. 84-GT-135.

7 Wu, C. S., and Louis, J. F., "A Comparative Study of the Influence of Different Means of Cooling on the Performance of a Combined (Gas and Steam Turbines) Cycle," ASME JOURNAL OF ENGINEERING FOR GAS TURBINES AND POWER, Vol. 106, No. 4, pp. 750–755.

A Comparative Study of the Influence of Different Means of Cooling on the Performance of a Combined (Gas and Steam Turbine) Cycle[1]

I. G. Rice.[2] The authors are to be commended on their paper for presenting steam as a viable short-term alternative to (*a*) water-blade cooling and (*b*) advanced air-blade cooling. The influence of the coolant on combined-cycle efficiency must be taken into consideration. This discusser is in general agreement with the four conclusions given at the close of the paper but not fully in agreement with the specific-optimum-cycle pressure ratios or turbine inlet temperatures derived from the computer model used. This discusser is also in general agreement with the figures presented, including Fig. 16; but in veiw of the reheat gas turbine specifically designed for combined-cycle operation and presently being tested in Japan [1], the paper should have included the reheat gas turbine.

Steam as both a blade coolant and a dual or binary working fluid is receiving limited, but overdue, and deserving attention at the present time. Recent tests by Allison Division of General Motors has added impetus to applying steam as both a working fluid and ultimately as a blade coolant [2, 3]. Previous work reported by this discusser [4] gives credit to Bruce Buckland for his efforts to use steam cooling in a closed cycle. Also this discusser's previous ASME papers [5–9], present analyses of using steam for convection cooling followed by film blanket cooling. Reference is also made to the fact that General Electric listed steam cooling as its second choice for blade cooling for its completed DOE/EPRI water blade-cooling research program [10]. Water blade cooling is recognized as a long-range goal, but it is very difficult to achieve; whereas steam, as the authors indicate, can be accomplished in the short-term using only modifications to the state-of-the-art hardware and established manufacturing techniques.

This discusser herewith presents two graphs, Figs. 1 and 2, of [5] and [6]. These graphs were produced by using a method of stream separation and by following steam as a working fluid and coolant through both the simple and reheat (gas and steam) cycles and heat recovery boiler. Appropriate expansion losses were included. Reference is made to Fig. 1 where steam cycle efficiency is plotted against cycle pressure ratio (CPR) for various inlet steam temperatures. It can be seen that steam

[1] By Chuan shao Wu and J. F. Louis, published in the October 1984 issue of the ASME JOURNAL OF ENGINEERING FOR GAS TURBINES AND POWER, Vol. 106, No. 4, pp. 750-755

[2] Consultant, Spring, Texas, Fellow ASME

to conserve velocity energy and help stabilize the boundary layers. The new manufacturing techniques will make this approach of slot "blowing" a viable contender. However, today's state-of-the-art manufacturing techniques can be used for steam cooling with only minor modifications without using full slot blowing. Regarding steam blade cooling, references [1–7] are given.

The first stage nozzle exit velocity for a given exit Mach number depends upon the inlet pressure and inlet temperature. The same is true with respect to the coolant's inlet temperature and pressure at its entrance to the main gas stream. The gas follows a near constant entropy expansion. The nose cooling air or steam has much more driving force than trailing edge coolant flow. The core flow between adjacent vanes has more enthalpy drop and thus exists at a higher velocity. The authors do not consider variations in exit velocity or distinguish between nose and trailing edge coolant.

Considering steam as the coolant, pumping loss calculated by equation (12) can be reduced because considerably less coolant steam is required to cool the rotating blades than that required by the already heated cooling air in the proposed arrangement of the authors. Further, disk and seal frictional drag factors can be reduced by using steam due to steam's lower viscosity.

There is another factor that affects expansion velocity and nozzle vane design and that factor is the circumferential temperature profile encountered. A multiple "can" type combustor (assumed to be the type applied by the authors with reference to Fig. 1) has high temperature spikes down the center of each can. The annular circumferential exit profile must be considered as well as radial profile. Oftentimes where "can" type combustors are used the nozzle vanes that are subjected to the temperature spikes will burn or develop trailing edge warp whereas the other vanes on either side exposed to the lower temperature will not so deteriorate. Therefore experience indicates that the nozzle vane cooling design must be based on the temperature spike and not the average circumferential temperature. The annular combustor with a greater number of fuel nozzles and no radial wall restrictions has a far superior circumferential temperature profile as is well known. A discussion of vane and blade cooling should include the combustor system employed.

In closing, this discusser does not believe there is any appreciable gain, if any gain at all, in combined-cycle efficiency when considering the second or third definition of firing temperature and the application of formulas (9) and (10). Also it is not known or proven that nozzle vanes can operate at 1400°C combustor outlet temperature by applying internal convection/impingement air cooling only without relying on external film cooling. Further, it is not known if pure steam, indeed a far superior coolant to air, can provide adequate nozzle vane cooling using internal convection/impingement cooling only without the benefit of external film cooling for combustor outlet temperatures above 1200°C. The authors might like to comment on any rig tests that have been run and the data obtained in support of their conclusions.

This discusser does compliment the authors on taking a step forward toward reevaluating blade cooling with respect to combined-cycle efficiency and suggests that a similar evaluation be made for steam cooling to include both the simple cycle and reheat cycle gas turbines.

References

1 Rice, I. G., "Steam-Cooled Blading in a Combined Reheat Gas Turbine/Reheat Steam Turbine Cycle: Part I, Performance Evaluation," ASME Paper No. 79-JPGC-GT-2.

2 Rice, I. G., "Steam-Cooled Blading in a Combined Reheat Gas Turbine/Reheat Steam Turbine Cycle: Part II, Design Considerations," ASME Paper No. 79-JPGC-GT-3.

3 Rice, I. G., "The Reheat Gas Turbine With Steam-Blade Cooling—A Means of Increasing Reheat Pressure, Output and Combined Cycle Efficiency," ASME JOURNAL OF ENGINEERING FOR POWER, Vol. 104, Jan. 1982.

4 Rice, I. G., and Jenkins, P., "Comparison of the HTTT Reheat Gas Turbine Combined Cycle With the HTTT Nonreheat Gas Turbine Combined Cycle," ASME JOURNAL OF ENGINEERING FOR POWER, Vol. 104, Jan. 1982.

5 Rice, I. G., "The Integrated Gas/Steam Nozzle With Steam Cooling: Part I, Application," ASME Paper No. 84-GT-134.

6 Rice, I. G., "The Integrated Gas/Steam Nozzle With Steam Cooling: Part II, Design Considerations," ASME Paper No. 84-GT-135.

7 Wu, C. S., and Louis, J. F., "A Comparative Study of the Influence of Different Means of Cooling on the Performance of a Combined (Gas and Steam Turbines) Cycle," ASME JOURNAL OF ENGINEERING FOR GAS TURBINES AND POWER, Vol. 106, No. 4, pp. 750–755.

A Comparative Study of the Influence of Different Means of Cooling on the Performance of a Combined (Gas and Steam Turbine) Cycle[1]

I. G. Rice.[2] The authors are to be commended on their paper for presenting steam as a viable short-term alternative to (*a*) water-blade cooling and (*b*) advanced air-blade cooling. The influence of the coolant on combined-cycle efficiency must be taken into consideration. This discusser is in general agreement with the four conclusions given at the close of the paper but not fully in agreement with the specific-optimum-cycle pressure ratios or turbine inlet temperatures derived from the computer model used. This discusser is also in general agreement with the figures presented, including Fig. 16; but in veiw of the reheat gas turbine specifically designed for combined-cycle operation and presently being tested in Japan [1], the paper should have included the reheat gas turbine.

Steam as both a blade coolant and a dual or binary working fluid is receiving limited, but overdue, and deserving attention at the present time. Recent tests by Allison Division of General Motors has added impetus to applying steam as both a working fluid and ultimately as a blade coolant [2, 3]. Previous work reported by this discusser [4] gives credit to Bruce Buckland for his efforts to use steam cooling in a closed cycle. Also this discusser's previous ASME papers [5–9], present analyses of using steam for convection cooling followed by film blanket cooling. Reference is also made to the fact that General Electric listed steam cooling as its second choice for blade cooling for its completed DOE/EPRI water blade-cooling research program [10]. Water blade cooling is recognized as a long-range goal, but it is very difficult to achieve; whereas steam, as the authors indicate, can be accomplished in the short-term using only modifications to the state-of-the-art hardware and established manufacturing techniques.

This discusser herewith presents two graphs, Figs. 1 and 2, of [5] and [6]. These graphs were produced by using a method of stream separation and by following steam as a working fluid and coolant through both the simple and reheat (gas and steam) cycles and heat recovery boiler. Appropriate expansion losses were included. Reference is made to Fig. 1 where steam cycle efficiency is plotted against cycle pressure ratio (CPR) for various inlet steam temperatures. It can be seen that steam

[1] By Chuan shao Wu and J. F. Louis, published in the October 1984 issue of the ASME JOURNAL OF ENGINEERING FOR GAS TURBINES AND POWER, Vol. 106, No. 4, pp. 750-755

[2] Consultant, Spring, Texas, Fellow ASME

cycle efficiency for the simple cycle exceeds the condensing steam turbine cycle efficiency by a considerable margin for a steam inlet temperature above 2000°F (1093°C) but starts to level off at a CPR of 18.

The real payoff of steam blade cooling is realized for the reheat gas turbine at CPRs of 38 and above as can be noted in Fig. 1. The full reheat of the total coolant steam mass flow used in the high-pressure gas generator gives an added boost in cycle efficiency as can be observed. Therefore, steam, even though a superior blade coolant for the simple cycle, is even a better cooling/working fluid for the reheat cycle.

Figure 1 also indicates that the quantity of steam blade cooling/injection is only limited by the vitiation effect on combustion and the quantity of water makeup required for both the simple and reheat gas turbine cycles, because the cooling/injection steam cycle efficiency is higher than the condensing steam cycle efficiency of 40.43 percent shown. It follows that it would be better to inject the steam into the gas turbine than to condense it after its full expansion to the condenser. It is important just how the coolant steam is injected from the blades to the gas stream and at what velocity.

Figure 2 shows the appreciable amount of extra work per pound of steam obtained by the blade coolant/injectant steam. The extra work of the cooling air not used but allowed to be heated and expanded, although not shown, is also appreciable. The amount of work per pound of steam for the reheat gas turbine, as can be noted, can be some 30 to 40 percent greater than that obtained by the condensing steam turbine.

The superior heat transfer qualities of saturated, but dry and separated, steam have long been known to the boiler manufacturers for designing superheater tubes operating at some 3000 psi (20.69 MPa) internal pressures with outside gas stream temperatures of some 2500°F (1371°C). Babcock and Wilcox [11] provides design data that can be used to calculate both steam convection temperature rise inside the blading and pressure drop. Reference is made to the following formula (1) of [11] where U_s is the steam film conductance, G is the area mass flow, C_p is the specific heat and μ is the absolute viscosity. This general formula also appeared in this discusser's coauthored paper [9].

$$U_s = \frac{0.0266}{(d/12)^{0.20}} \times G^{0.80} \times C_p \times \mu^{0.20} \tag{1}$$

Figure 3 is a plot taken from [11] showing 1/16-in.-dia channels and is for unity of the factor $C_p\mu^{0.20}$. This graph should be used in conjunction with Fig. 4, also taken from [11], which is a plot of the factor $C_p\mu^{0.20}$ versus steam temperature.

It can be noted that the value of $C_p\mu^{0.20}$ for 200 psi (1.38 MPa) saturated steam, point A of Fig. 4, is much lower than for 600 psi saturated-steam, point C. Considering a simple-cycle gas turbine operating at 100–200 psi (.689–1.38 MPa) pressure, it appears that the steam should be used for internal convection and impingement cooling to point B at about 800°F (427°C) and then expanded for outside film cooling. When considering the reheat gas turbine gas generator, the steam at a higher 600 psi (4.137 MPa) can be optimized for internal cooling to about 950°F (510°C), point D, before being expanded and discharged for film cooling. Steam at the higher pressure (C–D) has a much higher film conductance factor, as seen, and favors the reheat gas turbine.

Regarding steam pressure drop inside blade-cooling channels, the Darcy/Fanning formula can be applied. One such variation of this formula is given in [11] and presented below as formula (3), where

$$\mathrm{Re} = \frac{dG}{12\mu} \tag{2}$$

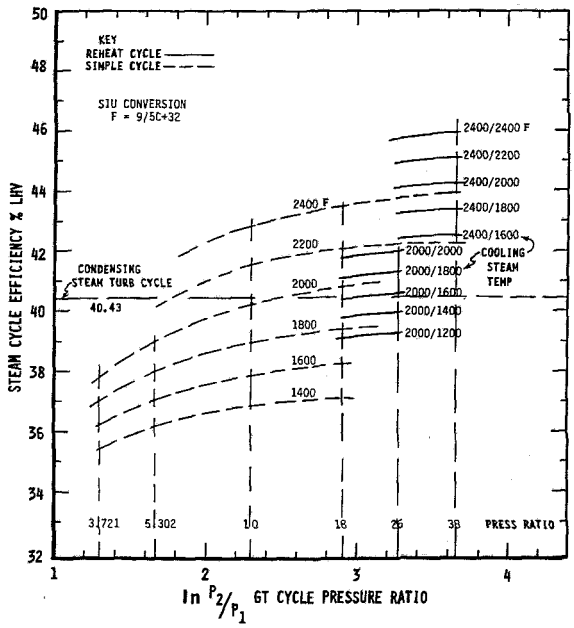

Fig. 1 Steam cycle efficiency versus gas turbine pressure ratio [5, 6]

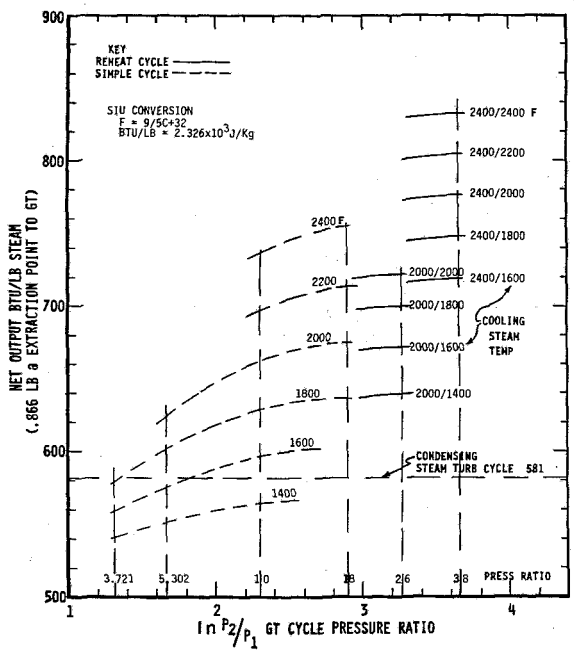

Fig. 2 Steam specific work versus gas turbine pressure ratio [5, 6]

Re = Reynolds number

d = equivalent diameter, in.

Inside tubes:

d = internal diameter, in.

In general:

$$d = 4 \times \frac{\text{area of channel, sq in.}}{\text{wetted perimeter, in.}}$$

$G = W/A$ = mass flow, lb/sq ft, hr

μ = absolute viscosity, lb(mass)/ft,hr

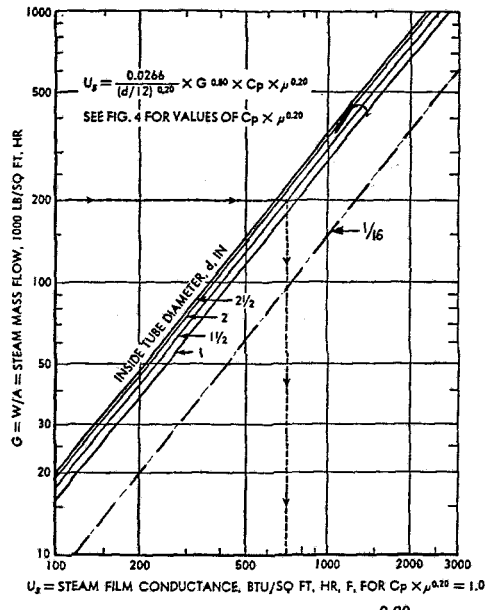

Fig. 3 Steam film conductance for unity $C_{p\mu}{}^{0.20}$ factor [11]

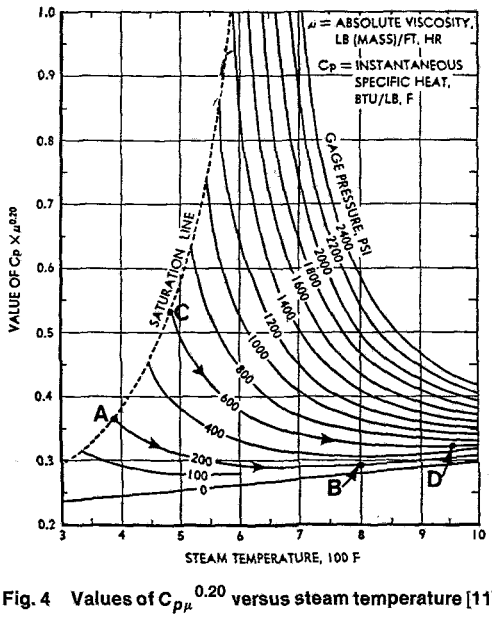

Fig. 4 Values of $C_{p\mu}{}^{0.20}$ versus steam temperature [11]

$$\Delta P = \frac{fL}{d} V \left(\frac{G}{100{,}000}\right)^2 \tag{3}$$

ΔP = pressure drop due to friction, lb/sq in.

f = friction factor

L = developed length of flow path including all bends and fittings in position, ft

V = specific volume, cu ft/lb

Friction factor f for small channels can run rather high (about .04 to .045) for the high Reynolds numbers encountered.

Applying Figs. 3 and 4 and formulas (1-3) will give reasonable steam temperature rises corresponding to points B and D of Fig. 4 and pressure drops of 20 to 30 psi (138 to 207 KPa) for nozzle vane and sidewall cooling and rotating blade and platform cooling.

Tables 1 and 2 of the authors' paper were not included with the original printing and therefore this discusser cannot comment on the parameters and design considerations used by the authors. However, it has been the discusser's approach to use actual and accurate computer-generated performance data on existing turbines such as the LM2500 and LM5000 and extrapolate to higher inlet temperatures and cycle pressures. These data yield higher optimum CPRs for the simple-cycle gas turbine combined cycle which peaks at about 18 for a 2000°F (1093°C) turbine inlet temperature.

The authors' paper did not discuss or define turbine inlet temperature (TIT). Where considerable coolant is used for cooling, particularly for the nozzle vane leading edge, there can be variations up to 200°F (111°C). Three different definitions of TIT have been used in the technical literature: (*i*) average combustor gas outlet temperature, (*ii*) average nozzle total inlet temperature of the mixture of the combustion gas and the nozzle coolant, and (*iii*) average turbine rotor inlet temperature of the mixture of the combustion gas and the nozzle coolant relative to the rotating blade, where the rotating velocity can be some 50 to 60 percent of that of the nozzle exit velocity and where there is a noticeable reduction in relative impact temperature. Here lies an appreciable difference between water cooling (closed-nozzle cooling) and either air or steam film cooling and leads to the term "overfiring" to compensate for heating the nozzle film coolant air or steam. The authors might like to comment on turbine inlet temperature, its definition, and its effects on combined-cycle efficiency.

The question of steam solid deposits and channel plugging has been raised to this discusser in the past. It is important to note that the cooling steam must be dry and free of carryover. Steam extracted from a steam turbine would be of this quality. Further, as the steam is heated any soluble impurities present as vapor will move away from condensing and plating out. In the case of the steam turbines, the steam becomes cool – particularly in the latter stages – and deposition does take place.

Steam cooling does require high-quality water makeup. This water, as condensate, can be obtained through heat exchange of the feedwater and little, if any, heat loss will occur. On the other hand, there would be a capital cost penalty involved.

Techniques for steam internal convection cooling and film cooling are not discussed by the authors. How the film cooling injection is handled can have an effect on the coolant's expansion efficiency. The authors might want to comment on this aspect as used for their analysis.

There are other gas turbine internal and external components requiring cooling to be considered besides the blading, and (12) and (13) are given in this regard. The authors are asked to comment on such cooling.

This discusser, in closing, again compliments the authors on their paper and encourages more theoretical studies followed by actual rig testing of blade steam cooling.

References

1 Hori, A., and Takeya, K., "Outline of Plan for Advanced Research Gas Turbine," ASME JOURNAL OF ENGINEERING FOR POWER.

2 Messerlie, R. L., and Tischler, A. O., "Dual-Fluid Cycle, Test Results of a Steam Injected Gas Turbine to Increase Power and Thermal Efficiency," IECEC paper, Orlando, Fla., 1983.

3 Messerlie, R. L., and Strother, J. R., "Integration of the Brayton and Rankine Cycle to Maximize Gas Turbine Performance—A Cogeneration Option," ASME Paper No. 84-GT-52.

4 Rice, I. G., "The Reheat Power Turbine with Steam Cooling—A Means of Increasing Reheat Temperature, Exhaust Temperature and Combined-Cycle Efficiency," ASME Paper No. 82-GT-134.

5 Rice, I. G., "Steam-Cooled Blading in a Combined Reheat Gas Turbine/Reheat Steam Turbine Cycle: Part I, Performance Evaluation," ASME Paper No. 79-JPGC-GT-2.

6 Rice, I. G., "Steam-Cooled Blading in a Combined Reheat Gas Turbine/Reheat Steam Turbine Cycle: Part II, Design Considerations," ASME Paper No. 79-JPGC-GT-3.

7 Rice, I. G., "The Reheat Gas Turbine With Steam-Blade Cooling—A

Means of Increasing Reheat Pressure, Output and Combined Cycle Efficiency," ASME JOURNAL OF ENGINEERING FOR POWER, Vol. 104, Jan. 1982, pp. 9–22.

8 Rice, I. G., and Jenkins, P., "Comparison of the HTTT Reheat Gas Turbine Combined Cycle with the HTTT Nonreheat Gas-Turbine Combined Cycle," ASME JOURNAL OF ENGINEERING FOR POWER, Vol. 104, Jan. 1982, pp. 129–142.

9 Jenkins, P. E., and Rice, I. G., "Blading Heat Transfer Considerations in a Reheat Gas Turbine Combine Cycle," ASME Paper No. 81-GT-155.

10 Alff, R. K. et al., "The High Temperature Water Cooled Gas Turbine in Combined Cycle with Integrated Low BTU Gasification," ASME Paper 77-JPGC-GT-7.

11 *Steam, Its' Generation and Use*, The Babcock & Wilcox Company, 1955.

12 Rice, I. G., "Steam-Cooled Gas Turbine Casings, Struts, and Disks in a Reheat Gas Turbine Combined Cycle: Part I, Compressor and Combustor," ASME JOURNAL OF ENGINEERING FOR POWER, Vol. 105, Oct. 1983, p. 844–850.

13 Rice, I. G., "Steam-Cooled Gas Turbine Casings, Struts, and Disks in a Reheat Gas Turbine Combined Cycle: Part II, Gas Generator Turbine and Power Turbine," ASME JOURNAL OF ENGINEERING FOR POWER, Vol. 105, Oct. 1983, pp. 851–858.

Authors' Closure

The authors would like to thank Dr. Ivan Rice for the thoughtful but also extensive comments. In response to his questions, we would like to say:

1 that we recognize the importance of the reheat turbine, we have a fairly extensive study of it and expect to present the results in a different paper; and

2 that we were very careful to make comparable or identical assumptions in the comparison of different types of cooling.

This led us (*a*) to choose the average combustion gas outlet temperature as turbine inlet temperature, because it is independent of the type of coolant being and in vane cooling; also (*b*) the techniques for internal convection and film cooling are taken as identical for steam and air, the practice of air cooling being used.

The authors agree with Dr. Rice that the cooling of other parts than blades, such as disks, shrouds, platforms, become more and more influential with the pressure ratio. They would be quite significant for example in the high-pressure turbine of the reheat gas turbine considered by Dr. Rice.